UNIVERSIDAD
DE GRANADA

Programa de doctorado de Física y Ciencias del Espacio

TESIS DOCTORAL

Climate Variability in the Levant Region

DOCTORANDO

ALA A. M. SALAMEH

DIRECTORAS

Dr. María Jesús Esteban Parra

Dr. Sonia Raquel Gámiz Fortis

Granada 2021

Editor: Universidad de Granada. Tesis Doctorales
Autor: Ala Salameh
ISBN: 978-84-1306-991-3
URI: http://hdl.handle.net/10481/70151

Acknowledgements

The completion of this Ph.D. dissertation would not have been possible without the support and guidance that I have received from many people, whom I appreciate and genuinely thank for their support morally and practically. I would like to thank all the people who enabled this Ph.D. dissertation to become true.

In this regard, I would like to express my deep thanks and gratitude to my supervisors, Dr. María Jesús Esteban Parra and Dr. Sonia Raquel Gámiz Fortis for their continuous support throughout the writing of this dissertation. I am also indebted to Dr. Yolanda Yolanda Castro Díez. Their pieces advice, suggestions, professional assistance, and their continuous motivations and encouragements have really inspired me to complete this work. I am lucky to have them as my supervisors for my Ph.D. thesis and without that support this work would not have seen light.

Many thanks also to Dr. Ahmad Abu Hammad for motivating me and providing the opportunity to work on some secondary NORHED scientific projects during my work to complete my Ph.D. This opportunity has encouraged me to overcome difficulties and to finish my scientific work.

Special thanks are also extended to Dr. Rahaf Al-Rawas, Dr. Farah Sawafta, Dr. Riad Qara Fallah, Dr. Mohammad Bahjat, and Dr. Rami Musa for the assistance in providing some basic data on Syria, Jordan, and Palestine. I also extend my thanks to Dr. Kamal Abdel Fattah, Dr. Basem Al Zubaidi, Dr. Murad Shaheen, Dr. Abdel Haj Ibrahim, Dr. Marwan Ghanem, Dr. Faisal Sabah, and Dr. Khalil Abushamsieh, who always motivated me and lifted my spirits. Special thanks are due to all the people who have taught me one day, who gave me their time, their knowledge, their support and their positive spirit to build a bridge toward successful and fruitful life.

Finally, and most importantly, I would like also to introduce a deep and heartfelt thanks to my mother and father, brothers and sisters for their continuous trust in me and my capabilities, their continuous encouragement and support to follow up my dreams during this challenging period.

ABSTRACT

Climate change is a topic of great interest around the world because it has serious environmental, agricultural, hydrological, and socio-economic consequences. The Levant region, as a part of the East Mediterranean, is considered a region particularly vulnerable to current and future climate change, which also occurs in the context of other developmental stresses, such as water scarcity, fatigue infrastructure, and frequent drought events. Furthermore, political and ethnic conflicts, population growth, and increasing demand for water, food, and energy all exacerbate the implications of climate change. Additionally, there is a lack of cooperation and sharing of climate data among the region's countries, as well as a lack of cooperation in dealing with potential climate changes in the region.

There have been no previous studies or comparisons in the literature assessing changes and variability in maximum (Tmax) and minimum (Tmin) temperatures, diurnal temperature range (DTR), precipitation, extreme temperature and precipitation indices, and drought in the entire Levant region (Syria, Lebanon, Jordan, Palestine, and Israel), using climatic data from ground stations. The majority of climate studies in the Levant are limited to specific areas or countries, primarily over Israel. Most of them measured climate change in terms of mean values, with low spatial and temporal coverage.

Thus, it is essential to study and investigate the climate variability in the Levant region at multiple time and space scales. The thesis aims to uncover and establish the relationships between climate variability and the most important climate indicators such as large-scale circulation patterns, Sea Surface Temperature (SST), and Sea Level Pressure (SLP) indicators in the Mediterranean Sea and North Atlantic Ocean in order to, better understand the causal mechanisms of such climate variability. Besides, it also aims to identify the regions that are most vulnerable to drought, and assess the dry spells that affected this area and the current trends on multiple drought time scales.

This thesis fills a real gap in climatic studies in this critical region of the world. It is the first study of its kind to focus on the climate of the Levant as a whole, using the largest amount of climate data ever collected. It does not focus on a single climate variable, but rather analyzes a number of

them. For the first time, data have been compiled and long, homogeneous and quality-controlled climatic time series have been obtained for temperatures and precipitation, covering as many meteorological stations as possible in the Levant. Finally, this thesis serves as the scientific foundation for any future joint efforts by Levantine countries to combat climate change through a unified scientific strategy.

The following thesis is divided into ten chapters. The first three chapters discuss and present in detail the objectives, geographic and climatic features of the study area, the raw data, data quality control methods, handling missing values, outliers, homogenization of data sets, and methodology applied in this work. Temperature, extreme temperature indices, precipitation, and extreme precipitation indices as well as their relationships with the large-scale circulation patterns are examined at multiple time scales in Chapters 4-7, respectively. Chapter 8 has been devoted to co-variability analysis between the seasonal temperature and precipitation in the Levant and the general patterns of the SST and SLP. In Chapter 9, droughts have been analyzed, studying their characteristics, and its relationship with large-scale circulation patterns, SST and SLP. Each chapter from 4 to 9 consists of three sections, introduction, results, conclusions and discussion. Finally, the main conclusions reached in this thesis are summarized in Chapter 10.

The preliminary records consisted of rainfall data for more than 2000 rain gauges and 89 temperature stations. All data, station by station, were subjected to a rigorous quality control for systematic errors, missing data, and outliers. All stations that did not meet a number of conditions were excluded, the most important of which was the homogeneity and continuity of the data up to the most recent time period. The time periods were determined based on the best spatial coverage (topography, climatic regions) and the highest data quality. The final stations list consisted of 61 stations for temperature covering the period 1987-2017 and 165 stations for precipitation covering the period 1970-2018. Missing data was less than 5% in all cases.

The thesis demonstrated that the Levant region has experienced rapid warming on multiple time scales. With the exception of October, November, December, and January, the Tmax and Tmin showed significant warming trends on the remaining time scales. More than 97% of the stations exhibited increasing trends in both Tmax and Tmin across all time scales, with the highest frequency of significant trends (> 74% of the stations) observed at the annual, spring, February, March, and August time scales. The Tmax increased faster than Tmin in winter, summer, and spring over the Levant from 1987 to 2018. In the autumn, May, and July, however, Tmin warmed faster than Tmax. The DTR for the cold months (December-April) increased, while it decreased for the warm months (May-November), being significant only for August and September. The south Levant-Tmax increased significantly at a higher rate than of the north Levant-Tmax in the annual, spring, summer, and autumn scales. On the contrary, the North Levant-Tmin rose at a higher rate than south Levant-Tmin in the annual, winter, and autumn scales. Jordan had the highest significant increasing Tmax trends for annual, winter, spring, and summer, while Syria had

the highest trend for autumn-Tmax. Furthermore, Syria-Tmin had the highest warming trend in the annual, winter, and autumn, while Palestine and Jordan had the highest warming trends in spring-Tmin and summer-Tmin.

Trends towards drier conditions has also been found in the Levant region, particularly in the spring and March. Except for Jordan in February, no significant increasing trends were detected for the Levant as a whole and for its sub-regions at any time scale. A percent of 55% of stations showed significant decreasing trends in spring, with the highest rates for Syria's easternmost locations, coastal stations, and northern Palestine. The averaged spring time series for the Levant, Palestine/Israel, Jordan, and Syria showed significant decreasing trends. Furthermore, in March, all sub-regions showed significant downward trends, and in April for Syria. The study area showed more spatial variability based on seasonal rainfall than seasonal temperatures, and it can be divided into three homogeneous regions corresponding to central and north Palestine and Jordan (PC-1), coastal and western Syria (PC-2), and eastern Syria and Jordan, and southern Palestine and Jordan (PC-3).

A total of 34 extreme rainfall and temperature indices developed by ETCCDI and ET-SCI (a few of which were modified to fit the study area) were analyzed for Palestine and Israel in the south Levant. Warming and drier conditions are also increasing, according to the results. Extremes related to minimum night-time temperature indices denoted more intense trends at annual and seasonal scales than those related to maximum day-time temperature indices. The most significant increasing trends were detected for summer-TXn, TNn, and TNx, with more than 90% of total stations. For TN90p-spring and TN90p-summer, a percent of 61% and 85% of the stations showed significant increasing trends. The study area had longer periods of extreme dry spells (CDD) and shorter periods of extreme wet spells in the winter, spring, and combined winter-spring (CWD). Spring extreme indices showed negative trends for most of the indices, significantly for R1mm, R20mm, CWD, RX1day, RX3day, RX5day, and SDII indices.

Drought has become more frequent and extended, within the region, especially after the mid-1990s. Drought features have increased significantly in all regions and for all SPI time scales in 1995-2018, compared to 1970-1994. Significant (at 0.05 level) decreasing trends were detected for the SPI-3 spring and SPI-6 spring/summer. The Levant region experienced drought episodes in 1999-2001, 2006-2011, and 2014-2018, all of which were more severe on long-term drought scales. According to PCA, the study area can be divided into three homogeneous regions at SPI-3, 6, and 12 month timescales, and into four regions at SPI-24 months timescale. The PC-1 regions (the central and northern locations from Palestine, northern locations from Jordan, and south Syria) showed heavy significant increasing trends in the DF and MDS at SPI-3 and 12 month timescales. Significant changes will occur in central and northern Palestine, as well as in eastern Syria. The PC-2 region (Syrian coast) had the highest DF, TDD, and TDS values but it showed mixed trends with no significance in the DF and MDS.

Regarding the influence of large-scale ocean-atmospheric circulation patterns on seasonal temperatures, precipitation and drought, the results strongly support the NCP, NAO, WEMO, and ENSO indices as predictors due to their high ability in explaining the interannual temperatures and rainfall variability in different seasons. The influence of the NAO, NCP, MO, and EA/WR indices is always negative on temperatures and positive on rainfall, except for the NAO, which has an inverse effect on rainfall. On the other hand, the effect of the ENSO and WEMO indices is positive on temperatures and negative on the rainfall.

The NCP index is the major influential atmospheric circulation index for the seasonal temperatures and rainfall over the Levant region (e.g., winter-Tmax and -Tmin, autumn-Tmax and -Tmin, winter rainfall, and winter drought). The effect of the ENSO index was mainly restricted in summer temperatures and autumn rainfall and drought. The WEMO index notably exerted influence in spring temperatures, rainfall and drought.

The SST-(winter temperatures and rainfall) coupled modes reflect the SSTs tripolar Atlantic Ocean patterns, which are influenced by the NAO atmospheric forces. The SST-(spring temperatures and rainfall) coupled modes reflect the SSTs horseshoe Atlantic Ocean patterns, which not resemble the NAO signature, but regional atmospheric-ocean interactions (like Mediterranean SLP, and the NCP index) because of the NAO's weaker influence in seasons such spring, summer and autumn.

The SST-autumn temperatures coupled mode clearly showed the regional influence of the east and west the Mediterranean Sea, as well as the North Sea, Baltic Sea, and west Europe. This coupled mode strongly resemble the NCP negative impact on the autumn temperatures. A similar SST structure was found for SST-summer temperatures and SST-autumn rainfall, which is strikingly resemble the ENSO's positive and negative effects on summer temperatures and autumn rainfall.

The role of the Atlantic SLP in explaining temperature and rainfall variability is significantly reduced, especially in the central latitudes, compared to winter. In summer and autumn, for example, the SLP shifted to the subtropical Atlantic, favoring the ENSO effect on summer temperatures and autumn rainfall. In a same line, the strong winter action centers over the Azores were completely absent in spring, summer, and autumn. On the other hands, the center action over the Europe, North Africa, and Mediterranean Sea remained constant from spring to autumn. These changes in the Atlantic SLP may led to enhance the role of regional interactions related to Mediterranean region and west Europe in spring and autumn, like NCP, WEMO, MO indices.

RESUMEN

El cambio climático es un tema de gran interés en todo el mundo debido a sus graves consecuencias ambientales, agrícolas, hidrológicas y socioeconómicas. La región de Levante, como parte del Mediterráneo oriental, se considera una región particularmente vulnerable al cambio climático actual y futuro, también afectada por otros factores del desarrollo, como la escasez de agua, la fatiga de las infraestructuras, los conflictos políticos y étnicos, el crecimiento de la población y la creciente demanda de agua, alimentos y energía, que exacerban las implicaciones del cambio climático. Además, existe una falta de cooperación e intercambio de datos climáticos entre los países de la región, así como una falta de cooperación para hacer frente a los impactos del cambio climático en la región.

Hasta el momento, no se cuenta con estudios previos en la literatura que evalúen los cambios y variabilidad en la temperatura máxima (Tmax) y mínima (Tmin), rango de temperatura diurna (DTR), precipitación, índices de temperatura y precipitación extrema, y sequía en toda la región de Levante (Siria, Líbano, Jordania, Palestina e Israel), utilizando datos climáticos obtenidos a partir de estaciones meteorológicas. La mayoría de los estudios climáticos en el Levante se limitan a áreas o países específicos, principalmente sobre Israel, y analizan la variabilidad climática y/o el cambio climático únicamente en términos de valores medios a partir de datos que presentan baja cobertura espacial y temporal.

Por lo tanto, esta tesis tiene como objetivo el análisis de la variabilidad climática en la región de Levante a distintas escalas temporales, analizando y estableciendo las relaciones entre el clima de la región y los patrones de circulación a gran escala, con el objetivo de comprender mejor los mecanismos causales de dicha variabilidad climática.

Así, esta tesis llena un vacío real en los estudios climáticos en esta región crítica del mundo, puesto que es el primer estudio de este tipo que se centra en el clima del Levante en su conjunto, utilizando la mayor cantidad de datos climáticos recopilados hasta ahora y analizando un conjunto completo de variables climáticas. Por tanto, los resultados de esta tesis podrían servir como base científica para cualquier futuro esfuerzo conjunto de los países levantinos para combatir el cambio climático a través de una estrategia científica unificada.

La tesis se divide en diez capítulos. Los primeros tres capítulos presentan en detalle los objetivos, las características geográficas y climáticas del área de estudio, los datos brutos, los métodos de

control de calidad de los datos, y la metodología aplicada en este trabajo. La temperatura, los índices de temperatura extrema, la precipitación y los índices de precipitación extrema, así como sus relaciones con los patrones de circulación a gran escala, se examinan en múltiples escalas de tiempo en los Capítulos 4-7. El capítulo 8 se ha dedicado al análisis de covariabilidad entre la temperatura y la precipitación estacionales en el Levante y los patrones generales de la SST y la SLP. En el capítulo 9 se realiza un análisis detallado de las sequías, estudiando sus características y su relación con los patrones de circulación a gran escala, la SST y la SLP. Cada capítulo del 4 al 9 consta de tres secciones: introducción, resultados, conclusiones y discusión. Finalmente, las principales conclusiones alcanzadas en esta tesis se resumen en el Capítulo 10.

Los registros iniciales consistieron en datos de lluvia obtenidos de más de 2000 estaciones pluviométricas y 89 estaciones de temperatura. Todos los datos, estación por estación, se sometieron a un riguroso control de calidad para detectar errores sistemáticos, datos faltantes y valores atípicos. Se excluyeron todas las estaciones que no cumplieron con una serie de condiciones, la más importante de las cuales fue la homogeneidad y continuidad de los datos hasta el período de tiempo más reciente. Los períodos de tiempo se determinaron en función de la mejor cobertura espacial (atendiendo también a factores como la topografía y las regiones climáticas) y la mayor calidad de datos. La lista final de estaciones seleccionadas consta de 61 estaciones para la temperatura que cubren el período 1987-2017 y 165 estaciones para la precipitación que cubren el período 1970-2018. Los datos faltantes fueron menos del 5% en todos los casos.

Los resultados de esta tesis demuestran que la región de Levante ha experimentado un calentamiento rápido en múltiples escalas de tiempo. Con la excepción de octubre, noviembre, diciembre y enero, Tmax y Tmin mostraron tendencias de calentamiento significativas en las escalas de tiempo restantes. Más del 97% de las estaciones exhibieron tendencias crecientes tanto en Tmax como en Tmin en todas las escalas de tiempo, con la mayor frecuencia de tendencias significativas (> 74% de las estaciones) observadas en las escalas de tiempo anual, primavera, febrero, marzo y agosto. La Tmax aumentó más rápido que la Tmin en invierno, verano y primavera en el Levante de 1987 a 2018. En otoño, mayo y julio, sin embargo, la Tmin se calentó más rápido que el Tmax. El DTR para los meses fríos (diciembre-abril) aumentó, mientras que disminuyó para los meses cálidos (mayo-noviembre), siendo significativo solo para agosto y septiembre. La Tmax de la región sur de Levante aumentó significativamente a una tasa mayor que la Tmax del norte en las escalas anual, primavera, verano y otoño. Por el contrario, la Tmin del norte aumentó a un ritmo mayor que la Tmin del sur en las escalas anual, de invierno y de otoño. Jordania tuvo las tendencias de aumento significativo de la Tmax más altas para la escala anual, invierno, primavera y verano, mientras que Siria tuvo la tendencia positiva más alta de Tmax de otoño. Además, Siria tuvo la mayor tendencia de calentamiento de la Tmin a escala anual, invierno y otoño, mientras que Palestina y Jordania tuvieron las mayores tendencias de calentamiento de la Tmin en primavera y verano.

También se han encontrado tendencias hacia condiciones más secas en la región de Levante, particularmente en primavera y en marzo. A excepción de Jordania en febrero, no se detectaron tendencias crecientes significativas para la precipitación del Levante en su conjunto y para sus

subregiones en ninguna escala de tiempo. Un porcentaje del 55% de las estaciones mostró tendencias decrecientes significativas en la precipitación de primavera, con las tasas más altas para las ubicaciones más orientales de Siria, las estaciones costeras y el norte de Palestina. La serie de tiempo de primavera promediada para el Levante, Palestina/Israel, Jordania y Siria mostró tendencias decrecientes de precipitación significativas. Además, en marzo, todas las subregiones mostraron importantes tendencias a la baja, y en abril para Siria.

En general, el área de estudio mostró más variabilidad espacial basada en las precipitaciones estacionales que en las temperaturas estacionales, y se puede dividir en tres regiones homogéneas correspondientes al centro y norte de Palestina y Jordania (PC-1), la costa y oeste de Siria (PC-2) y el este de Siria y Jordania, y el sur de Palestina y Jordania (PC-3).

Respecto al análisis de extremos, se han analizado un total de 34 índices de temperatura y precipitaciones extremas desarrollados por ETCCDI y ET-SCI (algunos de los cuales se modificaron para adaptarlos al área de estudio) para Palestina e Israel, en el sur del Levante. Las condiciones de calor y sequedad también están aumentando, según los resultados. Los extremos relacionados con los índices de temperatura mínima nocturna denotaron tendencias más intensas en escalas anuales y estacionales que las relacionadas con los índices de temperatura máxima durante el día. Las tendencias crecientes más significativas se detectaron para verano en los índices TXn, TNn y TNx, con más del 90% del total de estaciones afectadas. Para el índice TN90p de primavera y verano, el 61% y el 85% de las estaciones mostraron tendencias crecientes significativas, respectivamente. El área de estudio tuvo intervalos más largos con períodos secos extremos (CDD) e intervalos más cortos con períodos húmedos extremos (CWD) en el invierno, la primavera y para la combinación invierno-primavera. Los índices extremos de primavera mostraron tendencias negativas para la mayoría de los índices, significativamente para los índices R1mm, R20mm, CWD, RX1day, RX3day, RX5day y SDII.

Los resultados del análisis de la sequía revelan que la sequía se ha vuelto más frecuente y extendida dentro de la región, especialmente después de mediados de los noventa. Los parámetros característicos de la sequía han aumentado significativamente en todas las regiones y para todas las escalas de tiempo del SPI en el periodo 1995-2018, en comparación con 1970-1994. Se detectaron tendencias decrecientes significativas (a un nivel de 0.05) para el SPI-3 meses de primavera y SPI-6 meses en primavera/verano. La región de Levante experimentó episodios de sequía en los periodos 1999-2001, 2006-2011 y 2014-2018, más severos para escalas de sequía a largo plazo.

Según el PCA aplicado al índice SPI a distintas escalas temporales, el área de estudio se puede dividir en tres regiones homogéneas en escalas de tiempo 3-, 6- y 12-meses, y en cuatro regiones para el SPI-24 meses. Las regiones asociadas a la PC-1 (el centro y norte de Palestina, el norte de Jordania y el sur de Siria) mostraron fuertes tendencias crecientes significativas en la frecuencia (DF) y en la severidad (MDS) de la sequía en las escalas de tiempo SPI-3 y -12 meses. La región costera de Siria (PC-2) presentó los valores más altos de frecuencia (DF), duración (TDD) y severidad (TDS) de la sequía, aunque mostró tendencias mixtas no significativas en DF y MDS.

Con respecto a la influencia de los patrones de circulación océano-atmosféricos a gran escala sobre las temperaturas estacionales, la precipitación y la sequía, los resultados presentan a los índices de teleconexión NCP, NAO, WEMO y ENSO como potenciales predictores debido a su alta capacidad para explicar la variabilidad de las temperaturas interanuales y de las precipitaciones. La influencia de los índices NAO, NCP, MO y EA / WR es siempre negativa sobre las temperaturas y positiva sobre las precipitaciones, a excepción de la NAO, que tiene un efecto inverso sobre las precipitaciones. Por otro lado, el efecto de los índices ENSO y WEMO es positivo sobre las temperaturas y negativo sobre las precipitaciones.

El índice NCP es el índice de circulación atmosférica más influyente para las temperaturas estacionales y las precipitaciones en la región de Levante (por ejemplo, para la Tmax y la Tmin de invierno y otoño, y para la precipitación y la sequía de invierno). El efecto del índice ENSO estuvo restringido principalmente en las temperaturas de verano y las precipitaciones y sequías otoñales. El índice WEMO influyó notablemente en las temperaturas, las precipitaciones y la sequía de primavera.

Los modos acoplados entre la SST y las temperaturas y precipitación de invierno reflejan el patrón tripolar de la SST del Océano Atlántico, que está influenciado por el patrón atmosférico asociado a la NAO. Los modos acoplados de la SST y de las temperaturas y precipitaciones de primavera reflejan un patrón de herradura de la SST del Océano Atlántico, que no correlaciona con la NAO y que parece estar relacionado con otros patrones regionales asociados a la SLP mediterráneo y al índice NCP, en acorde con la influencia más débil de la NAO en las estaciones de primavera, verano y otoño.

El principal modo acoplado de la SST y las temperaturas de otoño mostró claramente la influencia regional del este y oeste del Mar Mediterráneo, así como del Mar del Norte, el Mar Báltico y el oeste de Europa. La influencia de este modo acoplado se asemeja al impacto negativo del NCP en las temperaturas otoñales. Se encontró una estructura similar de la SST acoplada a las temperaturas de verano y a la precipitación en otoño, relacionada con los efectos positivos y negativos del ENSO sobre las temperaturas de verano y las lluvias de otoño.

El papel de la SLP del Atlántico en la variabilidad de las temperaturas y las precipitaciones del Levante se reduce significativamente, especialmente en las latitudes centrales, excepto en invierno. En verano y otoño, por ejemplo, los centros de acción de la SLP se desplazan hacia el Atlántico subtropical, favoreciendo el efecto ENSO sobre las temperaturas de verano y las precipitaciones de otoño. En la misma línea, los fuertes centros de acción invernal sobre las Azores están ausentes en primavera, verano y otoño. Por otro lado, los centros de acción sobre Europa, el norte de África y el Mar Mediterráneo se mantienen constantes desde la primavera hasta el otoño.

CONTENTS

LIST OF FIGURES

LIST OF TABLES

LIST OF ACRONYMS

CL	Cluster
COR	Correlation
CV	Coefficient of Variation
DD	Drought duration
Diff.	Difference
DF	Drought frequency
DJF	December-January-February
DS	Drought severity
DTR	Diurnal Temperature Range
EA	East Atlantic
EM	East Mediterranean
ENSO	El Niño-Southern Oscillation
EOF	Empirical Orthogonal Function
MAM	March-April-May
MK	Mann-Kendall
MOI	Mediterranean Oscillation Index
NAO	North Atlantic Oscillation

NO	North Hemisphere
NCP	North Sea Caspian Pattern
PCA	Principal Component Analysis
PCI	Precipitation Concentration Index
QC	Quality Control
SC	Squared Covariance
SCF	Square Covariance Fraction
SD	Standard Deviation
SPI	Standardized Precipitation Index
Sig.	Significant
SLP	Sea Level Pressure
SMK	Sequential Mann-Kendall
SNHT	Standard Normal Homogeneity Test
SRA	Standardized Precipitations Anomaly
SST	Sea Surface Temperature
STR	String of Coupling between fields in SVD
SVD	Singular Value Decomposition
Tmax	Maximum Temperature
Tmin	Minimum Temperature
WA/WR	East Atlantic-Wesern Russia
WEMOI	Western Mediterranean Oscillation Index

CHAPTER 1

INTRODUCTION

In this chapter, the motivations and importance that support the research carried out in this work are presented. In addition, the objectives and structure of the thesis are described. More details of these topics and literatures review are included in the introduction to each chapter.

1.1 Overview

Climate change is an issue of particular interest globally since it involves serious environmental, economic, and social implications (Salameh et al., 2018; Wang et al. 2011; Osofsky 2014). Climate change refers to "a change in the state of the climate that can be identified by changes in mean or variability of its properties, and that persist for an extended period, typically decade or longer, as a result of human activity or natural factors" (IPCC, 2007). The Earth's climate system has demonstrably changed on both global and regional scales since the pre-industrial era due to increases in greenhouse gases concentration that is probably lead to increase temperatures, changes rainfall patterns, and increase the frequency of extreme events (IPCC 2001, 2007, 2013).

The East Mediterranean (EM) region has been classified as a hot spot of the Earth´s climate change. It is expected to experience future climate change above the global means (Giorgi, 2006). According to the Intergovernmental Panel on Climate Change (IPCC), the rate of warming in the southern and eastern Mediterranean regions over the present century is tending to be larger (drier and hotter) than the average global warming by 2.2–5.1 °C (IPCC, 2013). By the middle of this century, the temperature will increase between 2.5 to 3.7°C in summer and from 2.0 to 3.1°C in winter (Cruz et al., 2007). In addition, the number of warm days will increase by 50–60 additional days/year by the end of the 21st century (Lelieveld et al., 2012).

Regarding precipitation variations over the EM region, it is expected to reduce about 20% from the annual rainfall by the year 2050 (Black, 2009; Lelieveld et al., 2012; Smiatek et al., 2011). Furthermore, southern and eastern Mediterranean regions suffer from severe water shortages of up

to 100 m³/person/year, and some of them reach up to 500 m³/person/year (Simone, 2011; Droogers et al., 2012). Despite the fact that the Arab world contributes merely 4.2% to the global GHG emissions, the impact of climate change on the region's fragile environment and its people is expected to be immense, which demands urgent planning for adaptation measures (AFED, 2009). For the last decades, many studies have indicated the decreasing precipitation and increasing temperature trends over the Mediterranean and Middle East regions (Salameh et al., 2019; AlSarmi and Washington, 2011; Hochman et al., 2018; Alpert et al., 2002; Najafi and Moazami, 2017; Hassanean, 2001, 2004; Zhang et al., 2005; Hasanean and Abdel basset, 2006; Rehman, 2010; AlSarmi and Washington, 2011).

In general, the Mediterranean region is under intense anthropogenic pressures such as overfishing, habitat destruction, alteration of rivers inflow, and pollution (Ballesteros, 2006). The Levant, as a part of the EM, is considered a region very vulnerable to the current and future climate change, primarily due to its low adaptive capacity and its sensitivity to many of the projected changes (Al-Quinna et al., 2011; Shadeed, 2013). Furthermore, the climate change occurs in the context of other developmental stresses such as water scarcity, weakness of existing infrastructure, and frequent drought events (Erian et al., 2011; Kelleya et al., 2015; Mathbouta et al., 2018; Lelieveld et al., 2013). Moreover, all of these factors are escalated by political and ethnic conflicts (e.g., Arab-Israel conflicts and Arab Spring events) as well as the rapid population growth and demand for water, food, and energy (Lange, 2019; Ziv et al., 2006; Al-Qinna et al., 2011; Hammad and Salameh, 2018).

For example, Syria is one of the countries which are especially vulnerable to climate change due to the dependence of more than 62% of its agricultural lands (equivalent to about 14258 Km²) of rainfall as the main source of irrigation (Cafiero, 2009). In addition, rainfall represents 68.5% of all available water resources, and the agricultural water requirements were expected to increase by 6% in 2020 (ACSAD, 2011). Jordan is considered the fourth poorest country in terms of water resources (World Bank, 2013). According to the Ministry of Water and Irrigation (MWI), water availability has declined from 3600 m^3/person/year per capita in 1946 to 145 m^3/person/year per capita in 2007 (MWI, 2009). Increasing temperatures also lead to higher rates of evapotranspiration and increase the plant water requirements (Snyder et al., 2011). This may be particularly important in rainfed areas, like Levant regions (Syria, Lebanon, Jordan, Palestine and Israel), due to the lack of irrigation possibilities.

There are no previous studies in the literature assessing the variability in maximum (Tmax) and minimum (Tmin) temperatures, precipitation, extreme temperature and precipitation indices, and drought in the entire Levant region, based on climatic data from ground stations, nor comparison with other regions. Besides, most of the climate studies in the Levant are focused on limited areas or countries, mainly over Israel (Ziv et al., 2014; Shlomi and Ginat, 2009; Freiwan and Kadioğlu, 2008; Ben-Gai et al., 1994, 1998; Ghanem, 2011). In addition, most of them identified the climate change in term of mean values, using limited time scales and stations. One of the main reason for this is the difficulty for obtaining high-quality climate data due to the limitations imposed by many

meteorological departments in the Levant region, with the exception of Israel, to exchange data sets with different resolutions.
Understanding climate change necessitates paying attention to changes in climate variability and extremes. Thus, it is essential to study and investigate the climate variability in the Levant region. The study of climate variability and the establishment of relations between the most significant climate variables is crucial for understanding the causal mechanisms of such climate variability and for generating prediction models.

1.2 Objectives

The overall aim of this thesis is to increase the knowledge about climate variability in the Levant region in terms of both its determination and causal mechanisms. In particular, this thesis aims to provide for the first time a comprehensive spatio-temporal analysis for temperatures (Tmax and Tmin), precipitation, extreme temperature and precipitation, and drought variability over the entire Levant region, using more data from meteorological stations than ever before. Moreover, this work seeks out to explore the atmospheric-oceanic factors driving temperature, precipitation, and drought variability in the Levant region. Therefore, the results from this work could provide a baseline for the governmental decision makers in the Levant region for topics like water, agricultural, urban, transportation planning and also for disaster management. Specifically, the main objectives of this thesis are:

1) To develop a quality-controlled and homogeneous climate database covering the whole of the Levant area.
2) To analyze the spatio-temporal trend variability of Tmax and Tmin over the study area at annual, seasonal, and monthly time scales.
3) To analyze the spatio-temporal trends variability of precipitation at annual, seasonal, and monthly time scales.
4) To identify the impacts of the main teleconnection indices on the maximum and minimum temperatures and precipitation variability in the study area, at seasonal scales.
5) To provide a comprehensive temporal and spatial analysis of the extreme temperature and precipitation indices, and their relationships with the main large-scale circulation patterns.
6) To investigate and evaluate the potential relationship between the seasonal temperature and precipitation in the Levant region and two indicators of climate variability, which are the sea surface temperatures (SST), and the sea level pressure (SLP).
7) To analyze the spatio-temporal variability of the drought phenomena over the Levant region through the frequency (DF), duration (DD), and severity (DS) drought characteristics.
8) To investigate and evaluate the relationships between main teleconnection indices along with the coupled variability between the SST and SLP and the seasonal drought.

1.3 Structure of the thesis

The work is divided into ten chapters, including the introduction and conclusions chapters. An outline of the chapters that follow is provided here.

- Chapter 1 briefly discusses the main motivations and objectives that stand behind this work. It highlights some of the general characteristics of climate studies in the Levant region.
- Chapter 2 provides a description of the study area, its geographical and climate features. It also includes a description of the original data and the data Quality Control (QC) process.
- Chapter 3 summarizes the methods used in this work.
- Chapter 4 presents an overview of the spatial and temporal variability of the annual, seasonal, and monthly maximum and minimum temperatures over the Levant region during the period 1987-2017. This chapter also studies the relationships between the seasonal temperatures and the large-scale circulation pattern.
- Chapter 5 analyzes the spatio-temporal variability of the extreme temperature indices in Palestine and Israel during 1987-2017. It also provides a comprehensive evaluating between the extreme temperatures and the large-scale circulation patterns at annual and seasonal timescales.
- Chapter 6 presents an overview of the spatial and temporal variability of the annual, seasonal, and monthly precipitation over the Levant region during 1987-2017. This chapter also studies the relationships between the seasonal rainfall and the large-scale circulation patterns.
- Chapter 7 analyzes the spatio-temporal variability of the extreme rainfall indices in Palestine and Israel during 1987-2017. It also provides a comprehensive evaluating between the extreme rainfall and the large-scale circulation patterns at annual and seasonal scales.
- Chapter 8 analyzes the coupled variability between seasonal temperatures (Tmax and Tmin) and precipitation and SST and SLP. These couplings are explored using Singular Value Decomposition (SVD) technique.
- Chapter 9 examines the spatial and temporal variability of the drought over the Levant from 1970 to 2018. The drought characteristics (frequency, duration, and severity) are investigated. In addition, the relationships between seven large-scale circulation indices, along with the North Atlantic SST and the North Hemisphere SLP, and the seasonal drought, are studied.
- Chapter 10 summarizes the main conclusions and future work.

CHAPTER 2

STUDY AREA AND DATA

This chapter gives an overview of the geographic and climatic features of the Levant. It also contains details on the origin of data, sources, time scales, and station locations used in this work. The data quality control methods, handling missing values, outliers, and homogenization of the data sets are discussed.

2.1 The study area

2.1.1 Geographical features of the Levant

The study's geographical domain extends over the Levant region that encompasses Palestine, Israel, Jordan, Lebanon, and Syria, placed at the eastern edge of the Mediterranean Sea between latitudes 34^0N-42^0N, and longitudes 29^0E-37^0E. Turkey surrounds the Levant region in the north; Saudi Arabia, the Red Sea and the Sinai Peninsula in the south; and the Mediterranean Sea and Iraq in the west and east, respectively (Figure 2.1a). The Levant region has an area of about 311.979 km². Its topography sharply varies, with an elevation ranges from 459 m below the sea level at Jericho (Palestine) to 3090 m above the sea level at Qurnat Al-Aswadah (Lebanon). And with a big difference between the peaks of mountains (e.g., central Palestine Mountains, eastern and western Lebanon Mountains) and the lowlands in Palestine and Jordan (e.g., Arad and Jordan valleys), Syria (e.g., Al-Ghab plain), and Lebanon (e.g., Al-Bekaa plain) (Figure 2.1b). From a geomorphological point of view, four major geographical units that play an important role in the climate diversity for the region can be distinguished (Figure 2.1b) (Baly et al., 1984; Mart et al., 2005; Zohary, 1982):

1. The narrow lowlands (elevation: 0-250 m) along the western coastal areas, widening only in the southward up to 60 km. They extend from the Iskenderun plains in the north to the Sinai Peninsula in the south, with a length of more than 600 km.

2. The western highlands, which range between 550-950 m for the Central Palestine Mountains and the Upper/Lower Galilee, 550-1400 m for the Syrian coastal Mountains in the northwestern, and 550-3093 m for the eastern/western Lebanon Mountains.

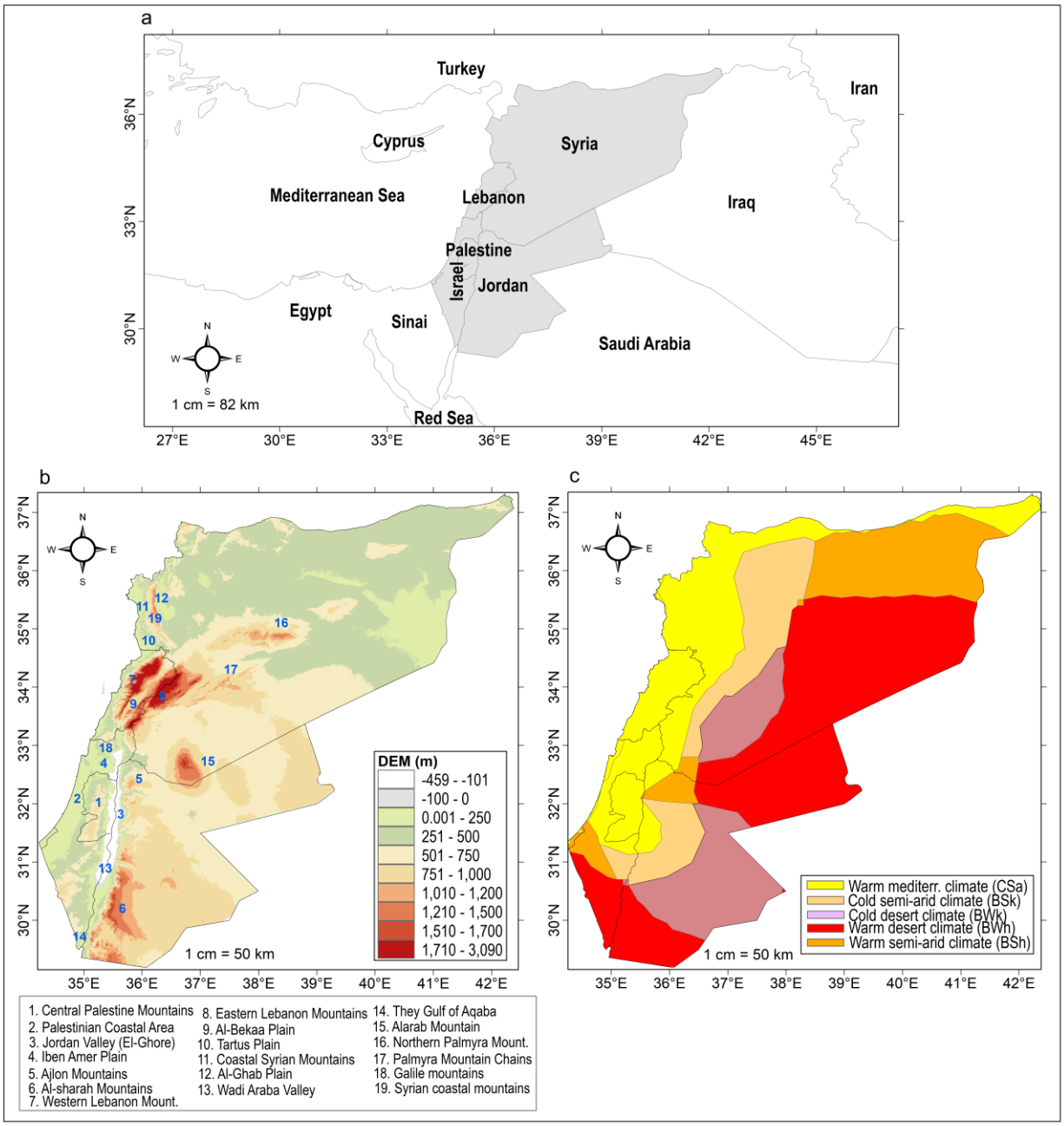

Figure 2.1. (a) Study area location, (b) Topography features, and (c) Köppen climate zones classification. Source: http://gdem.ersdac.jspacesystems.or.jp and http://koeppen-geiger.vu-wien.ac.at/.

3. The central Rift valley, which consists of three major segments, the Jordan Rift in the south (-495-0 m), that forms the lowest depression of the Earth's continental surface. The Syrian Ghab Rift in the north (100-250 m), and the Lebanese Fault (Al-Bekaa plain).

4. The eastern Plateau covers all the eastern areas from Jordan and the southeastern regions from Syria. It has several hills and isolated mountains. The Levant desert (Badia) in the east covers 60% of the total area, while the mountains formed around 30% of the area.

2.1.2 Climate characteristics of the Levant

The Levant climate is characterized by a complex interaction between the global air-ocean circulation system, the complex topography, and possibly anthropogenic factors. According to the Köppen Climatic classification (Figure 2.1c), 85% of the total area is classified as warm and cold arid-semiarid climate zones (types BWh, BWk, BSh, and BSk). These regions extend over the whole eastern Plateau and the southern provinces, from Palestine and Jordan. On the other hand, the Warm Mediterranean Climate (type Csa) corresponds only to 15% of the total area and covers the western coastal regions from Syria, Lebanon, and Palestine. The western mountains (Figure 2.1b), such as Lebanon and Central Palestine Mountains, play an essential role in distributing rainfall and temperature across the Levant. In this context, the Mediterranean Sea's humid influence diminishes sharply eastwards due to the orographic effects of the western mountains (Finkelstein and Langgut, 2014). Therefore, the western mountains and coastal strip are humid, while the eastern regions are semi-arid and arid (van Zeist and Bottema, 1991). The moisture that is blocked by the western mountains is stored as snowfall or rainfall. Later it runs off the surface or seeps into aquifers, which lead to the rise to the Levant Rivers such as Jordan River, Litany, and Assi in Lebanon (Assaf, 2014; Jason et al., 2004).

Climatically, the Levant is classified as a transition region, located between the Afro-Asian desert to the south and the temperate, mid-latitude westerly wind to the north (Saaroni et al., 2010; Lionello, 2012; Frumkin and Stein 2004). In addition, two large monsoon systems, north African and southwest Asia, extend over the region to the southwest and southeast. Both these monsoons have a significant impact on the climate of the region. The region's location between these hemispheric climate belts and the impact of the nearby Mediterranean Sea makes the region sensitive to changes in the global climate system (Kushnir et al., 2017).

Most rainfall is concentrated in the winter season and early spring (December-March) and is mainly caused by the passage of the extratropical cyclones over the east Mediterranean (EM) (Sharon and Kutiel, 1986; Alpertet al., 1990; Zivet al., 2006). These cyclones are called Cyprus depressions because most of them tend to pass, intensify or even develop over Cyprus and the Syrian coast (HMSO, 1962; Alpertet al., 1990; Shay-El and Alpert, 1991; Katsnelson, 1964; Shaaroni et al., 2010). The Cyprus lows are responsible for transporting cool air from eastern Europe over the warmer Mediterranean where it becomes humid and unstable and may produce rainstorms that typically last 2–3 days (Alpert et al., 2004; Shay-El and Alpert, 1991). About 90% of the rainfall occurs by the Cyprus low (Goldreich et al., 2004). The Levant's southern and eastern regions are located on the outskirts of these lows; therefore, these areas receive little rainfall.

In addition, the Red Sea Trough (RST) is another type of synoptic system, which can produce low and localized precipitation in the EM region (Heiblum et al., 2011; Enzel et al., 2008). It is a low-pressure system extending from eastern Africa (Ethiopia and Sudan) along the Red Sea toward the EM and the Levant (Armon et al., 2018; Ashbel, 1938; El-Fandy, 1948). The RSTs are most

common during fall and spring and are the dominant synoptic feature in the EM in October (Tsvieli and Zangvil, 2005; Goldreich, 2003).

2.2 The Original Data

2.2.1 Temperature and precipitation data

2.2.1.1 Monthly data

Monthly Tmax and Tmin temperature time series from 89 meteorological stations distributed across the Levant region (Figure 2.2a, Table 2.1) were obtained from the following resources: 1- The Meteorological Departments of Syria, Palestine, and Israel; 2- The National Oceanic and Atmospheric Administration (NOAA); 3- International Center for Agricultural Research in the Dry Areas (ICARDA), and 4- Lebanese Agricultural Research Institute (LARI). For the precipitation, the historical archive of monthly precipitation time series from 2482 stations (Figure 2.2b, Table 2.1) was taken from: 1- The Meteorological Departments of Syria, Palestine, Jordan, and Israel; 2- The Agricultural Ministries of Palestine and Syria, and 3- Water Authority of Jordan.

Country	Temperature	Precipitation
Syria	35	474
Palestine and Israel	31	1940
Jordan	12	61
Lebanon	7	7
Turkey and Saudi Arabia	4	-
Total	89	2482

Table 2.1. Number of temperature and precipitation stations for each country.

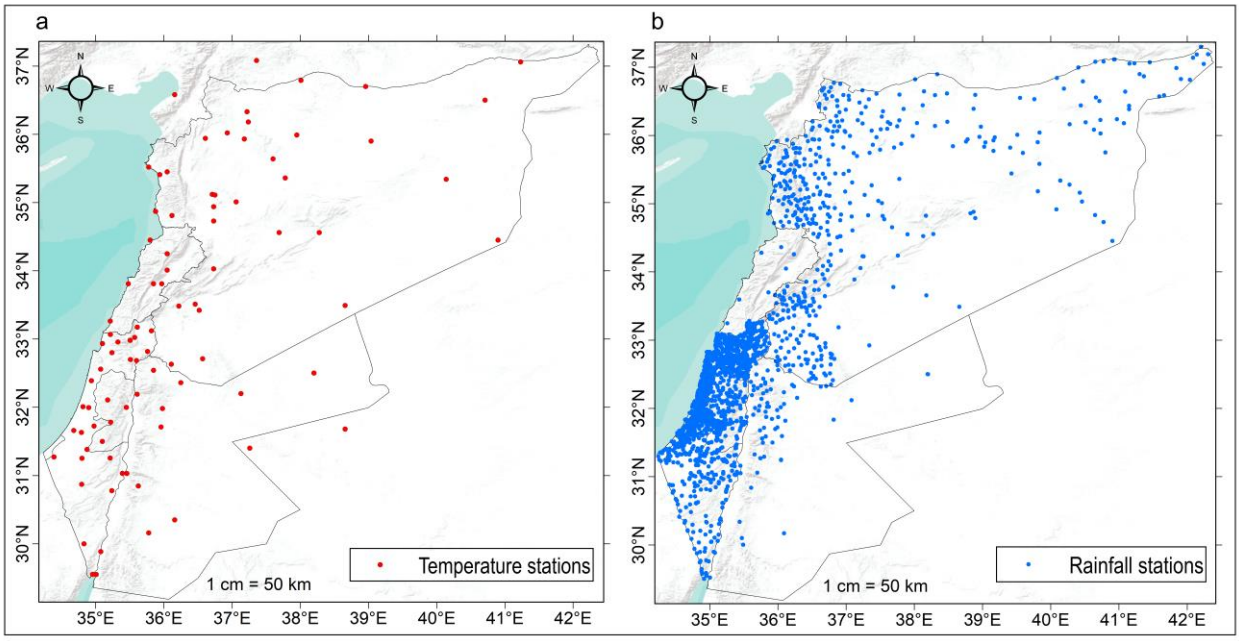

Figure 2.2. The spatial distribution of all available meteorological stations for (a) monthly temperature and (b) monthly precipitation.

2.2.1.2 Daily data

For this study, the daily data are available only for Historical Palestine, which nowadays is composed of Israel and Palestine territories. The historical archive of daily time series Tmax and Tmin from 118 stations was taken from the Israeli Meteorological Department (https://ims.data.gov.il) (Figure 2.3a). In addition, observed daily precipitation data from an initial number of 130 stations in the Israel and Palestine territories were obtained from the Israel and Palestine Meteorological Departments (https://ims.data.gov.il http://www.pmd.ps/, respectively) (Figure 2.3b).

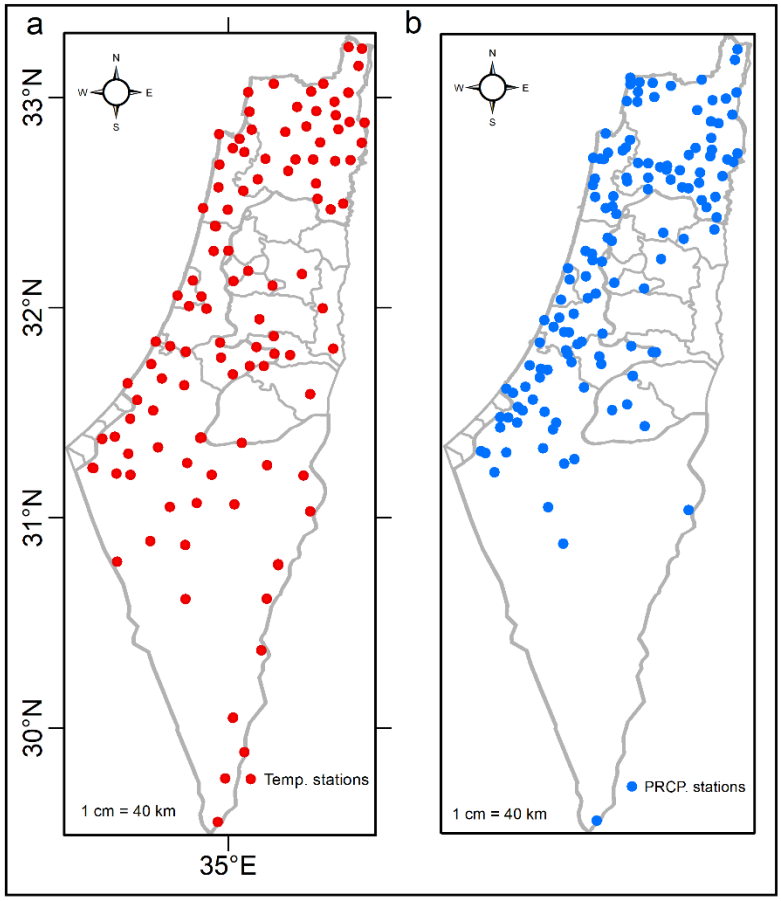

Figure 2.3. The spatial distribution of all available meteorological stations for (a) daily temperature and (b) daily precipitation.

2.2.2 Data Quality Control

Not all of the monthly/daily temperatures (Tmax and Tmin) and precipitation time series mentioned in Section 2.2.1 were used in the analysis. Each station was subjected to a rigorous quality control assurance (QC) to reduce data errors and choose the most reliable time series. Climate studies related to climate variability, climate change, and climate prediction require high quality and homogeneous time series. The QC guarantees that data reflect the climate characteristics of the location and time (Von Storch, 2008). In this context, the systematic errors/unreasonable values, missing data, and outliers were checked and evaluated (Klein Tank et

al., 2009; Alexander et al., 2006; El Kenawy et al., 2013). Generally, stations should be selected based on the length, completeness of records, and homogeneity (Trewin 2013; Ahmad et al. 2013). Firstly, the available time-series were filtered based on their record lengths. Three types of time series were discarded from the final list of stations:

1- Stations that have generally less than 30 years of monthly time series, based on the World Meteorological Organization (WMO) criterion for climate studies.
2- Stations with records not continuous for recent years.
3- Stations with more than 10% of missing monthly values (Huang et al. 2014; Meddi et al. 2014; Tan et al., 2019).

Although the stations with shorter records were not used for the analysis, they were still useful in assessing missing data, outliers, and homogeneity at nearby stations. In addition, stations have to be at well-spaced locations across the study area and represent the different climatic zones and topography. However, note that there is a lack of meteorological stations in the dryland, such as south of Palestine, Jordan, Dead Sea Rift valley, and eastern areas from Syria and Jordan, compared to the western coastal regions. The application of the three previous criteria resulted in:

1- A total of 60 out of 89 stations for monthly temperature time series.
2- A total of 520 out of 2482 stations for monthly precipitation with a length greater than or equal to 30 years. From these, only 316 stations had continuous records until 2018. In addition, 167 out of 316 stations had less than 10% of monthly missing data.
3- A total of 28 out of 118 stations and 66 out of 130 stations for daily temperature and precipitation time series, respectively, have passed the first stage.

To maximize the investigation period, taking into account the best spatial coverage, the periods 1987-2018 and 1970-2018, respectively, were selected to be the temporal limits for the monthly/daily temperatures (Tmax and Tmin) and precipitation analysis.

In a second stage, the monthly/daily temperature and precipitation time series were plotted to check for systematic errors (e.g., Tmin ≥ Tmax, Tmax > 60^0C, Tmin < - 30^0C, Rainfall < 0 mm, and typographical errors). These systematic errors were manually handled as missing values.

2.2.2.1 Missing data and outliers

Missing data (MD) is a widespread problem in climatology, and it is essential to estimate them for performing the analysis of climatic variables. They can produce biased results, and they can hinder the application of required statistical analyzes (Farzana et al., 2019; Vieux, 2001). In the literature, there are many approaches to missing data treatments (Aieb et al., 2019; Simolo et al., 2010; Presti et al., 2010):

1- “Internal” temporal interpolation when time series data (such as its long-term average or its values before and after the missing value) are used to infill the missing values in the same time series.
2- “External” spatial interpolation when gaps at a target station are calculated by using synchronous observations from surrounding stations.

The spatial interpolation approach contains many techniques such as the normal ratio (NR), arithmetic mean, aerial precipitation ratio, inverse weighting distance (IWD), and correlation coefficient (CC) (Silva et al., 2007; Suhalia et al., 2008). The arithmetic means method assumes equal weights from all nearby stations, and it is recommended when the annual value at each of the station differs by less than 10% from that of the station with the missing data (Singh, 1994; Chow et al., 1988; McCuen, 1998). While the NR method gives a weight for each surrounding station and is used if any of the surrounding stations has an annual value greater than 10% of the station considered. A comprehensive detail about these methods and their calculations is available in Tabios and Salas (1985), Singh (1994), and Yozgatligil et al. (2013).

In this study, three methods were used in infilling missing values:

1- If a monthly temperature and precipitation time series have only one missing value, it was replaced by the long-term average.
2- If a monthly time series have two or more missing values, the spatial interpolation methods, mainly the arithmetic mean and the NR methods were applied.
3- For a daily time series, only those months and years with more than 3 and 15 missing days, respectively, were handled. Note that the RClimDex v1.0 (Klein Tank et al., 2009) software used to calculate the extreme temperature and precipitation indices does not calculate monthly indices if more than 3 days are missing in a month, and more than 15 missing days in the annual values. If these missing days were not successive, the temporal interpolation was used based on the average of two values of consecutive days (before and after the missing day). Furthermore, if these missing days were successive, the spatial interpolation method was applied based on neighbouring stations with distance < 20 km and correlation value $r > 0.8$ (Sibson, 1981; Jiang et al., 2012).

In most cases, the arithmetic mean was used because of the small distance between the target and reference stations as well as the high correlation between them ($r > 0.85$). Special attention was given to zero monthly precipitation values in months of winter, spring, and autumn. To distinguish among months with no precipitation from those with no observation, the values were compared with the observed values at nearby stations. Moreover, the means and standard deviations were computed for the complete time series and those incomplete time series. The differences in mean and standard deviation did not result statistically significant.

The percent of missing data were listed for each station in (Tables 1-4, in Appendix A). Based on stations, the percent formed less than 5% for monthly temperatures and precipitation time series whereas, they comprised less than 1% and 4% for daily precipitation and temperatures time series, respectively.

Outlier values may be considered as errors of measurement or a result of exceptional climatic conditions that caused such values actually to occur (Stedinger et al., 1993). Such observations will negatively affect the data's compatibility and homogeneity and lead to erroneous and inaccurate results (Osborne et al., 2004). Therefore, it is essential to detect and handle them (correction, removing, or keep them) in the quantitative analysis's first steps.

In this study, the thresholds of outliers were defined within the range of ±3 and ±4 standard deviations for the monthly and daily temperature time series, respectively (Hunt, 2007; Harmel et al., 2002; Jones et al., 1999; Athar, 2014; Zhang et al., 2005; Brunet et al., 2006). For the monthly and daily precipitation time series, the interquartile range (3*IQR) technique was used to identify suspicious values (Peterson et al., 1998; González-Rouco et al., 2001).
After that, the visual comparison among neighbouring stations (spatial coherency) was also used to determine whether an outlier resulted from natural factors or systematic errors (Sutarya and Mahendra, 2014; Eischeid et al., 1995). All unreasonable outliers were manually edited by replacing them with monthly averages. Tables 2.2 and 2.3 summarize the total missing values and outliers detected in the monthly and daily temperatures and precipitation time series, respectively.

Country	Monthly temperature (Tmax, Tmin)			Monthly precipitation		
	Total stations	Total MD	Total outlier	Total stations	Total MD	Total outliers
Palestine and Israel	28	101 (0.5%)	33	78	343 (0.7%)	498
Jordan	9	26 (0.4%)	8	36	102 (0.4%)	523
Syria	15	83 (0.7%)	21	53	620 (1.9%)	539
Lebanon	4	74 (3.5%)	4	-	-	-
Turkey and Saudi Arabia	4	0	3	-	-	-
Total	60	284 (0.6%)	69 (0.1%)	167	1065 (1%)	1560 (1.5%)

Table 2.2. Summary of missing data and outliers detected in the monthly temperature and precipitation. The totals for temperature indicate the missing data and outliers detected in both Tmax and Tmin averages.

Country	Daily temperature (Tmax, Tmin)			Daily precipitation		
	Total stations	Total MD	Total outlier	Total stations	Total MD	Total outliers
Palestine and Israel	28	1598 (0.3%)	118 (0.02%)	66	797 (0.07%)	791 (0.07%)

Table 2.3. Summary of missing data and outliers detected in the daily temperature and precipitation. The totals for temperature indicate the missing data and outliers detected in both Tmax and Tmin averages.

2.2.3 Homogeneity

A homogeneous climate time series is defined as one in which variations are caused only by variation in the weather and climate (Conrad and Pollak, 1950; Aguilar et al., 2003). Homogenization is important because it produces climatic time series that consistently reflect a proper assessment of climate variation and change (Venema et al., 2012).
Long climatological time series often contain variations due to non-climatic factors, such as methods of preliminary data treatment, changes in measuring methods, instrumentation, changes in station locations, the urban heat island effect, and changes in the surrounding of the stations (e.g., urbanization, vegetation) (Peterson et al., 1998; Klok et al., 2009; Štěpánek et al., 2012; Hansen et al., 2001). Non-climatic factors make climatic recording unrepresentative of the actual climate variation. They may hide the climatic signals and lead to misinterpretation of climatic studies' conclusions (Costa and Soares, 2009, 2006).
Generally, homogeneity tests are classified into two groups as the ‘absolute method’ and the ‘relative method’. In the first type, the tests are applied to each station separately and based on the

station's available historical files to evaluate the change points. Furthermore, such tests are required in the low spatial density of stations and low correlation between neighboring stations (González et al., 2000; Dhorde et al., 2013; Göktürk 2008). In the second type, the climatic records from neighbouring stations are used to construct a reference time series, to be compared with the station being tested. This method assumes that stations within a geographical region have identical climatic patterns, so observations at any station within the area will reflect this similar pattern (Hänsel et al., 2016; Costa and Soares, 2009).

A comprehensive review of homogenization methods, approaches for developing homogenized climatic time series, and causes of inhomogeneities are available in Peterson et al. (1998), Aguilar et al. (2003), Venema et al. (2012), Trewin (2010) and Domonkos (2013).

2.2.3.1 Monthly time series

A total of 60 and 167 monthly temperatures (Tmax and Tmin) and precipitation time series, respectively, were subjected to homogeneity tests. It is recommended to apply more than one statistical test for detecting inhomogeneities in time series (Wijngaard et al., 2003; Costa and Soares, 2009). In this study, the method used follows the approach proposed by Wijngaard et al. (2003). Four absolute tests were applied at 5% significance level using XLSTAT tool, a user-friendly Microsoft Excel add-in, to evaluate the homogeneity of monthly time series, with null hypothesis (H0, data are homogeneous), and alternative hypothesis (Ha, data are non-homogeneous). The tests are: the Pettitt test (Pettitt, 1979), the standard normal homogeneity test (SNHT) for a single break (Alexandersson, 1986), the Buishand range test (Buishand, 1982), and the Von Neumann ratio test (Von Neumann, 1941). The SNHT is sensitive to change points at the beginning and end of the time series, whereas the Pettitt and the Buishand tests are more sensitive to detecting breaks in the middle of the time series (Costa and Soares, 2009; Arikan et al., 2019; Tan et al., 2019; Suhaila et al., 2008). We labelled time series as ‘useful’ if one or zero tests rejected the null hypothesis. If two tests rejected the null hypothesis, we labelled it as ‘doubtful’ and if three or four tests rejected the null hypothesis we labelled it as ‘suspect’.

Such this approach was used in many studies worldwide such as Turkey (Arikan et al., 2019; Firat et al., 2010; Dikbas et al., 2010), Peninsular Malaysia (Kang and Yusof, 2012; Suhaila et al., 2018), Pakistan (Ahmed et al., 2018), Portugal (De Lima et al., 2010), Brazil (Hänsel et al., 2016), and Iran (Salehi et al., 2020). In addition, time series plotting and comparison (spatial coherence) with neighboring stations (distance < 20 km, $r > 0.8$) were used in some cases to evaluate the change points. Finally, all non-climatic change points were fitted using software package AnClim v5.025. Table 2.4 shows the total stations that showed change points in their monthly temperatures and precipitation time series. The results indicated that 455 (31.5%) out of 1440 monthly Tmax and Tmin time series exhibited significant change points in two, three, or four tests. A total of 328 (72%) of them have occurred in March, June, July, and August. All change points were subjected to spatial evaluation. March exhibited significant change points in 59 and 41 stations for Tmax and Tmin, respectively. All change points in March were considered a result of climatic factors because they occurred in 2000. In addition, August exhibited significant change points in 38 and

50 stations for Tmax and Tmin, respectively. All of them were also considered a result of climatic factors because they occurred in 1997. However, note that many studies have indicated the relationship between the strong El Niño year 1997/1998 and the change points in temperature series during this year (Athar, 2014; AlSarmi et al., 2011). For this reason, the correlation coefficients between the ENSO pattern and the extreme temperature indices at annual and seasonal scales were calculated.

Month	Temperatures		Precipitation
	Tmax	Tmin	
January	1	6	3
February	12	23	2
March	59	41	4
April	0	15	2
May	0	16	1
June	20	44	-
July	33	43	-
August	38	50	-
September	8	40	3
October	0	6	2
November	1	2	0
December	1	1	0
Total	173	287	17

Table 2.4. Total stations in each month that showed change point in monthly temperature and rainfall time series.

2.2.3.1 Daily time series

Data homogeneity is assessed using the R-based RHtest software for the daily temperatures time series. This software can be used to detect and adjust multiple change points that could exist in a data series that may have first-order autoregressive errors (Tao, 2014; Wang et al., 2007; Wang, 2008). Software and user guide are available fromhttp://cccma.seos.uvic.ca/ETCCDMI/software.shtml. Furthermore, the R-based 'RHtests_dlyPrcp' software, based on the transPMFred algorithm (Wang and Feng, 2013, available at http://etccdi.pacificclimate.org/software.shtml), was used to detect multiple change points in the daily precipitation time series, and adjust them using the 'quantile-matching' algorithm (Wang et al., 2010). These methods have been widely used to detect change points in daily time series (Wang et al., 2015; Wu and Huang, 2016; Villafuerte et al., 2014). Finally, 16 breakpoints were detected in 15 out of 66 daily precipitation time series (Table 5 in Appendix A). For the daily temperatures, a total of 5 and 16 out of 28 stations exhibited inhomogeneities in their daily maximum and minimum temperatures, respectively (Table 6 in Appendix A).

2.2.4 Final list of meteorological stations

For monthly temperatures time series, available Lebanon´s stations only cover the period (1994-2017), and for representing it, four stations (Kfardan, Beyrouth, Tripoli, and Houche-Oumara) were included in this study. Furthermore, four stations from Turkey and Saudi Arabia were included in the stations' final list because of their geographical vicinity. Unfortunately, many

Syrian´s stations have long time series with good quality, but they stopped working in 2012 because of the war. Furthermore, there were no stations from Lebanon has passed the selection criteria for monthly precipitation. Only two specific stations in the database (Hazeva and Ariel) cover a shorter period (1988–2017 and 1990–2017, respectively) for the daily Tmax and Tmin time series. Two stations (Elqana and Karmel) from the West Bank cover a shorter period 1982-2018 for the precipitation dataset. The location of the final stations is shown in Figures 2.4, 2.5, and 2.6. The numbers indicating the stations and the metadata (names, coordinates, elevation, and percent of missing values) are listed in Tables 1-4 in Appendix A.

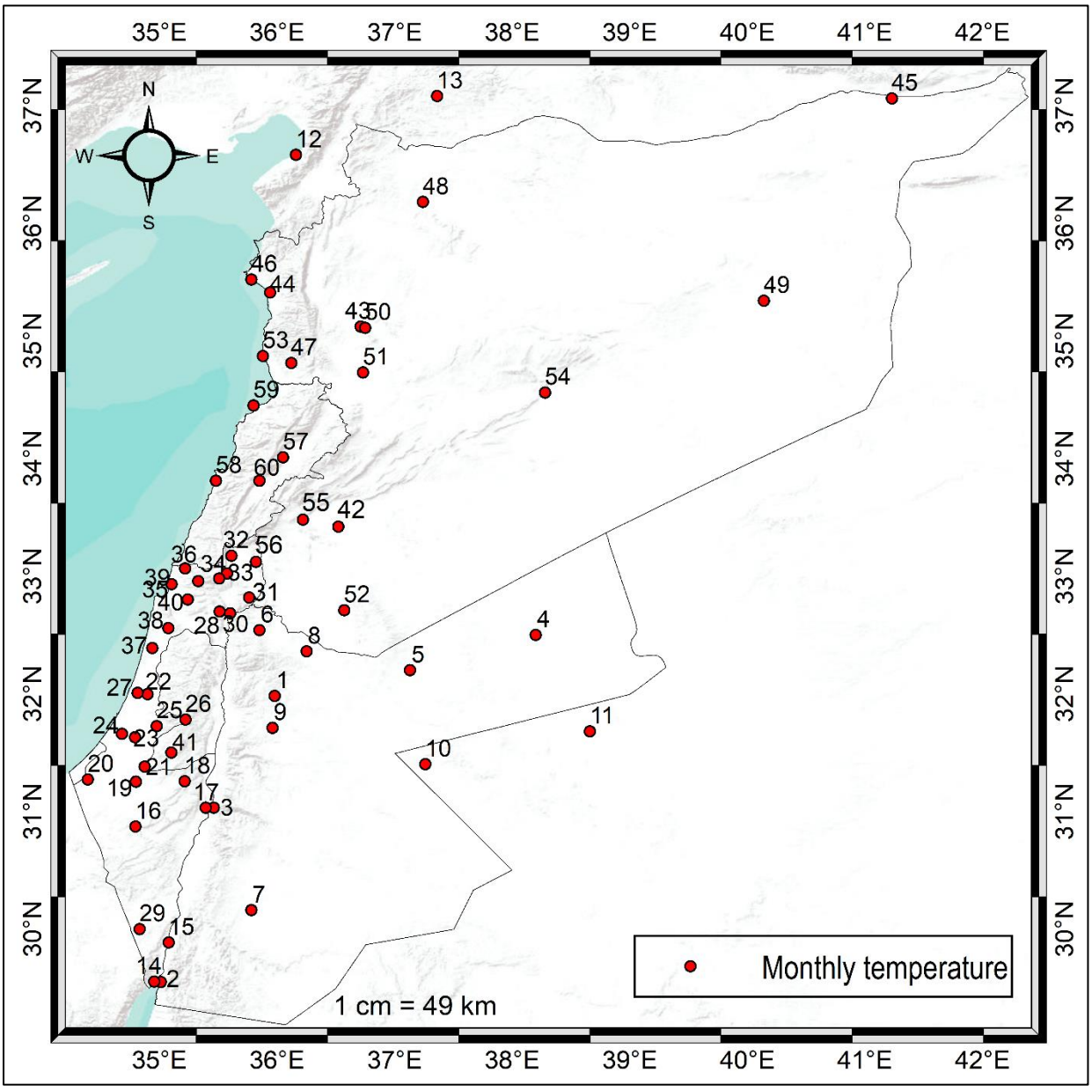

Figure 2.4. The location of the considered stations for monthly Tmax and Tmin averages. The numbers indicating the stations and the metadata (names, coordinates, elevation and percent of missing values) are listed in Table 1 in Appendix A.

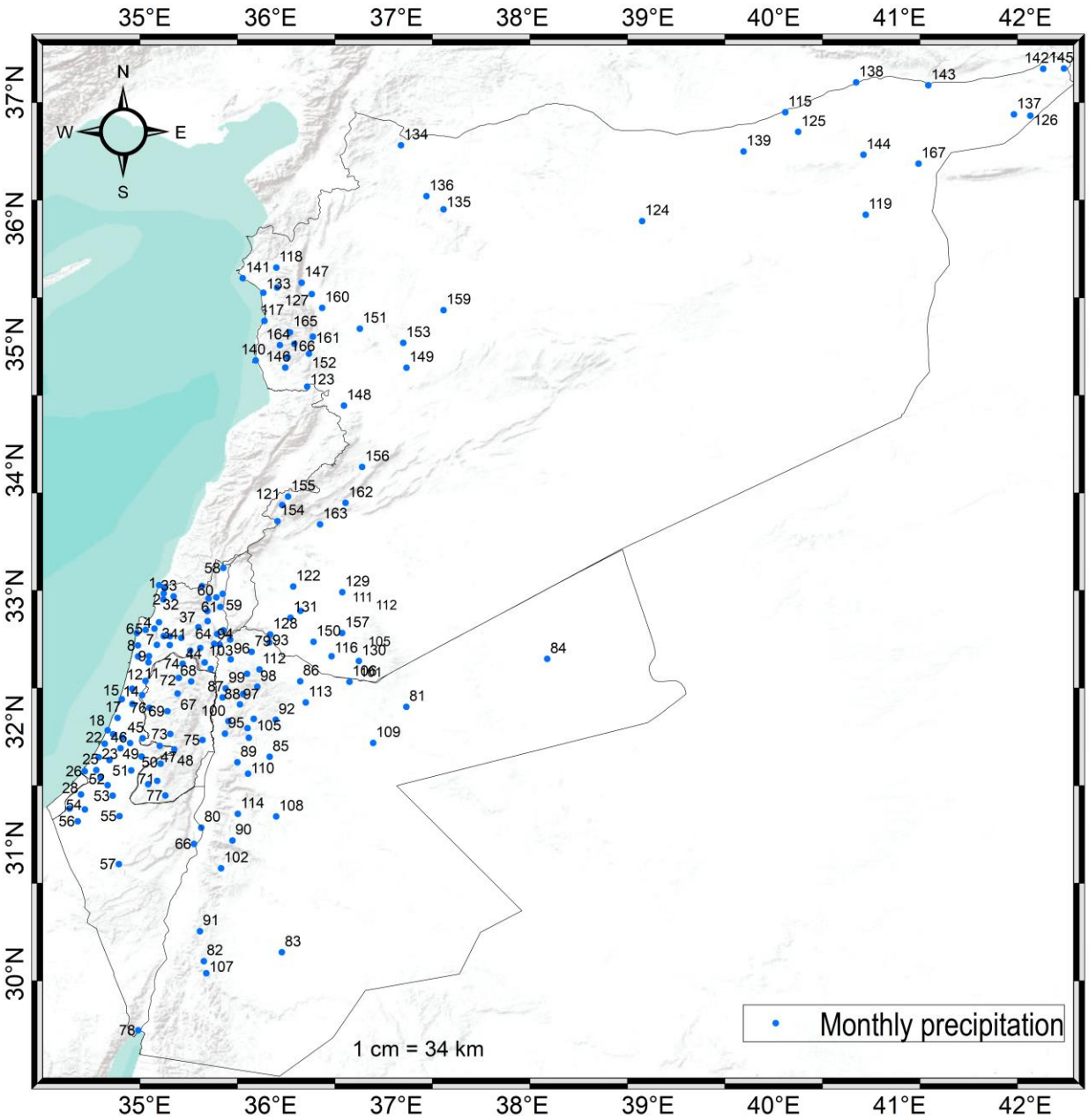

Figure 2.5. The location of the considered stations for monthly rainfall averages. The numbers indicating the stations and the metadata (names, coordinates, elevation and percent of missing values) are listed in Table 2 in Appendix (A).

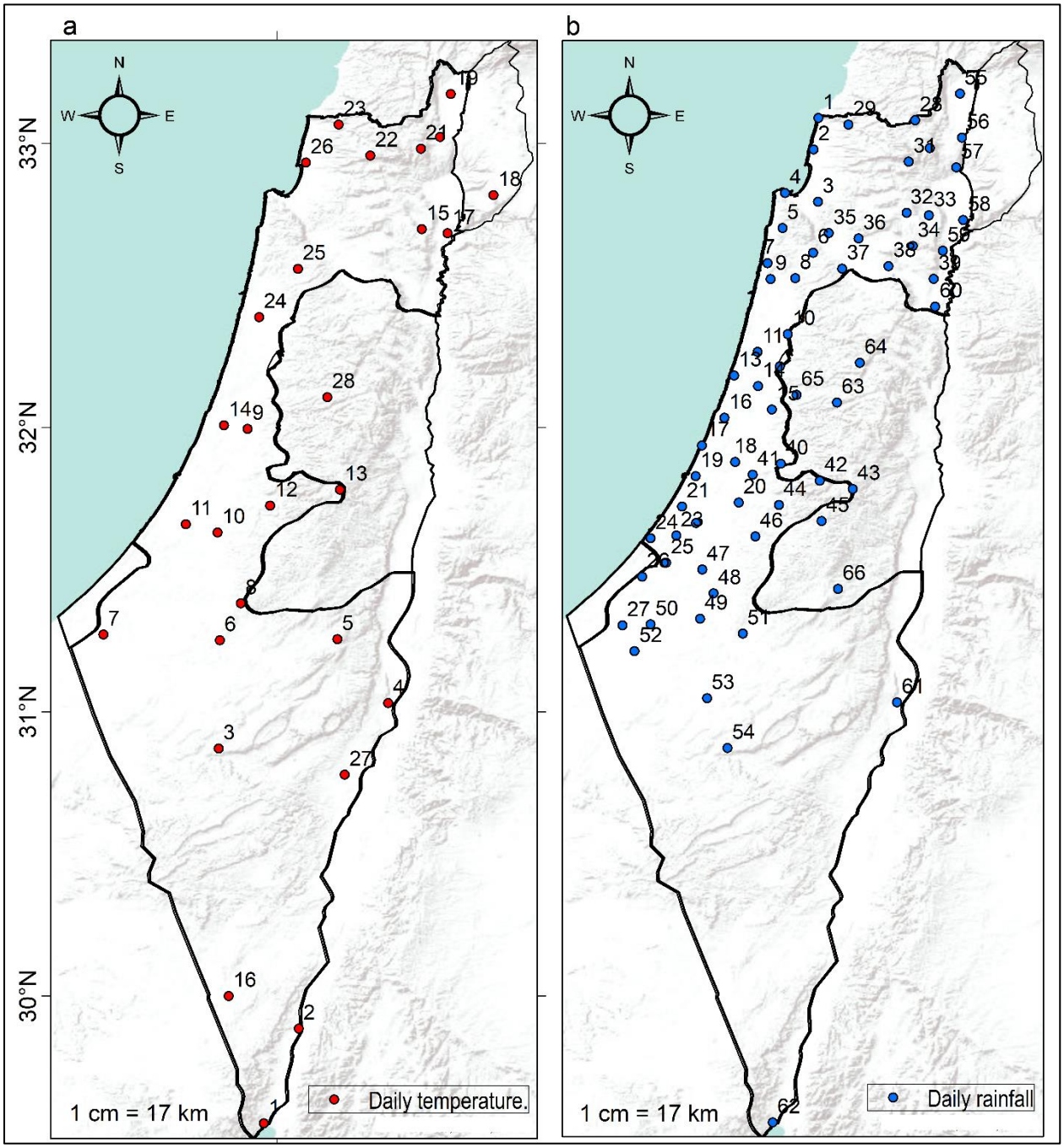

Figure 2.6. The location of the final stations for daily Tmax and Tmin values (a), and daily precipitation totals (b). The numbers indicating the stations and the metadata (names, coordinates, elevation and percent of missing values) are listed in Tables 3 and 4 in Appendix A.

2.3 The teleconnection indices

Seven teleconnection indices that can account for the influence of large-scale circulation patterns on temperatures and precipitation in the study region namely, North Atlantic Oscillation (NAO), East Atlantic pattern (EA), East Atlantic Western Russian pattern (EA-WR), Western

Mediterranean Oscillation (WEMO), El Niño Southern Oscillation (ENSO), North Sea Caspian Pattern (NCP) and Mediterranean Oscillation Indices (MOI) were selected.

Monthly values of these teleconnection indices for the period 1970–2018 were collected from the Climate Prediction Center of the National Oceanic and Atmospheric Administration (http://www.cpc.ncep.noaa.gov/data/teledoc/telecontents.shtml), from Climatic Research Unit of the University of Norwich (https://crudata.uea.ac.uk/cru/data/moi/) for MOI and NCP, and from the Group of climatology of the University of Barcelona (http://www.ub.edu/gc/en/2016/06/08/wemo/) for WEMO. A brief definition of each index, together with a schematic map indicating its location (Figure 2.7) is provided.

The North Atlantic Oscillation (NAO) was first identified in the 1920s by Sir Gilbert Walker (Walker, 1924; Walker et al., 1932), and it is one of the most prominent and recurrent patterns of atmospheric circulation variability over the northern hemisphere (NH, Greatbatch, 2000). It describes a large-scale meridional oscillation between the subtropical anticyclone, near the Azores, and the subpolar low pressure system, near Iceland (Wanner et al., 2001). It influences the climate variability extended from the United States' eastern seaboard to western/central Europe and Siberia and from the Arctic to the subtropical Atlantic, especially during the winter season. The NAO's positive phase reflects below normal geopotential heights and pressures across the high latitudes of the north Atlantic and above normal over the central north Atlantic, the eastern United States, and western Europe. The negative phase reflects the opposite pattern of height and pressure anomalies over these regions. Both phases of the NAO are related to basin-wide changes in the north Atlantic jet stream and storm track's intensity and location and with large-scale modulations of the normal patterns of zonal and meridional heat and moisture transport (Hurrell, 1995). Which, in turn, results in changes in temperature and precipitation patterns, from eastern north America to western and central Europe (Walker et al., 1932; Rogers et al., 1979).

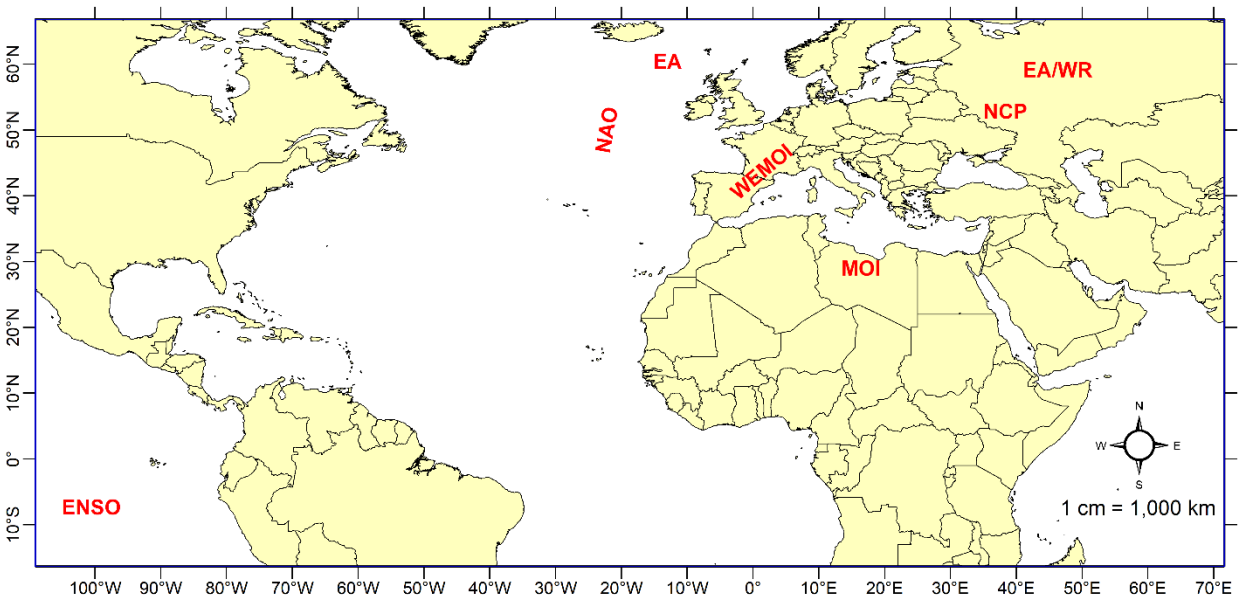

Figure 2.7. Approximate location of the main areas associated to the teleconnection indices used in this study.

The East Atlantic (EA) pattern is the second prominent mode of low-frequency variability over the north Atlantic and appears as a leading mode in all months. It was first described by Wallace et al. (1981) as positive 500 hPa height anomalies over the subtropical north Atlantic and eastern Europe when it is in its positive phase. This atmospheric pattern exhibits a well-defined SLP center of action near [55^0N, 20–35^0W]. Some authors describe the EA as a north-south dipole of anomaly centers spanning the north Atlantic from east to west (Bastos et al., 2016), while others characterize it as a well-defined SLP monopole to the south of Iceland and west of Ireland, near [52.5^0N, 22.5^0W] (Moore et al., 2012; Zubiate et al., 2017).

The East Atlantic/West Russia (EA/WR) (Barnston et al., 1987) pattern affects Eurasia throughout the year. The EA/WR was originally identified through an orthogonally rotated principal component analysis (RPCA), which applied to the monthly-mean geopotential height at 700 hPa. It consists of four main anomaly centers. Additionally, it is characterized by two central large-scale anomalies located over the Caspian Sea and western Europe (Barnston et al., 1987). And it is important not only because its impact extends across the European mainland, including the Mediterranean basin (Xoplaki, 2002; Krichak et al., 2013), but also because this impact reaches the Middle East (Krichak et al., 2002), Siberia, and mid-latitude east Asia as a planetary scale stationary wave pattern. The positive (negative) phase is associated with positive (negative) height anomalies located over Europe and northern China and negative (positive) height anomalies situated over the central north Atlantic and north of the Caspian Sea.

The Western Mediterranean Oscillation (WEMO) (Martin-Vide et al., 2006) is defined by the western Mediterranean basin's synoptic framework and its surrounding area. The WEMO index is constructed as the difference between normalized sea level pressure data at [35^0N–5^0W] (San Fernando, Spain) and [45^0N–10^0E] (Padova, Italy). The positive phase of this index corresponds to the anticyclone over the Azores enclosing the south-west Iberian quadrant and low-pressures in the Liguria Gulf. And its negative phase coincides with a central European anticyclone located north of the Italian Peninsula and a low-pressure center, often cut off from northern latitudes, in the Iberian southwest framework. In the eastern Iberian Peninsula, its effects are dominant compared to those from the NAO and the Atlantic Multi-decadal Oscillation (AMO) (Martín-Vide et al., 2006; Mariotti et al., 2012).

El Niño Southern Oscillation (ENSO) is one of the most important climate phenomena due to its ability to change the global atmospheric circulation, which in turn, influences temperature and precipitation worldwide (Niedzielski et al., 2014; Wallace et al., 1981). The changes in pressure gradient (Southern Oscillation/SO) across the Pacific are associated with changes in temperature and precipitation anomalies on the eastern and western Pacific coasts “El Niño” leading to worldwide climate variability (IPCC, 2007b). It is inherently caused by the interaction between the atmosphere and the ocean (Nicholls, 2015). El Niño refers to unusually warm ocean temperature that occurs every 2-7 years around Christmas time along Peruvian coast, extending into the equatorial eastern and central Pacific Ocean. The southern oscillation, named by its discover -Sir Gilbert Walker- on the other hand, refers to a “seesaw” of the atmospheric pressure between the Pacific and Indian oceans. The acronym ENSO has been widely used to describe this

interannual climate fluctuation, emphasizing the inherent ocean-atmosphere coupling (Zebiak et al., 2015).

North Sea Caspian Pattern (NCP) index (Kutiel et al., 2002) can be defined as the normalized 500 hPa pressure difference between averages of North Sea [0^0E, 55^0N and 10^0E, 55^0N] and north Caspian [50^0E, 45^0N and 60^0E, 45^0N] centers of action. Kutiel et al. (2002) have stated that the anomalous circulation in the eastern Mediterranean basin showed an increased southwesterly circulation during the NCP in the negative phase and an increased northeasterly circulation during the NCP in the positive phase. The negative phase of the NCP was defined for all cases when the standard score of the difference between the two poles was less than -0.5, and the positive case was defined for all cases when the standard score was greater than 0.5.

The Mediterranean Oscillation Index (MOI) can be calculated based on sea level pressure differences between Gibraltar northern frontier [36.1^0N, 5.3^0W] and Lod Airport Israel [32.0^0N, 34.5^0E] (Palutikof et al., 2003). There are different versions of this index, depending on the reference points (Criado-Aldeanueva et al., 2013). Conte et al. (1989) developed the MOI as the difference between the standardized 500 hPa geopotential heights of Algiers [36.4^0N, 3.1^0E] and Cairo [30.1^0N, 31.4^0E]. Brunetti et al. (2002) designed a specific MOI version for the central Mediterranean using the difference between Marseille's normalized sea level pressure and that of Jerusalem. This index was found to present a good correlation between total precipitation and the number of wet days in Italy (Brunetti et al., 2002). The MOI applied in this study is based on the normalized pressure difference between the Algiers and Cairo dipoles (Conte et al., 1989).

2.4 The SST and SLP data

The monthly mean data for the Sea Surface Temperature (SST) were obtained from the Hadley Centre Global Sea Ice and Sea Surface Temperature (HadISST, Rayner et al., 2003) for the period 1970-2018, with a spatial resolution of 1^0x 1^0 and a geographical domain encompassed between [70^0W-50^0E, 0^0N-60^0N]. On the other hand, monthly mean data for the Sea Level Pressure (SLP) were downloaded from the NCEP reanalysis (Kalnay et al., 1996) for the period 1970-2018, with a resolution of 2.5^0x 2.5^0 and a geographic domain covering [0^0-90^0N, 180^0W-180^0E]. The SST data composed a gridded set of 4829 cells and the SLP data of 5329 cells.

CHAPTER 3

METHODOLOGY

In this chapter, the methodology used in the Thesis is explicated. Methods about the calculation of trends, the obtaining of extreme temperature and precipitation indices, and the co-variability analysis, among other statistical techniques, are fully described and discussed.

3.1 Trend detection method

The trend detection can be carried out using parametric or nonparametric methods. Parametric methods are more suitable for normally distributed data (Onoz and Bayazit, 2003). Nonparametric methods lead to more reliable results for non-normally distributed data such as the hydrological and meteorological data (Hirsch et al., 1992; Salas, 1993). In this Thesis, the trend analysis was performed using the Sen's slope estimator (Sen, 1968); meanwhile, the Mann-Kendall (MK) nonparametric test (Mann, 1945; Kendall, 1975) was applied to evaluate the trend significance. The MK test is a rank-based procedure, less sensitive to the non-normality of the distribution, and less affected by outliers in the series (Birsan et al. 2005; Zhang et al., 2000; Ouarda et al., 2014). However, some assumptions are associated with this test, such as independent time series data (Mulugeta et al., 2019; Razavi et al., 2016). The presence of significant serial correlation in hydroclimatic time series affects trend testing resulting, for example, an increased detections of trends (Type II errors) or a high rejection rate of the null hypothesis (Type I error) (Mulugeta et al., 2019; Yue et al. 2002). All the time series were pre-whitened in order to correctly apply the MK test for serial autocorrelation (Pingale et al., 2016; Abeysingha et al., 2016; Wagesho et al., 2013; Hamed, 2009, Zhang et al., 2000; Wang and Swail, 2001; von Storch, 1995; Vincent, 2006; Yue et al. 2002).

According to the MK test, the null hypothesis indicates no trend (the time series is independent and randomly ordered), and the alternative hypothesis indicates a trend (Onoz and Bayazit, 2012). The nonparametric MK test has been widely used to assess the monotonic trend in climatic studies

(Salameh et al., 2018; Jain et al., 2012; Rajand, 2012; Alexander et al., 2006, Kunkel et al., 1999, Klein Tank and Können, 2003; New et al., 2006; Zhang et al., 2009; Zhang et al., 2015; Gu et al., 2017; Deng et al., 2018; Sarricolea et al., 2019). The detailed calculation procedure can be found in Hirsch et al. (1982) and Yue et al. (2002). The related equations for calculating the MK statistic, S, is the following:

$$S = \sum_{i=1}^{n-1} \sum_{j=i+1}^{n} sign\ (T_{j-}\ T_i) \tag{3.1}$$

where n is the length of the time series, T_j and T_i are the ith and jth data point in the time series ($j > i$), respectively. The $sign()$ is the sign function which can be defined as:

$$sign(Tj\ -\ Ti) = \begin{cases} 1\ if\ Tj\ -\ Ti > 0 \\ 0\ ifTj\ -\ Ti = 0 \\ -1\ if\ Tj\ -\ Ti < 0 \end{cases} \tag{3.2}$$

Under the assumption that the data are independent and identically distributed, the mean of the *S* statistic is given by (Kendall, 1975):

$$E(S) = 0 \tag{3.3}$$

E is the expected value of the S, and the variance (σ^2) is obtained as:

$$\sigma^2 = \frac{n(n-1)(2n+5) - \sum_{k=1}^{m}(i)(i-1)(2i+5)}{18} \tag{3.4}$$

In which m is the number of tied groups and i is the number of ties for the kth value.

The standard test statistic Z_s is calculated as follows:

$$Z_s = \begin{cases} \frac{s-1}{\sigma}\ for\ S > 0 \\ 0\ for\ S = 0 \\ \frac{s+1}{\sigma}\ for\ S < 0 \end{cases} \tag{3.5}$$

The Z_s is used as a measure of significance of trend when the sample size $n > 10$. A positive or negative value of Z_s indicates an upward or downward trend, respectively. The statistical significance of the trends was assessed at the 0.1, 0.05, 0.01, and 0.001 levels.

3.2 Sen's approach

The Sen's estimator is used for determining the magnitude of a trend in climatic studies. It is a non-parametric alternative to linear regression slope and is usually used in conjunction with the MK test (Lv et al., 2016). The Sen's slope estimator is the median of all pairwise slopes in the data set (Fortin and Hétu, 2014). This method can be calculated as (Some'e et al., 2012; Tabri and Aghajanloo, 2013; Xu et al., 2003):

$$Qmed = median\,(Q), \tag{3.6}$$

$$Q = \frac{X_j - X_i}{j - i}, i < j, \tag{3.7}$$

where the X_j and X_i are data points at time j and i, respectively.

3.3 Analysis of sub-periodical variation

For analysis of sub-periodical variation, Cramer's test (Lawson et al., 1981; WMO, 1966) was used to compare the means of the sub-periods with the mean of the entire period. The Cramer's t-statistics is defined as the departure of the sub-period mean from the long-term mean, divided by the long-term standard deviation (Sahai et al., 2003). The tk statistic is computed as:

$$t_{\mathrm{k}} = l_{\mathrm{k}} \left[(n\,(N-2) \,/\, \{N - n\,(1 + l_{\mathrm{k}}{}^2)\} \right] ½ \tag{3.8}$$

where n and N are the number of years constituting the sub-period and the entire period, respectively, and l_{k} is a standardized measure of difference between the means of sub-period and total period obtained as:

$$l_{\mathrm{k}} = (m_{\mathrm{k}} - \mu)/\sigma \tag{3.9}$$

where μ is the mean and σ is the standard deviation of the series for the total number of years (N); m_{k} is the mean for each successive n-year. For significance of Cramer's t_{k} value at 5% level, the required t value is ±1.96 or more (Mooley et al., 1984).

3.4 Change point detection

In hydroclimatic time series data, identifying the starting period of the significant trends is also of great interest. The sequential Mann-Kendall (SMK) test, introduced by Sneyers (1990), is typically used to define the start of any notable change or significant trend in the considered time series (Lu et al. 2004; Partal and Kahya 2006; Tabari et al. 2011; Shifteh Somee et al. 2012). The SMK test is computed using ranked values, y_i of the original values$(X_1, X_2, X_3, \ldots\ldots, X_n)$. The magnitudes of y_i $(i = 1, 2, 3, \ldots, n)$ are compared with y_j $(j = 1, 2, 3, \ldots, i-1)$. For each comparison, the cases where $y_i > y_j$ are counted and denoted by n_i. A statistic t_i can, therefore, be defined as (Bisai et al,. 2014; Gerstengarbe and Werner, 1999; Adarsh and Janga Reddy, 2015):

$$t_i = \sum_{j=1}^{i} n_i \tag{3.10}$$

The distribution of test statistic ti has a mean as

$$E(t_i) = \frac{i(i-1)}{4} \tag{2.11}$$

and a variance as

$$Var(t_i) = \frac{(i(i-1)(2i+5))}{72} \tag{3.12}$$

The sequential values of a reduced or standardized variable, called statistic $u(ti)$ is calculated for each of the test statistic variable ti as follows:

$$u(t_i) = \frac{t_i - E(t_i)}{\sqrt{var(t_i)}} \quad (3.13)$$

While the forward sequential statistic, $u(t_i)$ is estimated using the original time series $(X1, X2, X3, \ldots\ldots, Xn)$, values of the backward sequential statistic, $u'(t_i)$ are estimated in the same manner but starting from end of the series. In estimating $u'(t_i)$ the time series is resorted so that last value of the original time series comes first

When $u(t)$ and $u'(t)$ are plotted, the intersection of curves $u(t)$ and $u'(t)$ within ±1.96 (that corresponds to the bounds at 5% significance level) of the test statistic indicates the approximate time of occurrence of the trend (Dipak. et al., 2014). If $u(t)$ exceeded the confidence line, there was a significant upward or downward trend in the time series (Liu et al., 2008; Olmo et al., 1995).

3.5 Principal Component Analysis

The Principal Component Analysis (PCA) is a multivariate analysis technique that identifies and obtains the dominant spatio-temporal patterns of the simultaneous variations of a field or variable (Preisendorfer, 1998). Climatologists have widely used this method as a tool in the study of the spatial and temporal variability of climatic fields (Cerón et al., 2020; Nair and Mohanty, 2013; Santos et al. 2017). Its fundamental objective is to reduce the multidimensional data sets analyzed. The purpose of PCA is to transform the highly associated variables in the original data into smaller independent or unrelated variables, called Principal Components (PCs), and to use these few variables to reflect most of the variability in the original data (Zhang et al., 2020; Keyantash and Dracup, 2004). Thus, the PCA consists of an orthogonal linear transformation of the original data set to identify new variables, which are linear combinations of the original data set, subject to the maximization of covariance or correlation (von Storch and Zwiers, 1999). Each PC explains percentage of variance of the original data, with the first PC explaining the greatest amount of variance.

In this study, the PCA is conducted using Varimax rotation on standardized and detrended annual and seasonal temperatures and precipitation time series. The Varimax rotation is an orthogonal method used to maximize the variance between the PCs, and it is used to identify areas with independent temperature and precipitation variability. The number of PCs to retain was determined based on the North rule of Thumb (North et al., 1982), based on the degeneration of eigenvalues. If the spacing between two consecutive eigenvalues is smaller than the error of the first one, they cannot be considered different true eigenvalues. The loading corresponding to each data set was mapped to show the spatial patterns of variability across the Levant region. A brief outline of the important features of PCA is given below:

If the data matrix is defined as:

$$Z = (z_{ij}: i = 1, \ldots\ldots n, j = 1, \ldots\ldots p) \quad (3.14)$$

And the symmetric correlation matrix as (Preisendorfer, 1988):

$$R = Z^T Z \tag{3.15}$$

The `p' PCs of Z are the columns of an $(n(time)\ x\ p(stations))$ matrix F containing PC scores obtained by linear combination of the original variables with conditions of mutual orthogonality and maximum variance and given by:

$$F = ZA \tag{3.16}$$

where `$i$' and `j' represent individuals or cases and variables, respectively, superscript `T' represents the transpose of the matrix, and matrix A contains unit length eigenvectors providing PC loadings. The eigenvectors are uncorrelated and they are orthogonal to each other. Because of this, they are commonly named Empirical Orthogonal Function (EOFs).
The basic eigen-structure of the correlation matrix can be represented as

$$ADA^T \tag{3.17}$$

where D is the diagonal matrix of eigenvalues of R arranged in descending order of magnitude. It can be shown that variances of column vectors of F are numerically equal to the elements of matrix D.
The sum of variances is thus $trace(D)$ or $trace(R)$ and the proportion of the total variance attributed to each PC is

$$[\{di/trace(D)\}x100]\ percent, \tag{3.18}$$

whered_i is ith elements of D.

In PCA, the matrices A and F are further rescaled according to:

$$L = AD^{1/2} \tag{3.19}$$

$$F = FD^{1/2} \tag{3.20}$$

so that elements of matrix L provide correlation between PCs and original variables and matrix F contains standardised PC scores having zero means and unit variances.

3.6 The K-means clustering algorithm

The K-means algorithm (Mac Queen, 1967; Hartigan and Wong, 1979) is used to reveal structures in the data set and minimize large dimension data sets. It is an indirect clustering method relies on the similarity measure between observations based on the nearest neighbor method (Xiong et al. 2011; Tan et al. 2019). This algorithm distributes n observations into k clusters in which each observation belongs to the cluster with the nearest centroid, and the similarity between clusters is lower. In this algorithm, the number of clusters (K) is randomly selected among n observations, each of which represent the centroid of a cluster. The n remaining observations are allocated to

the closest cluster based on the distance between the observation and each cluster's centroid. After that, the centers or centroids are recalculated, and observation reallocates until the criterion function converges or remain constant (Jinming et al., 2015; Kim and Ahn 2008; Salehnia et al., 2019). More details about this method are in (Fränti and Sieranoja, 2018; Everitt et al. 2011; Jain, 2010).

In practice, the most popular similarity measure is Euclidean distance due to its computational simplicity and sum-squared error (SSE) is used as the objective function. The error for each observation that represents the Euclidean distance to the nearest centroid are calculated, and then the sum of squared errors (SSE) are calculated as follow (Liu et al., 2013; Zeng et al., 2020):

$$SST = \sum_{j=1}^{k} \sum_{i=1}^{n} d_{ij}(x_i, c_j) \tag{3.21}$$

where d is the Euclidean distance. The centroid of the ith cluster is defined by formula

$$c_i = \frac{1}{n_i} \sum_{j=1}^{n_i} x_i \tag{3.22}$$

where $x = (x_i 1, x_i 2, \dots, x_i d)$.

It was mainly used to identify the thresholds that separate stations into homogeneous regions. The K-means clustering technique was applied to the rotated PC scores (Mills, 1995). The homogeneity of each cluster was studied by the ratio value of between-classes variance and total variance. If the ratio is high, the corresponding cluster must be considered homogeneous and vice versa. The optimal number of clusters was decided using the R "NbClust" Package (Charrad et al., 2014). It provides 30 indexes for determining the optimal number of clusters in a data set, and it offers the best clustering scheme from different results to the user.

3.7 Extreme temperature and precipitation indices

In this study, 16 extreme indices derived from daily maximum and minimum temperatures (Table 4.1), and 15 extreme precipitation indices (Table 4.2) were selected from a total of 27 temperature and precipitation indices recommended by the Expert Team on Climate Change Detection Monitoring and Indices (ETCCDI) (Folland et al., 1999; Alexander and Herold, 2015; Peterson et al., 2001).

The extreme temperature indices can be divided into four categories (Fonseca et al., 2016; Scorzini et al., 2018): 1. Absolute extreme temperature (TXx, TXn, TNx, TNn and ETR); 2. Percentile-based extreme temperature (TX90p, TX10p, TN90p and TN10p); 3. Duration-based (warm spell duration index (WSDI) and cold spell duration index (CSDI)); and 4. Fixed threshold (SU25/30, TR20/25 and frost days). Similarly, the extreme precipitation indices can be divided into five broad categories (Alexander et al., 2006): 1. Threshold indices (R1mm, R10mm, R20mm, and R50mm), 2. Absolute indices (e.g., Rx1day, Rx3day, and Rx5day), 3. Extreme percent (R95P and R99P), 4. Duration indices (CDD and CWD), and 5. Other indices (PRCPTOT, SDII, R95Ptot and R99Ptot). For the study area, the thresholds 30ºC and 25ºC were applied for very summer days (SU30) and very tropical nights (TR25) indices, respectively, based on the long-term summer averages for

Tmax and Tmin, and in a detailed review of the literature for the surrounding regions such as the Arabian Peninsula and Saudi Arabia (Athar, 2014; Attada et al., 2019), Iran (Rahimzadeh et al., 2009; Rahimi and Hejabi, 2018) or Turkey (Erlat and Türkes¸, 2013). In addition, the derived extreme precipitation indices such as consecutive dry days (CDD) and consecutive wet days (CDD) were performed for the wet months (e.g., CDD/CWD-DJF, CDD/CWD-MAM, and CDD/CWD-DJFMAM).

All extreme temperature indices were computed at annual time scale, and at seasonal scale for absolute and percentile indices as well as for SU25/30 and TR20/25 indices. For extreme rainfall indices, the indices were computed at annual time scale, and at seasonal scale for PRCPTOT, R1mm, R10mm, R20mm, RX1day, RX3day, RX5day, and SDII indices. Days from December 1 to the end of February were considered for winter (win), March–April–May for spring (spr), June–July–August for summer (sum), and from September to November for autumn (aut).

A brief description and definition of each index with acronyms are given in Tables 4.1 and 4.2, and further details are available in Zhang et al. (2011) and http:// etccdi.pacificclimate.org/list_27_indices.shtml. Extreme indices were performed using the software package RClimDex v1.0 (Zhang and Yang, 2004) developed at the Climate Research Branch of the Meteorological Service of Canada. The software and documentation are available at http://etccdi.pacificclimate.org. Such software performs the calculations using daily data and provides monthly and annual data of the indices

Index	Indicator name	Description	Index type	Unit
TXx	Max Tmax	Maximum value of daily maximum temperature	Absolut	ºC
TXn	Min Tmax	Minimum value of daily maximum temperature	Absolut	ºC
TNx	Max Tmin	Minimum value of daily minimum temperature	Absolut	ºC
TNn	Min Tmin	Maximum value of daily minimum temperature	Absolut	ºC
ETR	Range	MaxTmax – MinTmin	Absolut	ºC
TX90p	Warm days	Count of days when Tmax >90th percentile	Percentile	Day
TX10p	Cold days	Count of days when Tmax < 10th percentile	Percentile	Day
TN90p	Warm nights	Count of days when Tmin >90th percentile	Percentile	Day
TN90p	Cold nights	Count of days when Tmin < 10th percentile	Percentile	Day
WSDI	Warm spell duration index	Count of days with at least six consecutive days when Tmax >90th percentile	Percentile Duration	Day
CSDI	Cold spell duration index	Count of days with at least six consecutive days when Tmin <10th percentile	Percentile Duration	Day
SU	Summer days	Count of days when Tmax >25 ∘C	Threshold	Day
SU30	very summer days	Count of days when Tmax >30 ∘C	Threshold	Day
FD	Frost days	Count of days when Tmin <0 ∘C	Threshold	Day
TR	Tropical nights	Count of days when Tmin >20 ∘C	Threshold	Day
TR25	very tropical nights	Count of days when Tmin >25 ∘C	Threshold	Day

Table 3.1. Definition of extreme temperature indices used in this study.

Index	Indicator name	Definition	Unit
PRCPTOT	Annual total wet-day precipitation	Annual total precipitation from days ≥1 mm	Mm
R1mm	Number of wet days	Annual count of days when precipitation ≥1 mm	Days
R10mm	Number of heavy precipitation days	Annual count of days when precipitation ≥10 mm	Days
R20mm	Number of very heavy precipitation days	Annual count of days when precipitation ≥20 mm	Days
R50mm	Number of days above 50 mm	Annual count of days when precipitation ≥50 mm	Days
R95P	Very wet days	Annual total precipitation when RR > 95th percentile	mm
R99P	Extremely wet days	Annual total precipitation when RR > 99th percentile	mm
R95Ptot	Contribution from very wet days	100*R95P/PRCPTOT	%
R99Ptot	Contribution from extremely wet days	100*R99P/PRCPTOT	%
RX1day	Max 1-day precipitation amount	Monthly maximum 1-day precipitation	mm
RX3day	Max 3-day precipitation amount	Monthly maximum consecutive 3-day precipitation	mm
RX5day	Max 5-day precipitation amount	Monthly maximum consecutive 5-day precipitation	mm
SDII	Simple daily intensity index	Annual total precipitation divided by the number of wet days (defined as precipitation ≥1 mm) in the year	mm/day
CWD	Consecutive wet days	Maximum number of consecutive days when precipitation ≥1 mm	Days
CDD	Consecutive dry days	Maximum number of consecutive days when precipitation <1 mm	Days
CDD-DJF	Consecutive dry days	Maximum number of consecutive days when precipitation <1 mm, between December to February	Days
CDD-NDJFM	Consecutive dry days	Maximum number of consecutive days when precipitation <1 mm between November to March	Days

Table 3.2. Description of extreme precipitation indices used in this study.

3.8 The teleconnection patterns influence

The influence of teleconnection indices on the Levant's seasonal Tmax and Tmin and precipitation was examined by mean of Pearson correlation as in other studies (Efthymiadis et al., 2011; Unkaševic and Tošic, 2013; Popov et al., 2018) based on detrended series for each station. In addition, the seasonal averaged time series for temperatures and precipitations were calculated for entire Levant and its sub regions "Jordan, Palestine/Israel, Syria and Lebanon". After that, the correlation was also applied between these averaged time series and the teleconnection patterns. The statistical significance of the correlations was assessed at the 5% significance level.

The teleconnection maps, which describes the linkage between a region of interest and other points in the domain that are farther than the de-correlation length scale of the variable were constructed and analyzed. Teleconnection maps thus provide information about the structure of recurrent climate variability that is characterized by the correlation at a distance feature.

In addition, the frequency of significant correlations and their magnitudes between teleconnection patterns and the seasonal averaged time series for entire Levant and its sub regions were also calculated and analyzed. Those teleconnection indices excluded from teleconnection maps did not

show significant concurrent correlations with any of the meteorological stations or they showed very small frequency of significant correlations. RStudio (version 3.6.2) and ArcMap (version 10.4.1) software were used to perform all calculations and to produce teleconnection maps, respectively.

3.9 Co-variability analysis

To determine the mechanisms governing climatic variations, it is essential to characterize the large-scale interactions between the ocean and the overlying atmosphere. In this thesis, the possible relationship between the seasonal temperatures and precipitation in the Levant region and two indicators of climate variability, sea surface temperatures (SST) and sea level pressure (SLP), will be evaluated to identify significant associated regions have a coupled variability. The coupled relationships between two spatial-temporal fields (such as SST-winter Tmax, SLP-spring rainfall) were examined using Singular Value Decomposition (SVD).

The use of SVD in the meteorological context is quite recent. Prohaska (1976) was the first to use it to study the relationship between two meteorological fields. After that, not many studies using SVD to relate geophysical fields were published until Bretherton et al. (1992) and its companion paper, Wallace et al. (1992). After that, the use of SVD for climatological purposes increased considerably. It has been used in numerous studies to identify coherent spatial patterns of climate variability in regions around the world for several variables such as drought (Rajagopalan et al., 2000), Precipitation (Wang et al., 2000; Uvo et al., 1998; Enfield et al., 1999), streamflow (Soukup et al., 2009; Sagarika et al., 2015), runoff (McCabe et al., 2014).

The SVD has usually been applied to two data fields together by using the cross-covariance matrix to identify modes that explain the greatest covariance between such fields (Martín et al., 2011, Venegas et al 1995). Detailed discussions on SVD analyses can be found in Bretherton et al. (1992), Wallace et al. (1992), von Storch and Navarra (1995), and Newman and Sardeshmukh (1995). In this study, the calculations related to SVD followed these steps:-

1- A matrix of standardized and detrended SST, SLP, seasonal (Tmax, Tmin) and precipitation were developed.
2- The cross-covariance matrix "C" was then computed for each coupled spatio-temporal matrices (such as SST-summer Tmax, SLP-winter rainfall). Let's X and Y be the left and right data fields representing the climatic variable, SST/SLP and seasonal temperatures/precipitation, respectively. The dimension of X is $N \times m_\chi$ and the dimension of Y is $N \times m_\gamma$, where N represents times (years), m_χ the number of grid points and m_γ the number of gauging stations. The temporal cross-covariance matrix can be constructed as:

$$C = XY = \begin{bmatrix} X1Y1 & \cdots & X1Ym_\gamma \\ \vdots & \ddots & \vdots \\ Xm_\chi Y1 & \cdots & Xm_\chi Ym_\gamma \end{bmatrix} \quad (3.23)$$

Which has m_χ x m_γ dimension, with each element of the matrix, <$XiYj$>, corresponding to the spatial cross-covariance between the time series Xi and Yj at grid i and station j, respectively.

3- After that, the SVD was applied to the cross-covariance matrices and physical information or SVD coefficients regarding the relationship between the coupled fields was obtained. The resulting SVD of the cross-covariance matrix created two matrices of singular vectors "U and V" and one matrix of singular values "L". Based on the cross-covariance matrix, matrices U, V and L are related by:

$$C = ULV^{\mathrm{T}} \tag{3.24}$$

The singular vectors for X are the columns of U (often-called left patterns), and the singular vectors of Y are the columns of V (right patterns). Each pair of singular vectors is a mode of co-variability between the fields X and Y.

These vectors, a set of Nx dimensional orthogonal vectors U_{k} $(k = 1, .., Nx)$ for X, and a set of Ny dimensional orthogonal vectors Vq $(q = 1, \dots, Ny)$ for Y, are determined so the covariance between the projections of the fields on them is maximized, subjected to orthogonalty:

$$UU^{\mathrm{T}} = I \tag{3.25}$$

$$VV^{\mathrm{T}} = I \tag{3.26}$$

4. The matrix L is an $m_\chi \, x \, m_\gamma$ diagonal matrix holding the singular values. Each pair of singular vectors (ui, vi) corresponds to a singular value in L. Bretherton et al. (1992) defines the squared covariance fraction (SCF_{k}) as a useful measurement for comparing the relative importance of modes in the decomposition. The relative importance of each SVD mode is indicated by the percentage of square covariance (SC) for the associated mode. For each singular value. This quantity is defined by:

$$SCF_{\mathrm{k}} = \frac{{I_{\mathrm{k}}}^2}{\sum_{i=1}^{R} {I_{\mathrm{i}}}^2} \tag{3.27}$$

The modes are ordered with respect to their singular values so that the first pair accounts for the largest SCF_{k} and the remaining pairs describe a maximum fraction unexplained by the previous pairs.

5. As mentions before, the two matrices of singular vectors "U" and "V" generally referred to as the left (SST/SLP) matrix and the right (seasonal temperatures or rainfall) matrix. The columns of the left matrix was projected onto the standardized (SST/SLP) matrix and the columns of the right matrix was projected onto the standardized (seasonal temperatures or rainfall) matrix. These are the temporal expansion series of the left "A" and right "B" fields, respectively, , which describe the time variability of each mode, and are given by

$$A = XU \tag{3.28}$$

$$B = YV \tag{3.29}$$

The Kth columns of the A and B matrices contain the expansion coefficients for the kth SVD mode for fields X and Y, respectively. Since both U and V are orthogonal, the original fields can be easily reconstructed as:

$$X = AU^{\mathrm{T}} \tag{3.30}$$

$$Y = BV^{\mathrm{T}} \tag{3.31}$$

Hence, using equations (1), (2), (7) and (8), the temporal covariance between the two fields can be expressed in terms of the expansion coefficients as follows:

$$A^{\mathrm{T}} B = L \tag{3.32}$$

That is, an expansion coefficient of the left field is correlated only with the time series of the same mode in the right field.

6. After that, the correlation between the expansion coefficients corresponding to the left and right fields, called string of coupling, (STR_{k}) was calculated. For example, in case of the kth mode:

$$STR_{\mathrm{k}} = \mathrm{r}A_{\mathrm{k}}B_{\mathrm{k}} \tag{3.33}$$

Moreover, the total variance of individual field, explained by each mode, was also calculated by determine the eigenvalues of the covariance matrix for the left/right expansion coefficient and divided by its trace.

7. The left homogeneous correlation values (for the 1st mode) were determined by correlating the left matrix values (here SST/SLP) with the left field's 1st temporal expansion series. The right heterogeneous correlation values (for the 1st mode) were determined by correlating the right matrix (seasonal temperatures or rainfall) with the left field's 1st temporal expansion series. The homogenous correlation map is an indicator of the geographic localization of covering parts of the field. In contrast, the heterogeneous correlation map indicates how well the grid points of one field relate to the other's kth expansion coefficient. In this study, special; attention is given to the heterogeneous correlation maps as we seek the influence of SST or SLP over temperature and precipitation.
8. The SCF and STR are only meaningful when they are associated with significant SC. Newman and Sardeshmukh (1995) suggest, from a different perspective, that SVD modes are physically meaningful only if they explain significant portions of the variance of their respective fields. We assess the statistical robustness of the results obtained from the SVD analysis, with a significance test using a Monte Carlo approach focusing on the square covariance (SC) rather than the SCF or correlation coefficient (Venegas et al., 1997). The SC is a direct measure of the relationship between SST/SLP-rainfall and temperature; whereas, the SCF and the correlation coefficient indirectly measure the relationship between the coupled SVD patterns. To test the significance of the SVD analysis, a Monte Carlo simulation is performed by randomizing the SST/SLP in time. After that, the SVD

analysis is performed 100 times. The randomized SVD analyses exceed the number of times the original squared covariance (SC) indicates its significance level. For example, if the randomized SC exceeds the original SC less than five times, then the significance level would be 95%.

3.10 Standardized Precipitation Index (SPI)

This study uses the SPI to understand meteorological droughts in the study region. There are many drought indices available, such as the Palmer drought severity index (PDSI), China Z index (CZI), effective drought index (EDI), and the Standardized Precipitation Evapotranspiration index (SPEI) (Palmer 1965; Kendall and Stuart, 1977; Byun and Wilhite, 1999; Vicente-Serrano et al., 2010; Tian et al. 2018). The SPI is a multi-timescale drought index developed by McKee et al. (1993) that uses the monthly precipitation aggregates over a range of time scales (1, 3, 6, 12, 18, and 24 months, etc.) to describe precipitation changes. The SPI values refer to the strength of the anomaly, with positive values indicating water surpluses due to above-normal rainfall and negative values indicating water shortages due to below-normal precipitation (Brito et al., 2018; Yenigun and Ibrahim, 2019). It was chosen because it has been widely used and recommended for characterizing meteorological droughts by the World Meteorological Organization (WMO), as well as by international meteorological and drought monitoring centers (WMO, 2012; Vogt et al., 2011; Svoboda et al., 2002). It is also a flexible indicator with robust underlying probability functions that can be calculated for many timescales, has high spatial coherence, only requires precipitation data, and SPI values from different climatic regions can be easily and directly compared (Kim et al., 2014; Ford and Labosier, 2014; Spinoni et al., 2014).

The first step entails estimating the parameters for a specific distribution of precipitation totals for the observed stations and over the desired timescale. Despite the fact that no single distribution is optimal, the Gamma distribution has proven to be the most reliable and is thus the most commonly used (Guttman 1999; McKee et al., 1993; Wilks, 1995):

$$G\,(x) = \frac{1}{\beta^{\gamma}\mathbb{\Gamma}(\gamma)} \int_0^x x^{\gamma-1} e^{-\frac{x}{\beta}}\ x > 0 \tag{3.34}$$

where γ is the shape parameter, β is the scale one, x is the precipitation amount, and $\mathbb{\Gamma}(\gamma)$ is the Gama function. The γ and β can be obtained by the maximum likelihood estimation method, as follow.

$$\gamma = \frac{1+\sqrt{1+4A/3}}{4A} \tag{3.35}$$

$$A = \ln(x) - \frac{1}{n}\sum_{i=1}^{n} \ln x_i \tag{3.36}$$

$$\beta = \bar{x}/\gamma \tag{3.37}$$

Where $\bar{x}$ is the mean value of the precipitation, n is the number of observations, and x_i is the quantity of precipitation in the sequence of data. The gamma distribution is undefined for $x = 0$, so the cumulative probability distribution given a zero value is derived as follows:

$$H(x) = q + (1 - q)G(x) \quad (3.38)$$

Where q is the probability of no precipitation.

The cumulative probability distribution is then transformed into the standard normal distribution to calculate SPI (Türkeş and Tatlı, 2019). More detailed descriptions of the SPI calculation are provided in (McKee et al., 1993; Wu et al., 2005; Guttman, 1999; Gumus and Algin, 2017). McKee et al. (1993) have classified the SPI values into seven levels as shown in Table 3.3.

SPI value	Class
SPI ≥2.0	Extremely wet
1.5 ≤ SPI < 2.0	Severe wet
1.0 ≤ SPI < 1.50	Moderately wet
0 < SPI < 1	Slightly wet
−1.0 < SPI < 0	Slightly dry
−1.50 < SPI ≤ −1.0	Moderately drought
−2.0 < SPI ≤ −1.5	Severe drought
SPI ≤ −2.0	Extremely drought

Table 3.3. Classification used for SPI by McKee et al. (1993).

For this study, the drought event is defined as a period in which the SPI is continuously negative and reaches a value of −1.0 or less (McKee et al., 1993). The drought frequency (DF) is defined by the number of drought events (SPI≤ -1) per time period (49 years) (Tian and Quiring, 2019). The drought duration (DR) is the period length in which the SPI is continuously negative, starting when the SPI values is equal to -1 and ending when the SPI values turn out to be positive, in this analysis for at least two consecutive months (Mishra et al., 2009; Spinoni et al., 2014). The drought severity (DS) was defined as the sum of the absolute monthly SPI values when they are ≤−1(Tan et al., 2015; Spinoni et al., 2014).

CHAPTER 4

TREND ANALYSIS OF MAXIMUM AND MINIMUM TEMPERATURES

This chapter aims to analyze the spatial and temporal changes in the annual, seasonal, and monthly trends of the maximum, minimum, and diurnal temperatures range as indicators of climate change over the entire Levant in 1987-2018. The trends are analyzed based on observational data from 60 stations at multiple time and space scales. The relationships between seven large-scale circulation patterns and seasonal temperature are also investigated where the correlation maps are constructed and analyzed.

4.1 Introduction

At the global and continental scales, most of the warming observed in recent decades is attributed to anthropogenic influences (Houghton et al., 2001; Stott, 2003; IPCC, 2007, 2013). During the 1906-2005 and 1850-2012 periods, global mean temperature has increased by 0.74°C and 0.85°C, respectively, and the rate of warming during the last 55 years of the 1906-2005 period is nearly twice that of the first half (0.12±0.03°C/decade vs. 0.07±0.02°C/decade) (Trenberth et al., 2007; IPCC, 2013). Moreover, global warming has been remarkably rapid since the mid-1970s (WMO 2006).

In the eastern Mediterranean, temperature showed a negative trend during 1950-1990 (e.g., this decrease exceeds -0.2°C/decade in southeastern Turkey) (Sahsamanoglou and Makrogiannis, 1992; Repapis and Philandras, 1988; Proedrou et al., 1997; Domroes and El-Tantawi, 2005). In addition, Ben Gai et al. (1999), analyzed the trends of maximum and minimum temperatures in Israel using data from 40 stations for the period 1960-1994, and the results showed a significant ($p < 0.1$) decreasing trend in annual maximum and minimum temperatures by -0.03 and -0.05°C/decade, respectively. Hasanean et al. (2001), investigated the surface air temperature

variations in eastern Mediterranean using the annual temperature data from 8 stations before 1991, and the decreasing temperature trends were observed in Amman, Lattakia, and Alexandria stations by -0.16 (Sig.), -0.13 and -0.10°C/decade, respectively. Over Turkey, the mean annual maximum and minimum temperatures showed decreasing trends of -0.04 and -1.33°C/decade during 1955-1989 (Kadiog˘lu, 1997). Freiwan and Kadioglu et al. (2008), analyzed the maximum and minimum temperatures at the annual and seasonal scales in Jordan, using data from 14 stations during the period 1950-2000, and found a decreasing trend in maximum temperature with the highest rate in Amman (-2.03°C/decade).

On the other hand, the warming trend has been generally observed since the early 1990s for the eastern Mediterranean (Repapis et al., 2007; Saaroni et al., 2003). In Israel, Kafle and Bruins (2009) investigated the mean annual temperature for the period 1970-2002, and they found that the last 6 years from 1994 to 2002 were among the warmest years within the period 1970-2002 for almost all 12 weather stations, which shows the increasing warming effects in the last decade from 1970-2002. In addition, Tangborn (2003) analyzed daily maximum and minimum temperatures observations for the 1932-1999 period at 74 weather stations in the United States, Europe, Asia, and Australia. The results suggested that abrupt climate change occurred in the 1980s, and since 1990, positive temperature anomalies have been observed at almost all stations during the winter season.

Indeed, the smallest changes in maximum (Tmax) and minimum (Tmin) temperatures can cause noticeable changes in physical, hydrological, and biological systems, as well as in crop yields, plant growth, water resources, drought, and human health (Parmesan, 2006; IPCC, 2001; Walther et al., 2002; Zhang et al., 2015). Changes in global mean surface temperature are a useful indicator of climate change and variability, but these changes may be due to changes in maximum and minimum temperatures (Braganza et al., 2004) with different impacts. In addition, the difference between Tmax and Tmin, defined as the diurnal temperature range (DTR), is also a good indicator of climate variability and change.

On the other hand, teleconnection indices indicate the degree to which these patterns are modes of atmospheric variability and allow the study of their temporal variations and their effects on regional climate (Quadrelli et al., 2004; Brunettiet et al., 2002). They have a direct impact on human activities, as they are often associated with floods, droughts, heat or cold waves, and other factors that can directly influence and disrupt agriculture and water supplies (Jerez et al., 2013; Bastos et al., 2016). They are also often responsible for the occurrence of abnormal weather patterns (Barnston et al., 1987). Some of these indices are expected to increase under increased anthropogenic pressure (Zheng et al., 2013; Cai et al., 2014).

Numerous studies indicate that temperature and precipitation variations at the global and regional level are controlled by different large-scale teleconnection patterns, such as North Atlantic Oscillation (NAO), North Sea Caspian Pattern (NCP), and El Niño Southern Oscillation (ENSO). The relationship between climate and teleconnection patterns has been well documented in many regions of the world, including Europe (Hurrell, 1995; Ulbrich and Cristoph, 1999; Trigo et al., 2002; Zanchettin et al., 2008; Gámiz--Fortis et al., 2011), and in various parts of Middle East such

as Turkey (Türkes and Erlat, 2009; Kutiel and Türkes, 2005; Unal et al., 2010), Iran (Nazemosadat et al., 2006; Sabziparvar et al., 2011; Araghi et al., 2017; Ghasemi and Khalili, 2008), Egypt (Hasanean et al., 2004; Hasanean et al., 2006), and Saudi Arabia (Almazroui et al., 2020; Hasanean and Almazroui, 2016; Attada et al., 2018).

Very few previous studies in the literature evaluate changes in air temperature in the Levant as a whole. All studies have used individual countries (especially Israel), a very small number of stations, small areas or basins, and a limited time scale (Al Qatarneh et al., 2018; Matouq et al., 2013; Ben Gai et al., 1999; Kafle and Bruins 2009; Freiwan et al., 2008). On the other hand, the changes in air temperature in many other countries were well documented in the Middle East and north Africa. For example, in Turkey (Türkeş et al., 2002; Toros, 2012), Iran (Ghasemi, 2015; Soltani et al., 2016), Saudi Arabia (Almazroui et al., 2012; AlSarmi et al., 2011), Egypt (Tonbol et al., 2018; Domroes et al., 2005; Hassanean, 2006), and Libya (Kenawy et al., 2009).

Concerning the teleconnection patterns, till now, the relationships between atmospheric circulation indices and the Levant temperature have not been completely identified. There are few studies on this topic, and all of them have dealt with limited areas, seasons, meteorological stations, teleconnection patterns, climate variables, and periods of investigation. The vast majority of these studies focused on Israel (Yosef et al., 2009; Ben Gai et al., 2001; Ziv et al., 2006), and very few studies were for the Levant as a whole. This study uses seven teleconnection patterns for the period 1987-2018. Details on the data of the large-scale circulation patterns, resources, locations, and definitions are given in Chapter 2, Section 2.3.

This chapter aims to analyze the spatial and temporal changes in the annual, seasonal, and monthly trends of the maximum (Tmax), minimum (Tmin), and diurnal temperature range (DTR) in the Levant region over the period 1987-2018. In addition, it will be determined which of the large-scale variability modes influence the Levant seasonal temperatures (Tmax and Tmin). The temporal averages for the annual and seasonal (Tmax, Tmin, and DTR) were calculated based on monthly data for 60 stations distributed over the study area. Figure 2.4.1a shows the geographical distribution of the stations, while Table 1 in Appendix (A) contains the names, coordinates, and elevations of the stations. Details on the Data Quality Control (QC), the data, and homogeneity are available in Chapter 2, Section 2.2.

The analysis was conducted for the entire Levant and its countries (Palestine/Israel, Jordan, Lebanon, Syria, north Levant, and south Levant). The spatial and temporal trends for the three variables were calculated on the annual, seasonal, and monthly scales using the nonparametric Mann-Kendall test (Mann, 1945; Kendall, 1975) and Sen's slope estimator (Sen, 1968). In addition, the mean difference between the two sub-periods (1987-2000 and 2001-2011), and the change points detection was assessed at the three temporal scales. For the seasonal analysis, each year was divided into four climatic seasons, namely winter (December-February), spring (March-May), summer (June–August), and autumn (September–November).

The temporal mean values calculated on the annual and seasonal scales were plotted. They were also fitted by using the non-parametric Lowess smoothing technique (Appendix C.1) to smooth the temperature variability during the period under study (Cleveland, 1979, 1981). This method is

useful for tracking changes in temporal behavior in climatic time series (Costa and Soares, 2009; Kvamstø et al., 2012; Cioffi et al., 2015). In addition, the K-mean cluster algorithm was used to analyze the trends in annual and seasonal Tmax, Tmin, and DTR according to the clusters obtained. Observations in the same cluster were jointly analyzed according to certain characteristics, such as their geographical distribution and the rates of temperature warming. Finally, correlation maps between the teleconnection indices and the seasonal temperatures were constructed and analyzed.

4.2 Results

4.2.1 Temporal behavior for the annual and seasonal averages

Table 4.1 shows some descriptive statistics for the annual, seasonal, and monthly averaged time series for Tmax, Tmin, and DTR for the period 1987-2018. The temporal behavior for the annual and seasonal averages is shown in Figure 4.1. The long-term annual mean values (Tmax, Tmin, and DTR) reached 25.5°C, 13.9°C, and 11.6°C, respectively. In winter/summer, they reached 16.1/33.7°C, 6.7/20.7°C, and 9.4/12.9°C, respectively. It is noticeable that the long-term autumn averages of Tmax and Tmin are higher than those for spring by 3–3.5°C, where they ranged for spring/autumn 24.6/27.6°C for Tmax and 12.2/15.7°C for Tmin (Table 4.1).

Scale	Tmax (°C)				Tmin (°C)				DTR (°C)			
	Max	Min	Mean	Stdv.	Max	Min	Mean	Stdv.	Max	Min	mean	Stdv.
Annual	27.5	23.6	25.5	0.70	15.5	12.3	13.9	0.63	12.1	11.2	11.6	0.25
Winter	18.9	12.1	16.1	1.2	8.6	4.4	6.7	0.84	10.8	7.9	9.2	0.6
Spring	26.3	22.3	24.6	1.1	13.7	10.5	12.2	0.81	13.2	11.7	11.9	0.4
Summer	34.7	32.3	33.7	0.67	22.1	19.6	20.7	0.70	13.5	12.2	12.5	0.3
Autumn	30.1	26	27.6	0.87	17.5	14.3	15.7	0.82	12.6	10.9	11.5	0.4
January	18.0	11.5	14.9	1.5	8.4	3.0	5.8	1.3	10.2	7.7	9.1	0.7
February	20.1	11.8	16.4	1.7	8.9	3.8	6.5	1.3	11.8	7.8	9.9	0.9
March	23.9	16.2	19.8	2.1	11.2	6.2	8.8	1.5	12.7	9.5	11.0	0.8
April	28.4	21.9	24.7	1.6	14.3	10.0	12.1	1.1	14.8	11.2	12.6	0.8
May	31.5	26.8	29.0	1.1	17.5	14.5	15.8	0.9	14.5	12.2	13.2	0.6
June	34.1	30.8	32.2	0.8	20.6	17.6	18.9	0.7	13.9	12.2	13.3	0.5
July	36.4	32.4	34.2	0.9	24.5	19.8	21.5	0.9	14.0	11.6	12.7	0.5
August	36.7	32.1	34.4	0.9	23.9	20.0	21.7	0.9	13.4	11.7	12.6	0.4
Sept.	34.2	31.0	32.2	0.7	21.9	18.1	19.6	0.9	13.5	11.7	12.6	0.5
October	30.4	25.8	28.4	1.3	18.6	14.3	16.3	1.2	13.8	11.2	12.1	0.6
November	26.2	18.8	22.2	1.6	13.1	8.3	11.2	1.3	13.3	8.4	11.0	0.9
December	20.0	13.2	16.9	1.7	10.1	4.7	7.4	1.4	11.6	7.6	9.5	1.1

Table 4.1. Some fundamental statistics for the annual, seasonal, and monthly Tmax and Tmin averages over the Levant in the period 1987-2018.

In 1987-2018, the warmest/coldest annual mean values in 2010/1992 were 27.5/23.6°C for Tmax and 15.5/12.4°C for Tmin (Table 4.1, Figure 4.1). January is the coldest month with averages of 14.9 and 5.9°C for Tmax and Tmin, while August is the hottest month with 34.4 and 21.7°C, respectively. The standard deviation values shown in Table 4.1 indicate a greater variability of Tmax than Tmin for all time scales, except for summer. The highest variability was observed in March with standard deviation values reached 2.1°C for Tmax and 1.5°C for Tmin. The highest

annual mean values in 2010 were at Elat station (southernmost of Palestine) by 33.6°C for Tmax and at Sedom station (southeast of the Negev desert) by 23.7°C for Tmin (not shown).

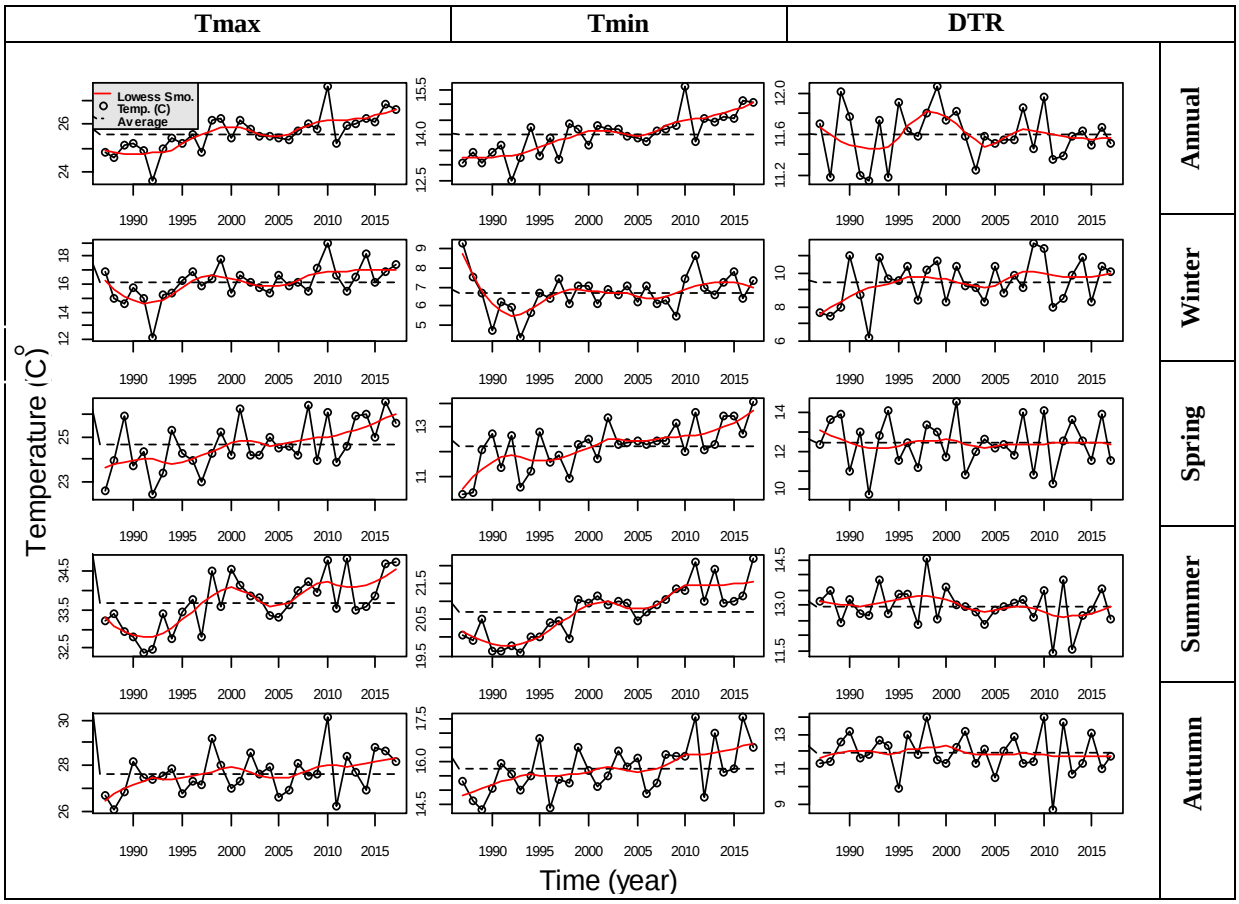

Figure 4.1. Temporal behavior for the annual and seasonal averages of Tmax, Tmin, and DTR over the study area. The red line indicates the Lowess smoothing, dashed line indicates the long-term average of the whole period 1987-2018.

As shown in Figure 4.1, the annual, spring, and autumn averages of Tmax and Tmin have generally undergone three major stages: a marked increase below their long-term averages from 1987 until 2000, followed by a decrease near the long-term averages in 2000-2006, and then, a rise above the long-term averages from 2006 onward. The general behavior for winter and summer Tmax and Tmin followed a similar pattern, except in 1987-1992, when they decreased below the long-term means.

Over the study area, annual and seasonal Tmax and Tmin tended to increase in the last decade of the 20th century. Interestingly, annual DTR generally decreased as both Tmax and Tmin tended to decline in 2000-2006, while it tended to remain constant, although both Tmax and Tmin increased in 2006-2018, which can be attributed to the higher annual Tmin warming than Tmax in that period by 0.90 and 0.71°C/decade, respectively.

4.2.1.1 Analysis of the means difference

The mean differences for the annual, seasonal, and monthly averages for the two sub-periods 1987-2000 and 2001-2018 are listed in Table 4.2. The results confirmed the tendency toward warming in the period 2001-2018 compared to the period 1987-2000. For Tmax, the study area exhibited a high and significant ($p < 0.05$) increase of spring and winter mean values by 0.9 and 1.1ºC, respectively. For the Tmin, a strong and significant increase in spring and summer means by 1.1ºC was found for both. The results also showed that winter showed a non-significant increase in the mean DTR by 0.6°C. In contrast, summer and autumn showed a non-significant decrease of -0.3 and -0.2ºC, respectively.

Level	Tmax (°C)		Diff.	Tmin (°C)		Diff.	DTR (°C)		Diff.
	Period (1)	Period (2)		Period (1)	Period (2)		Period (1)	Period (2)	
Annual	25.1	25.9	0.8***	13.4	14.3	0.9***	11.6	11.6	0
Winter	15.6	16.5	0.9*	6.5	6.8	0.3	9.1	9.7	0.6
Spring	24	25.1	1.1***	11.6	12.7	1.1***	12.4	12.4	0
Summer	33.3	34	0.7***	20.1	21.2	1.1***	13.1	12.8	-0.3
Autumn	27.4	27.9	0.5	15.4	16	0.6*	12	11.8	-0.2
January	15.0	15.8	0.8	6.0	6.5	0.5	9.0	9.3	0.3
February	16.1	17.5	1.4*	6.3	7.4	1.2*	9.9	10.1	0.2
March	18.9	21.4	2.4***	8.2	9.9	1.7**	10.7	11.4	0.7*
April	24.8	25.4	0.6	12.1	12.8	0.7+	12.8	12.6	-0.2
May	29.2	29.4	0.1	15.8	16.3	0.5+	13.4	13.0	-0.4+
June	31.9	32.6	0.7*	18.5	19.5	0.9***	13.4	13.1	-0.3+
July	33.8	34.5	0.7*	21.0	22.0	0.9***	12.8	12.5	-0.2
August	33.9	34.7	0.8**	21.2	22.4	1.2***	12.7	12.3	-0.3*
September	32.1	32.5	0.4	19.4	20.2	0.8**	12.7	12.3	-0.4**
October	28.3	28.9	0.6	16.2	17.0	0.7+	12.1	11.9	-0.2
November	22.5	22.8	0.3	11.5	11.9	0.5	11.0	10.9	-0.1
December	17.2	17.7	0.5	7.8	7.9	0.1	9.4	9.8	0.4

Table 4.2. The means difference for temporal annual, seasonal, and monthly averages of Tmax, Tmin, and DTR, and their significance level over the study area between the periods 1987-2000 (1) and 2001-2018 (2). *** indicates significant differences at 0.001 level, ** at 0.01 level, and * at 0.05 level, + indicate positive differences at 0.1 level of significance.

Over the period 2001-2018, Tmax and Tmin averages increased in all months compared to 1987-2000 (Table 4.2). The maximum increase was significant in March, by 2.4°C for Tmax, 1.7°C for Tmin, and 0.7°C for DTR. In addition, the monthly averages of Tmax for February, June, July, and August showed significant increases of 1.4, 0.7, 0.7, and 0.8°C, respectively. For Tmin, the February, June, July, August, and September mean values showed significant increases of 1.2, 0.9, 0.9, 1.2, and 0.8°C, respectively. The results also showed that the Tmin averages for April, May, and October increased significantly by 0.7, 0.5, and 0.7°C at a significance level of 0.1. For DTR, all monthly averages in the second period showed decreases, except for the winter months (December, January, and February) and March, with increases ranging from 0.2°C for February to 0.7°C (Sig.) for March. The significant mean decreases were in August (-0.4°C) and September (-0.4°C).

4.2.2 Temporal trends for the annual, seasonal, and monthly averages

Table 4.3 shows the trends estimated by the Sen's slope and their significance for Tmax, Tmin, and DTR. The annual and seasonal averages showed significant warming trends for Tmax and Tmin, with the warming in the Tmax being slightly stronger than for the Tmin, except for autumn. In the analyzed region, significant warming was observed at the level of 0.001 for annual Tmax and Tmin, with values of 0.33 and 0.30°C/decade, respectively. The annual DTR average showed a weak and non-significant decreasing trend by -0.03°C/decade.

Among the seasons, spring exhibited a very strong and significant warming trend of 0.53°C/decade for Tmax and 0.51°C/decade for Tmin. Winter showed a strong warming trend in Tmax by 0.50°C/decade, while it was of little significance for Tmin. In particular, it showed a rising trend in DTR by 0.30°C/decade, although it was not significant. On the other hand, autumn showed strong warming in Tmin by 0.52°C/decade, whereas it showed a low significance for Tmax. The results also revealed the warming in winter (0.50°C/decade) is notably stronger than in summer (0.34°C/decade), especially for Tmax.

Level	Tmax (°C/decade)	Tmin (°C/decade)	DTR (°C/decade)
Annual	0.33***	0.30***	-0.03
Winter	0.50**	0.27+	0.30
Spring	0.53**	0.51**	-0.07
Summer	0.34**	0.29***	-0.21
Autumn	0.36*	0.52***	-0.27
January	0.49	0.26	0.26+
February	0.83*	0.63*	0.31
March	1.05*	0.72*	0.33+
April	0.55	0.42+	0.06
May	0.16	0.43*	-0.15
June	0.48*	0.27*	-0.012
July	0.41*	0.45***	-0.12
August	0.47***	0.45***	-0.20*
September	0.35+	0.46***	-0.17*
October	0.12	0.36	-0.05
November	0.32	0.40	-0.01
December	0.49	0.26	0.21

Table 4.3. The temporal trends for the annual, seasonal, and monthly averages of Tmax, Tmin, and DTR over the study area during (1987-2018), and their significance level. *** indicates significant differences at 0.001 level, ** at 0.01 level, and * at 0.05 level, + indicate positive differences at 0.1 level of significance.

Table 4.3 also shows the monthly trends across the Levant for the period 1987-2018. There are more months significantly affected by warming trends in Tmin than in Tmax. Of all months, March showed the highest rising trends with 1.05°C/decade for Tmax, 0.72°C/decade for Tmin, and 0.33°C/decade for DTR. In the other spring months, the significant warming was only observed in the Tmin averages of 0.42°C/decade (Sig. at 0.1 level) for April and 0.43°C/decade for May. In addition, only February for the winter months exhibited significant warming tendencies by 0.83°C/decade for Tmax and 0.63°C/decade for Tmin. In addition, the months of October and November showed weak and insignificant warming trends, while September showed significant

trends with values of 0.35°C/decade (Sig. at 0.1 level) for Tmax, 0.46°C/decade for Tmin, and -0.17°C/decade for DTR. Interestingly, all summer months (June, July, and August) witnessed significant rising trends with values of 0.48, 0.41, and 0.74°C/decade for Tmax and 0.27, 0.45, and 0.45°C/decade for Tmin. In addition, August showed a significant downward trend for DTR of -0.2°C/decade.

4.2.2.1 Trend change points detection

The sequential Mann-Kendall (SMK) test was applied to estimate the qualitative changes in the trends for the annual, seasonal, and monthly averaged time series. The results are listed in Table 7, Appendix A, which shows the significant change points detected, and some of these are shown in Figure 4.2. The SMK test results show the statistically significant change points in the annual, seasonal, and monthly time series (Table 7, Appendix A). Figure 4.2 shows that the annual and seasonal Tmax and Tmin average series show strongly increasing trends. The decreasing trends corresponded to very short periods, especially in 1987-1992 for winter, spring, and summer.

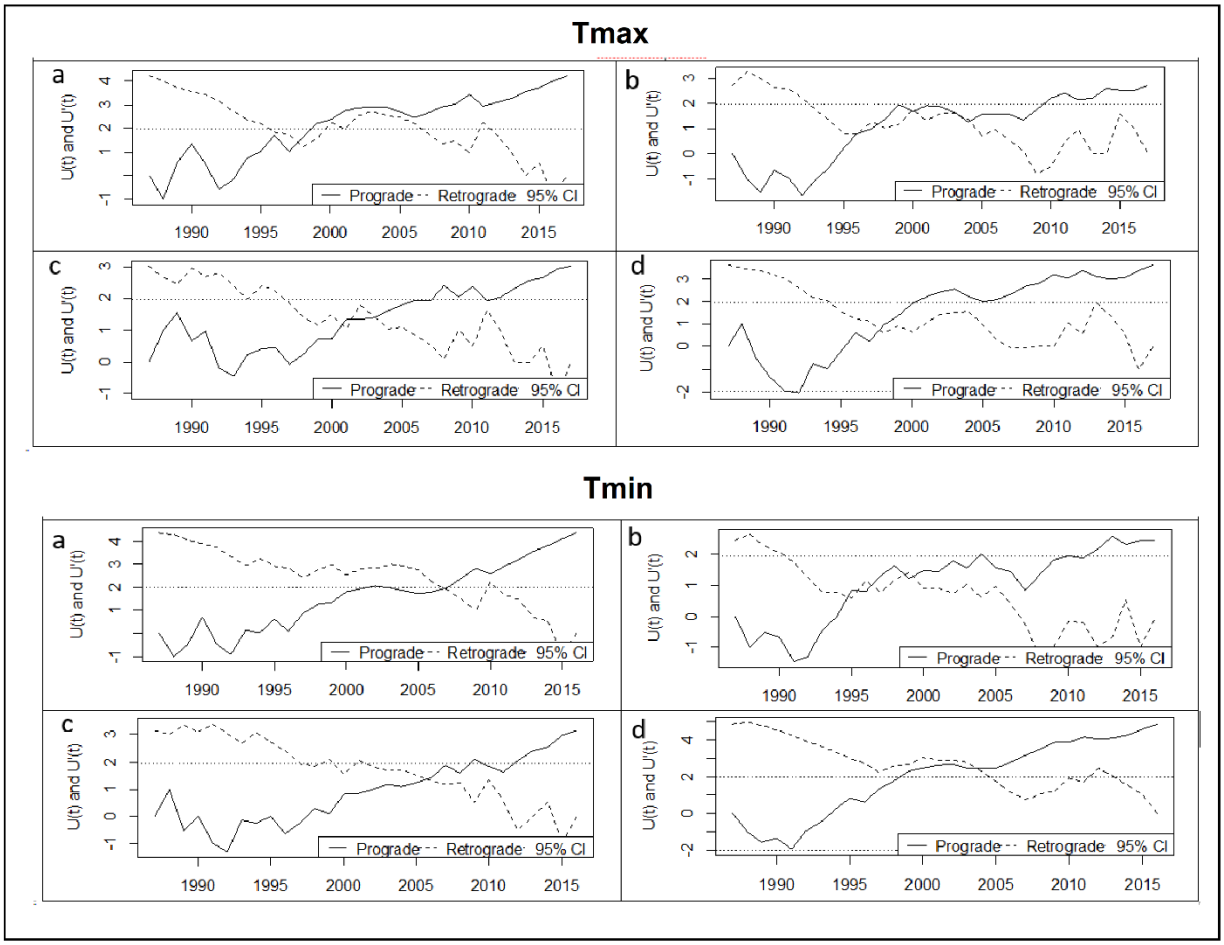

Figure 4.2. Graphical representation of the forward, U(t) and the backward, U'(t) series of the Sequential Mann-Kendall test for annual (a), winter (b), spring (c), and summer(d) Tmax and Tmin averaged time series. The computed U(t) and U'(t) values are depicted respectively by solid and dashed lines, while the horizontal dotted lines demonstrate confidence limits at the 5% significance level.

The significant turning points for the Tmax averages were observed in 1997 for the annual and summer series (Figures 4.3 a and d), and in 2002 for winter and spring (Figure 4.2 b and c). Furthermore, the increasing trends have become significant in 2010 for winter and spring Tmax and Tmin, in which U(t) is placed outside the 95% confidence band, whereas they became significant in the second half of the 1990s for the yearly and summer Tmax averages.
For the averaged Tmin time series (Figure 4.2, bottom), the curves significantly intersect each other in 2007, 1998, 2007, 2004, 2006 for winter, spring, summer, and autumn. In general, the significant change points of the Tmin series were concentrated in the years 2005 and 1997 (Table 7, Appendix A). For example, the months of February, March, August, and September had a significant change point in 2005, and the months of June and July in 1997 had significant change points in their Tmin averages (Table 7, Appendix A).

4.2.3 Spatial analysis of annual, seasonal, and monthly trends

In this section, the frequency and strength of trends were spatially analyzed at the regional and local scales. The annual, seasonal, and monthly Tmax, Tmin, and DTR time series were averaged for each country (Palestine/Israel, Jordan, Lebanon, and Syria). After that, the trends were calculated for all countries. We have followed this subjective division or non-climatic criterion because it helps us make comparisons with other works done on a local level in the Levant region. The results are presented in Figure 4.3 (a and b), Table 4.4, and Table 8 (Appendix A) for the trend magnitudes and significance. Furthermore, each station's annual, seasonal, and monthly Tmax, Tmin, and DTR trends were calculated. Figures 4.4 (a-c) and Table 9 (Appendix A) show the total number of stations that showed positive (significant positive) and negative (significant negative) trends for the annual, seasonal, and monthly Tmax, Tmin, and DTR. Figures 4.5 and 4.6 represent the spatial distribution for the annual and seasonal trends. Figure 4.7 and the attached Table 9 (Appendix A) show some fundamental statistics for the annual and seasonal Tmax and Tmin trends. The spatial distribution of the monthly Tmax, Tmin, and DTR trends are shown in Figures 4.8 (A) to 4.8 (C). Note that the results for Lebanon are not shown in Figure 4.3, but they were listed in Table 8 (Appendix A) because the Lebanon time series covers a shorter period 1994-2018 compared to Palestine/Israel, Jordan, and Syria.

4.2.3.1 Trends analysis for the Levant´s countries

The results shown in Figure 4.3a revealed all countries, except Lebanon, were significantly affected by the warming trends in annual Tmax and Tmin. Tmax trends ranged from 0.32ºC/decade for Palestine to 0.39ºC/decade for Jordan. In comparison, Tmin trends ranged from 0.23ºC/decade for Jordan to 0.28ºC/decade for Syria. Although all counties showed significant warming trends in annual Tmax and Tmin, their annual-DTR trends were weak (less than -009ºC/decade) (Figure 4.3a, Table 8 in Appendix A).
For seasonal trends, spring trends contribute to the highest percentage of annual warming trends for Tmax and Tmin. They ranged from 0.49ºC/decade (Lebanon) to 0.59ºC/decade (Jordan) for Tmax, and from 0.47ºC/decade (Syria and Jordan) to 0.48ºC/decade (Palestine and Lebanon) for

Tmin. Moreover, the highest seasonal warming trends were observed in spring for all countries, except Syria-Tmax, where the warming was slightly stronger in winter (0.51ºC/decade) than in spring (0.50ºC/decade), and in autumn-Tmin (0.58ºC/decade) than in spring-Tmin (0.47ºC/decade). It should be noted that the increasing trends for autumn-Tmin were higher than those for summer and winter for all counters (Figure 4.3a, Table 8 in Appendix A). The winter-Tmax increased at higher rates than the summer for all regions, with higher rates for Jordan (0.53 ºC/decade).

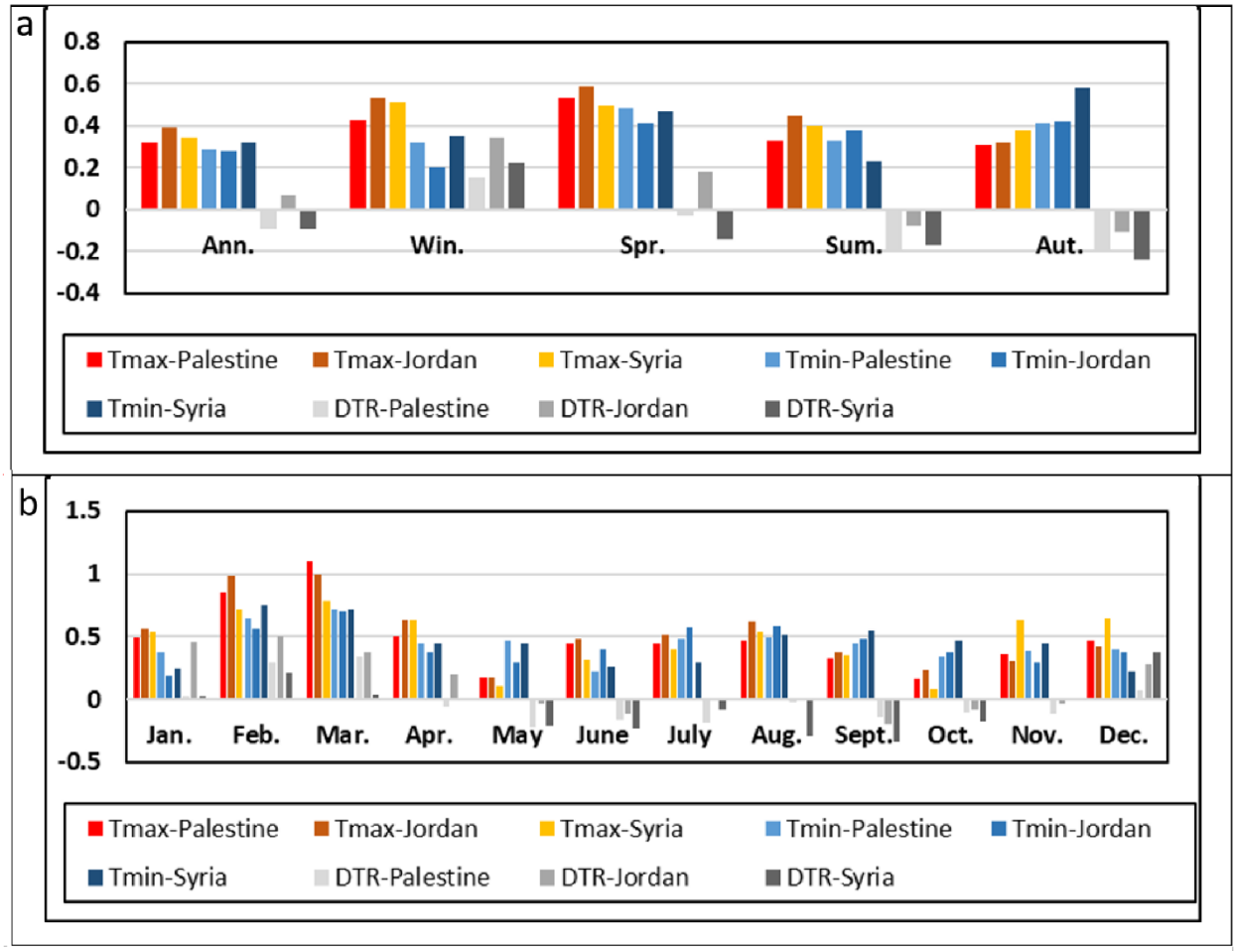

Figure 4.3. Annual and seasonal Tmax, Tmin and DTR trends (°C/decade) calculated for countries (a), and those for the monthly trends (b). The significance level are in Table 7, Appendex A.

The sharply rising winter-Tmax trend for Jordan has led to a significantly increasing winter-DTR trend by 0.34ºC/decade (Figure 4.3a, Table 8 in Appendix A). The results shown in Figure 4.3 indicated that all countries witnessed higher warming of their annual and seasonal Tmax than Tmin, except for autumn. Furthermore, all countries showed declining trends in autumn-DTR, which were significant only for Palestine at -0.19ºC/decade. The analysis for the south (Palestine and Jordan) and north (Lebanon and Syria) Levant trends (Table 4.4) indicated the south Levant-Tmax increased at a higher rate than the north Levant-Tmax in the annual (0.34ºC/decade), spring

(0.57ºC/decade), summer (0.38ºC/decade), and autumn (0.36ºC/decade). Only in winter, the north Levant-Tmax rise at a higher rate than south Levant by 0.50ºC/decade. On the contrary, the Tmin of the north Levant increased at higher rates than south Levant in annual (0.32ºC/decade), winter (0.34ºC/decade), and autumn (0.35ºC/decade). Both the south and north Levant significantly exhibited increasing winter-DTR trends at 0.24 and 0.26ºC/decade, respectively. In addition, south Levant showed a significant declining trend in summer DTR by -0.15ºC/decade, whereas the north Levant exhibited a significant declining trend in autumn-DTR by - 0.27ºC/decade.

Month	Southern Levant Tmax/Tmin/DTR (°C/decade)	North Levant Tmax/Tmin/DTR (°C/decade)
Ann.	0.34**/0.28**/-0.01	0.32**/0.32**/0
Win.	0.47+/0.27+/0.24*	0.50*/0.34+/0.26+
Spr.	0.57*/0.48**/0.091	0.49*/0.43*/0.018
Sum.	0.38*/0.36**/-0.15*	0.20/0.23*/-0.08
Aut.	0.36*/0.41*/-0.13	0.31/0.53**/-0.27*

Table 4.4. The annual and seasonal Tmax, Tmin, and DTR trends for the south and north Levant in (1987-2018).

Overall, the significant upward trends in Tmax and Tmin for all countries were mainly observed in February, March, and August (Figure 4.3b). On the other hand, they were not observed for any region and temperature variable in January, October, November, and December, except for Jordan in January-DTR by 0.46ºC/decade (Table 8, Appendix A). For all countries of the Levant, the maximum monthly warming trends Tmax and Tmin occurred in the cold months, especially for February and March (Figure 4.3b). For Palestine and Jordan, a gradually increasing Tmax trend was observed from October to March, from 0.15 to 1.1ºC/decade for Palestine and 0.23 to 1ºC/decade for Jordan. In addition, warming Tmax gradually increased from May to August for Jordan and Syria, from 0.18 to 0.62ºC/decade and from 0.11 to 0.49ºC/decade, respectively (Figure 4.3b, Table 8 in Appendix A). For Tmin, the countries showed the maximum upward trends in February and March. Upward trends for February-Tmin ranged from 0.56ºC/decade for Jordan to 0.75ºC/decade for Syria, and all countries showed similar upward trends for March-Tmin (0.71ºC/decade).

4.2.3.2 Trend analysis at the local scale

4.2.3.2.1 Annual and seasonal scales

The results provide strong indications of significant warming trends in the entire Levant region (Figures 4.5a, Table 9 in Appendix A). The decreasing trends showed a very isolated and random pattern compared to the broad, intense, and coherent warming trends in Tmax and Tmin (Figures 4.6 and 4.7). The maximum frequency of significant increasing trends was found for annual and spring with 84% and 74% of the stations (60 stations) for Tmax and 84% and 79% for Tmin (Figure 4.4a, Table 9 in Appendix A).

For the annual Tmax (Figure 4.5), the highest warming trends (0.32-0.47°C/decade) were observed significantly at most Jordanian stations, and in the central (31ºN and 32ºN) and northern (31.8ºN and 32.3ºN) locations from Palestine. The Syrian coastal area showed a lower value of significant

warming trends (0.23-0.27°C/decade). Annual Tmax trends ranged from 0.01°C/decade at Kfardan in Lebanon to 0.48°C/decade at Ayelet Hashahar in northwestern Palestine, with a mean of 0.30°C/decade and a standard deviation of 0.09°C/decade, indicating very highly concentrated trends around the mean (Figure 4.7, Table 10 in Appendix A).

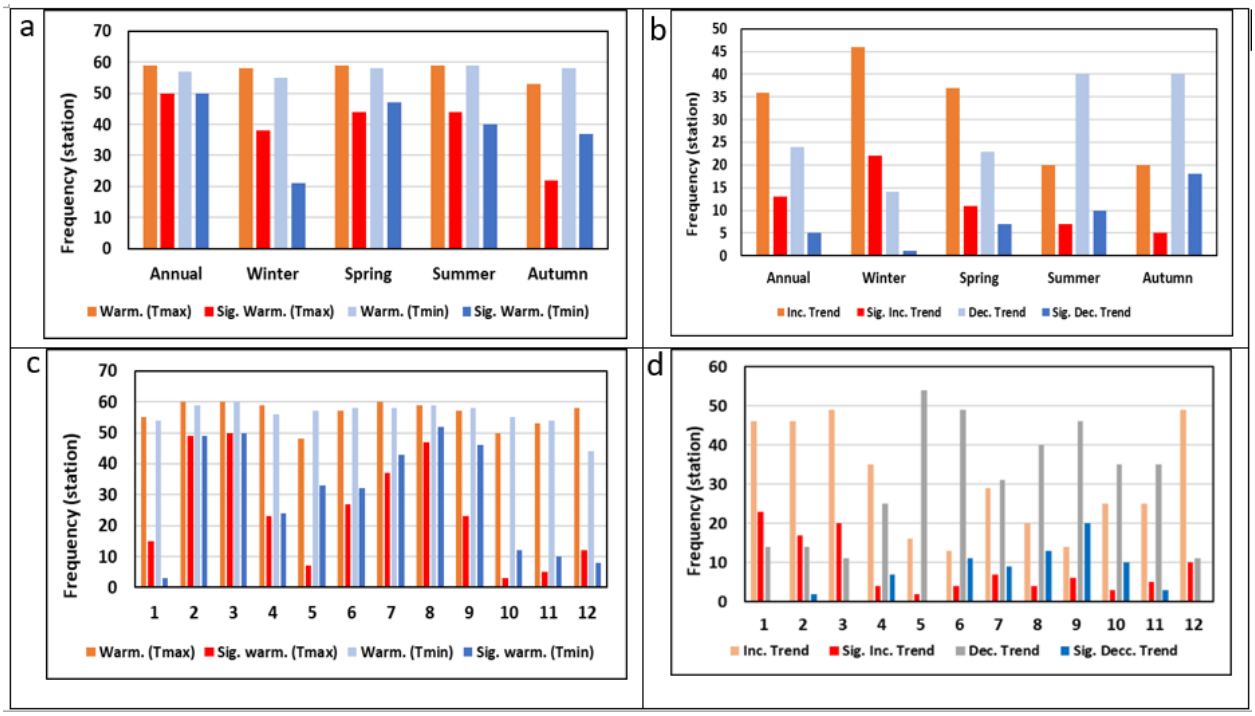

Figure 4.4. (a) Frequencies of warming and significant warming trends for the annual and seasonal Tmax and Tmin averages. (b) Frequencies of trends for the annual and seasonal DTR averages. The panels (c) and (d) are for the monthly Tmax and Tmin averages.

The annual Tmin trends ranged from -0.23°C/decade to 0.45°C/decade, with an average value slightly less than for Tmax (0.27°C/decade) and a standard deviation of 0.12°C/decade (Figure 4.7, Table 10 in Appendix A). For most Syrian and Lebanon stations, the rate of Tmin warming was slightly higher than that of Tmax. In contrast, most Palestine and Jordan stations notably exhibited higher values of warming trends in Tmax than in Tmin. For example, Palestine's central and northern locations showed less warming trends in Tmin than in Tmax, where their Tmin trends were less than 0.30°C/decade (Figure 4.5).

For the seasonal Tmax trends (Figure 4.6), the strong significant warming trends (0.60-0.74°C/decade) occurred in winter and spring and spatially covered the entire Jordan, central and northern locations from Palestine. Note that the strong warming trend extended to cover more sites in spring for central, north Palestine, and Syrian areas in the south and north. The summer and autumn seasons exhibited less significant warming trends (with values lower than 0.60°C/decade) for all locations.

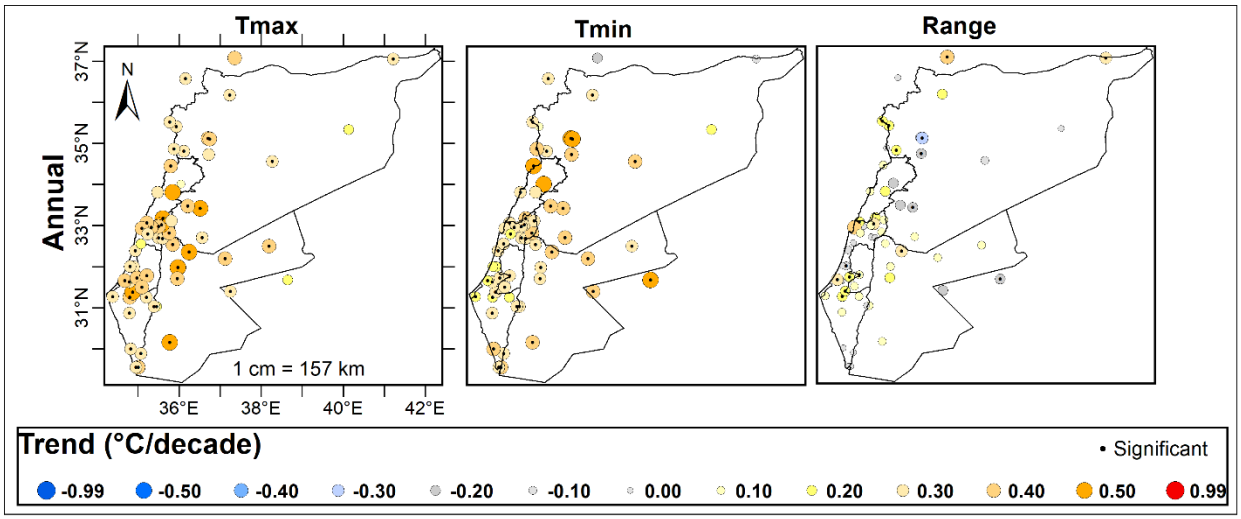

Figure 4.5. Spatial trends for the annual averages of Tmax, Tmin, and DTR over the study area during (1987-2018). Trends for Lebanon stations were calculated during (1994-2018).

At the seasonal Tmin scale, the strong significant warming trends (0.45-0.88°C/decade) were observed in autumn and spring, whereas winter and summer exhibited less value of significant warming trends (< 0.50°C/decade) for all locations. In autumn, the high band of trends mainly covered the sites between 33ºN-35ºN.

In spring, the same regions were affected by the strong warming trend and the eastern and northern areas of Jordan and the West Bank's southern areas. The highest significant increase trend was in autumn at Hama station by 0.94°C/decade. The frequency of significant decreasing DTR trends ranged from 2% in winter to 30% in autumn, whereas the significant increasing trends ranged from 8% in autumn to 37% in winter (Figure 4.4b). Spatially, the significant annual-DTR upward trends (0.14-0.24°C/decade) covered some locations in the central and northern parts of Palestine and the Syrian coastal area.

In summer and autumn, most stations were affected by decreasing trends, except in few cases, such as the Syrian coastal area and some central and northern Palestine locations. The important and significant decreasing trends (-0.45 to -0.88°C/decade) occurred in autumn, mainly in Syria between 33ºN-35ºN. The same areas were affected by significant decreasing trends but with lower rates (from -0.14 to -0.32°C/decade) during summer and spring. Note that six stations in Palestine's central area exhibited significant increasing spring-DTR trends by an average of 0.30°C/decade. In winter, most stations revealed increasing trends with significant in the northern locations from Jordan and Palestine and Palestine's central stations by 0.26-0.63°C/decade.

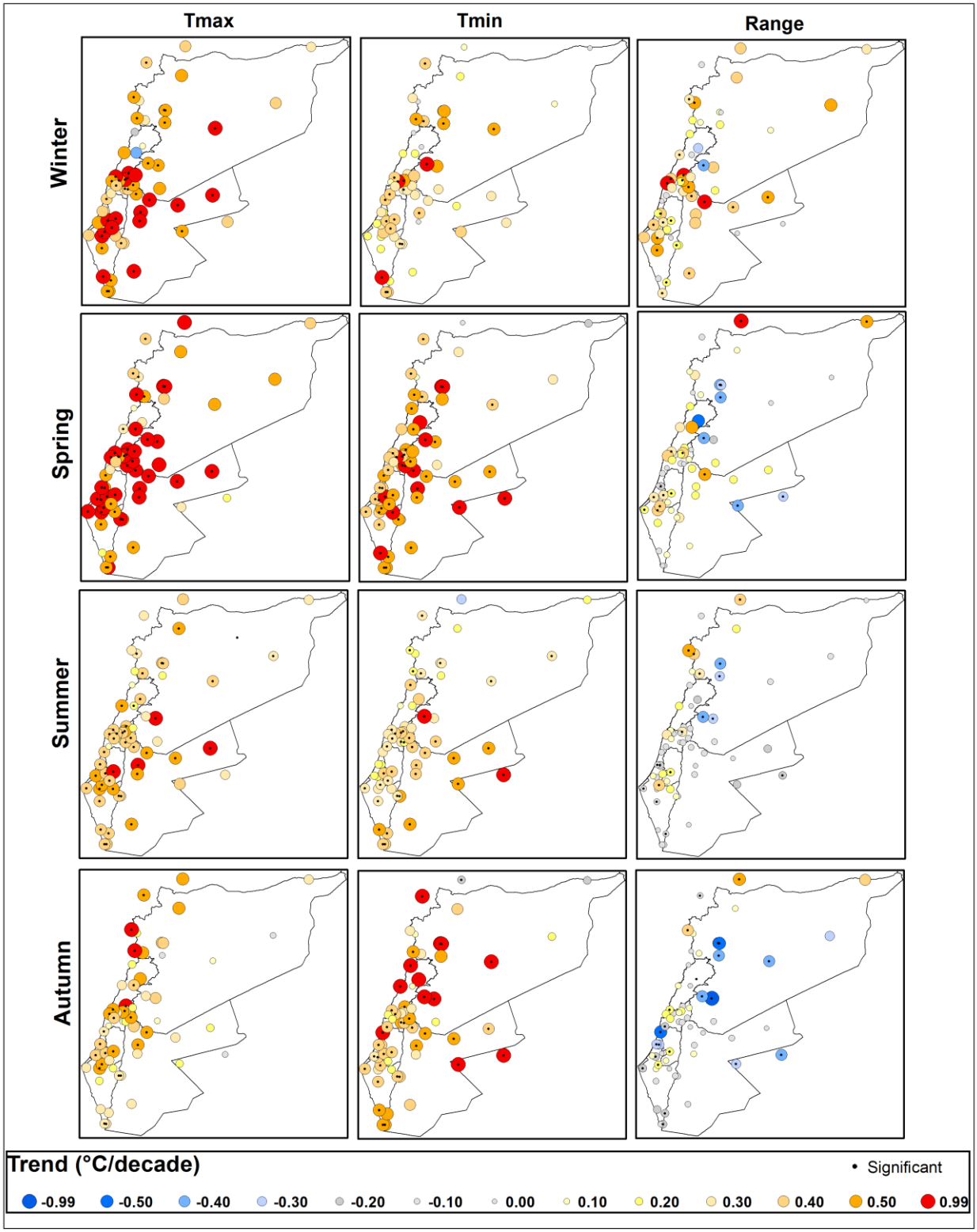

Figure 4.6. Spatial trends for the seasonal averages of Tmax, Tmin, and DTR over the study area during (1987-2018). Trends for Lebanon stations were calculated during (1994-2018).

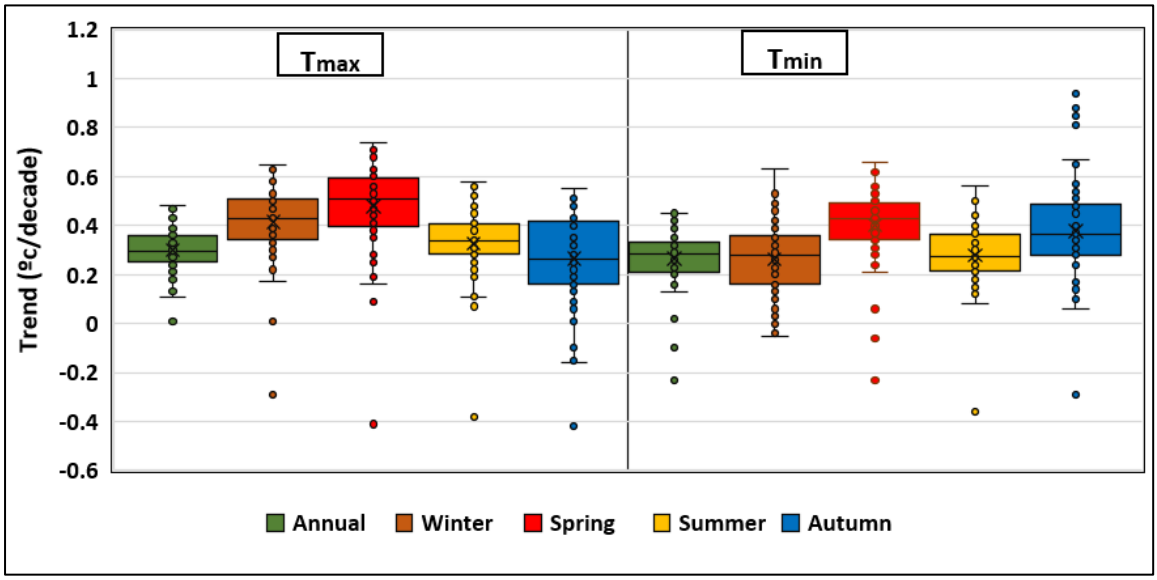

Figure 4.7. Boxplots for the annual and seasonal Tmax and Tmin trend.

4.2.3.2.1 Monthly trends

In all cases, the significant decreasing trends formed less than 2% (one station) of total stations, such as the Qunitera station in December-Tmin by -0.61°C/decade. On the other hand, more than 89% (53 stations) exhibited warming trends in the Tmax and Tmin for all months, except for May-Tmax and December-Tmin, which showed warming trends in 80% and 74% of the stations, respectively (Figure 4.4c, Table 9 in Appendix A). The findings showed most months exhibited more frequencies of a significant warming trend in Tmin than Tmax, especially for the hot months May-November (Figure 4.4c). The cold months (December-April) generally exhibited equal frequencies in Tmax and Tmin, except for January and December (Figure 4.4c).

Although the minimum temperature exhibited equal or higher percentages of the warming trend than the maximum temperature, it showed fewer magnitudes at most stations for the most months. In this context, a percentage of 88%, 78%, 88%, 71%, 58%, 58%, 58%, 51%, and 83% of the stations had higher trend values in the Tmax than Tmin, for January, February, March, April, June, July, August, November, and December, respectively. Only in May, September, and October, most stations displayed higher warming trends in the Tmin than Tmax by 68% of the stations for the three months.

The analysis of the monthly DTR trends reflected the results obtained from the monthly Tmax and Tmin. When the Tmin is decreasing, or the Tmax is increasing, the DTR is expected to increase. As mentioned before, the Tmax trends for December, January, February, March, and April exhibited higher values of warming than Tmin at most locations. This led to a much higher frequency of increasing DTR trends by 82%, 77%, 77%, 82%, and 58% of the stations, respectively (Figure 4.4d, Table 9 in the Appendix A). On the contrary, the Tmin trends for May, September, and October displayed higher values of the warming than Tmax at most locations, which led to a much higher frequency of decreasing DTR trends by 90%, 77%, and 58% of the stations, respectively.

Figures 4.8 (A) to 4.8 (C) show the spatial distribution of the monthly trends from 1987 to 2018. We mainly discuss here the February and March trends due to their vast and strong warming compared to other months. The February trends were higher than for other winter months (December and January) at more than 92% (55 stations). In addition, the February Tmax trends increased with higher rates than those for the Tmin for all locations, except for very few cases in the North Levant (Lebanon and Syria). The highest warming trends (0.90-1.70°C/decade) mainly and extensively covered the southern Levant region (Palestine and Jordan), between 29ºN-34ºN, while the northern regions showed fewer magnitudes of warming trends (< 0.75°C/decade).
For the February-Tmin trends, much fewer frequencies for the high band (0.90-1.70°C/decade) were observed for the southern Levant, although the same areas still show high rates of trends between (0.7-0.85°C/decade). For the DTR, Jordan's northern areas were affected by the highest significant increasing trends (from 0.50 to 0.70°C/decade).

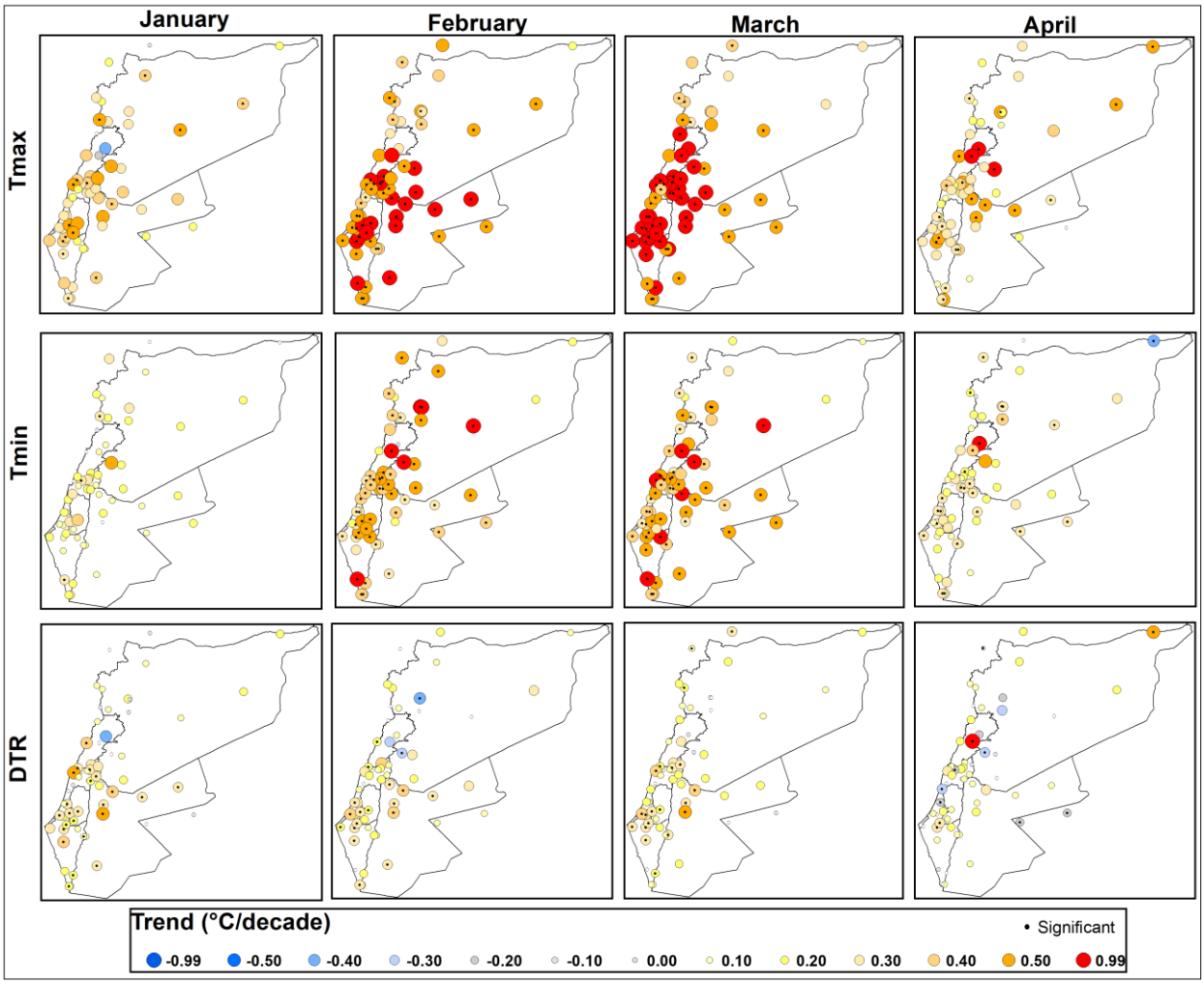

Figure 4.8 (A). Spatial trends for the January, February, March, and April averages of Tmax, Tmin, and DTR over the study area during the period 1987-2018. Trends for Lebanon stations were calculated for the period 1994-2018.

A comparison between spring months (March, April, and May) reveals that March-Tmax and Tmin trends were higher than May at 100% (60 stations), and at 92% (4 stations) for April. In addition, the March-Tmax increased with higher rates than those for the Tmin for all locations. Among all monthly Tmax trends, the March-Tmax exhibited the highest warming trend values at more than 92% (55 stations) of the stations. Similar to February, with more intensive and spread significant warming trends, the high band of the March-Tmax trends (0.90-1.70°C/decade) covered the southern Levant region (Palestine and Jordan), while the most Syrian areas showed fewer magnitudes of warming trends (< 0.75°C/decade). The high band of warming trends covered the northern locations from Jordan, southern locations from Syria, central and north locations from Palestine between 31ºN-32ºN and 31.5ºN-32.5ºN, and the Lebanon locations.

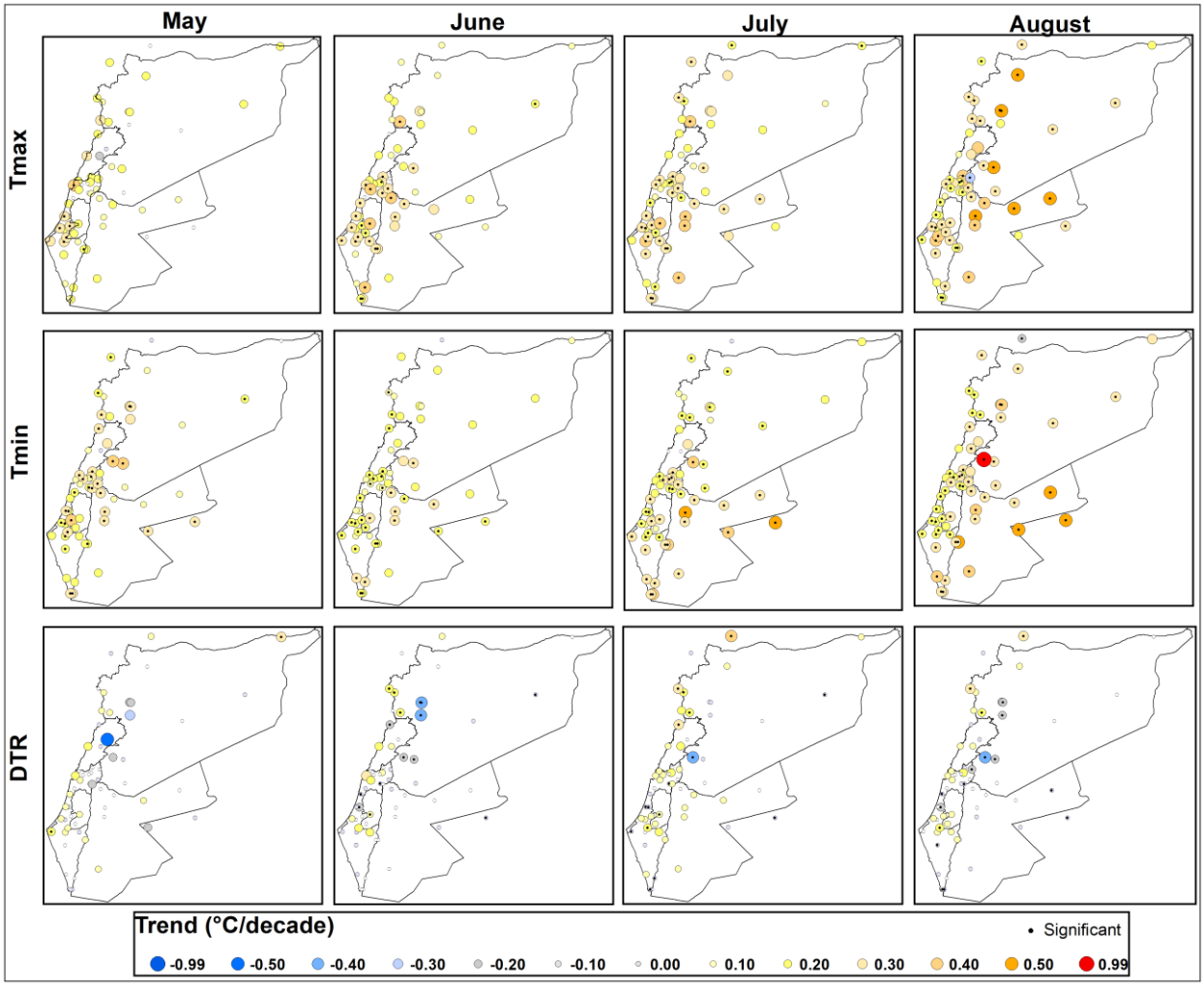

Figure 4.8 (B). Spatial trends for the May, June, July, and August averages of Tmax, Tmin, and DTR over the study area during the period 1987-2018. Trends for Lebanon stations were calculated for the period 1994-2018.

For the March-Tmin trends, much fewer frequencies for the high band of trend were observed for the southern Levant, although the same areas still show high trends (0.70-0.85°C/decade) (Figure 4.8 (A)). The highest significant increasing trends in the DTR (from 0.59 to 0.72°C/decade)

occurred in Jordan's northern areas. Moreover, southern locations from the Palestinian coastal area showed a significant increasing trend (0.45 – 0.66°C/decade).

In June (Figure 4.8B), warming Tmax trends increased compared with May-Tmax, especially over the southern regions (Palestine and west of Jordan). On the contrary, the June-Tmin trends decreased compared with May-Tmin, especially over entire Palestine and between 31ºN-35ºN from Syria and Lebanon. High warming trends (0.30 – 0.45°C/decade) covered northern areas in Jordan and Palestine's central regions for June-Tmax. All stations showed rising trends in June-Tmin (less than 0.25°C/decade), except for some north location in Jordan and Damascus from Syria by up to 0.35°C/decade. In September (Figure 4.8 (C)), locations showed low warming Tmax rates compared with August and July. The majority of stations exhibited warming trends ranged from 0.16 to 0.43°C/decade. They had higher warming trends in Tmin than Tmax. High increasing trends were found in western areas from Syria and entire Lebanon (0.52 to 0.61°C/decade).

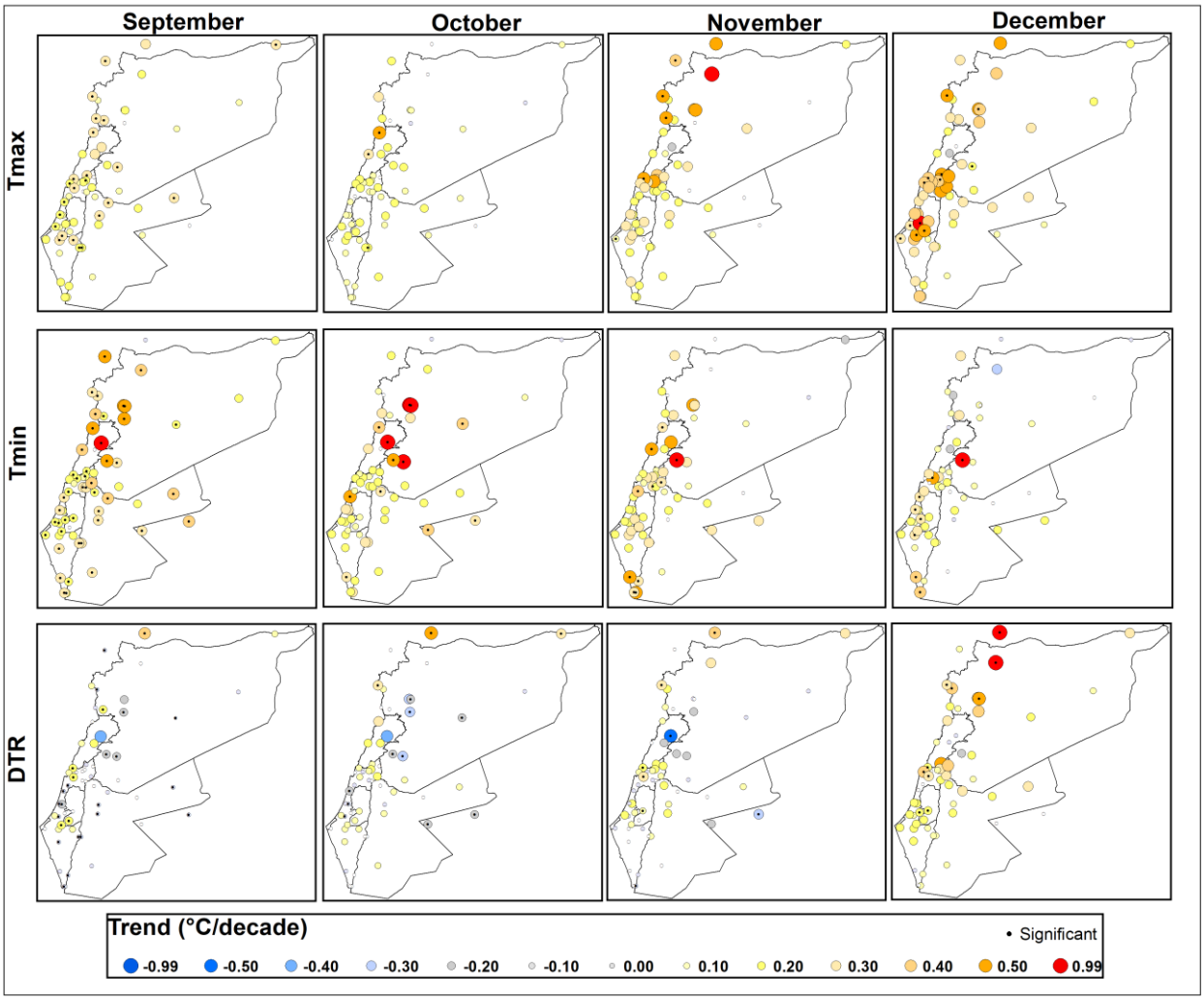

Figure 4.8 (C). Spatial trends for the September, October, November, and December averages of Tmax, Tmin, and DTR over the study area during the period 1987-2018. Trends for Lebanon stations were calculated for the period 1994-2018.

4.2.4 Clustering analysis for the annual and seasonal trends

The K-means clustering algorithm was used to identify and represent the regional aggregation in the temperature trends discussed before. It was applied to the annual and seasonal Tmax, Tmin, and DTR trends. Figure 4.9 shows that the resulting clustering leads to three categories, each identified by a color, for both the annual and seasonal variables. The optimal number of clusters was decided based on 30 indices available in the R NbClust Package (Charrad et al., 2014). The high number of these indices indicated the 2 and 3 clusters are the best number of groups.

Most of the Jordan stations, northern and central locations of Palestine, and Hama and Damascus stations from Syria formed a cluster characterized by very high warming trends by rates of 0.37°C/decade for annual Tmax, and seasonal Tmax trends ranged from 0.39°C/decade in autumn to 0.59°C/decade in spring.

In addition, eastern Syrian locations (east to 37ºE), southern Palestinian locations (south to 31.2ºN), and the locations between 31ºN-31.8ºN from the Palestinian coastal area showed the second cluster with lower rates of warming trends for annual and seasonal series between 0.18°C/decade (for autumn), to 0.46°C/decade (for spring). The third cluster contains only three stations from Lebanon. They exhibited decreasing trends in winter-Tmax (-0.22°C/decade) and increasing trends in spring, summer, autumn, and annual Tmax by 0.41, 0.19, 0.30 0.25°C/decade, respectively.

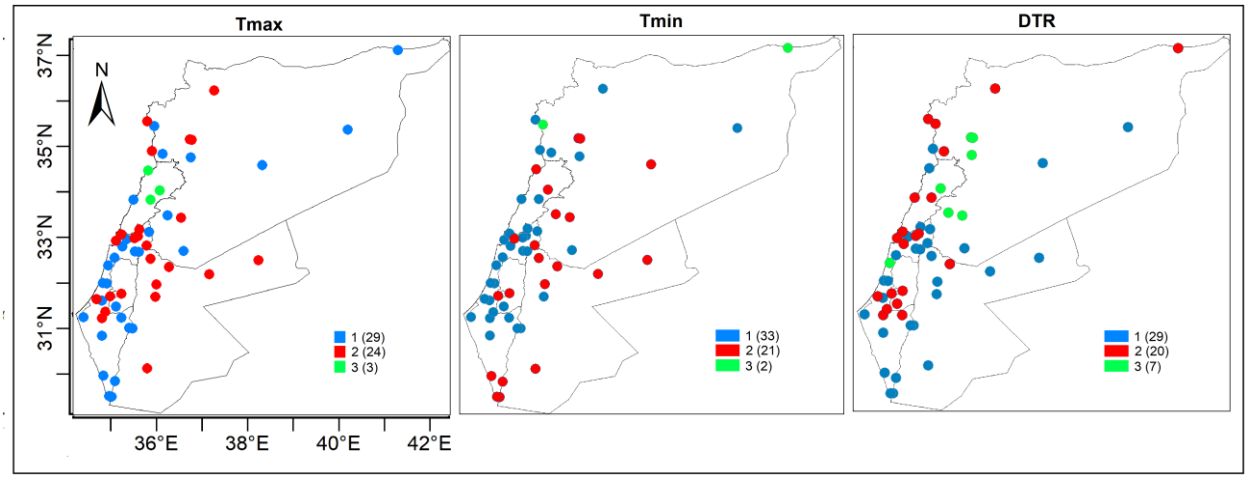

Figure 4.9. The clustering of annual and seasonal Tmax, Tmin and DTR in 1987-2018.

Most of the Jordan stations also formed the high cluster trend in the annual and seasonal Tmin, whereas only four stations from central and northern Palestine were included in this cluster. On the other hand, the most southern locations from Palestine, Damascus, Maze Airport, Tadmur, Hama from Syria, and Tripoli and Kfardan from Lebanon were also included in this cluster trend. These regions showed increasing trends by 0.34, 0.31, 0.48, 0.36, and 0.52°C/decade, for annual, winter, spring, summer, and autumn-Tmin, respectively. Other regions such as Syrian coastal areas and most Palestine locations, except the most southern sites, formed the second cluster with less increasing trends by 0.24, 0.25, 0.38, 0.23, and 0.31°C/decade. The third cluster contains two

stations from Syria, Kamishli and Basil Airport, with low decreasing trends (less than -0.1°C/decade) for the annual and seasonal Tmin.

The DTR's increasing trend cluster was spatially grouped in Palestine's central and northern locations, the coastal and northern areas from Syria, and the Beyrouth Airport and Houche Oumara stations from Lebanon. These locations showed increasing trends of 0.15, 0.27, 0.24, 0.13, and 0.09°C/decade, for annual, winter, spring, summer, and autumn, respectively. On the other hand, the Syrian locations situated in the Damascus and Hama governorates formed a cluster of decreasing trends, by notably high rates of reducing in their annual, spring, summer, and autumn by -0.26, -0.36, -0.32, and -0.55°C/decade, respectively, whereas they showed a lower value in winter by -0.06°C/decade. The results also showed that Jordan, southern locations from Palestine (< 31ºN), and the stations of Tadmur and Deir Ezzor from Syria formed a cluster of increasing trend in winter-DTR by 0.23°C/decade and a decreasing trend on their summer and autumn-DTR by -0.11 and -0.16°C/decade, respectively.

4.2.5 Influence of the large-scale circulation patterns on the seasonal temperatures

Based on the frequency of significant correlation (Table 4.5), the NCP index showed the highest frequency with the Levant seasonal temperatures, where its impact extends to all seasons compared to other patterns by more than 91%, 67%, 38%, and 94% of the stations, for winter, spring, summer, and autumn, respectively. The results indicate the EA/WR and NAO indices come second place in terms of significant correlations except for autumn. Furthermore, the rest of the patterns showed notable correlations in some cases, such as ENSO/summer-Tmin (55% of the stations), WEMO/autumn-Tmax (67% of the stations), MO/winter (Tmax, Tmin) (> 90% of the stations).

		WEMO	EA/WR	NAO	EA	MO	NCP	ENSO
Winter	**Tmax**	0	59	46	0	58	60	0
	Tmin	0	50	53	0	54	55	1
Spring	**Tmax**	55	33	32	3	7	56	16
	Tmin	41	51	36	7	1	40	7
Summer	**Tmax**	3	18	22	15	14	37	23
	Tmin	4	11	15	12	9	23	33
Autumn	**Tmax**	40	0	7	7	0	59	1
	Tmin	4	0	4	6	0	56	3

Table 4.5. The total stations that showed significant ($p < 0.05$) correlation with the large-scale circulation patterns based on each season.

Figure 4.10 exhibits the correlation coefficients calculated between the indices and one single averaged seasonal (Tmax and Tmin) time series for the Levant and sub-countries. In the first place, it must be announced that the NCP index significantly and negatively correlated with all Levant´s seasonal Tmax and Tmin, with higher values than other patterns. These correlations ranged from -0.49 for summer-Tmax to -0.79 for winter-Tmax, and from -0.40 for summer-Tmin to -0.74 for winter-Tmin. Moreover, the NCP index showed negative correlations with all Levant countries' seasonal temperatures that are always significant except for three cases, Palestine and Syria summer-Tmin and Lebanon spring-Tmax. The maximum values were found in autumn (Tmax and

Tmin) for all countries by > -0.57 for Tmax and > -0.45 for Tmin. Among the indices, only the NCP index had significant correlations with the autumn Tmin for the Levant and countries.
Indices EA/WR, NAO, and MO also showed strong negative correlations with the Levant's winter Tmax and Tmin between -0.44 for NAO-winter-Tmax and -0.53 for MO-winter-Tmin. In winter, these three indices also had a significant correlation for all countries by values ranged from -0.35 for NAO-winter-Tmax at Syria to -0.59 for the MO-winter-Tmax at Palestine and from -0.34 for NAO-winter-Tmin at Lebanon to -0.60 for MO-winter-Tmin at Syria. In general, it can be concluded that the MO index is the second most influential index, after NCP, which affects the Levant's winter Tmax and Tmin (Figure 4.10).

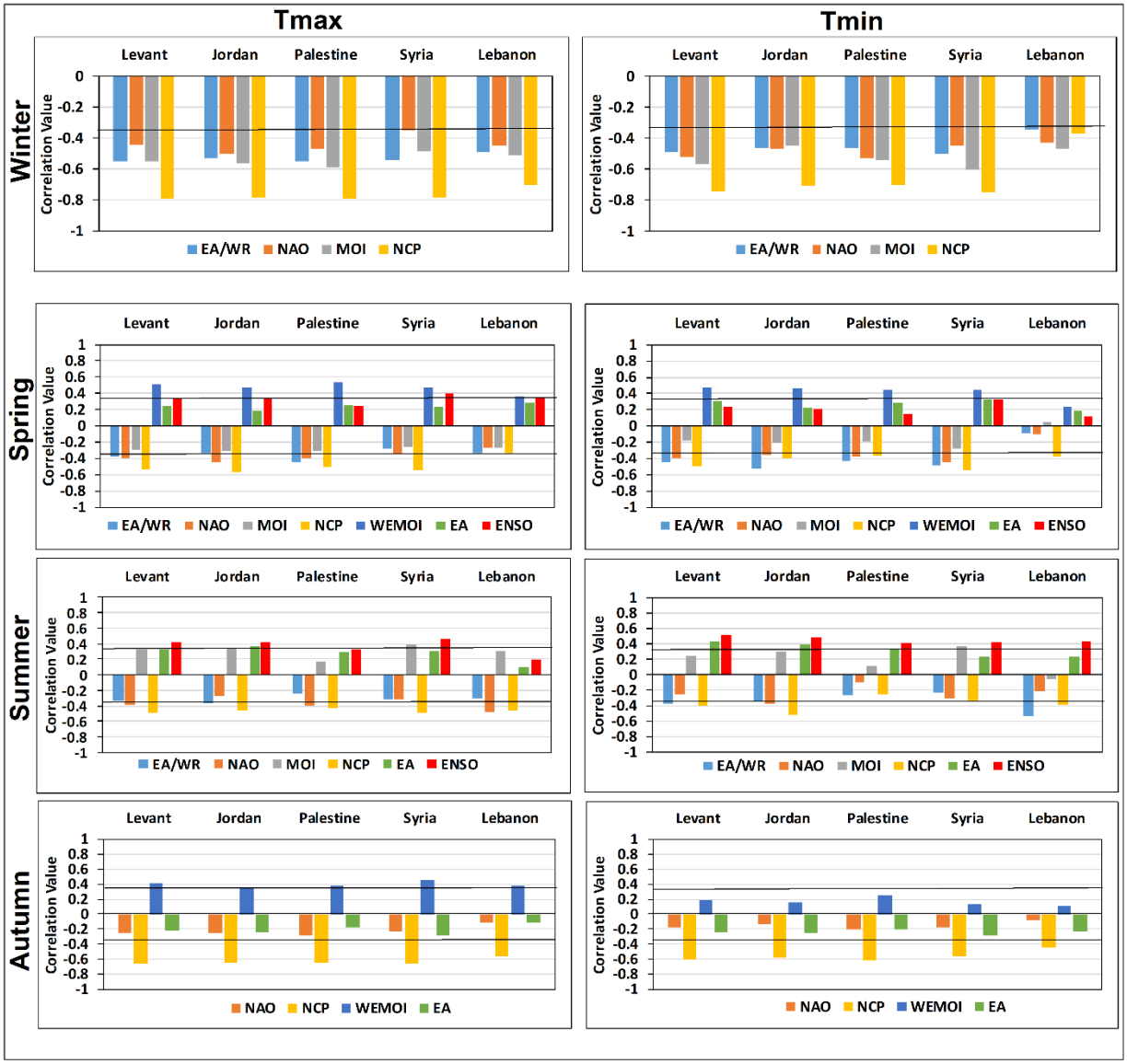

Figure 4.10. Correlation coefficients between the teleconnection patterns and seasonal temperature averaged series for the Levant and countries. Bold Horizontal line refers the significant limits.

For the Levant's spring Tmax and Tmin, a significant and negative correlation was found with the EA/WR, NAO indices, ranging from -0.38 to -0.45. Furthermore, the WEMO index highly correlated with the Levant´s spring temperatures by 0.51 for Tmax and 074 for Tmin. The significant influence of WEMO has included all countries of Levant, except for Lebanon-Tmin, by 0.36 for Lebanon-Tmax and 0.54 for Palestine-Tmax, and 0.24 for Lebanon-Tmin to 0.46 for Jordan-Tmin. Consequently, the WEMO index is the second most important index that affects spring temperatures. In some cases, it affects the spring temperatures more than the NCP index, such as Palestine-Tmax and Jordan-Tmin. It is also the second most important index that affects the autumn-Tmax for all regions by correlations values ranging from 0.37 to 0.45.

4.2.5.1 Correlation maps for the winter temperatures

Figure 4.11 represents the patterns of the correlations between the four-teleconnection indices EA/WR, NAO, MO, and NCP and winter Tmax and Tmin. For both Tmax and Tmin, the spatial correlation patterns with NCP are similar, although its influence on Tmin for Lebanon and some locations in the Palestinian coastal area (up to -0.47) is relatively less than Tmax (up to -0.79) (Figure 4.11). For Tmax (Figure 4.11, upper panels), the NCP index showed significant negative correlations (r < -0.70) for all locations, reaching values of r < -0.77 for some stations.

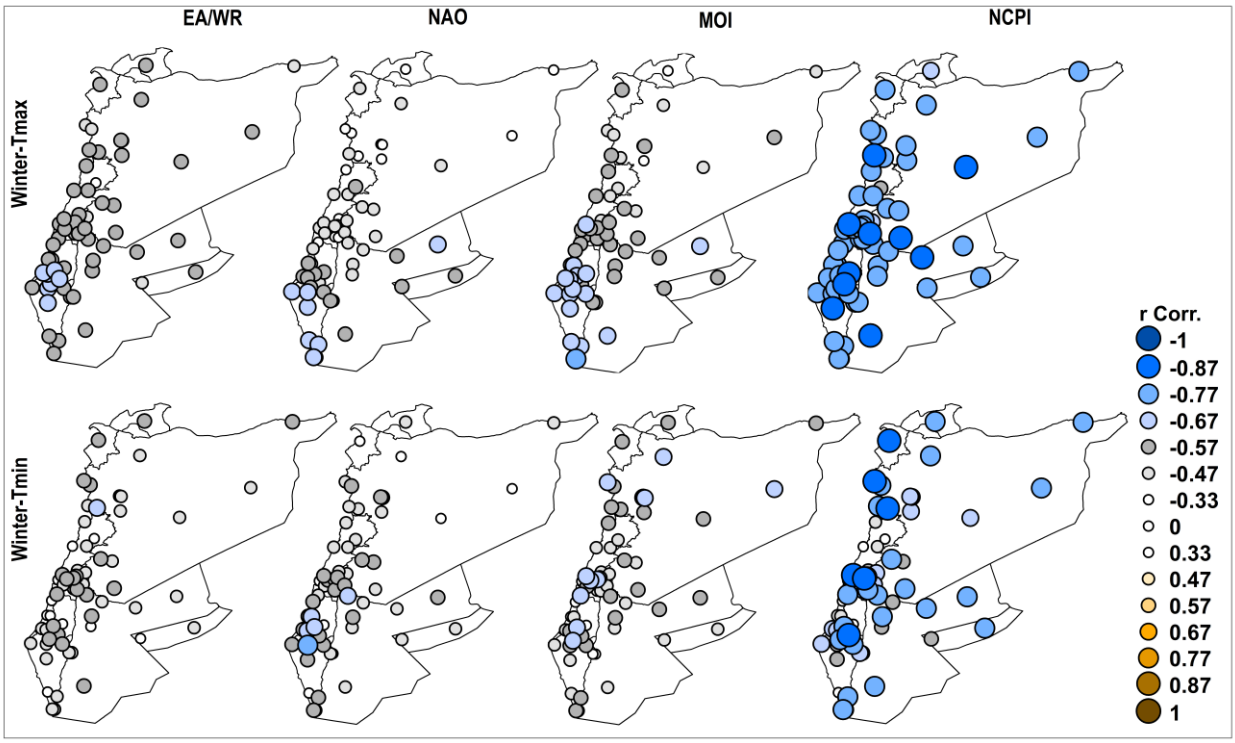

Figure 4.11. Spatial distribution of correlation coefficients between winter Tmax (top panels) and Tmin (bottom panels) and most significant teleconnection indices in the period 1987-2018.

A comparison between the EA/WR, NAO, and MO indices show that the MO had more influence than the NAO and EA/WR indices, especially in Palestine's southern locations (-0.57 to -0.66). For the EA/WR index, the high values of correlations (between -0.57 and -0.66) were mainly

concentrated in the south and west locations of Jerusalem and the upper Negev desert. For the NAO index, its influence ranged from -0.33 to -0.46 for all sites in north Palestine and Jordan and between -0.57 and -0.66 for Palestine's southeastern areas. The NAO and MO indices generally exerted more influence on the south Levant than the Northern Levant.

For Tmin (Figure 4.11, bottom panels), the MO index presented higher correlations with the winter Tmin, especially for Syria's areas compared with its influence on Tmax and compared to other indices. While EA/WR index generally showed a lower influence on Tmin than Tmax for most locations. The results also pointed to the high correlation coefficients (-0.50 to -0.69) for the EA/WR, NAO, and MO indices, which mainly covered Palestine's northern locations and locations located to the west and south Jerusalem.

4.2.5.2 Correlation maps for the spring temperatures

As shown in Figure 4.12 (upper panels), considerable positive correlations were recorded for WEMO index and negative for the NCP index. In this context, the strongest effect of WEMO on spring-Tmax was observed in Palestine, especially in the northern locations, with correlation coefficients between 0.51 and 0.69. In contrast, the NCP index showed the highest negative correlations (from -0.51 to -0.69) in the northern regions of Jordan and Palestine, southern regions of Jerusalem, and Syria's southern and eastern regions. The EA/WR and NAO indices generally showed a lower significant correlation ranging from -0.40 to -0.49 for all locations and mainly concentrated over Palestine and Jordan. The ENSO's effect was pronounced on Syria, north Lebanon, and Jordan by correlations from -0.33 to -0.47.

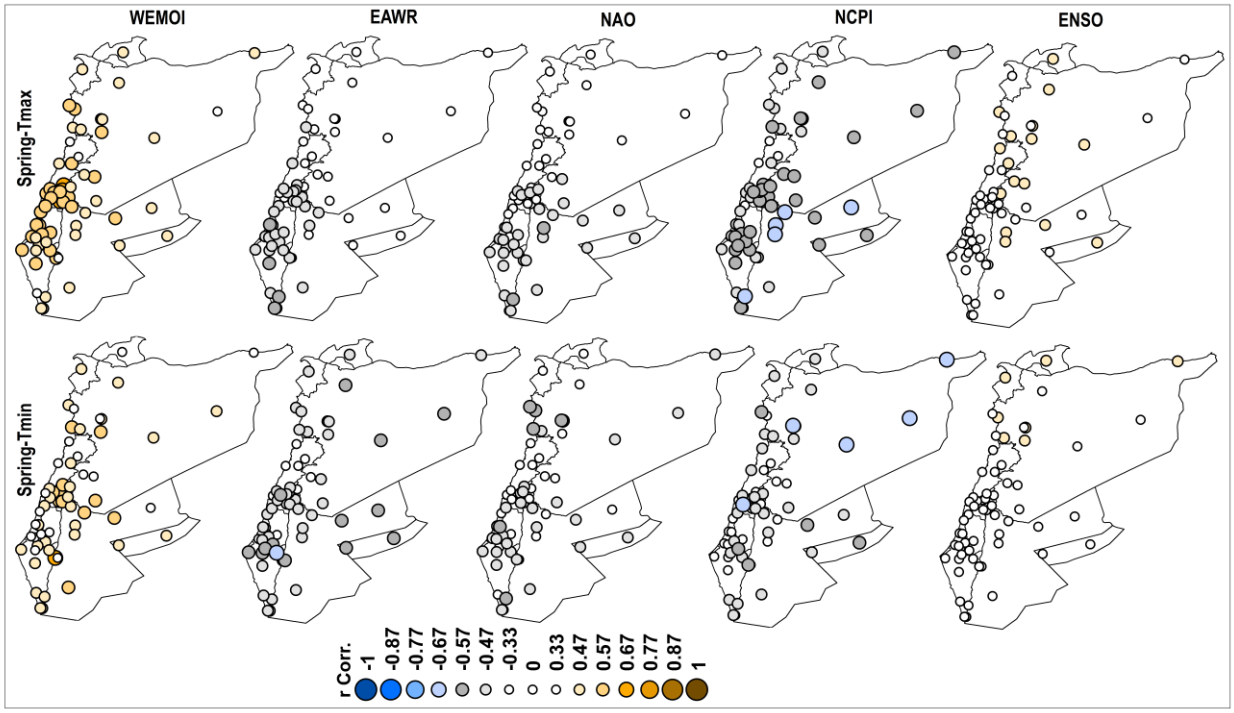

Figure 4.12. Spatial distribution of correlation coefficients between spring Tmax (top panels) and Tmin (bottom panels) and teleconnection indices in the period 1987-2018.

For spring-Tmin (Figure 4.12, bottom panel), the highest effect was found for the WEMO index on the northern regions of Palestine due to high correlations (0.57 to 0.66). The NCP index showed a high negative correlation (-0.57 to -0.66) for Syria's eastern locations. On the other hand, it obviously showed a low correlation for southern Levant (Palestine and Jordan) for most sites ($r < -0.47$), compared with its effect on Tmax. It is also noticed that the EA/WR´s influence was more pronounced on the southern Levant than the NCP´s impact. In this context, most locations, especially the Syrian locations (-0.37 to -0.57), eastern locations from Jordan (-0.57), and upper parts of the Negev desert in Palestine correlated strongly (-0.57 to -0.67) with the EA/WR. On the contrary, its influence was lower on Lebanon-Tmin (< -0.27) than its impact on Tmax. The NAO index also showed a high effect on Tmin for Syrian coastal stations (-0.57), and similar to EA/WR, its influence was lower on Tmin for Lebanon locations (< -0.27) than Tmax.

4.2.5.3 Correlation maps for the summer temperatures

Figure 4.13 shows the correlation maps between the EA/WR, NAO, EA, MO, NCP, and ENSO indices and summer-Tmax/Tmin for 60 stations distributed across the study area. It can be seen that the relations between NCP and ENSO indices and summer-Tmax are stronger compared to other indices. The significant negative correlation coefficients between the NCP index and summer-Tmax are generally homogeneous in the Levant. However, for some places in east and south Jerusalem, they show high values.

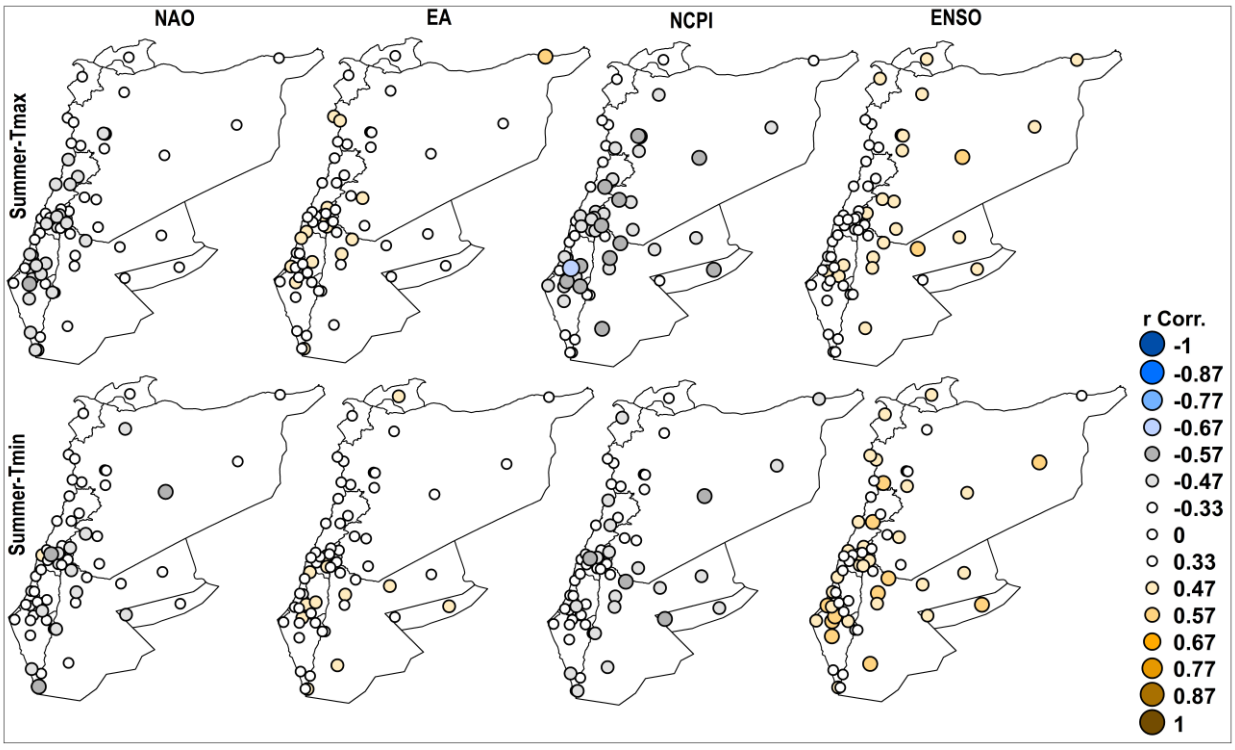

Figure 4.13. Spatial distribution of correlation coefficients between summer Tmax (top panels) and Tmin (bottom panels) and teleconnection indices in the period 1987-2018.

For Syria, the NCP index exerted an effect on the central and eastern stations (-0.47 to -0.57). The results also revealed that the NCP index's impact was generally lower on Tmin than Tmax, especially in Palestine's northern/central regions and in Syria's northwestern areas (< -0.37). The ENSO index showed a remarkably influence on summer-Tmax for the eastern sites more than for the western sites. In general, its influence was weaker (< 0.37) between 34ºE-35.5ºE than its influence between 35.5ºE-42.3ºE (0.37< r <0.57).

For Tmin, the effect of the ENSO index was more pronounced than its impact on Tmax. In this context, its significant influence was greatly expanded, encompassing more locations between 34ºE-35.5ºE, especially the coastal areas of Syria, Lebanon, and Palestine (0.37 < r < 0.47). In addition, it showed more frequency of high correlations band (r < 0.57) with some locations in the upper part of the Negev desert in Palestine and east Jordan. The EA's effect was more pronounced on Tmax than Tmin, and mainly concentrated in the southern Levant (Jordan, northern and central locations from Palestine) by correlation from 0.37 to 0.47.

4.2.5.4 Correlation maps for the autumn temperatures

The NCP index (Figure 4.14) showed a high and negative correlation with most of the study area locations. The correlations varied from -0.57 to -0.66 for Palestine and Syria's coastal regions and Palestine's northern locations. Furthermore, it showed very high correlations (> -0.67) with ten stations, such as Jerusalem, and Amman. The significant effect of WEMO index on the autumn-Tmax was homogeneous for locations between 29.5ºN-35ºN by 0.33 to 0.46, while it reached values from 0.33 to 0.56 for north Syria between 35ºN-37.5ºN. The results confirmed the NCP index as the main driver of the autumn-Tmin. For most places, such as the Palestinian coastal region and north Jordan, it showed relatively less impact on Tmin than Tmax. The highest correlations (up to -0.77) were found with some places in northern Palestine.

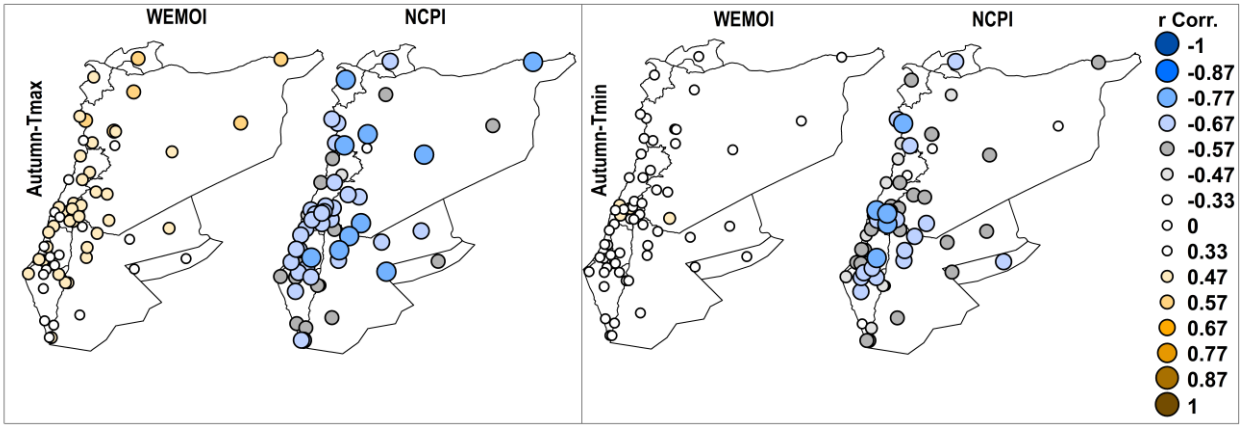

Figure 4.14. Spatial distribution of correlation coefficients between autumn Tmax (top panels) and Tmin (bottom panels) and teleconnection indices in the period 1987-2018.

4.3 Conclusions and discussion

The aim of this study was to identify the spatial and temporal changes in annual, seasonal, and monthly trends of maximum, minimum, and diurnal temperature range over the entire Levant region during the period 1987-2018. In addition, it was to determine which of the large-scale variability modes influence the seasonal temperatures of the Levant. The conclusions can be drawn as follows:

1. The annual and seasonal Tmax and Tmin have shown an increase below long-term averages from 1987 to 2000. After that, they showed a decrease near long-term averages in 2000-2006, and they began to increase above long-term averages from 2006 onward. A different behavior was observed in 1987-1992 for winter and summer when the averages decreased below long-term means. The annual and seasonal Tmax and Tmin have increased since the last decade of the 20th century. In the Levant, the warmest/coldest annual averages were in 2010/1992 for Tmax and Tmin.

Such tendency was also found in Turkey, Saudi Arabia, Egypt, Iran, Spain, and eastern Mediterranean (Repapis et al., 2007; Saaroni et al., 2003; Türkeş et al., 2002; Almazroui et al., 2012; Domroes et al., 2005; Gonzalez-Hidalgo et al., 2016; Asakereh et al., 2020). Interestingly, the warmest year was globally also in 2010 (WMO, 2011) as well as at the regional scales in Saudi Arabia, Egyptian Mediterranean coast, Turkey, Spain, Iraq, and Iran (Nazrul Islam et al., 2015; Tonbol et al., 2018; Hadi et al., 2018; Gonzalez‐Hidalgo et al., 2016; Ghasemi, 2015; Muslih et al., 2017). Furthermore, the world was also cold during 1991/1992, probably due to the eruption of Mt. Pinatubo (Jones, 1994).

2. During the period 2001-2018, the means of Tmax and Tmin for annual, spring, summer, January, February, June, July, and August have significantly increased over the Levant region compared to the period 1987-2000. The highest Tmax and Tmin significant increases were registered for spring and March. Moreover, the means of Tmax and Tmin for the 10-years non-overlapping periods, 1987-1996, 1997-2006, and 2007-2018 have gradually increased. The last decade 2007-2018, significantly was the hottest decade for all Tmax and Tmin temporal scales.

These increases are in the same line as those of the global temperature. The rise of 0.21°C in the decadal temperature averages of global, from 1991–2000 to 2001–2010, is larger than for any other two successive decades since the beginning of instrumental records (WMO, 2013). Based on the WMO Statement on the State of the Global Climate in 2019, the last five-year (2015–2019) and ten-year (2010–2019) averages are also the warmest on record. In Jordan, Matouq et al. (2013), analyzed the mean annual Tmax and Tmin in 1979-2008. The results showed the mean maximum annual temperature was around 30.65°C during the first decade (1979–1988), and then increased to 34.7°C during the second decade (1989–1998).

3. In 1987-2018, the significant warming trends affected both daytime (Tmax) and nighttime (Tmin) temperatures in the Levant, but at a higher rate for Tmax than Tmin in winter (December-February), summer (June and August), and spring (Mach-April). On the contrary, the Levant-Tmin has experienced a higher warming rate than Tmax in autumn

(September-November), May, and July. The highest monthly warming trends for Tmax and Tmin were observed in February and March. Only September-Tmin from autumn months showed a significantly increasing trend. Furthermore, a very strong and significant seasonal warming trend (> 0.50ºC/decade) was observed for spring-Tmax and spring-Tmin, winter-Tmax, and autumn-Tmin. Note that the summer-Tmax trend (0.34ºC/decade) in particular showed a less strong warming trend than the winter-Tmax.

4. The DTR of the cold months (December-April) increased, while it decreased for the warm months (May-November), being significant only for August and September. The highest monthly increase in DTR was in March, although non-significant. A strong and widespread significant decrease in March rainfall (Chapter 7) could be associated with a decrease in cloud cover and an increase in the March-DTR. Many authors pointed to the inverse effect of changes in cloud cover (New et al., 2000; Geerts, 2003).

These results are consistent with studies from many regions of the Levant and the world. The trend towards a warmer climate has been reported in Mediterranean countries such as Spain (0.15-0.35ºC/decade), Italy (0.2ºC/decade), and Romania (0.15 to 0.28°C/decade) (del Rio et al., 2012; Toreti and Desiato, 2008; Viola et al., 2013; Micu D et al., 2015). Furthermore, it has been well documented in Europe over the last three decades (Stott, 2003; Luterbacher et al., 2007), with warming in most regions being stronger in winter than in summer (Micu D et al., 2015; Vogelsang and Franses, 2005). Ghasemi (2015) analyzed the annual and seasonal Tmax and Tmin mean values over Iran based on data from 38 stations during the period 1961-2010, and the results showed significant warming trends in the mean values. They also indicated that the spring-Tmax average showed a strong significant warming of 0.42°C/decade. Malekian and Kazemzadeh (2016) analyzed regional trends in southwestern Iran based on data from 15 stations in the years 1972-2011 and found that the mean temperature series on the monthly scale for February and March showed the highest magnitude of warming trends. Robaa and AL -Barazanji (2013) investigated the annual mean temperature at 11 stations in Iraq, using time series of different lengths over the period 1941-2010. The results confirmed a warming trend at all stations at an increased rate of 0.50°C/decade, with the highest warming trend occurring after 1995. Toros (2012) examined the variation of extreme daily temperatures over Turkey during the period1961-2008, and the results showed that a total of 69% of the stations (165 stations) showed positive trends in annual Tmax averages and 66% positive trends in annual Tmin averages. AlSarmi et al. (2011) analyzed the trends in temperature and precipitation parameters for Arabian Peninsula based on data from 21 stations during the years 1980-2008. They found significant increasing trends in annual and seasonal Tmax and Tmin mean values and decreasing trends at the DTR level, where annual Tmax and Tmin significantly increased at a rate of 0.32 and 0.55°C/decade, respectively, and the autumn showed very strong warming trends in Tmin average by 0.70°C/decade. Kenawy et al. (2009) found a significant warming trend in the annual minimum temperature as well as in DTR over Libya by 0.23°C/decade and -0.28°C/decade, respectively, and spring showed the highest significant warming trend by 0.29°C/decade for Tmin.

5. In all seasonal temperatures, the Tmax warming was higher than Tmin for all countries, except for the autumn. Spring showed the highest increasing trends for all countries. Moreover, the Tmax of south Levant increased significantly at a higher rate than north Levant in the annual, spring, summer, and autumn. Only in winter, the Tmax of north Levant rise at a higher rate than south Levant. On the contrary, the Tmin of the North Levant rose at a higher rate than south Levant in the annual, winter, and autumn. Of all countries, Jordan had the highest significant increasing trends in Tmax for annual, winter, spring, and summer, whereas Syria had the highest trend for autumn-Tmax. In addition, Syria-Tmin had the highest warming trend in the annual, winter, and autumn, while Palestine and Jordan showed the highest trends in spring-Tmin and summer-Tmin.
6. On a monthly basis, in January, October, November, and December, no country showed significantly increasing trends of Tmax and Tmin. The Jordan-Tmax and Tmin showed the highest increase in the summer months of June, July, and August. It also showed the highest increasing trends in autumn Tmax and Tmin months, of September and October. Palestine-Tmax and Tmin showed the highest trend values in March, November, and December, although they were significant only for March.
7. The widespread significant warming trends (> 80% of the stations) were mainly observed during the course of the year, in March, February, and August, both in Tmax and Tmin. Spatially, most stations from Jordan and northern and central areas of Palestine showed very high warming trends for annual, winter, spring, summer, and autumn Tmax with the highest value for spring. These regions also showed very high warming trends for the summer-Tmin and winter-DTR.

Fallah-Ghalhari et al. (2019) examined the effects of climate change on the Tmax and Tmin over Iran using data from 45 stations in the years 1976-2005. They showed more than 80% of the stations with warming trends in their Tmax and Tmin, and only one station showed a significantly decreasing trend. The trend slope for maximum and minimum temperature was 0.23 and 0.39°C /decade, respectively. Al Qatarneh et al. (2018) studied the impact of climate change on water resources in the Azraq Basin in Jordan using data for only two stations in the years 1980-2014. The results showed that the mean maximum temperature increased significantly with an average of 1°C/decade, while an increase in the mean minimum temperature of 0.5°C/decade was observed. The mean annual temperature above the Azraq Basin increased by 0.75°C/decade during the 46 years studied.

8. The NCP index was the major influential atmospheric circulation index for the seasonal temperatures in the Levant. In this context, it showed more significant negative correlations compared to other patterns. For winter Tmax and Tmin, more than 55 stations showed significant correlations with this index by mean values of -0.77 and -0.56, respectively. For autumn Tmax and Tmin, the NCP index showed significant correlations with more than 56 stations and mean correlations of -0.64 and -0.56. Furthermore, it was the main regulator in summer Tmax with 37 stations that correlated significantly with a mean value of -0.47. Significant negative correlations reached more than 40 stations for spring Tmax and Tmin.

Its strong influence on the spring Tmin mainly covered the northern Levant areas in Lebanon and Syria. The NCP index was also the second most important pattern affecting the summer-Tmin. In contrast, the ENSO pattern with an average correlation of 0.46 and significant correlations with 33 stations was the most important driving force for the summer minimum. All other patterns showed no particularly significant correlations for summer temperatures, with the exception of the EA/WR index on the Lebanon-Tmin.

9. The WEMO index was the second most important index, affecting autumn-Tmax and spring-Tmax and Tmin. Apart from the NCP and WEMO indices, the other patterns did not have a major impact on autumn and spring temperatures, except for some cases in spring-Tmin such as the EA/WR on the eastern locations from Jordan and Syria and for the northern stations from the Negev desert. The highest impact of the EA/WR, NAO, and MO indices occurred in winter. For example, the MO index influenced the winter-Tmax for the southern regions of Palestine. The NAO index had a significant influence on the winter-Tmax and Tmin for the southern Levant.

Kutiel et al. (2002), who found, on the basis of monthly temperatures and precipitation from 33 stations across Greece, Turkey, and Israel, that the temperature were significantly higher during the NCP in its negative phase as compared with the NCP in its positive phase. Their results placed the NCP as the most influent of the teleconnections over the Middle East. The NAO and Southern Oscillation (SO) present an ability to differentiate between below-normal or above normal temperatures, and as one of the main teleconnections affecting the climate of the Balkans, the Anatolian Peninsula and the Middle East. Ghasemi and Khalili (2008) investigated the relationship between the NCP and winter temperature variability in Iran, showing that the NCP has a strong negative correlation with winter temperatures. Furthermore, it was found that the positive phase of the NCP is associated with strong cyclonic activity over Iran, causing enhanced cloudy conditions and precipitation. Ben-Gai et al. (2001) analyzed the temperature and surface pressure anomalies in Israel and the NAO using data of maximum and minimum monthly temperatures from 6 stations, covering a period of 45 years (1950-1994). The result revealed a high negative correlation between the NAO index and temperature variation in Israel. This result are also confirmed in this study, where NAO showed negative correlation with all seasonal temperatures in Palestine and Israel, although with high rates in winter-Tmax and Tmin as well as in summer-Tmax. Hasanean (2004) studied the wintertime surface temperature in Egypt in relation to the associated atmospheric circulation, using data for 18 stations. The results indicated very weak correlations between ENSO and EA patterns and winter temperature for all stations. On the other hand, the highest significant effect occurred between the EA/WR pattern and all stations. The NAO also showed significant negative correlations with 10 out of 18 stations. Ramadan et al. (2011) studied the sensitivity of the temperature and precipitation response over the Litani basin in Lebanon to 13 different global and regional climate circulation patterns. In their study used satellite data during the period 1950-2008, and the result showed temperature variability over the entire Litani Basin shows an overall annual negative correlation with NAO index. Meanwhile, mean temperature shows to be negatively correlated with NAO in all seasons. The EA/WR pattern did

not showed significant correlation with the Litani precipitation with any temporal and spatial data used. However, the connection with temperature variation is evident. An annual negative correlation between the Litani's temperature and EA/WR pattern is detected.

Abualnaja et al. (2015) analyzed the impacts of climate modes on air–sea heat exchange in the Red Sea and they found that the Red Sea climate was strongly and negatively influenced by the NAO and the EA/WR indices with maximum impact on the northern part of the Red Sea, especially in winter. The negative heat flux anomalies generated by the NAO and EA/WR indicate that these modes are associated with a greater heat loss by the sea during winter. This is because of the transfer of colder air masses from higher latitudes during the positive phase of the NAO and EA/WR over a broader region including the eastern Mediterranean Sea.

CHAPTER 5

ANALYSIS OF EXTREME TEMPERATURE INDICES

This chapter aims to analyze the spatial and temporal changes in the annual and seasonal extreme temperature indices over the southern Levant for the period (1987-2018) Also, the influence of the seven large-scale circulation patterns on the extreme temperature indices is spatially and temporally analyzed.

5.1 Introduction

Climatic extreme events can have serious impacts on environment and society compared with the changes in the average climate (Vörösmarty et al., 2000; Parmesan et al., 2000). Furthermore, extremes are more sensitive to climate change than mean values (Katz and Brown, 1992). However, most analyses of long-term global climate change using observational temperature and precipitation data have focused on changes in mean values (Alexander et al., 2006), and there are few studies about climate extremes, especially in a region like Levant. The analysis of changes in extremes depends on daily data, which are generally difficult to access in countries like Jordan, Lebanon, Syria and Palestine, which impose restrictions on the accessibility of climatic data.

According to the studies of the IPCC, the warming in southern and eastern Mediterranean over this century will be larger than the global average warming and the annual precipitation is very likely to decreases (IPCC, 2007, 2013). For example, Lelieveld et al. (2012) predict a continual, gradual and relatively strong warming of about 3.5-7°C between the period 2070-2099 and the 1961-1990 reference period and under an intermediate IPCC SRES scenario. The IPCC's scenarios for the eastern Mediterranean indicate that average summer temperatures will gradually increase around 0.5-0.9˚C/decade, and the number of warm days will increase by 20-40 additional days/year by the end of the 21st century (Lelieveld et al., 2012). Note as was indicated by Lelieveld et al. (2012), the expected changes in precipitation could be associated with a reduction of

cloudiness, which allows more solar radiation to be absorbed at the surface, being able to contribute to the increase of temperature. In addition, the Levant region in general, and Historical Palestine (Israel and Palestine) in particular, are considered more vulnerable and sensitive to the negative impacts of climate change, because these regions are affected by many developmental stresses such as the water resources shortage, weakness of existing infrastructure, low adaptive capacity, and frequent drought events. Moreover, all of these factors are escalated by the political conflicts and the rapid population growth (Hammad and Salameh, 2018; Al-Qinna et al., 2011; Ziv et al., 2006; Lelieveld et al., 2012; Sowers et al., 2011; Terink et al., 2013).

For Levant region, there are very few studies focused on changes in climate extremes indices. Zhang et al. (2005) analyzed changes in several indices over the Middle East region for the period 1964-1999, using data from 52 stations of 15 countries, but only 4 stations belonged to Levant region. Donat et al. (2014) examined changes in extreme temperature and precipitation in the Arab region, but their study did not include stations from the Historical Palestine. However, changes in the frequency and intensity of climate extreme indices have been already well documented in other countries such as Saudi Arabia (Islam et al., 2015; Almazroui et al., 2014; Athar, 2014), Arabian Peninsula (AlSarmi and Washington, 2014), Iran (Rahimi and Hejabi, 2018; Rahimzadeh et al., 2009) and Turkey (Toros, 2012; Erlat and Türkeş, 2013).

Therefore, the present study has a dual objective. Firstly, it tries to fill the gap in the studies related to extreme temperature indices in the Levant region. Secondly, it provides a comprehensive temporal and spatial analysis of extreme temperature indices and their relationships with the main large-scale circulation pattern in the northern Atlantic and the Mediterranean Basin, i.e., the North Atlantic Oscillation (NAO), the East Atlantic (EA) pattern and the EA/Western Russia (EA/WR) pattern, the Western Mediterranean Oscillation (WEMO), the Mediterranean Oscillation (MO), and the North Sea-Caspian pattern (NCP).

The study also includes an analysis of the El Niño-Southern Oscillation (ENSO) influence over Levant extreme temperature indices, as the main global climate variability pattern. The methodology and the list of extreme temperature indices used in this work along with their definition are in Section 3.7 and Table 3.1, respectively. In addition, Figure 2.6a shows the geographical distribution of the stations used for this analysis, while Table 3 in the Appendix A provides names, coordinates, and elevations of the stations. Details related to data, Quality Control (QC), and homogeneity are available in Chapter 2, Section 2.2.

5.2 Results

5.2.1 Annual trends of extreme temperature indices averaged over the study area

Figure 5.1 depicts the time series of anomalies for the annual extreme temperature indices averaged over the whole study area during the period 1987-2018, and Table 5.1 shows their temporal trends. Although the absolute extreme indices (TXx, TNx, TXn and TNn) showed increasing trends by 0.17, 0.40, 0.05 and 0.18ºC/decade, respectively, only TNx trend resulted significant at the 90% confidence level (Table 5.1). It is also noted that, meanwhile hot absolute extreme indices (TXx, TNx) were found to increase with rates higher than those of their corresponding cold extreme

indices (TXn, TNn), the hot percentile TX90p and TN90p indices increased with rates lower than the decreasing rates of the TX10p and TN10p indices. Furthermore, in all absolute and percentile-based extreme temperature indices the increasing trends related to minimum temperature (night-time) indices were higher than those of maximum temperature (daytime) indices (Table 5.1).
Figures 5.1c and 5.1d depict the percentile-based extreme temperature indices TX90p, TX10p, TN90p and TN10p, where the temporal behaviors for TX10p and TN10p clearly pointed to a decreasing trend along the period 1987-2018. Increasing trends by 2.20 and 3.17 days/decade were found, significant at the 99% confidence level, for TX90p and TN90p, respectively; while TX10p and TN10p showed non-significant decreasing trends by -3.94 and -5.52 days/decade, respectively. These results strongly confirmed the general tendency toward the warming over the study area.

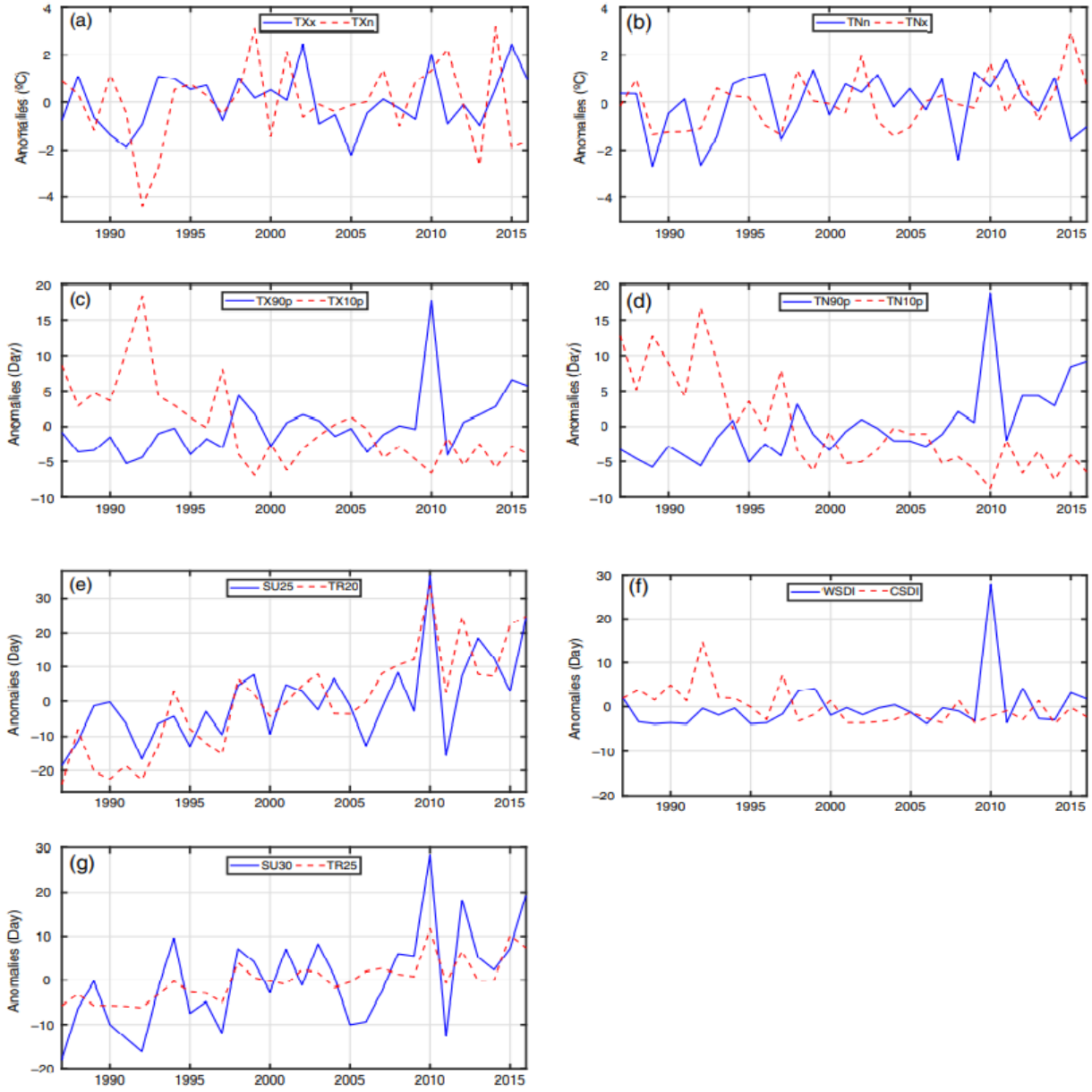

Figure 5.1. Time series of anomalies for the annual extreme temperature indices averaged over the study area during the period 1987–2018.

The tendency towards warming in the analyzed region was also confirmed by the duration and fixed threshold extreme temperature indices SU25/30 (summer and very summer days), TR20/25 (tropical and very tropical nights), WSDI (warm spell duration) and CSDI (cold spell duration) (Figures 5.1e, f, and g). The temporal behavior for SU25/30 and TR20/25 indices showed increasing trends along the period 1987-2018. The SU25 and TR20 indices displayed significant increasing trends at 0.001 significance level by 8.15 and 14.4 days/decade, respectively. Moreover, very summer days (SU30) and very tropical nights (TR25) indices exhibited significant increasing trends at the 95% and 99.9% confidence levels by 7.10 and 3.74 days/decade, respectively. Furthermore, WSDI index showed significant increasing trend at the 95% confidence level by 0.63 days/decade, whereas the CSDI index had a significant decreasing trend at the 99% confidence level by -1.79 day/decade (Table 5.1).

Index	Trend	Index	Trend
TXx	0.17 (^{0}C/decade)	**TN10p**	-5.52 (days/decade)
TXn	0.05 (^{0}C/decade)	**WSDI**	0.63* (days/decade)
TNx	0.40+ (^{0}C/decade)	**SU25**	8.15*** (days/decade)
TNn	0.18 (^{0}C/decade)	**SU30**	7.10* (days/decade)
ETR	-0.01 (^{0}C/decade)	**FD**	0 (days/decade)
TX90p	2.20** (days/decade)	**CSDI**	-1.79** (days/decade)
TX10p	-3.94 (days/decade)	**TR20**	14.40*** (days/decade)
TN90p	3.17*** (days/decade)	**TR25**	3.74** (days/decade)

Table 5.1. Trends for the annual extreme temperature indices averaged over the study area. Symbols ***, **, * and +, indicate a significant trend at $\alpha = 0.001$, $\alpha = 0.01$, $\alpha = 0.05$ and $\alpha = 0.1$ level, respectively.

5.2.2 Annual trends of extreme temperature indices at local scale

5.2.2.1 Absolute extreme temperature indices

Table 5.2 and Figure 5.2 show the results of the trend analysis for the absolute extreme temperature indices, at annual scale. In general, most stations in the central and southern regions exhibited increasing trends for all absolute indices, although except for TNx trends, they did not show significant increasing trends at the 95% confidence level. The hot absolute extremes (TXx and TNx) were found to increase at more stations compared to cold extremes (TXn and TNn). In addition, the number of locations that were affected by increasing trends in the minimum temperature indices (TNx and TNn) was larger than those of the maximum temperature indices (TXx and TXn). In detail, maximum values of minimum temperatures (TNx) intensively exhibited increasing trends in 89% (25 stations) of total stations, and 36% (10 stations) with significant increasing trends by values ranging between 0.45 and 1.14ºC/decade. High and significant increasing trends (up to 0.68ºC/decade) were mainly distributed over the Palestinian Coastal Plain regions (Lod Airport, Bet Dagan and En Hahoresh stations) and at some stations in the north (Kefar Blum and Elon stations) and in the south (Elat and Hakfar Hayarok). The results did not detect any significant decreasing trend in the five absolute indices, except for one station (Hazeva) in ETR index.

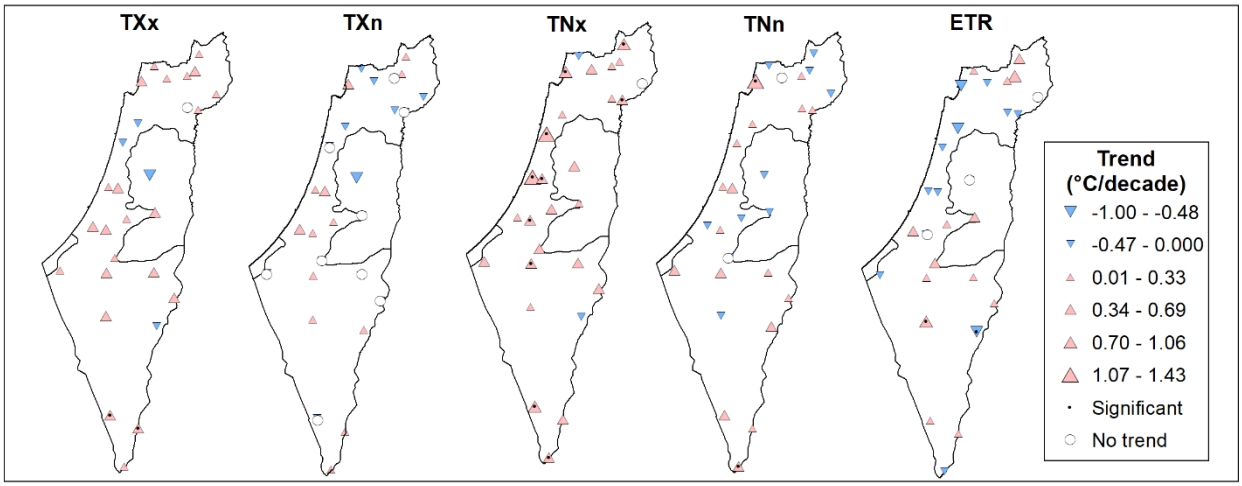

Figure 5.2. Spatial distribution of trends (ºC/decade) for absolute extreme temperature indices.

Index	Positive	Negative	Percentage of stations (%)
TXx	23 (2)	4 (0)	7.1 / 0
TXn	13 (0)	6 (0)	0 / 0
TNn	17 (2)	9 (0)	7.1 / 0
TNx	25 (10)	2 (0)	36 / 0
ETR	14 (1)	11 (1)	3.5 / 3.5
TX90p	28 (25)	0	89 / 0
TX10p	0	28 (1)	0 / 3.5
TN90p	28 (26)	0	93 / 0
TN10p	0	28 (3)	0 / 10.7
WSDI	13 (11)	0	39 / 0
CSDI	2 (1)	8(6)	0 / 21
SU25	27 (23)	1 (0)	82 / 0
SU30	26 (16)	1 (0)	57 / 0
FD	3 (0)	16 (1)	0 / 5)
TR20	28 (24)	0	86 / 0
TR25	12 (8)	0	28.5 / 0

Table 5.2. Number of stations showing positive and negative trends for each extreme temperature index at annual scale. In bracket the number of stations showing significant trends at the 95% confidence level. Right column shows the percentage of stations with significant increasing/decreasing trends.

5.2.2.2 Percentile-based extreme temperature indices

The results shown in Table 5.2 and Figure 5.3 clearly indicated homogeneous patterns of the increasing/decreasing trends for all percentile-based extreme temperature indices. The results also confirmed the tendency toward warming over the study area where all locations exhibited decreasing trends in their cold extreme (TX10p and TN10p) indices whereas they showed increasing trends in their hot extreme (TX90p and TX10p) indices. In this context, 100% of total stations exhibited increasing trends in their TX90p and TN90p, with 89% (25 stations) and 93% (26 stations), respectively, showing significant trends with values up to 2.74 and 3.20 days/decade, respectively. The high band of increasing trends higher than 2.39 days/decade affected more locations for TN90p than those for TX90p, such as some stations in the Palestinian Coastal Plain

region (En Hahoresh, Galed, Lod Airport and Bet Dagan) (Figure 5.3). Coherently, TX10p and TN10p indices displayed decreasing trends in 100% of total stations but with a smaller number of significant stations, only 1 and 3 stations, respectively (Table 5.2).

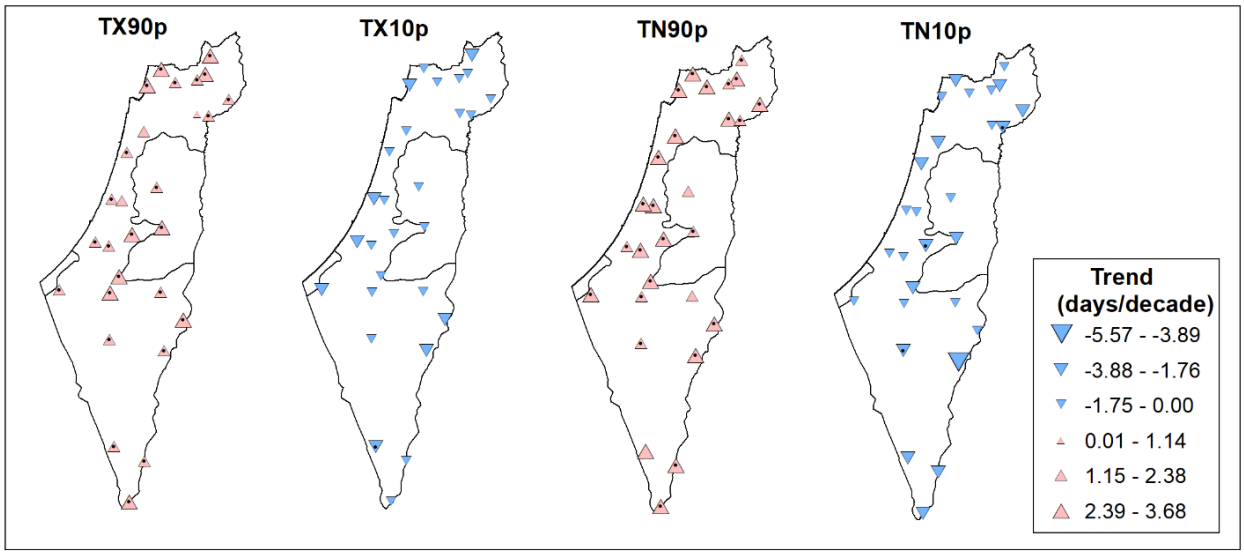

Figure 5.3. Spatial distribution of trends (days/decade) for annual percentile-based extreme temperature indices. Significant trends at the 95% confidence level are marked by a dot.

5.2.2.3 Duration and fixed threshold extreme temperature indices

The tendency toward a warming was also confirmed by the results shown in Table 5.2 and Figure 5.4 for the annual duration and fixed threshold extreme temperature indices, where decreasing trends were not observed for WSDI, SU25/30 and TR20/25 indices, except for Ariel station, although was not significant. In addition, the WSDI index showed increasing trends while the CSDI index showed decreasing trends.

Summer days (SU25) and tropical nights (TR20) indices exhibited very intense and significant increasing trends in 82% and 86% (23 and 24 stations, respectively). All stations that showed significant positive trends in their SU25 index, also showed significant positive trends in their TR20 index. Furthermore, most regions in the study area were affected by a high band of significant increasing trends (between 6.90 and 11.09 days/decade) in both indices (Figure 5.4).

For very summer days (SU30) and very tropical nights (TR25) indices, the significant increasing trends intensively occurred at more locations for SU30 (57%, 16 stations) than those of TR25 index (28.5%, 8 stations). The very high and significant increasing trends (between 17 and 22 days/decade) covered the north-western regions at Elon and Akko stations for SU30, while the high and significant increasing trends (from 11 to 14 days/decade) found over the south-eastern areas at Elat, Yotvata and Hazeva stations, and the north-eastern areas at Yavne'el and Massada for TR25 index (Figure 5.4).The warm spell duration index (WSDI) denoted increasing trends in 52% (13 stations), and only 39% (11 stations) resulted significant at the 95% significance level (Table 5.2). The positive increasing trends (between 1.26 and 2.83 days/decade) were mainly distributed over the northern and center regions (Figure 5.4).

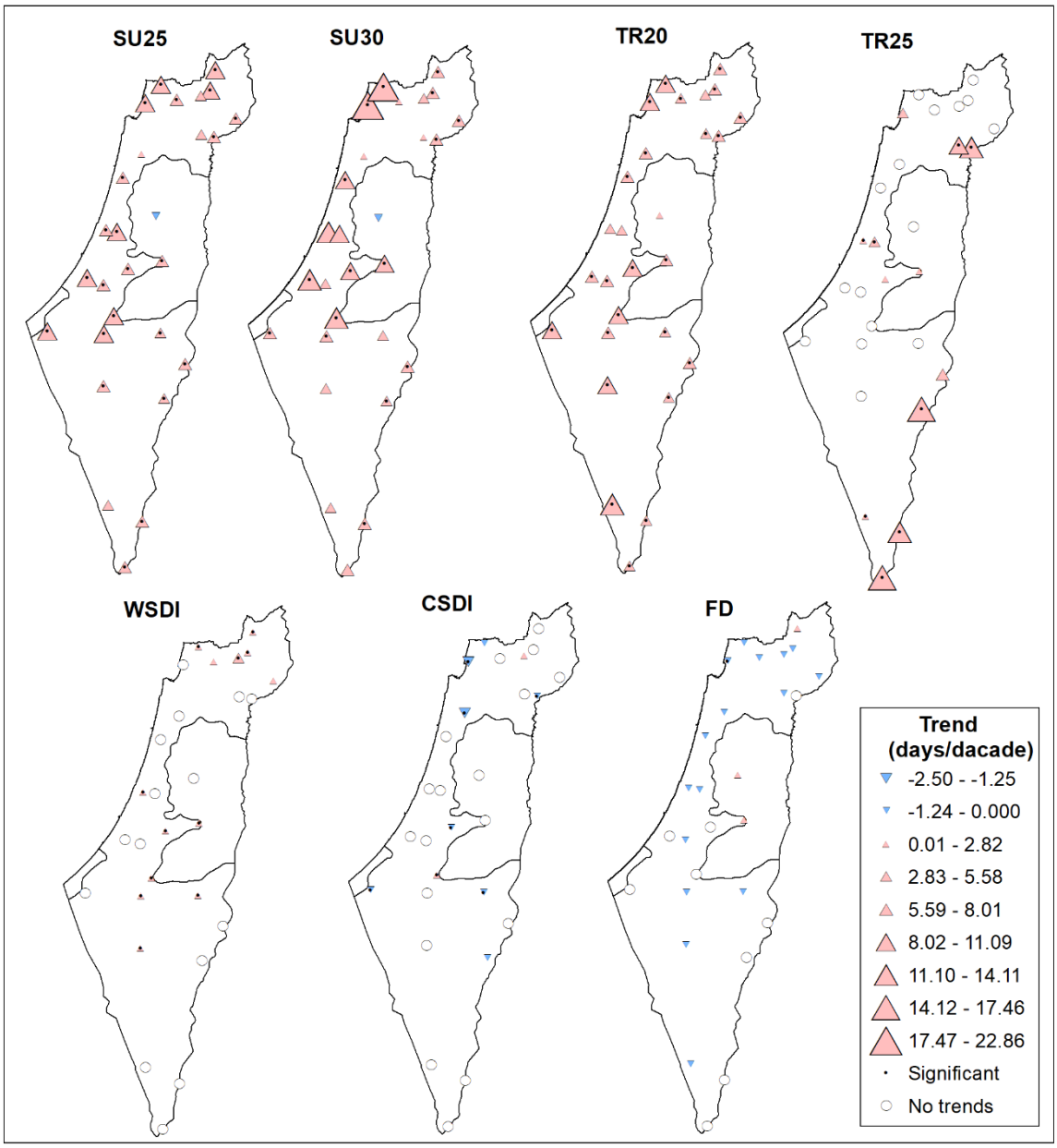

Figure 5.4. Spatial distribution of trends (days/decade) for annual duration and fixed threshold extreme temperature indices. Significant trends at the 95% confidence level are marked by a dot.

The negative trends for cold spell duration index (CSDI) and frost days (FD) also confirmed the tendency toward the warming, with 28.5% of the locations (8 stations) showing decreasing trends for CSDI index and 21% of them (6 stations) with significant trends. Only one station (Lahav) displayed significant increasing trend by 1.00 day/decade for CSDI. High decreasing trends of CSDI between -1.99 and -2.49 days/decade occurred in the north-western region. For FD index, most stations (57%) showed negative trends, but only 1 station (Akko station) resulted significant with a value of -0.12 days/decade. In addition, for this latter index, only few isolated stations presented positive trends although non-significant.

5.3 Seasonal trends of extreme temperature indices at local scale

5.3.1 Absolute extreme temperature indices

Results presented in Table 5.3 and Figures 5.5 and 5.6 did not reveal any significant decreasing trend for all the seasonal absolute extreme temperature indices. Furthermore, warming trends affected more locations than the decreasing trends for all the seasonal absolute extreme temperature indices, except for TXx-spring and TXx-autumn (Table 5.3 and Figure 5.5), when non-significant decreasing trends affected more locations, mainly distributed in the northern region. The analysis for frequency and intensity of trends also revealed that the total number of locations that was affected by significant/non-significant warming trends for the minimum temperature indices (TNx and TNn, Figure 5.6) were more than those for the maximum temperature indices (TXx and TXn, Figure 5.5), especially for spring and autumn (Table 5.3).

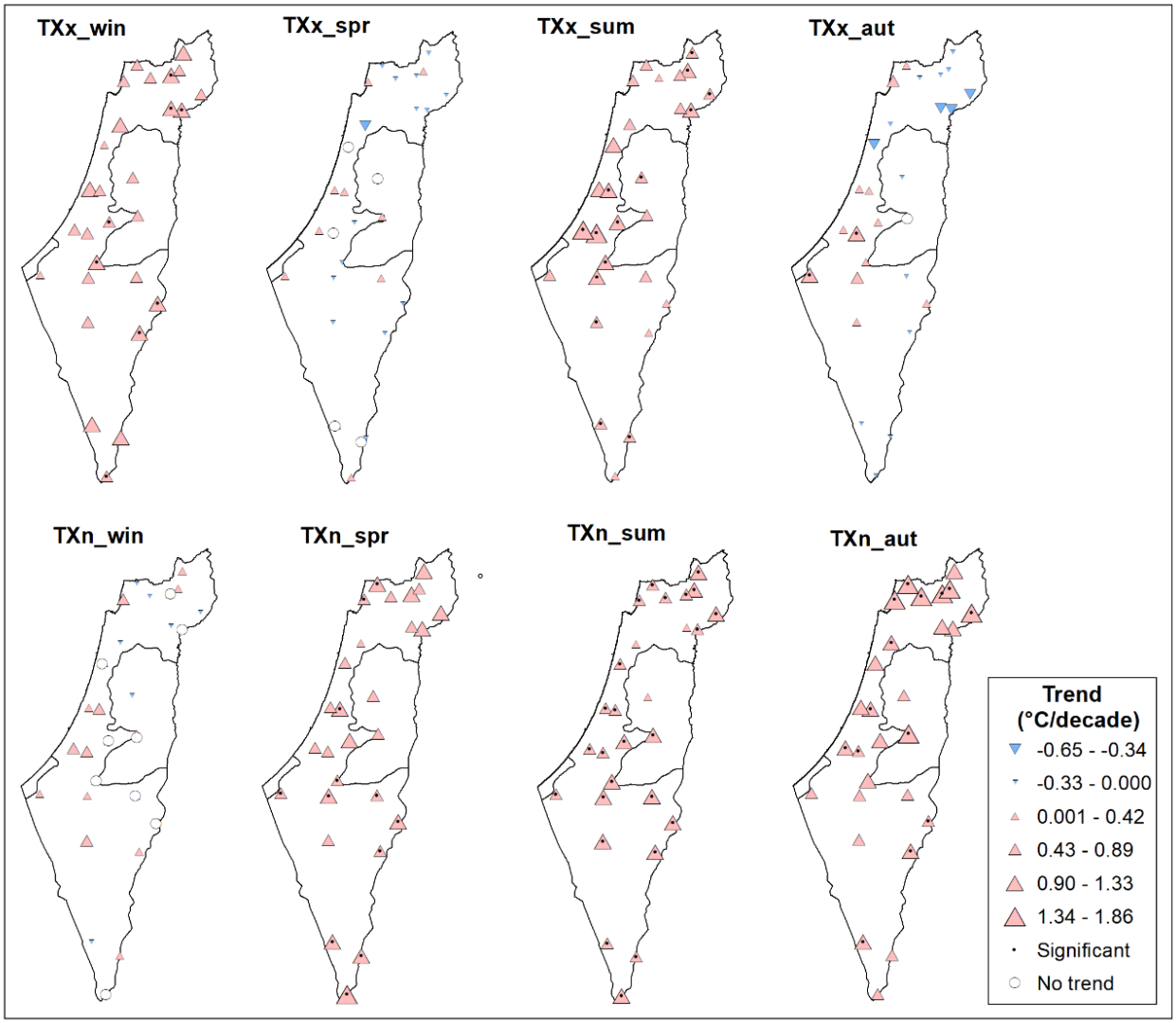

Figure 5.5. Spatial distribution of trends (ºC/decade) for seasonal absolute extreme maximum temperature indices. Significant trends at the 95% confidence level are marked by a dot.

More than 96% of total stations showed positive trends for all absolute summer extreme temperature indices (Table 5.3). Moreover, summer did not show any decreasing trend at all stations and for all indices. It is also interesting to note that it exhibited the highest total of stations with significant warming trends in 50%, 89%, 96% and 89% of total stations for the TXx, TXn, TNn and TNx indices, respectively (Table 5.3). For spring and autumn, they showed dominant warming trends (> 96% of total stations) in the minimum values of the absolute temperature indices (TXn and TNn), with significant trends for more than 43% of total stations, while winter showed dominant occurrence of warming trends for maximum values of temperature indices (TXx and TNx), with significant results for more than 29% of total stations.

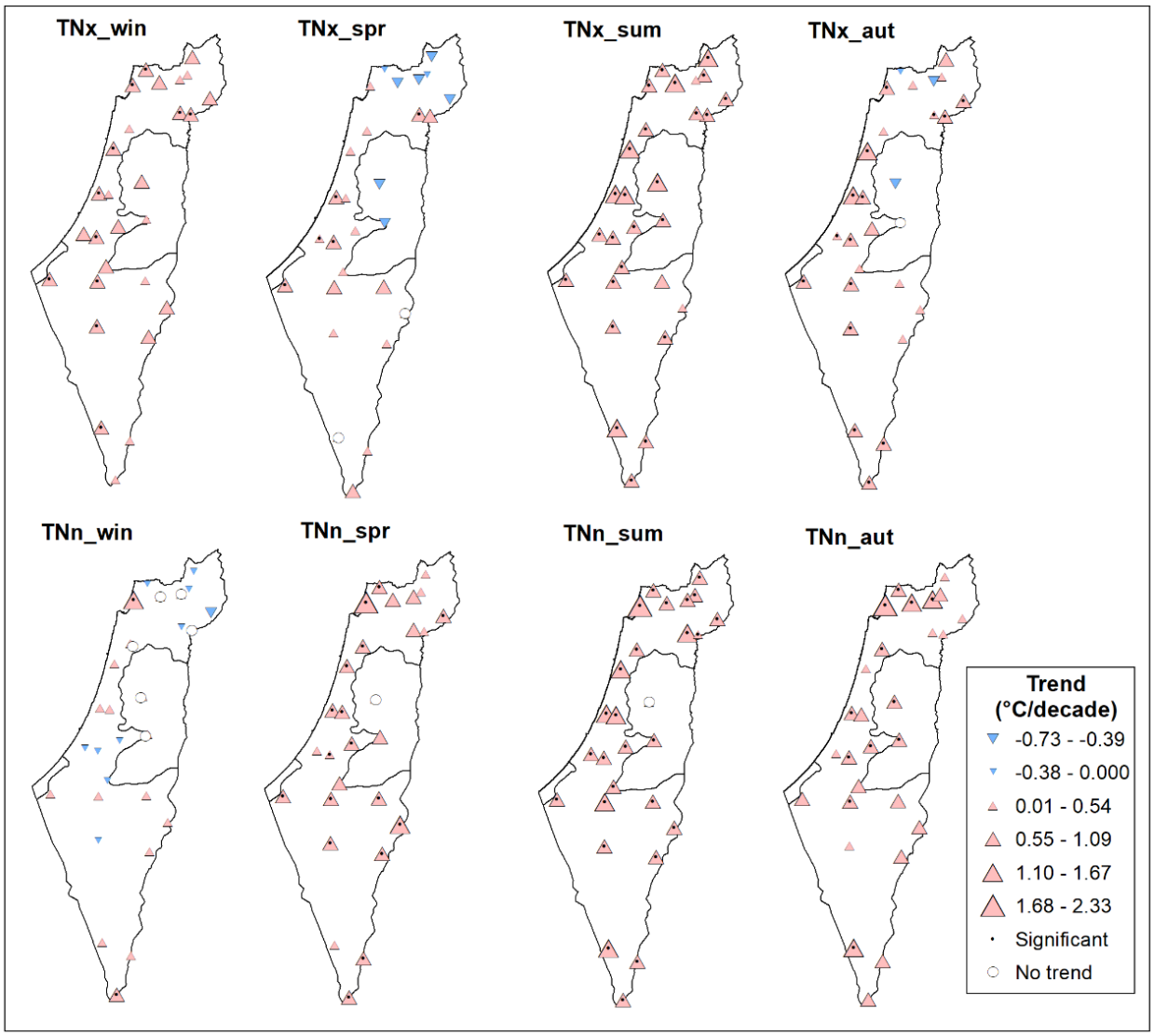

Figure 5.6. Spatial distribution of trends (ºC/decade) for seasonal absolute extreme minimum temperature indices. Significant trends at the 95% confidence level are marked by a dot.

Regarding decreasing trends, spring and autumn displayed decreasing trends in 50% of total stations for TXx index. They also displayed decreasing trends in 29% and 11% of total stations for

TNx index, respectively. Furthermore, the decreasing trends occurred in TXn-winter and TNn-winter in 25% and 36%, respectively (Table 5.3). The coherent spatial of decreasing trends, although nonsignificant, were found in some cases such as for TXx-spring in the northern regions, TNx-spring in the northern and central areas of the West Bank, and TXx-autumn in the regions that extended from central West Bank to the most north-eastern regions for the northern regions (Figures 5.5 and 5.7).

Index	Seasonal scale							
	Winter		Spring		Summer		Autumn	
	Positive	Negative	Positive	Negative	Positive	Negative	Positive	Negative
TXx	28 (8)	0	9 (0)	14 (0)	28 (14)	0	12 (2)	15 (0)
TXn	12 (0)	7 (0)	28 (12)	0	28 (25)	0	28 (14)	0
TNn	12 (2)	10 (0)	27 (17)	0	27 (27)	0	28 (12)	0
TNx	28 (11)	0	18 (5)	8 (0)	28 (25)	0	24 (15)	3 (0)
TX90p	28 (17)	0	28 (9)	0	28 (21)	0	16 (1)	12 (0)
TX10p	0	28 (0)	0	28 (2)	3 (0)	25 (5)	0	28 (24)
TN90p	28 (12)	0	28 (17)	0	28 (24)	0	26 (9)	2 (0)
TN10p	3 (0)	25 (0)	0	28 (14)	0	28 (5)	0	28 (16)
SU25	22 (20)	0	27 (21)	0	5 (3)	0	25 (4)	2 (0)
SU30	1 (1)	0	21 (7)	6 (0)	21 (8)	1 (0)	26 (4)	2 (0)
TR20	0	0	23 (11)	5 (1)	25 (23)	0	26 (18)	2 (0)
TR25	0	0	6 (2)	0	20 (15)	0	6 (4)	2 (1)

Table 5.3. Number of stations with positive and negative trends for each extreme temperature index at seasonal scale. In bracket the number of stations with significant positive or negative trends at the 95% confidence level.

The analysis of the intensity of warming trends revealed that summer significantly showed the highest warming trends between 0.98 and 1.36ºC/decade for TXx index and spatially covered the regions extended eastward and northward of the Gaza strip. It is also exhibited a significant warming trend between 0.6 and 1.0ºC/decade in the north-eastern region. In addition, spring and autumn exhibited warming trends in TXn index stronger and more pronounced than their trends in TXx index. The highest rates of warming trends occurred in autumn for TXn index, from 0.90 to 1.86ºC/decade, distributed over the northern regions of the study area (Figure 5.5). Furthermore, the high significant increasing trends for summer (from 1.0 to 1.22ºC/decade) covered the north-eastern regions and the upper areas of the Negev desert.

For the minimum temperature indices (TNx and TNn), the results shown in Figure 5.6 generally indicated that spring and autumn exhibited more intense and positive trends for (TNx) index than their (TXx) index. Similar conditions were also found in summer, especially for the northern and south-eastern regions. Moreover, summer showed more intense increasing trends for TNn index than TXn index, especially for all coastal regions that extends from Gaza strip in the south to Akko in the north (with rates from 0.98 to 1.47ºC/decade). For TNx index, the highest and significant warming trends, in the interval 1.11-1.23ºC/decade, appeared in summer, and spatially distributed in the Palestinian Coastal Plain regions (Beit Dagan, Lod Airport and En Hahoresh stations) as well as at Kefar Hayarok and Harashim stations in the north. For TNn index, autumn showed high increasing trends in the northern regions with some locations reaching 2.33ºC/decade.

5.3.2 Percentile-based extreme temperature indices

In general, all seasons showed significant increasing trends in the TN90p index (Figure 5.8) for more locations and with higher intensity than the TX90p index (Figure 5.7), except for winter. For the TX90p index, winter and summer displayed higher frequency and intensity of the significant increasing trends compared with those for spring and autumn, when 61%, 32%, 75% and 3.5% of total stations exhibited significant increasing trend for winter, spring, summer and autumn, respectively (Table 5.3). The strongest significant increasing trends (from 3.74 to 4.27 days/decade) covered the most northern and southern regions in winter and they covered all regions, except for very few locations in summer (Figure 5.7). In spring, the area extended eastward and northward of the Gaza strip showed a significant increasing trend in their TX90p index by 2.70 days/decade on average.

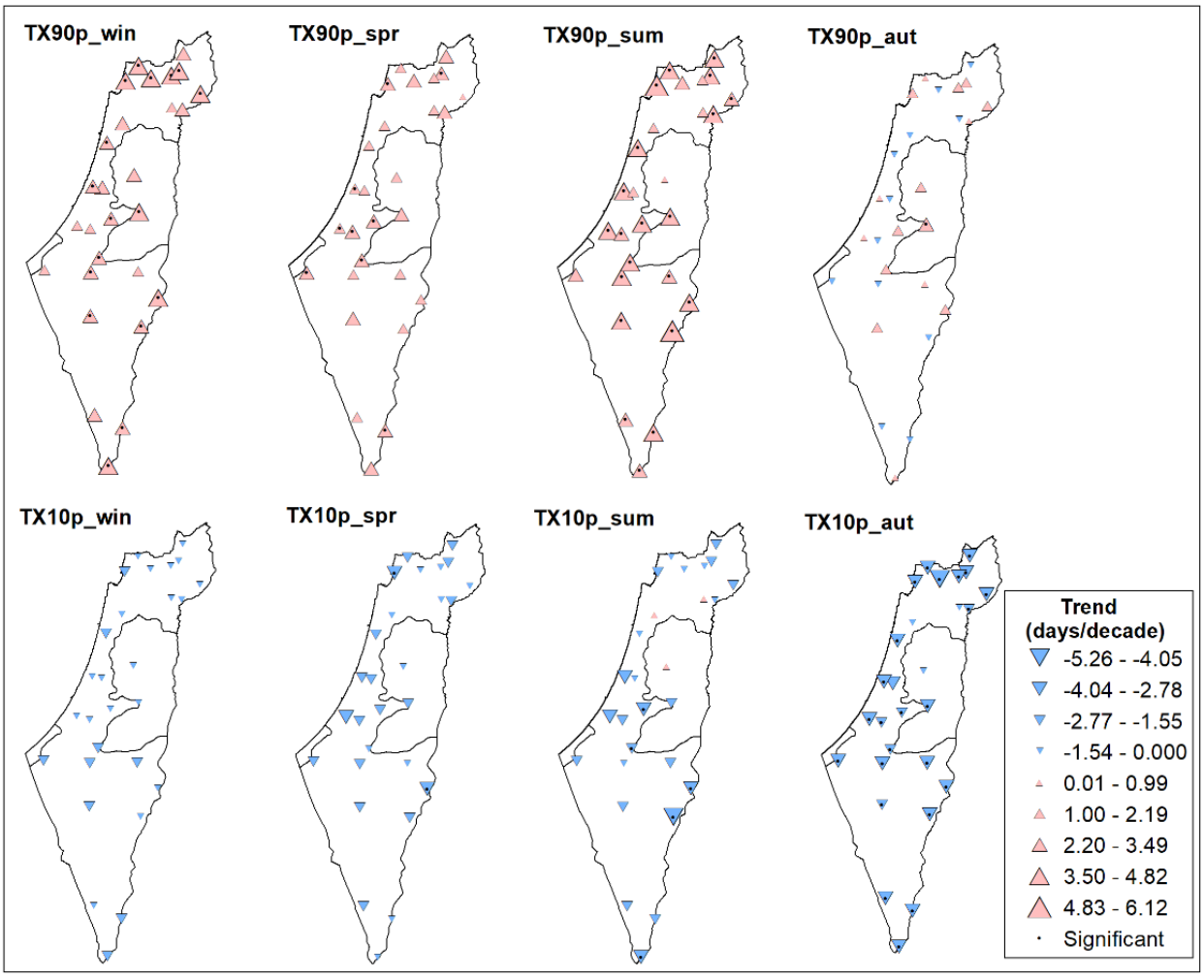

Figure 5.7. Spatial distribution of trends (days/decade) for seasonal percentile-based extreme temperature indices. Significant trends at the 95% confidence level are marked by a dot.

For TN90p index, 43%, 61%, 86% and 32% of total stations had significant increasing trends for winter, spring, summer and autumn, respectively (Table 5.3). The strongest significant positive

trends were in summer (by 4.79-5.31 days/decade) and spatially covered all the study area. For the rest of seasons, the increasing trends were, in general, less intense (< 3.22 days/decade) for all regions (Figure 5.8). Regarding TX10p and TN10p indices, all seasons had decreasing trends for all locations, except a total of six stations (three in TX10p-summer and three in TN10p-winter) which showed very weak and non-significant increasing trends. The results also indicated that winter did not show significant decreasing trends in both indices and for all locations. Contrariwise, autumn showed the highest occurrence and intensity of decreasing trends, significant for the 86% of the total number of stations for TX10p index and the 57% for TN10p index (Table 5.3). For TX10p-autumn index (Figure 5.7), the highest significant decreasing trends (between -2.78 and -5.36 days/decade) covered the entire study region. For TN10p-autumn (Figure 5.8) the intensity of decreasing trends reached values even higher in general.

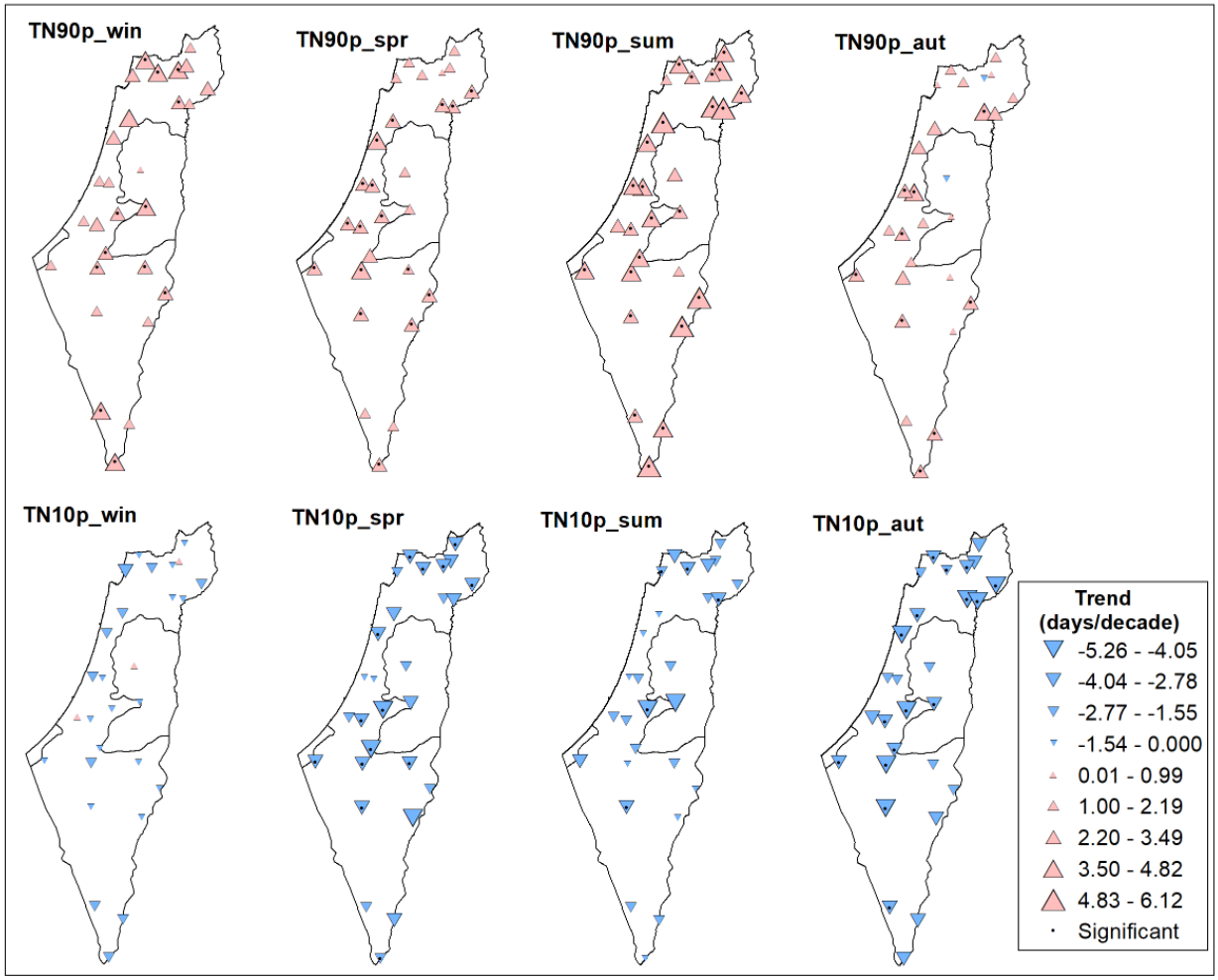

Figure 5.8. Spatial distribution of trends (days/decade) for seasonal percentile-based extreme temperature indices. Significant trends at the 95% confidence level are marked by a dot.

Spring, showed significant decreasing trends at more locations and with higher intensity in TN10p index than TX10p index (50% and 7% of total stations, respectively, Table 5.3). For TN10p-spring, most locations showed significant decreasing trend (from -2.52 to -3.57 days/decade). In addition,

the significant decreasing trends showed a generalized pattern in TX10p-summer and TN10p-summer, but only with five significant results (Figures 5.7 and 5.8).

5.3.3 Duration and fixed threshold extreme temperature indices

The results presented in Figure 5.9 and Table 5.3 indicated 82% of total stations (23 stations) remarkably showed significant and positive trends for TR20 index (between 4.39 and 7.53 days/decade) in summer. The regions extended eastward and northward of the Gaza strip had the highest positive trends in summer, with rates from 6.28 to 7.53 days/decade. Furthermore, 64% and 39% of total stations had significant increasing trends respectively in autumn and spring. For autumn, the trends ranged between 3.14 and 3.77 days/decade, whereas they were lower than 1.43 days/decade for most locations in spring. In addition, the northern regions showed decreasing trends for TR20-spring by -0.62 days/decade (Table 5.3, Figure 5.9).

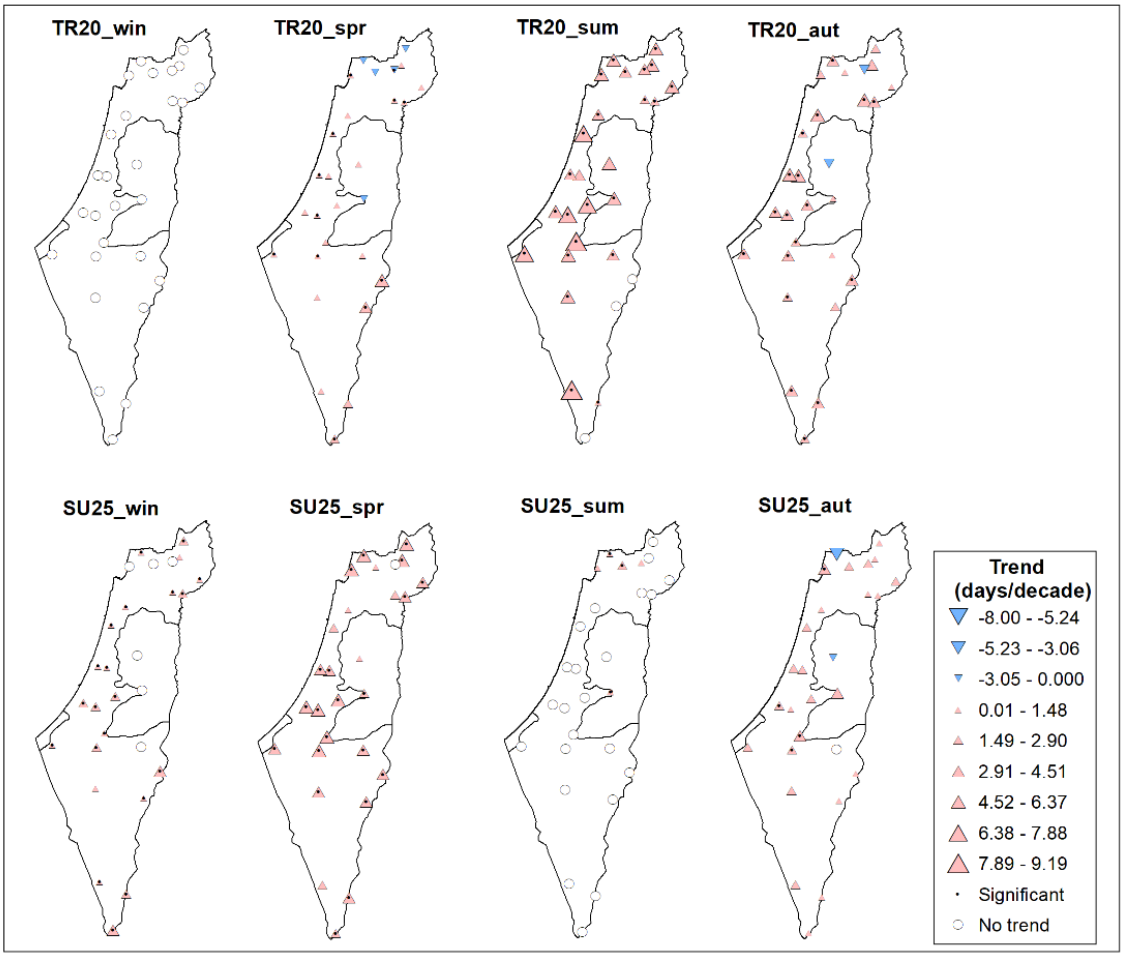

Figure 5.9. Spatial distribution of trends (days/decade) for duration and fixed threshold extreme temperature indices. Significant trends at the 95% confidence level are marked by a dot.

For SU25 index, summer did not exhibit remarkably increasing or decreasing trends in 89% of total stations, whereas winter showed significant increasing trends in 71% of the cases (20 stations), autumn in 14% (4 stations) and spring in 75% (21 stations). Spring had the highest

significant and generalized increasing trends, up to 4.39 days/decade, which are mainly distributed over the whole area (Figure 5.9).

For autumn and summer, the frequency and intensity of increasing trends related to the minimum temperature (TR20) were greater than those of maximum temperature (SU25) at all locations. Contrary, the frequency and intensity of increasing trends for winter and spring were greater for SU25 than for TR20 at all locations.

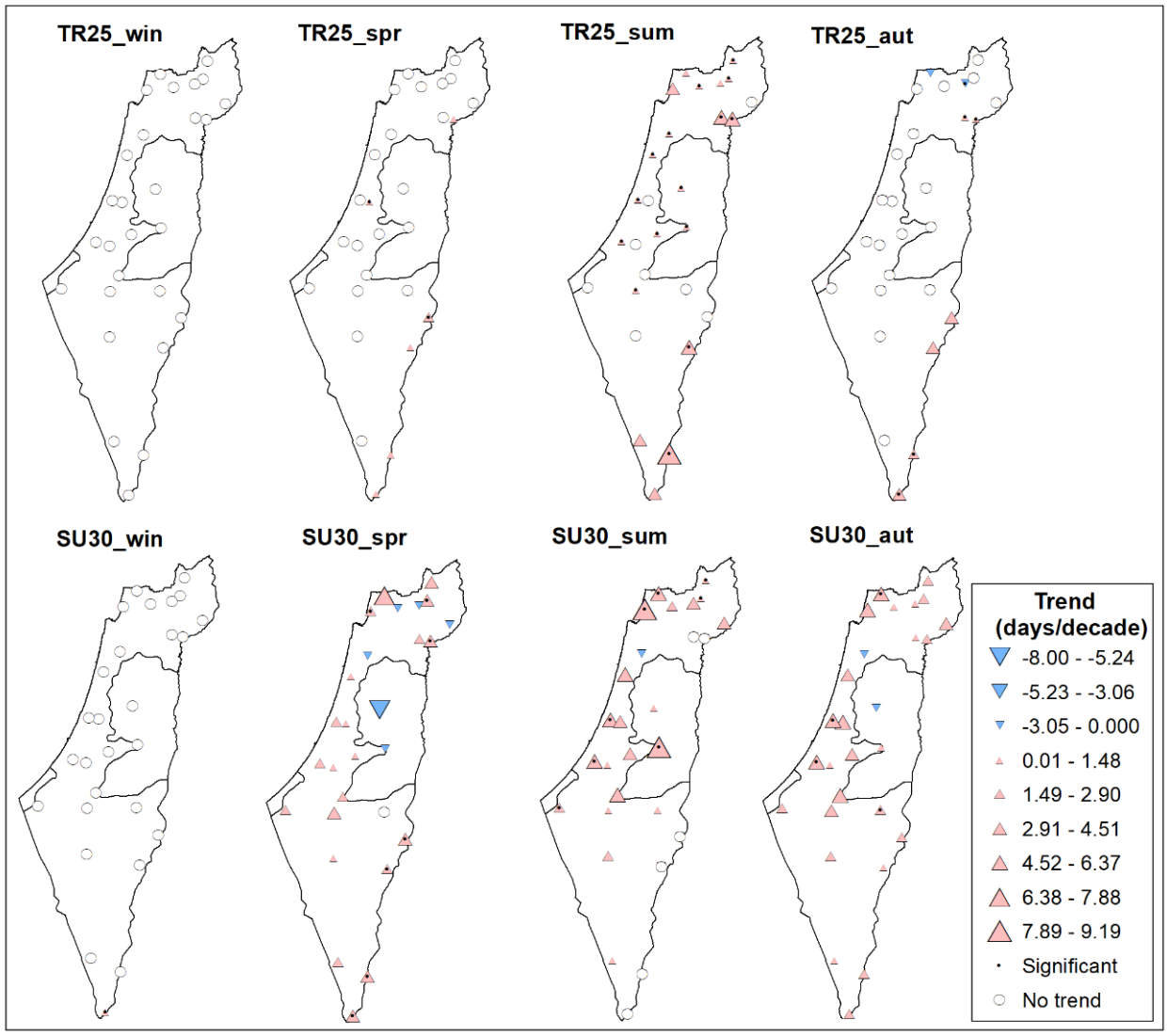

Figure 5.10. Spatial distribution of trends (days/decade) for duration and fixed threshold extreme temperature indices. Significant trends at the 95% confidence level are marked by a dot.

For very extreme threshold indices, the increasing trends for SU30-spring were more pronounced than those for TR25-spring for all regions, except at Ariel and Jerusalem stations which exhibited non-significant decreasing trends (Figure 5.10). In this context, for TR25-spring only 6 stations showed increasing trends with 2 stations of them being significant, while 75% (21 stations) showed increasing trends for SU30-spring index with 33.4% (7 stations) of them being significant.

Spatially, the south-eastern regions along the border with Jordan exhibited increasing trends for both indices, but with higher rates (from 2.52 to 3.77 days/decade) for SU30 index (Figure 5.10). For winter, the results did not detect any trend for TR25 and SU30, except at Elat station which exhibited a significant increasing trend for SU30 by 0.43 days/decade (Figure 5.10).
In summer, TR25 index significantly showed increasing trends at more locations (53% of total stations) than those for SU30 index (28% of total stations), whereas SU30 generally showed higher intensity of increasing trends than TR25 in most locations, especially in the Palestinian Coastal Plain areas and some locations in the northern regions. Most stations in the Palestinian Coastal Plain showed significant increasing trends for TR25 index (from 0.64 to 1.26 days/decade). These regions also showed high increasing trends, although nonsignificant, for SU30 index (from 5.65 to 6.28 days/decade). It is also noticed that the southern regions showed higher rates of increasing trends in TR25 index (from 5.02 to 6.28 days/decade). For autumn, TR25 index did not show increasing/decreasing trends in 71% of total stations. On the other hand, SU30 index exhibited increasing trends in 93% of the cases (26 stations), but only 4 stations of them being significant at the 95% confidence level.

5.4 Extreme temperature indices and teleconnection patterns

In this section, the relationships between the extreme temperature indices and the selected large-scale circulation patterns were examined, with the aim to identify whether any specific circulation pattern could have some influence on the occurrence of the extreme temperatures over the study area. Tables 5.4 and 5.5 summarize the number of stations with significant correlations between the extreme temperature indices and the NAO, EA, EA/WR, WEMO, MO, ENSO and NCP teleconnection indices at annual and seasonal scales, respectively.
The results listed in Tables 5.4 and 5.5 generally demonstrated the NCP is the main driver of the extreme temperature indices over the study area. For the sake of saving space, we present here only the correlation coefficients between NCP and the extreme temperature indices at annual and seasonal scales (Figures 5.11 and 5.12, respectively). Moreover, we provide four supplementary files in the Appendix B (Figures 1, 2, 3 and 4) of the main correlation coefficients for EA/WR, NAO and ENSO patterns. In addition, Figure 5.13 shows the temporal variability of the NCP standardized index along with some standardized temperature indices time series.

5.4.1 Annual scale

According to Table 5.4, the NCP pattern intensively showed the most significant influence on TXx, TXn, TX90p, TX10p, TN90p, TN10p, WSDI, SU25, SU30, CSDI, TR20 and TR25 indices in 28.6%, 57%, 93%, 82%, 86%, 75%, 71.5%, 46%, 64.3%, 71.4%, and 60.7% of total stations, respectively. Moreover, all correlation coefficients between the NCP index and all extreme temperature indices were negative, except for TN10p and for TX10p, CSDI and FD indices in some locations. The highest negative correlation coefficients (between -0.56 and -0.63) were found with the TX90p, TN90p and WSDI indices and spatially covered the most southern regions, the upper parts of the Negev desert as well as the northern regions (Figure 5.11). High correlation

coefficients (between -0.43 and -0.56) covered the northeastern regions and Jerusalem district for TXx, while for TXn, correlations up to -0.50, covered the southern areas of the Palestinian Coastal Plain and northeastern regions. For TN10p, most stations showed significant and positive correlations (up to 0.47) (Figure 5.11).

Regarding the other patterns, the EA/WR represented the second most important pattern affecting the extreme temperature indices over the study area (Table 5.4). Its influence mainly occurred over SU25 index in 86% of total stations which presented significant negative correlations with it. High and significant correlations (up to -0.63) covered the Palestinian Coastal Plain, Beer Sheva and the northeastern districts (Figure 1 in the Appendix B). In addition, it showed significant correlations, although lower, with TX10p (43% of total stations), TN10p (39%), SU30 (43%), WSDI (43%) and CSDI (46%) indices at more locations than other patterns (Table 5.4).

The main influence of the EA pattern was on TXx, TNx and TX90p indices in 28.5%, 39% and 28.5% of the total stations, respectively, and with correlation coefficients ranging from 0.31 to 0.48 (not shown). The NAO pattern also exhibited significant and positive correlations with TNx in 36% of total stations, with correlation coefficients ranging from 0.32 to 0.48. Furthermore, the NAO index displayed significant negative correlations with TX90p and TN90p in 61% and 50% of total stations, respectively. For TX90p, high correlation between -0.41 and -0.61 occurred in the most southern region as well as in the eastward and northward of the Gaza strip. For TN90p, the highest significant correlations were reached at the centre region, up to -0.72 (Figure 2 in the Appendix B). The significant correlations were very weak between MO, WEMO and ENSO patterns and all extremes indices, except the positive correlation in 32% of total stations between MO and WSDI, 32% of total stations between WEMO and TN10p and 50% of total stations between ENSO and TN10p

Index	NAO		EA		EA/WR		WEMO		MO		NCP		ENSO	
	(+)	(-)	(+)	(-)	(+)	(-)	(+)	(-)	(+)	(-)	(+)	(-)	(+)	(-)
TXx	1	0	8	0	0	2	5	0	0	2	0	8	0	0
TXn	0	1	1	0	0	0	0	3	0	0	0	16	0	0
TNx	10	1	11	0	1	0	0	0	0	0	0	9	0	0
TNn	0	1	1	1	0	1	0	1	0	0	0	0	0	3
TX90p	0	17	8	0	0	12	0	0	0	5	0	26	0	0
TX10p	1	0	0	0	12	0	0	0	1	0	8	15	4	0
TN90p	0	14	7	0	0	14	0	0	0	4	0	24	0	0
TN10p	2	0	0	0	11	0	0	9	0	0	21	0	14	0
WSDI	0	0	1	0	0	12	1	1	9	0	0	20	0	0
SU25	0	7	1	0	0	24	3	0	0	0	0	16	0	0
SU30	0	7	6	0	0	12	5	0	0	0	0	13	0	0
CSDI	0	1	0	1	12	1	3	0	0	0	0	18	3	0
TR20	0	8	7	0	0	9	4	0	0	0	0	20	0	2
TR25	0	8	6	0	0	4	0	0	1	0	0	17	0	0
FD	0	0	0	0	5	0	5	1	0	0	4	0	0	0

Table 5.4. Number of stations with significant positive or negative correlations between extreme temperature and teleconnection indices at annual scale. Only significant results at the 95% confidence level are shown.

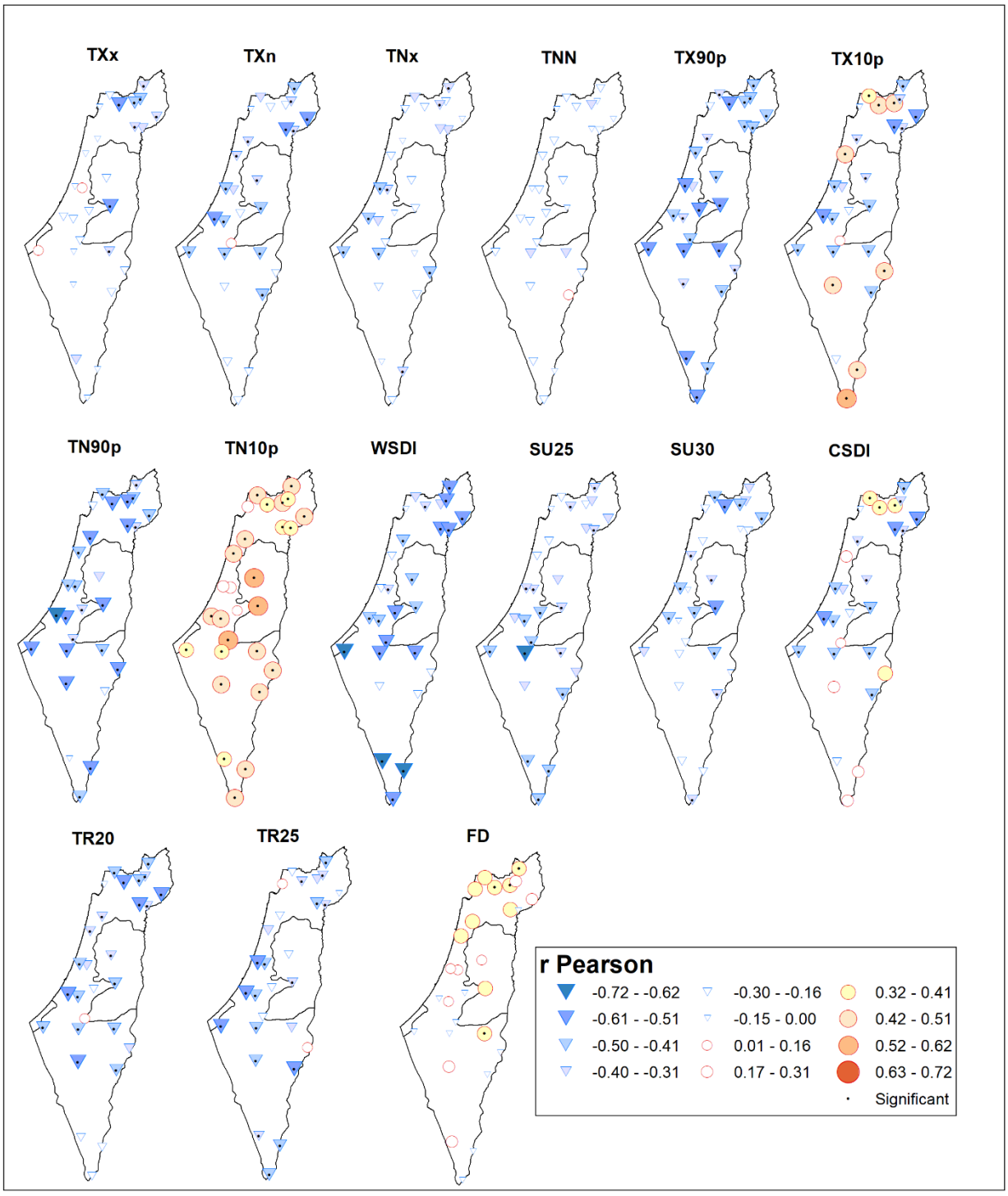

Figure 5.11. Spatial distribution of Pearson correlation coefficients between the NCP index and the extreme temperature indices at annual scale.

5.4.2 Seasonal scale

Table 5.5 summarizes the number of stations with significant correlations between the extreme temperature indices and the teleconnection patterns at seasonal scale. The results also indicated the NCP pattern was the main driver of extreme temperature indices in winter for 5 out of 12 indices, and in autumn for 8 out of 12 indices, while EA/WR was the main driver of extreme indices in spring for 5 out of 12 indices. In summer, the ENSO pattern showed a big influence on 5 extreme temperature indices. In general, the main influence seems be exerted by the NCP pattern, concentrated over the percentile extreme temperature indices for winter and autumn (for all percentile extremes) and in summer (for TX90p and TN90p).

In winter, the NCP pattern intensively presented the highest correlation coefficients, compared with the other patterns, on TXn, TNn, TX90p, TN90p, TX10p and TN10p indices with 100%, 86%, 75%, 61%, 79%, and 96% of total stations, respectively (Table 5.5, Figure 5.12). High and negative correlations (between -0.52 and -0.72) covered mostly the study area for TXn, TNn, TX90p and they concentrated in the north-eastern regions for TN90p. For positive correlations with TX10p and TN10p, very high and significant values (from 0.63 to 0.72) spatially covered all the study area for both indices. Figure 5.13b illustrates the strong positive correlation between the temporal variability of the standardized NCP and TN10p indices averaged for all locations along the period 1986-2016 in winter.

In spring, the NCP also had the highest influence on TNn with 39% of total stations showing significant correlations as well as it exhibited high occurrence of significant correlations with TXn, TX90p and SU25/30 with 68%, 32% and 68/50%, respectively (Table 5.5). The NCP in summer was the main controller for TX90p, TN90p and TR25 indices respectively in 61%, 50% and 32% of total stations.

In autumn, the NCP pattern showed high influence on 8 out of 12 indices, TNn, TX90p, TN90p, TX10p, TN10p, SU25/30 and TR20 indices, with 79%, 96%, 79%, 32%, 61%, 100/68% and 75% of total stations, respectively, with significant correlations. It also showed high occurrence of significant correlations with TXn and TNx indices with 61% and 39% of total stations, respectively (Table 5.5). For TX90p and TN90p, high correlation coefficients (from -0.59 to -0.67) spatially covered the complete study region (Figure 5.12). A similar pattern was found for TNn index, but with lower correlations. For TN10p index, the correlation pattern showed positive values extended over all the region. The temporal variability of the standardized NCP and TX90p (Figure 5.13a) and SU25 (Figure 5.13c) autumn indices showed the strong negative correlations along the period 1986-2016.

Regarding EA/WR pattern, it resulted the main controller for TXx, TXn, TN90p and TR20/25 indices for 96%, 82%, 36% and 50%/29% of total stations, respectively, in spring (Table 5.5). Spatially, high correlation coefficients (from -0.42 to -0.50) were found in the Palestinian Coastal Plain and north-western areas for TXn index, as well as in all regions of the study area for TXx index (Figure 3 in Appendix B). The EA/WR pattern also displayed a high frequency of significant correlations with SU25/30 indices in 79%/50% of total stations (Table 5.5).

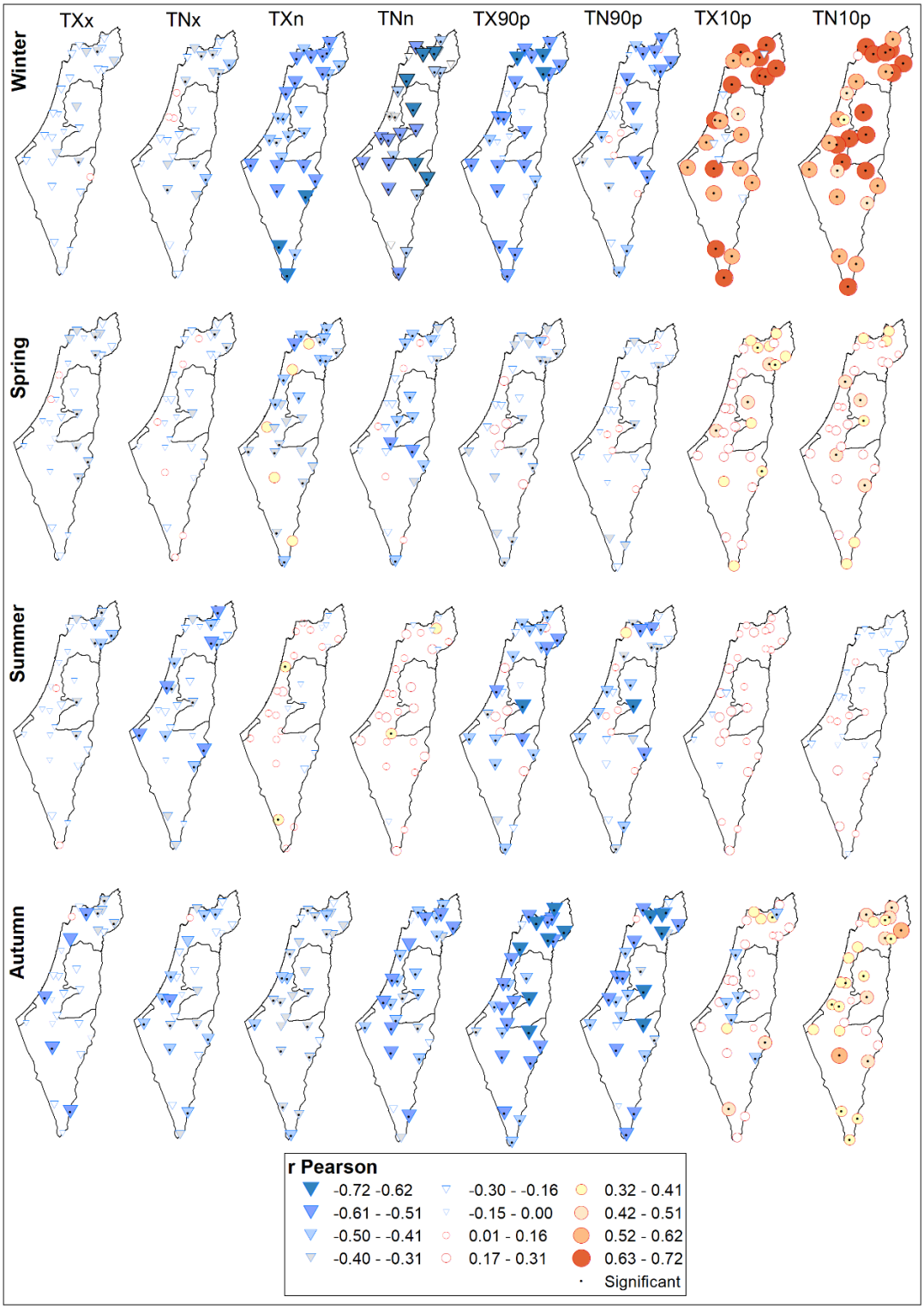

Figure 5.12. Spatial distribution of Pearson correlation coefficients between the NCP index and the extreme temperature indices at seasonal scale.

In summer, the EA/WR pattern was the main controller for all absolute extreme temperature indices in 53%, 61%, 100% and 89% of total stations for TXx, TNx, TXn and TNn, respectively.

The highest correlation coefficients were found for TXn and TNn indices, between -0.41 and -0.61 (Figure 3 in Appendix B). On the other hand, in autumn, the EA/WR pattern displayed the highest influence on TXx and TNx for 96% and 75% of total stations. All regions showed correlations coefficients (between -0.41 and -0.50) for TXx, except for the northeastern region where the correlations were lower (Figure 3 in Appendix B).

Compared with the other patterns, the NAO showed the highest effect on SU25/30 for 71%/68% of total stations in winter (Table 5.5). Strong correlation coefficients (between -0.51 and -0.72) were found in the area extended from the centre to the south of the region for SU25index. A similar pattern was also found for SU30, but showing lower correlations (Figure 4 in Appendix B). In autumn, NAO pattern had the highest significant correlations with TXn for 89% (Table 5.5).

It is noticed that the ENSO pattern showed the highest influence on TX10p and TN10p indices for 68% and 61% of total stations, respectively, during spring and summer. Spatially, high and significant correlations between 0.42 and 0.62, were expanded over the study region (Figure 4 in Appendix B).

Indices	**Seasons**	**Extreme temperature indices**										
		TXx	**TNx**	**TXn**	**TNn**	**TX 90p**	**TN 90p**	**TX 10p**	**TN 10p**	**SU 25/30**	**TR 20/25**	**Tot.**
NAO	Winter	3	11	2	6	1	0	6	9	20/19	0/0	77
	Spring	0	8	0	1	4	2	0	4	19/7	5/0	50
	Summer	0	0	0	1	13	11	1	1	2/3	4/3	39
	Autumn	0	5	25	5	6	2	0	0	½	6/2	54
EA	Winter	0	0	0	4	0	0	0	0	0/0	0/0	4
	Spring	1	6	0	1	4	6	0	2	1/5	11/6	43
	Summer	6	5	0	7	0	5	1	0	0/2	0/3	29
	Autumn	0	1	0	1	0	0	0	0	14/4	0/0	20
EA/WR	Winter	0	12	19	12	15	2	17	16	11/0	0/0	104
	Spring	27	6	23	3	6	10	2	7	22/14	14/8	142
	Summer	16	17	28	25	1	9	3	0	2/2	5/6	114
	Autumn	27	21	18	0	0	0	0	2	0/2	0/0	70
WEMO	Winter	0	0	7	18	0	1	0	0	0/0	0/0	26
	Spring	2	10	0	0	10	7	16	4	24/12	3/0	88
	Summer	0	0	1	2	0	0	1	1	2/2	1/1	11
	Autumn	3	0	15	20	8	3	4	0	20/2	1/1	74
MO	Winter	0	6	5	5	22	16	1	3	17/8	0/0	83
	Spring	1	0	1	2	0	0	1	0	14/4	4/0	27
	Summer	1	0	1	3	0	0	5	1	2/5	2/0	20
	Autumn	9	2	7	0	0	0	0	0	6/0	0/10	34
NCP	Winter	2	8	28	24	21	17	22	27	4/3	0/0	156
	Spring	6	2	17	11	9	2	6	5	19/14	2/0	93
	Summer	7	12	2	1	17	14	0	0	0/4	5/9	71
	Autumn	7	11	17	22	27	22	9	17	28/19	21/4	204
ENSO	Winter	1	0	2	3	0	1	9	1	2/2	1/0	22
	Spring	0	0	0	0	0	0	19	17	4/1	2/0	41
	Summer	0	0	2	8	0	2	17	15	5/10	10/3	72
	Autumn	0	0	0	7	1	1	1	0	0/0	0/5	15

Table 5.5. Number of stations with significant correlations between extreme temperature and teleconnection indices at seasonal scale. Only significant results at the 95% confidence level are shown.

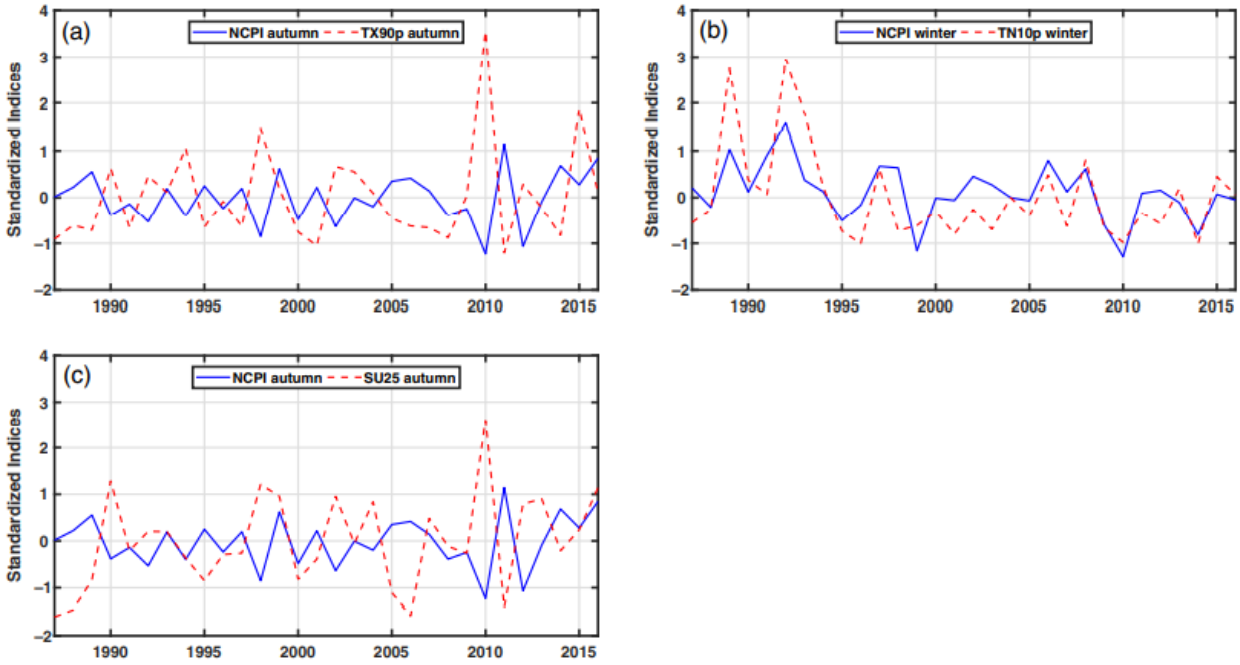

Figure 5.13. Temporal variability of the standardized NCP index along with some standardized temperature indices time series.

5.5 Conclusions and discussion

Topic such as spatio-temporal analysis for extreme temperature indices over Israel and Palestine in the Levant region were not fully explored by previous studies, and it is required further attention. Thus, the main aim of this study was to provide a comprehensive analysis of this topic using more stations and for a recent period of time. In this study, trends for 16 extreme temperature indices computed from daily data of 28 stations homogeneously distributed over the territory were spatially and temporally analyzed at annual and seasonal scales, for the period 1987-2018. In addition, the relationships between these extreme indices and large-scale circulation patterns were examined for each station. The main conclusions can be summarized as follow:

1. The analysis of 16 extreme temperature indices revealed a dominant warming tendency for the last three decades over the study area. Extremes related to minimum night-time temperature denoted more intense trends compared to those of maximum day-time temperature indices, at annual and seasonal scales.
2. Regarding the averaged extreme indices over the study area, significant increasing trends for seven extreme temperature indices (TNx, TX90p, TN90p, SU25, SU30, TR20 and TR25) were detected at annual scale, whereas the significant decreasing trends were detected for the CSDI and TN10p indices.

These results are consistent with other studies in regions around the study area. Donat et al. (2014) analyzed the changes in extreme temperature and precipitation over the Arab region based on data of 61 stations, and they found increasing trends in the averages of TXx, TX90p, TN90p and WSDI indices by 0.23ºC/decade, and 1.6, 2.1 and 0.76 days/decade, respectively. They also found decreasing trends in CSDI, TX10p and TN10p indices by -3.3, -2.2 and -3.2 days/decade,

respectively. Over Central Asia, Feng et al. (2018) studied the spatio-temporal variations in extreme temperature, based on data of 108 stations from six countries for the period 1981-2015. The results revealed that both TX90p and TN90p experienced significant increasing trends by 1.1 and 1.4 days/decade, respectively as well as TX10p and TN10p showed significant decreasing trends by -1.01 and -0.62 days/decade, respectively. Furthermore, Almazroui et al. (2014) analyzed trends of temperature extremes in Saudi Arabia based on data of 27 stations during the period 1981-2010, and they found significant increasing trends in the TNx, TX90p, TN90p and WSDI indices by 0.7ºC/year, 16.9, 12.7 and 3 days/decade, respectively. The results also indicated the significant decreasing trends in CSDI, TX10p and TN10p index by -2.4, -19.4 and -16.3 days/decade, respectively. Finally, Erlat and Türkeş (2013) analyzed trends of SU25 and SU30 indices over Turkey based on data of 97 stations during the period 1976-2010 and the results revealed significant increasing trends by 6.8 and 7.2 days/decade, respectively.

3. At annual and local scales, the analysis of trends for extreme temperature indices revealed significant warming trends in TNx index (36% of total stations). Moreover, the analysis revealed significant increasing trends in WSDI, SU25/30 and TR20/25 indices. For SU25 and TR20, more than 82% of total stations were affected by significant increasing trends while SU30 and TR25 indices exhibited significant increasing trends in 46% and 29% of total stations. For WSDI index, 39% of total stations were affected by significant increasing trends. In addition, the percentile-based extreme temperature indices showed very coherent patterns for significant increasing trends with 89% and 92% of total stations respectively exhibited significant increasing trends for TX90p and TN90p indices. Furthermore, TX10p and TN10p indices showed decreasing trends in 100% of total stations.

In agreement with these results, studies carried out in surrounding regions provide results in the same line. Rahimzadeh et al. (2009) analyzed the variability of extreme temperature over Iran during the period 1951-2003, and the results revealed that 46%, 74%, 46%, 44% and 85% of total stations (27 stations) exhibited significant increasing trends in their TNx, TN90p, TX90p, SU25 and TR20 indices, respectively. For TX10p and TN10p indices, Rahimzadeh et al. (2009) also found decreasing trends in more than 55% of total stations. Furthermore, Rahimi and Hejabi (2018) studied extreme temperature indices over Iran during 1960-2014 and they found 88%, 71%, 76%, 61% and 73% of total stations (33 stations) had statistically significant increasing trends in their TNx, TX90p, TN90p, SU25 and TR20 indices, whereas TX10p and TN10p indices exhibited significant decreasing trends in 39% and 64% of total stations, respectively. The TNx, TR20 and WSDI indices also showed intensive significant increasing trends in 70%, 74% and 70% of total stations (27 stations) over Saudi Arabia (Almazroui et al., 2014). Finally, Erlat and Türkeş (2013) found 95% and 94% of total stations (97 stations) showed upward trends in their annual averages of SU25 and SU30 indices, respectively over Turkey.

4. At seasonal scale, the results did not indicate significant decreasing trends for any absolute extreme temperature indices. For TX10p-autumn, 86% of total stations showed significant decreasing trends as well as 50% and 57% of total stations in TN10p-spring and TN10p-autumn, respectively. Contrary, at annual scale, the analysis showed intense and broad

significant increasing trends in all the absolute extreme temperature indices. For summer, more than 90% of total stations exhibited significantly increasing trends for TXn, TNn and TNx indices. For autumn and spring, more than 40% of total stations had significant increasing trends of TXn and TNn indices. In winter, 39% of total stations showed significant increasing trends in. The intense and coherent increasing trends were found also in TX90p and TN90p indices in 61% and 75% of total stations for TX90p-winter and TX90p-spring, respectively. For TN90p, 61% and 85% of total stations showed significant increasing trends for TN90p-spring and TN90p-summer.

These results are in agreement with those obtained in surrounding areas. Islam et al. (2015) analyzed the changes in seasonal temperature extremes over Saudi Arabia during the period 1981–2010, and they found that summer exhibited significant warming trends for all absolute extreme temperature indices more than those for other seasons in 63% for TXx, 48% for TXn, 59% for TNn and 70% for TNx of total stations (27 stations). The analysis of seasonal trends in frequency of extreme temperature indices revealed significant increasing trends of SU25 index in winter and spring (71% of total stations) with averages ranging between 0.1 and 5.87 days/decade. In summer and autumn, more than 64% of total stations exhibited significant increasing trends of TR20 index by averages ranging between 1.3 and 5.14 days/decade. TR25 showed significant increasing trend in 54% of total stations for summer with averages ranging in the interval 0.04-9.19 days/decade. Note that the warming process in densely populated regions like Jerusalem, Akko and Beer Sheva is expected to be even faster due to the urban heat island, at least partly (Ziv et al., 2005). Many studies indicated the effect of urbanization on the increasing temperature in cities, especially during summer, when urban heat islands are stronger due to a greater storage of heat in urban structures (Fujibe, 2009). Itzhak Ben Shalom et al. (2016) studied the trends of urban warming during the period 1980-2014 in four Israeli cities (Jerusalem, Beer Sheva, Elat and Tel Aviv) to estimate the urbanization effect on the local climate, and they found that the urban minus rural temperature showed a more intense warming in the daytime in the 4 cities.

In the present study, the urban locations of Jerusalem and Akko showed the highest increasing trends above 6.38 days/decade in SU30-summer index, but other urban stations as Elat and Beer Sheva did not show significant increases in this index. Other rural locations, such as Elon and Bet Dagan, also exhibited significant increasing trends in SU30-summer. Moreover, for TNx index in summer almost all the locations showed significant trends with similar values, independently of the urban or rural character. Therefore, from our study we cannot confirm the urban heat effect as the responsible of the warming trends in Levant region. The generalized warming trends could be due to the global warming (Parker, 2004).

5. For the analysis of the influence of teleconnection indices on the extreme temperature over Israel and Palestine, the study revealed the NCP pattern was the main driver of extreme temperature variability over the study area, particularly at annual, winter and autumn scales. It displayed strong influence compared with other patterns on 11 out of 12 indices for the annual extremes, 5 out of 12 indices for winter and 8 out of 12 indices for autumn. In addition, EA/WR and ENSO displayed notably effects on the extreme temperature

indices in some cases, especially in spring and summer. The study also revealed the main influence of the NCP generally concentrated in the percentile extreme temperature indices for winter (all percentile extremes), summer (TX90p and TN90p) and autumn (all percentile extremes). EA/WR represented the second most important pattern affecting the extreme temperature indices over the study area, and its main influence occurred on the absolute extreme temperature indices for winter (TNx), summer (all absolute extremes), autumn (TXx and TNx) and spring (TXx and TXn). At annual scale, strong significant correlations were observed between the NCP and TX90p, TX10p, TN90p, TN10p, WSDI and TR20 indices respectively, in 93%, 82%, 86%, 75%, 71.5%, and 71.4% of total stations. In winter and autumn, the NCP broadly and intensively exhibited significant correlations with TXn-winter, TNn-winter, TN10p-winter, TX90p-autumn and SU25-autumn respectively in 100%, 86%, 96%, 96% and 100% of total stations, respectively. On the other hand, EA/WR had the highest effect compared with other patterns on TXx-spring, TXn-spring, TXn-summer, TNn-summer in 96%, 82%, 100% and 89% of total stations. For ENSO pattern, it exhibited the highest effect in summer on TX10p, TN10p, SU25/30 and TR20 in 61%, 53.5%, 18/36% and 36%, respectively. Other teleconnection patterns (NAO, EA, WEMO and MO) did not show significant correlations, except in very few cases such as WEMO in spring with TNx (36% of total stations), TX90p (36% of total stations) and SU25 (86% of total stations).

These results are in accordance with those carried out in surrounding areas. Kutiel and Benaroch (2002) concluded that the main impact of the NCP mode should be exhibited over the Balkans and the eastern Mediterranean basin mainly in autumn, winter and spring, and is less frequent in summer. Furthermore, Kutiel et al. (2002) used data of NCP, monthly mean air temperature and monthly total rainfall from 33 stations across Greece, Turkey and Israel for the period 1958-1998 to analyze the implication of the NCP on the regional climate of the eastern Mediterranean basin. Their results confirmed that the NCP was the main atmospheric teleconnection affecting the climate of the Balkan, the Anatolia Peninsula and the Middle East region. The positive phase of this pattern is associated with below normal temperature, while the negative phase temperature is related with above normal temperature. In addition, they found the impact of NCP on air temperature was more pronounced in the mountainous inland regions for Israel. In addition, the results found there was more rainfall during the positive phase of the NCP over all regions in Israel. Ghasemi and Khalili (2008) analysed the effect of the NCP on winter temperatures in Iran based on data of 31 stations for the period 1958-2000, and they found negative and significant correlations between the NCP and minimum, maximum and mean winter temperature for 90%, 87% and 97% of total stations, respectively. Their results shown that the positive NCP is associate with enhanced precipitation and cloudy conditions, which causes below normal temperatures over Iran. As noted by Brunetti and Kutiel (2011), during the positive phase of NCP in winter, the anomaly circulation is mainly northerly over major parts of eastern Europe, the Black and the Caspian Seas and the eastern Mediterranean area, leading to a considerable decrease in

temperatures compared to the normal conditions. The opposite is true during the negative phase of NCP.

For the impact of EA/WR pattern, Baltacı et al. (2018) analyzed relationships between teleconnection patterns and Turkish climatic extremes based on data of 94 stations for 1965-2014, and the results indicated that EA/WR pattern intensively exhibited negative and significant correlations with TNx, TNn and TXn indices in winter, stronger than those from the NAO and EA patterns. These authors established that the positive phase of EA/WR is associated with a prevalence of north flow over the eastern Mediterranean area, which can explain the sign of the correlations found. Other studies have been also identified the influence of the EA/WR pattern on the climate of the region, but they do not use the temperature (Yosef et al., 2009; Krichak and Alpert, 2005).

CHAPTER 6

SPATIO-TEMPORAL ANALYSIS OF PRECIPITATION

This chapter aims to analyze the spatial and temporal variability of precipitation in the Levant region. It also aims to analyze the annual, seasonal, and monthly trends for the period 1970-2018. Besides, the relationships between seven large-scale circulation patterns and seasonal precipitation will be studied using a correlation analysis.

6.1 Introduction

Identifying the spatio-temporal variability of precipitation is a crucial issue in the management of water resources and for the mitigation of hydrological hazards (floods and droughts), especially in the Levant region, where arid and semi-arid climates account for the largest part of the region. Fluctuations in precipitation can also lead to socio-economic and natural problems (Asakereh, 2020; Boroujerdy et al., 2017). According to the IPCC report (2013), precipitation increased significantly in the eastern parts of North and South America, in northern Europe, and north and central Asia. In contrast, rainfall declined in the Mediterranean coast, southern Africa, and parts of south Asia in the period 1900-2005. Declining trends in annual and seasonal precipitation have also been observed in Italy (Brunetti et al., 2000), India (Pal and Al-Tabbaa, 2011), Turkey (Partal and Kucuk, 2006), Iran (Najafi and Moazami, 2015; Soltani et al., 2015) and Iraq (Al-salihi et al., 2014; Al-Barazanji, 2015). The majority of the Middle East countries cannot meet their current water needs (World Bank, 2007). Jordan, for example, is one of the countries in the world with more limited water resources. The available water resources per capita will decrease from less than 160 m^3/capita/year to about 90 m^3/capita/year by 2025 (MWI and GTZ, 2005).

Until now, there are not studies to assess changes in mean precipitation and trends at annual, seasonal, and monthly time scales for the Levant as a whole. Most studies focused just on local areas and used a limited number of stations or time scale. Also, on the basis of observational data,

the relationship between the large-scale circulation patterns and the rainfall in the Levant is not fully investigated (Gai et al., 2001; Ziv et al., 2006).

This chapter aims, therefore, to analyze the spatio-temporal variability of precipitation in the Levant region, along with a trend analysis at annual, seasonal, and monthly scales during the period 1970-2018. In addition, the influence of the main large-scale climate variability modes on the Levant seasonal rainfall will be explored. Annual and seasonal rainfall time series were obtained on the basis of monthly data from 165 stations distributed over the study area. Figure 2.5 showed the stations' geographical distribution, while Table 2 in the Appendix A contains names, coordinates, and stations' elevations. Details regarding data quality control (QC) and homogeneity are available in Chapter 2, Section 2.2. The analysis was carried out for the entire Levant and its sub-regions (Palestine/Israel, Jordan, and Syria).

Some basic statistics, the seasonal/monthly contributions to the annual rainfall, and the temporal fluctuations for the annual/seasonal rainfall are investigated. The non-parametric Mann-Whitney (U) test was used to analyze the mean differences between the two sub-periods 1970-1990 and 1991-2018. In addition, the Cramer's test was used to evaluate the mean deviations of five non-overlapping 10-year periods, and four overlapping 20-year periods at the three-time scales.

Moreover, the main variability spatial patterns of the annual and seasonal rainfall are investigated using Principal Component Analysis (PCA) and K-means cluster algorithm. The factor loadings are computed and their spatial distribution is discussed. The component scores were used as input in the K-means cluster to divide the study area into homogeneous rainfall sub-regions. Furthermore, salient statistics (e.g., mean and standard deviations) along with the box–whisker plots were calculated and graphically plotted for each cluster.

A precipitation trend analysis at annual, seasonal, and monthly scales was carried out using the non-parametric Mann-Kendall test (Mann, 1945; Kendall, 1975) and Sen's slope estimator (Sen, 1968). Besides, the sequential Mann-Kendall (SMK) test was applied to detect the significant change points. Finally, correlation maps between the teleconnection indices and precipitation time series over the area under study were constructed and analyzed.

6.2 Results

6.2.1 Fundamental statistics for the Levant rainfall

Some statistics (e.g., mean, maximum, minimum, and standard deviation) of the averaged precipitation in the Levant for the period 1970-2018 are listed in Table 6.1. In addition, Figure 6.1a to d shows the box plots for annual and seasonal precipitation for the Levant and its countries, and Figure 6.4 shows the temporal behavior of the annual and seasonal mean rainfall. The Levant's annual rainfall varies from 246.3 mm in 1999 to 677.8 mm in 1991, with a standard deviation of 101.6 mm and a mean value of 453.8 mm (Table 6.1). The 1991/1992 rainy season was also the highest annual rainfall for Palestine/Israel (832.7mm) and Jordan (453mm), while Syria had the highest average (808.1 mm) in 2003. On the other hand, the years 1999, 1995, and 2015 had the lowest averages for Palestine (233.2 mm), Jordan (125 mm), and Syria (285.7 mm) (Figure 6.1a, Figure 6.4b to d).

Series	Mean (mm)	Max. (year)	Min. (year)	SD (mm)	CV (%)	Skew.	Kurt.	% to annual rainfall
Ann.	453.8	677.8 (1991)	246.3 (1999)	101.6	22.4	0.20	-0.50	100.0
Win.	281.6	521.2 (1992)	79.1 (2014)	86.7	30.8	0.25	-0.08	62.1
Spr.	93.6	202.0 (1971)	28.2 (2008)	36.4	38.9	0.43	-0.07	20.6
Aut.	81.2	241.3 (1976)	19.6 (2016)	46.5	57.2	1.45	2.20	17.9
Jan.	105.9	236.1	14.5	43.0	40.5	0.7	1.0	23.3
Feb.	85.0	215.2	21.1	42.8	50.3	1.2	1.8	18.7
Mar.	58.0	125.8	10.1	29.4	50.6	0.2	-0.6	12.8
Apr.	27.1	150.5	2.3	23.5	86.8	3.3	15.5	6.0
May	8.8	31.9	0.4	8.3	94.2	1.4	1.2	1.9
Sep.	2.1	12.1	0.0	2.8	130.0	2.1	3.9	0.5
Oct.	21.8	54.1	2.2	14.8	67.8	0.5	-0.8	4.8
Nov.	53.2	173.5	11.5	35.7	67.2	1.4	2.7	11.7
Dec.	92.2	232.4	21.0	48.5	52.6	0.6	-0.1	20.3

Table 6.1. Statistics of annual, seasonal and monthly rainfall for the Levant (1970-2018).

No appreciable precipitation is recorded during summer months in all the region. For the entire Levant, the spring, May, September, and October had the lowest standard deviation with values of 36.4, 8.3, 2.8, and 14.8 mm, respectively (Table 6.1). The highest values were in winter (86.7 mm) and December (48.8 mm). As can be seen in Figure 6.4e and f, the spring rainfall are tightly grouped around the long-term mean, whereas the winter rainfall relatively spread around the long-term mean and the year-to-year fluctuations are high. The annual rainfall had a skewness value of 0.20, indicating an asymmetric distribution for the annual Levant precipitation, and it lies to the right of mean "right-skewed". The kurtosis reached -0.53, indicating platykurtic shape. Based on the skewness and kurtosis guidelines provided by Hair et al. (2017), the distribution for annual, winter, spring, January, March, October, and December precipitation are considered normal, when the values of skewness and kurtosis are between +1 and -1. On the contrary, the distribution for autumn, February, April, May, September, and November are not considered normal, when skewness and kurtosis values higher than +1, that is "substantially right-skewed" and "too peaked", respectively (Table 6.1).

As shown in Figure 6.1a to d, Jordan had the lowest minimum, maximum, and mean annual and seasonal precipitation. Palestine recorded the maximum precipitation for the annual (832.7 mm, 1991), for winter (680.5 mm, 1992), and for autumn (274.5 mm, 1986), while Syria recorded the maximum in spring (252.7 mm, 1971). In addition, Palestine had a higher mean precipitation value in winter (323.8 mm) than Syria, while Syria recorded higher mean values in the annual mean, spring, and autumn. On all time scales, Syria had a higher minimum precipitation than Palestine and Jordan, which may indicates that Syria has less rainfall variability than Palestine and Jordan as will be seen in the following section.

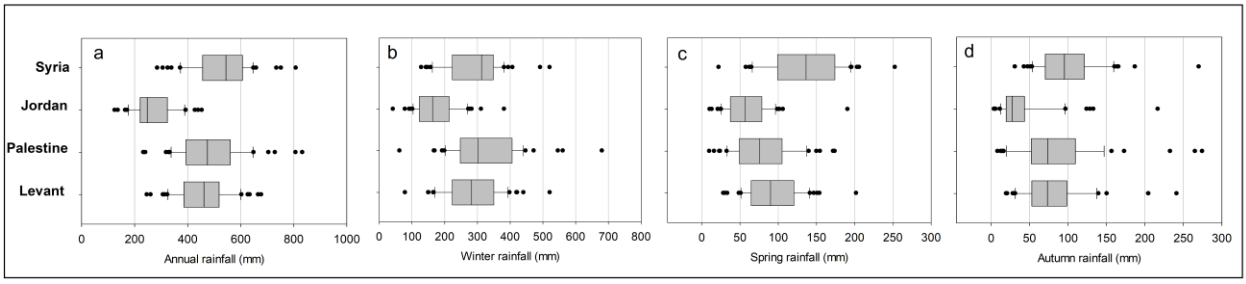

Figure 6.1. Boxplot showing the rainfall variability at annual (a), and seasonal, winter (b), spring (c), and autumn (d) over the Levant and sub-regions.

6.2.1.1 Coefficient of variation

The coefficient of variation (CV) is a measure of the dispersion of the data around the mean value, which is 22.4% for the annual Levant precipitation (Table 6.1). They increased gradually from January (40.5%) to September (130.0%) and decreased gradually from October (67.7%) to December (52.6%), indicating the strong inverse relationship between rainfall and CVs values. According to Hare (2003) and Tessema et al. (2017), CVs values between 20% and 30% show a moderate variability in precipitation conditions. Therefore, all monthly averaged time series showed high variability conditions when their CVs were above 30% (Table 6.1).

The CVs calculated for the annual averaged time series for Palestine/Israel, Jordan, and Syria (Figure 6.2) showed moderate variability in annual precipitation for all regions, with 26.7% for Palestine, 29.2% for Jordan, and 21.7% for Syria. At seasonal scale, the variability was high for all sub-regions except Syria, which showed a moderate variability of 30.3% in winter. The highest variability was found in autumn, with 68% for Palestine, 98.3% for Jordan, and 43.4% for Syria. It is also noticeable that Jordan had the highest CVs for annual and seasonal rainfall, while Syria had the lowest.

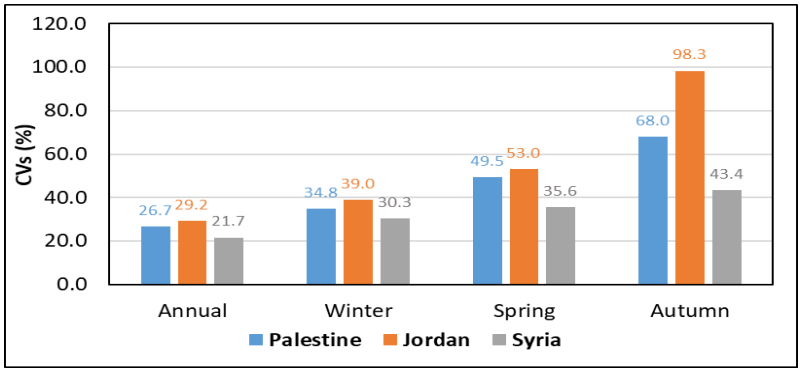

Figure 6.2. Annual and seasonal coefficient of variations (%) for the Levant sub-regions (1970-2018).

6.2.1.2 Seasonal contributions to the annual precipitations

In this section, the contribution of seasonal rainfall to the annual average is analyzed. These seasonal contributions vary spatially, with the highest amounts observed from winter (61%-70%) for all locations in Palestine, Jordan (except the eastern locations), and southern Syria. In contrast, the lowest contributions (42%-50%) were observed at the easternmost stations from Syria, and

contributions in northwestern Syria ranged from (51%-60%) (Figure 6.3a). This means that the spring and autumn contributions in the northern Levant are higher than in the southern Levant. For Jordan and southern Syria, the contributions in autumn (13%-20%) were significantly lower than in spring (21%-30%) (Figures 6.3b and c). Moreover, for all Palestine stations, the spring and autumn contributions were generally close (13%-20%), except for the southern coastal regions, which receive higher rainfall in autumn than in spring. The highest spring contributions (31%-37%) were recorded for Syria's eastern areas (31%-37%).

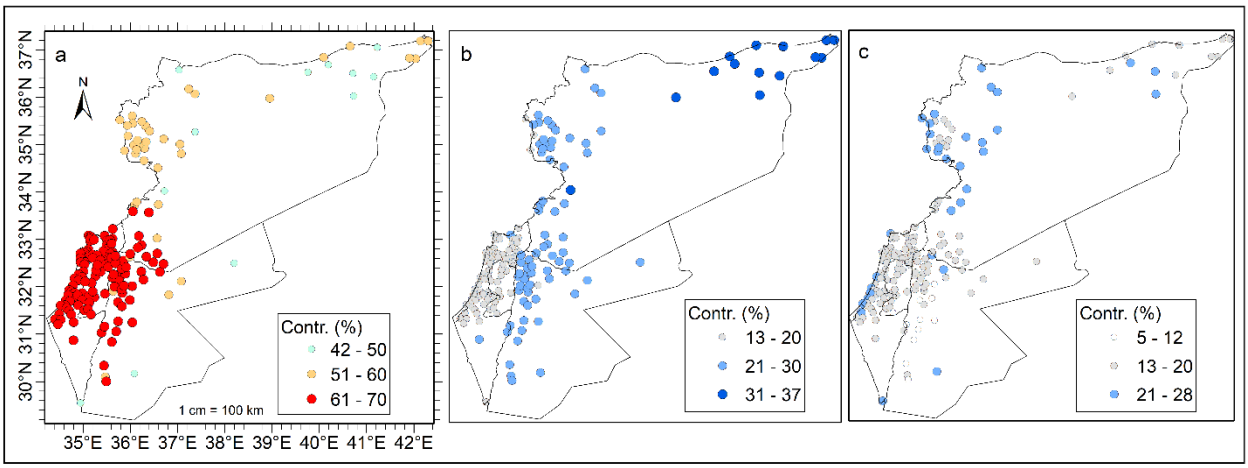

Figure 6.3. Spatial distribution of seasonal contributions to annual mean rainfall for winter (a), spring (b), and autumn (c).

The decadal contributions (%) of seasonal and monthly rainfall to the long-term annual average in the Levant region are shown in Table 6.2. From this, it can be concluded that the decadal contribution for autumn and November decreased gradually from 1980-1989 (21.1% and 15.6%, respectively) to 2010-2018 (17% and 11.9%, respectively). The contribution for March fell from 15.7% in 1990-1999 to 7.4% in 2010-2018. It is interesting to note that the sharpest decline was in spring, from 22.5% in the first decade to 14.2% in the last decade, and the autumn contribution was significantly higher in the last decade than in spring.

	1970-1979	1980-1989	1990-1999	2000-2009	2010-2018
Winter	60.8	60.3	61.4	66.8	61.0
Spring	22.5	18.6	19.8	13.8	14.2
Autumn	19.6	21.1	18.4	17.9	17.0
January	26.3	24.0	27.6	29.2	29.1
February	16.4	23.4	22.1	23.0	17.1
March	14.4	14.1	15.7	9.6	7.4
April	7.8	3.7	3.4	3.5	5.1
May	0.3	0.8	0.8	0.8	1.7
September	0.1	0.1	0.2	0.3	0.4
October	4.3	5.0	3.1	6.1	4.1
November	13.0	15.6	15.1	11.5	11.9
December	27.6	21.4	24.4	23.3	23.1

Table 6.2. Contribution (%) of the seasonal and monthly rainfall to the annual Levant rainfall, by decades.

6.2.2 Temporal variability for the rainfall averages

Figure 6.4a to d depicts the temporal variability of annual precipitation for the Levant and sub-regions during the years 1970-2018, and Figure 6.4e to g shows the seasonal variations of precipitation over the Levant. Interestingly, the regions exhibited similar annual precipitation patterns, but the order of magnitude varies between them (Figure 6.4a to d). For Jordan, all annual averages were below the long-term average of the Levant (453.8 mm) (Figure 6.4c). The long-term averages reached 528.8 mm for Syria and 488.6 mm for Palestine/Israel. The estimated annual mean of precipitation was about 50.7% for Jordan, 92.4 % for Palestine and 85.8 % for the Levant from the annual mean for Syria.

The temporal behavior of annual rainfall that reflected in the Lowess line (Appendix C.1) has shown a cyclical pattern since the late 1980s. In this context, a decreasing pattern was observed for the Levant and sub-regions in 1993-1999, 2003-2008, and 2012-2018 (Figures 6.4a to d). On the other hand, an increasing pattern for shorter periods was observed in 2000-2003 and 2008-2012. For Syria (Figure 6.4d), a different pattern was observed in the years 1970-1985, where it showed an increasing pattern, while other regions showed a constant variation or a very slightly decreasing pattern. For the Levant's seasonal rainfall (Figure 6.4e to g), a similar variability was observed for annual and winter rainfall (Figure 6.4a and e). In addition, spring fluctuations gradually decreased during the period under study (Figure 6.4f), and autumn precipitation (Figure 6.4g) decreased in 1990-1999 and increased slightly from 1998 onwards.

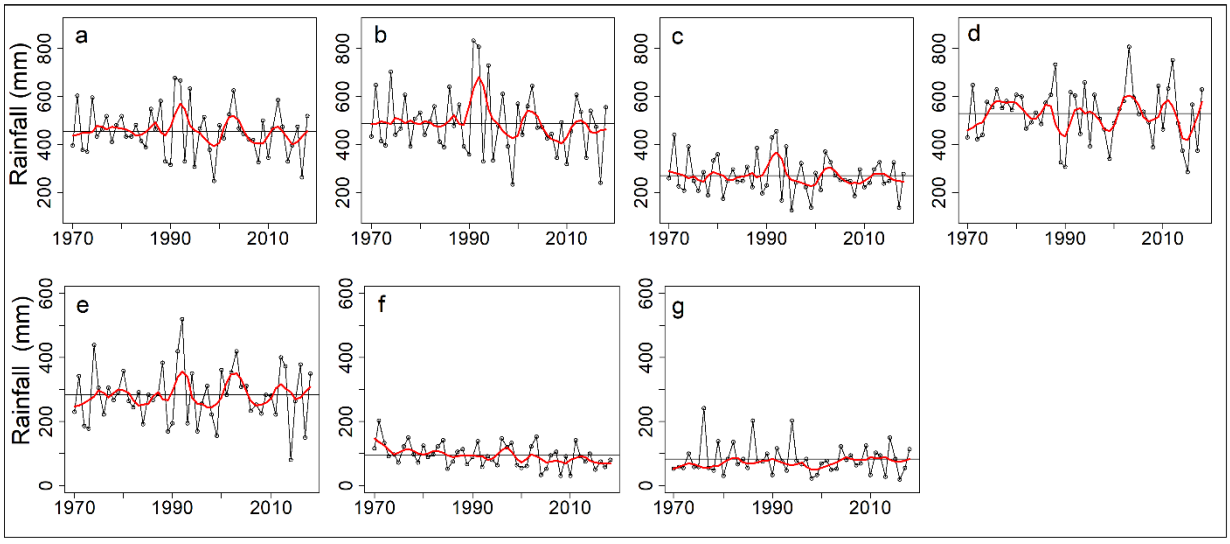

Figure 6.4. Temporal behavior of the annual mean rainfall with Lowess (red) and long-term average lines for Levant (a), Palestine (b), Jordan (c), and Syria (d). Bottom panels indicate Levant seasonal rainfall fluctuations for winter (e), spring (f), and autumn (g).

For the years 1987-2017, the results indicated an inverse relationship between precipitation and temperature in the Levant (see Section 5.2.1 for temperate behavior). For example, when the temperature tended to increase in 1987-2000, precipitation decreased, and when the rainfall decreased in 2012-2018, temperature notably increased. Moreover, 1992 was the year with the

coldest annual averages for Tmax and Tmin, while it was the year with the highest annual average precipitation. The cross correlation matrix calculated between the temperature variables (Tmax, Tmin, DTR, and Tmean) and the precipitation amount showed a significant and negative correlation between annual-Tmax/DTR and rainfall by -0.46/-0.81. All seasonal-Tmax averages significantly correlated with their precipitation. For example, winter -Tmax and rainfall correlated by -0.53, spring-Tmax and rainfall by -0.46, and autumn-Tmax and rainfall by -0.36. No significant correlations were found between all seasonal-Tmin and rainfall. The correlations with the Tmean were significant for winter, spring, and autumn by -0.38, -0.46, and -0.36 respectively. Figure 6.5 shows some of these relationships, and Table 11 in the Appendix A shows the overall cross-correlation matrix.

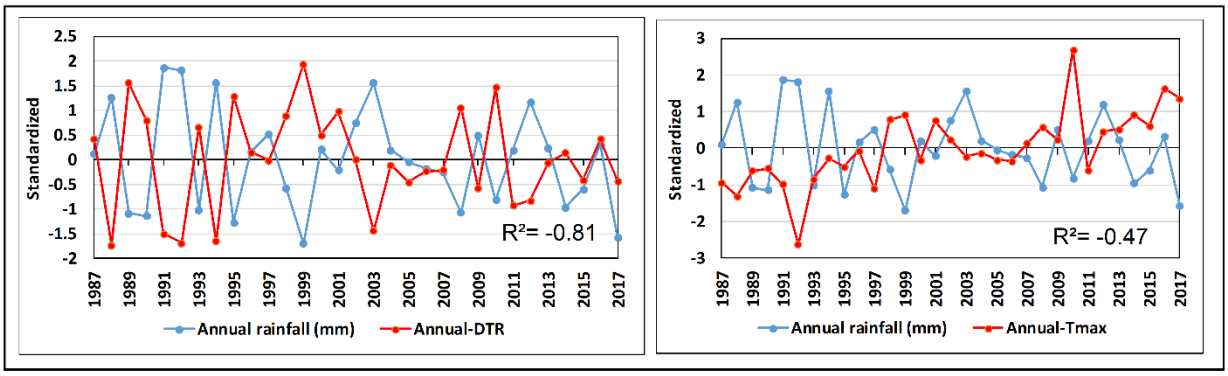

Figure 6.5. Temporal variability of the standardized annual rainfall and annual-DTR (left panel) and annual-Tmax (right panel).

The correlation between the annual precipitation averages of the Levant and the sub-regions was also performed to understand their interrelationship (Figure 6.6). Palestine had a maximum correlation ($r^2 = 0.95$), while Syria had the minimum ($r^2 = 0.81$).

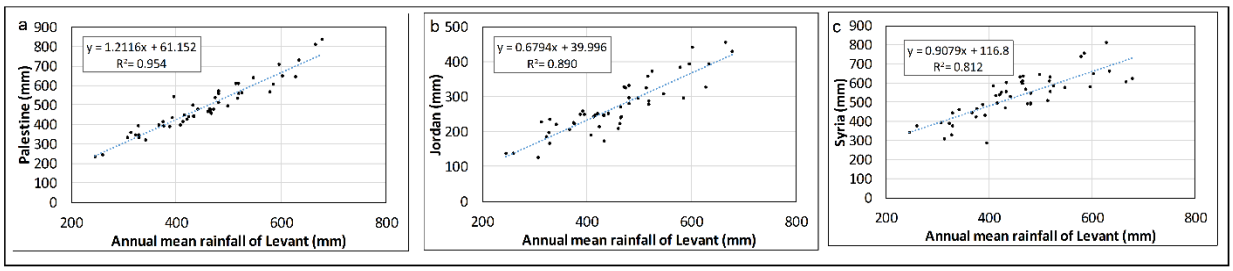

Figure 6.6. Relationship between average annual rainfall of Levant and its sub-regions: Palestine (a), Jordan (b), and Syria (c).

6.2.2.1 Sub-periodical variation

The Cramer test was applied to two types of sub-periods, the non-overlapping 10 years and the overlapping 20 years, to assess their mean deviations from long-term averages. This test was applied to annual and seasonal precipitation for the Levant and sub-regions, and the results are shown in Figure 6.7. No significant ($p < 0.05$) mean deviations of the non-overlapping 10-year

averages were found for the Levant and sub-regions at annual and seasonal scale (Figure 6.7, left column). However, the positive and negative values of t_k indicate a shift towards wetter or drier conditions. In general, the regions have slightly witnessed wetter conditions ($t_k > 0$) in their annual, spring, and autumn mean values for the first (1970-1979) and second (1980-1989) sub-periods. In contrast, they showed slightly drier conditions ($t_k < 0$) in winter for the first and second 10-years sub-periods. In addition, all regions generally had drier conditions in their annual and seasonal rainfall during the last 10-year sub-period (2010-2018), which was more pronounced for the annual and spring. The highest negative variations over the last two decades were recorded in spring, although they were not significant for all regions.

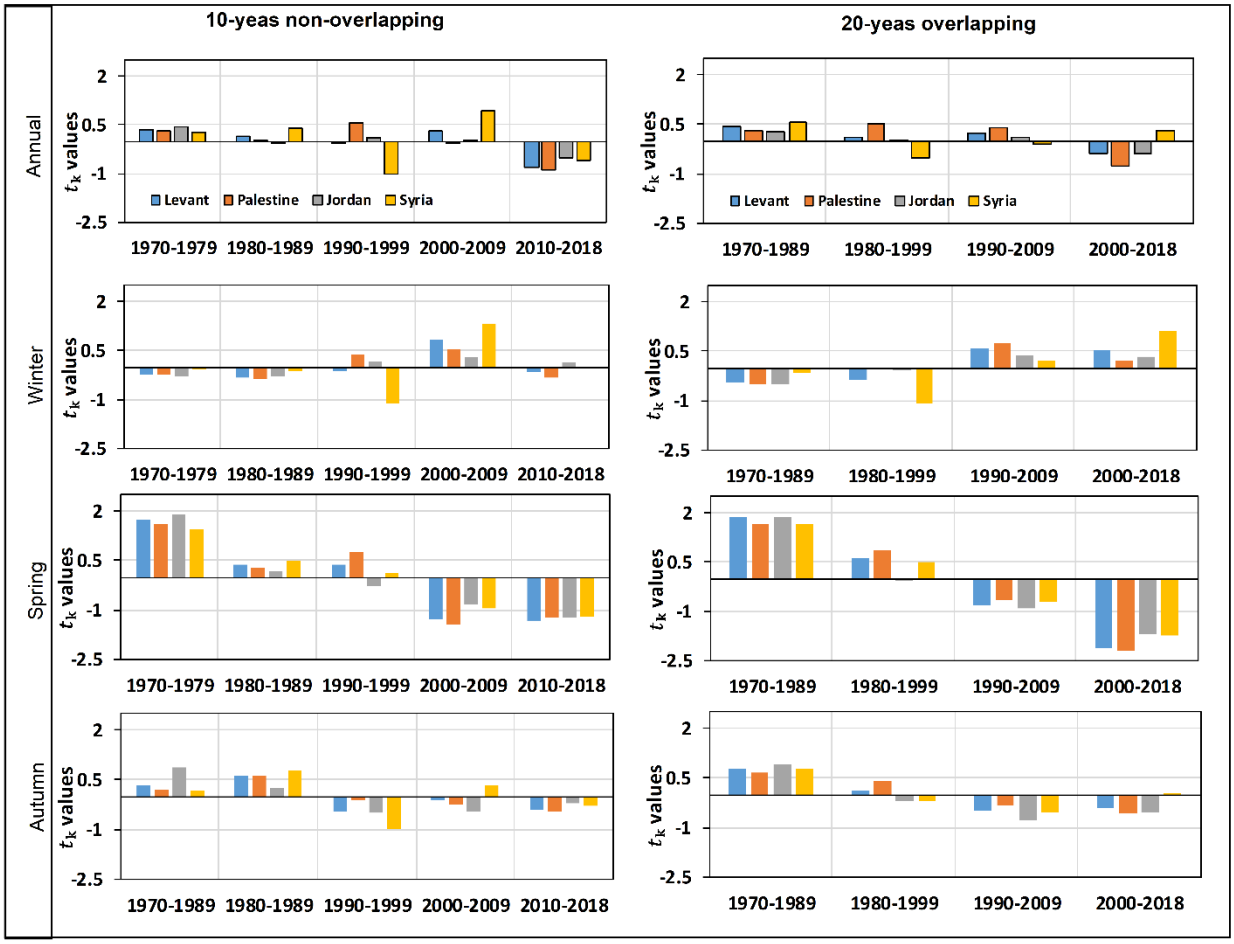

Figure 6.7. Mean departures for annual and seasonal precipitation using 10-years non-overlapping and 20-years overlapping sub-periods for Levant and its sub-regions.

The analysis for 20-year overlapping periods (Figure 6.7, right column) showed a significant and negative spring mean deviation for the Levant and Palestine in 2000-2018; in contrast, the Levant and sub-regions showed a positive annual, spring, and autumn mean deviation for the period 1970-1989, with a high rate for spring. These positive departures continued only for the Levant and Palestine during the years 1980-1999. For winter, all regions showed negative t_k values in the years 1970-1989 and 1980-1999, while they showed positive values in 1990-2009 and 2000-2018. In

general, it can be said that the Levant and its sub-regions have shown a different pattern since 1990. In addition, the mean annual and seasonal differences between the two sub-periods 1970-1990 and 1991-2018 were also assessed using the Mann-Whitney test. The results indicate that the Levant, Palestine, and Jordan experienced a significant decrease in spring precipitation by 17.5, 18 and 20 mm, respectively, during the years 1991 to 2018. Apart from spring, no significant mean increase or decrease was observed for any time scale or region.

In addition, these significant declines in spring averages in the periods 2000-2018 and 1991-2018 with respect to the previous one (1970-1999 and 1970-1990, respectively) were spatially evaluated (Figures 6.8a and b). In 1991-2018, the strongest decrease was observed at stations in the northern Syrian coastal region and in the governorates of Amman, and Jerusalem by 44-65 mm. Furthermore, the most inland sites in the West Bank and north-east Palestine, north Jordan, the southern coastal areas, and most eastern stations from Syria recorded decreases by 24-43 mm. On the other hand, the stations covering the Palestinian coastal areas showed relatively fewer decreases in their spring averages (0-23 mm) (Figure 6.8a), while they showed higher decreases by 24-43mm over the period 2000-2018 (Figure 6.8b).

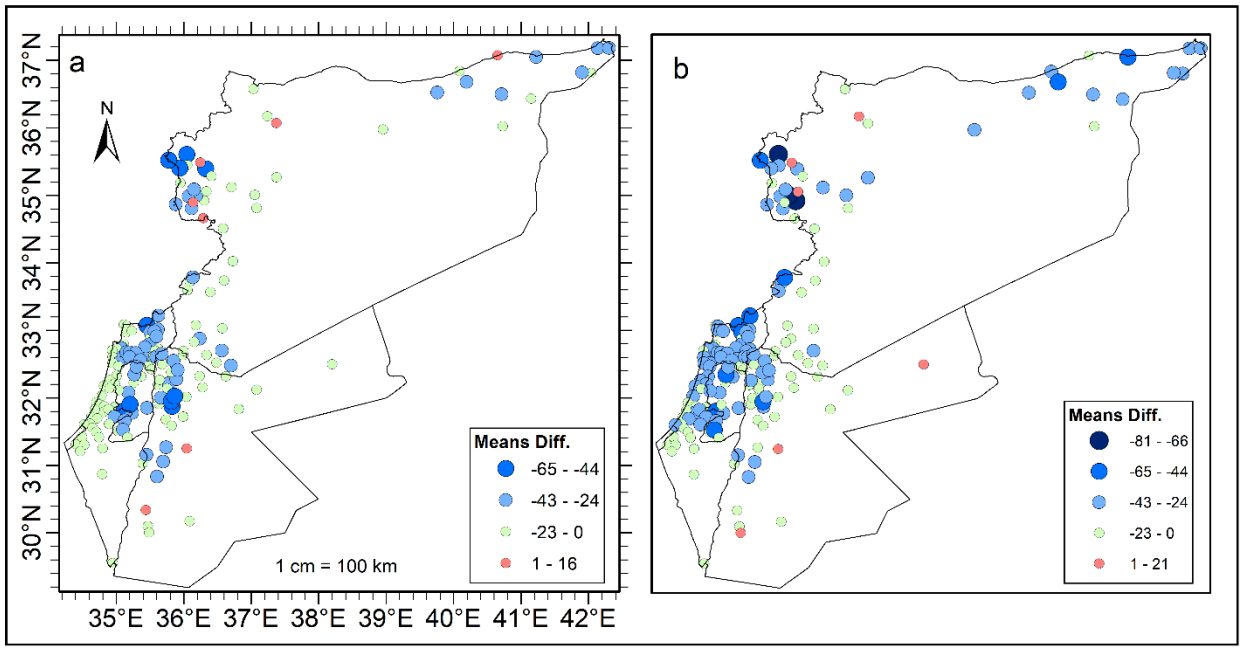

Figure 6.8. Differences in mean spring precipitation between the periods 1970-1990 and 1991-2018 (a), and 1970-1999 and 2000-2018 (b).

6.3 Spatial rainfall variability

In this part, the spatial distributions of annual precipitation, coefficient of variation (CVs), and precipitation concentration index (PCI) (Appendix C.2) were analyzed. Figure 6.9a to e shows isohyet patterns of annual mean, maximum, minimum, coefficients of variation (CVs), and the index of annual precipitation concentration (PCI) in the years 1970-2018. The mean annual precipitation varied widely in the Levant region. The lowest annual mean was in the Elat station

(25.6 mm) in the southernmost part of Palestine, while the highest mean was in the En Halaqeim station (1491.1 mm) in the governorate of Tartus. The northwestern part of the study area (Syrian coastal region) receives the highest annual precipitation (755-1491 mm) (Figure 6.9a). In these regions, both the annual precipitation of each site and the local average are higher than the overall average over the study area. The northernmost locations in Palestine represented the second most important region receiving annual precipitation amounts between 600 and 700 mm. The highest precipitation in these regions is due to the proximity of the sea which increases the interaction between land and sea (condensation barrier effect), resulting in a high and evenly distributed precipitation throughout the year in this region.

A general pattern of decreasing annual average precipitation is recognizable while passing through west to east and from north to south. The lowest annual precipitation (300 mm) was observed in the eastern and southern areas of the Levant, east to 36.5ºE and south to 31.2ºN, especially in Syria and Jordanian Badias and in the Negev desert in southern Palestine. In these regions, both the annual rainfall of each location and the local average are lower than the overall average (Figure 6.9a). It is important to note that a wide and extended area receives an average of less than 300 mm of precipitation, while those areas that receive an average of more than 400 mm of precipitation form a small part that is concentrated on the west coasts.

Similar to annual precipitation, the Syrian coastal region had the highest maxima and minima of annual precipitation, while the eastern and southern locations had the lowest (Figure 6.9b and c). The maximum annual mean values ranged from 76.6 mm at Elat station to 2779.5 mm at Shatha station (northwest of Syria), while the minimum mean values ranged from 0 at Elat and Petra stations to 684.2 mm at En Halaqeim. A very strong positive correlation ($r > 0.91$) was found between the annual precipitation, maximum, and minimum averages.

The spatial pattern of the coefficients of variation (CVs) (Figure 6.9d) corresponds inversely with that of the annual precipitation (Figure 6.9a), with an increase in average precipitation being expected to cause a decrease in CV. This significant and inverse relationship ($r = -0.60$) indicates that northern Palestine and western Syria show high precipitation averages with regular precipitation occurrences, and then relatively low CVs (< 30%), while southern and eastern regions show fewer precipitation averages with strong irregularity and then high CVs (> 30%). The highest CVs values (> 60%) were found in the most southern regions of Palestine and Jordan (e.g. in the Elat and Aljafer stations).

According to Oliver (1980) and based on the values of the precipitation concentration index (PCI) (Figure 6.9e), the annual precipitation of the study area is classified as a non-uniform distribution. In the same line, the values of PCI vary spatially over the study area, whereby (i) the values between 13 and 15 (moderate precipitation concentration) covered the coastal areas from the Syrian governorates (Lattakia and Tartus), (ii) the values between 16 and 20 (irregular distribution) covered the largest area of the Levant (rest regions from Syria, northern regions of Jordan and central and northern regions of Palestine), and (iii) the values greater than 20 (strong irregularity) in the southern regions of the area under investigation and east of Jordan. The average range of

PCI < 10 was never recorded for any station. The lowest average value of PCI (13.3) was achieved at the Qadamos station in the governorate of Tartus.

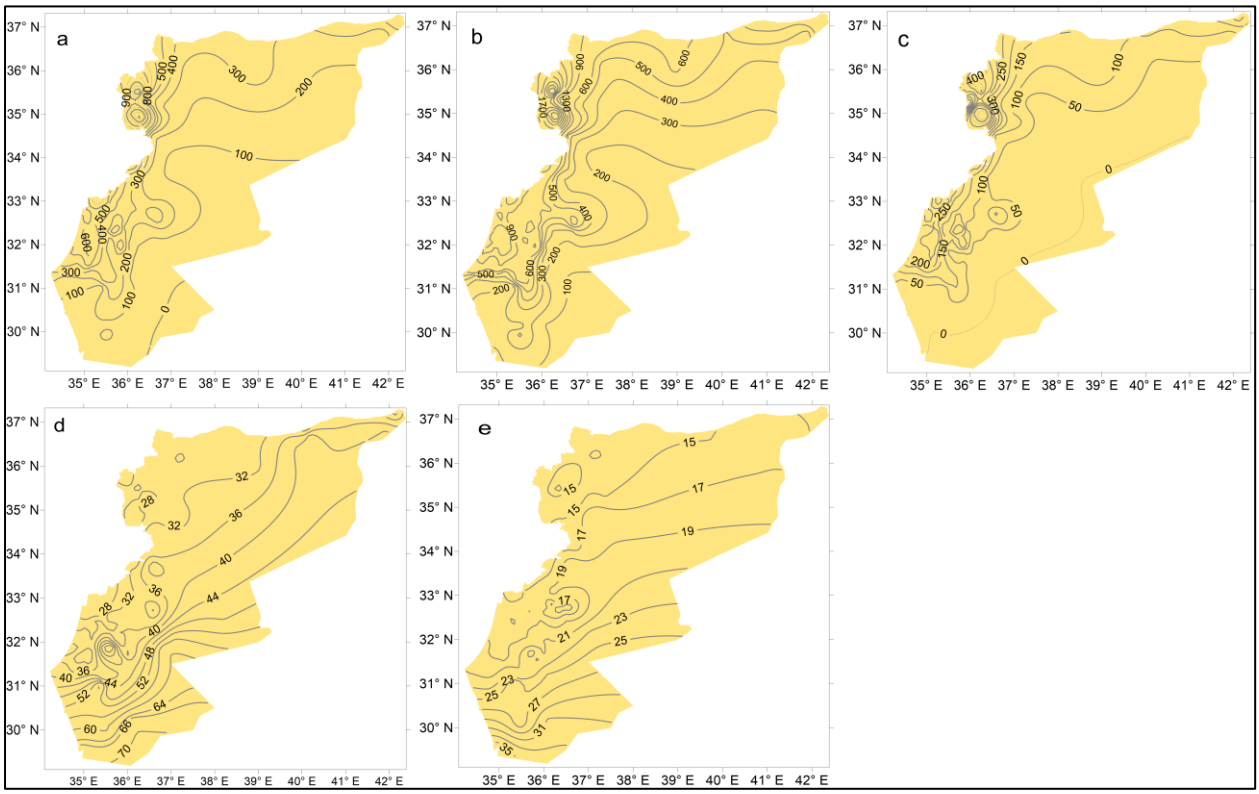

Figure 6.9. Spatial distribution of long term mean annual rainfall (a), maximum mean annual (b), minimum mean annual (c), CVs (d), and annual PCI values (e) in 1970-2018.

The annual PCI values increase towards the south where the maximum values were found at Elat and Aljafer stations by 37 and 31, respectively. A high positive and significant correlation was found between PCI and the CVs by (r = 0.77). Furthermore, the spatial pattern of the annual mean values PCI reflects the climate zone map of the Levant. Since the rainy season is very short and heavy precipitation is limited in the southern regions as arid and semi-arid zones, relatively high PCI values are expected in these regions. Conversely, smaller PCI values were expected in regions with a relatively long and heavy rainy season and a uniform temporal distribution of precipitation over time, e.g. Syrian coastal areas and northern regions of Palestine.

6.3.1 Spatio-temporal variability of annual rainfall

Principal Component Analysis (PCA) was used in conjunction with the K-means cluster to study the spatial and temporal variability and to delineate precipitation clusters for annual and seasonal precipitation in the Levant region. The data of the standardized input matrix (MxN) were constructed with columns for 167 stations and rows for 49 years. Based on the North rule of thumb (Figure 6.10a), three PCs were retained for the annual precipitation, and consequently they were rotated using the varimax approach (Bortz, 1993) to maximize the correlation and large loading, and minimize the small loading between the rotated PCs and the original variables, which

facilitates their interpretation (Raziei et al., 2008; Gocic and Trajkovic, 2014). As can be observed in Table 6.3, the first three PCs explained 70.2% of the total variance and the first three rotated components explained 42.4%, 17.9%, and 9.9% of the total variance, respectively.

Variance (%)	PCs			Cumulative
	PC1	PC2	PC3	
Un-rotated (%)	53.3	10.3	6.6	70.2
Varimax rotated (%)	42.4	17.9	9.9	70.2

Table 6.3. Explained variance (%) by the both un-rotated and rotated PCs for annual precipitation.

Figure 6.10b to d shows the time series (factor scores) for the three rotated PCs, and Figure 6.11a to c displays the spatial distribution of factor loadings for these PCs. The spatial patterns of the factors loading for each PC (Figure 6.11) showed that each component was well connected to a different region, with the highest loading factor for each PC being associated with a particular region. Factor loading is essentially the correlation coefficient between the stations and the PCs that were rotated PCs. For example, PC-1 represents the central and northern locations in Palestine and the southern locations in Syria, where high correlations ($r > 0.65$) were observed between the stations and PC-1 in these regions. PC-2 represents the Syrian coastal region, and PC-3 represents the eastern areas of Syria and Jordan.

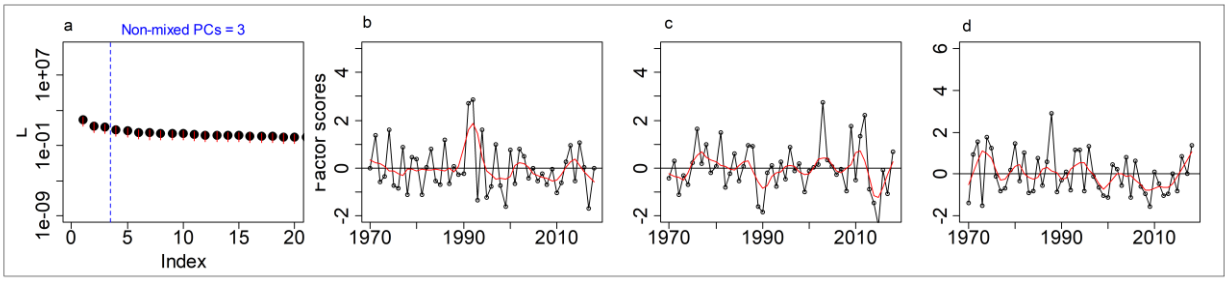

Figure 6.10. Number of the retained PCs based on the North rule (a). The factor scores for the PC-1 (b), PC-2 (c), and PC-3 (d). Redline refers to Lowess line.

To identify the thresholds separating the stations into homogeneous precipitation regions, the K-means clustering technique was applied to the rotated PC scores (Mills, 1995). The homogeneity of each cluster was examined by the ratio of the variance between the classes and the total variance. If the ratio is high, the corresponding cluster must be considered homogeneous and vice versa.
The ratio calculated for the annual precipitation reached 0.72, where the sum of the squares within the cluster is 282.3, and the sum of the squares between the clusters is 571.6. Figure 6.12a illustrates the annual spatial pattern of precipitation such that three different sub-zones have been identified in the Levant region. The central and northern areas of Palestine between 31.5ºN-33.3ºN, northern Jordan and southern Syria, comprising 96 stations, formed the first homogeneous precipitation subzone. Cluster 2, comprising 40 stations, is located mainly in the Syrian coastal area between 34.5ºN-36ºN. The third cluster covered the largest area in the eastern regions from Syria and Jordan and the southern locations from Palestine and Jordan. From this it can be concluded that the first and second clusters represent the Mediterranean climate zones, while the third cluster is related to the arid and semi-arid climate zones (Figure 6.12a, Figure 2.1c).

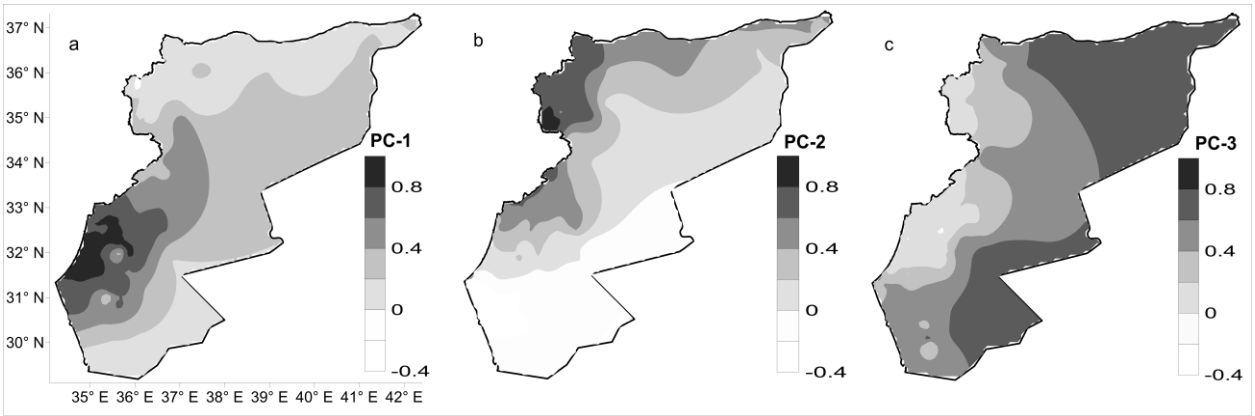

Figure 6.11. Spatial distributions of factor loading for the rotated PC-1 (a), PC-2 (b), and PC-3 (c).

The second cluster (the Syrian coastal rainfall cluster), has the highest annual mean value of precipitation at 723.8 mm with a standard deviation of 164.5 mm (Figure 6.10c). It also has the lowest CVs and the lowest precipitation concentration index (Figure 6.9d and f). In contrast, the third cluster (eastern and southern regions) has the lowest mean annual precipitation of 209.8 mm, with a standard deviation of 52.9 mm. It also showed the highest inter-annual variability and the highest precipitation concentration index. The mean annual precipitation of the second cluster is three and a half times higher than that of the third cluster, indicating the high precipitation variability in the Levant. The first cluster has a mean annual precipitation of 467.7 mm and a standard deviation of 126.4 mm. It showed relatively higher CVs (28%-36%) and PCI (17-19) values than the second cluster. The highest annual precipitation was observed in 1992 and 2003 for the first and second cluster with 791.7 mm and 1142.1 mm, respectively (Figure 6.12b). Finally, the extreme values were not observed in any of the clusters (Figure 6.12b).

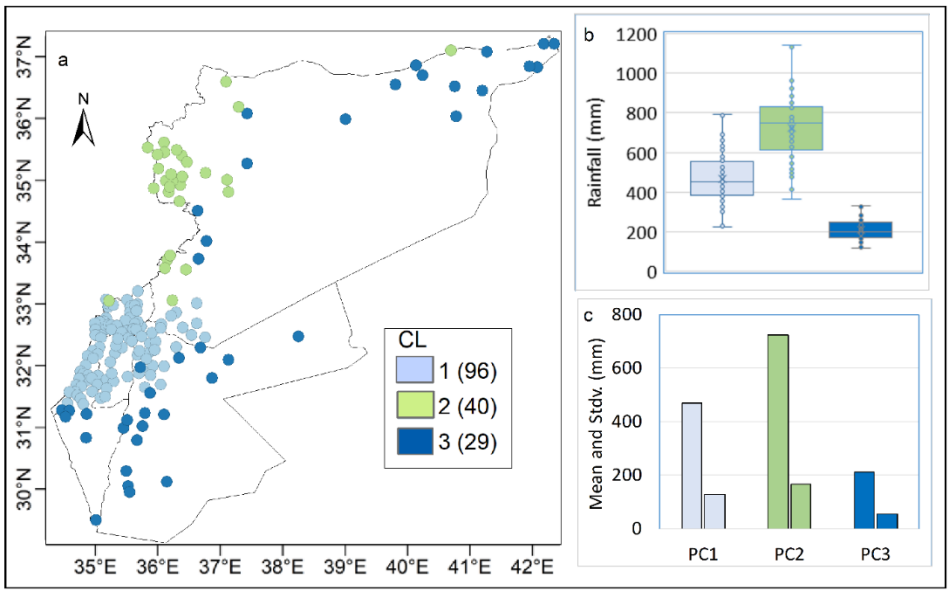

Figure 6.12. (a) Homogeneous rainfall sub-regions outlined through cluster analysis. (b) Boxplots, and (c) standard deviation and mean of annual rainfall for each cluster.

6.3.2 Spatial regionalization of seasonal rainfall

Based on the North rule of thumb (Figure 6.13, panels (a)), three PC were retained for each season. Table 6.4 summarizes the explained variance for each un-rotated and rotated PCs, with the first three PCs explaining 75.9%, 70%, and 80% of the total variance for winter, spring, and autumn, respectively. Figure 6.13 (panels (b) to (d)) shows the seasonal factor scores for the first three retained PCs. The spatial distribution of seasonal factor loadings are shown in Figure 6.14 (panels (a) to (c)). In addition, Figure 6.15 panels (a), show the homogeneous sub-regions (clusters) for each season and some descriptive statistics related to each cluster are presented in the panels (b) and (c). In general, the existence of high loading factors in more than one component was not observed, i.e. each PC refers to a different region for all seasons (Figure 6.14). The spatial pattern of the clusters varies slightly across the seasons and the year together with the variation in the number of stations in each cluster. A close spatial pattern was generally observed between winter, autumn, and annual precipitation (Figures 6.12a) 6.15 (winter a), and 6.15 (autumn, a)).

In winter, the first component (PC-1) explained 45.2% of the total variance in the datasets (Table 6.6), and is concentrated in the central and northern areas of Palestine, north Jordan, and south Syria by rainfall average of 306.4 mm and a standard deviation of about 109 mm (Figure 6.15). The stations in these regions highly correlated with the first component ($0.65 < r < 0.85$) (Figure 6.14, winter (a)). For this PC, the rainfall ranged from 666.6 mm (an extreme value) in 1992 to 55.2 mm (680.3 mm) in 2014 (Figure 6.15, winter (b)). The second component that explained 18.7% of the total variance was dominant in north Syria, including the coastal areas, the most northeastern locations at the borders with Turkey, locations in the west of Damascus district, and most northern locations in Palestine. It receives the highest winter rainfall by an average of 430.3 mm and a standard deviation of 132.8mm. Moreover, this cluster showed the highest rainfall of 763.2 mm in 2003. A decreasing trend can be seen from 2002 onward for this PC (Figure 6.13, winter (c)).

Season	Variance (%)	PCs			Cumulative
		PC1	PC2	PC3	
Winter	Un-rotated (%)	57.6	10.0	8.4	75.9
	Varimax rotated (%)	45.2	18.7	12.1	75.9
Spring	Un-rotated (%)	49.7	9.1	8.2	70
	Varimax rotated (%)	42.5	13.3	11.2	70
Autumn	Un-rotated (%)	62.9	11.8	5.3	80
	Varimax rotated (%)	38.4	32.3	9.3	80

Table 6.4. Summarizes the explained variance (%) for each un-rotated and rotated PCs.

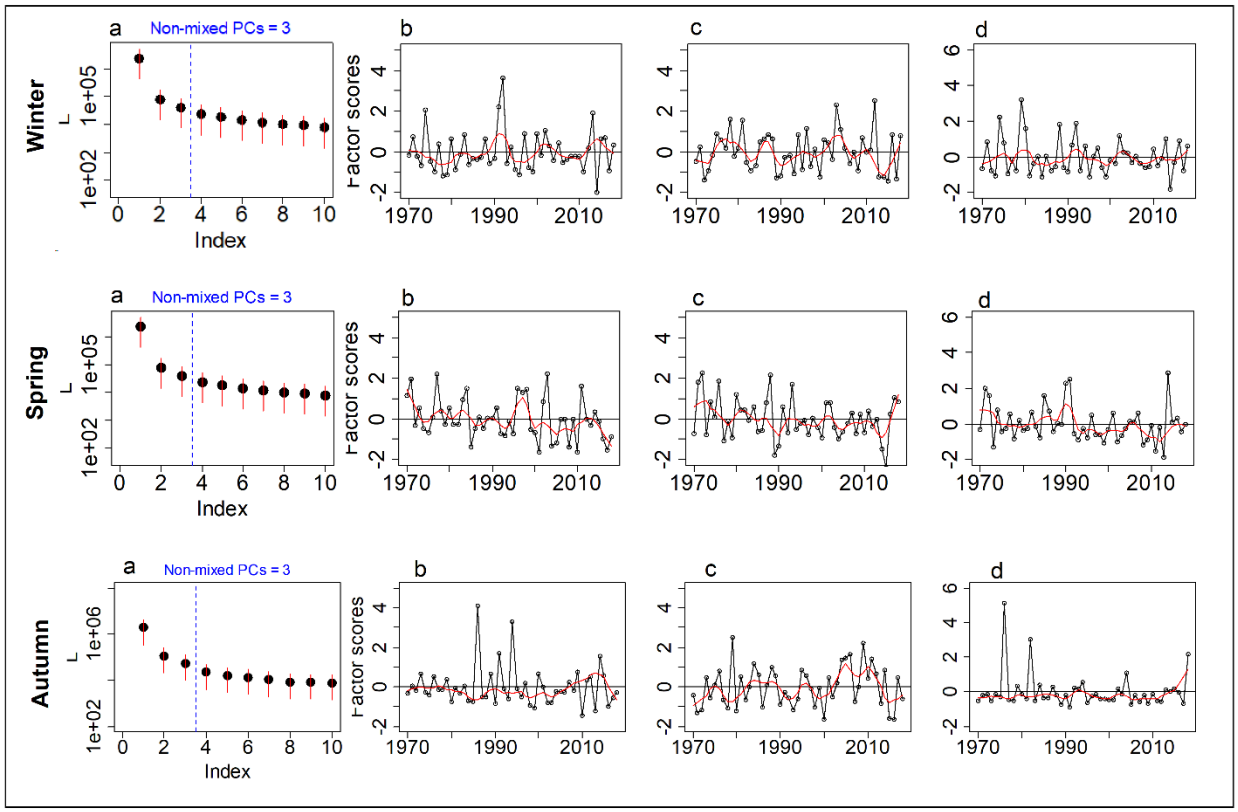

Figure 6.13. The Panels (a) represent the number of the retained PCs based on the North Rule of Thumb for each season. The panels (b), (c), and (d) are factor scores for the PC1, PC2, and PC3 of winter, spring, and autumn.

Figure 6.14, winter (c), shows that the maximum loadings correspond to south Palestine and Jordan, east Jordan and Syria, and central locations in Syria (east and north Damascus). Stations in these regions formed the third cluster sub-region (Figure 6.15, winter (a)). Note that these regions represent the arid and semi-arid climate zones, with the lowest mean precipitation of 142.4 mm and a standard deviation of 44 mm. This cluster reflects the third PC which explains 12.1% of the total variance and contains 33 stations. Winter rainfall ranged from 61.5 mm to 256.2 mm in 1979.

In spring, the first PC is strongly connected to the central and northern areas of Palestine and north Jordan (> 0.70) (Figure 6.14, spring (a)). A percentage of 42% of the total variance can be explained by this PC, while the first three PCs explain 70% of the total variance (Table 6.4). The K-means cluster indicated that these regions had an average spring precipitation of 87.1 mm, and a standard deviation of 43.5 mm (Figure 6.15, spring (a and b)). As can be seen in Figure 6.13, spring (a), the PC-1 showed a decreasing pattern along the study period. In fact, the second and third PCs also showed a similar pattern of decreasing over the period 1970-2018.

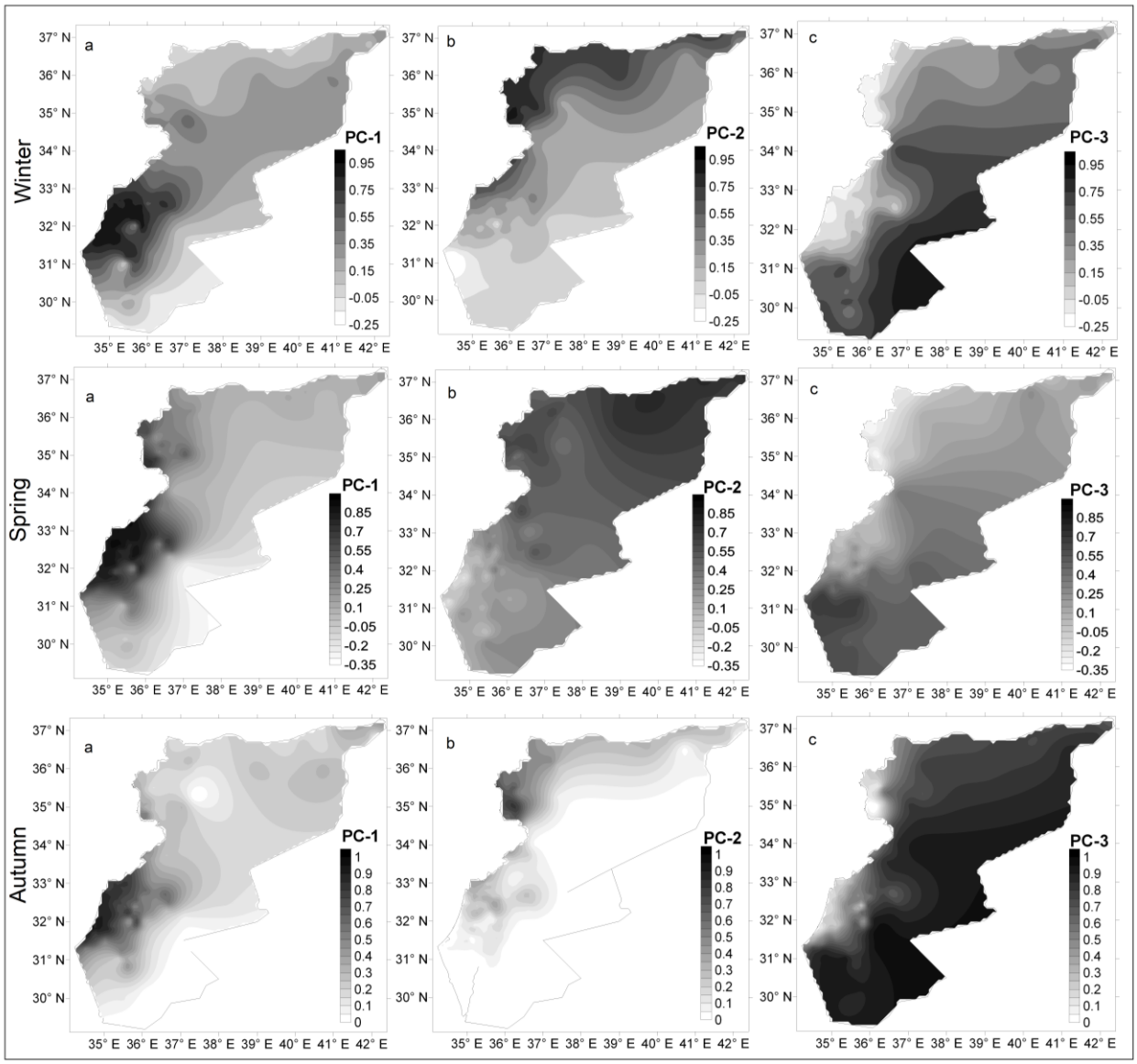

Figure 6.14. Spatial distributions of loading factors for the rotated PC-1 (a), PC-2 (b), and PC-3 (c), of winter, spring, and autumn.

The second component covers the whole of Syria (48 stations) with the highest average precipitation (135.2 mm) and a standard deviation of 47.8 mm. It explained 13.3% of the total variance (Table 6.4), although it covered the largest area compared to other PCs. For this PC-2, the maximum (252.4 mm) and minimum values (21.9 mm) calculated based on the averaged stations belonging to it were in 1972 and 2015, respectively. Finally, the southern regions of Palestine and Jordan and the eastern part of Jordan formed the third PC, which referred to the third cluster (35 stations). These regions always had the lowest rainfall in all seasons.

For the autumn, the first three PC explained 80% of the total variance by 38.4%, 32.3% and 9.3% for the PC-1, PC-2 and PC-3, respectively (Table 6.4). Similar to winter and spring, the central and northern stations from Palestine correlated strongly (0.75-0.80) with the largest area of the Levant that covered southern Palestine, Jordan, and Syria, and with all of the eastern areas from

Jordan and Syria (Figure 6.14, autumn (b)). As can be seen in Figure 6.15, autumn (b), the PC-1 and PC-3 had extreme values. For example 224.3 mm and 132.3 mm, in 1976 and 1982, for the PC-1, and 287.6 mm and 271.5 mm in 1986 and 1994, for the PC-3.

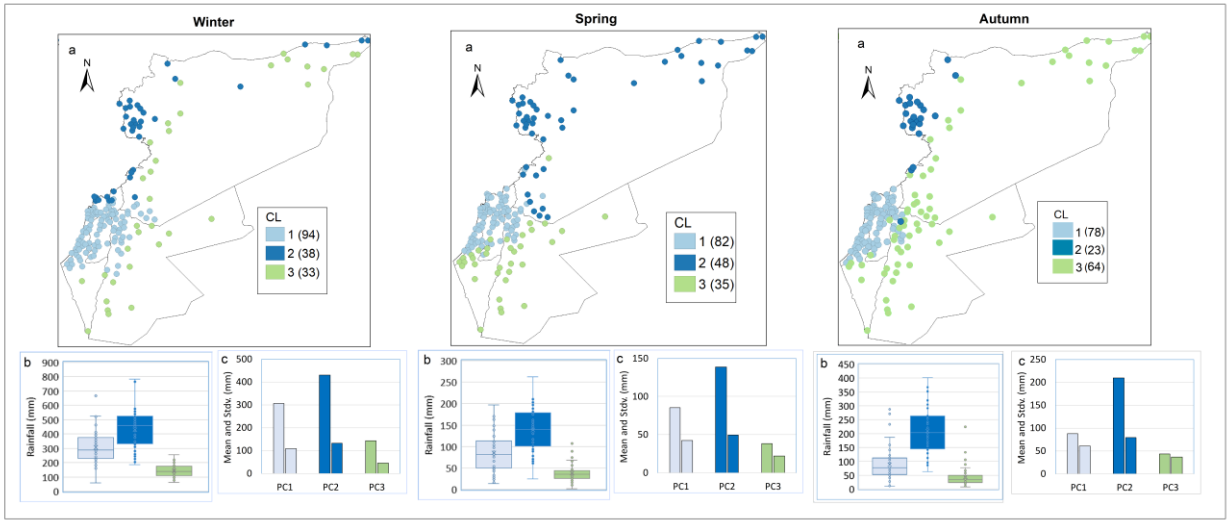

Figure 6.15. (a) Homogeneous winter, spring, and autumn rainfall sub-regions outlined through cluster analysis. (b) Boxplots, and (c) standard deviation and mean of annual rainfall for each cluster.

6.4 Trend analysis (Spatial and Temporal)

In this section, the temporal and spatial trends for annual, seasonal and monthly precipitation are examined. The precipitation time series were averaged for the Levant and sub-regions over the period 1970-2018, and the trends were calculated for each region on the three time scales (Table 6.5). The frequency of increasing and decreasing trends is shown in Figure 6.16. In addition, the trends were also calculated for each station, and the results were presented spatially in Figure 6.17a to d for the annual and seasonal scale, and in Figures 6.19a to c and 6.20a to c for the monthly scale.

6.4.1 Annual and seasonal trends

The analyses showed that average annual precipitation decreased, although not significantly, by -13.8, -15.2, -5.4, and -9.5 mm/decade for Levant, Palestine, Jordan, and Syria, respectively (Table 6.5). At the local level, annual trends ranged from -50.4 mm/decade for Hiffeh to 33.8 mm/decade for Mesiaf, with an average of -11.7 mm/decade (Table 6.5).

As shown in Figure 6.16, the annual precipitation decreased at 144 of 167 stations, with 23 stations of them showing significant decreasing trend. On the other hand, only 2 stations in Jordan showed a significant increasing trend (Ras en-Naqab by 21.7 mm/decade and Mulih by 18.8 mm/decade) (Figure 6.17a). The results also showed that of 78 stations distributed in Palestine/Israel, only 5 stations showed rising trends at weak rates (less than 2 mm/decade), with the exception of Nablus, which showed a rising trend by 11.5 mm/decade. In contrast, homogeneous declining trends were observed in Palestine, southern and eastern Syria, while annual trends were mixed in Jordan and

western Syria (Figure 6.17a). The significant decreasing trends were intensively covered Ar-Raqqa and Hasakah (east Syria, east of 39°E longitude, related to cluster 3 and PC-3) with an average of -26.8 mm/decade. They were also observed in the West Bank (-17.9 mm/decade at Tubas, 50.1 mm/decade at Salfit, -43.9 mm/decade at Meithalon, and -30.3 mm/decade at Jericho) and in Jordan (-19.4 mm/decade at Ira, and -36.1 mm/decade at Wadi Es-sir) (Figure 6.9a). Among the significant increasing trends, they were observed at only two Jordanian sites, Ras en-Naqab by 21.7 mm/decade, and Mulih by 18.8 mm/decade (Figure 6.17a).

Time series	Levant	Palestine	Jordan	Syria	Max.	Min.	Mean	Median
Annual	-13.8	-15.2	-5.4	-9.5	33.8	-50.4	-11.7	-11.3
Winter	-0.6	0.9	2.3	-2.8	35.3	-21.3	0.7	-0.8
Spring	-8.7**	-8.4**	-5.3*	-12.0**	8.8	-25.3	-9.2	-9.1
Autumn	-0.8	-03.3	-1.4	0.5	24.2	-13.3	-1.9	-2.2
January	5.3	4.7	6.2*	4.5	22.5	-6.4	4.0	3.4
February	-1.1	-0.9	4.4	-3.9	9.1	-13.6	-1.3	-1.3
March	-6.9**	-7.3**	-5.4**	-6.2*	8.6	-16.0	-6.8	-7.1
April	-2.6	-1.8	-0.2	-5.4**	0.2	-17.6	-2.5	-1.8
May	0.7	0.4**	0.3*	1.0	6.5	-2.2	0.3	0.0
September	0.2	0.1***	0.05	0.4	2.2	-1.2	0.1	0.0
October	0.08	0.04	0.06	0.9	8.5	-4.5	0.5	0.2
November	-2.3	-3.8	-7.1	-1.3	15.8	-9.7	-2.3	-2.0
December	-0.1	-3.7	1.6	1.3	18.8	-14.4	-1.4	-1.4

Table 6.5. Results of annual, seasonal and monthly rainfall trend (mm/decade) using Mann-Kendall test and Sen's slope estimator, along with some statistical parameters for the trends. Note: *** is for 0.001 level of significance, ** for 0.05, and * for 0.1.

A significant downward trend was observed in the averaged seasonal time series only in spring, with -8.7, -8.4, -5.3, and -12.0 mm/decade for the Levant, Palestine, Jordan, and Syria (Table 6.5). The non-significant positive trends were found only in winter for Palestine and Jordan by 0.9 and 2.3 mm/decade, but they showed negative trends in autumn by -3.3 and -1.4 mm/decade, respectively (Table 6.5). At the local level, the lowest seasonal trend in spring was -25.3 mm/decade at Hiffa station and the highest in winter by 35.3 mm/decade at Shatha station (Table 6.5).

For all seasons, the decreasing trends formed higher percentages than the increasing trends, with 92 (55%), 162 (97%), and 124 (74%) of 167 stations showing decreasing trends for winter, spring, and autumn, respectively (Figure 6.16). Among the seasons, strikingly rising trends are mainly concentrated in winter. In this context, although 45% of the stations showed increasing trends, only three dispersed stations were significant; namely, the Kufranja dam (29.9 mm/decade), Ras en-Naqb (18.1 mm/decade), and Muleih (18.9 mm/decade) (Figure 6.17b). It is also noticeable that the increasing winter trends were concentrated in the Levant's western parts, with an average increase of 13.8 mm/decade in the Syrian coastal districts (Latakia and Tartu, Cluster-2 and PC-2). On the contrary, the declining trends were significantly grouped over the eastern areas from Syria (Hasakia and Ar-Raqqa Governorates, Cluster-3 and PC-3) with an average of -14.0 mm/decade (Figure 6.17b).

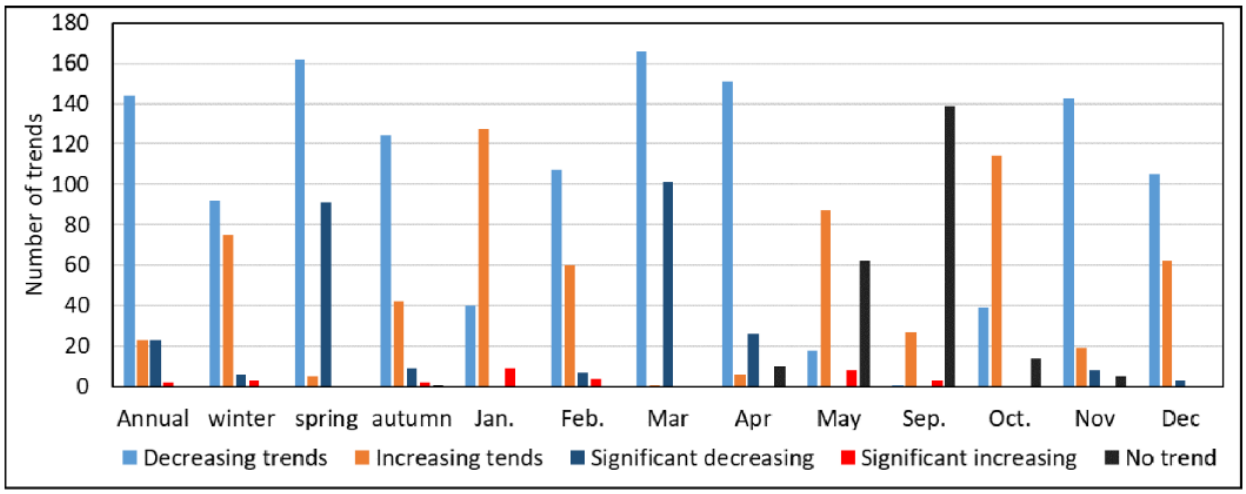

Figure 6.16. Number of trends for the annual, seasonal and monthly series, during period 1970-2018.

The widespread and intensive, significant decreasing trends have occurred in the spring. A percent of 54% (91 stations) of 167 stations showed significantly decreasing trends (Figures 6.16 and 6.17c). These trends showed a very coherent pattern for all regions and clusters in spatial terms. For Palestine, 100% (78 stations) of the total number of stations showed decreasing trends, and 65% (51 stations) reported significantly reduced trends. In addition, the sum of the significantly declining trends reached 15 out of 36 stations for Jordan and 25 out of 53 stations for Syria (Figures 6.16 and 6.17c). Furthermore, significantly increasing trends were not observed at any of the sites. The northern Levant (Syria) showed stronger declining trends (-12.0 mm/decade) than the southern Levant (Palestine and Jordan) (-7.9 mm/decade) (Table 6.5). In spatial terms (Figure 6.17c), the Syrian coastal areas, which showed increasing trends in winter, showed decreasing trends in spring precipitation by an average of -15.4 mm/decade, significantly for Al Basil Airport (-19.0mm/decade), Latakia (-20.4mm/decade) and Hiffa (-25.2mm/decade) stations. Similar to winter, the easternmost regions of Hasakia showed significant declining trends, averaging -13.9 mm/decade. In Palestine and Jordan, fewer values of significant declining trends (< -14.0 mm/decade) were observed for all locations.

In autumn, the trends calculated for the averaged time series were weak, -0.8, -3.3, -1.4, and 0.5 mm/decade for the Levant, Palestine, Jordan, and Syria, respectively. In addition, only 5% (9 stations) of the stations showed significantly decreasing trends (Figure 6.16 and 6.17d). It can be seen that the highest decreasing trends are mainly found in the central areas of Palestine between 31.3ºN-32ºN by an average of -9.1 mm/decade, with significant decreasing trends for the Jerusalem (-10.4 mm/decade), Bet Guvrim (-7.8 mm/decade), and Dura (-9.0 mm/decade) stations. Similar to winter, the Syrian coastal areas, especially the governorate of Tartus, showed coherently increasing trends by an average of 7.9 mm/decade, only significant at Messiaf (8.5 mm/decade).

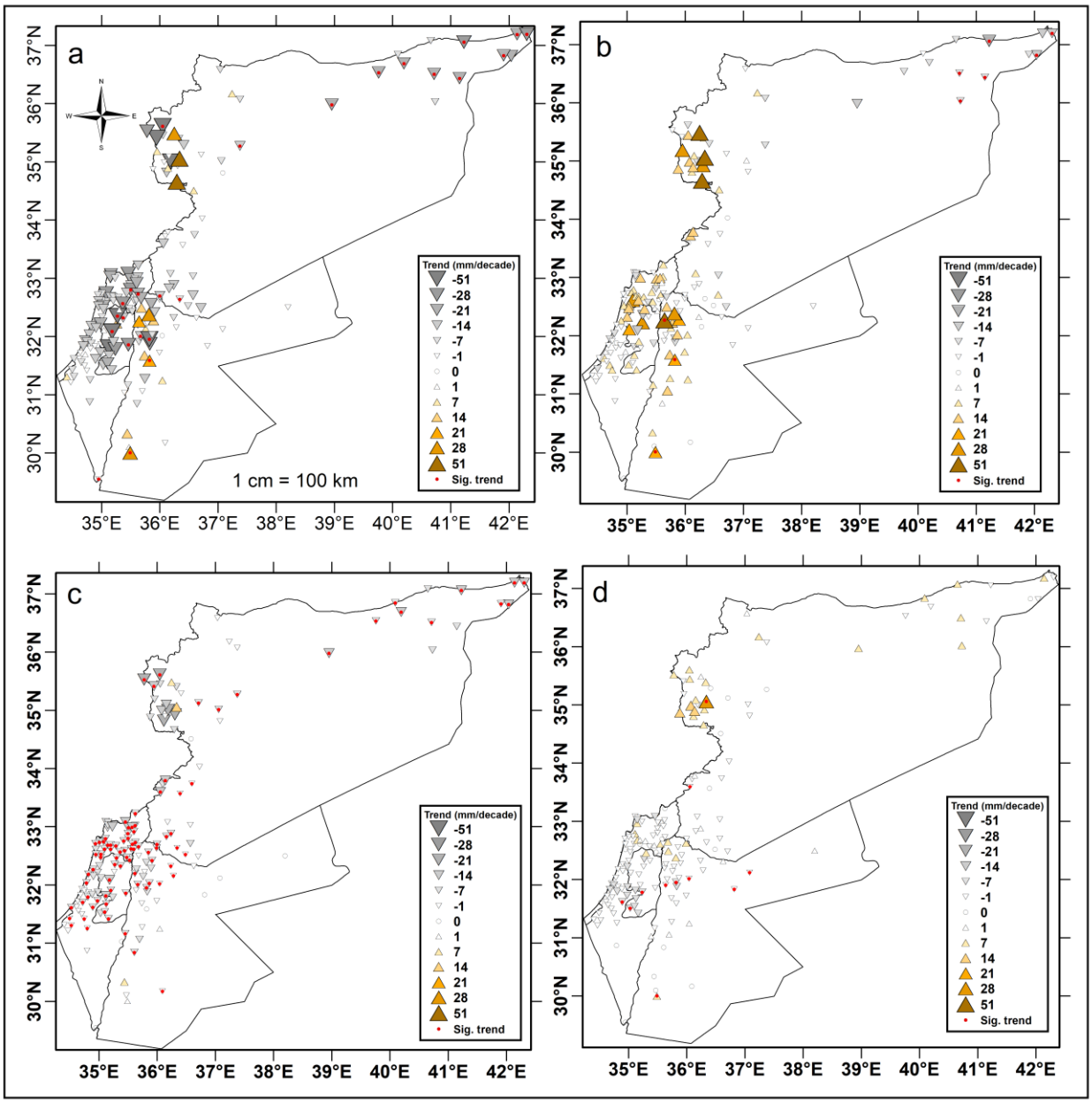

Figure 6.17. The spatial distribution of trends for (a) annual, (b) winter, (c) spring, and (d) autumn precipitation during 1970-2018.

The trend profiles of annual precipitation along latitudes 30ºN to 36.5ºN and longitudes 34.7ºE to 38ºE, were also calculated (Figure 6.18a to d). Trend profiles were recorded every 0.5ºN and 0.5ºE. For illustration purposes, we present here only the trend averages of the latitude and longitude profiles (Figure 6.18a and b) and the highest decreasing trends of a longitude and latitude (Figure 18c and d). The longitudinal profiles across all latitudes "west-east" exhibited a decreasing pattern with an average of -0.11 (mm/decade)/(3 Km) (Figure 6.18a). The results also showed that the latitudinal profile (north-south) averaging all longitude trends showed a decreasing pattern with an average of -0.016 (mm/decade)/(3 Km) (Figure 6.18b). The strongest decrease was observed along

the 35.5ºN latitude by -0.20 (mm/decade)/(3 Km) eastward and along the 35.0ºE longitude by -0.20 (mm/decade)/(3 Km) northward (Figures 6.18c and d).

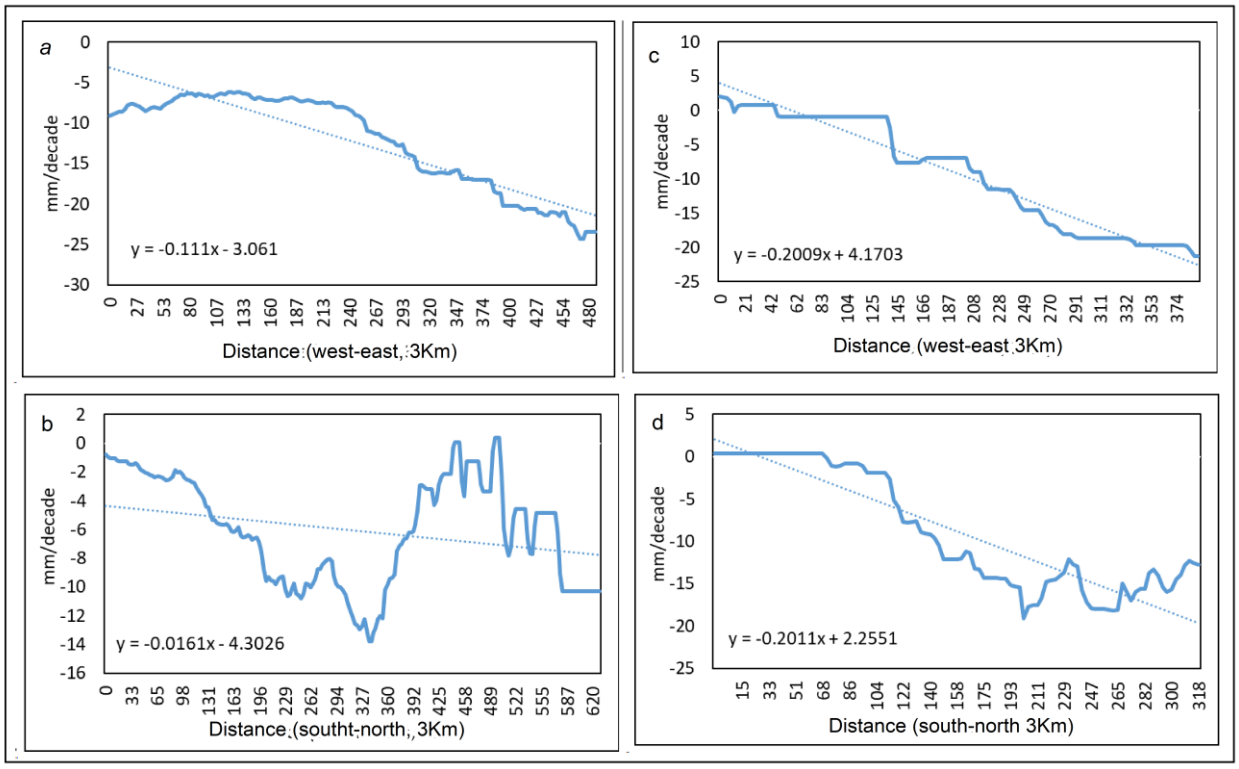

Figure 6.18. Spatial profiles of mean annual precipitation averaged along all latitudes (a), longitudes (b), for the latitude of highest decreasing trend (34.50N) (c), and for the longitude of highest decreasing trend (3.050E) (d).

6.4.2 Monthly trends

Based on the monthly averaged time series over regions (Table 6.5), the main results are:

(i). All regions (Levant, Palestine, Jordan, and Syria) showed significant decreasing trends in March, with -6.9, -7.3, -5.4, and -6.2 mm/decade. A significant downward trend was also observed for Syria in April with 5.4 mm/decade. Furthermore, all regions showed a downward trend in April by -2.6, -1.8, 0.2 and -5.4 mm/decade and in November by -2.3, -3.8, -7.1 and -1.3 mm/decade.

ii). A monthly significant increasing trend was only observed for Jordan in January by 6.2 mm/decade. It can also be noted that Jordan showed rising trends in all winter months (Dec-Feb.).

iii). Apart from January, the rising trends (sig. or not sig.) in May, September, and October were generally weak (less than 0.9 mm/decade).

iiii). Palestine showed the highest downward trend in December and March, by -3.7 and -7.3 mm/decade, respectively. In addition, Jordan showed the highest downward trend in November by -7.1 mm/decade, and Syria in April by -5.4 mm/decade.

Concerning the frequency of trends (Figure 6.16), the decreasing trends were dominant in the months of a high contribution to the annual precipitation, except for January (Table 6.5 and Figure 6.16). The highest total of decreasing trends was observed in March and April with 166 and 151

stations, respectively, while the highest total of increasing trends was observed in January with 127 stations. The significant increasing trends were not observed for March, April, October, November, and December. In addition, the months of May and September (transition months) showed very high percentages of cases without trend, with 62 and 139 stations, respectively.

The maximum trend was in January by 22.5 mm/decade at Shatha station, whereas the minimum trend was in April by -17.6 mm/decade at Wade Al'ouun station (Table 6.5). The range of May, September, and October trends was very small (less than 12 mm/decade). In addition, these months had a high percentage of cases where no trend was observed and a very low percentage of significant rising or decreasing trends. For these reasons, the spatial variability of the monthly trends is analyzed only for December, January, February, March, April, and November.

In December and January (Figure 6.19a and b), trends were positively concentrated in the Syrian coastal region, with average values of 5.8 and 13.2 mm/decade, respectively. The results also showed that all sites in the Palestinian coastal region showed declining trends with high rates for the northwestern sites (-15 mm/decade) in December. In January, they showed especially increasing trends with high rates for the northwestern sites (10.7 mm/decade). The different trends between December and January were also observed at the southern sites from Palestine, Jordan, and Syria.

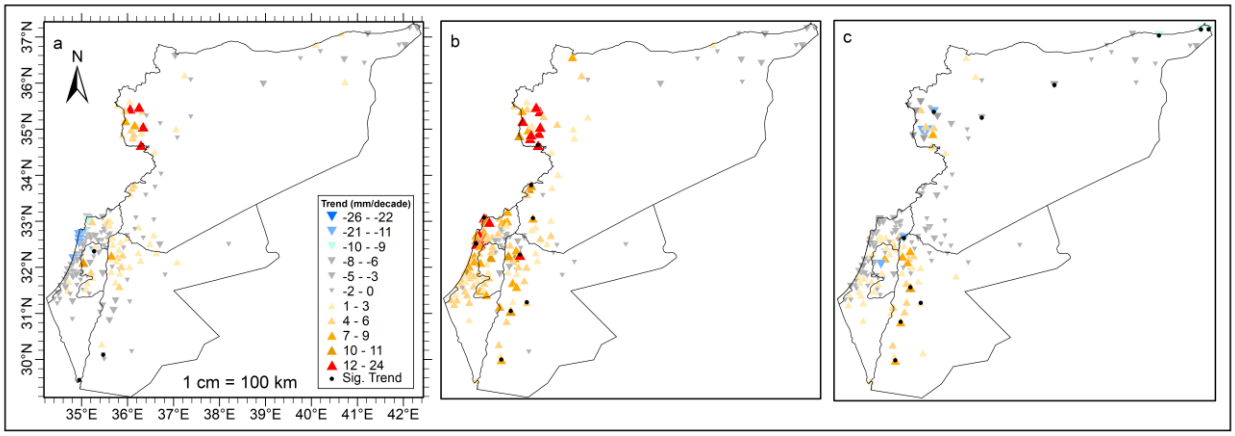

Figure 6.19. Spatial distribution of trends for winter months of December (a), January (b), and February (c), during 1970-2018.

It is also noticeable that the eastern regions of the Levant (east to 36.6ºE) in January formed a region with low declining trends with an average of -2.1 mm/decade. Significant declining trends were not observed in January, while they were observed in December at three scattered stations (Meithelon -14.4 mm/decade, Elat -0.8 mm/decade, and Ma'an -0.7 mm/decade). Figure 6.19b shows the significant upward trends found in January at 9 sites, mainly east to 36.6ºE, with a high value at the Ala'reda station (15.7 mm/decade), and two of these sites are in the Palestinian coastal region, Kefar Harosh (11.1 mm/decade) and Binyamina (14.3 mm/decade).

In February (Figure 6.19c), a dominant increasing trend was observed for the West Bank along the 35.4ºE, which was significant at Tafileh (6.1 mm/decade), Ras En-Naqab (7.4 mm/decade), Qatraneh (2.6 mm/decade), and Muleih (1.1 mm/decade). On the other hand, most of the eastern

locations in the Hasakah Governorate showed a declining trend of -5.1 mm/decade. The significantly decreasing trends also occurred at seven stations between 35.5ºN and 36.8ºN, with a high rate at the Al Karim station (-10.4 mm/decade).

A very coherent and homogeneous pattern of significant decreasing trends was observed in March (Figure 6.20a). A percentage of 60.5% (101 stations) of the stations were affected by significantly decreasing trends, and 166 of 167 stations showed decreasing trends. Spatially, most stations in the West Bank and east of the Haifa district showed the highest decreasing trends, with averages of -15.5 and -9.8 mm/decade, respectively. In addition, the easternmost stations in Syria showed significant declining trends of -6.4 mm/decade.

In April (Figure 6.20b), 160 of 167 stations recorded a decreasing trend, while only 26 stations reported a significant decreasing trend. The high significant trends were observed at most eastern locations of Hasakah and in the coastal areas of Syria with -7.2 and -11.5 mm/decade respectively. On the contrary, all southern sites in Palestine and all in Jordan showed very low frequencies and orders of magnitude of decreasing trends (sig. or not) compared to their March trends, with less than -5.5 and -3.2 mm/decade for all sites.

In November, the high declining trends were found in the Jerusalem district (-5.2 mm/decade), the areas from Nablus to Miethalon in the West Bank (-5.4 mm/decade), and the northern areas from Palestine (-4.2 mm/decade) (Figure 6.20c).

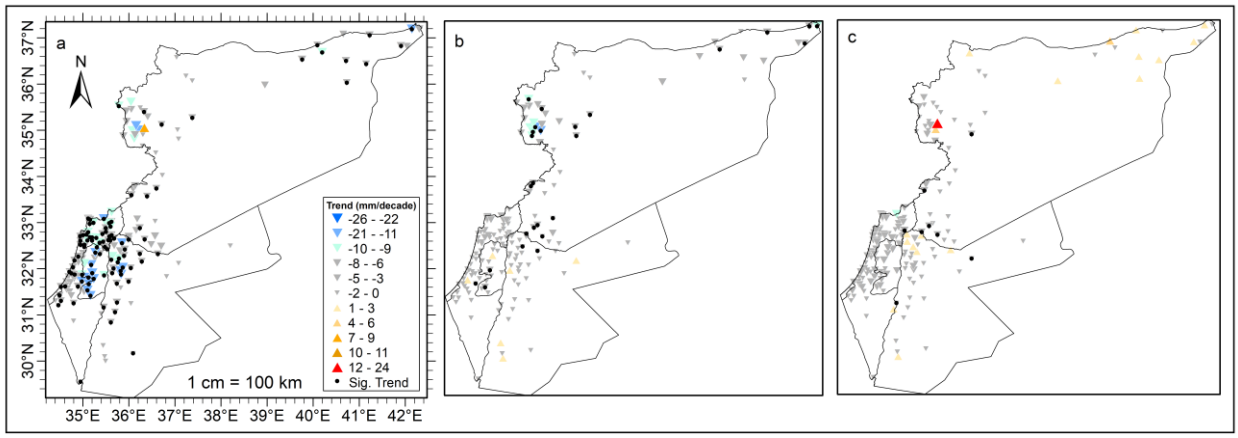

Figure 6.20. Spatial distribution of trends for (a) March, (b) April, and (c) November, during 1970-2018.

6.5 Change points detection

The sequential Mann-Kendall (SMK) test was applied to the time series averaged in spring and March due to their significantly decreasing trends. The results were plotted for all regions (Figure 6.21, upper and lower panel). For the spring-averaged time series (Figure 6.21, upper panel)), there are several intersections of $U'(t)$ and $U(t)$ for all regions mainly in the years 1975-1985, which means a large variability in this period. The results also indicate that significant change points were observed around 1992 for the Levant, Palestine and Jordan and around 1997 for Syria. The downward trend became significant in 1995, with the $U(t)$ for all regions outside the 95% confidence bands, except Syria, which showed a starting point for a significant trend around 2015. The trends were totally significant after 2008 onward for the Levant, Palestine and Jordan, where

the $U(t)$ line did not return to within the 95% confidence band. Furthermore, the significant upward trends in the years 1970-2018 were not observed in any region where the declining behavior during the period under study can be easily observed.

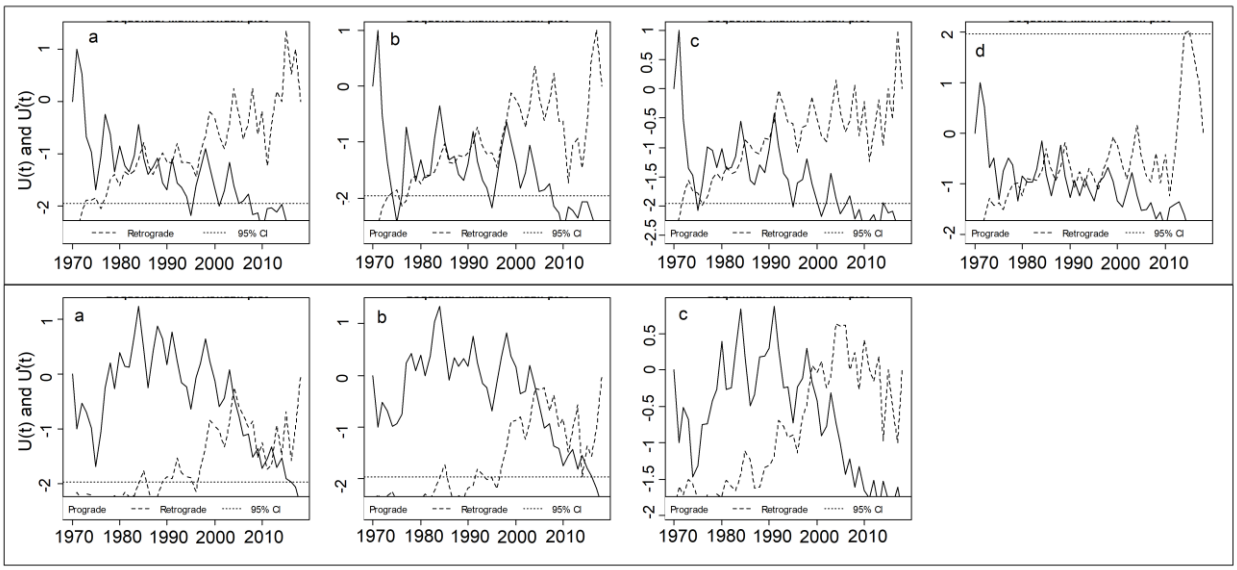

Figure 6.21. Top panel: Graphical representation of the forward, U(t) (solid line) and the backward, U'(t) (dashed line) series of the Sequential Mann-Kendall test for spring averaged time series over (a) Levant, (b) Palestine, (c) Jordan, and (d) Syria. Bottom panel: the same for March averaged time series over (a) Levant, (b) Palestine, and (c) Jordan. The horizontal dotted lines indicate confidence limits at the 5% significance level.

In contrast to the spring, the averaged time series for March showed an upward trend for all regions in the period 1970-1990, although non-significant one, while they have shown a downward trend since 1991 onward (Figure 6.21, bottom panel). The significant change points were found for the Levant in 2013, for Palestine in 2015 and for Jordan in 1999. In addition, the March trends since 2015 have been clearly downward for all regions.

6.6 Influence the large-scale circulation patterns on the seasonal temperatures

Table 6.6 summarizes the number of stations with significant correlations between winter, spring, and autumn precipitation, and the teleconnection indices. Figure 6.22 shows the correlation coefficients between the teleconnection indices and the averaged seasonal precipitation series for the Levant and its countries. Based on the results presented in Table 6.8, the NCP, WEMO, and ENSO indices showed the highest frequency of significant correlations in winter, spring, and autumn, with 83, 80, and 118, respectively, out of 167 stations. Other indices showed remarkable significant correlations in winter (MO and EA/WR indices with 76 and 46 out of 167 stations, respectively), spring (NCP and EA indices with 35 and 19 stations), and autumn (WEMO and EA /WR with 16 and 17 stations).

According to the magnitude of the correlations (Figure 6.22), the NCP index also showed the highest magnitude of positive correlation with the averaged time series of winter rainfall for the

Levant (r = 0.30), Jordan (r = 0.32), and Palestine (r = 0.39). The MO index showed slightly lower correlation values than the NCP index, by 0.30, 0.31, and 0.37. Interestingly, no teleconnection pattern showed a significant correlation with the winter rainfall in Syria.

For spring, the highest correlation coefficients with the averaged time series were found for the WEMO index by -0.40 for the Levant, -0.30 for Jordan, -0.39 for Palestine, and -0.34 for Syria. It is also noteworthy that the indices EA and NCP showed an effect on Syria's rainfall through an average correlation of -0.36 and 0.31, respectively. Only the ENSO pattern showed a significant effect on autumn precipitation for all regions, except Syria, with -0.34 for the Levant, -0.39 for Jordan, and -0.34 for Palestine/Israel (Figure 6.22).

	WEMO	EA/WR	NAO	EA	MO	NCP	ENSO
Winter	0	46	5	1	76	83	5
Spring	80	2	0	19	1	35	4
Autumn	16	17	4	1	0	0	118

Table 6.6. The total stations that showed significant ($p<0.05$) correlation with the large-scale circulation patterns based on each season.

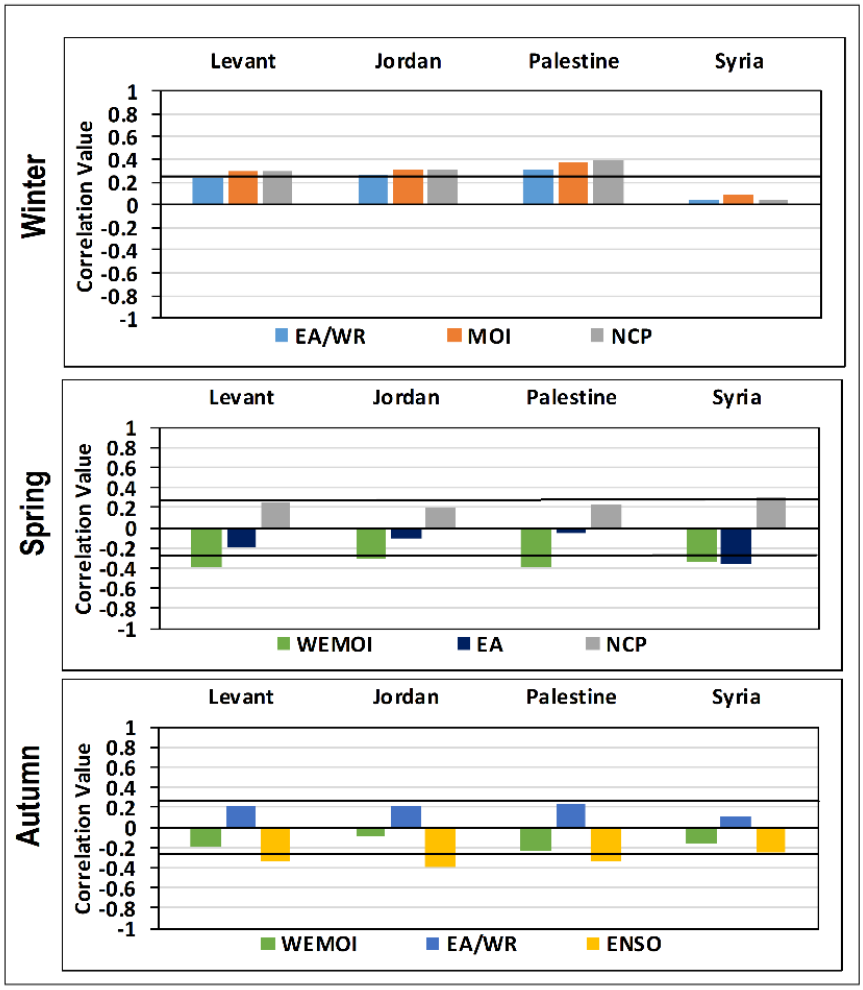

Figure 6.22. Correlation coefficients between the teleconnection indices and seasonal rainfall averaged series for the Levant and countries. Bold Horizontal line refers the significant limits.

6.6.1 Correlation maps for the winter rainfall

Spatially, during winter, the impact of the EA/WR, MO, and the NCP (Figures 6.23a to c) is concentrated on the central and northern Palestine sites and the northern Jordan sites. For the NCP index, the highest effect ($0.47 < r < 0.57$) was on the southern and central regions of the Palestinian coastal region and all sites covering the central Palestinian mountains from the Jenin governorate in the north to Hebron in the south. It is also noticeable that the NCP index did not show any significant effect on the northernmost locations in Palestine. For Syria, the NCP index showed an influence on some locations in As-Suwayda governorate (south of Syria) (0.37-0.46) (Figure 6.23). Like the NCP index, the MO index showed the highest values of correlations in the southern locations of the Palestinian coastal region and the western locations of Jerusalem (0.47-0.57).

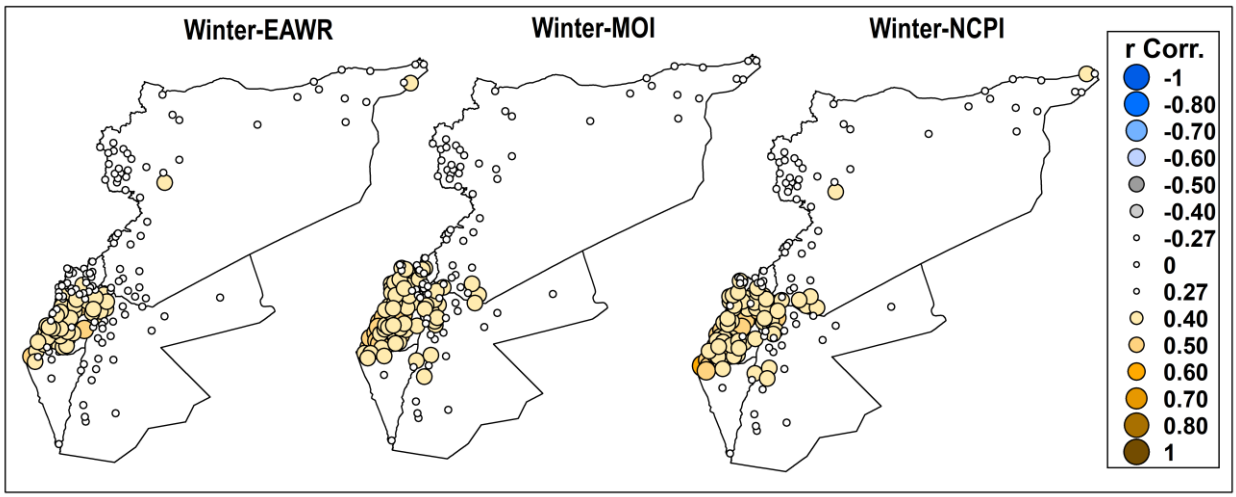

Figure 6.23. Spatial distribution of correlation coefficients between winter rainfall and teleconnection indices in 1970-2018.

6.6.2 Correlation maps for the spring rainfall

During spring, the WEMO showed a widespread significant correlation (-0.37 to -0.56) over the coastal areas in Palestine and Syria and over the northern locations of Palestine and Jordan (Figure 6.24). The effect of the EA index occurred only in the Syrian locations, especially the easternmost locations in the governorate Al-Hasaka (-0.37 to -0.66). In addition, the NCP had significant positive correlations with some eastern and western locations in Syria (0.37-0.56) (Figure 6.24).

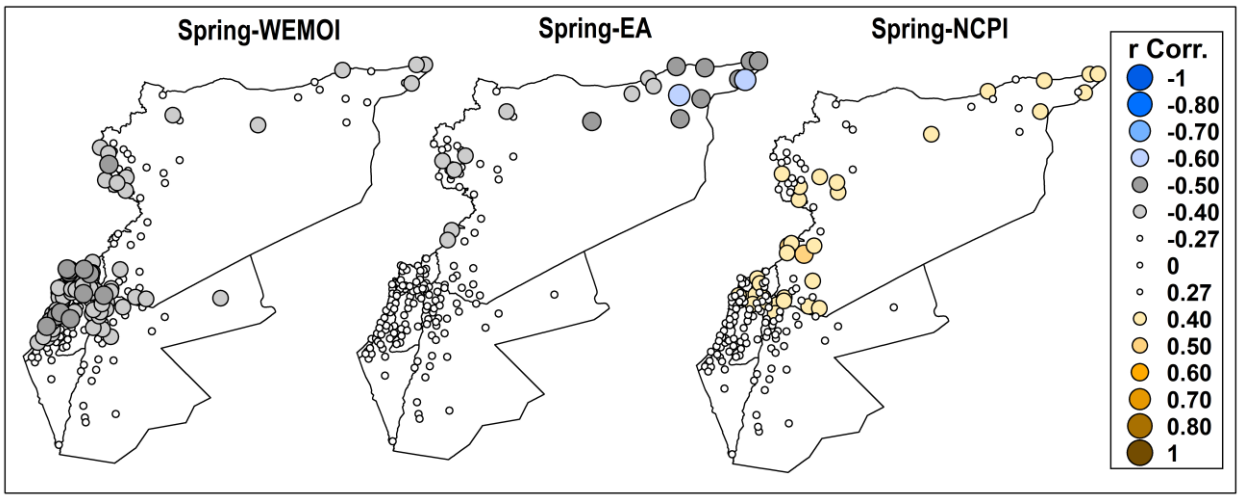

Figure 6.24. Spatial distribution of correlation coefficients between spring rainfall and teleconnection indices in 1970-2018.

6.6.3 Correlation maps for the autumn rainfall

In general, all sites show significant negative correlations with the ENSO pattern (-0.37 to -0.56) during autumn, except for the Syrian coastal areas. Its effect also extended to the southern sites of Jordan and Palestine (Figure 6.25). The WEMO index showed some impact (ranging between -0.37 and -0.46), which occurred in 16 Palestinian coastal stations. Furthermore, a significant correlation with the EA/WR index (0.37-0.46) for 16 stations in the northeastern area of Palestine and southern Syria was found.

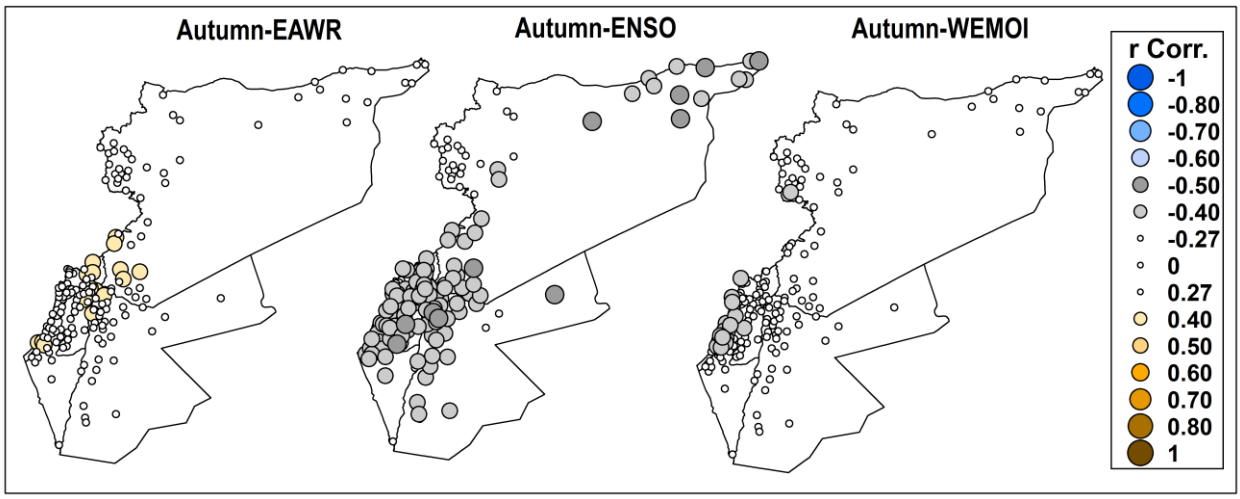

Figure 6.25. Spatial distribution of correlation coefficients between autumn rainfall and teleconnection indices in 1970-2018.

6.7 Conclusions and discussion

This chapter examined the spatial and temporal changes in monthly, seasonal, and annual rainfall averages and trends in the Levant region for the period 1970-2018. The conclusions can be summarized as follow:

1. Annual rainfall in the Levant varies from 246.3 mm in 1999 to 677.8 mm in 1991, and the rainy season of 1991/1992 was the wettest for Palestine/Israel and Jordan. The decadal autumn and November contribution decreased gradually from 1980-1989 to 2010-2018. The March contribution also decreased from 1990-1999 to 2010-2018. The large decline was recorded in spring.
2. A cyclical pattern in the temporal behavior of annual precipitation has been observed, particularly since the late 1980s. A decreasing pattern in the years 1993-1999, 2003-2008, and 2012-2018 was observed for the Levant and all sub-regions, while in the years 2000-2003 and 2008-2012 an increasing pattern was observed for shorter periods. In addition, the spring fluctuations gradually decreased during the whole period of investigation.
3. An inverse and significant relationship between precipitation and maximum/mean temperature was observed in the Levant during the period 1987-2018. In addition, a high positive correlation was found between the annual Levant precipitation and the precipitation in Palestine/Israel ($r^2 = 0.95$). Kafle and Bruins (2009) studied climatic trends in Israel for the period 1970–2002 and found a negative correlation between temperature and precipitation and it was significant for the Negba, Kefar Blum, Har Kena'an, Beer Sheva and Sedom Pans places. Saaroni et al. (2015) studied the dry periods in the Levant region and found that the daily precipitation in Israel (2 grid cells covering the area 31°N–33°N, 35°E–36°E) was correlated with that in the Levant region, which showed a high correlation of $r = 0.87$.
4. In 2000-2018, spring rainfall in the Levant and Palestine has decreased significantly compared to 1970-2018. In addition, the Levant, Palestine, and Jordan have recorded a significant decrease in their spring mean values for the period 1991-2018 compared to 1970-1990.
5. The precipitation is not spatially monotonously distributed over the Levant. The study area was divided into three different homogeneous zones using the PCA and CA for the annual and seasonal precipitation. In general, Palestine's central and northern regions and the northern regions of Jordan formed the first cluster. The Syrian coastal area is the second cluster, and the third cluster was located in southern Palestine/Jordan and eastern Jordan/Syria. A slightly different classification was observed in the spring, when the whole of Syria formed the second cluster, while southern Palestine/Jordan and only east Jordan formed the third cluster. Furthermore, the first and second clusters represent the Mediterranean climate zone, while the third cluster reflects the arid and semi-arid climate zone.
6. In all cases, the mean precipitation is lowest in cluster 3 (southern and eastern regions) and highest in cluster 2 (Syrian coastal areas). Furthermore, the standard deviation of

precipitation is lowest for cluster 3 and highest for cluster 2. The first cluster had the precipitation concentration index (PCI) between 17 and 19, the second cluster had PCI < 15, and the third cluster (eastern and southern stations) had the highest annual PCI. Finally, the extreme values were not observed for any cluster on the annual scale, whereas they were observed for the first and third clusters in autumn.

7. A significantly decreasing trend was observed in the time series averaged in spring for the Levant, Palestine/Israel, Jordan, and Syria. In addition, the sub-regions showed a significant downward trend in March and in April for Syria. In spring, the significant change points were observed around 1992 for the Levant, Palestine, Jordan, and around 1997 for Syria. Furthermore, March's average precipitation showed significant change points in 2013 for the Levant, 2015 for Palestine, and 1999 for Jordan.
8. In spatial terms, a total of 91 out of 167 stations showed significant decreasing trends in spring, with the highest rates for the easternmost locations of Syria, coastal stations of Syria, and northern Palestine. In March, a percentage of 60.5% (101 stations) was affected by significant downward trends, with high rates for most stations in the West Bank, east to Haifa district, and the most eastern stations of Syria. In autumn, only nine stations showed a significantly decreasing trend, with high rates in Palestine's central areas. In contrast, the Syrian coastal region showed rising trends in autumn. For winter, only the eastern areas of Syria showed significantly decreasing trends, while other regions showed increasing, though not significant, with the highest rate for the Syrian coastal region. In April, 26 stations showed significantly decreasing trends and were spatially concentrated in most eastern locations and the coastal areas of Syria. A significant monthly upward trend was observed in January for Jordan, with the highest rate for the Syrian coastal region. In addition, a dominant upward trend was observed in February for West Jordan along the 35.4ºE, which was significant for some places. On the other hand, most of the eastern sites in Syria showed a declining trend.

The trends observed are consistent with the results of previous studies in regions around the Levant. Fathian et al. (2020) analyzed the changes and trends in climate extremes throughout Iran using precipitation and temperature data from 76 stations for the period 1981–2010, noting that more than 90% of the stations showed a decreasing trend in annual rainfall, and for almost 26% of them, the trend was significant. Raziei et al. (2014) examined the spatial patterns and temporal trends of precipitation in Iran using raster data (0.5° spatial resolution) for the period 1951–2009. The results showed that winter and January showed an upward trend in most parts of the country, while spring seems to be a downward trend in most parts of Iran. Tabari et al. (2011) analyzed the annual and seasonal precipitation trends of 41 stations in Iran in the period 1966–2005. The results showed a decreasing trend in annual precipitation at about 60% of the stations, and the trends in the time series of spring precipitation were mostly negative. Negative decreasing trends in annual and seasonal rainfall were well documented for Iran in many other studies (Modarres and Sarhadi, 2009; Kousari et al., 2011; Najafi and Moazami, 2015; Soltani et al., 2015).

Salman et al. (2018) studied the unidirectional trends of daily precipitation extremes in Iraq between 1950 and 2015 using data from 15 stations. The results showed a decreasing trend in annual precipitation between -0.6 and -39.5 mm/decade. Similar results were obtained by Al-salihi et al. (2014) and Al-Barazanji (2015), who analyzed precipitation trends in Iraq for the periods 1981-2010 and 1972-2011, respectively. Raja et al. (2017) examined the precipitation variability in Turkey for the period 1976-2010 and noted a general decrease in Turkey's annual precipitation trend in recent years. Oezguer and Koçak (2019) and Unal et al. (2012) examined the annual and regional trend of total precipitation based on observations collected at 237 and 271 meteorological stations, respectively, over Turkey. According to the results of the regional Mann-Kendall test, a decreasing trend was observed for all regions. Toros (2012), examined the spatio-temporal precipitation change at 165 stations across Turkey for the period from 1961 to 2008. The results showed a decreasing trend of annual precipitation by -9.7 mm/decade and a decreasing trend in the rainy season (October-April) by -10.0 mm/decade. Brunetti et al. (2006) investigated the precipitation variability in Italy over the last two centuries. They observed a decrease in annual precipitation of 5% per century due to the decline in spring precipitation (∼9 %). Furthermore, Italy's strong decrease in precipitation trends was well documented (Longobardi and Villani, 2010; Diodato, 2007).

Sahour et al. (2020) studied the aridity trends in the Middle East and adjacent areas from 1948 to 2018 using Data Assimilation System (GLDAS-Noah). The result showed a significant downward trend (up to 8.0 mm/decade), which was detected in March for Turkey's western side, eastern Iran, northern Iraq, northern Syria, Lebanon, and Israel. In addition, significant downward trends (2 to 6 mm/year) were observed in April for north Syria and Israel. Philandras et al. (2011) analyzed long-term precipitation trends and variability within the Mediterranean region in the 1901-2009 and 1951-2010 periods using a monthly grid ($0.5^{o} \times 0.5^{o}$) and based on station data. The results showed decreasing trends in annual precipitation for the east (-15 mm/decade), the west (-36.1 mm/decade), and central Mediterranean (-30 mm/decade). In Egypt, the trend analysis of precipitation at 31 stations showed that 77% of the observed trends decreased, suggesting a decrease in rainfall (Gado et al., 2019). Zakhem and Kattaa (2016) reported a 17% decrease in the mean annual precipitation of Damascus (Syria) for the period 1970–2000. Kafle and Bruins (2009) examined climatic trends in Israel for the period 1970-2002 using data from 34 stations. The results showed decreasing annual precipitation trends ranging from -5.1 to -16.6 mm/decade.

9. The study revealed that the NCP index, with average correlations of 0.39 for Palestine and 0.32 for Jordan, is the main controller of winter rainfall in the Levant, especially for southern Levant. The MO and EA/WR represented the second and third most important patterns that influenced winter rainfall. The results indicated that the WEMO pattern was the main driver of rainfall in spring, where it influenced 80 of 167 stations. In addition, the NCP was the second most important pattern affecting spring rainfall for 35 stations. The WEMO influence was concentrated in Palestine and Syria's coastal areas and Palestine and Jordan's northern areas. For autumn, the results clearly showed that the ENSO was the most

important pattern influencing negatively precipitation for 118 stations. Its influence extended to all areas except the Syrian coastal region.

These results are consistent with other studies conducted at the sub-regional level, mainly in Israel within the Levant region. Tobias Tornros (2013) examined the relationship between Mediterranean Oscillation (MO) and the winter precipitation in southern Levant, using precipitation data for 30 stations of Israel and Jordan in the years 1960-1993. The results showed the correlation coefficients between the MO index and single precipitation series reach values up to 0.60. The results also identify the EA/WR and NCP as strongly associated with winter precipitation. During negative (positive) MO phases the probability of above average winter precipitation is 22% (59%), respectively.

A positive MO phase characterized by high pressure above central Europe and the West Mediterranean, and a Cyprus low in the East Mediterranean. Since the western "Algiers" and eastern "Cairo" centers of the MO is above and below normal, respectively. In winter, a low pressure tends to penetrate the East Mediterranean and form a Cyprus low; the resultant cyclone favours the formation and introduction of moist westerly winds into the Levant region. The location of the cyclone centered south or east of Cyprus is known to be associated with above normal levels of rainfall in southern parts of the EM (Saaroni et al., 2010).

Yosef et al. (2009) examined trends in daily precipitation intensity over Israel 1950-2003 using 32 stations throughout Israel. They also investigated the influence of some telecommunication indices on total precipitation by correlation. They found higher correlations between total annual rainfall and the NCP and EA/WR for the central and southern regions, although they are also significant for the north. Some significant correlations were also found with MO, especially in the south. Kutiel et al. (1998, 2002) found that rainfall in Israel during the positive phase of the NCP is far greater than rainfall during the negative phase of NCP and that NCP's effect on the rainfall regime in Israel increases from the northern parts of the country to the south. The same result was also found in this study, where the NCP pattern weakly correlated with the northern locations in Israel (<0.27) compared with central and southern locations (0.47-0.56).

The negative phase of the NCP refers to an increased counterclockwise anomaly around the western center of the NCP "the north of the Caspian Sea" and an increased clockwise anomaly circulation around the eastern pole. These anomalous imply increased westerly anomaly circulation towards central Europe and an increased easterly anomaly circulation towards Georgia, and eastern Turkey. Which leads to an increase in southwesterly anomaly circulation towered the Balkans, western Turkey, and the Middle East, causing above normal temperatures and below normal rainfall in these regions. The opposite occurs with the positive phase of the NCP index.

Krichak et al. (2005) examined the decadal trends in the pattern East Atlantic-West Russia (EA /WR) and the Mediterranean precipitation in the period 1590-2000 using gridded (0.5°lat×long) monthly precipitation data over land from the Climate Research Unit (CRU). Their results showed that the EA/WR winter precipitation correlations are statistically positive significant and over the eastern Atlantic and the southeastern Mediterranean, including Israel. Extreme wet (dry) winter months over the Mediterranean region were characterized by anomaly patterns projecting to the

negative (positive) phase of EA/WR. Krichak et al. 2005 and 2002, found the precipitation in south Levant will increase when the EA/WR in its positive phase where the Levant is affected by more cyclones due to the advection to the EM of the air masses from central Europe. Hatzaki et al. (2010) showed a significant correlation between East Mediterranean precipitation and EA pattern during the spring, winter, and autumn seasons. This study shows that the EA teleconnection pattern is negatively correlated with spring precipitation, especially for eastern Syria locations by (-0.47--0.66).

Balach (2011) and Eshel and Farrell (2000) suggest that the EM precipitation is correlated with the North Atlantic Oscillation (NAO). Krichak and Alpert (2005) showed that when the NAO and the EA-WR are in positive phase the rainfall in Israel is above normal. On the other hand, Ben-Gai et al. (2001) and Ziv et al. (2006) reported that precipitation over Israel is poorly correlated with the NAO index. This is also confirmed by the results obtained in this study and shown in Table 6.6 and Figure 6.23. Concerning the ENSO, Price et al., 1998 investigated the link between El Niño and precipitation in Israel and they showed that statistically significant relationships exist in the late autumn between El Niño and weather in EM after mid-1970s. On the other hand, Ouachani et al. (2011) found that there are a link between ENSO and precipitation in the southern Mediterranean region. However, the relationship is less clear between ENSO and the eastern Mediterranean (EM) region. In this study, and based on observational data more than ever before and well cover the whole Levant region, the link between ENSO and EM precipitation were strongly confirmed in autumn, especially in south and east Levant.

CHAPTER 7

ANALYSIS OF EXTREME RAINFALL INDICES

This chapter aims to analyze the spatial and temporal changes in the annual and seasonal extreme rainfall indices over the southern Levant (Historical Palestine) in the period 1970-2018. Furthermore, the influence of the seven large-scale circulation patterns on the extreme rainfall are spatially and temporally analyzed.

7.1 Introduction

The assessment of changes in extreme precipitation indices is essential due to their broad implications for society, agricultural land, river runoff, crop yields, natural vegetation, health, tourism, infrastructure design, and economic development (Najafi and Moradkhani, 2014; Radinović and Ćurić, 2009; Peterson et al., 2008; Wang et al., 2012). The effects of climate change on extreme precipitation indices have recently received considerable attention. Global warming has the potential to increase the intensity of extreme precipitation, as a warmer atmosphere with enhanced water vapour and moisture content creates a more active hydrological cycle (Rosenzweig et al., 2001; Easterling et al., 2000; Trenberth, 2011). Furthermore, small changes in mean precipitation due to global warming can cause significant changes in extreme precipitation (Katz and Brown, 1992; De Lima et al., 2013). Numerous studies have reported increasing trends of extreme precipitation events in Greece (Nastos and Zerefos, 2007), India (Ravadekar and Preethi, 2010; Deshpande et al., 2011), Switzerland (Schmidli and Frei, 2005), and the Mediterranean Basin (Alpert et al., 2002; Goodess and Jones 2002; Barrera-Escoda et al., 2014). The Mediterranean region also experienced a decreasing precipitation trend in the second half of the 20th century (Xoplaki et al., 2003). This trend is expected to continue, with a decrease in total annual precipitation of up to 20% by 2050 (Black, 2009).

The Levant is considered one of the most sensitive areas with regard to climate change and future extreme climate conditions. In the literature, most climate studies on climate change in the Levant

region have focused on long and mid-term averages (Ziv et al., 2014; Shlomi and Ginat, 2009; Freiwan and Kadioğlu, 2008; Ben-Gai et al., 1994, 1998; Ghanem, 2011). This was mainly due to the limitations in providing high quality daily data from many meteorological departments in the Levant region, except Israel, with the exchange of data sets with daily or hourly resolution. Yosef et al. (2019), however, examined the annual changes in extreme temperature and precipitation indices in Israel over the period 1950-2017; their study did not include stations from the area West Bank. In addition, looking at precipitation changes on an annual basis often hides considerable variation between seasons (Garnaut, 2008). Zhang et al. (2005) analyzed the changes of several indices in the Middle East region for the period (1964-1999), using data from 52 stations from 15 countries, but only four stations belong to the Levant region. Donat et al. (2014) studied changes in extreme temperatures and precipitation in the Arab region, but their study did not include stations from Israel and Palestine. Therefore, a topic such as spatio-temporal analysis for extreme precipitation indices over Israel and Palestine in the southern Levantine region has not been fully explored by previous studies and needs further attention.

This study has two objectives. First, it attempts to provide a comprehensive spatio-temporal analysis for the annual and seasonal extreme precipitation indices (15 indices) over Israel and Palestine in the period 1970-2018. The methodology and the list of extreme precipitation indices and their definition are presented in Section 3.7 and Table 3.2. The second objective is to study the effects of the main large-scale circulation patterns in the northern Atlantic and Mediterranean Basin (NAO, EA, EA/WR, WEMO, MO, NCP, and ENSO) on the extreme precipitation indices. Figure 2.6b shows the stations' geographical distribution for this analysis, while Table 4 in Appendix A contains the names, coordinates, and elevations of the stations. Details regarding data Quality Control (QC), and homogeneity are available in Chapter 2 Section 2.2.

7.2 Results

7.2.1 Annual extreme rainfall indices

7.2.1.1 Spatial distribution

In order to better understand the relationships between the indices of extreme precipitation and their spatial variability, the long-term mean values for the period 1970-2018 were calculated for each index and each station. Then the cross-correlation matrix between the indices and some geographical factors (e.g., longitude, latitude, and elevation) was established based on the detrended time series. Table 7.1 summarizes the links between some precipitation indices and geographical factors. Figure 7.1 shows the spatial distribution of some precipitation indices over the period 1970-2018, and Figure 7.2 shows some strong relationships between indices and geographical factors. For more information about the overall cross-correlation matrix, see Table 12 in the Appendix A.

Over the study area, total annual precipitation (PRCPTOT) exhibited a strong positive correlation with all extreme indices and geographical factors, except for the index of consecutive dry days (CDD) which showed a significant negative correlation of -0.72 (Table 7.1). As shown in Figure 7.1a, the spatial distribution of the PRCPTOT index shows a distinct north-south gradient or

latitudinal pattern with a significant positive correlation of PRCPTOT-latitude, reaching 0.66 (Table 7.1).

Variable	PRCPTOT	CDD	CWD	R50mm	R95P	R99P	RX3Day	RX5Day	SDII
PRCPTOT	1	-0.72	0.86	0.83	0.99	0.97	0.93	0.95	0.89
CDD	**-0.72**	1	-0.77	-0.42	-0.68	-0.66	-0.53	-0.56	-0.41
CWD	**0.86**	**-0.77**	1	0.46	0.80	0.77	0.71	0.74	0.62
R50mm	**0.83**	**-0.42**	**0.46**	1	0.89	0.89	0.90	0.90	0.90
R95P	**0.99**	**-0.68**	**0.80**	**0.89**	1	0.99	0.96	0.97	0.91
R99P	**0.97**	**-0.66**	**0.77**	**0.89**	**0.99**	1	0.95	0.96	0.91
RX3Day	**0.93**	**-0.53**	**0.71**	**0.90**	**0.96**	**0.95**	1	1.00	0.98
RX5Day	**0.95**	**-0.56**	**0.74**	**0.90**	**0.97**	**0.96**	1.00	1	0.97
SDII	**0.89**	**-0.41**	**0.62**	**0.90**	**0.91**	**0.91**	**0.98**	0.97	1
Long.	**0.49**	**-0.67**	**0.64**	0.14	**0.42**	**0.38**	0.24	**0.27**	0.14
Latit.	**0.66**	**-0.80**	**0.88**	0.21	**0.57**	**0.55**	**0.42**	**0.45**	**0.31**
Elev.	**0.43**	-0.17	0.23	**0.50**	**0.46**	**0.44**	**0.45**	**0.45**	**0.45**

Table 7.1. The correlation coefficients calculated between some of extreme rainfall indices and geographical factors. Bold number means significant correlation at $p < 0.05$.

Since mean precipitation cannot reflect the extreme annual precipitation values, the maximum annual precipitation (Pmax) was plotted in the study area (Figure 7.1b). Over the last 49 years, Pmax with values of 1000 mm between 31.5ºN and 32.2ºN are found at many locations in West Bank, central and southern locations from the central coastal region, the southern locations in the district of Haifa, and the northernmost locations. These sites also had the highest average values for the CWD, SDII, RX5day, and R99P indices (Figure 7.1d, e, g, and h).

Simultaneously, the CDD, CWD, and SDII indices (Figure 7.1c to e) show a consistent spatial distribution with the PRCPTOT index. As precipitation increases towards the central and northern regions, CWD and SDII are expected to increase and the CDD index to decrease, as confirmed in Figure 7.1. In this context, the central coastal area and the northern regions, in general, showed the highest values for CWD and SDII by more than 5 days and 12 mm/day, respectively, while the southern stations showed the lowest values by less than 4 days and 10mm/day, respectively. These two indices are significantly and positively correlated at 0.62, and they show a significant positive correlation with the PRCPTOT index by 0.86 and 0.89, respectively (Table 7.1). They also show a significant positive correlation with latitude by 0.88 and 0.31, respectively (Figure 7.2b). The results also showed that the SDII index (Figure 7.1e) correlates better with Pmax (Figure 7.1b) than the PRCPTOT index, with a correlation value of 0.95 (not shown).

On the contrary, the central and northern locations had the lowest CDD index values (< 180 days) compared to the southern places, which had an average value of 220 days (Figure 7.1c). The CWD and CDD indices are the indicators of the spells of rainy days and drought periods, which are good indicators of the beginning and end of the drought in a region. Furthermore, they are important indices from the agriculture perspective (Casanueva et al., 2014). For example, they help in identifying appropriate sowing dates and irrigation scheduling. Areas that received a lower CDD value showed a complementary higher value of the CWD and SDII indices (Figure 7.1c and d) with a significant negative correlation of -0.77 and -0.46 between CDD-CWD and CDD-SDII, respectively (Table 7.1). Furthermore, the CDD index showed significant negative correlations

with all extreme precipitation indices and geographical factors, except for its correlation with altitude. Figure 7.2a is a demonstration of the strong negative correlation of CDD-latitude.

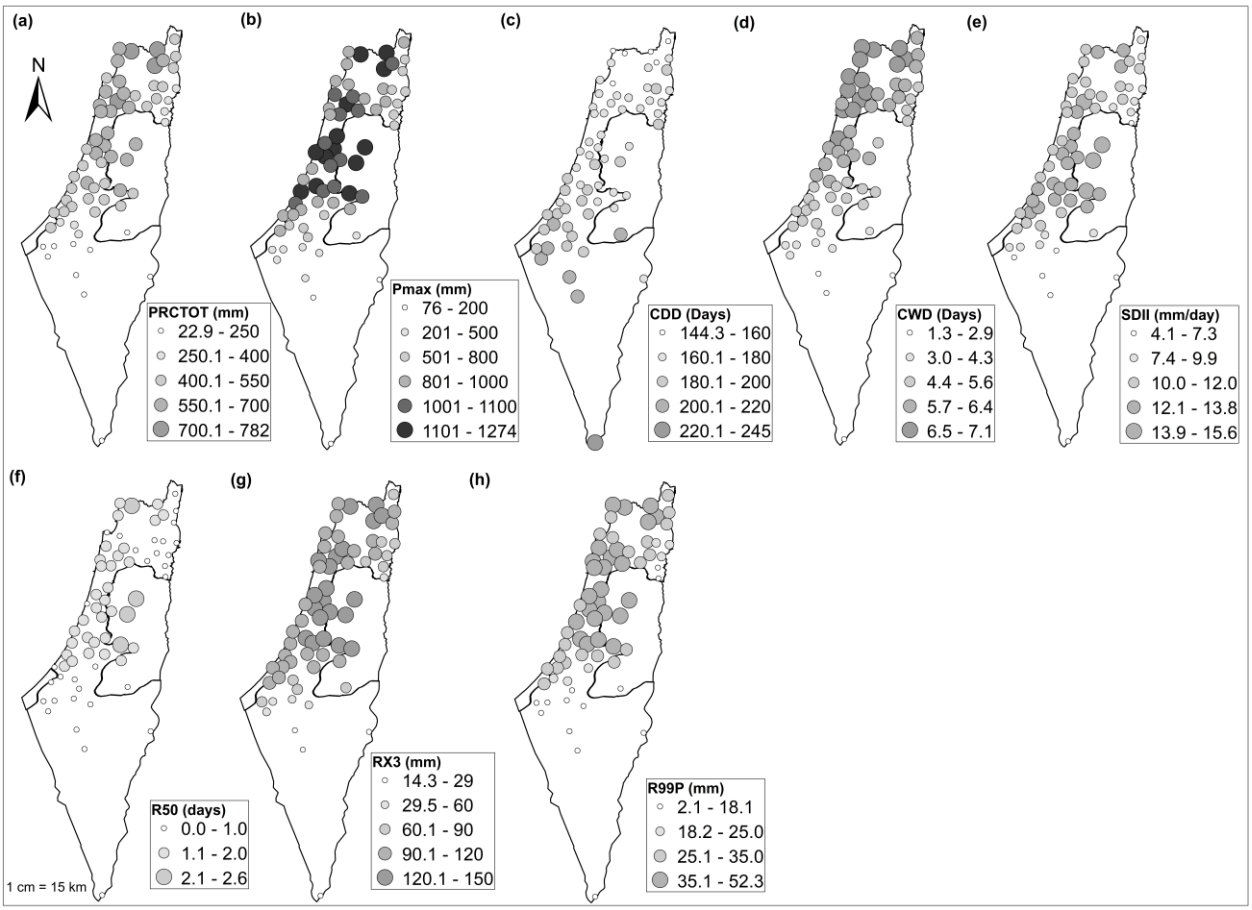

Figure 7.1. Spatial distribution of some rainfall extreme indices in the period 1970-2018.

Similar results were found for R50mm, RX5days, and R99P (Figures 7.1f to h). These indices show significant positive correlations with the PRCPTOT (by 0.83, 0.95, and 0.99, respectively) and CWD indices, and significant negative correlations with the CDD index (by -0.42, -0.56, and -0.66, respectively. The highest frequency of the number of days above 50 mm (R50mm), between 2.1-2.6 days, was found at Qiryat Anavim, the Salfit, Nablus, and Elon stations (Figure 7.1f). Apart from the CDD index, the lowest annual mean values of all extreme precipitation indices were found both for the southern locations and the regions located at the north-eastern borders of the West Bank (Figure 7.1a to h). These locations are characterized by their low altitudes and far from marine influences. The significant positive correlations can confirm this between altitude and all extreme events, except the CDD index (Table 7.1). The altitude effect is positive for all extreme precipitation indices with a high rate (0.50) for the R50mm index (Figure 7.2c).

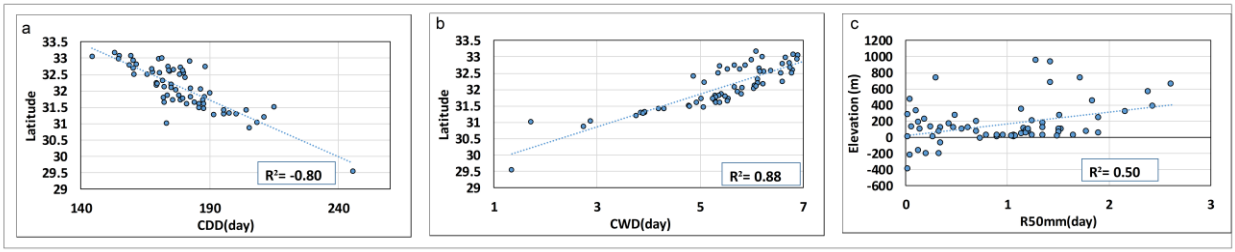

Figure 7.2. Relationships between some indices and geographical factors.

7.2.1.2 Principal component patterns

In this section, the PCA was applied to the annual indices to capture an overall view of the 15 extreme precipitation indices' temporal evolution, averaged over the study area. A matrix of 49 (years/rows) x 15 (indices/columns) was created for each station. After that, the 49 x 15 matrix across the stations' network based on the standardized averaged time series over the study area was also constructed. Based on the North rule of thumb, three components were retained and rotated (varimax rotation). Table 7.2 shows the factor loadings and the explained variance for each PC and Figure 7.3 shows the factor scores for each PC.

The first component explains 51.1% of the variance in the Palestine/Israel-wide matrix with the highest loadings (> 0.90) for the indices R95Ptot, R99P, R99Ptot and RX1day, and > 0.80 for the indices R50mm, R95P, RX3day, RX5day, and SDII (Table 7.2). In addition, the temporal variance of 9 out of 15 indices can be summarized by the first component. As shown in Figure 7.3a, the component scores showed a no significant increasing trend over 1970–2018 by 0.11 per decade.

Index	Comp. 1	Comp. 2	Comp. 3	Index	Comp. 1	Comp. 2	Comp. 3
PRCPTOT		0.89		**R99P**	0.94		
CDD			-0.96	**R99Ptot**	0.94		
CWD		0.65		**RX1day**	0.90		
R1mm		0.94		**RX3day**	0.87		
R10mm		0.94		**RX5day**	0.83		
R20mm		0.84		**SDII**	0.87		
R50mm	0.85			**Eigenvalues**	10.2	2.4	1.0
R95P	0.83			**Variability (%)**	51.1	32.0	7.4
R95Ptot	0.96			**Cumulative %**	51.1	83.1	90.5

Table 7.2. Components loadings for 15 extreme rainfall index for 66 stations in Historical Palestine.

The second component explains 32% of the composite matrix variance and had high positive loadings on the PRCPTOT, CWD, R1mm, R10mm, and R20mm indices (Table 7.2). In addition, this component shows a significant ($p < 0.05$) negative trend of -0.19 per decade with a decrease in the mid-1990s (Figure 7.3b). On the other hand, the third component explains 7.4% of the total variance, with a negative loading (-0.96) on the CDD index. The negative loading indicates the strong inverse relationship between this component and the CDD index, which shows a significant upward trend of 0.2 per decade (Table 7.2, Figure 7.3c).

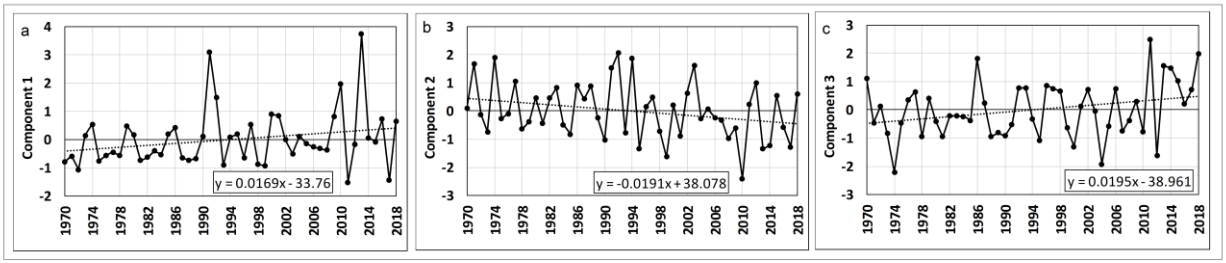

Figure 7.3. Time series plot of standardized scores for the components related to the extreme rainfall indices over the period 1970-2018.

7.2.1.3 Explaining variance in extreme rainfall

To explain the temporal variability of the extreme precipitation indices in the study area, the relationship between the three significant PCs obtained in the previous section and seven teleconnection indices has been studied. For more details on these indices, see Section 2.3. The Pearson correlation was used to link the temporal variability of the first three PCs to the annual values of the teleconnection indices. Table 7.3 shows the correlation coefficients and their significance level obtained on the basis of detrended time series.

The results show that PC1 (mainly related to the intensity and percent indices of extreme events) is significantly and positively correlated with the WEMO index by 0.29 with a significance level of 0.05 (Table 7.3, Figure 7.4a). For PC2, related to the frequency of extreme events, a significant ($p < 0.01$) positive correlation with the MO index by 0.40 is obtained (Figure 7.4b). In addition, this component shows a significant correlation with NCP (Figure 7.4c), ENSO, and EA/WR indices by 0.32, -0.31, and 0.29, respectively. The results generally showed a correspondence between the PC2 and NCP pattern since 1997 (Figure 7.4c). As shown in Table 7.3, no statistically significant link between the predictors and the scores for component 3 could be established.

	EA/WR	NAO	EA	MO	ENSO	NCP	WEMO
PC1	-0.04	-0.05	0.05	-0.10	-0.10	-0.09	0.29**
PC2	0.29**	0.25	0.08	0.40***	-0.31**	0.32**	0.03
PC3	0.23	0.11	0.25	-0.16	-0.18	0.19	-0.15

Table 7.3. Correlation coefficients between PCs and teleconnection patterns in the period 1970-2018. Asterisks indicate significance level: * = ($p < 0.1$), ** = ($p < 0.05$), *** = ($p < 0.01$).

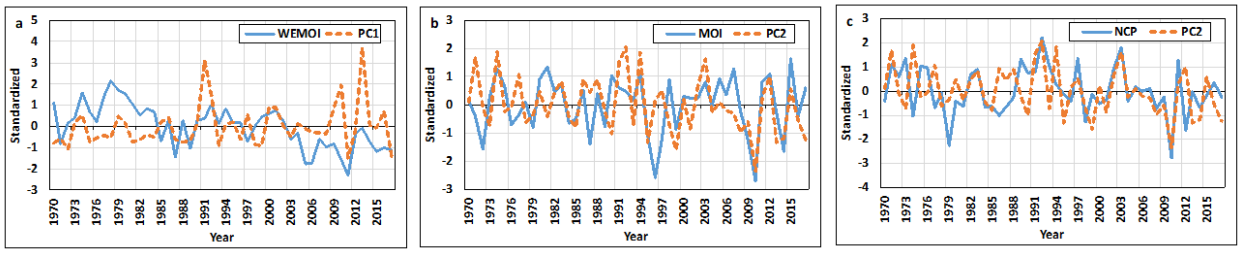

Figure 7.4. Time series plot of standardized scores for the components and some teleconnection patterns in the period 1970-2018.

7.2.1.4 Annual temporal variation and trends

Table 7.4 summarizes the number of stations with increasing/decreasing trends, as well as the averaged time series trends for the study area from 1970 to 2018. The temporal behavior for the PRCPTOT, R1mm, R10mm, R20mm, R95P, R99P, R95PTot, R99PTot, RX1Day, RX3Day, RX5Day, SDII, CWD, and CDD indices were plotted and smoothed using the LOWESS line to describe their temporal evolution (Figure 7.5(a to n)). Furthermore, the spatial distribution of the trends for the extreme indices are presented in Figure 7.6(a to k).

From Table 3, the frequency-based rainfall extreme indices show generally decreasing trends. On the other hand, the intensity and percent-based rainfall extreme indices show rising trends. Although more than 86% of the stations showed decreasing trends in the PRCPTOT, R1mm, R10mm, R20mm, and CDD indices, but they showed few frequency of significant trends by 4, 21, 6, 4, and 17 stations, respectively (Table 7.4).

The intensity extreme indices, RX1day, RX3day, RX5day, and SDII, showed upward trends in 70%, 64%, and 61% of total stations, respectively (Table 7.4), with very low significant increasing or decreasing trends (3 stations). Furthermore, in the R50mm, R99P, R99PTOT, and CWD, more than 77% of total stations showed no discernible positive or negative trends (Table 7.4).

No.	Index	Total (+) trends (Sig.)	Total (-) trends (Sig.)	No trend	Trend for averaged time series
1	PRCPTOT	6(0)	60(4)	0	-12.3 (mm/decade)
2	R1mm	1(0)	65(21)	0	-1.5* (days/decade)
3	R10mm	0	58(6)	8	-0.5 (days/decade)
4	R20mm	5(0)	34(4)	27	-0.1 (days/decade)
5	R50mm	12(0)	7(0)	58	0.03 (days/decade)
6	R95P	35(2)	26(0)	5	2.5 (mm/decade)
7	R99P	7(6)	0(0)	58	3.3 (mm/decade)
8	R95Ptot	51(0)	18(0)	6	0.6 (%/decade)
9	R99Ptot	5(4)	0(0)	61	0.6** (%/decade)
10	RX1day	46(3)	20 (0)	0	1.3 (mm/decade)
11	RX3day	42(0)	24(0)	0	1.5 (mm/decade)
12	RX5day	40(0)	26(0)	0	0.8 (mm/decade)
13	SDII	40(0)	26(0)	0	0.04 (mm/decade)
14	CWD	5(0)	10(0)	51	0.02 (days/decade)
15	CDD	9(0)	57(17)	0	-2.8** (days/decade)

Table 7.4. Number of stations that showed increasing and decreasing trends along with the trend values for the averaged time series in the period, 1970-2018. The number in brackets represents the counts of stations with statistically significant trends at the 95% confidence level. Asterisks indicate significance level: * = ($p < 0.1$), ** = ($p < 0.05$).

Across the study area, the overall trend of the PRCPTOT index was found to be non-significant decreasing by -12.3 mm/decade (Table 7.4). Spatially (Figure 7.6a and Table 7.4), a percent of 91% of the stations showed downward trends and only four stations of them with significant, namely Kefar YehezqeL, Salfit, Sede Boqer, and Elat by -30.3, -8.8, -3.8, and -42.4 mm/decade, respectively.

The number of wet days index (R1mm) showed a significant ($p < 0.1$) downward trend by -1.5 days/decade in 1970-2018, with a declining amount from 58 days to 23 days during the period

1994–2010 (Figure 7.5b). The regionally averaged R10mm, and R20mm trends were non-significant, decreasing by -0.5 and -0.1 day/decade, respectively, whereas the R50mm index trend was non-significant, increasing by 0.03 day/decade (Table 7.4).

As can be seen in Table 7.4 and Figure 7.6b, a percent of 99% of stations exhibited decreasing trends in the R1mm index, 21 stations of them distributed in northeastern regions, Haifa district, and West Bank exhibited significant negative trends. The highest rates (-2.5- -3.0 days/decade) were found for Jerusalem and Nablus stations from West Bank, Yiron, Har kena'an, Gazit, kefar Yehezqel, and Tirat Zevi stations from northeastern region, and Nir'ezyon station from Haifa district. A percent of 88% and 52% of the stations showed decreasing trends for the R10mm and R20mm indices (Table 7.4), only 6 and 4 stations of them, respectively with significant trends. For example, the kefar Shemaryahu, kefar Yehezqel, Salfit, and Haon stations (-1.0- - 2.0 days/decade) for the R10mm index, and Regavim, Yir'on, Jerusalem, and Salfit stations (-0.53- -0.99 days/decade) for the R20mm index (Figure 7.6c).

Figures 7.5a to d show a similar temporal behavior pattern for the PRCPTOT, R1mm, R10mm, and R20mm indices, with a significant positive correlation ($r > 0.82$). For these indices, the lowest values were registered in 1999 and 2017 and the highest values were registered in 1991/1992. It's also worth noting that the annual mean variations from 2004 to 2011 were totally lower than the long-term averages, with a general declining pattern from 1991 to 2010.

For the (R95P) index, there was a non-significant rising trend (2.5 mm/decade) in the study area (Table 7.4). Only two stations, Regba and Nablus, had significant increasing trends, by 24.7 and 21.1mm/decade, respectively (Figure 7.6g). In 1991, 1992, and 2013, the R95P and R99P indices showed three strong peaks of 339/124, 283/83, and 238/119mm, respectively (Figure 7.5e and f). When the trend was calculated for the R99P index without the abnormal values, it revealed a significant increase of 3.6 mm/decade. For R99P index, six stations showed significant rising trends at the local level in the northwest, by 1, 1.4, 2.6, and 2.8mm/decade at Kefar Rosh, Regba, Haifa Port, and Nir Ezyon stations, and 2.3 and 1.3mm/decade at Gadot and Kefar Yehezqel stations (Figure 7.6f).

The contribution of the very wet days index (R95Ptot) showed a non-significant positive trend of 0.6%/decade (Table 7.4). On the other hand, the contribution from extremely wet days (R99Ptot) showed a generally significant ($p < 0.05$) positive trend of 0.6%/decade in the period 1970-2018 (Figure 7.5h). The stations that showed a significant upward trend in their R99P index, also showed a significant upward trend in their R99Ptot index (Kefar Rosh, Regba, Haifa Port and Kefar Yehezqel and Gadot stations) between 0.01-0.8%/decade (not shown). The highest values for these two indices were found in 1991 (42/15%) and 2013 (44/22%) whereas the lowest values were found in 1999 (10/1%) and 2017 (5/0%) (Figure 7.5g and h).

The intensity extreme indices RX1day, RX3day, and RX5day indices showed non-significant positive trend of 1.5, 1.0, and 0.8 mm/decade over 1970-2018, with no significant increasing or decreasing trends were found for all observed stations (Figure 7.6h to j). These indices exhibited similar temporal variation with two maximum values, in 1992 (78/146/196mm) and 2013 (79/154/189mm) (Figure 7.5i to k).

The SDII index showed a positive trend over the study area by 0.04 (mm/decade) (Table 7.4). The highest values were found in 1991, 1992, and 2013 of 16.3, 13.8, and 15.6 mm/day, respectively (Figure 7.5l). The high average values of the PRCPTOT index in 1991 and 1992 led to high average values in the SDII index, while the relatively low average of the R1mm index in 2013 led conversely to a high average in the SDII index in that year (Figures 7.5(a and b)).

Figure 7.5m shows the evolution of consecutive wet days (CWD) in 1970-2018. Two periods of decreasing and increasing pattern can be seen, 1970-1978/1992-1999, and 2007-2018/1998-2003, respectively. Based on the general trend line (0.02 days/decade) (Table 7.4), there was no significant interannual variability of CWD from 1970 to 2018.

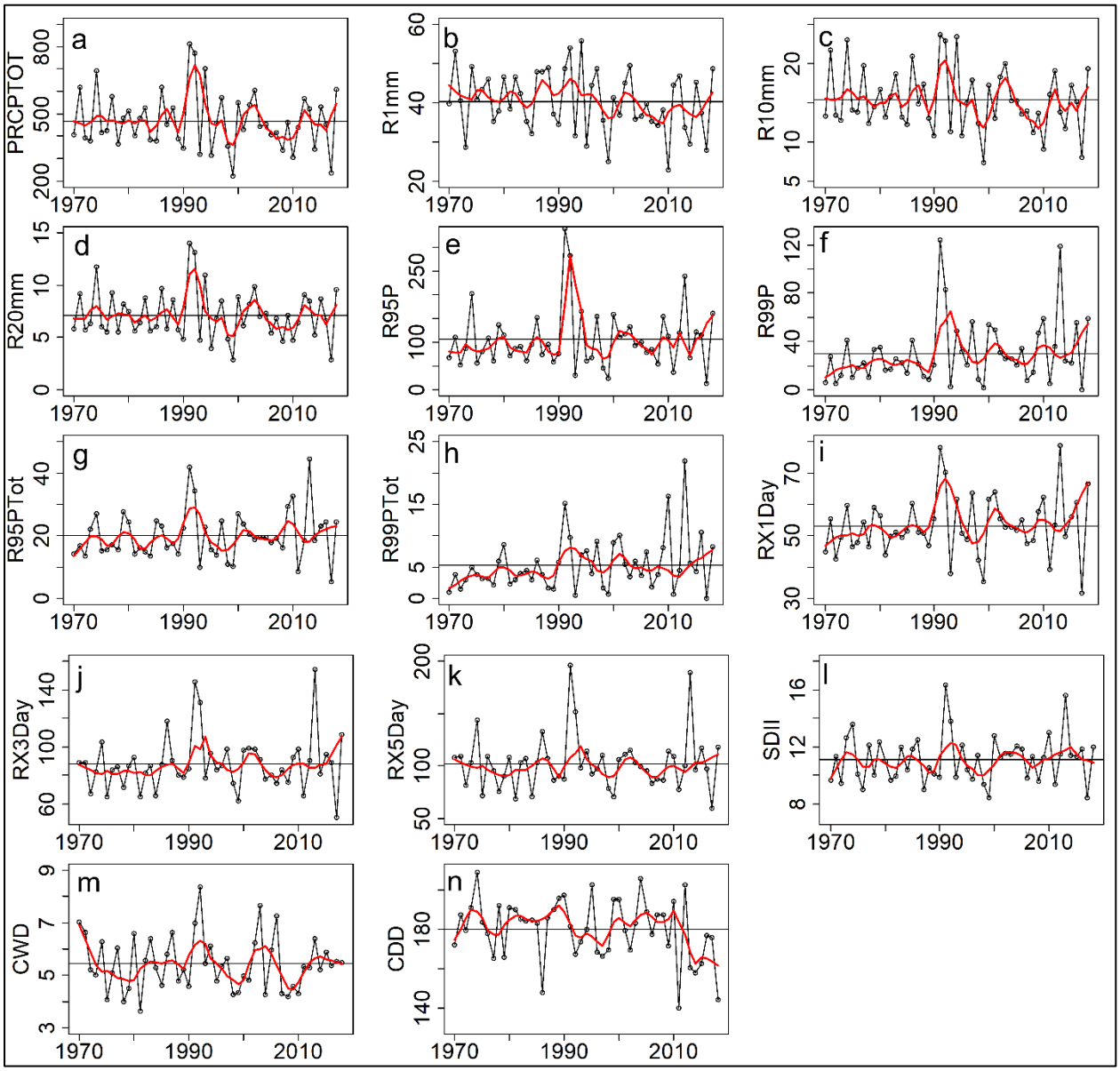

Figure 7.5. The temporal evolution for extreme rainfall indices in the period 1970-2018.

Figure 7.5n shows the evolution of consecutive dry days (CDD) over the period 1970-2018, with the overall trend for this period showing a significant ($p < 0.05$) downward trend of -2.8 days/decade (Table 7.4). The highest average (208 days) was observed in 1974, while the lowest average (139 days) was observed in 2011. It is also noticeable that the CDD averages have not risen above the long-term average (180 days), since 2013, with a general decreasing pattern since 2007. The trend calculated for 2007-2018 was also statistically significant and decreased by -25.7 days/decade.

Spatially (Figure 7.6e), the index of consecutive dry days for 17 stations in the northernmost regions and southern locations from the coastal area shows significant negative trends. The highest trends <-18.7 days/decade were observed for six stations such as Gadot and Almagor in the northeastern regions, Regba in the northwest of the study area, Ziqim and Nir'am at the northern boundary of Gaza Strip. Additionally, eight stations randomly showed a non-significant increasing trend between 0.1-5.8 days/decade.

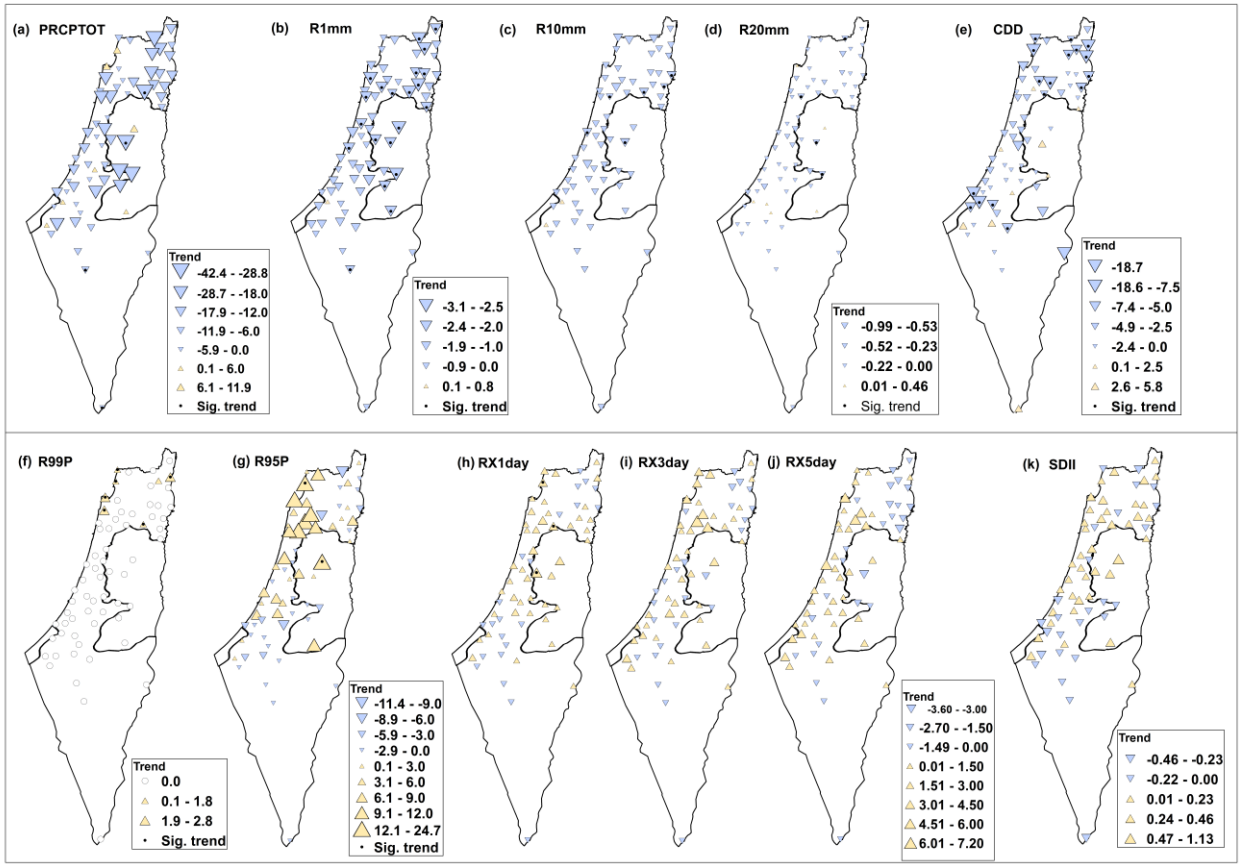

Figure 7.6. Spatial distribution of trends for some indices that exhibited notably decreasing or increasing trends in the period 1970-2018.

Although the intensity extreme indices RX1day, RX3day, RX5day, and SDII did not show significant trends, it is essential to assess their trends spatially because of their direct association with floods and landslides (Figures 7.5h to k). For example, the RX1day index causes flash floods, while RX3day and RX5day are more likely to cause long-term river floods. For RX1day index, a

percentage of 90% of the total coastal stations that extended from Akko governorate in the far northwest, to the direct eastern locations of the Gaza Strip in the south, and all stations in West Bank, and the southeastern sites from the north district, showed positive trends. However, only three of them were significant trends, Regba, Giv'at Oz, and Elqana stations between 4.5 and 5 mm/decade. The coastal stations from north to the south showed rising trends in the RX5day index more frequently than in the RX1day and RX3day indices. For these three indices, the magnitude of the decreasing trends was less than for the increasing trends. The declining trend mainly affected the southern coastal area and the northeastern stations, which is more pronounced in the RX5day.

7.2.2 Trends in the seasonal extreme indices

In this section, the seasonal trends for the indices PRCPTOT, R1mm, R10mm, R20mm, RX1day, RX3day, RX5day, SDII, CWD and CDD were calculated for each station and for the entire study area on the basis of the averaged time series (Table 7.5). Figures 7.7, 7.8 and 7.9 show the spatial distribution for the trends of the winter, spring and autumn indices.

7.2.2.1 Winter trends

Significant trends for the spatially averaged time series were not found for all extreme winter indices (Table 7.5). However, the winter indices showed increasing trends for the PRCPTOT, RX1day, RX3day, RX5day, SDII, and CDD indices by 1.4, 1.4, 2.7, 1.1, 0.13 mm/decade, and 0.20 days/decade, respectively (Table 7.5). On the other hand, the declining trend is observed only for the number of wet days index (R1mm) by -0.7 days/decade. As shown in Table 7.5, the R10mm, R20mm, and CWD indices did not show any notable trends over 1970-2018.

The spatial distribution of most significant trends for winter indices is shown in Figures 7.7a to d. Overall, the extreme indices do not locally seem to change very quickly, as very few significant trends were observed (< 7 stations) for all indices during this season. As shown in Figure 7.7a, the PRCPTOT index did not show significant increase or decrease in all observed station. In addition, its spatial trend reflects a generally complex pattern, except for the stations in the Haifa district and the northeast area, which showed increasing trends in the interval (6.8 - 5.6) mm/decade. However, a percentage of 42% (28 stations) showed decreasing trends with the highest values (between -9 and -13.5 mm/decade) for the Salfit, Negba, and Miqwe Yisrael stations. On the other hand, a high increasing trend (9 to 22.2 mm/decade) was observed at Karmel, Nablus, and Elqana stations in West Bank and the Ramat Hashofet, Haifa Port, and Giv'at Oz stations in Haifa district. According to Figure 7.7b in connection with the RX1day-winter index, the central and northern regions (> 32.0ºN) vastly showed increasing trends, but only in three stations with a significant trend, namely Regba, Ramat Hashofet and Giv'at Oz by 3.8, 5.3, and 3.8 mm/decade, respectively. In contrast, the decreasing trends (0 to -1.4 mm/decade) are mainly concentrated in the southern locations from the coastal area and the study area's southern locations. Different trends at neighboring locations, such as the southern coastal locations, indicated that while a flash flood may occur in one area, a water shortage may be expected in the next area at the same time.

Index	Season	Tot. (+) trends (Sig.)	Tot. (-) trends (Sig.)	No trend	Trend for averaged time series
PRCPTOT	Winter	38(0)	28(0)	0	1.4 (mm/decade)
	Spring	2(0)	64(36)	0	-8.5 (mm/decade)
	Autumn	12(0)	53(0)	1	-1.8 (mm/decade)
R1mm	Winter	0	66(4)	0	-0.70 (days/decade)
	Spring	2(0)	64(29)	1	-0.70* (days/decade)
	Autumn	20(0)	19(0)	27	0 (days/decade)
R10mm	Winter	0	21(0)	45	0 (days/decade)
	Spring	0	58(22)	8	-0.10 (days/decade)
	Autumn	14(0)	25(0)	27	0 (days/decade)
R20mm	Winter	25(0)	22(0)	19	0.02 (days/decade)
	Spring	0	31(9)	35	-0.04** (days/decade)
	Autumn	2(0)	29(3)	35	-0.01 (days/decade)
RX1day	Winter	50(3)	16(0)	0	1.4 (mm/decade)
	Spring	1(0)	65(27)	0	-2.4** (mm/decade)
	Autumn	3(0)	63(9)	0	-1.9 (mm/decade)
RX3day	Winter	53(0)	13(0)	0	2.7 (mm/decade)
	Spring	2(0)	64(22)	0	-4.2** (mm/decade)
	Autumn	8(0)	58(9)	0	-2.2 (mm/decade)
RX5day	Winter	38(0)	28(0)	0	1.1 (mm/decade)
	Spring	3(0)	63(15)	0	-4.1* (mm/decade)
	Autumn	15(0)	51(3)	0	-1.9 (mm/decade)
SDII	Winter	46 (7)	20(1)	0	0.13 (mm/decade)
	Spring	2(0)	64(26)	0	-0.61** (mm/decade)
	Autumn	7 (0)	59 (7)	0	-0.60 (mm/decade)
CDD	Winter	43(0)	23(0)	0	0.20 (days/decade)
	Spring	59 (12)	7(0)	0	1.5** (days/decade)
	Winter spring	58(11)	8(0)	0	1.3 (days/decade)
CWD	Winter	13	22	31	-0.03 (days/decade)
	Spring	3	52 (21)	11	-0.2** (days/decade)
	Winter-spring	20	22	24	-0.01 (days/decade)

Table 7.5. Number of stations that showed increasing and decreasing trends along with the trend values for the averaged time series in the period 1970-2018. The number in brackets represents the counts of stations with statistically significant trends at the 5% level. * = ($p < 0.1$), and ** = ($p < 0.05$).

All stations exhibited decreasing trends in number of wet days index (R1mm winter) (Figure 7.7c), with significant results for the stations Salfit, Nablus, Zefat Har Kenaan, and Kefar Yehezqel by -2.1, -1.5, -1.9, and -1.7 days/decade, respectively. In general, the magnitude of the declining trends was higher for the northern regions (> 32.5ºN, > 1.5 days/decade) than for the southern regions (< 1 day/decade). Moreover, these large declining trends are consistently reflected in the rising trends for the simple day intensity index (SDII winter), which were mainly observed in the northern regions of the study area (Figure 7.7d). Seven northern locations showed significant rising trends in the SDII index: Nablus, Zefat Har Kenaan, Elon, Ramat Hashofet, Haifa Port, Kefar Hamakkabbi and Regba stations by 1.3, 0.75, 0.67, 1.1, 0.51, 0.5 and 0.53 mm/decade respectively.

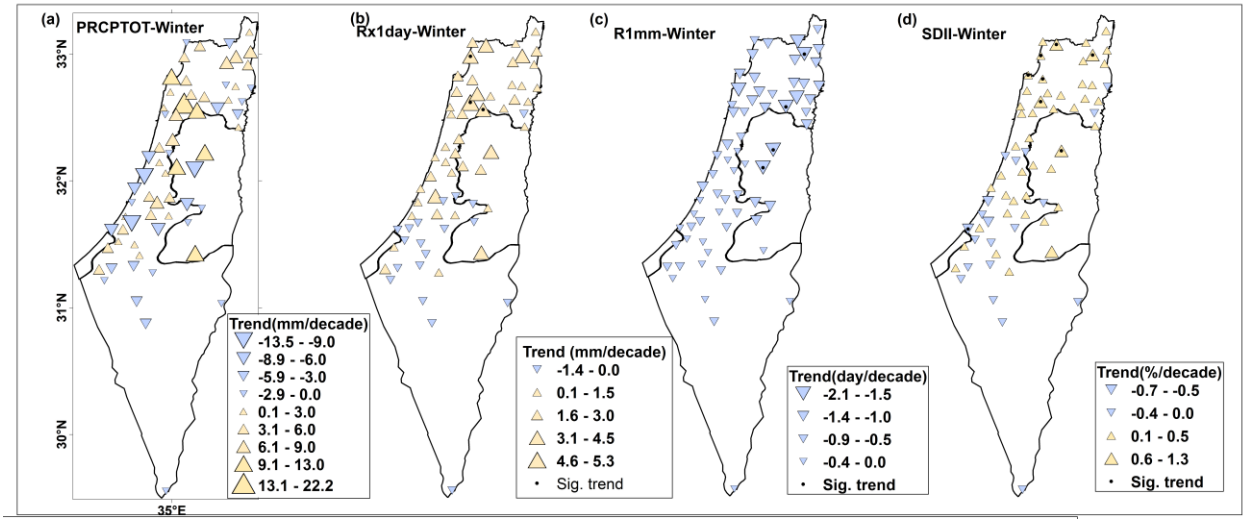

Figure 7.7. Spatial distribution of winter trends for some indices that exhibited notably decreasing or increasing trends in the period 1970-2018.

7.2.2.2 Spring trends

Compared with other seasons, all spring extremes showed very rapid changes. The results indicate that the trends at the level of p = 0.05 for the R20mm, RX1day, RX3day and SDII indices decreased significantly by -0.04 days/decade, -2.4, -4.2, and -0.61 mm/decade, respectively (Table 7.5). Furthermore, at a significance level of 0.1, the R1mm and RX5 day indices were statistically significant at -0.70 days/decade and -4.1 mm/decade, respectively (Table 7.5). In contrast, the CDD index showed a significant increasing trend of 1.5 days/decade. (Table 7.5).

For the total precipitation index for wet days in spring (PRCPTOT), a percentage of 97% of the stations (64 stations) showed a decreasing trend, with 56% (36 stations) showing a significant trend at the level of 0.05 (Table 7.5). Decreasing trends ranged from -1.1 mm/decade for Sedom Man to -17.3 mm/decade for Yiron, while increasing trends, which occurred at only two sites, ranged from 0.1 mm/decade for Regba to 2.4 mm/decade for Niram. Locally, a coherent and intense pattern (Figure 7.8a) of significantly decreasing trends can be seen. The highest values (< -9.0 mm/decade) were for the northernmost station, Jerusalem Governorate at Qiryat Anavim and Beit Jimal, and the central region from the coastal areas at Kefar Shemaryahu and Miqwe Yisrael.

For the index of wet days (R1mm), 97% of the stations (Table 7.5) showed decreasing trends, and 44% (29 stations) reported significant trends. The R1mm index showed a lower frequency of significant trends at the northern sites than the PRCPTOT, while it showed higher frequencies at the central and southern sites. It is also interesting that the significant trends affected all stations in West Bank. The highest rates (-0.90 to -1.07 days/decade) were observed at West Bank in the Jerusalem district, Nablus and Elqana stations, and northeastern Kefar Blum, Gazit, and Hazore'im stations.

As shown in Table 7.5 and Figure 7.8c, a percentage of 88% of the stations (58 stations) showed decreasing trends in the occurrence of heavy precipitation events (R10mm); in 38% of these stations, a significant decreasing trend was observed. This index showed decreasing trends in the

interval from 0 to -0.2 days/decade and was thus below the R1mm index for all stations. Although the R1mm and R10mm precipitation events in spring showed similar spatial patterns, the R1mm index showed a higher frequency of significantly decreasing trends in the central and southern regions than the R10mm index (Figures 7.8b and c). Therefore, it can be stablished that the decrease in the frequency of extreme precipitation events (R1mm and R10mm) indices also plays a major role in the main decrease of precipitation in spring.

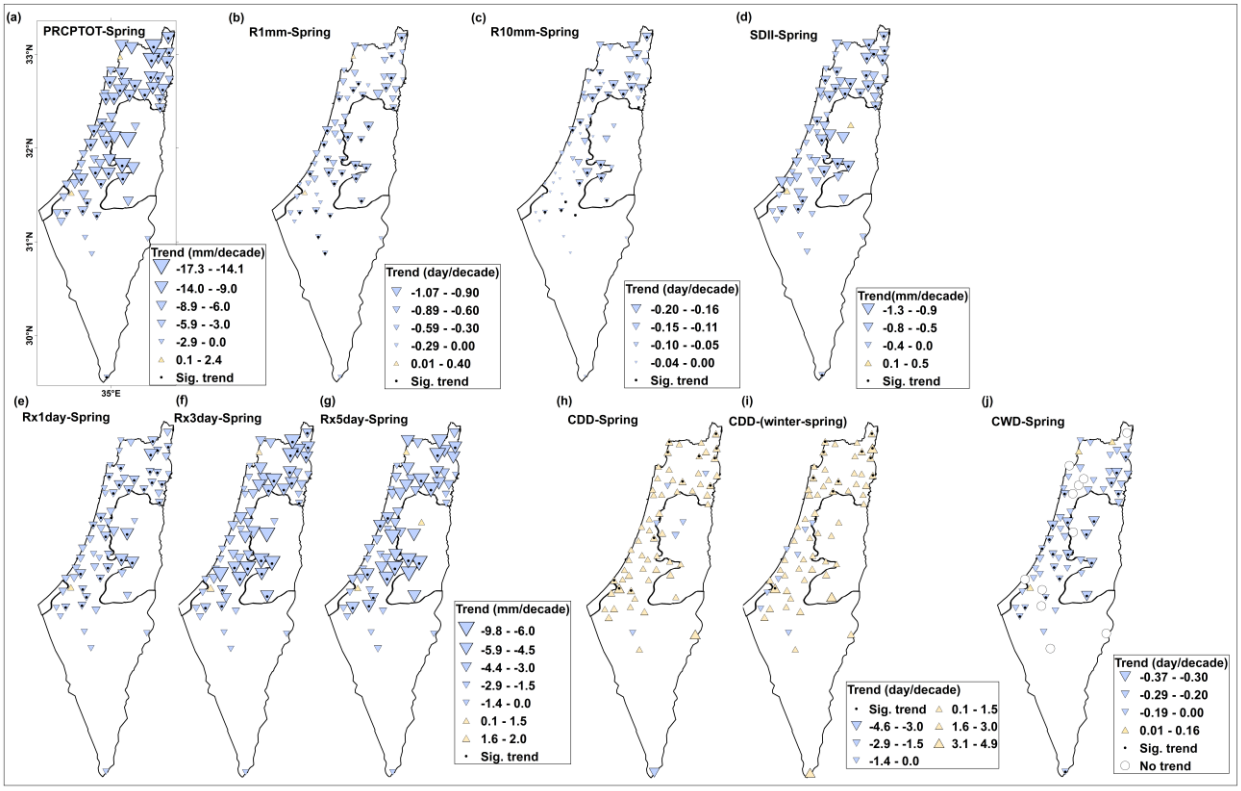

Figure 7.8. Spatial distribution of spring trends for some indices that exhibited notably decreasing or increasing trends in the period 1970-2018.

With respect to the simple daily intensity index (SDII) (Figure 7.8d), 97% of the stations showed a decreasing trend, and 40% (26 stations) of them showed a significant trend (Table 7.5). Although the R1mm index decreased at most sites, the SDII index decreased due to the large decreases in the PRCPTOT index. In this context, a very close spatial pattern was observed for the PRCPTOT and SDII indices. All stations showing a significant decreasing trend in the PRCPTOT index also showed a significant decreasing trend in the SDII index. The highest significant decreasing trends (-0.9 to -1.3 mm/decade) were observed at ten sites in the northern regions, such as Regavim, Yir'on, Ginnegar, and Almagor stations, and in the Jerusalem district at Qiryat Anavim, Beit Jimal, and Jerusalem St. Anne stations.

For maximum 1-day, 3-day, and 5-day (RX1day, RX3day, and RX5day) rainfall, more than 95% (> 63 stations) of the total stations showed decreasing trends, with significant trends at 41%, 33%, and 23% of the stations, respectively (Table 7.5, Figures 7.8e to g). The RX1day index showed less declining trends than the RX3Day and RX5Day indices. The highest significant declining

trends (between -5.9 and -4.5 mm/decade) for the R1Xday index occurred at four locations: Jerusalem, Qiryat Anavim, Salfit, and Parod stations. In addition, the significant trend band extends over more sites (around Jerusalem and in the northern regions of the study area) than for the RX3day and RX5day indices.

The Consecutive Dry Days Index (CDD) in spring showed rising trends in 89% (59 stations) of the total station, with significant trends in 20% (12 stations) of them (Figure 7.8h and Table 7.5). Very similar results were obtained for the CCD index for the combined winter and spring season, which also showed increasing trends in 88% (58 stations) of the stations, with significant trends in 19% (11 stations) of them (Figure 7.8i and Table 7.5). For both indices, the significant increasing trends coherently covered the northeast locations at the Gadot, Almagor, Haon, and Kefar Blum stations by rates between 1.8 and 3.6 days/decade, and the northwest locations at the Kefar Rosh Haniqra and Regba stations by rates between 1.7 and 2.7 days/decade (Figures 7.8h and i). In addition, the stations located north of the Gaza Strip (Ziqim, Niram, and Ruhama) also showed significantly increasing trends in their CDD-spring index with 2.3, 4.9, and 2.7 days/decade, respectively. The broad increasing trends in the CDD-spring index have led to the broad decreasing trends in the CWD spring index (Table 7.5, Figure 7.8j). One percent of 79% of stations had declining trends in the CWD-Spring Index, with significant trends in 40% of stations (Table 7.5). High significant decreasing trends (-0.30 days/decade) were observed at ten stations, namely, Salfit, Nablus, Jerusalem, and Carmel at West Bank, Eyal, and Kefar Shemaryahu in the central coastal region, and Hazore'im, Gazit, and Almagor in the northeast area (Figure 7.8j).

7.2.2.3 Autumn trends

The results for the autumn trends were similar to those for the winter, with no significant decreasing or increasing trends observed for any of the autumn indices (Table 7.5). Also, the frequency-based indices (R1mm, R10mm, and R20mm) did not reflect any remarkable changes in the area under investigation in 1970-2018. However, the PRCPTOT, RX1day, RX3day, and RX5day indices showed declining trends of -1.8, -1.9, -2.2, and -1.9 mm/decade, respectively. In terms of stations, 80%, 29%, 38%, and 44% of the stations showed declining trends in the PRCPTOT, R1mm, R10mm, and R20mm indices, respectively, with no significant trend. On the other hand, the intensity extreme indices RX1day, RX3day, RX5day, and SDII showed decreasing trends for more than 77% of the total stations, with 9, 9, 3, and 7 stations respectively showing significant decreasing trends.

The spatial distribution of trends for some indices is shown in Figures 7.9a to d. The same stations that had significantly decreasing trends in the RX1day index also had significantly decreasing trends in the RX3day index (Figures 7.9b and c). These significant trends included sites around the Jerusalem district and the Salfit, Parod, and Haon stations (at rates < -3.0 mm/decade). Significant declining trends were also found for the SDII index (Figures 7.9e) at seven dispersed stations, Regavim, Nir Gallim, Yiron, Jerusalem, Ruhama, Haon, and Karmel, with values ranging from -0.9 mm/decade at Karmel to -2.3 mm/decade at Nir Gallim and Yiron.

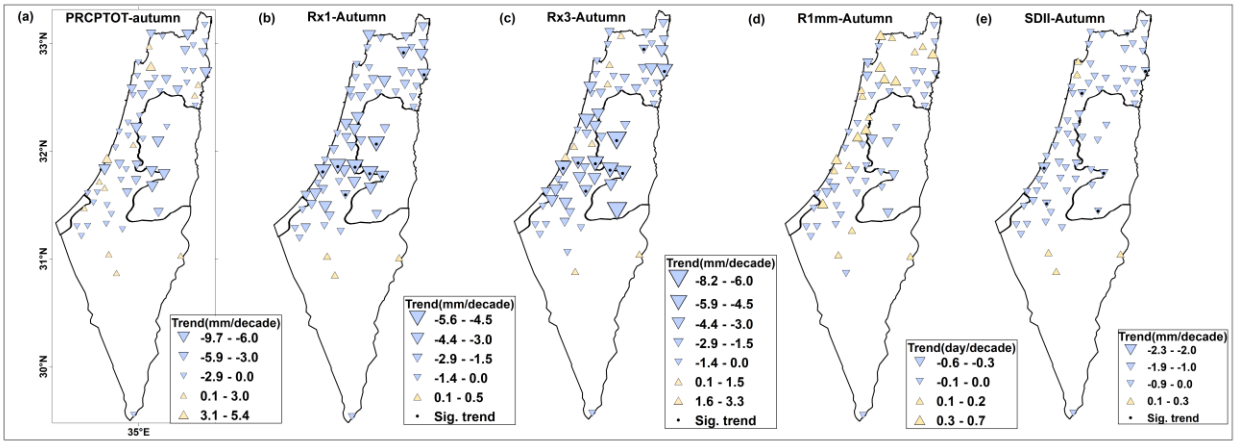

Figure 7.9. Spatial distribution of autumn trends for some indices that exhibited notably decreasing or increasing trends in the period 1970-2018.

7.2.3 Extreme rainfall indices and teleconnection patterns

In this section, the relationships between 15 extreme rainfall indices and seven large-scale circulation patterns, WEMO, EA/WR, NAO, EA, MO, NCP, and ENSO were investigated to determine whether a particular circulation pattern could have some influence on the occurrence of precipitation extremes. Tables 7.6 and 7.7 summarize the number of stations with significant correlations between the extreme value indices and the long-distance circulation patterns on the annual and seasonal scales. Figure 7.10 shows the spatial distribution of the correlation coefficients for the most important patterns that particularly influenced the annual extreme precipitation indices. Figures 7.11, 7.12, and 7.13 also show the spatial distribution of the correlation coefficients for the extreme precipitation indices in winter, spring, and autumn.

7.2.3.1 Annual scale

According to the results listed in Table 7.6, the large-scale circulation patterns had a more significant impact on the frequency-based indices than the intensity and percent-based indices. For the intensity and percent-based indices, the effect was less than 30% of the stations and was mainly related to the WEMO index. The results also revealed the MO index was the main driver for the PRCPTOT, R1mm, R10mm, and R20mm and R99Ptot indices. These results are consistent with the results obtained between the teleconnections pattern and PCs (Table 7.3).

In detail, when compared to other patterns, the MO index showed the highest frequency of significant positive correlation for the indices PRCPTOT, R1mm, R10mm, and R20mm with 59%, 65%, 61%, and 42% of the stations respectively (Table 7.6). Its effect is intensively concentrated between 31.4ºN to 33.2ºN by correlation coefficients between 0.27 and 0.37 for the PRCPTOT, R1mm and R20mm indices (Figures 11a, b, and d) and between 0.27 and 0.53 for the R10mm index (Figure 7.10c). MO was also the main driver for the R99Ptot index (Table 7.6, Figure 7.10e) for 20% of the stations that correlated negatively with it between -0.27 and -0.37 and spatially covered some northern sites.

Index	WEMO		EAWR		NAO		EA		MO		NCP		ENSO	
	+	-	+	-	+	-	+	-	+	-	+	-	+	-
PRCPTOT	3	0	0	2	10	0	0	0	39	0	3	0	0	33
CDD	0	0	1	14	1	6	9	0	3	0	8	0	0	5
CWD	2	0	8	0	0	0	3	0	5	0	31	0	0	28
R1mm	0	0	26	0	8	0	0	0	43	0	31	0	0	39
R10mm	3	0	5	0	6	0	2	0	40	0	6	0	0	28
R20mm	15	0	5	0	8	0	1	0	28	0	2	0	0	8
R50mm	14	0	2	0	2	3	0	0	3	0	4	0	0	8
R95P	19	0	1	0	1	0	1	1	3	0	2	0	0	1
R95Ptot	10	1	0	0	0	8	2	1	2	2	2	0	0	0
R99P	11	1	0	0	0	8	2	1	2	0	2	0	0	0
R99Ptot	2	0	5	0	0	8	0	0	1	12	5	0	0	0
RX1day	9	0	1	0	0	2	2	1	3	2	2	0	0	3
RX3day	6	5	2	0	6	5	1	0	0	2	0	0	0	1
RX5day	2	0	2	0	2	2	1	0	2	1	0	0	0	0
SDII	15	0	0	0	1	3	1	0	1	0	0	0	0	0

Table 7.6. Number of stations with significant positive or negative correlations between extreme precipitation and teleconnection indices at annual scale. Only significant results at the 95% confidence level are shown.

In addition, the ENSO pattern was the second most important pattern affecting the PRCPTOT, CWD, R1mm, and R10mm indices (Table 7.6). A percentage of 50%, 42%, 59%, and 42% of the stations showed significant negative correlations with the ENSO pattern in their PRCPTOT, CWD, R1mm, and R10mm indices, ranging from -0.27 to -0.53. These high frequencies of significant correlations place the ENSO index in second place after the MO index for the PRCPTOT, R1mm, and R10mm indices and the NCP index for the CWD index. Spatially speaking (Figures 7.10n to q), the pattern was generally the same for the ENSO and MO modes, but with lower frequency in the northern locations and higher frequency in the southern regions for the ENSO mode. For example, the ENSO showed a more significant correlation for the PRCPTOT, R1mm and R10mm indices between 31.2ºN and 31.4ºN at the Magen, Eshel Hanasi, Urim, Omer, and Gevulot stations. The NCP index was the main controller of the CWD index, showing a significant positive correlation with 47% of the stations (Table 7.6). Its effect extended over all stations at the northern boundaries of West Bank (with correlation coefficients between 0.27 and 0.53), the northernmost locations, and the central and southern locations from the coastal area (Figure 7.10f). In addition, 47% of the stations showed remarkable positive significant correlations with the R1mm index (Figure 7.10r). The significant effect for the EA/WR pattern occurred at 23% and 39% of the stations showing negative and positive significant correlations on the CDD and R1mm indices (Table 7.6). Spatially (Figures 7.10g and s)), the EA/WR effect mainly covered some central locations between 31.3ºN and 32.0ºN (with correlations between -0.27 and -0.4 for the CDD index and between 0.27 and 0.44 for the R1mm index).

The WEMO index had a dominant significant influence on the six extreme indices (R50mm, R95P, R95Ptot, R99P, RX1day, and SDII), with 21%, 29%, 17%, 18%, 14% and 23% of the stations showing a significant positive correlation with it (Table 7.6). Figure 7.10h to m shows the spatial distribution for the correlation coefficients between the WEMO index and the six indices

mentioned before. For all six indices, the geographical domain of the WEMO effect was mainly concentrated between 31.3ºN and 32.0ºN at some locations in the Jerusalem district and north-eastern locations from Gaza Strip. Its influence also affected some stations in the Haifa district for the R50mm, R95P and SDII indices. Finally, the EA and NAO indices are poorly correlated with the annual extreme precipitation indices, except for the NAO effect on the RX3day index at 17% of the stations (Table 7.6). Its influence was negative for the northernmost locations (-0.27 to -0.53) and positive for some southern coastal locations (0.27 to 0.37).

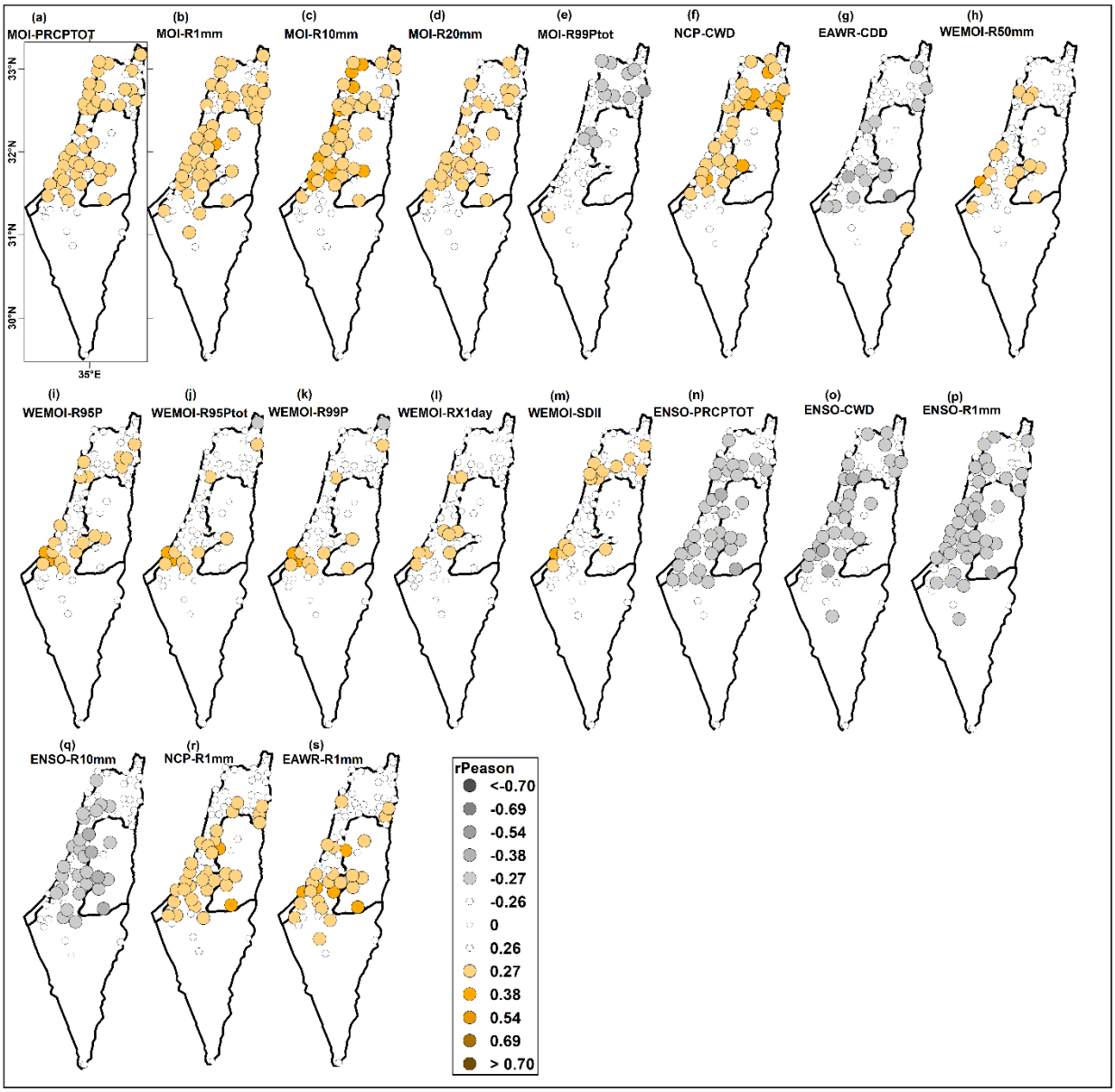

Figure 7.10. Spatial distribution of Pearson correlation coefficients between the teleconnection patterns and the precipitation indices at annual scale.

7.2.3.2 Seasonal scale

Based on the frequency of significant correlations (Table 7.7), the results indicated no single dominant pattern on the seasonal rainfall extremes, as different patterns generally influence the different seasons. In this context, the NCP pattern appeared as the dominant pattern on the winter extreme rainfall indices. The MO and EA/WR indices also showed a considerable frequency of significant correlations. On the other hand, the ENSO and WEMO indices showed high frequencies of significant correlations with the extreme precipitation indices in autumn and spring. Similar to the annual results, the strength and frequency of these correlations were low for all patterns with the seasonal intensity and percent-based extreme rainfall indices, especially for the RX1day, RX3day, and SDII indices.

Index	Season	WEMO		EA/WR		NAO		EA		MO		NCP		ENSO	
		+	-	+	-	+	-	+	-	+	-	+	-	+	-
PRCPTOT	Winter	0	0	20	0	0	0	0	0	43	0	51	0	0	2
	Spring	0	37	0	0	0	1	0	0	5	0	8	0	0	1
	Autumn	0	20	4	0	9	0	0	0	2	0	0	0	0	48
R1mm	Winter	0	7	41	0	0	0	0	0	53	0	58	0	0	1
	Spring	0	57	0	0	3	0	0	2	3	0	27	0	0	5
	Autumn	0	35	7	0	14	0	0	0	6	0	0	0	0	56
R10mm	Winter	0	0	30	0	1	0	1	0	58	0	55	0	0	5
	Spring	0	37	1	1	0	1	0	0	9	1	9	1	0	1
	Autumn	0	26	5	0	6	0	1	0	4	0	0	0	0	33
R20mm	Winter	0	0	6	0	2	0	0	0	32	0	30	0	0	6
	Spring	0	4	0	4	0	0	1	0	4	0	2	0	2	4
	Autumn	0	15	3	0	2	0	1	0	2	0	0	0	0	20
RX1day	Winter	1	2	3	1	1	2	1	0	2	1	4	0	0	5
	Spring	1	9	1	1	0	1	2	1	2	0	0	0	2	2
	Autumn	0	8	4	0	3	1	0	1	1	0	0	0	0	15
RX3day	Winter	0	3	7	0	0	9	2	0	6	0	15	0	0	7
	Spring	0	8	0	0	0	0	0	1	4	0	3	0	0	2
	Autumn	0	9	0	0	13	0	0	0	0	0	1	0	0	19
RX5day	Winter	0	2	7	0	3	5	1	0	9	0	20	0	0	3
	Spring	0	16	0	0	0	0	0	0	1	0	16	0	0	1
	Autumn	0	5	0	0	28	0	0	0	0	0	1	0	0	38
SDII	Winter	0	0	0	0	0	1	3	0	1	0	1	0	0	4
	Spring	0	0	0	1	1	0	3	0	2	0	1	0	1	1
	Autumn	0	2	1	0	0	0	0	2	1	0	0	0	0	5
CDD	Winter	0	1	0	2	0	32	1	0	0	14	0	15	0	1
	Spring	7	0	1	3	0	12	12	0	1	0	0	9	1	3
CWD	Winter	0	1	50	0	0	0	1	0	1	0	48	0	1	25
	Spring	0	37	0	0	2	0	0	10	4	0	33	0	0	2

Table 7.7. Number of stations with significant positive or negative correlations between extreme precipitation and teleconnection indices at seasonal scale. Only significant results at the 95% confidence level are shown.

As shown in Table 7.7, the NCP index had a greater impact on seven winter extreme rainfall indices (PRCPTOT, R1mm, R10mm, R20mm, RX3day, RX5day, and CWD). It positively and significantly correlated with them at 77, 88, 83, 45, 23, 30, and 73% of the stations, respectively, which may indicate that the NCP index has had a major impact on the study's rainfall regime area

over the last decades. Figure 7.11a shows the spatial distribution of these significant correlation coefficients in winter, with the highest correlations (0.55-0.69) for the R1mm index being found in the southern parts of the coastal area and around the Gaza Strip. Its effect was extensive and covered a large extent, ranging from 30.8ºN to 33.3ºN for the PRCPTOT, R1mm, R10mm, R20mm, and CWD indices, except for the northernmost location for the PRCPTOT index. On the other hand, there was less frequency of significant correlations with a small area of its effect on the RX3day and RX5day indices that generally extended between 31.0ºN and 32.0ºN (r values between 0.27 and 0.38).

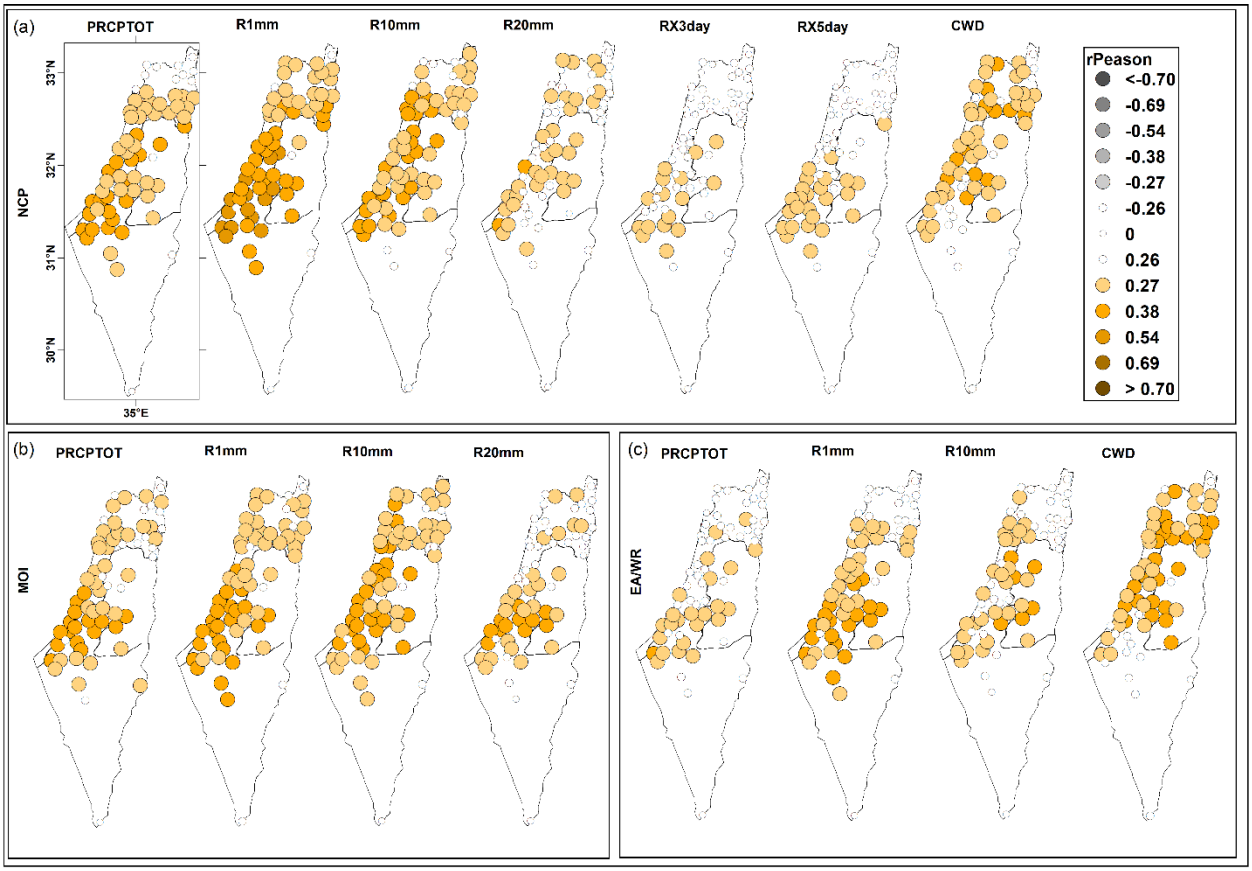

Figure 7.11. Spatial distribution of Pearson correlation coefficients between the NCP (a), MO (b), and EA/WR (c) teleconnection indices and the precipitation indices in winter.

The results also showed that the MO and EA/WR indices had remarkable effects on four winter extreme precipitation indices. The PRCPTOT, R1mm, R10mm, and R20mm winter indices are positively and significantly correlated with the MO index with 65, 80, 88, and 48% of the total stations. The correlation coefficients showed similar spatial patterns to the NCP index (Figure 7.11b). For the R20mm index, MO covered more sites in the southern coastal region with significant correlations (0.38-0.53) higher than the NCP index. The EA/WR index (Figure 7.11c) showed a lower frequency of significant correlations for the PRCPTOT, R1mm, and R10mm indices at 30, 62, and 45% of the stations, respectively, compared to the NCP and MO indices. In contrast, it showed a very high frequency of significant correlations with the CWD index in 76%

of the total stations, with a similar spatial pattern as in the NCP and CWD, and with a higher frequency of the higher correlation band (0.38-0.53) at the northern locations.

In spring, the WEMO index proved to be the most influential pattern on six spring extreme precipitation indices (PRCPTOT, R1mm, R10mm, RX1day, RX5day, and CWD) of 56, 86, 56, 14, 24, and 56% of the total station with significant negative correlations (Table 7.7). The highest significant negative correlations (-0.38 to -0.53) were with the R1mm index for most stations and with the PRCPTOT index at some central and northeast locations (Figure 7.12a). The RX5day significant correlations are concentrated at coastal and northeastern locations while for the RX5day index, they showed a scattered pattern. In addition to the WEMO index's effect, the NCP index also exerted a certain positive influence on the R1mm, RX5day, and CWD indices, but with a lower frequency and significant magnitude correlations (Figure 7.12b). As shown in Figure 7.12c, the effect of the EA index on the CDD index occurred only in spring at 13% of the stations with significant positive correlations in the range of 0.27 to 0.37. The NAO pattern also had some negative impact on 13% of stations for the CDD index and spatially distributed in the northern locations (Figure 7.12c).

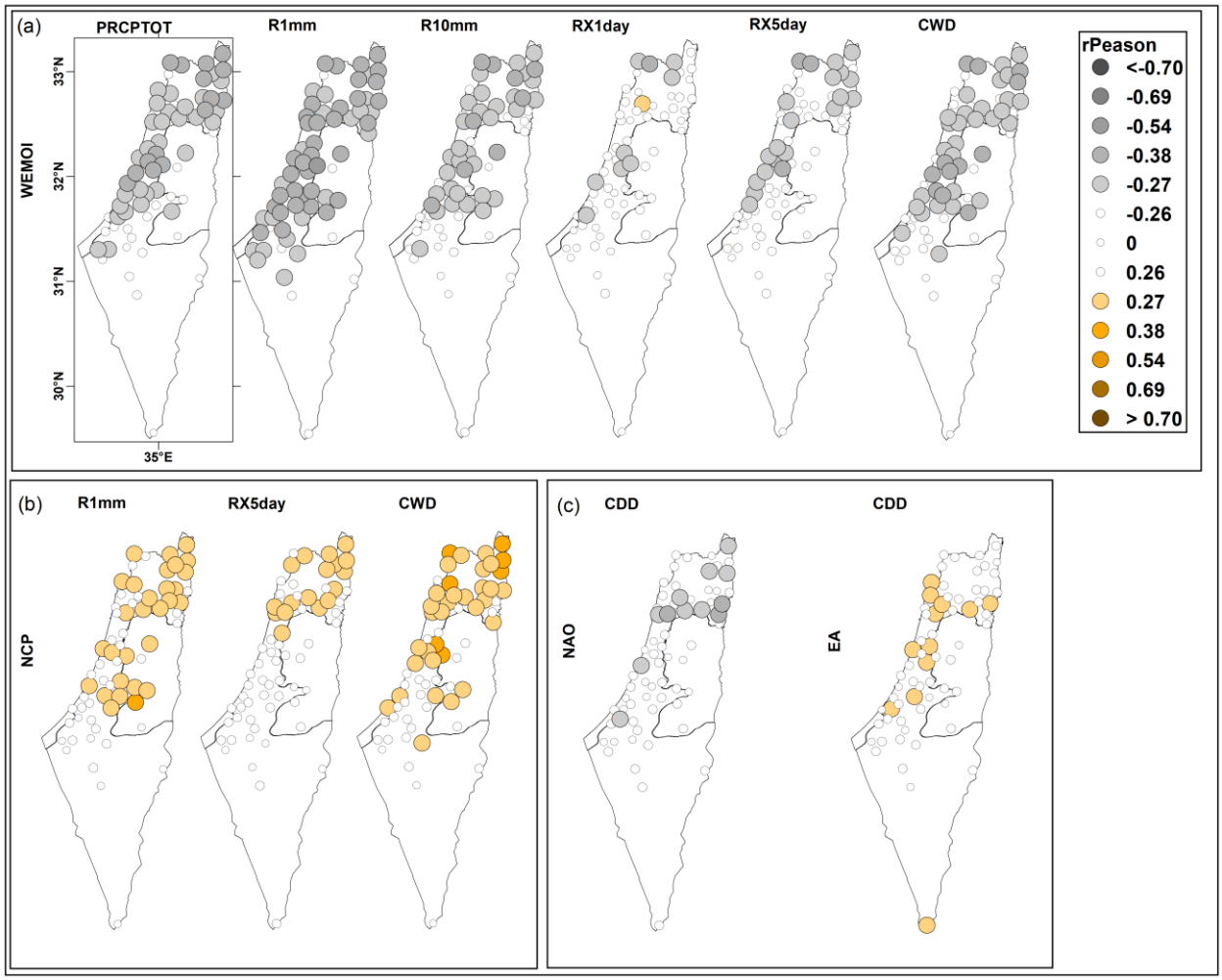

Figure 7.12. Spatial distribution of Pearson correlation coefficients between the WEMO (a), NCP (b), and NAO (c) teleconnection indices and the precipitation indices in spring.

For autumn, the results listed in Table 7.7 show that the ENSO pattern is the main regulator for seven extreme precipitation indices (PRCPTOT, R1mm, R10mm, R20mm, RX1day, RX3day, and RX5day). For these indices, 73, 58, 50, 30, 23, 29, and 58% of the total stations showed significant negative correlations with the ENSO pattern in autumn. In addition, the indices PRCPTOT, R1mm, R10mm, and R20mm correlated negatively with the WEMO for 30, 53, 39, and 23% of the stations, respectively. The NAO pattern also showed some positive effects on the RX1day and RX5day indices at 20 and 42% of the stations. Figures 7.13a to c show the spatial distribution of correlation values between the three patterns and extreme precipitation autumn indices. Most stations in the northern, coastal, and West Bank areas were significantly affected by the ENSO pattern, especially for the PRPTOT, R1mm, R10mm, and RX5day indices (Figure 7.13a). Other indices (R20mm, RX1day, and RX3day) showed spatially almost isolated patterns for the significant correlations, except for stations in the Jerusalem Governorate. The ENSO pattern affected more stations in all regions than the WEMO index.

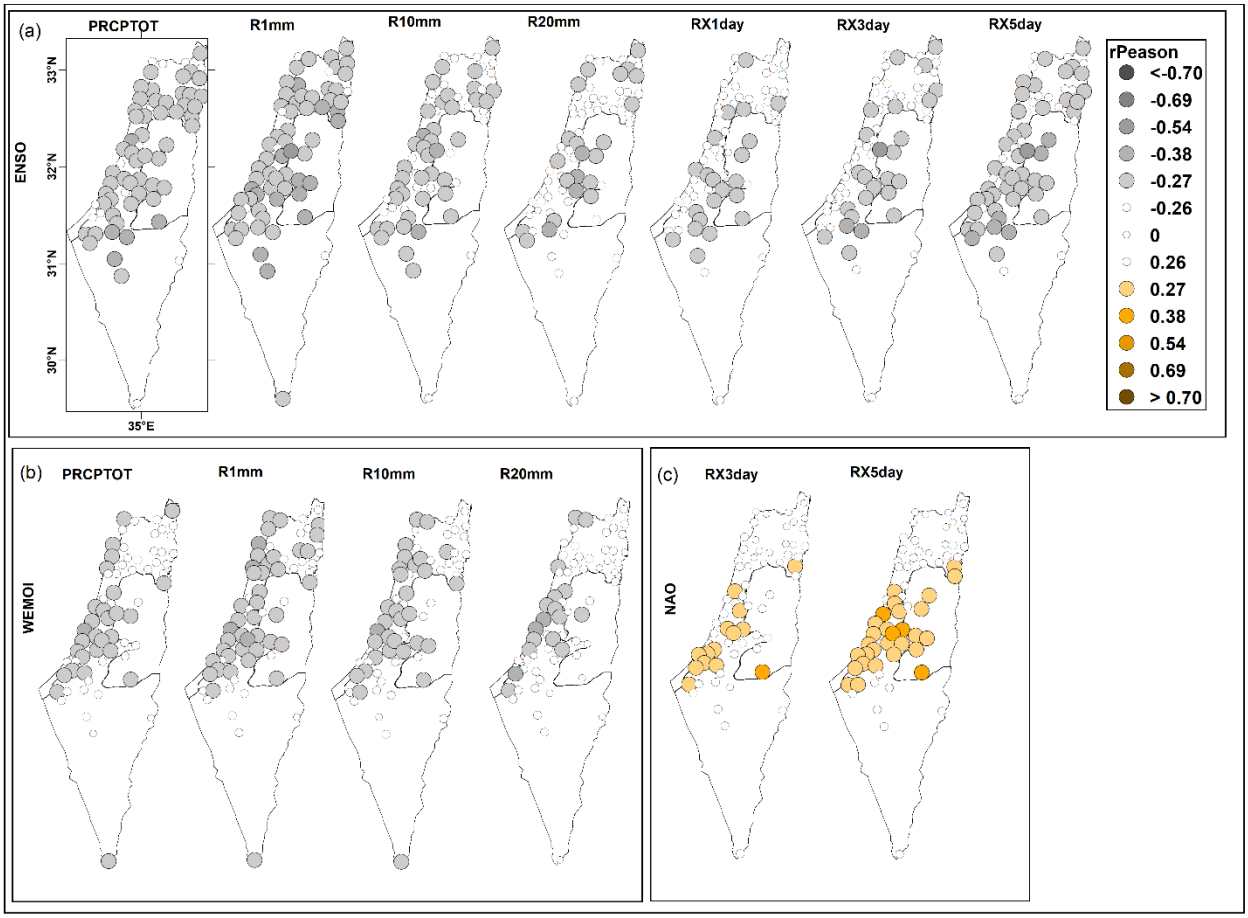

Figure 7.13. Spatial distribution of Pearson correlation coefficients between the ENSO (a), WEMO (b), and NAO (c) teleconnection indices and the precipitation indices in autumn.

7.3 Conclusions and discussion

In this study, a set of 15 different extreme precipitation indices were computed using homogeneous and quality controlled daily records for 66 stations distributed in Israel and Palestine covering 1970-2018. The study's main goals were to provide a Spatio-temporal analysis for the extreme rainfall indices at the annual and seasonal scales. It also tried for the first time to investigate the relationships between these indices and some large-scale circulation patterns in the Atlantic Ocean and the Mediterranean Sea. The main conclusions can be summarized as follows:

1. In 1970-2018, the spatial distribution for the extreme precipitation indices generally followed a north-south gradient, with the highest mean values found in the central and northern regions and the lowest mean values in the southern regions, except for the CDD index. The CDD index correlated negatively with all extreme precipitation indices and geographical factors, while a significant positive correlation was found between all other indices. In addition, the influence of latitude, longitude, and elevations on all extreme indices was significantly positive, except for the CDD index.
2. We found three underlying components in the data that explain 90% of the variance in the composite matrix of annual extreme precipitation indices. The first component appeared in the context of the intensity and percentage indices of extreme events and showed a non-significant upward trend over the period 1970-2018, and showed a significant positive correlation with the WEMO mode. The second component connected to frequency-based extreme events and showed a significant decreasing trend. The PC2 showed a positive correlation with the mode MO mode and with the EA /WR, ENSO and NCP modes. The third component relates only to the CDD index with a significantly decreasing trend.
3. A decreasing pattern for all extreme indices in the period 1991-1999, which is continuous until 2010 for many indices was detected. Furthermore, common peaks were observed in 1991/1992 and 2013 for most indices. The lowest values were observed in 1999 and 2010 for the most extreme indices.
4. The annual averages for frequency-based extreme indices exhibited decreasing trends, significant for the R1mm and CDD indices. Significant decreasing trends affected 32% and 26% of the stations respectively for the R1mm and CDD indices, and they covered the northern, northeastern, and West Bank stations for the R1mm index, and some southern coastal locations for the CDD index. In contrast, the percent and intensity based-extreme indices showed increasing trends, significant for the R99Ptot index. The significantly decreasing trend in the index CDD did not lead to an increase in the CWD index, suggesting that the changes in the indices of precipitation frequency are mainly reflected in the decrease of precipitation events with heavy and very heavy rainfall in most parts of the study area.
5. With more than 86% of the stations showed decreasing trends in the PRCPTOT, R1mm, R10mm, and R20mm indices, the area under investigation may be subjected to drought episodes in the future. The dominant decreasing trends in the PRCPTOT led to a decrease in the frequency of wet, heavy, and very heavy rainfall day’s indices, while they led to an increase in the intensity and percent of extreme indices.

Many studies have shown a decreasing precipitation trend and a reduction in the annual number of precipitation days for the Mediterranean and Middle East regions (AlSarmi and Washington, 2011; Hochman et al. 2018; Shohami et al. 2011; Alpert et al. 2002; Christensen et al. 2007; Nastos and Zerefos 2007; Najafi and Moazami 2017; Ziv et al. 2014; Philandras et al. 2011). The results are also consistent with Alexander et al. (2006) and Donat et. al. (2014) who studied extreme precipitation around the world using data from 5948 stations and global gridded data. They found a decreasing trend in the R10mm index and an increasing trend in the R99Ptot index in the eastern Mediterranean, including Israel and Palestine.

The general line of our results are also in agreement with the results obtained by Yosef et al. (2019), who studied the annual changes in extreme temperature and precipitation indices in Israel for the period 1950-2017. Their results showed the frequency-based extreme indices were affected by decreasing trends whereas the percent and intensity based-extreme indices were affected by increasing trends. On the other hand, their study did not document any significant increasing or decreasing trends while our study showed significant trends for R1mm, R99Ptot, and CDD indices. This can be attributed to the different base periods. Alpert et al. (2002) and Yosef et al. (2009) described a regional increase in percentage from the total annual amounts of "Moderate-Heavy" (16–32 mm/day) and "Heavy" (32–64 mm/day) categories for the north and center of Israel, despite the decreases in total rainfall amount. On global and regional scales, many studies predicted that under the global warming, a greater increase is expected in extreme precipitation, as compared to the mean values (IPCC 2007, 2008, 2011; Groisman et al. 2005; Kundzewicz et al. 2005; Dai 2011; Klein Tank and Können, 2003; Yilmaz 2015; Sensoy et al. 2013; Najafi and Moazami 2016; Rahimzadeh et al. 2009).

6. On a seasonal scale, no significant trends were observed for the averaged winter extreme indices. However, clearly positive trends were observed for the PRCPTOT, RX1day, RX3day, RX5day, CDII, and CDD indices. The increasing trend of the PRCPTOT index, together with the decreasing trend of the R1mm index, led to an increase of the SDII index, which is significant for the northwestern sites. In addition, the northern locations have experienced intensively rising trends in the RX1day index. The rising trends in both RX1day and the SDII index in the northern regions may indicate an increase in precipitation intensity and the possibility of flooding in these areas; particularly, they affected many sites with an annual precipitation maximum of more than 1000 mm.
7. One of the most important findings of this study relates to spring extreme indices that showed negative trends for most of the indices, significantly for R1mm, R20mm, CWD, RX1day, RX3day, RX5day, and SDII. These indices showed significant decreasing trends in more than 32% of the stations covering central and northern locations. With the exception of the CDD index, there was a very consistent pattern of declining trends across the study area, with more than 75% of stations showing declining trends in all indices.
8. During the autumn, significant decreases in RX1day, RX3day, and SDII were observed in 11-14% of the stations, primarily in the central regions. Spring and autumn, according to these findings, are the seasons that contribute the most to annual declines in the PRCPTOT,

R1mm, R10mm, R20mm, and CDD indices, while winter is the season that contributes the most to annual increases in the RX1day, RX3day, RX5day, and SDII indices.

9. The study area had longer periods of extreme dry spells (CDD) and correspondingly shorter extreme wet spells (CWD) for winter, spring, and the combined winter-spring.

Sillmann and Roeckner (2008) estimate a significant increase in the (CDD) index in regions around the Mediterranean Sea. This finding is consistent with a study by Tebaldi et al. (2006), who also found a significant increase in dry days. Ziv et al. (2014) found that the declining trend in annual precipitation during the period under study is mainly due to the spring season. Our results are also consistent with Hertig et al. (2013), who examined the changes in some seasonal extreme precipitation indices such as the PRCPTOT and CDD indices for the Mediterranean region, for the period 1950-2006. Their results showed a decrease in total precipitation over the Mediterranean region, especially in spring, while total precipitation increased especially in winter. Concerning the CDD index, they noted an increase in the CDD spring over the Mediterranean's southern and eastern parts.

10. The influence of teleconnection modes on the extreme precipitation indices was more pronounced for the frequency-based extreme rainfall indices than for the intensity and percent-based indices. In winter, the NCP index had a greater influence on seven winter extreme precipitation indices (PRCPTOT, R1mm, R10mm, R20mm, RX3day, RX5day, and CWD), mainly between 30.8ºN and 33.3ºN. The MOI and EA/WR indices had a remarkable impact on four winter extreme rainfall indices with the highest on the R10mm for the MO index, and on the R1mm for EA/WR. In spring, the WEMO index emerged as the most influential pattern on six spring extreme precipitation indices (PRCPTOT, R1mm, R10mm, RX1day, RX5day, and CWD). For the autumn, the results showed that the ENSO pattern is the main regulator for seven extreme precipitation indices (PRCPTOT, R1mm, R10mm, R20mm, RX1day, RX3day, and RX5day). In general, the EA and NAO patterns showed a weak influence on the annual and seasonal extreme precipitation indices. The NAO's remarkable effect was in autumn for the RX3day and RX5day index, and in winter for the CDD index.

No work in the literature establishes a direct link between the extreme precipitation indices and large-scale circulation patterns in Israel and Palestine. Most studies analyzed the influence of the large-scale circulation pattern on the mean values. However, it is important to note that some of these studies confirm some of the results obtained in this study. Kutiel and Benaroch (2002), based on monthly average temperatures and monthly precipitation totals from 33 stations in Greece, Turkey, and Israel, showed that the NCP is more pronounced in winter and transitional seasons. The negative episodes of the NCPs tend to increase the circulation of the south-western anomaly towards the Balkans, western Turkey, and the Middle East, causing precipitation in these regions to be below normal, while the opposite occurs in the positive episodes. Kutiel and Paz (1998) found that precipitation in Israel during the positive phase of the NCP is far greater than precipitation during the negative phase of the NCP, and that the influence of the NCP on the precipitation regime in Israel increases from the northern parts of

the country to the south. Toernros (2013) analyzed the relationship between the index Mediterranean Oscillation (MO) and winter precipitation in Southern Levant (Israel and Jordan) for the period 1960-1993. The results showed that winter precipitation is significantly associated with positive MO phases. Price et al. (1998) used monthly data for four stations in 1922-1990 to investigate whether there is a statistical correlation between ENSO conditions and precipitation in Israel. According to the results, there seems to be a correlation between El Niño events and precipitation in Israel since the mid-1970s, and these correlations are statistically significant for the last 20-25 years. Hurrell et al. (2003) and Kelley et al. (2012) have shown that the relationship between NAO and precipitation is not uniform throughout the Mediterranean region. The effects are large in the Western Mediterranean and weaker and opposite in the Levant. On the other hand, Oikonomou et al. (2010) investigated the relationship between extreme droughts (CDD) in the Eastern Mediterranean with large-scale circulation using daily precipitation for 56 stations in Eastern Mediterranean for 1958 2000. They showed that the CDD index via EM is influenced by teleconnection patterns centered on Northern Atlantic (NAO).

CHAPTER 8

COVARIABILITY ANALYSIS

In this chapter, Singular Value Decomposition (SVD) technique is used to examine and evaluate the possible relationships between the seasonal temperatures and precipitation in the Levant region and two indicators of climate variability, the sea surface temperatures (SST) and the North Hemisphere sea level pressure (SLP), in order to identify associated regions that may have coupled impacts.

8.1 Introduction

In the previous chapters, the influence of seven main teleconnection indices (such as the NCP, NAO, and ENSO) on the seasonal temperatures (Tmax and Tmin) and precipitation in the Levant region was spatially and temporally investigated. These teleconnection indices represent a part of ocean-atmospheric variability but they are spatially referred to specific regions (e.g., the pressure differences between two centers of action). This implies they do not take into account additional information of the climatic system that could have an influence on the seasonal temperatures and precipitation in the Levant region. Furthermore, the non-stationarity of the teleconnection patterns (Batehup et al., 2015; López-Moreno, 2008) due to external factors such as anthropogenic climate change (Müller and Roeckner, 2008; Herceg Bulic et al., 2011) and internal factors such as the non-linear interactions with other regulators of climate variability (Fogt et al., 2011), compels us to seek new variables that can provide information regarding the variability of the climate system. Xoplaki et al. (2003, 2002) and Matulla et al. (2003) showed the combination of various large-scale climate fields can account for a higher amount of explained variance of the local or regional climate fields than a single circulation parameter alone.

The oceans are playing an important role in driving of internal climate variability, affecting climate around the globe (Shukla, 1998). In this sense, Donat et al. (2016) compared century-long SST-

driven runs from one atmospheric GCM with gridded observations and reanalysis data and found that SST variability could explain about 50% of the inter-annual variability of globally averaged temperature extremes and about 15% for precipitation extremes. The majority of radiation from the sun is absorbed by the ocean, which also helps to distribute heat around the globe. For example, ocean water is constantly evaporating, increasing the temperature and humidity of the surrounding air to form rain and storms that are then carried by trade winds (Olbers et al., 2012; Gill, 1982). In fact, the ocean dynamics should be considered since it plays a significant role in temperature and precipitation variability (Deser et al., 2010). Hence, the SST or the sea level pressure (SLP) can provide important information about hydrologic variability in regions around the world. For example, slow variations in SST provide a source of potential predictability for climate fluctuations on timescales of seasons and longer (Deser et al., 2010). Therefore, the identification of coupling modes between these climatic variables and the seasonal temperature and precipitation variability could be a useful tool to improve our understanding of the interactive relationships between them.

In the literature, there are various methods to evaluate coupled modes of variability between two spatial-temporal fields. Bretherton et al. (1991), in their work entitled "An Inter-comparison of methods for finding coupled patterns in climate data", provided a unified conceptual framework for five methods that isolate important coupled modes such as the singular value decomposition (SVD) of the covariance matrix between two fields, the canonical correlation analysis (CCA), and the companied principal component analysis (CPCA). They compared SVD with others techniques mentioned before andfound the SVD is the most preferable for general use and it directly produces explicit measures of relationships between the derived coupled patterns. In addition, it has advantages such as its lack of systematic bias and good general performance. Their results also indicated that SVD was simpler to apply, interpret, and require no user-supplied parameters.

In their study between wintertime SST and 500 mbar height (Z500) anomalies, Wallace et al. (1992) illustrated SVD applied to a geophysical problem, and they compares SVD to CCA and CPCA and PCA, showing that SVD clearly isolates the two most important extratropical modes of variability in this case. Furthermore, while principal components analysis (PCA) is very common for this type of analysis, SVD has the advantage of being able to establish the similarities between two spatio-temporal fields by evaluating the cross-covariance matrix. In contrast, PCA evaluates only one spatial-temporal field (Sagarika et al., 2015).

The role of SST or SLP, in shaping the climate of the Levant region is still mostly unclear and unexplored. To determine the mechanisms governing climatic variations, it is essential to characterize the large-scale interactions between the ocean and the overlying atmosphere. In this Chapter, the possible relationships between the seasonal temperature and precipitation in the Levant region and two indicators of climate variability, the SST and North Hemisphere SLP will be evaluated in order to identify significant associated regions that have coupled impacts. The first goal is to identify the principal modes of behavior of the SST/SLP and the overlying atmospheric circulation, in order to provide insight into the variability of the coupled atmosphere–ocean system on interannual timescales. A secondary goal is to determine whether these modes of variability are

connected with any of the well-known teleconnection patterns. The geographical domain, periods, resources of the SST and SLP data are available in Chapter 2, Section 2.3. The methodology related to SVD used in this study is included in Chapter 3, Sections 3.8 and 3.9. The SST, SLP, precipitation, and temperature data are averaged for the winter (December, January, February), spring (March, April, May), summer (June, July, August), and autumn (September, October, November) for the periods 1987-2017 for temperature and 1970-2018 for the precipitation.

8.2 Results

8.2.1 Covariability between SST and seasonal temperatures

To examine and quantify the link between the SST and seasonal temperatures (Tmax and Tmin), the SVD was performed by analyzing the covariance matrices of the two fields. The results are displayed using homogenous and heterogeneous correlation maps (Wallace et al., 1992). The statistics for the first three leading SVD modes, including the temporal correlation between pairs of expansion coefficients, strength of the coupling (STR) and the percentage of squared covariance (SCF) are listed in Table 8.1. Furthermore, Table 8.2 shows the variance in individual fields (SST, seasonal temperatures) explained by each mode. Table 8.3 shows the correlations between the left SST expansion coefficients of the selected SVD modes and the seven teleconnection indices chosen for this study.

In all SVD analyses, only the coupling coefficients associated with the first three modes were evaluated because they accounted for 80% or more of the SCF. As can be seen in Table 8.1, the SCF for the third mode drops below 6% in all cases, and the SCF for the second mode was less than 8% in most cases, which means that the amount of information accounted for the second and third modes respecting the two fields is not very relevant. Moreover, the total number of stations that exhibited significant correlations with the second and third modes was less than 12 stations. Because of the reasons above, only the first mode was included in our discussion.

Season	Variable	STR			SST-seasonal temperatures SCF (%)			Total sig. stations (Heterogeneous)
		Mode1	Mode2	Mode3	Mode1	Mode2	Mode3	Modes (1,2,3)
Winter	**Tmax**	0.59	0.58	0.66	91	4	1	(55,0,0)
	Tmin	0.73	0.67	0.66	89	5	2	(58,5,3)
Spring	**Tmax**	0.70	0.64	0.55	84	6	4	(59,0,0)
	Tmin	0.79	0.62	0.77	81	8	2	(54,3,0)
Summer	**Tmax**	0.68	0.64	0.73	84	5	3	(53,6,1)
	Tmin	0.76	0.73	0.78	76	8	6	(53,4,12)
Autumn	**Tmax**	0.64	0.69	0.73	80	7	3	(57,1,0)
	Tmin	0.73	0.80	0.70	65	16	4	(57,2,0)

Table 8.1. Summary of the strength of the coupling (STR) and the square covariance fraction (SCF) corresponding to the selected modes from SVD of SST and seasonal temperatures for the period 1987-2017.

Season	Variable	SST variance (%)			Seasonal Temp. variance (%)		
		Mode1	Mode2	Mode3	Mode1	Mode2	Mode3
Winter	**Tmax**	19	21	9	85	4	2
	Tmin	19	22	8	71	4	4
Spring	**Tmax**	11	24	16	77	3	4
	Tmin	12	27	10	66	5	3
Summer	**Tmax**	24	8	8	55	11	5
	Tmin	23	14	7	41	8	9
Autumn	**Tmax**	11	17	8	79	4	2
	Tmin	7	21	11	67	4	3

Table 8.2. The variance in individual fields (SST and seasonal temperatures) that are explained by each mode.

Season	Variable		WEMO	EA/WR	NAO	EA	MO	NCP	ENSO
Winter	**Tmax**	**M1**	-0.18	-0.20	**-0.66**	0.08	**-0.48**	**-0.39**	0.07
		M2	-0.42	0.12	-0.61	-0.40	-0.16	0.11	0.13
		M3	-0.17	0.07	0.11	-0.05	0.18	0.08	0.23
	Tmin	**M1**	-0.13	-0.20	**-0.65**	0.10	**-0.48**	**-0.40**	0.00
		M2	0.43	-0.08	0.58	0.43	0.14	-0.08	-0.27
		M3	0.03	-0.06	-0.12	-0.10	-0.09	0.08	0.06
Spring	**Tmax**	**M1**	**0.43**	**-0.47**	-0.10	0.18	-0.16	-0.21	0.28
		M2	0.19	0.00	0.63	0.07	0.20	0.38	-0.25
		M3	-0.18	-0.26	-0.47	0.02	-0.01	-0.24	-0.16
	Tmin	**M1**	-0.25	**0.51**	0.25	-0.19	0.15	0.26	-0.22
		M2	-0.20	0.03	-0.62	-0.05	-0.11	-0.34	0.13
		M3	-0.11	-0.15	-0.22	0.04	0.16	-0.12	-0.47
Summer	**Tmax**	**M1**	**-0.44**	**-0.56**	-0.28	0.06	0.02	**-0.46**	**0.56**
		M2	0.22	0.29	-0.03	0.13	0.10	0.07	-0.17
		M3	-0.21	-0.21	0.02	0.12	0.00	-0.12	0.09
	Tmin	**M1**	**-0.42**	**-0.55**	-0.26	0.09	0.03	**-0.43**	**0.58**
		M2	0.28	0.21	0.04	0.11	0.28	0.07	-0.08
		M3	-0.39	-0.24	-0.19	0.00	-0.11	-0.28	0.06
Autumn	**Tmax**	**M1**	0.08	-0.24	**-0.45**	-0.16	-0.16	**-0.66**	0.35
		M2	0.16	0.14	0.46	0.00	0.08	0.03	-0.23
		M3	-0.49	0.12	-0.01	0.19	-0.13	0.19	-0.12
	Tmin	**M1**	0.18	-0.15	-0.25	-0.16	-0.11	**-0.67**	0.16
		M2	-0.14	-0.14	-0.44	0.04	-0.11	-0.12	0.24
		M3	-0.39	0.15	-0.08	0.15	-0.14	0.15	-0.16

Table 8.3. Correlations between the left expansion coefficients of the selected SST modes and the teleconnection indices, from the SVD of SST and seasonal temperatures.

8.2.1.1 Winter Tmax and Tmin covariability

The first SVD mode explains 91% of the squared covariance between the SST and winter-Tmax (Table 8.1). The temporal correlation between pairs of expansion coefficients for the first mode is 0.59, significant at 99.99% (Table 8.1, Figure 8.1c). In addition, the first pattern itself explains 19% of the total SST variance and 85% of the total Levant's winter-Tmax variance (Table 8.2).

The homogenous and heterogeneous correlation patterns, as well as the temporal correlation between the left (SST) and right (winter-Tmax) standardized expansion coefficients for the first mode, are shown in (Figure 8.1, upper panels). The first SVD mode of winter-Tmax has a well-defined pattern over the domain where high positive significant correlations are found in 55 out of

60 stations (Figure 8.1b, Table 8.1). The SST homogeneous correlation map (Figure 8.1a) generally resembles the Atlantic tripolar pattern (Sutton et al., 2001), showing a significant positive correlation up to 0.70 in north and south of the North Atlantic Ocean, and a different sign in the central Atlantic ocean (30°N to 40°N). A positive correlation in the western/eastern Mediterranean Sea were also detected. When the SST in the north and south of the Atlantic Ocean is abnormally warm, and the SST is abnormally cold in the central Atlantic Ocean, the winter-Tmax in the Levant is abnormally warm increase. Most Levant's locations showed positive correlations (r> 0.55) with this pattern. In general, this mode is characterized by the NAO/MO-SST relationship, which is also confirmed by the significant correlation between the left expansion coefficient and the NAO/MO indices by -0.66/-0.48 (Table 8.3). The NAO and MO indices also showed significant negative correlations with winter-Tmax, especially for southern locations in the Levant (Figure 4.10). These correlations are generally less than those for this SST mode.

In addition, the homogenous correlation map also exhibited a significant negative correlation over the Baltic Sea and east of the North Sea, with a high negative dipole correlation in the Baltic Sea (r > 0.80). These regions are negatively and significantly correlated to winter-Tmax. The left expansion coefficient significantly presented a correlation by 0.39 with the NCP index (Table 8.3). It is also noted that the NCP which has a center of action in the North Sea exhibited a significant negative correlation with the Levant winter-Tmax (-0.79) (Figure 4.10).

For winter-Tmin, the first SVD mode individually explains 85% of the squared covariance between SST and winter-Tmin (Table 8.1). The temporal correlation between the left (SST) and right (winter-Tmin) standardized expansion coefficient reached 0.73, which indicates a tight coupling between them (Table 8.1, Figure 8.1c, bottom panels). For the first mode, the SST pattern itself explains 19% of the total SST variance, while the first SVD mode of winter-Tmin explains 71% of the Levant winter-Tmin variance (Table 8.2).

The homogeneous map (Figure 8.1a, lower panel) associated with this mode shows a similar pattern of the winter-Tmax. It shows a couple of significantly correlated areas. A positive in the north and south parts of the North Atlantic Ocean (up to 0.85) and eastern Mediterranean Sea (up to 0.70), which are positively and significantly associated with winter-Tmin in the Levant. On the other hand, the Atlantic Ocean's central area (30°N to 40°N), the Baltic Sea, and east of the North Sea negatively correlated with the left expansion coefficient and the winter-Tmin. Similar to winter-Tmax, the left expansion coefficient significantly correlates with the NAO, MO, and NCP indices by -0.72, -0.56 and -0.40 (Table 8.3). Theses indices negatively affected the Levant´s winter-Tmin. It can be concluded that the NAO and MO indices are negatively related to SST in the North Atlantic and the Eastern Mediterranean, while the NCP positively correlated with SST in the North and Baltic Seas. As shown in Figure (8.1b), 58 stations exhibited a significant positive correlation with this mode, with the highest values (0.70-0.84) in southern locations in Palestine and Jordan and at the eastern locations from Jordan.

It seems that there is a relevant contribution from SST to the long-term behavior and variability in winter Levant temperatures (Figures 8.1, c panels). Small deviations between the SST's left and winter Tmax/Tmin right expansion coefficients are observed. For example, the warming winter

Tmax and Tmin anomalies in 1991-1999 (Figure 8.1) are perfectly associated with the SST warming in the north and south of the Atlantic Ocean.

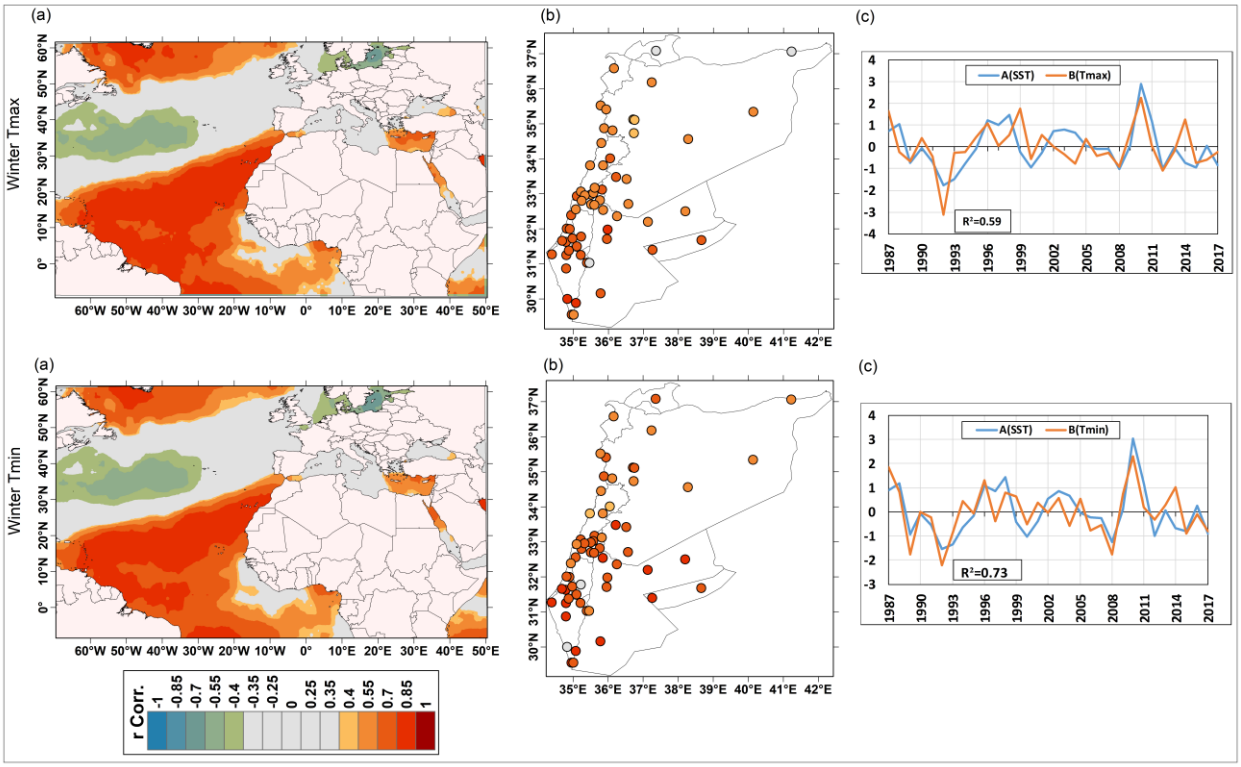

Figure 8.1. (a) Homogeneous maps, (b) heterogeneous maps and (c) left (SST) and right (winter temperature) normalized expansion coefficient time series of winter SST-Tmax (upper panel) and winter SST-Tmin (bottom panel) SVD. Colored areas and circles in homogeneous and heterogeneous maps respectively represent regions and stations with significant correlations at 0.05 significance level (higher than +0.35 and lower than -0.35).

8.2.1.2 Spring Tmax and Tmin covariability

The first SVD mode comprises 84% of the square covariance fraction between SST and spring-Tmax. The correlation between the left and right expansion coefficient reached 0.70 (Table 8.1, Figure 8.2c, upper panels). Moreover, the SST pattern explains 11% of the total SST variance, while the first SVD mode explains 77% of the Levant´s spring-Tmax variance (Table 8.2). According to the homogenous map (Figure 8.2a, upper panel), the pattern showed a positive correlation (0.70-0.84) in the east and the central Mediterranean Sea, the Black Sea, and central/southern parts of the Atlantic Ocean. The spring-Tmax are significantly and positively associated with the SST of these regions for all locations and with high values (> 0.70) in the northern areas of Palestine and coastal locations of Lebanon and Syria (Figure 8.2b). In the same context, the results also showed the left expansion coefficient significantly correlates with the WEMO and EA/WR indices by 0.43 and -0.47, respectively (Table 8.3). In addition, these two indices showed significant correlations with the averaged spring-Tmax over the Levant by 0.51 and -0.38, respectively (Chapter 4, section 4.2.5.2).

For spring-Tmin (Figure 8.2, bottom panels), the fraction of the square covariance explained by the first mode reached up 81%, and the strength of the coupling was 0.79 (Table 8.1, Figures 8.2c). the first mode explains 66% of the spring-Tmin variance, much higher than the second mode, which presents only 8% (Table 8.2). The SST pattern describes 12% of the total SST variance (Table 8.2). The homogenous map (Figure 8.2a) revealed significant negative correlations (-0.40 - -0.70) in south and central Atlantic, Black Sea, and east of the Mediterranean Sea. The SST of these regions positively correlated with spring-Tmin. On the contrary, this mode showed a positive correlation to the west of the Iberian Peninsula. The heterogeneous map (Figure 8.2b) displayed significant negative correlations in all stations except for Lebanon. The results also showed the left expansion coefficient significantly correlates with EA/WR index by 0.51 (Table 8.3).
In spring, the strength of coupling between the left (SST) and right (temperature) expansions coefficients was generally higher than for winter and other seasons (Figures 8.2, c panels). Closed variation is noted between the left and right expansion coefficients, especially in 1987-1999 and 2011-2018, where the increasing temperature well coincides with the SST increasing periods.

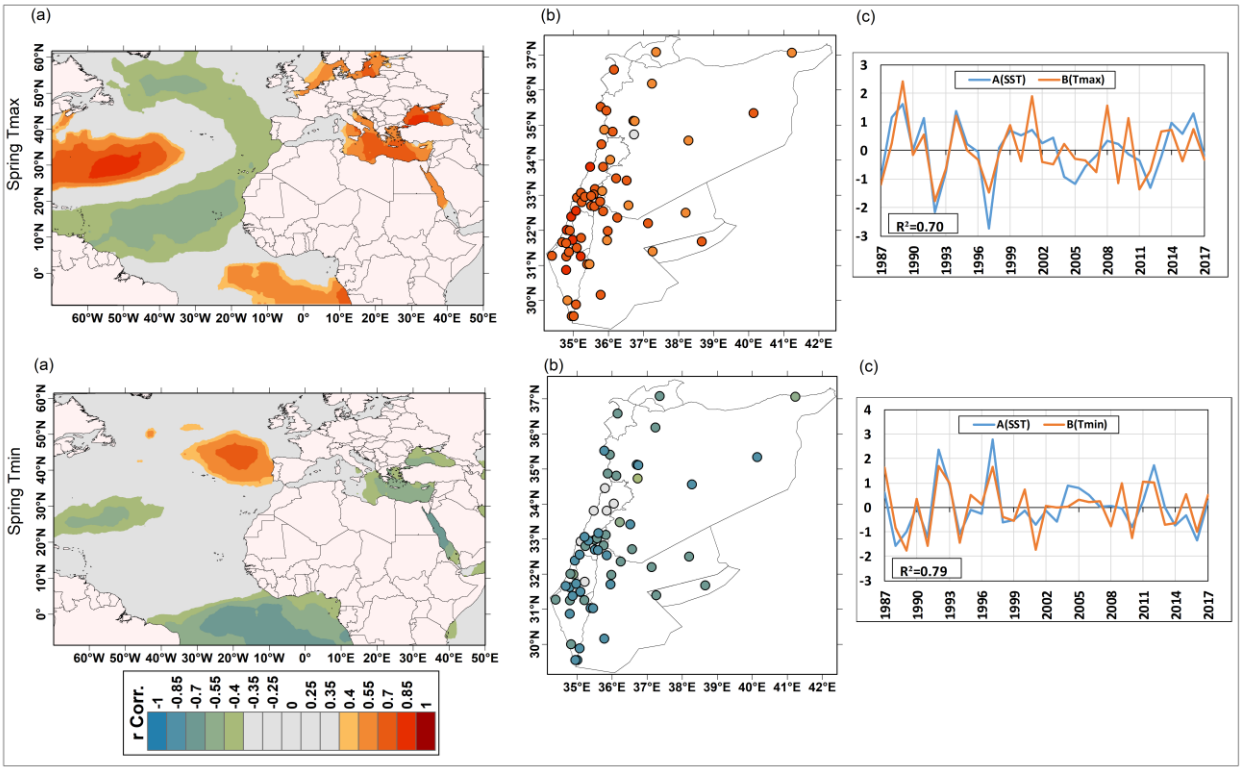

Figure 8.2. As Figure 8.1 but for spring.

8.2.1.3 Summer Tmax and Tmin covariability

The results showed a significant correlation between the left (SST) and right (summer-Tmax) expansion coefficient by 0.68 (Table 8.1, Figure 8.3c, upper panel). In addition, the first mode from the SVD comprises 84% of the square covariance (Table 8.1). This mode strongly showed positive correlations in the north and tropical Atlantic Ocean, eastern parts of the Mediterranean Sea, and Black Sea (Figure 8.3a). The heterogeneous map (Figure 8.3b, upper panel) also showed

high and significant positive correlations for most locations. Significant correlations were found between the left expansion coefficient and the EA/WR, NCP, and ENSO indices by -0.56, -0.46, and 0.56, respectively (Table 8.3).

For summer-Tmin (Figure 8.3, bottom panel), a significant positive correlation was found between the left and right expansion coefficient by 0.76 (Table 8.1, Figure 8.3c). The first mode from the SVD comprises 76% of the square covariance (Table 8.1). Similar to the results obtained for the SST/summer-Tmax, this mode strongly showed positive correlations in the north and tropical Atlantic Ocean and east of the Mediterranean Sea (Figure 8.3a). The heterogeneous map (Figure 8.3b, lower panel) also showed high and significant positive correlations for most locations. Significant correlations were found between the left expansion coefficient and the EA/WR, NCP, and ENSO indices by -0.55, -0.43, and 0.58, respectively (Table 8.3). Close deviations between the left SST and right summer Tmax/Tmin expansions coefficients are observed. When the SST in the north and tropical Atlantic Ocean and east of the Mediterranean Sea increases,the summer temperatures increases. For example, the decreasing and increasing summer (Tmax and Tmin) in 1987-1991 and 1992-1999, respectively (Figure 8.3c) are associated with decreasing and increasing SST in the north and south of the North Atlantic Ocean.

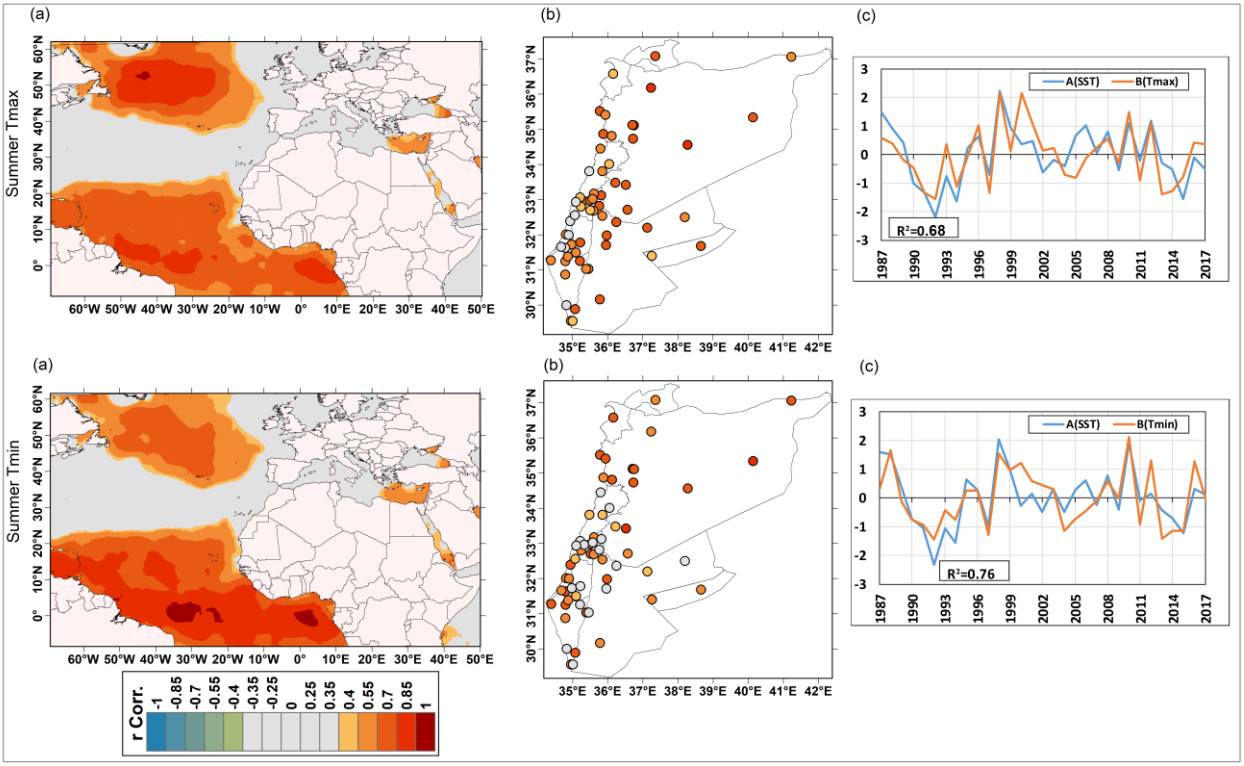

Figure 8.3. As Figure 8.1 but for summer.

8.2.1.4 Autumn Tmax and Tmin covariability

The three leading SVD modes together account for 90% of the total SST/autumn-Tmax variance. Individually, they explain 80%, 7%, and 3% of the variance (Table 8.1). A significant correlation (0.64) was found between the left (SST) and right (autumn-Tmax) expansion coefficients (Table

8.1, Figure 8.4c, upper pannel). The SVD SST pattern explains 11% of the total SST variance, whereas the first SVD mode of autumn-Tmax explains 79% of the Levant's autumn-Tmax variance (Table 8.2).

The correlation maps analysis revealed that this first SST mode shows significant positive correlations in the north and the tropical part of the Atlantic Ocean and east the Mediterranean Sea (Figure 8.4a, upper panel). It also shows significant positive correlations with the most locations in the Levant. It can be concluded that the Levant's autumn-Tmax positively and significantly correlates to the SST in the northern Atlantic Ocean and eastern Mediterranean Sea. On the contrary, the autumn-Tmax negatively correlated with the SST for the North and Baltic Seas and the western Mediterranean Sea (Figure 8.4a, upper panel). The heterogeneous map (Figure 8.4b, upper panel) indicated that this mode is highly associated with autumn-Tmax variability in most Levant locations. It showed significant positive correlations for 57 out of 60 stations. The highest correlations (up to 0.7) were found for the eastern places from Jordan and Syria and some northern Palestine locations. Based on the correlations coefficients calculated between the first SST mode and the teleconnection indices (Table 8.3), the NAO and NCP indices presented significant negative correlations by -0.45 and -0.66, respectively. Furthermore, the NCP index showed a significant negative correlation with the Levant's autumn-Tmax (Chapter 2, section 4.2.5.4).

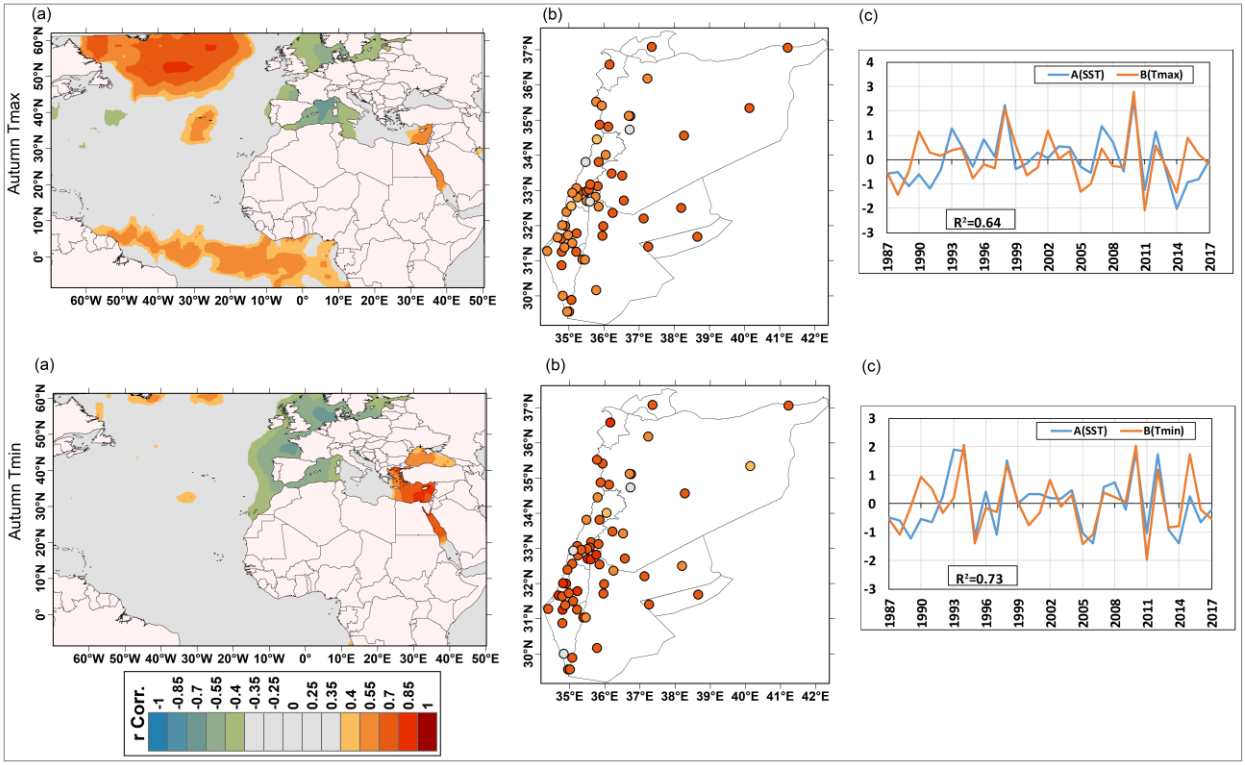

Figure 8.4. As Figure 8.1 but for autumn.

A percent of 65% of the total covariance of the system is explained by the first mode SST-autumn Tmin, and the correlation coefficients between the reconstructed SST and autumn-Tmin time series based only on the first mode is equal to 0.73 (Table 8.1). The first SVD mode of autumn-Tmin and SST formed 0.67% and 7% of the total variance, respectively (Table 8.2).

As shown in Figure 8.4a (bottom panel), the eastern Mediterranean Sea and the Black Sea showed a high positive correlation (up to 0.85). In addition, the heterogeneous map (Figure 8.4b, lower panel) indicated that this mode is highly and positively associated with autumn-Tmin variability in 57 out of 60 stations in the Levant. The highest correlations (>0.85) were found in some locations around Jerusalem and northern Palestine. On the other hand, the North and Baltic Seas and the western area from the Mediterranean Sea exhibited a significant negative correlation with the left expansion coefficients, which means autumn-Tmin negatively correlated with these regions. Based on the correlation coefficients calculated between the first SST mode and the teleconnection indices (Table 8.3), only the NCP index presented significant negative correlations by -0.60. In addition, the NCP index exhibited a significant negative correlation with autumn-Tmin by an average of -0.66 (Chapter 2, section 4.2.5.4).

8.2.2 Covariability between SST and seasonal precipitation

The fractional variance of the SST-precipitation covariance matrix explained by the first three leading SVD modes and the correlations between the left and right expansion coefficients of the SST and precipitation modes are listed in Table 8.4. Table 8.5 shows the percentage variances explained by the individual SST and seasonal precipitation fields. Additionally, Table 8.6 shows the correlations between left expansion coefficients of the selected SVD modes and the teleconnection indices.

Season	STR			SST-seasonal rainfall SCF (%)			Total Sig. Stations (Heterogeneous)
	Mode1	Mode2	Mode3	Mode1	Mode2	Mode3	Modes (1,2,3)
Winter	0.46	0.56	0.59	36	31	8	(103,44,/3)
Spring	0.56	0.40	0.69	38	29	7	(102,6,13)
Autumn	0.53	0.66	0.47	80	7	5	(135,30,12)

Table 8.4. Summary of the strength of the coupling (STR) and the square covariance fraction (SCF) corresponding to the selected modes from SVD of SST and seasonal rainfall for the period 1970-2018.

Season	SST variance (%)			Seasonal rainfall Variance (%)		
	Mode1	Mode2	Mode3	Mode1	Mode2	Mode3
Winter	6	16	4	55	8	8
Spring	6	28	4	40	12	6
Autumn	17	5	11	61	11	7

Table 8.5. The variance of individual fields (SST and seasonal rainfall) that is explained by each mode.

Season		WEMO	EA/WR	NAO	EA	MO	NCP	ENSO
Winter	M1	-0.22	0.18	**-0.50**	-0.28	-0.09	0.03	0.00
	M2	-0.10	-0.10	**-0.61**	0.01	**-0.36**	-0.28	0.07
	M3	0.33	**-0.37**	0.01	-0.23	-0.08	**-0.29**	**0.32**
Spring	M1	**0.33**	-0.09	-0.20	0.13	0.00	**-0.33**	**-0.36**
	M2	-0.08	-0.06	**-0.47**	0.10	0.08	-0.17	-0.16
	M3	0.23	0.08	-0.12	-0.08	-0.21	-0.12	0.08
Autumn	M1	0.15	0.17	**0.37**	0.01	0.05	0.09	**-0.41**
	M2	0.01	0.19	0.13	0.02	0.28	0.09	-0.06
	M3	0.19	-0.02	**0.30**	-0.10	-0.06	-0.16	-0.03

Table 8.6. Correlations between the left expansion coefficients of the selected SVD SST modes and the teleconnection indices, from the SVD of SST and seasonal rainfall.

8.2.2.1 Winter covariability

Figure 8.5 shows the first three modes obtained through the SVD analysis applied to the seasonal series of the SST anomalies and the winter-rainfall anomalies in the Levant during the entire period 1970-2018. The first three coupled modes explain 75% of the fractional variance for the covariance matrix (SST–winter rainfall) (Table 8.4). The first SVD mode explains 36% of the fractional variance between the SST and winter-rainfall, with a strength of the coupling of 0.46 (Table 8.4, Figure 8.5c, Mode 1). Furthermore, the first mode itself explains 6% of the total SST variance and 55% of the total winter precipitation variance (Table 8.5).

The SST of the Atlantic resembles the Atlantic tripolar pattern, showing two centers of action with positive correlations (up to 0.70) located in the northernmost latitudes and in the tropical region, and two centers of action with negative correlations (up to 0.40) in the north-central Atlantic, the North Sea, and central Mediterranean Sea. The heterogeneous map (Figure 8.5b, Mode 1) indicated that this mode is intensively associated with winter rainfall variability in most Levant locations by 103 out of 165 stations, with high magnitudes of correlations (0.55-0.69) in north Palestine. This implies that the Levant tends to have more precipitation in winter when the northern and southern parts of the North Atlantic Ocean are abnormally warm. Based on the correlation coefficients calculated between the first mode and teleconnection indices (Table 8.6), only the NAO index presented significant negative correlations by -0.50. Note that colored areas and circles in the homogeneous and heterogeneous maps represent regions and stations with significant correlations at a 0.05 significance level (higher than +0.30 and lower than -0.30).

The second SVD mode explains 31% of the fractional variance between the SST and winter-rainfall, with a strength of the coupling of 0.56 (Table 8.4, Figure 8.9c, Mode 2). Furthermore, the second coupled-mode explains 16% of the total SST variance and only 8% of the total precipitation variance (Table 8.5). The homogeneous map (Figure 8.5a, Mode 2) exhibited significant negative correlations (up to 0.70) in the north, and the area extended from southern Spain to the eastern coastal area of the southern America content between (0º-20ºN), which also negatively correlated with winter rainfall. This mode seems similar to the tripolar pattern of the Atlantic but with displaced centers of action. On the other hand, the central area of the Atlantic Ocean, North and Baltic Seas, presented positive correlations (up to 0.55) with the left expansion coefficients, and these regions positively correlated with winter rainfall. The heterogeneous map (Figure 8.5b, Mode 1) indicated that this mode is associated with winter rainfall variability only in the central regions from Palestine between (31.5ºN-32.5ºN) by 44 out of 165 stations, with correlations values (0.40-0.54). Based on the correlation coefficients calculated between the left SST expansion coefficients and the teleconnection indices (Table 8.6), only the NAO and MOI indices presented significant negative correlations by -0.61 and -0.36, respectively. However, note that the NAO did not exhibited significant correlation with the winter rainfall whereas the MOI index showed a notably positive correlation with winter rainfall in Palestine (Chapter 6, section 6.6.1).

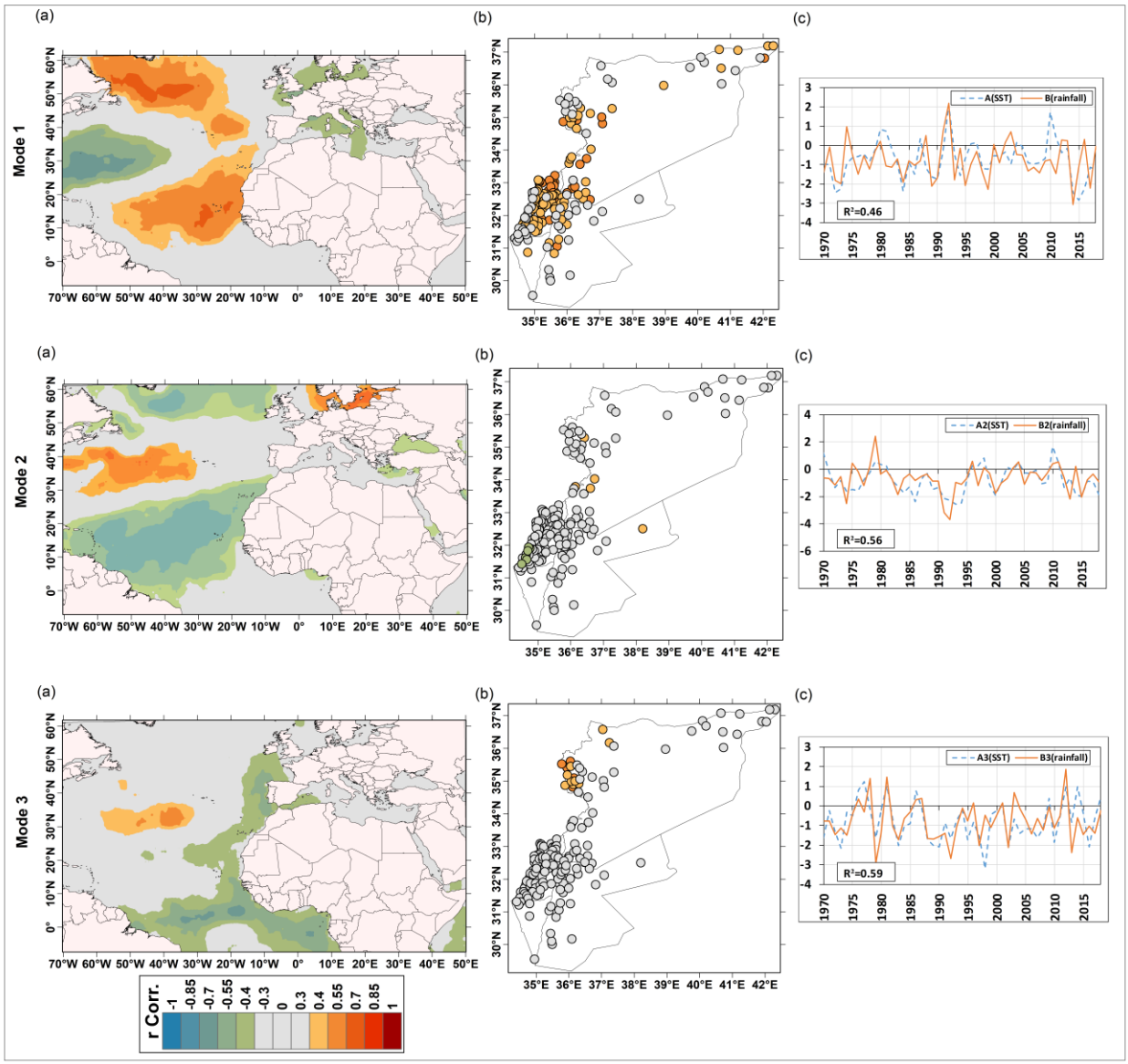

Figure 8.5. (a) Homogeneous map, (b) heterogeneous map and (c) left (SST) and right (winter-rainfall) normalized expansion coefficient time series for the Mode 1 (upper panel), Mode 2 (central panel), and Mode 3 (bottom panel) from winter SST-precipitation SVD. Colored areas and circles in homogeneous and heterogeneous maps represent regions and stations with significant correlations at 0.05 significance level (higher than +0.30 and lower than -0.30).

The third coupled mode between the winter SST and winter-rainfall (Figure 8.5, Mode 3) explains 8% of the SCF between both fields (Table 8.4). The correlation between the SST and winter-rainfall expansion coefficients is 0.59, showing, therefore, an important coupling force between these two fields for this third mode. The spatial pattern found for the SST presents negative SST values in the equatorial strip of the Atlantic and bordering the African and Portuguese coasts. There are center of positive correlations in the central Atlantic. The heterogeneous correlation map for winter-rainfall in the Levant (Figure 8.5b, Mode 3) shows significant positive correlations in the

Syrian coastal area with an average of 0.40, which positively correlated with the center of positive correlation in the central Atlantic.

8.2.2.2 Spring covariability

Figure 8.6 shows the first three modes of SST obtained by the SVD in spring, along with the map of heterogeneous correlations for spring-rainfall (Figures 8.6, b panels) and temporal variability of each mode, represented by its respective coefficients of expansion (Figure 8.6, c panels).

The first three coupled modes explain 74% of the fractional variance for the covariance matrix (SST–spring rainfall) (Table 8.4). The first associated pattern is responsible for 38% of the SCF, with a strength of the coupling of 0.56 (Table 8.4, Figure 8.6c, Mode 1). Furthermore, the first mode itself explains 6% of the total SST variance and 40% of the total precipitation variance (Table 8.5). The homogenous map (Figure 8.6a, Mode 1) presents a horseshoe shape with significant positive correlation in the Atlantic Ocean and a significant negative correlation in the central part of the Atlantic Ocean, the North Sea, and the western coast of Italy.

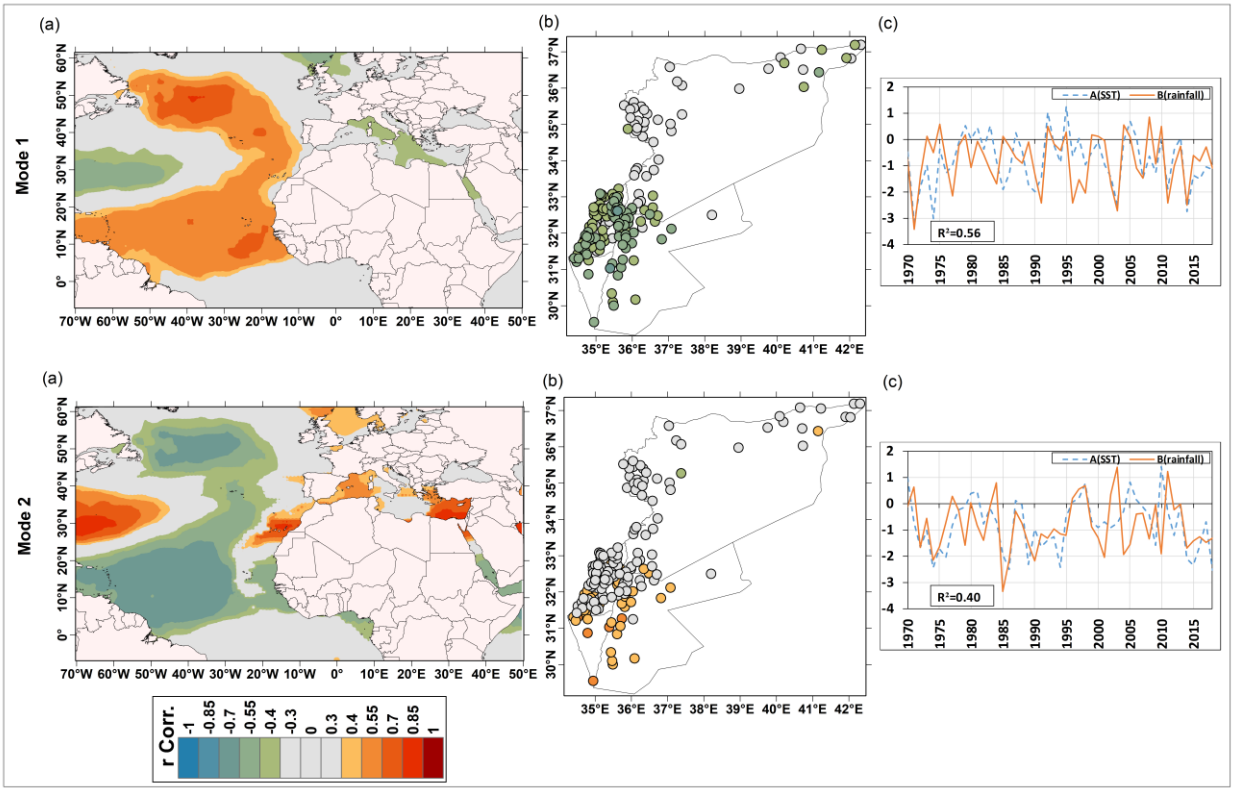

Figure 8.6. As Figure 8.5 but for the first two coupled modes from the spring SST-rainfall SVD.

As shown in Figure (8.6b, Mode 1), the heterogeneous map showed significant negative correlations with 102 stations concentrated in the south of Levant (Palestine and Jordan) and at some locations in eastern Syria. The highest correlations (-0.55- -0.69) covered the western and northern sites from Jordan and the northeastern locations in Palestine. Hence, the Levant will receive less precipitation in spring when the horseshoe shape area's SST is abnormally cold. The correlations with teleconnection indices were significant and moderate for WEMO (0.33), NCP (-

0.33), and ENSO (-0.36) indices (Table 8.6). Besides, the WEMO index negatively correlated with the spring Levant rainfall by an average of -0.40 (Chapter 6, section 6.6.2).
The second mode explains 29% of the squared variance, with a strength of the coupling of 0.40 (Table 8.4, Figure 8.6c, Mode 2). This mode also explains 28% of the total SST variance and 12% of the spring rainfall (Table 8.5). It exhibited a horseshoe shape pattern of significant negative correlations in the Atlantic Ocean with a significant positive correlation centre in the central area of the Atlantic Ocean, the North Sea, and western and eastern Mediterranean Sea (Figure 8.6a, Mode 2). For the heterogeneous map (Figure 8.6a, Mode 2), a significant positive correlation was found in the southern regions, especially in the south of Palestine and Jordan, as well as eastern locations from Jordan. In addition, a significant negative correlation was found between the NAO index and the left SST expansion coefficients by -0.47 (Table 8.6).

8.2.2.3 Autumn covariability

Table 8.4 shows the first three coupled modes, which explain 92% of the covariance matrix's fractional variance (SST–autumn rainfall). The first coupled pattern is responsible for 80% of the SCF, with a strength of the coupling of 0.53. Furthermore, the variance explained for this first mode was 17% of the total SST variance and 61% of the total precipitation variance (Table 8.5).
The homogenous map (Figure 8.7a, Mode 1) presents a significant negative correlation in the north and tropical Atlantic Ocean. The correlations between the left (SST) expansion coefficients and the teleconnection indices were significant for NAO (0.37) and ENSO (-0.41) indices (Table 8.6). The heterogeneous map (Figure 8.7a, Mode 1) showed significant positive correlations with 135 stations covering all locations, except Syria's coastal area. The high correlations (0.55-0.69) were more pronounced for the western and northern sites from Jordan, the northeastern locations in Palestine and southern locations from Jerusalem, and the Palestinian coastal area (Figure 8.7b). The homogeneous and heterogeneous maps indicated the Levant tends to have more precipitation in autumn when the northern and tropical Atlantic Ocean's SST is remarkably cold.
The second coupled mode (Figure 8.7, Mode 2) between the SST and the autumn rainfall explains 7% of the SCF. It presents a high coupling force between the two fields; the correlation coefficient is 0.66, significant at the 95% confidence level. The variance explained by each field for the second mode was only 5% of the total SST variance and 11% of the total precipitation variance (Table 8.5). This pattern did not show any significant correlation with the large-scale circulation patterns (Table 8.6), where the SST homogeneous map showed very small areas of significant correlation in the Atlantic Ocean (Figure 8.7a, Mode 2).
For the third mode, the two fields explained the 5% of the square covariance and the correlation between their expansion coefficients time series was 0.47 (Table 8.4). This mode itself explains 11% of the total SST variance and 5% of the total precipitation variance (Table 8.5). Again, the SST spatial pattern for this mode indicates the tripolar Atlantic SST pattern with a displacement for its subtropical center (Figure 8.7a, Mode 3). Also, this pattern is associated with the NAO index, with the correlation between the time series of the SST expansion coefficients and the NAO index being 0.30 (significant at a 95% confidence level). The heterogeneous correlation map shows

significant negative correlation values at the 95% confidence level over the Syrian coastal region, indicating an increase in autumn rainfall in these areas when the SST abnormally high.

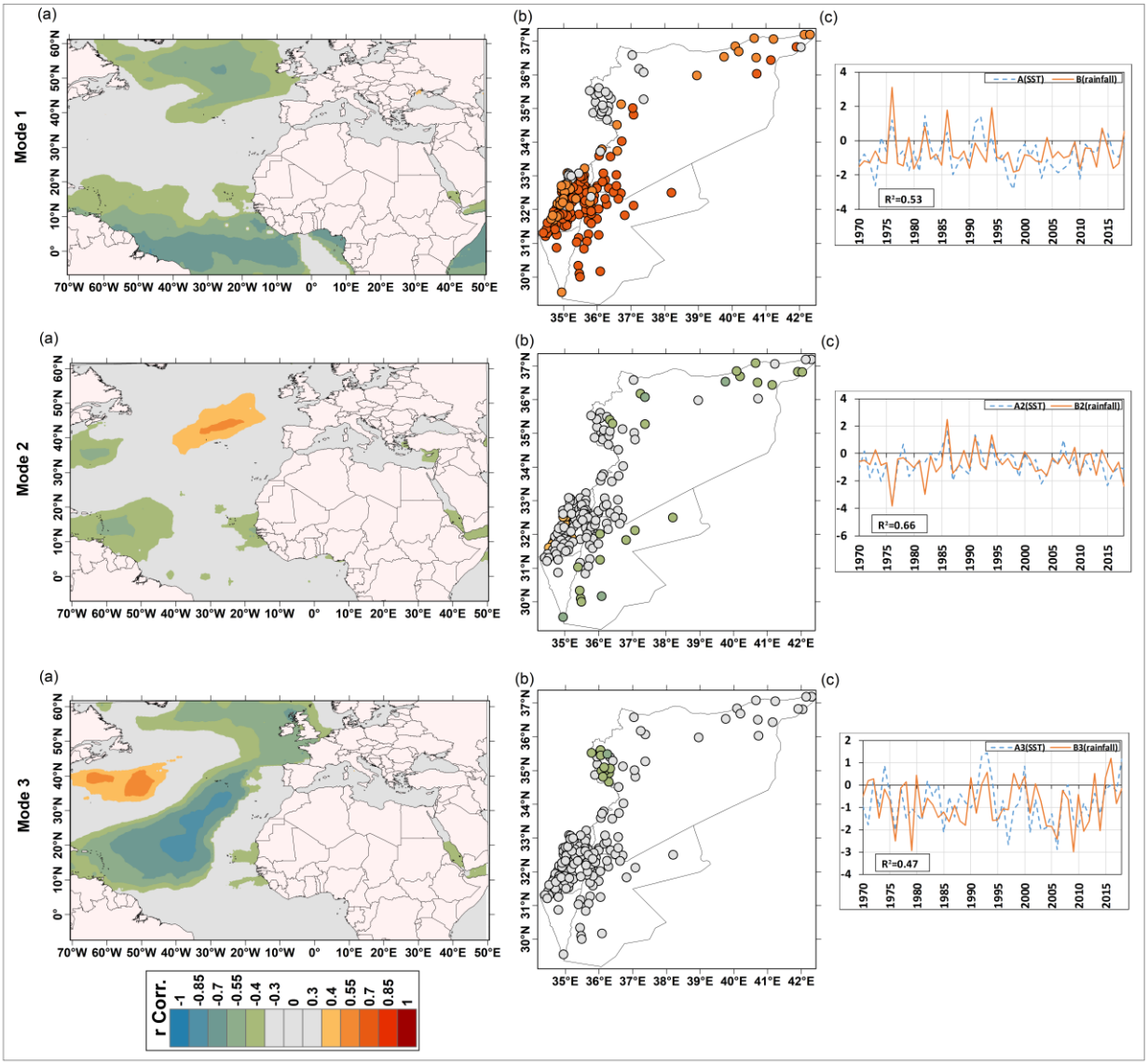

Figure 8.7. As Figure 8.5 but for autumn rainfall.

8.2.3 Covariability between SLP and seasonal temperature

The statistics for the first three SVD modes, including strength of the coupling (STR) and the percentage of squared covariance explained by each mode, that is, the relative importance of each SVD mode (SCF), are listed in Table 8.7. Furthermore, Table 8.8 shows the variance for individual fields (SLP and seasonal temperatures) explained by each mode. Table 8.9 shows the correlations between the left (SLP) expansion coefficients and the teleconnection indices. As can be noted in Table 8.7, SCF shows that the first coupled mode is, for all cases, the most important one, being it is much higher than SCF for modes 2 and 3.

Season	Variable	STR			SLP-seasonal temperatures SCF (%)			Total Sig. Stations (Heterogeneous)
		Mode1	Mode2	Mode3	Mode1	Mode2	Mode3	Modes (1,2,3)
Winter	**Tmax**	0.67	0.63	0.76	97	1	0.3	(59,1,0)
	Tmin	0.80	0.63	0.74	94	2	0.8	(58,1,0)
Spring	**Tmax**	0.57	0.69	0.56	87	4.5	2.9	(56,0,0)
	Tmin	0.59	0.61	0.81	78	4.9	4.4	(53,1,0)
Summer	**Tmax**	0.73	0.67	0.59	70	10	5.5	(53,2,1)
	Tmin	0.74	0.68	0.69	64	10.6	7.5	(50,1,1)
Autumn	**Tmax**	0.68	0.78	0.82	83	5.4	3	(59,1,2)
	Tmin	0.72	0.86	0.77	69	11	5.5	(58,1,1)

Table 8.7. Summary of the strength of the coupling (STR) and the square covariance fraction (SCF) corresponding to the selected modes from SVD of SLP and seasonal temperatures for the period 1987-2017.

Season	Variable	SLP variance (%)			Seasonal Temp. Variance (%)		
		Mode1	Mode2	Mode3	Mode1	Mode2	Mode3
Winter	**Tmax**	36	8	12	85	4	0.5
	Tmin	26	14	5	72	5	3.5
Spring	**Tmax**	19	10	12	77	5	4
	Tmin	15	11	16	65	5	1.7
Summer	**Tmax**	11	19	8.5	56	6	8.5
	Tmin	14	15	13.8	42	7.7	5.8
Autumn	**Tmax**	11	14	7.7	79	3	2.8
	Tmin	6	17	8	72	3	3

Table 8.8. The variance in individual fields (SLP and seasonal temperatures) that are explained by each mode.

Season	Variable		WEMO	EA/WR	NAO	EA	MO	NCP	ENSO
Winter	**Tmax**	**M1**	-0.01	**0.44**	**0.73**	0.08	**0.57**	**0.65**	0.08
		M2	0.44	-0.17	0.61	0.32	0.32	-0.12	0.23
		M3	-0.05	-0.30	0.05	-0.59	0.15	0.03	0.39
	Tmin	**M1**	0.02	**0.43**	**0.76**	0.14	**0.59**	**0.65**	0.10
		M2	-0.05	-0.37	-0.03	-0.62	0.16	-0.11	0.66
		M3	0.07	0.42	0.20	0.25	0.34	0.35	-0.68
Spring	**Tmax**	**M1**	**-0.45**	0.19	**0.52**	-0.04	**0.66**	**0.57**	**-0.47**
		M2	-0.11	0.31	0.38	-0.16	0.12	0.26	0.56
		M3	0.07	0.03	0.56	0.24	0.44	0.47	-0.07
	Tmin	**M1**	**-0.43**	0.26	**0.56**	-0.04	**0.64**	**0.55**	**-0.45**
		M2	-0.11	-0.16	0.32	0.11	0.53	0.43	-0.48
		M3	-0.11	0.18	0.46	-0.05	0.25	0.45	0.43
Summer	**Tmax**	**M1**	-0.19	**-0.38**	**-0.37**	0.18	0.21	**-0.41**	**0.74**
		M2	0.21	-0.31	0.55	0.50	0.29	0.32	0.05
		M3	-0.05	-0.02	0.40	0.01	0.36	0.22	0.47
	Tmin	**M1**	-0.21	-0.34	-0.20	0.18	0.18	-0.26	**0.78**
		M2	0.12	-0.34	0.23	0.42	0.06	0.08	-0.06
		M3	0.14	-0.12	0.81	0.28	0.21	0.54	0.23
Autumn	**Tmax**	**M1**	**-0.53**	0.12	**0.60**	-0.08	0.26	**0.71**	-0.14
		M2	0.02	-0.35	-0.25	-0.17	-0.10	-0.13	0.63
		M3	-0.46	0.20	-0.29	-0.11	-0.25	-0.08	0.20
	Tmin	**M1**	**-0.41**	-0.14	**0.52**	-0.08	0.09	**0.70**	**0.39**
		M2	0.23	-0.28	-0.46	0.00	-0.29	-0.40	0.62
		M3	-0.20	0.21	-0.25	-0.21	0.29	0.00	-0.33

Table 8.9. Correlations between the left expansion coefficients of the selected SLP modes and the teleconnection indices, from the SVD of SLP and seasonal temperatures.

8.2.3.1 Winter Tmax and Tmin covariability

The results show that the first three leading modes of the coupled variability from the SLP and winter-Tmax of the Levant account for 98.3% of the total square covariance (Table 8.7). The SCF value for the first leading mode is found to be 97%, which means that the first leading mode explains 97% of the combined covariance of the SLP and winter-Tmax (Table 8.7). Furthermore, the first mode explains 36% of the total SLP variance and 85% of the total winter-Tmax variance (Table 8.8). The correlation coefficient is then calculated between the expansion coefficients of SLP and winter-Tmax to indicate the strength of each mode's coupling (Table 8.7). The first, second, and third-leading modes have correlations equal to 0.67, 0.63, and 0.76, respectively, significant at $p < 0.05$ level (Table 8.7). For winter-Tmin, the SCF value for the first leading mode is f 94%, with the strength of the coupling of 0.80 (Table 8.7). Furthermore, the first mode explains 26% of the total SLP variance and 72% of the total winter-Tmin variance (Table 8.8).

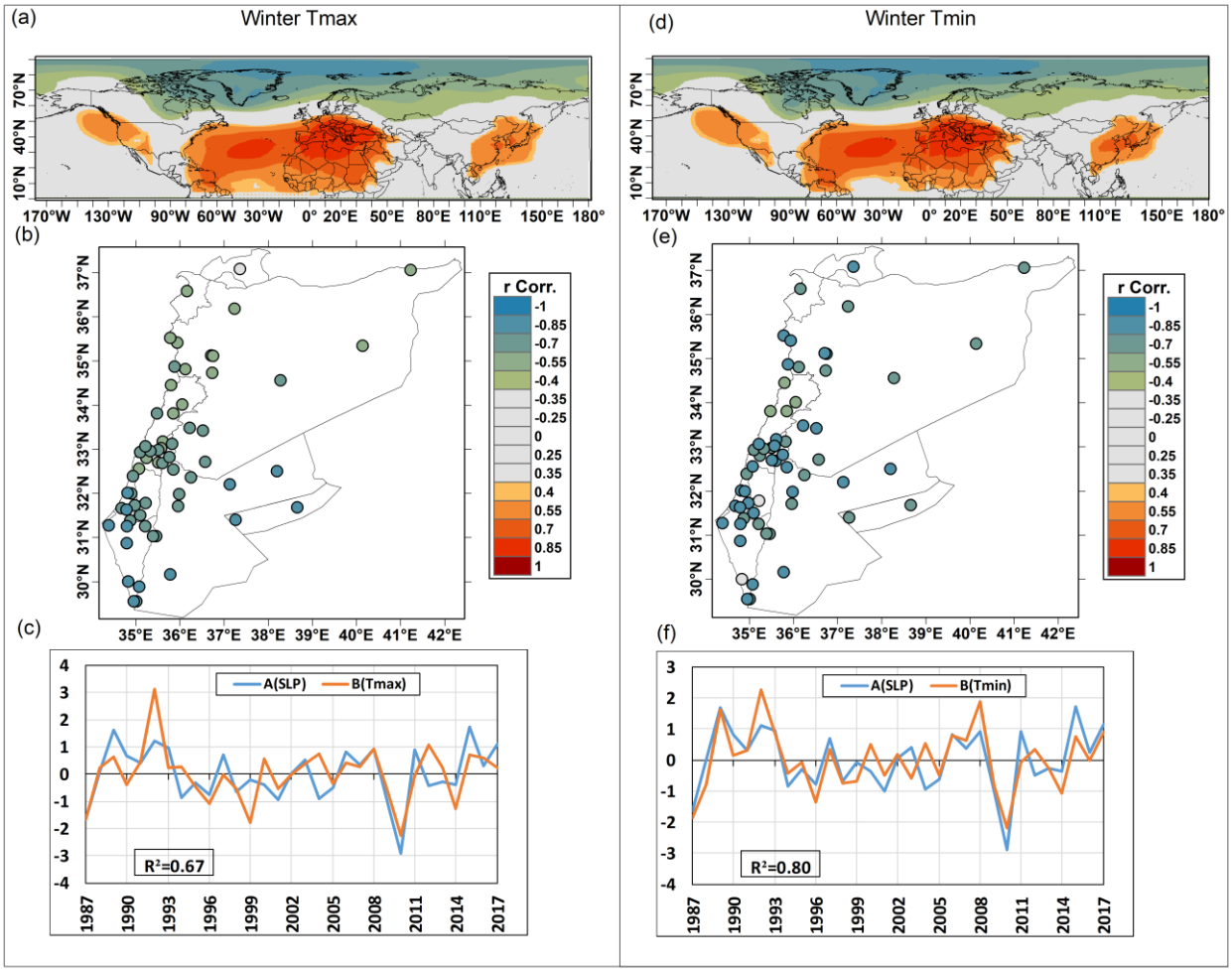

Figure 8.8. (a) Homogeneous map, (b) heterogeneous map, and (c) left (SLP) and right (winter temperature) normalized expansion coefficient time series for the mode 1 from the SDV of SLP and winter-Tmax. (d), (e), and (f) as (a), (b) and (c) but for winter-Tmin, respectively.

Figure 8.8 shows the heterogeneous and homogeneous correlation maps, and the expansion coefficients time series for the first leading SLP and winter-temperature (winter-Tmax, from a to

c, and winter-Tmin, from d to f) coupled mode, which determine how well the right (winter-Tmax/Tmin) field can be reconstructed from the left (SLP) field. The homogeneous maps (Figures 8.8a and 8.8d) show a significant correlation center (up to 0.85) over the central part of the Atlantic Ocean that extends over the Mediterranean Sea and Europe, while negative correlations are found at higher latitudes. When correlating the left expansion coefficients of the first modes with the teleconnection indices (Table 8.9), the highest and significant correlations were found with the NAO, NCP, MO, and EA/WR indices by 0.73, 0.65, 0.57, and 0.44 for winter-Tmax, and 0.76, 0.65, 0.59, and 0.43 for the winter-Tmin, respectively.

In addition, winter-Tmax and Tmin exhibited significant negative correlations with the NAO, NCP, MOI, and EA/WR indices (Figure 4.10). More than 97% of the stations for winter-Tmax and Tmin) significantly correlated with this mode (Table 8.7, Figures 8.8b and 8.8e, respectively). These results provide us the evidence that SLP is a crucial factor that explains the variability of the regional winter-Tmax and Tmin.

8.2.3.2 Spring Tmax and Tmin covariability

Figure 8.9 shows the results of the SVD between SLP and spring-Tmax and Tmin over the Levant region for the first coupled mode. For spring-Tmax, a total of 87% of the square covariance is explained by the first mode, and the strength of coupling between both variables is 0.73 (Table 8.7, Figure 8.9c). The first mode also explains 19% of the SLP variance and 77% of the spring-Tmax variance (Table 8.8). For the spring-Tmin, the first SVD mode accounts for 78% of the variance from the joint SLP and spring-Tmin dataset. The expansion coefficients of SLP and spring-Tmin are highly correlated, yielding a correlation coefficient of 0.59 (Table 8.7, Figure 8.9f). The first mode also explains 15% of the total SLP variance and 65% of the spring-Tmin variance (Table 8.8).

Figures 8.9a and 8.9d show the SLP spatial pattern for the first coupled mode for the spring-Tmax and Tmin, respectively. It is characterized by a center of high significant positive correlations (> 0.70) over the Middle latitudes (e.g., Europe, North Africa, Mediterranean Sea, Red Sea, and southern Asia). Moreover, significant negative correlations for the SLP are seen over high latitudes (60ºN-90ºN). The spring-Tmax and Tmin patterns in Figures 8.9b and 8.9e are marked by widespread significant negative correlations over all parts of the Levant region. Additionally, the SLP pattern is positively connected with the MO, NAO, and NCP indices, whereas it is negatively associated with the WEMO and ENSO indices (Table 8.9). In Figure 4.10, the MO, NAO, and NCP indices are negatively correlated with the spring-Tmax and Tmin, which indicates when these indices and the second SLP mode increase, the spring-Tmax and Tmin are expected to decrease.

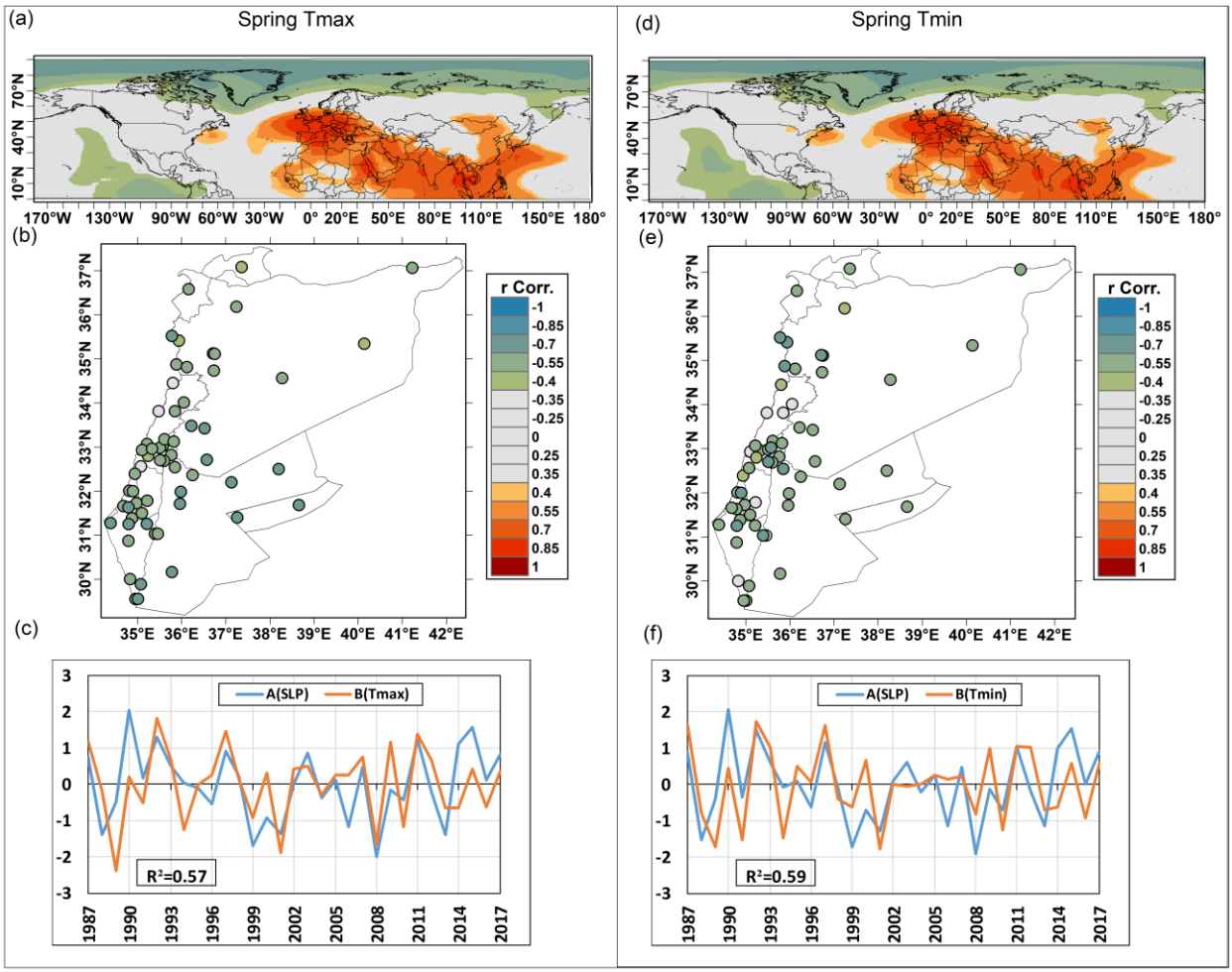

Figure 8.9. As Figure 8.8 but for spring temperatures.

8.2.3.3 Summer Tmax and Tmin covariability

For summer-Tmax (Figure 8.10, left panel), the first SVD mode explains 70% of the square covariance between the SLP and summer-Tmax, and the strength of the coupling between both variables is 0.73 (Table 8.7, Figure 8.10c). The first mode also explains 11% of the SLP variance and 56% of the summer-Tmax variance (Table 8.8).

For summer-Tmin (Figure 8.10, right panel), the first SVD mode accounts for 64% of the variance from the joint SLP and summer-Tmin dataset. The expansion coefficients of SLP and summer-Tmin are highly correlated, yielding correlation of 0.74 (Table 8.7, Figure 8.10e). The first mode explains 14% of the SLP variance and 42% of the summer-Tmin variance (Table 8.8).

Figures 8.10a and 8.10d show that the SLP pattern for this first coupled mode is characterized by significant positive correlations ($r > 0.70$) in the tropical Pacific region, which indicates the ENSO signature. Furthermore, the southern parts of the North Atlantic Ocean and northern Europa display negative SLP anomalies. A strong correlation of 0.74 was found between the left (SLP) expansion coefficients and the ENSO index for the summer SLP-Tmax and of 0.78 for the summer SLP-Tmin (Table 9). From the heterogeneous summer- Tmax and Tmin maps (Figures 8.10b and

8.10e), more than 83% of the stations exhibited a significant positive correlation with this mode. In addition, the summer-Tmax and Tmin positively correlated with the ENSO pattern by an average of 0.41 and 0.52, respectively (Figure 4.10).

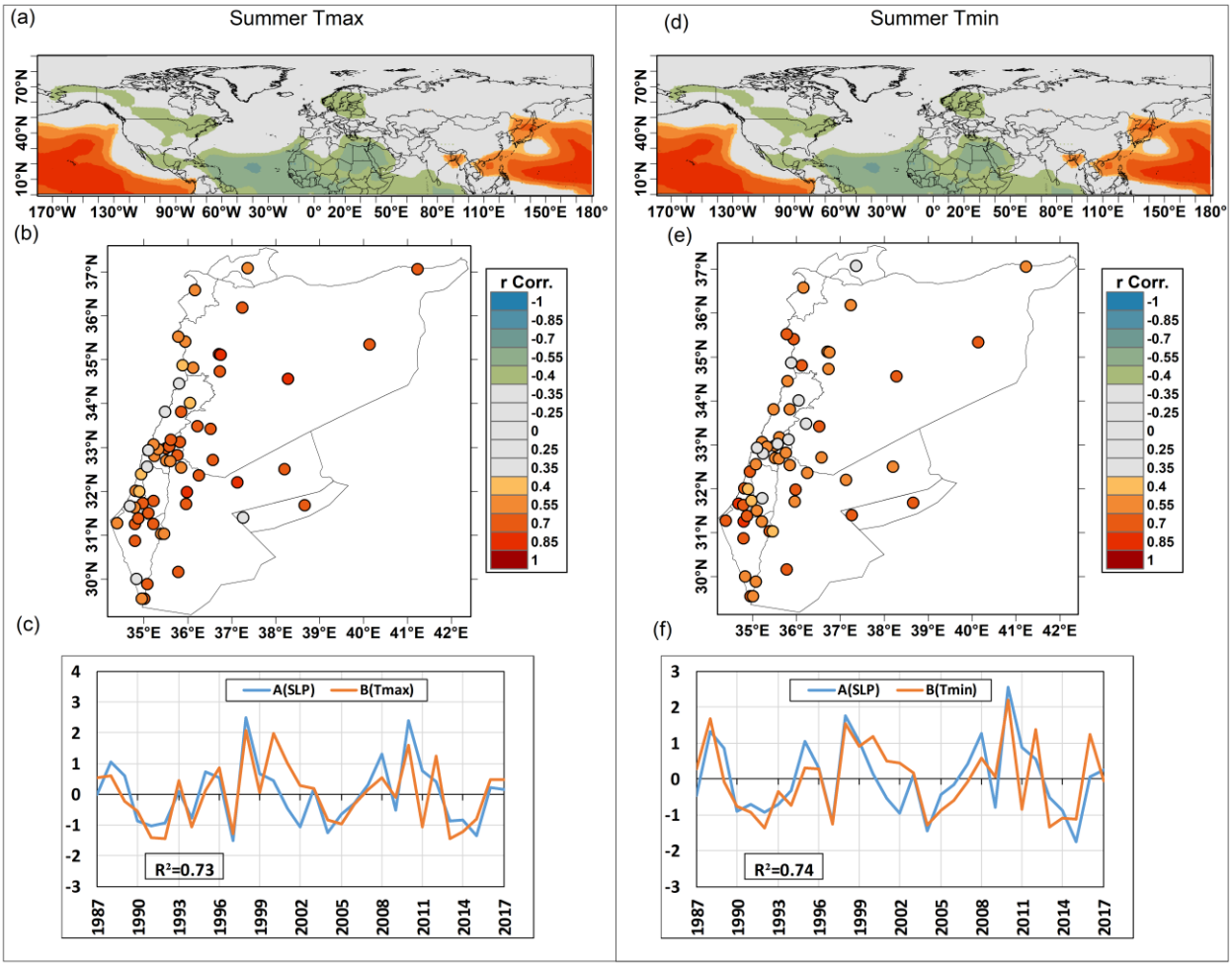

Figure 8.10. As Figure 8.8 but for summer temperatures.

8.2.3.4 Autumn Tmax and Tmin covariability

The first coupled pattern between SLP and autumn-Tmax (Figure 8.11, left panel) is responsible for 83% of the SCF, with a strength of the coupling is 0.68 (Table 8.7). The first SVD mode explains 11% and 79% of SLP and autumn-Tmax variance, respectively (Table 8.8). For the autumn-Tmin, the first SVD mode accounts for 69% of the variance from the joint SLP and autumn-Tmin dataset. The expansion coefficients of SLP and autumn-Tmin are highly correlated, yielding a correlation coefficient of 0.72 (Table 8.7). In addition, the first mode explains 6% of the SLP variance and 72% of the autumn-Tmin variance (Table 8.8).

The homogenous maps (Figures 8.11a and d) present a significant positive correlation center that extends from Europe to the Mediterranean Sea and northern Africa. On the other hand, the heterogeneous maps (Figure 8.11b and e) show significant negative correlations with 97% of the stations. The left (SLP) expansion coefficient for the first mode are positively correlated with the

NCP index by 0.71 and 0.70 for autumn-Tmax and -Tmin (Table 8.9), and the NCP index showed a negative correlation with the autumn-Tmax and -Tmin of -0.66 and -0.61(Figure 4.10).

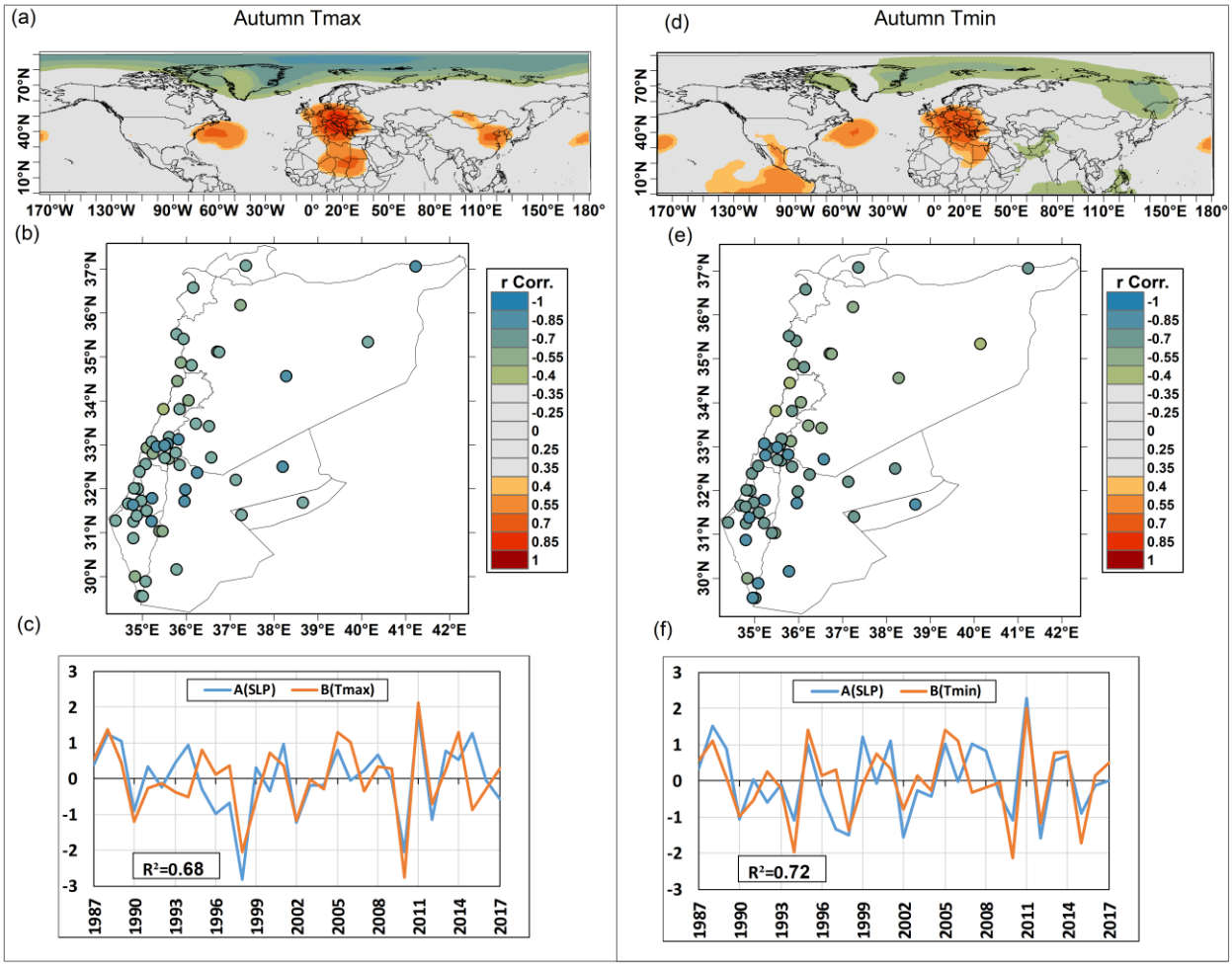

Figure 8.11. As Figure 8.8 but for autumn temperatures.

8.2.4 Covariability between SLP and seasonal rainfall

In this section, the Levant rainfall and the SLP relationships are investigated using an SVD analysis. Table 8.10 shows the percentage of the SCF and the temporal correlation between the pairs of expansion coefficients for the first three modes of the SVD analysis to give us an idea of the coupling strength. Furthermore, Table 8.11 shows the variance for individual fields (SLP and seasonal rainfall) explained by each mode. Table 8.12 shows the correlations between the left (SLP) expansion coefficients of the selected SVD modes and the teleconnection indices.

Season	STR			SLP-seasonal precipitation SCF (%)			Total Sig. Stations (Heterogeneous)
	Mode1	Mode2	Mode3	Mode1	Mode2	Mode3	Modes (1,2,3)
Winter	0.47	0.54	0.62	42	30	7	(102,22,8)
Spring	0.57	0.54	0.57	65	12	6	(100,24,16)
Autumn	0.58	0.63	0.52	77	7.8	4.9	(145,15,11)

Table 8.10. Summary of the strength of the coupling (STR) and the square covariance fraction (SCF) corresponding to the selected modes from SVD of SLP and seasonal rainfall for the period 1970-2018.

Season	SLP variance (%)			Seasonal rainfall Variance (%)		
	Mode1	Mode2	Mode3	Mode1	Mode2	Mode3
Winter	7	18.5	8.8	53	11	4
Spring	17	10	8	40	13	7
Autumn	13	9	6	61	10	7

Table 8.11. The variance in individual fields (SLP and seasonal rainfall) that are explained by each mode.

Season		WEMO	EA/WR	NAO	EA	MO	NCP	ENSO
Winter	**M1**	-0.11	-0.01	**0.56**	-0.13	0.21	0.27	**0.40**
	M2	-0.18	**0.58**	**0.74**	0.17	**0.55**	**0.68**	-0.20
	M3	0.04	0.24	0.21	0.01	0.10	0.11	**-0.42**
Spring	**M1**	**-0.43**	0.13	**0.52**	-0.11	**0.44**	**0.57**	-0.14
	M2	0.06	0.21	**0.58**	0.26	**0.58**	0.21	-0.20
	M3	0.11	-0.20	-0.11	0.26	0.26	-0.15	-0.57
Autumn	**M1**	-0.17	**0.38**	**0.35**	0.03	-0.01	0.22	**-0.79**
	M2	-0.05	0.17	**0.48**	-0.12	-0.06	0.17	-0.27
	M3	0.38	-0.26	-0.38	0.16	-0.39	-0.51	-0.10

Table 8.12. Correlations between left expansion coefficients of the selected SLP modes and teleconnection indices, from the SVD of SLP and seasonal rainfall.

8.2.4.1 Winter covariability

The first coupled mode (Figure 8.12, left panel) explains 42% of the square covariance, and the strength of the coupling is 0.47, significant at the 95% confidence level (Table 8.10, Figure 8.12c). The first mode also explains 7% of the total SLP variance and 53% of the winter-rainfall variance (Table 8.11). The homogeneous map (Figure 8.12a) shows a center of significant positive correlation (r> 0.70) over the central area of the Atlantic Ocean, which extends to the Mediterranean Sea, and also significant correlations (r>0.55) are in the equatorial and higher latitudes in the Pacific Ocean. These correlations are indicating the potential NAO and ENSO effects that significantly correlate with the left (SLP) expansion coefficients time series by 0.56 and 0.40, respectively (Table 8.12). The heterogeneous map couples this mode with rainfall variability in central Palestine, northern Palestine and Jordan, and the Syrian coastal area (Figure 8.12b). Therefore, this pattern is responsible for a generalized decrease in winter-rainfall in these regions.

The second mode (Figure 8.12, right panel) explains 30% of the square covariance with a strength of the coupling of 0.54, significant at the 95% confidence level (Table 8, Figure 8.12f). Furthermore, the second mode explains 18.5% of the total SLP variance and 11% of the winter-rainfall variance (Table 8.11). The homogeneous map (Figure 8.12d) shows a center of high significant positive correlation (up to 0.85) that extends from the Atlantic over Europe, north of Africa, and the Mediterranean Sea. This result is associated with the effects of the NCP, MO, and NAO indices, which significantly correlate with the second left (SLP) expansion coefficients time series by 0.68, 0.55, and 0.74, respectively (Table 8.12). The heterogeneous map couples this mode with rainfall variability in the Syrian coastal area (Figure 8.12e).

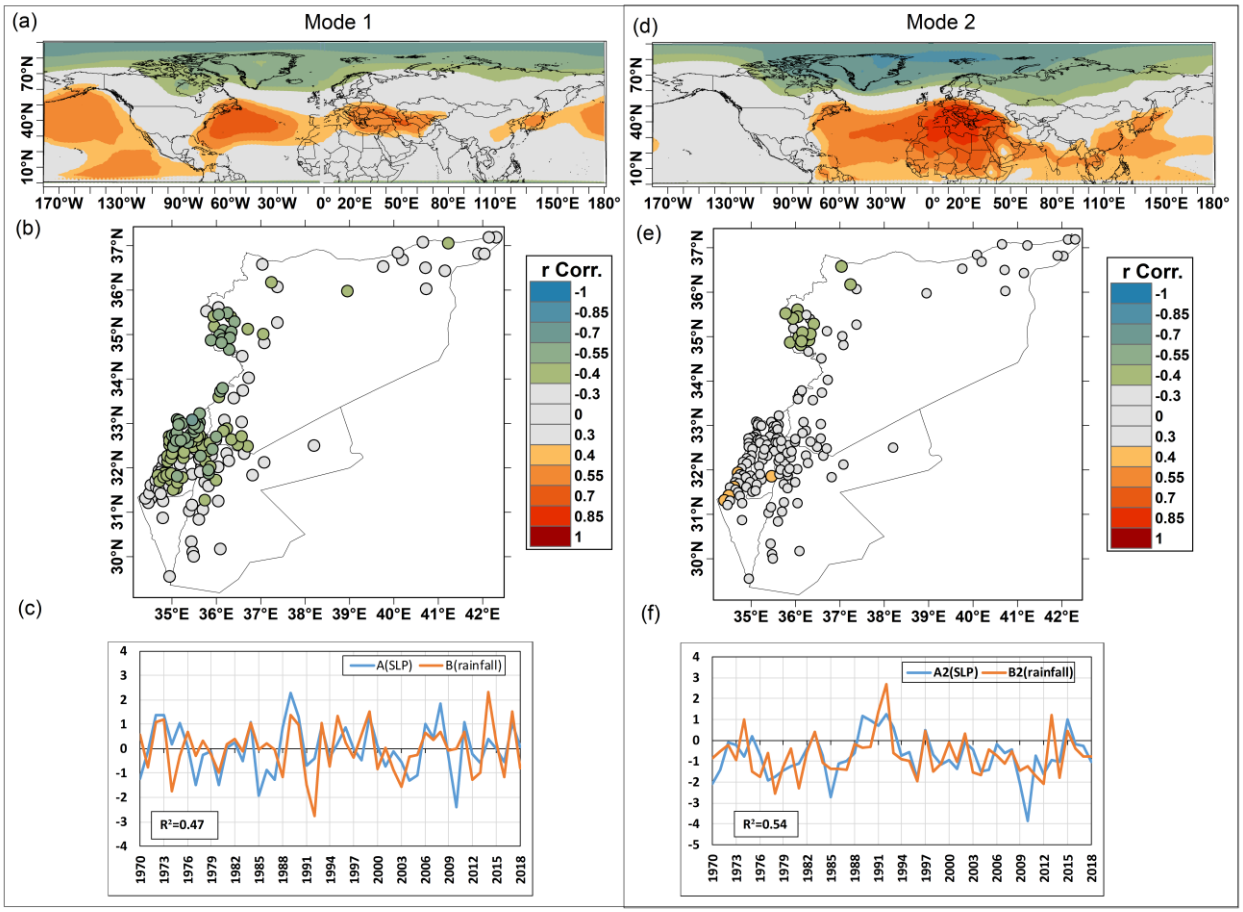

Figure 8.12. (a) Heterogeneous map, (b) homogeneous map, (c) left (SLP) and right (winter-rainfall) normalized expansion coefficient time series for the coupled Mode 1 obtained from SVD of SLP and winter-rainfall. (d), (e), and (f) are as (a), (b) and (c) respectively but for the coupled Mode 2.

8.2.4.2 Spring covariability

Figure 8.13 presents the results of the homogeneous correlation maps (Figures 8.13a and d) for the first two SLP modes obtained by the SVD in spring, together with the heterogeneous correlation maps for spring-rainfall (Figures 8.13b and e), and the temporal variability of each mode, represented by their respective expansion coefficient time series (Figures 8.13c and f).

The first mode explains 65% of the squared covariance, and the strength of the coupling reached 0.57 (Table 8.10, Figure 8. 13c). Furthermore, the first SVD mode explains 17% and 40% of the total variance for the SLP and spring rainfall, respectively (Table 8.11). The homogeneous map (Figure 8.13a) exhibits a pattern of positive correlations (r> 0.70) over Europe and western Mediterranean that extends through the Atlantic until North America. The NCP, MO, and NAO indices significantly correlate with this left expansion coefficient time series by 0.57, 0.44, and 0.52, respectively (Table 8.12). The heterogeneous map couples this mode with rainfall variability in the southern Levant, mainly in Palestine (Figure 8.13b). This pattern is responsible for a generalized increase in spring-rainfall, mostly in Palestine.

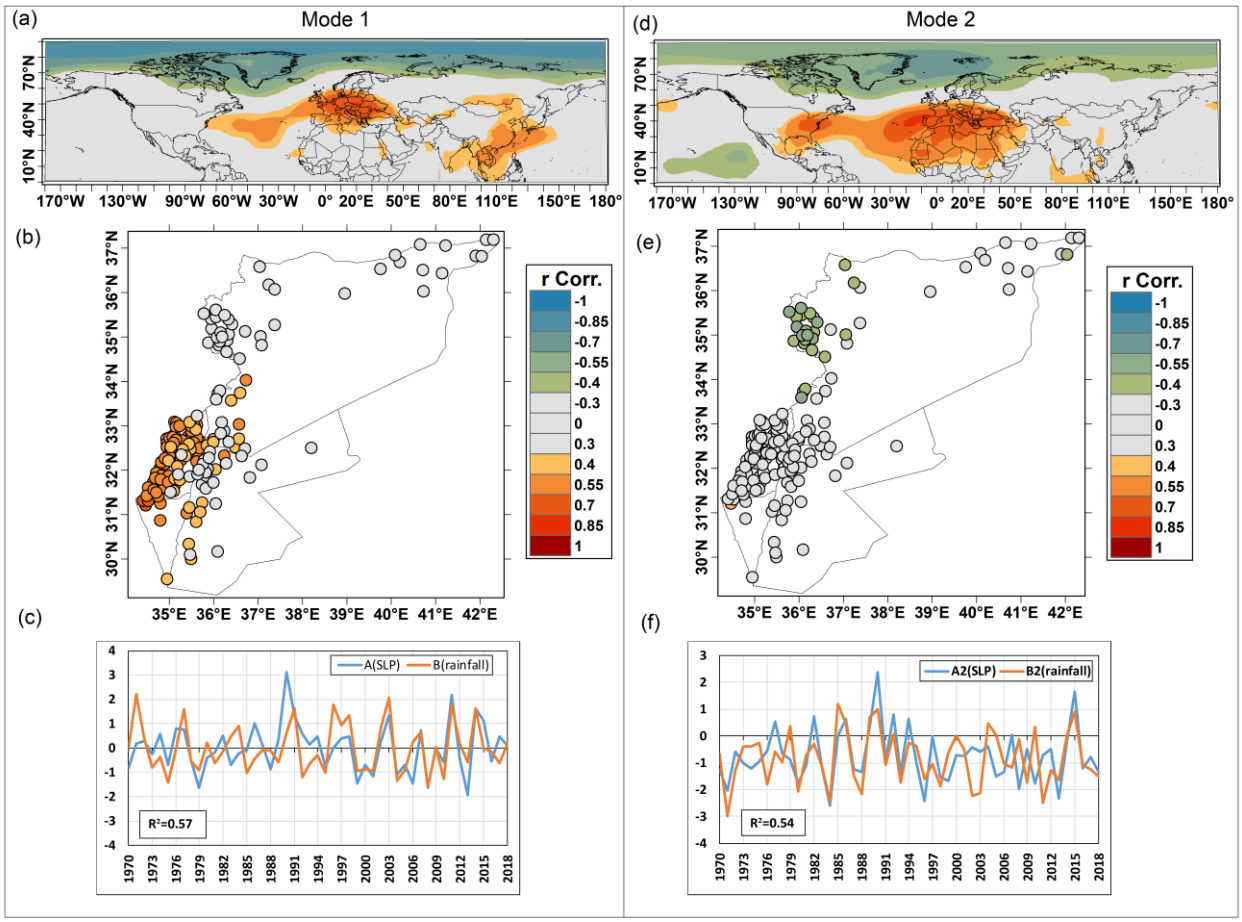

Figure 8.13. As Figure 8.12 but for spring rainfall.

The second coupled mode (Figure 8.13, right panels) between the SLP and the spring-rainfall explains 12% of the SCF and presents a strength of the coupling of 0.54 (Table 8, Figure 8.13f). It explains 10% and 13% of the total variance of the SLP and spring-rainfall, respectively (Table 8.11). From the homogeneous pattern (Figure 8.13d), the most intense positive values of correlation (> 0.70) are located over Europe, extending through the central Atlantic Ocean to the eastern coasts of North America (Figure 8.13d). Again, this pattern is associated with the NAO and MO indices. The correlation between the time series of the SLP expansion coefficients and these teleconnection indices is 0.58, significant at the 95% confidence level (Table 8.12). The heterogeneous correlation map (Figure 8.13e) shows a significant negative correlation at the 95% confidence level over the Syrian coastal area. It is indicating a decrease in spring-rainfall in these areas of the Levant during this mode's positive phase.

8.2.4.3 Autumn covariability

During autumn, the first coupled mode explains 77% of square covariance, with a couple of strength between the SLP and the autumn-rainfall of 0.58, which provides the highest square covariance among all the seasons (Table 8.10, Figure 8.14c). Also, it is important to note that the second mode of coupled variability in autumn explains the lowest SCF (7.8%) compared to that

explained by the second mode for winter (30%) and spring (12%) (Table 8.10). The first mode explains 61% of the total variance of the autumn-rainfall and 13% of the SLP variance (Table 8.11). Its homogeneous SLP spatial pattern (Figure 8.14a) shows a structure associated with ENSO index, with two action centers varying in opposite phase located over the western and eastern parts of the tropical Pacific Ocean. The correlation between the SLP expansion coefficient time series associated with the first mode and the ENSO index is -0.79 (Table 8.12), being significant at the 95% confidence. In addition, the autumn-rainfall averaged for the Levan was found negatively correlated with the ENSO index by -0.34 (see Figure 6.22 in Chapter 6). This implies a decrease in autumn rainfall when the SLP over the western and eastern parts of the tropical Pacific Ocean increases and vice versa. On the contrary, positive correlation were found in the southern part of the North Atlantic Ocean, South Africa and Asia, with high value in the northern Indian Ocean (r > 0.85) (Figure 8.14c). As shown in Figure 8.14b, all locations except Syrian coastal area showed positive and significant correlation with the SLP in these regions.

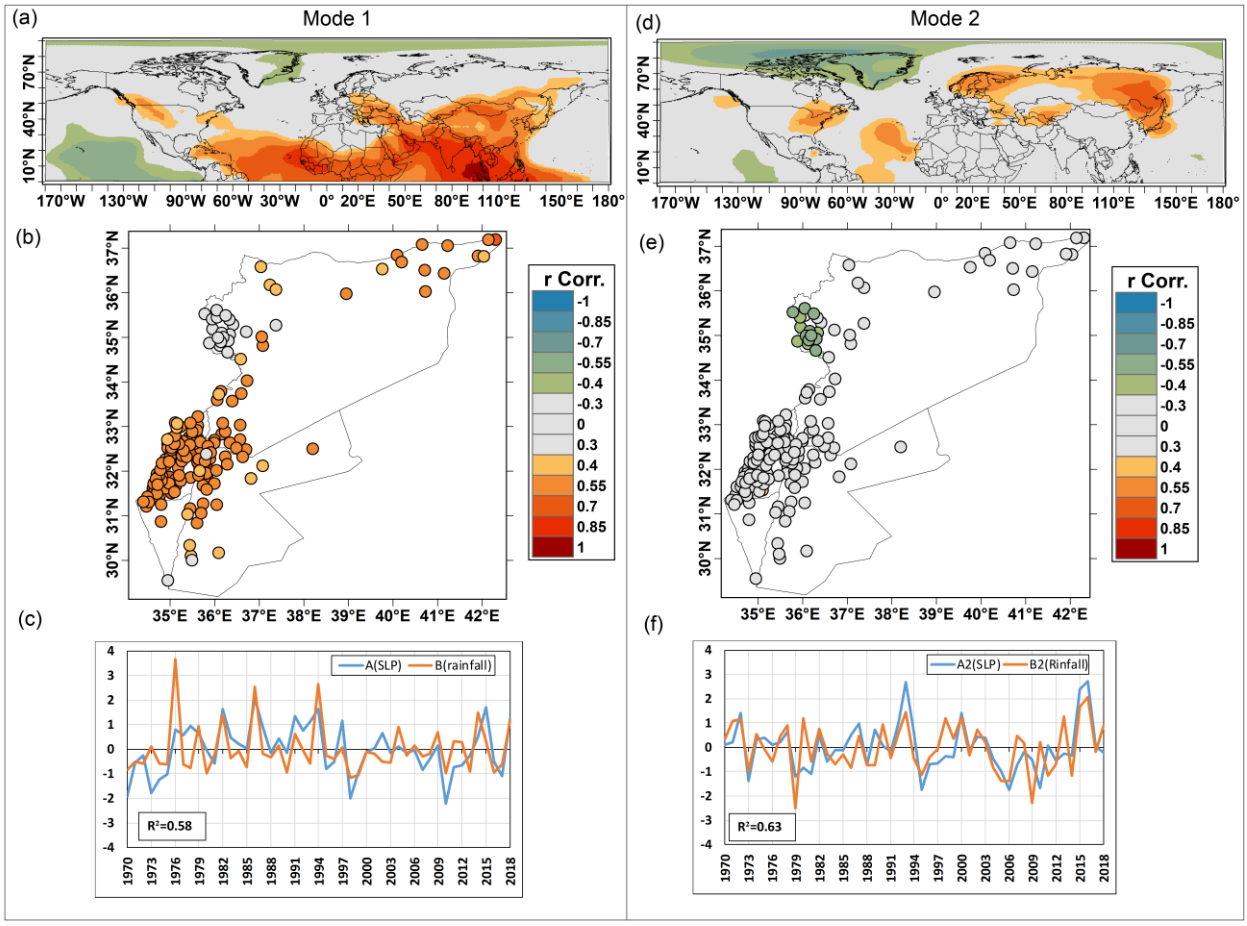

Figure 8.14. As Figure 8.12 but for the autumn rainfall.

The second coupled mode (Figure 8.14, right panels) between the SLP and the autumn-rainfall explains 7.8% of the SCF and presents a strength of the coupling of 0.63 (Table 8, Figure 8.14f). It explains 9% and 10% of the total variance of the SLP and spring-rainfall, respectively (Table 8.11). The second mode exhibited positive significant correlations over the northeastern Asia, the

Scandinavian Peninsula, and eastern coast of America. The SLP over these regions negatively correlated with the rainfall in the Syrian coast. On the other hand, negative significant correlations were found over the Greenland and most northern Canada, which positively correlated with the rainfall in the Syrian coast.

8.3 Conclusions and discussion

In this study, the SVD technique was applied to investigate the influence of two indicators of climate variability, Atlantic and Mediterranean SST and North Hemisphere SLP, on the seasonal temperatures (Tmax and Tmin) and precipitation variability over the Levant region. The main conclusions can be given as follow:

1. The analysis provides strong evidence for the influence of the Atlantic Ocean and Mediterranean Sea SST and the North Hemisphere SLP on the long-term behavior and variability in the Levant seasonal temperatures and precipitation. The leading SVD modes suggest that along with the complex topography of the Levant, many physical processes that are linked to large-scale ocean-atmospheric circulation interactions (e.g., winds speed, air temperatures, humidity, and heat flux) dominates the Levant temperatures and precipitation variability.
2. The strength of SST/SLP-seasonal temperature coupling (> 0.59) is much higher than the strength of the first SST/SLP-seasonal rainfall coupling mode (<0.59). Both the SST and the SLP account for roughly the same percentage of seasonal temperature variation (up to 85% of the winter-Tmax). Similarly, the SST and SLP account for similar percentages of total precipitation variance (up to 61% of the autumn rainfall). In addition, the SCF values calculated for SST/SLP-seasonal temperatures are generally higher than those calculated for SST/SLP-seasonal rainfall. These two large-scale indicators, SST and SLP, explain temperature variability better than precipitation variability, which could be due to the higher spatial and temporal variability of precipitation, especially in transition seasons, than temperatures.
3. Only the first mode was chosen for seasonal temperatures because the SCF values for the second and third SST/SLP-seasonal temperature coupled modes are always below 10%, and only a small number of stations are significantly correlated with them. On the other hand, this indicates that the temperatures in the study area are fairly consistent. When the North rule was used to determine the number of principal components that should be retained from PCA, the same results were obtained.
4. With the exception of spring for the first and second modes, the Mediterranean SST had a little impact on all seasonal rainfall. It is possible that the relationship between Mediterranean SST and seasonal precipitation in the Levant is not entirely causal, or that both fields are influenced by atmospheric processes. The influence of the Mediterranean SST on seasonal temperature, on the other hand, was more pronounced. Warmer SST in the eastern Mediterranean and Black Sea, are associated with warmer temperatures in all seasons (more details can be found in the following points).

5. The SLP-winter temperatures and rainfall coupled modes revealed that rising SLP over the central North Atlantic (near the Azores), the Mediterranean region, Africa's northern coast, and Europe, which is accompanied by decreasing SLP over the northern latitudes [70ºN-90ºN], leads to lower winter temperatures and rainfall in the Levant. The left SLP expansion coefficients show high significant positive correlations with the NAO, NCP, MO, and EA/WR indices, although its expansion coefficients, with the NAO and NCP showing the highest correlation values. The influence of the NAO, NCP, MO, and EA/WR indices is always negative on temperatures and positive on rainfall, except for the NAO, which has an inverse effect on the first winter rainfall mode.

The homogeneous patterns detected in these coupled modes are also similar to those found in some studies carried out in the Middle East and North Hemisphere region (Attada et al., 2019; Papadimas et al., 2012). The results are also in line with Beranová and Kyselý (2016), who studied the links between teleconnection indices (NAO, MO, and WEMO) and precipitation in the Mediterranean, and they found a similarity of the NAO and MO indices in explaining the drier conditions for positive phases over most of the Mediterranean area. Furthermore, they showed the eastern part of the Mediterranean presents an exception, as there is a positive MO index associated with wetter conditions while a positive NAO index is associated with drier conditions.

Iqbal et al. (2013) studied the influence of Azores High pressure on Middle Eastern rainfall and they found a negative significant correlation between the winter rainfall and the NAO and Azores High pressure and a positive significant correlation with the Icelandic Low pressure. Donat et al. (2014) and El Kenawy et al. (2016) confirmed that the links between the NAO and Middle East climate are best expressed during winter time, compared with the other seasons.

Several studies explain the dynamical mechanism of the NAO influence on the climate variability and general overview of NAO characteristics can be found (Cullen et al., 2002; Hurrell, 1995; Diao et al., 2015; Pinto and Raible, 2012; Visbeck et al., 2001). Note that most studies in literature have focused on central and western Europe, while there are few studies that have examined the effect of the NAO on the east Mediterranean.

The pressure gradient's intensity is determined by the pressure values in the Azores and Iceland, and it is enforced when the NAO index is positive and reduced when it is negative. When the NAO index is positive, the surface wind and winter storm tracks moving from west to east across the North Atlantic are stronger than usual, and vice versa. Wetter and warmer winter conditions are experienced in northern Europe, Scandinavia, and the east coast of the United States as a result of these westerly winds and winter storms track. Winters in Greenland, the Mediterranean, and the Middle East, including the Levant region, are cooler (lower temperatures) and drier (less rainfall). The negative phase of the NAO index, on the other hand, results in a weak westerly wind that may can penetrate south Europe to the Levant region, causing unstable winter conditions (wetter and warmer), while the opposite occurs over northern Europe.

The findings also revealed an inverse relationship between the SLP over central Europe and the air winter temperatures in the Levant region, which can be attributed to strong northerly flow over the Middle East, caused by anticyclones formed over Europe, being responsible for low air

temperatures there (van Loon and Rogers 1978; Bartzokas and Metaxas 1993; Papadimas et al., 2012). In a similar line, Eshel and Farrell (2000) demonstrated that when Greenland's pressure is elevated (negative NAO), an anomalous low/cyclone covers the Mediterranean and southern Europe, extending from the Azores, resulting in EM southerlies (warm wind), enhancing the ascent and thus intensifying rainfall. When Greenland's pressure is reduced, EM northerlies (cold wind) prevail, enhancing subsidence and resulting in less rainfall and drier conditions.

Ghasemi and Khalili (2007) found that a positive NCP (high SLP over the North Sea and low over the Caspian Sea) is linked to increased precipitation and cloudiness, resulting in below-normal temperatures over Iran. During the positive NCP phase, when the anticyclone is amplified in the North Sea, decreased temperature is linked to an increase in northeasterly (cold air) stream, according to Kutiel et al. (2002) and Nastos et al. (2011). Increasing temperature, on the other hand, is associated with increased southeasterly (warm air) stream during the negative NCP phase, as a result of the combined effect of an increased cyclonic anomaly circulation pattern over the North Sea and an increased anticyclone over the Caspian Sea.

Positive pressure anomalies near the British Isles (leading to less rainfall) characterize the EA/WR index's positive phase, while negative pressure anomalies in the Caspian Sea region characterize the index's negative phase (leading to more rainfall from northeast Africa to eastern Turkey and Black Sea region). The Azores High pressure center expands towards continental Europe in the positive phase, resulting in cold air advection from the north towards the southern part of Europe and the eastern Mediterranean region, with increased moisture transport from the Black Sea (Krichak and Alpert, 2005; Lim, 2014; Baltac et al., 2017). The negative phase is characterized by the occurrence of opposite conditions.

For the MO index, it generally shows similarities with the NAO pattern compared to other Mediterranean indices, with both positive (negative) phases characterized by higher (lower) SLP anomalies over the Mediterranean (Criado-Aldeanueva et al., 2014; Criado-Aldeanueva and Soto-Navarro, 2020). The effect of the MO on the winter temperatures and rainfall is mainly due to inforce the Mediterranean cyclogenesis. Both the NCP and MO indices affect temperature and rainfall in a similar way or seesaw behavior inside the Mediterranean basin (Ciarlo`and Aquilina, 2015; Conte et al., 1989). During the MOI positive phase, positive SLP is found in the west Mediterranean and negative in the east, resulting the east Mediterranean affected by a northerly circulation bringing cold air masses and lower temperatures to that region (Maheras and Kutiel, 1999; Conte et al., 1989). The pattern of positive MO index leads to positive precipitation anomalies in eastern Mediterranean and Levant, and the negative MO leads to negative precipitation anomalies (Beranová and Kyselý, 2016; Redolat et al., 2019; Ramadan et al., 2012; Törnros, 2013). This is due to the high geopotential height over the west that inhibits upward movement (that is required for rainfall) and leads to stable and sunny weather in these regions. This condition is primarily due to an atmospheric blocking generated in the western Mediterranean, where westerlies are reduced and storm tracks such as Cyprus Low along the eastern Mediterranean are favored (Redolat et al., 2019).

6. The results of the SST-winter temperatures reflect the tripolar SST structure marked by the same sign in the north and south of the North Atlantic Ocean and a different sign in the middle. This pattern is accompanied by a bipolar positive structure in the eastern Mediterranean, Red Sea, and eastern Black Sea. Furthermore, the findings could point to a shared action between the synoptic Atlantic SST and the Mediterranean Sea's regional SST. The NAO, MO, and NCP indices showed significant negative correlations with the left SST expansion coefficients.
7. The tripolar pattern, in which the Levant receives more precipitation when the SSTs in the north and tropical Atlantic are abnormally warm, is also reflected in the first and second SST-winter rainfall coupled modes. These two modes highly showed significant negative correlations with the NAO index, and significantly correlated with the most locations in the Levant for the first mode, and few locations in south Palestinian cost for the second mode.

The SST variability in the Atlantic has been shown to influence global and regional climate, particularly in the Northern Hemisphere (Sutton and Hodson, 2005; Sutton and Dong, 2012; Ehsan et al., 2020; Zhou and Wu, 2016; Black, 2011). The intrinsic modes of atmospheric circulation variability, such as the NAO index, imprint themselves on the SST field primarily via surface energy fluxes, wind regimes, and latent heat exchanges (Deser et. al., 2010). This tripole SST structure is dominant in the subpolar-tropical Atlantic during the winter (Wallace et al. 1990; Da Costa and Colin de Verdiere 2002), and the SST tripole has been shown to be influenced by the NAO's atmospheric forcing (Cayan, 1992; Marshall and Johnson, 2001; Wallece et al., 1990; Cullen et al., 2002; Kumar et al., 2017).

Kumar et al. (2017) found a trioplar SST structure similar to that found in this study when they investigated the north Atlantic effect on wintertime warm extremes trends in the Middle East. Compared to other indices, we found higher significant correlations between the NAO and the left SST expansion coefficients, ranging from -0.53 to -0.66 for both temperature and rainfall patterns, indicating that the tripole and the NAO have a strong relationship.

Because of stronger westerly and northeast trade winds, the Atlantic Ocean loses energy to the atmosphere over the subpolar and tropical regions during the NAO positive phase. The increased turbulent heat flux from the ocean to the atmosphere is caused by these strong winds. The Atlantic, on the other hand, gains energy in the middle latitudes due to lower wind speeds, resulting in a lower turbulent heat flux out of the ocean (Cayan 1992; Marshall et al., 2001; Visbeck et al., 2003; Jing et al., 2020). This means that when the NAO is in a positive phase, the SST in the subpolar and tropical Atlantic will be colder than normal, and in the multitudes higher than normal, resulting in a drop in winter Levant temperatures and rainfall, and vice versa.

Many studies have found that atmospheric processes in the Atlantic influence SST variability in the Mediterranean Sea (Traigo et al., 2002; Skliris et al., 2011; Marullo, 2011; Oguz, 2005; Türkes, 1996). In this context, the results showed a significant negative correlation between the NAO and SST of the east Mediterranean and Black Seas, which is also documented in many other studies (Rixen et al., 2005; Skliris et al., 2011; Oguz, 2005; Kazmin and Zatsepin 2007).

In general, the SST of the Eastern Mediterranean and Black Seas is strongly and positively related to all seasonal temperatures. As previously stated, a positive NAO pattern indicates strong westerlies, whereas a negative case indicates westerlies weakening. If the westerlies are weak, another large-scale process may take over, bringing a local northeasterly cold wind regime over the Caspian and Black Seas. The combination of a negative NAO phase and a positive NCP and EAWE patterns, according to Krichak et al., (2002), motivates the conditions for the predominance of northeasterly winds over the east Mediterranean. Northeasterly winds dominate over the Caspian and Black Seas during the positive phase of the NCP index, bringing cold air to the region and causing a decrease in SST, which leads to lower seasonal Levant temperatures. Similarly, during the negative phase of the NCP index, the winds blow primarily from the southwest, bringing warm air from these regions and, as a result, increasing SST, which leads to higher seasonal temperatures (Kazmin and Zatsepin, 2007; Tutsak et al., 2015).

Kumar et al. (2017) indicated that large and persistent Atlantic SST anomalies appear to modulate the occurrence of warm winter spells via the mediation of Mediterranean SSTs, thereby creating the conditions for the development of extended and persistent anticyclonic structures over the Middle East. Warmer SSTs over the eastern Mediterranean enhance evaporation, and the strong anticyclonic structures prevailing over the eastern Mediterranean and Middle East all help to suppress deep convection and initiate and sustain winter warm spells.

8. The SLP-spring temperatures coupled mode showed rising SLP from the Azores to west Pacific Ocean, Europe, north Africa, Middle East, and Indian Ocean, is associated with lower than normal temperatures over the Levant, while rising SLP in east Pacific Ocean and northern latitudes is associated with higher normal temperatures. The NAO, MO, and NCP indices are also linked to this coupled pattern.
9. The first SLP-spring rainfall coupled mode indicates when the SLP over central Atlantic, central Europe, the North and Caspian Seas, central Mediterranean Sea, Africa's northern coast, and southeastern coastal of Asia is higher than normal, the rainfall in south Levant increases. The second SLP-spring rainfall coupled mode is only relevant in the Syrian coast region, where increasing SLP over the central Atlantic, Europe, the Mediterranean Sea, North Africa, and the Middle East is associated with decreased rainfall, while increasing SLP in northern latitudes is associated with increased rainfall. For the first mode, rainfall in the south Levant was positively correlated with the NCP and MO indices, but negatively correlated with the WEMO index. Furthermore, the second mode resembles the NAO index effect on the Syrian coast area.

A similar SLP structure was also found in studying air temperature variability over the Arabian Peninsula and its links to circulation patterns (Attada et al., 2019). The mechanisms related to the NAO, MO, and NCP influence of temperature and precipitation in the Levant were discussed in conclusion 5.

10. The SST-spring temperatures coupled mode indicated a circulation pattern with a same sign in the central and east of the Mediterranean, Black, Red Seas, and North Seas. The

EA/WR index was the only one that had a significant correlation with SST expansion coefficients.

The EA/WR mechanism that affects temperatures was discussed in conclusions 5 and 6. Note that the EA/WR and NCP mechanisms are similar with both indices related to the SLP differences between the west Europe and Caspian Sea regions.

11. The first spring SST-precipitation coupled mode showed a horseshoe SST shape in the North Atlantic with a different sign, while the SST of the central Mediterranean Sea and North Red Sea showed a same SST sign was found in. This coupled mode exhibited significant correlations with the WEMO, NCP, and ENSO indices. For the second mode, the SST also showed a horseshoe in the North Atlantic with a different sign, while the SST of the east and west Mediterranean Sea exhibited a same sign. This SST pattern only exhibited significant correlation with the NAO index that affects the spring rainfall in the most southern locations from palatine/Israel and Jordan.

In spring, the atmospheric circulation related to the NAO is very weak and no significant, compared to the winter, which may enhances the regional Mediterranean, Black, and Red Seas effects on the climate conditions in the Levant region. The large-scale circulation patterns that connected generally with the Mediterranean area like the EA/WR, WEMO, and NCP indices are significantly correlated with the left SST expansion coefficients.

A warmer SST in the Mediterranean Sea will lead to enhance the water vapor in the atmosphere and a decrease of the vertical stability, which in turn, leads to increase rainfall in the adjacent areas like Levant. Rowell (2003), discovered evidence of increased Sahel rainfall with increased lower tropospheric moisture content, when the Mediterranean SST happened to be warmer than average.

12. The SST-summer temperatures leading mode revealed that warmer-than-normal SST in the subtropical/equatorial and north Atlantic, east Mediterranean, and Caspian Seas leads to higher-than-normal temperatures in the Levant.
13. The SLP-summer temperatures coupled mode revealed that increasing SLP in the tropical/subtropical Pacific Ocean causes temperature increases, while increasing SLP over the tropical/subtropical Atlantic Ocean, Africa, the Indian Oceans, and North Europe causes temperature decreases.

Ehsan et al. (2020) and Attada et al. (2019) found similar SST-summer temperatures and SLP-summer temperatures structures, respectively, for the Arab Peninsula and Middle East. In summer, the Azores High extends eastwards meeting the Balkan High pressure to form one common system (Bitan and Saaroni 1992; Alpert et al., 1990). For SST/SLP-summer temperatures coupled modes, the patterns are strongly correlated with the ENSO index, with significant positive correlations between the left (SST/SLP) expansion coefficients.

Regarding the influence of the Atlantic Ocean on the Middle East summer temperature, Ehsan et al. (2020) suggested that basin-wide North Atlantic SST warming is closely associated with warmer than normal conditions over the Middle East, and conversely, basin-wide North Atlantic SST cooling is closely associated with cooler than normal conditions over the Middle East. They also found a significant positive correlation (0.71) between the leading mode of the summer ME

temperature and spatially averaged SST anomalies in the Atlantic region, which is very close to our results where the STR between SST-summer Tmax/Tmin reached 0.68/0.76.

This Atlantic−ME connection during summer involves ocean–atmosphere interactions through multiple ocean basins, with an influence from the Indian Ocean and the Arabian Sea. Recent studies suggested that the mid-latitude/extratropical Eurasian Rossby wave is an important factor in describing the regional temperature variability during summer (Yadav, 2017). With the subtropical jet stream acting as a waveguide for Rossby waves (Branstator, 2002; Ding and Wang, 2005), successive troughs and ridges of Rossby waves travel along the jet stream and influence the characteristics of the Middle East regional climate (Yadav et al., 2009). Many studies also indicate the tropical Atlantic SST variability is associated with the ENSO (Enfield and Mayer, 1997), which was also documented in this study due to the positive significant correlation between the ENSO and left SST expansion coefficients by 0.56. The ENSO-related Atlantic warmings occur as a result of reductions in the surface NE trade wind speeds, which in turn reduce latent and sensible heat losses (increase SST) over the Tropical Atlantic, which in turn leads to increase summer temperatures in the Levant.

14. For the SLP-autumn temperatures, the coupled structure had a different sign in the area extending from Europe to the Mediterranean Sea and central northern Africa, while it had a same sign in the northern latitudes. In the east Mediterranean and Red Seas, the SST-autumn temperatures coupled mode showed the same sign while in the North Sea, western Mediterranean, and Europe, it showed an opposite sign. The left (SLP/SST) expansion coefficients had high significant correlations (0.70/-0.67) with the NCP index, indicating that this pattern resembles the NCP effect.

Furthermore, it was also documented that the NCP has a high negative impact on autumn temperatures, compared to other indices. In general, the SLP/SST homogeneous patterns are similar to those detected by Attada et al. (2019). The physical mechanism of the NCP index, which has a negative impact on temperatures, was discussed in detail in points 5 and 6. It should be noted that rising SST and SLP over the North Sea and west of Europe result in lower Levant temperatures in the autumn, which could be due to the NCP entering a positive phase (high SLP over the North Sea and low SLP over the Caspian Sea).

15. The first SLP-autumn rainfall coupled mode revealed increasing rainfall in all Levant locations, except the Syrian coast, when the SLP increases over the tropical/subtropical (Atlantic Ocean, Africa, Indian Ocean, and west pacific), Middle East and East Asia. The SLP pattern also indicated to increase rainfall when the SLP over the east Pacific Ocean is abnormally low.
16. Similarly, the first SST-autumn rainfall coupled pattern indicated to increase rainfall in most Levant location, except the Syrian coast, when the SST in the north and tropical/subtropical Atlantic Ocean is abnormally cold. The second and third mode of the SLP/SST-autumn rainfall only correlated with the NAO index,

The left SLP and SST expansion coefficients exhibited a strong negative correlation of -0.79 and -0.41 with ENSO index, respectively, compared to other indices. Note that the precipitation

structure linked to these SLP/SST patterns in the heterogeneous correlation maps exactly coincide with those autumn precipitation areas connected to the ENSO in (Figure 6.25). In addition, the SST-autumn rainfall displayed similar homogeneous structure of the SST-summer temperatures, where the SST pattern in both cases is highly correlated with the ENSO index.

In addition, the analysis may also indicates the positive (negative) links between the SST in tropical/subtropical Atlantic (SLP in tropical/subtropical Atlantic) and the ENSO index. Many studies have indicated the negative influence of the ENSO on the autumn rainfall in Iran (Nazemosadat and Cordery, 2000; Soltani and Gholipoor, 2006). Nazemosadat and Ghasemi (2004) assessed the impact of the Southern Oscillation index (SOI) on dry and wet periods in Iran. It has been found that El Niño (negative phase of the SOI) increases the autumn precipitation in the southern parts of this country, while La Niña (positive phase of the SOI) reduces the amount of precipitation. Alpert et al. (2005) found El Niño increased rainfall over the north Israel after 1970s due to the changes in the jet stream position, because if the jet stream shifts equatorward (El Niño) or poleward (La Niña) by a few degrees, significant changes in precipitation amounts can occur. Sandeep and Ajayamohan (2018) suggested that the ENSO influences the Middle East precipitation variability through an equatorward shift of the subtropical jet streams. They also found the moisture transport from the Red and Arabian Seas toward the Arabian Gulf is stronger and covers the entire Gulf during El Niño years. During El Niño events, they suggested the polar jet streams moved further south causing increased storms and thus increased rainfall. The potential mechanism that the ENSO affects the SST in the Tropical/subtropical Atlantic was discussed in points 12 and 13.

CHAPTER 9

DROUGHT ANALYSIS USING THE STANDARDIZED PRECIPITATION INDEX

Using data from 165 stations, this chapter examines the spatial and temporal variability of the drought over the Levant from 1970 to 2018. Drought characteristics (frequency, duration, and severity) are analyzed. In addition, the relationships between seven large-scale circulation patterns along with two climate indicators, the sea surface temperatures (SST), and the North Hemisphere sea level pressure (SLP) and the seasonal drought are studied.

9.1 Introduction

Drought is a complex natural disaster, which has various negative environmental, economic, agricultural, social, and political consequences (Zeinali and Safarian, 2017; Shamsniya et al., 2008). There is no universally agreed-upon definition of drought at the international level although it generally occurs when there is a shortage of water at a specific location and time (Correia et al., 1991; IPCC, 2007). In literature, drought can be divided into four types: meteorological, agricultural, hydrological, and socioeconomic (Fiorillo and Guadagno, 2010; Nalbantis, 2008; Wilhite, 2000; Wilhite and Glantz, 1985; Wilhite and Buchannan-Smith, 2005). The meteorological drought is defined as the degree of dryness in a specific region as measured by a deviation from climatological precipitation. Agricultural drought is caused by a lack of soil moisture caused by a lack of water available for crop or plant growth, resulting in biomass loss. Hydrological drought, on the other hand, is associated with a decrease in mean level water in surface and subsurface water resources. Finally, the socioeconomic drought has ramifications for human activities, including direct and indirect effects on agricultural production and other economic activities.

Many studies have shown that climate change is causing more drying conditions in the Mediterranean region due to temperature increases and precipitation decreases (IPCC, 2013;

Seager et al., 2014; Spinoni et al., 2018; Ulbrich et al., 2006; Tanarhte et al., 2012), which has been also documented from this Thesis for the Levant region (see chapters 4 and 6). Furthermore, all Levantine countries face constant threats of soil degradation, desertification, water scarcity, overpopulation, large-scale changes in land use and cover, increased urbanization, among others (Avni et al., 2006). As a result, in a region like the Levant, where also most agricultural systems rely on rainfall, the drought vulnerability will be very high. In addition, and because drought can be quite destructive at times, a better understanding of the spatial distribution of the drought and its parameters is required. Drought characteristics (e.g., frequency, duration, and severity) must be accurately estimated in order to plan the efficient use of water resources, as well as agricultural production. Where due to a lack of accurate information about the spatiotemporal characteristics of droughts, poor decision-making may result in increased drought-related costs and damages.

The meteorological drought analysis using the Standardized Precipitation Index (SPI) has been performed in many regions and countries in the Levant (Mathbout et al., 2018; Kelley et al., 2015; Gleick, 2014; Mohammed et al., 2020; Al-Qinna et al., 2011; Inbar and Bruins, 2004), Turkey (Sirdas and Sen, 2003; Karabulut, 2015; Dabanli et al., 2017), Iran (Shahabfar and Eitzinger, 2013; Mohammadrezaei et. al., 2020; Golian et. al., 2020), Iraq (Jasim and Awchi, 2020; Hameed et al., 2018; Awchi and Kalyana, 2017), and Saudi Arabia (Almazroui, 2019). However, until now, there are no detailed studies on drought in the Levant as a whole. All studies were conducted on a specific region or country using a small number of stations and few SPI-time scales. In addition, the relationships between drought and the large-scale circulation patterns and some climate indicators like SST or SLP have not been explored yet in the previous studies.

The main objectives of this chapter are as follow:

1) To identify the spatial and temporal patterns and trends of the drought over the Levant region at multiple SPI timescales (3, 6, 12, and 24 months) for the period 1970-2018.

2) To assess several drought characteristics, drought frequency (DF), drought duration (DD), and drought severity (DS), through the construction of the Levant DF, DD, and DS maps for different periods between 1970 and 2018.

3) To understand the relationships between the seasonal drought in the Levant and large scale circulation patterns in the Mediterranean Sea and North Atlantic Ocean via the teleconnection indices, as well as with the North Atlantic SST and North Hemisphere SLP.

In this study, the 3-, 6-, 12-, and 24-month timescales have been used as reference periods to monitor the meteorological and hydrological drought events. In order to compute the seasonal SPI, new cumulative time series from the original monthly data were obtained for winter (December-February, SPI-3 Feb), spring (March-May, SPI-3 May), autumn (September-November, SPI-3 Nov), September-February (SPI-6 Feb), December-May (SPI-6 May), March-August (SPI-6 Aug), and January–December (SPI-12 Dec). Figure 2.5 showed the stations' geographical distribution, while Table 2 in the Appendix A contains names, coordinates, and stations' elevations. Details regarding data quality control (QC) and homogeneity are available in Chapter 2, Section 2.2. The methodology used to calculate the SPI, along with the definitions of drought characteristics are provided in detail in Chapter 3, Section 3.10.

9.2 Results

9.2.1 Temporal variation of drought

Interannual and annual drought variations were investigated. In this regards, the SPI values for winter (SPI-3 Feb), spring (SPI-3 May), autumn (SPI-3 Nov), September-February (SPI-6 Feb), December-May (SPI-6 May), March-August (SPI-6 Aug), January-December (SPI-12 Dec), and SPI-24 were calculated for each station and averaged over the study area. Figure 9.1(a-p) depicts the temporal variations of the mean SPI time series along with the proportion of drought at stations in 1970-2018 for each drought category (extreme, severe, moderate, and slightly). The trends in the number of stations showing drought conditions based on the different drought categories were also calculated (Table 9.1). Furthermore, the historical drought events that resulted in widespread drought conditions in the region have been mapped and analyzed (Figure 9.2).

9.2.1.1 SPI-3 months

9.2.1.1.1 SPI-3 Feb

The extremely wet conditions are observed in 1992 for SPI-3 Feb (Figure 9.1a). Drought events were detected in 55% of the years (26 years), with 22 years falling into the slightly drought category and 4 years falling into the moderate drought category ($-1.50 < SPI \leq -1.0$), in 1973, 1984, 1999, and 2014 (Figure 9.1a). The SPI distribution shows that some stations, primarily in 1973, 1982, 1984, 1987, 1999, 2008, 2009, 2014, and 2015, exceeded the category threshold for extreme (SPI< -2) and severe (-2 <SPI<-1.5) droughts (Figure 9.1b). With 22 and 39 stations, respectively, the highest proportion of drought at stations was found in 2014 for the extreme drought and 1984 for the severe drought. At this timescale, the total number of stations that were affected by extreme and slightly drought events increased non-significantly by 0.37 and 1.50%/decade, while the total number of stations affected by severe and moderate drought decreased non-significantly by -1.1 and -1.3%/decade, respectively (Table 9.1).

In 2014, the spatial distribution of SPI-3 Feb (Figure 9.2a) revealed that marginally wet conditions covered a small region in the south of the Palestinian coast. On the other hand, severe and extreme drought conditions hit the Syrian coast, as well as several areas in northern and eastern Syria and northern Jordan. In 1970-2018, droughts in SPI-3 Feb lasted the longest in 1984-1987 and 2005-2009 (Figure 9.1a). Figure 9.1b also shows that the wettest winters were found in 1981, 1988, 1992, and 2003.

9.2.1.1.2 SPI-3 May

The variation of mean SPI-3 May values shows that the year 2008 is classified as extreme drought event (Figures 9.1c). The percent of drought years in SPI-3 May (51%, 24 years) was smaller than that in SPI-3 winter (Figures 9.1c and d). On the other hand, the severity and duration of drought, increased after 1992 for SPI-3 May compared to SPI-3 Feb. Drought events were also more frequent in the winter SPI-3 before 1992 than in spring SPI-3. Except for the years 2004 (moderate drought, covering 31.5% of the stations), 2008 (extremely drought, covering 50% of the stations), and 2010 (severe drought, covering 16% of the stations), all drought events were rated as slightly

drought (Figure 9.1c and d). During 1970-2018, the total number of stations that was affected by extreme, severe, and moderate drought significantly increased by 4.1, 3.2, and 3.3%/decade, respectively (Table 9.1). As shown in Figure 9.2b, the extreme drought event in 2008 occurred in the central and northern areas of Palestine and Jordan, while the north of Levant and the southern/eastern locations of Jordan had less severity for most locations. The longest drought duration in SPI-3 May/spring was found in 1992-1995, 1999-2001, and 2015-2018 (Figure 9.1c).

9.2.1.1.3 SPI-3 Nov

The variation of mean SPI values for SPI-3 autumn (Figures 9.1e and f) indicates that only 20 out of 49 years had drought occurrences, all of which were classified as slightly drought, with the exception of 1998, 1999, 2010, 2013, and 2016, which were classified as moderate drought. Extreme and severe droughts were mostly observed in 1998, 1999, 2010, 2013, and 2016, with 23%, 13%, 27%, 18%, and 25% of the stations experiencing extreme drought and 29%, 22%, 19%, 23%, and 29% of the stations experiencing severe drought, respectively. Between 1970 and 2018, the stations that experienced extreme, severe, and moderate drought increased non-significantly by 2.2, 2.4, and 0.3%/decade, respectively, whereas the stations that experienced slightly drought decreased significantly by -5.8%/decade (Table 9.1). The extreme drought event in 2010 (Figure 9.2c) intensively covered the coastal and northern stations from Palestine, while the north Levant, especially the west Syria showed slightly wet conditions. The lowest drought duration was found for SPI-3 Nov compared to those for winter and spring, when there were 2 consecutive autumns with drought throughout the record. In any case, the drought duration did not persist for more than two years (Figure 9.1e).

9.2.1.2 SPI-6 months

Based on the averaged values, only 2008 was determined to have extreme drought for SPI-6 Aug and the event of extreme wet is observed in 1992 for SPI-6 Feb (Figure 9.1g and k). A total of 24 years is rated as dry years based on the SPI-6 Feb mean values (Figures 9.1g and h), with only four years (1973, 1984, 1999, and 2014) falling into the moderate drought. The highest proportion of extreme drought at stations was found in 1973, 1999, and 2014 by 13%, 21%, and 19% of the stations. For the severe drought, the highest proportion was recorded in 1999 (34%) and 2014 (25%) and for the moderate drought, in 1999 (34%) and 2014 (25%). The SPI-6 Feb drought duration generally spanned for three years in the periods 1999-2001, 2006-2009, and 2016-2018.
For SPI-6 May (Figure 9.1i and j), the drought events were found in 26 years, three years of them, 1973, 1999, and 2008 were classified as moderate drought, and the remaining years were classified as slightly drought. Based on stations (Figure 9.1j), extreme drought affected the highest percentage of stations in 1999 and 2014 by 18 and 14% of the stations, and the severe drought in 1999 (25%) and 2008 (18%). Among the hydrological drought at the SPI-6 timescale, the longest drought duration was found in 1994-1997, 1999-2001, 2005-2010, and 2014-2018 (Figure 9.1i). In 1970-2018, the percent of stations that were affected by all drought categories was increased non-significantly by 0.71(extreme), 0.46 (severe), 0.66 (moderate), and 3.4 (slightly) %/decade.

The mean annual SPI-6 Aug values over the study region (Figure 9.1k and l) indicated drought events in 24 years, with one extreme drought year (2008), one severe drought year (2010), one moderate drought year (2004), and 21 slightly drought years. The highest extreme drought events were observed in 2004, 2008, 2010, 2015, and 2017 affecting between 17% and 50% of the stations. similar to SPI-3 May, the total stations that were affected by extreme, severe, and moderate drought in 1970-2018 significantly increased by 4.2, 3.1, and 3.4%/decade, respectively (Table 9.1).The drought duration generally spanned during the periods 1992-1995, 1999-2001, and 2015-2018 (Figure 9.1k).

9.2.1.3 SPI-12 and -24 months

For both hydrological drought timescales, a percent of 45% of the total years showed drought events, all of them were classified as slightly drought, except for (1999 and 2017, severe for SPI-12), and (2000, moderate for SPI-24). For SPI-12 (Figure 9.1n), the most diffused drought event took place in 1999 with more than 44% and 24% of the stations showing extreme and severe dry conditions. A diffused drought was also observed in 2017 with more than 33% and 23% of the stations showing extreme and severe dry conditions (Figure 9.1n). The highest moderate drought events was observed in 2008 covering approximately 38% of the stations. Slightly drought-affected stations showed a non-significant decrease of -6%, whereas extreme, severe, and moderated drought-affected stations increased by 2.2, 2.0 (Significant), and 1.6%, respectively (Table 9.1). Spatially, the extreme and severe drought in 1999 were widespread in the central and north Palestine, North Jordan, and south Syria (Figure 9.2d). Other regions generally showed less severity within the moderate drought. According to the SPI-12 scale, the study area have witnessed episodes of drought in 1999-2001, 2005-2011, and 2014-2018 (Figure 9.1m).

For mean annual SPI-24 (Figures 9.1o and p), the highest occurrence extreme and severe droughts were observed in 2000 covering about 25% and 23% of the stations, respectively. Furthermore, the number of stations affected by extreme, severe, moderate, and slightly droughts has increased in 1970-2018 by 0.9, 2.2, 4.0, and 5.4%/decade, respectively (Table 9.1). As can be seen in Figure 9.2e, all regions were affected by the extreme drought in 2000, with the exception of the central and northern sites in Palestine and west of Syria, which showed moderate and slightly drought. The maximum drought duration was observed during1999-2002, 2006-2012 and 2014-2018.

SPI lags	Extreme (%)	Severe (%)	Moderate (%)	Slightly (%)
SPI-3 FEB	0.37	-1.1	-1.3	1.5
SPI-3 MAY	4.1*	3.2*	3.3*	3.7
SPI-3 NOV	2.2	2.4	0.3	-5.8*
SPI-6 FEB	0.36	-0.27	-1.5	1.4
SPI-6 May	0.71	0.46	0.66	3.4
SPI-6 Aug	4.2*	3.1*	3.4*	3.2
SPI-12	2.2	2.0*	1.6	-0.6
SPI-24	0.90	2.2	4.0	5.4

Table 9.1. Trends in the number of stations that show drought conditions based on the drought categories for the period 1970-2018. * indicates significant trend at the 95% confidence level.

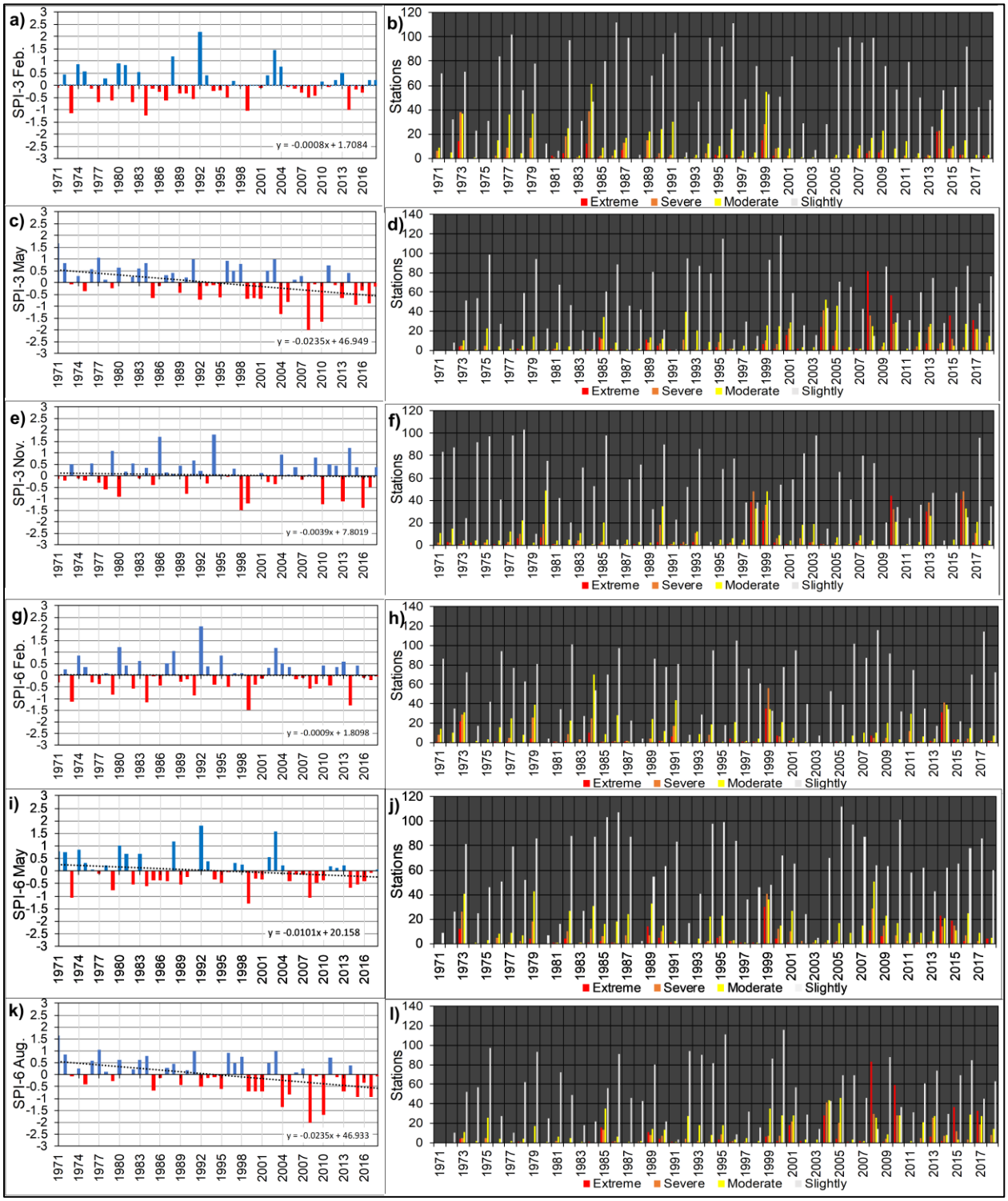
a)
SPI-3 Feb.
y = -0.0008x + 1.7084
b)
Stations
Extreme
Severe
Moderate
Slightly
c)
SPI-3 May
y = -0.0235x + 46.949
d)
Stations
Extreme
Severe
Moderate
Slightly
e)
SPI-3 Nov.
y = -0.0039x + 7.8019
f)
Stations
Extreme
Severe
Moderate
Slightly
g)
SPI-6 Feb.
y = -0.0009x + 1.8098
h)
Stations
Extreme
Severe
Moderate
Slightly
i)
SPI-6 May
y = -0.0101x + 20.158
j)
Stations
Extreme
Severe
Moderate
Slightly
k)
SPI-6 Aug.
y = -0.0235x + 46.933
l)
Stations
Extreme
Severe
Moderate
Slightly

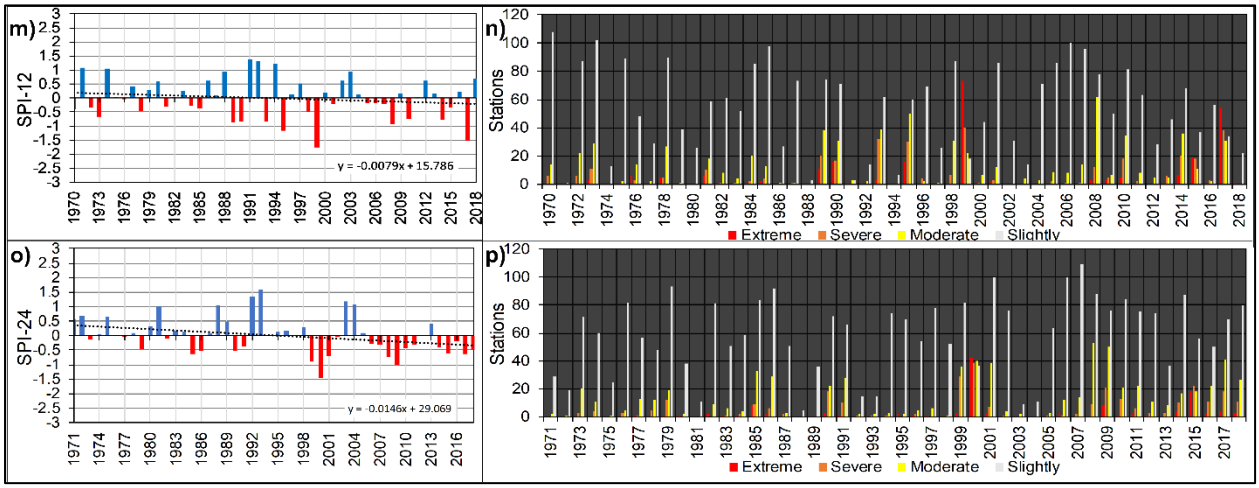

Figure 9.1. The annual SPI-3, -6, -12, and -24 months timescales series over the study area along the proportion of stations presenting drought conditions during 1970-2018 for each drought categories, extreme, severe, moderate, and slightly.

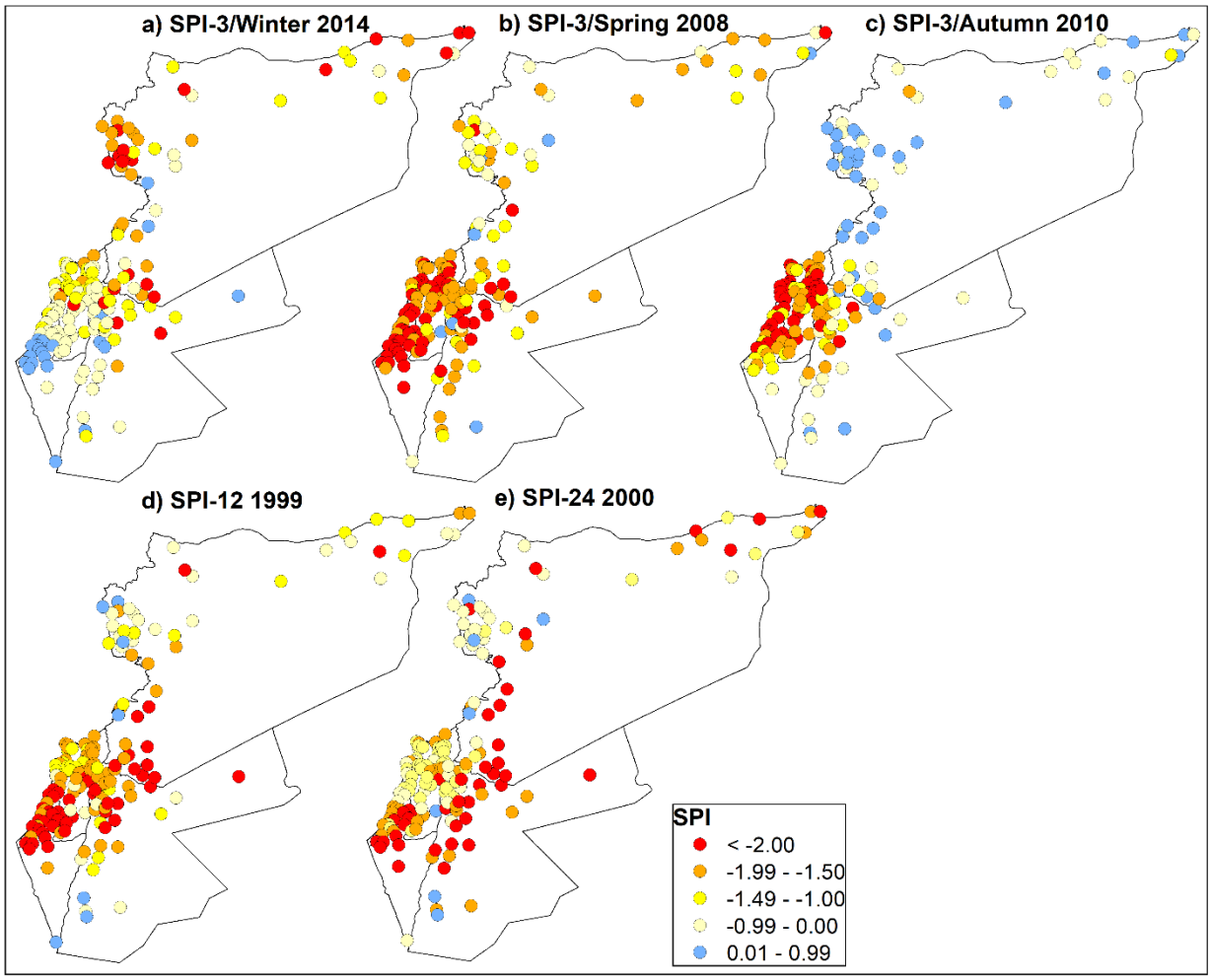

Figure 9.2. Drought maps of major historical drought events at various SPI timescales.

9.2.2 Spatial characteristics of drought

In order to analyze the spatial variation of drought in the Levant region and to detect homogeneous drought areas, the principal component analysis (PCA) and the K-means cluster were used. The factor loadings (Figure 9.3) are mapped to display the drought's spatial patterns, and the corresponding factor scores (Figure 9.4) are plotted to determine each PC's temporal behavior. The North Rule of Thumb (North et al., 1982) was used to determine the number of PCs retained, and they were rotated using the varimax technique (Bortz, 1993). Table 9.2 displays the overall variance described by each PC for SPI at various timescales in the Levant from 1970 to 2018.

The results listed in Table 9.2 show the first three PCs were retained for the SPI-3, -6, and -12 months timescales and they explained 70.7%, 66.6%, and 68.3% of the total variance. For the SPI-24 months, the first four PCs were retained and they explain 72.3% of the total variance. The first PC explains the highest percent of the total variance between 33.9% for SPI-24 and 39.1% for SPI-3. For the PC-2, the percent ranged from 16.1% for SPI-3 and 21.6% for SPI-24, and from 10.2% (SPI-24) to 15.5% (SPI-3) for the third PC. The PC-4 for the SPI-24 months timescale explains only 6.6% of the total variance.

SPI timescales	PC1 (%)	PC2 (%)	PC3 (%)	PC4 (%)
SPI-3	39.1	55.2	70.7	-
SPI-6	36.5	55.5	66.6	-
SPI-12	35.2	57.1	68.3	-
SPI-24	33.9	55.5	65.7	72.3

Table 9.2. The cumulative variance explained by each PC for different SPI timescales in 1970-2018.

The first three patterns for the SPI-3, -6, and -12 months and the first four patterns for the SPI-24 months were mapped (Figure 9.3) using the loading factors which represent the correlation between each PC and the SPI time series at 165 rainfall stations. In general, the results indicated a similar drought spatial distribution for all SPI time scales in the Levant region during 1970-2018. In addition, the results generally did not showed overlapping between PCs with high correlations ($r > 0.55$), where they clearly divided the study area into separated regions. At SPI-3 and -6 months timescales (Figure 9.3a to f), the three retained PCs are related to the same regions where the first PC represents the central and northern locations from Palestine, northern locations from Jordan, and south Syria. The second PC showed the highest correlations in western and coastal locations from Syria. In general, the Mediterranean climate zone in the south and north Levant is represented by the first and second PCs at these SPI timescales. The third PC is associated to the eastern and southern locations of the Levant, which represents the arid and semi-arid climate zones.

Similar results were generally obtained at SPI-12 and -24 timescales (Figure 9.3g to m), with little differences, where the second PC extended to cover many locations in north Palestine at SPI-12 and -24. In addition, the third PC is confined to the eastern regions of Syria whereas the south Palestine and all stations in Jordan, except the northern stations, conformed the fourth PC at SPI-24 timescale.

Figure 9.4 (from a to m) shows the temporal evolution of the PCs. At shorter SPI timescales, the drought duration is shorter, and as the SPI timescale increases, the duration of drought increases. Several extreme drought episodes were detected for many areas in the Levant, particularly for SPI-

12 and SPI-24 months. For example, the longest and most extreme drought for SPI-12 was observed from Feb./1999 to Nov./1999 for the PC-1 region (north Jordan, central and northern locations from Palestine, except most north locations) (see also Figure 9.2d), from Feb/2000 to Nov./2000 for PC-3 (east and south Levant), and from April/2014 to Nov./2014 for the second PC-2 (western and coastal regions from Syria) (Figure 9.4(j-i)).

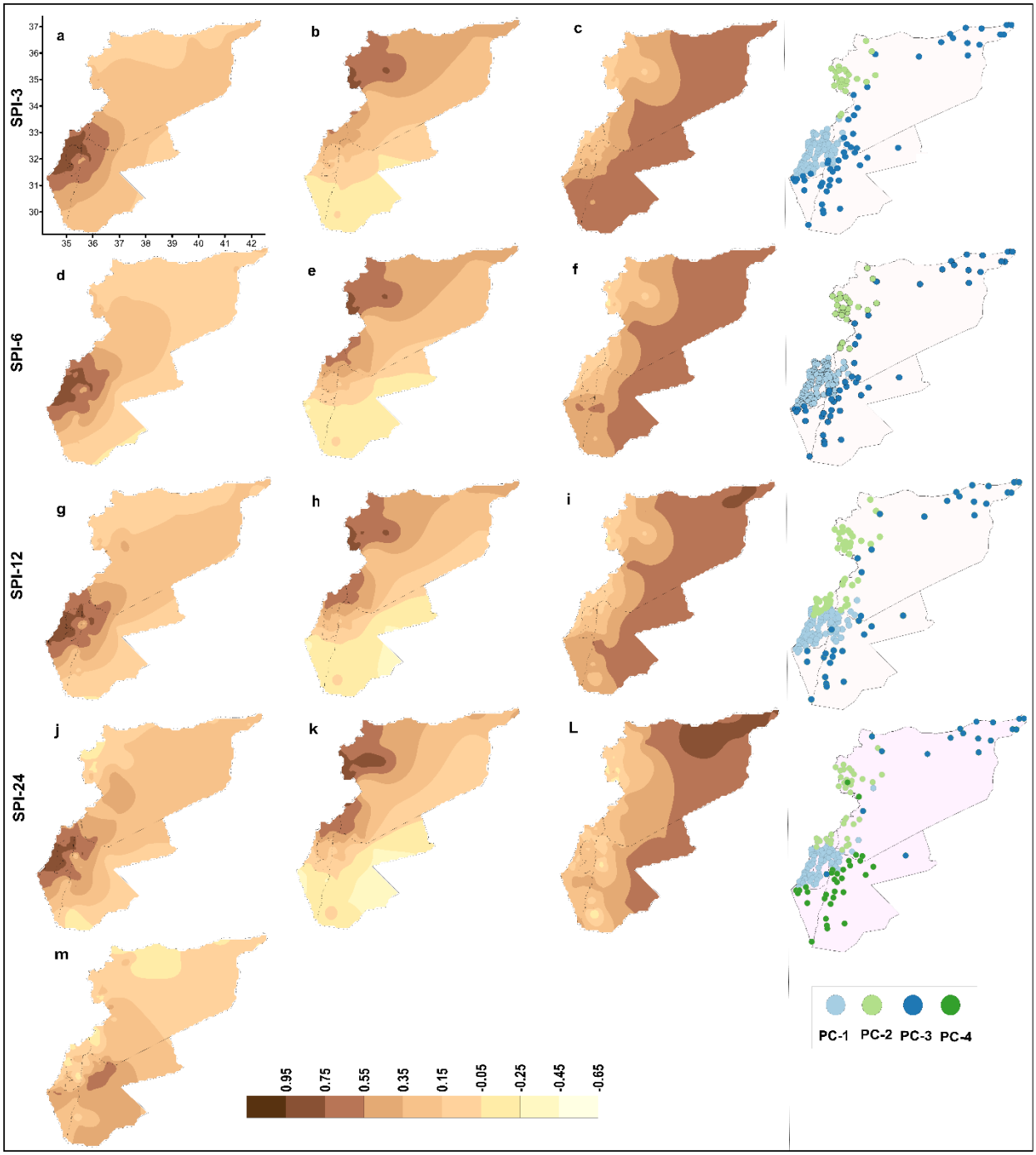

Figure 9.3. Spatial distribution of the PCs loading factors selected (EOFs) for the SPI-3, -6, -12, and -24 months timescales. The fourth column shows the delineated regions using the K-means cluster algorithm.

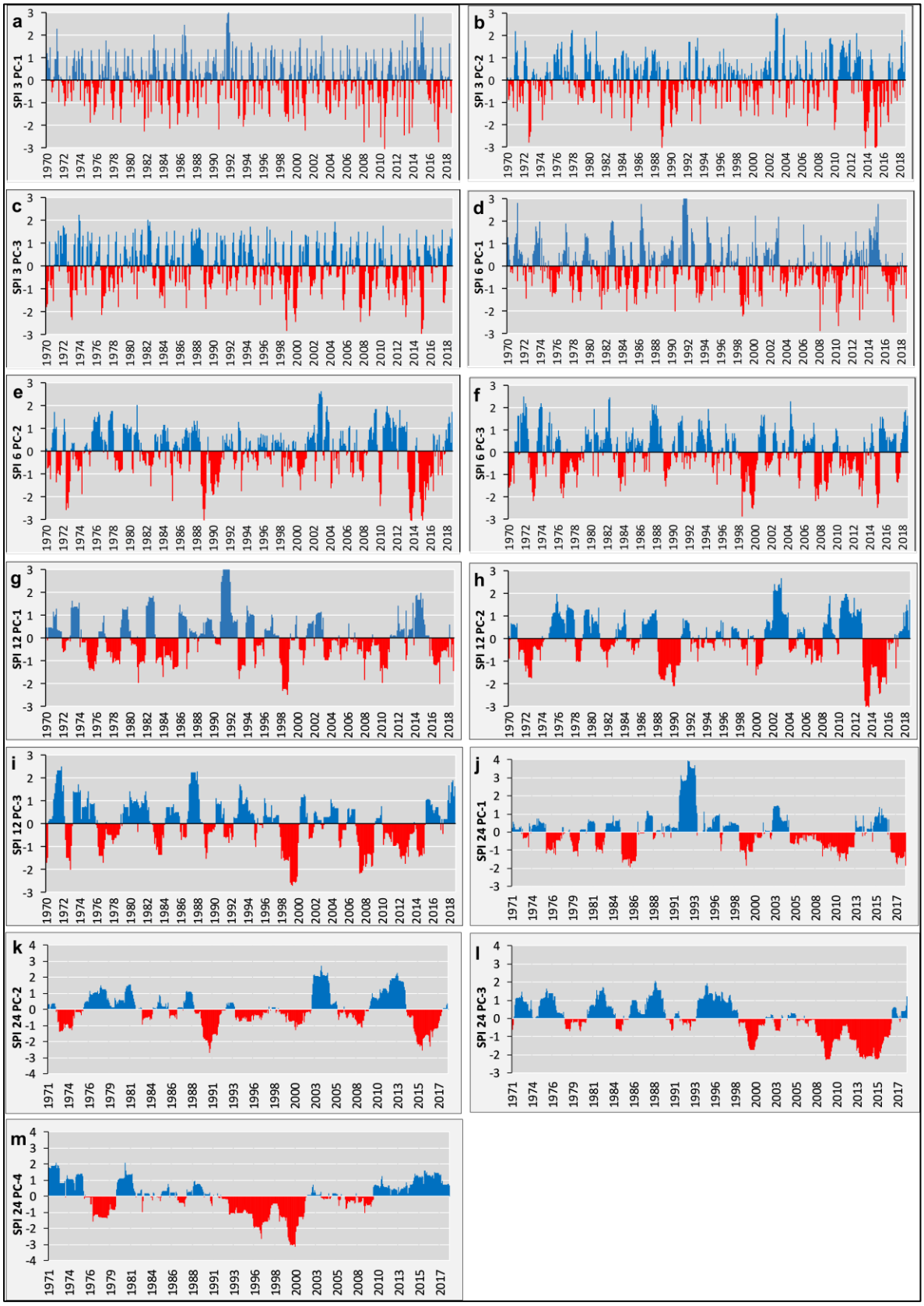

Figure 9.4. Temporal evolution for different SPI timescales from the series representing PCs.

For SPI-24, the longest extreme drought were extended from May/2013 to Sept./2015 for the PC-3 region (Figure 9.4l), from Jan./2000 to Dec./2000 for PC-4 (Figure 9.4m and Figure 9.2e), and from April/2009 to Nov./2009 for PC-3 (Figure 9.4L). For SPI-3, the longest drought period was observed in Jan/2015-Nov./2016 by average SPI value reached -1.2 for the PC-2 region (Syrian coast) (Figure 9.4b). Some drought parameters, drought frequency (DF), drought duration (DD), and drought severity (DS) for each PC-region at different SPI time scales will be analyze in the next section.

9.2.3 Drought parameters

In this section, the drought frequency (DF), total drought duration (TDD), and total drought severity (TDS) were calculated and spatially analyzed at different SPI timescales. These parameters were spatially evaluated to highlight the drought hot spots for the whole period 1970-2018 and for the two sub-periods 1970-1994 and 1995-2018 (Figures 9.6, 9.7, and 9.8), providing maps of the areas most affected by drought in the last 49 years. The whole period was splitted into two sub-periods because many SPI time scales generally showed turning points in the mid-1990s (see Figure 9.9 in the next section). The DF, TDD, and TDS were also averaged for the entire Levant and the studied countries as well as for the PCs time series (Figure 9.5).

9.2.3.1 Drought frequency

Based on the averaged values of DF (Figure 9.5a), a percent of 10.7, 14.1, 13.4, and 14.9% of the total months over the Levant showed DF (SPI≤ -1) at SPI-3, -6, -12, and -24 months, respectively. Syria showed the highest DF at the SPI-3, -6, and -12 by 11.7, 15.4, 13.8% of the total months, while Jordan showed the lowest by 9.5, 12.5, and 13.1%, respectively. At SPI-24 timescale, Palestine showed the highest DF with 15.4% of total months that showed moderate and above drought events.

The total months above moderate drought (SPI≤ -1) were calculated for each station and at different timescales (3-, 6-, 12-, and 24-months) during the whole period 1970-2018 (Figure 9.6, upper row) and for the two sub-periods 1970-1994 and 1995-2018 (Figure 9.6, middle and lower rows). The results show the DF for above moderate drought (SPI <-1) at each station is between 5.1 and 16% for the SPI-3 and between 5.1 to 21% for the SPI-6, -12, and -24. The stations affected by the lowest DF (< 12%, 69 months) decreased from 115 stations for SPI-3 to 29 stations for SPI-6, and only 17 stations for SPI-24. This indicates an increase in DF in most of the studied stations, from short-term drought to mid and long-term drought.

In general, most locations in north Jordan showed the lowest DF (5%< DF<12%) for all SPI timescales (Figures 9.6a to d). Based on SPI-3 months (Figure 9.6a), the highest DF was concentrated in the PC-2 region, the Syrian coast stations, (12-16%, 69-92 months) whereas the rest Levant locations (70% of the stations) showed DF <12% (69 months).

For SPI-6 months (Figure 9.6b), 100% of the stations showed higher DF than SPI-3 months. The highest DF with values around 16-18% (90-103 months) at this timescale was observed in 20% of the stations and spatially occurred in north Palestine and for many locations in coastal and eastern

areas of Syria, while the lowest DF values, around 10-12% of total months, were concentrated in northern Jordan and West bank. Based on PCs regions (Figure 9.5d), the PC-2 region also exhibited the highest DF by an average of 16% of the total months, while the PCs 1 and 3 exhibited similar DF values around 13.8%.

The southern locations of Palestine and Jordan, and eastern Syria (regions associates with the PC-3) showed the highest DF for SPI-12 (16-21% of total months) while the northern Jordan and West Bank showed the lowest (<12% of total months) (Figure 9.6c and Figure 9.5d). The highest DF for SPI-24 was mainly concentrated in southern part of Palestinian coast by average of 17.7% of total months (Figure 9.6d). The calculations based on PCs regions give to the regions associated with the PCs 3 and 4 the highest DF by averages of 16 and 15%, respectively. Although the PC-1 region has relatively less DF for all SPI timescales (Figure 9.5d), however the locations around Haifa district, in northern Palestine, showed considerable DF values mainly for SPI-3, -6, and -12 months compared to other locations considered into the PC-1 region.

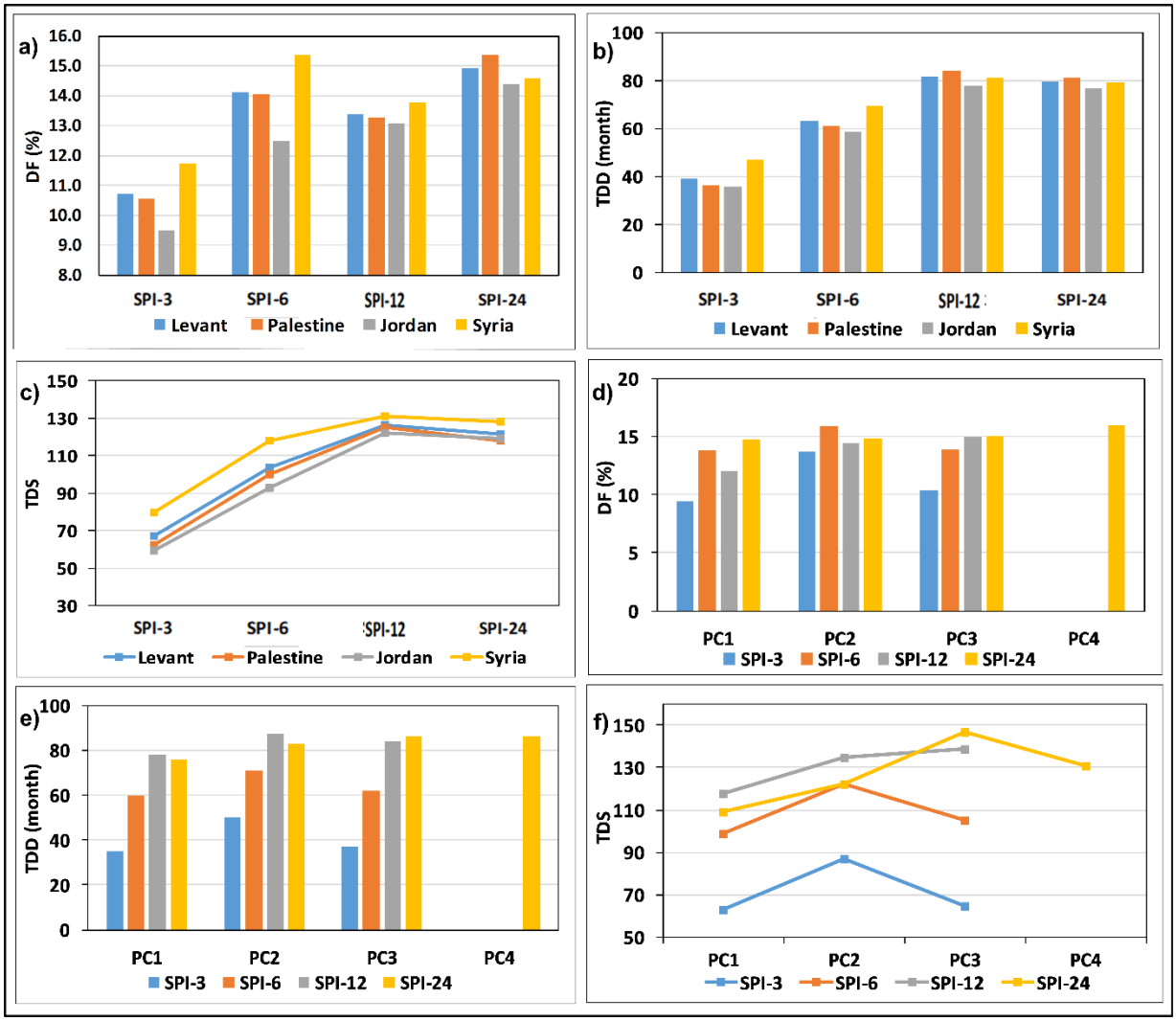

Figure 9.5. The averaged values of DF, TDD, and TDS over the Levant in 1970-2018.

Moreover, drought became more frequent during the second sub-period 1995-2018 compared to the first sub-period 1970-1994 for all SPI timescales (Figure 9.6, middle and lower rows). In this regard, the percentage of stations that showed DF > 20% of total months increased from < 2% of the total stations for SPI-6, -12, and -24 months in the first sub-period to 13%, 25%, and 50% of the total stations in the second sub-period, respectively. For example, the eastern locations from Syria showed the highest DF (> 20% of total months) for SPI-6, -12, and -24 during the second sub-period while they displayed DF with an average of 14% of total months in the first sub-period.

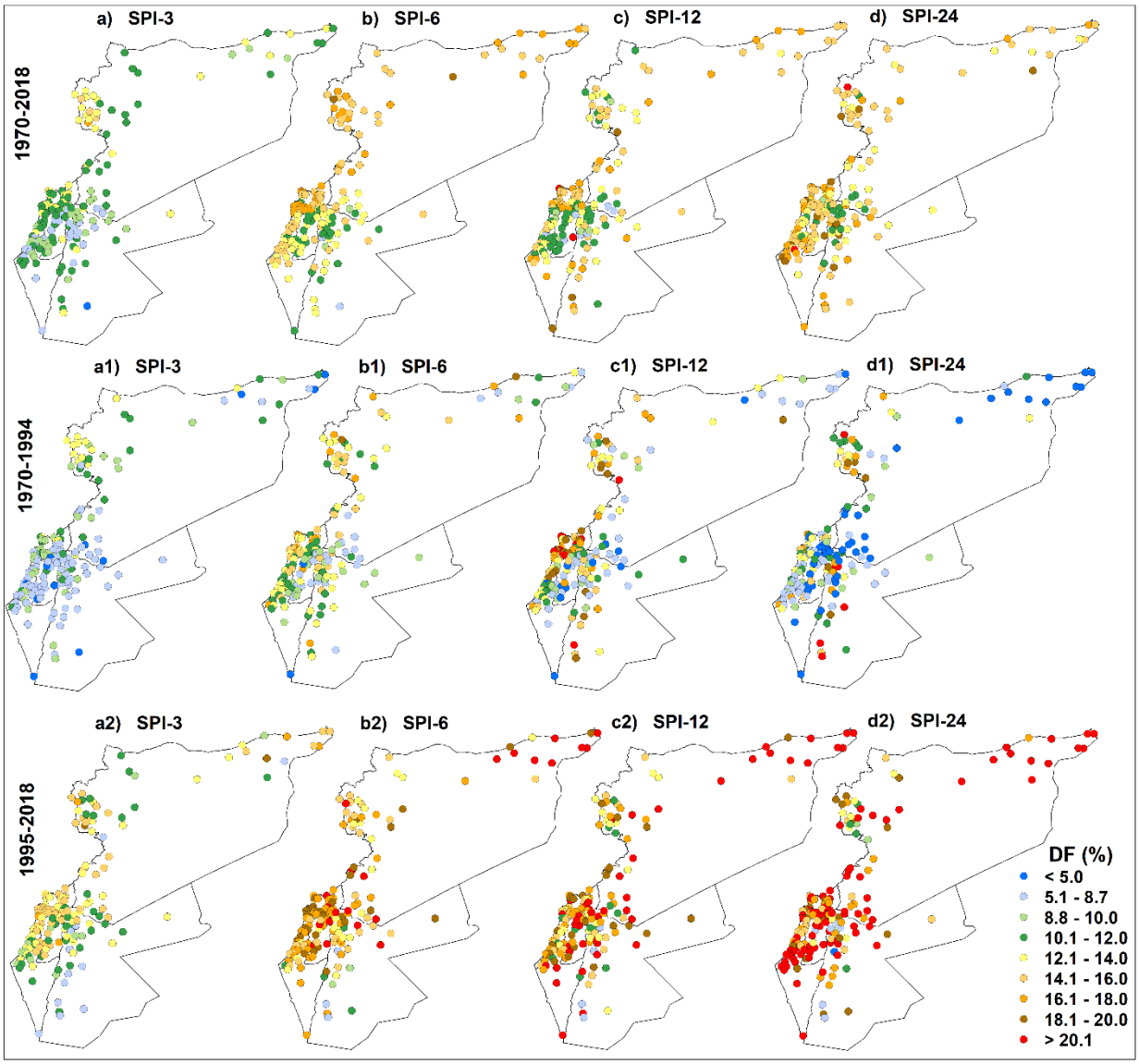

Figure 9.6. Drought frequency maps at different SPI timescales for the total period 1970–2018 (upper row), the first sub-period 1970–1994 (middle row), and the second sub-period 1995-2018 (lower row).

9.2.3.2 Drought duration

The average total drought duration (TDD) over the Levant from the SPI-3, -6, -12, and -24 months timescale are 39.4, 63.1, 81.6, and 79.5 months, respectively (Figure 9.5b). The highest average TDD was found for Syria with 47 and 69 months from the SPI-3 and -6, whereas Palestine showed the highest averages at SPI-12 and -24 by 84 and 82 months, respectively. On the other hand, Jordan showed the lowest averages from all SPI timescales with 35, 58, 77, and 76 months for SPI-3, -6, -12 and -24 months, respectively.

Overall, the PC-1 region (central Palestine and northern Jordan) had the lowest TDD at all SPI timescales, while the PC-2 region (western Syria) at SPI-3 and -6, and the PC-2 region (western Syria and northern Palestine) at SPI-12 and -24 had the highest TDD at all SPI lags.

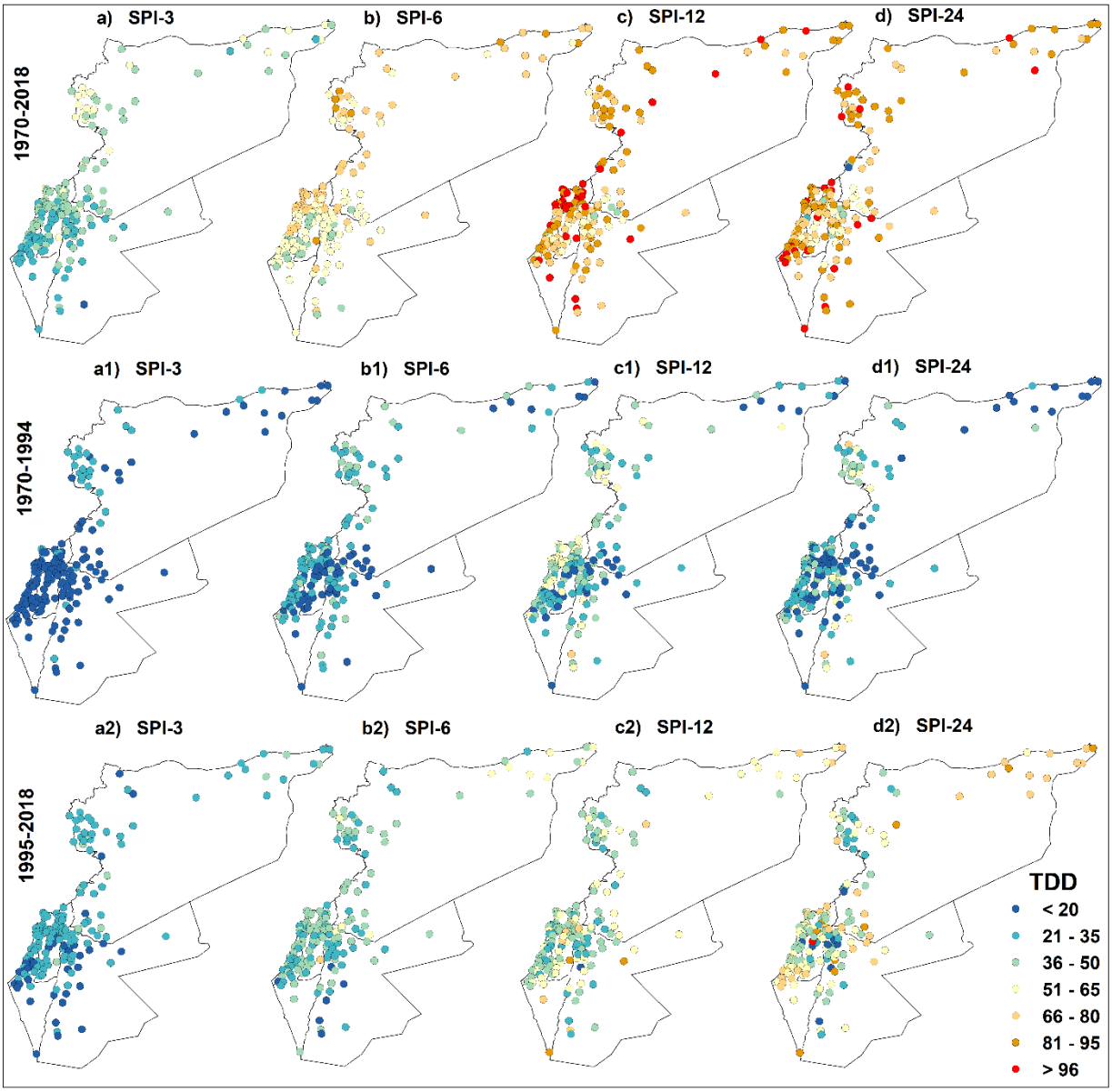

Figure 9.7. Drought duration maps at different SPI timescales for 1970–2018 (upper row), 1970–1994 (middle row), and 1995-2018 (lower row).

As can be seen in Figure 9.7a, the highest TDD values (around 51-65 months) at SPI-3 months were concentrated in the Syrian coast area (PC-2 region) and at some stations located to the east of Syria. On the other hand, the lowest values (between 21-35 months) were found in southern part of the Palestinian coast, West Bank, and northern Jordan (PC-1 region). At SPI-6 months' timescale (Figure 9.7b), both stations and regions showed higher values in their TDD than those for SPI-3 months. In this regards, the northern Palestine regions showed values between 51 and 65 months, while the highest values (between 81-95 months) affected many locations in Syrian coast and eastern Syria.

At the SPI-12 timescale (Figure 9.7c), the highest TDD is intensified and clustered in the north of Palestine region, which is a part of the PC-2 region, with an average value of 93 months. In general, the PC-2, PC-3, and PC-4 regions had identical TDD (between 83-87 months) for the SPI-24 timescale, while the PC-1 region (center of Palestine including the West Bank and northern Jordan) had TDD values lower, with an average of 76 months (Figure 9.5d). Locally, the southern part of Palestinian coast, which is a part of the PC-4 region of the SPI-24 timescale exhibited the maximum values of TDD with an average of 95 months.

The TDD between 1970-1994 and 1995-2018 (Figure 9.7, central and lower rows) shows that the TDD increased for most stations and regions during the second sub-period relative to the first one. The total number of stations that showed TDD < 20 months decreased substantially in the second sub-period compared to the first one. For example, the TDD for the central and northern stations in Palestine and Jordan increased from 20 months in the first sub-period to 21-35 months in the second sub-period for the SPI-3 months timescale. Increases for SPI-6, -12 and -24 timescales from TDD averages of 26, 26, and 12 months in the first sub-period to 49, 60, and 75 months in the second sub-period are also visible in areas of eastern Syria. On the other hand, the central and northern stations along the Palestinian coast, have seen a decrease of TDD from 48 months in 1970-1994 to 41 months in 1995-2018, at SPI-12 timescale.

9.2.3.3 Drought Severity

Over the Levant, the total drought severity (TDS) at SPI-3, -6, -12, and -24 month timescale are 67.2, 103.9, 126.4, and 121.3, respectively (Figure 9.5c). The results also showed the TDS for the northern Levant (Syria) was much higher than those for the southern Levant (Palestine and Jordan) at all SPI timescales (Figure 9.5c). In this context, the highest TDS was found for Syria by 79.7, 117.8, 131.1, and 127.9 at SPI-3, -6, -12, and -24, respectively. On the other hand, Jordan showed the lowest TDS for all SPI timescales by 59, 92.7, 121.9, and 119, respectively. For Palestine, the values reached 62.5, 99.7, 125.4, and 117.9, respectively (Figure 9.5c). According to the PCs regions (Figure 9.5f), the PC-2 region displayed the highest TDS at SPI-3 and -6 timescales, while the PC-3 region displayed the highest values at SPI-12 and -24 timescales. The PC-1 area had the lowest TDS at all SPI timescales.

Figure 9.8 depicts the spatial distribution of TDS in the Levant from 1970 to 2018 (upper row), as well as for the two sub-periods, 1970-1994 and 1995-2018 (middle and lower rows). The highest TDS values (between 76-100) were found along the Syrian coast (PC-2 region) and for many locations eastern Syria at the SPI-3 timescale (Figure 9.8a), while the lowest TDS values (between

26–50) were found at many Jordinean locations along the Palestine border. The values for the center and north of Palestine (PC-1 region) ranged from 51 to 75.

The maximum TDS values (126-150) for the mid-term drought SPI-6 (Figure 9.8b) were also grouped in the Syrian coast (PC-2 region) and some eastern Syria locations. At this time scale, the northern Palestine regions had significantly higher TDS than for the SPI-3 months, with values ranging from 101 to125, with the lowest values (between 76-100) located in the West Bank, southern part of the Palestinean coast, and in Jordan.

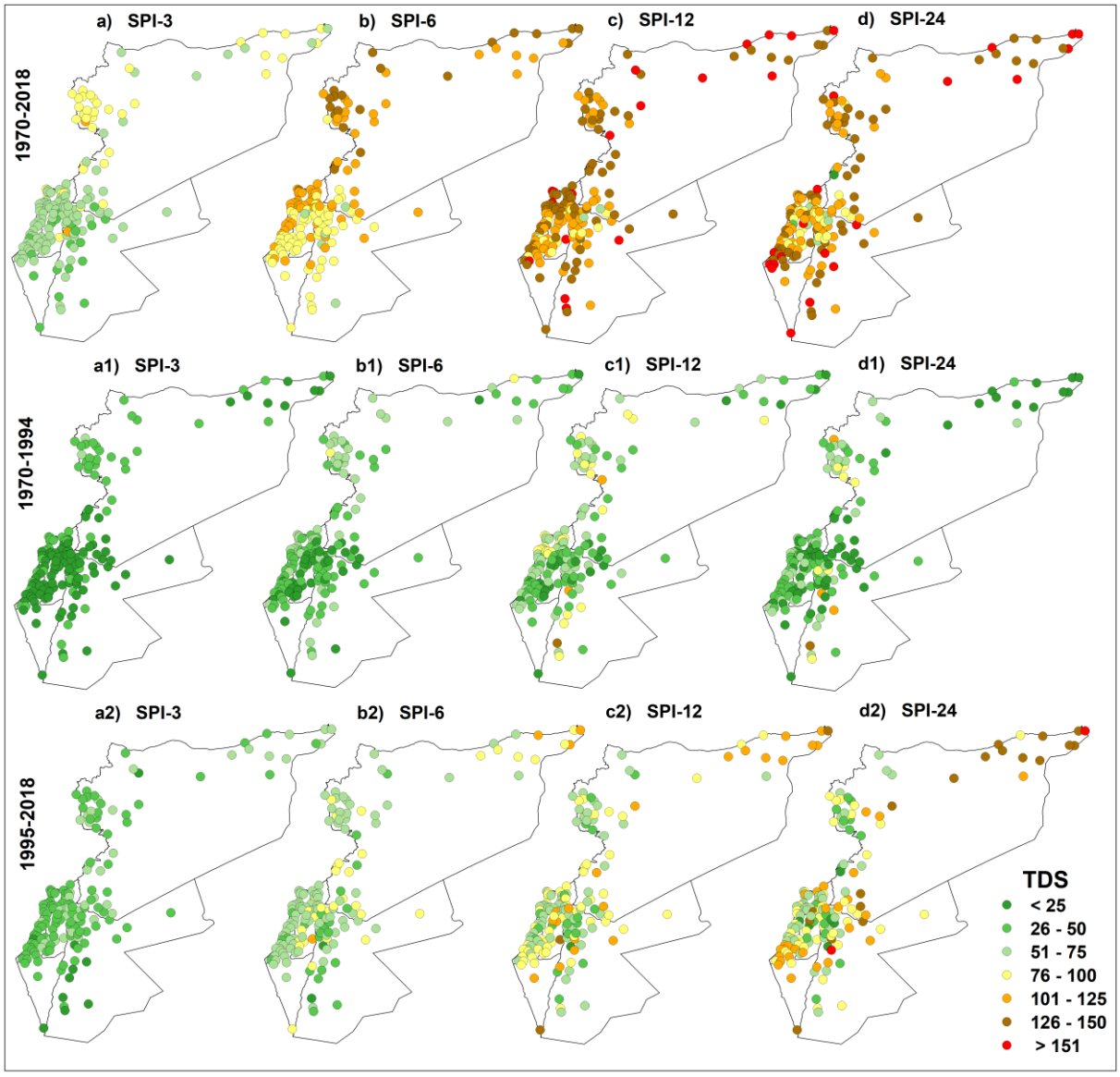

Figure 9.8. Drought severity maps at different SPI timescales for the total period 1970–2018 (upper row), the first sub-period 1970–1994 (middle row), and the second sub-period 1995-2018 (lower row).

Many locations to the east of Syria and Jordan were primarily affected by the highest TDS values (> 150) at SPI-12 months, as represented by the PC-3 area, which had the highest average TDS value by 139 (Figure 9.8c and Figure 9.5f). With an average of 135, the coastal and western areas

of Syria and north Palestine (PC-2 region) came in second place. And, as in all cases, the lowest TDS values was observed in central Palestine and northern Jordan, with an average of 117.5. According to the SPI-24 timescale analysis, the maximum TDS values (>126) clustered in the southern portion of the Palestinean coast and easten locations of Syria (Figure 9.8d).
Regarding the comparison between sub-periods, the TDS clearly increased for most locations and regions in 1995-2018 relative to 1970-1994, for all SPI timescales (Figure 9.8 middle and lower rows). TDS increased from values < 25 in the first sub-period to values between 26-50 in the second sub-period for PC-1 area (central and northern Palestine and Jordan) at SPI-3 months. It was also increased at SPI-6 months for the same area, from TDS values around 50 in the first sub-period to between 51-75 in the second one. The TDS in Syria's eastern locations (PC-3 region) increased from an average of 40 in the first sub-period to 106 in the second sub-period. At the SPI-24 timescale, TDS increased from an average of 17 to 133 for the same areas.

9.2.4 Temporal and spatial trends

The overall trends for the mean SPI-3 Feb, SPI-3 May, SPI-3 Nov, SPI-6 Feb, SPI-6 May, SPI-6 Aug, SPI-12, and SPI-24 months time series were estimated using the Mann Kendal test (Table 9.3), and the temporal evolution for the SPI averages at different timescales was evaluated using the Sequential Man kendall test (Figure 9.9). Only SPI-3 Feb reported statistically non-significant positive trend of 0.023 unit/decade (Table 9.3). The trends estimated for the spatially averaged SPI time series exhibited non-significant and negatives trends by -0.018, -0.019, -0.073, -0.11, and -0.15 unit/decade for SPI-3 Nov, SPI-6 Feb, SPI-6 May, SPI-12, and SPI-24, respectively. On the other hand, the SPI-3 May (-0.20 unit/decade) and SPI-6 Aug (-0.19 unit/decade) showed significantly (at 0.05 level) decreasing trends. In addition, in 1997, significant change points for the SPI-3 May and SPI-6 August were detected (Table 9.3, Figure 9.9b and f). During the periods 1999-2018 and 1978-1997/2000-2018, respectively, the notably rising SPI pattern was observed for SPI-3 Feb, SPI-3 Nov, and SPI-24 (Figure 9.9a, c, and h). In contrast, the sharp decreasing SPI pattern was noted in the period 1990-2018 for SPI-3 May, SPI-6 Aug, and SPI-12 (Figure 9.9b, f, and g). For SPI-6 May (Figure 9.9e), decreasing pattern was noted in 2002-2018. For SPI-24, two periods of decreasing pattern can be characterized, 1971-1980 and 1998-2018 (Figure 9.9h).
The trends of the different SPI timescales were also examined spatially, with the findings shown in Table 9.4 and Figure 9.10. Table 9.4 shows that for SPI values in winter, spring, autumn, and autumn/winter, few stations (< 4 stations) showed significant negative or positive trends. In the spring and spring/summer, however, significant decreasing trends affected more than 36% of the stations. Furthermore, the SPI-12 showed a significant decreasing trend in 27% of the stations. Due to their notably significant decreasing trends, the trends for SPI-3 spring, SPI-6 spring/summer, and SPI-12 have been spatially evaluated (Figure 9.10). Similar trend patterns were observed for SPI-3 spring and SPI-6 spring/summer values. For both SPI timescales, only 4 stations showed negative trends at the 99% significance level. Furthermore, central and north Palestine, north Jordan as well as several locations in east Syria displayed significant decreasing trends at the 95% confidence level. At SPI-12 months, many stations in West Bank and northern Jordan exhibited significant decreasing trends at the 99% confidence level.

SPI timescales	Trend (per decade)	Change points detected
SPI-3 Feb.	0.023	-
SPI-3 May	-0.20*	1997
SPI-3 Nov.	-0.018	-
SPI-6 Feb.	-0.019	-
SPI-6 May	-0.073	-
SPI-6 Aug.	-0.19*	1997
SPI-12	-0.11	-
SPI-24	-0.15	-

Table 9.3. Trends calculated for SPI values at different lags in 1970-2018. Trend units are standardized unit/decade.

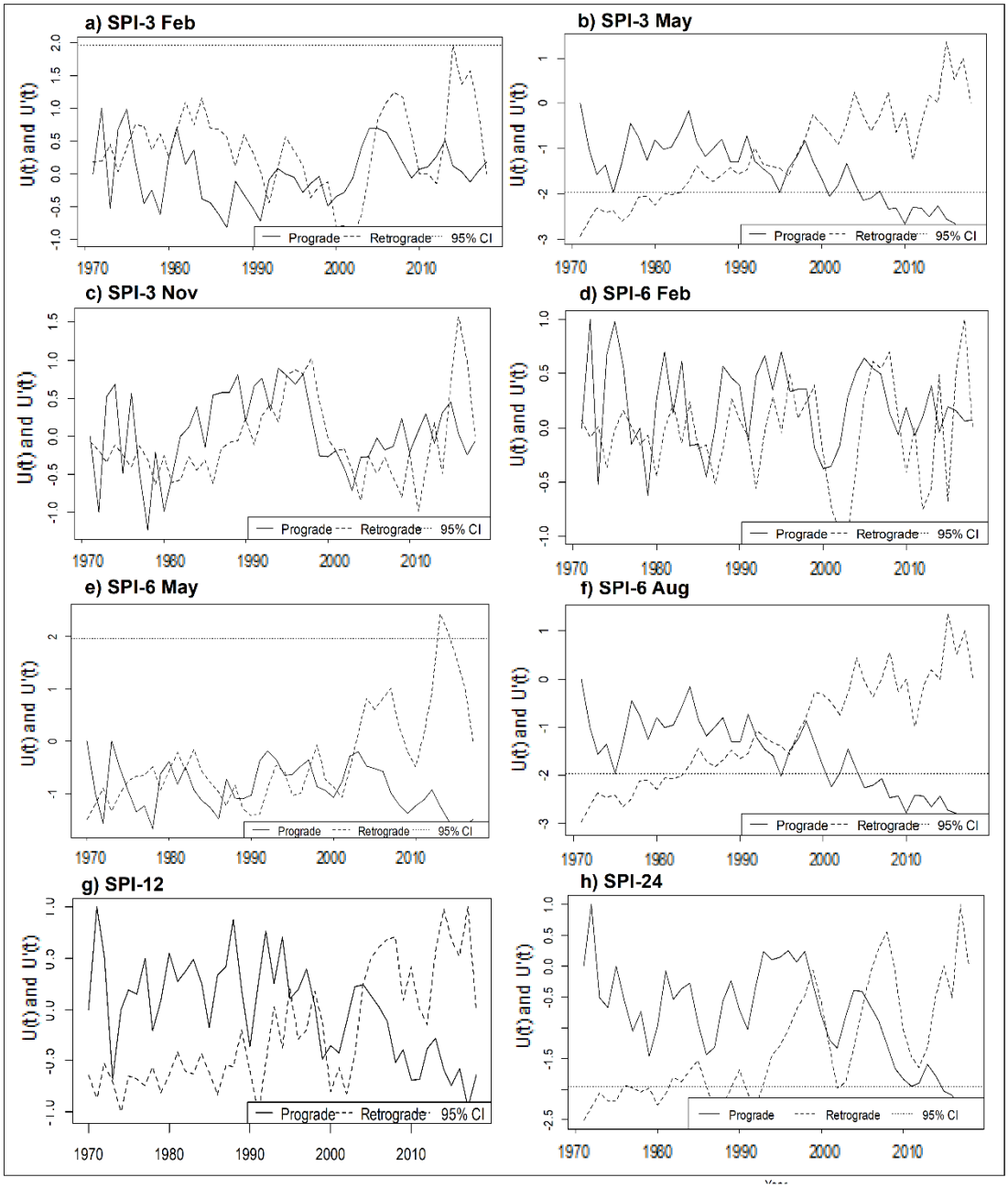

Figure 9.9. Temporal behaviour for different SPI timescales in the period 1970-2018.

SPI lags	Positive (Sig.)	Negative (Sig.)
SPI-3 winter	91(3)	74(4)
SPI-3 spring	8(0)	157(60)
SPI-3 autumn	56(2)	109(1)
SPI-6 autumn/winter	66(1)	99(4)
SPI-6 winter/spring	30(1)	135(4)
SPI-6 spring/summer	7(0)	158(60)
SPI-12 annual	22(4)	143 (44)
SPI-24 annual	26(4)	139(5)

Table 9.4. Number of stations that showed increasing (significant increasing) and decreasing (significant decreasing) trends at 5% significance level.

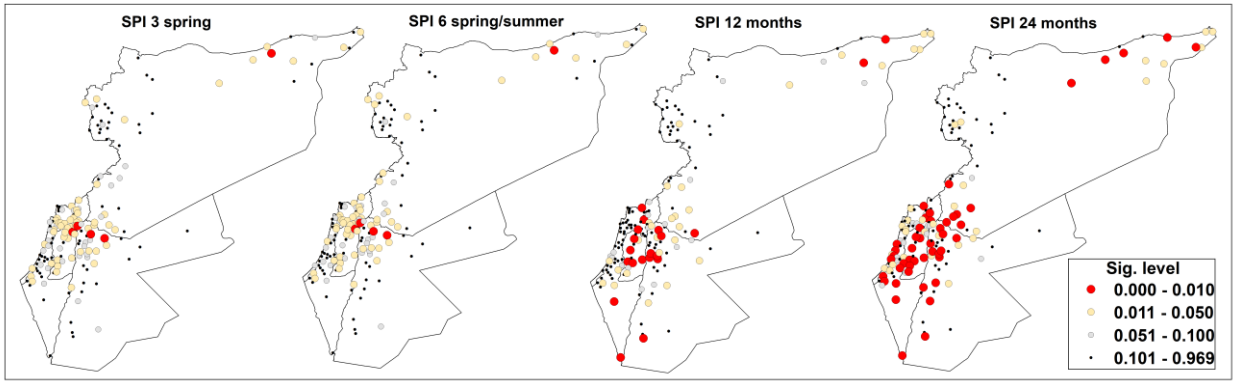

Figure 9.10. Spatial distribution of trend signification for different SPI timescales during the period 1970-2018.

At SPI-3 and -12 months timescales, the drought frequency (DF) and the maximum drought severity (MDS) were calculated for each station, and the values were averaged over the study area. The findings supported the trend toward drier conditions, with non-significant increases in DF at SPI-3 and -12 timescales of 0.20 and 0.58 event/decade, respectively (not shown). For both SPI-3 and SPI-12 timescales, decreasing trends in MDS of -0.07 (significant at 0.1 level) and -0.01 unit/decade, respectively were detected (not shown).

The spatial distribution of trends calculated for these two parameters is depicted in Figure 9.11. For both SPI-3 and -12 timescales, 128 out of 165 stations in the DF (Figure 9.11a and b) were affected by increasing trends, which were distributed throughout the Levant. They covered central and northern Palestine (PC-1 region), as well as southern and eastern Syria, intensively and uniformly, while the Syrian coast area (associated with the PC-2 region) and northern Jordan showed mixed trends, with many locations showing negative trends for DF. Many locations in the West Bank and northeastern Palestine at SPI-3 and -12 timescales, as well as the east of Syria at SPI-12 timescale, were affected by significant increasing trends (0.51-0.75 event/decade). In addition, the magnitudes of trends increased at SPI-12 compared to SPI-3, from 0.31 to 0.62 event/decade for the east of Syria, and from 0.29 to 0.38 event/decade for the north of Palestine.

The dry conditions were also confirmed by the MDS (Figure 9.11c and d), which showed decreasing trends in the study area of -0.096 and -0.11 unit/decade at SPI-3 and SPI-12, respectively (not shown). Furthermore, at SPI-3 and -12, more than 132 out of 165 stations showed

decreasing trends, with 22 and 31 stations showing significant decreases. The PC-1 regions also had the most significant decreasing trends (between -0.15 and -0.20 unit/decade). On the other hand, many locations in PC-2 regions and western Jordan along the border with Palestine showed increasing trends. In comparison to the SPI-3 timescale, the band of high decreasing trends (-0.15 - -0.20) was intensified at SPI-12 scale in north Palestine and southern/eastern Syria.

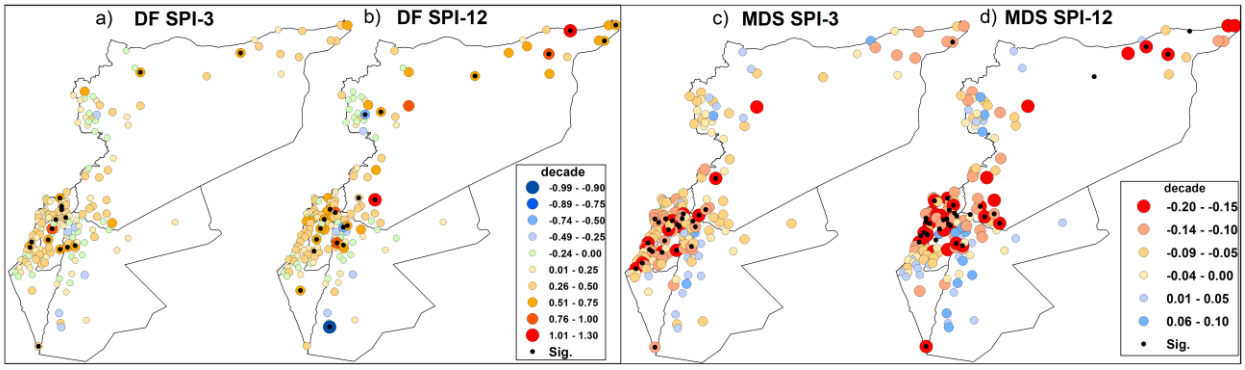

Figure 9.11. Spatial distribution of the DF and MDS trends calculated for the period 1970-2018.

9.2.5 Influence of the large-scale circulation patterns on seasonal drought

The number of stations that showed significant correlations between annual and seasonal SPI values (SPI-12, SPI-3 Feb. for winter, SPI-3 May for spring, and SPI-3 Nov. for autumn) and the teleconnection indices, is listed in Table 9.5. Based on the frequency of significant correlations, the WEMO index is a key driver of drought in Levant in spring, showing 58 stations that are strongly and negatively correlated with it. It is also the second index related with drought in autumn, with 38 stations. The NCP index is the main controller of drought at annual and winter timescales in the Levant, where it showed negative significant correlations with 74 stations. Its effect also was notably on the autumn drought by 43 stations. The ENSO index has the greatest impact on autumn drought, with 93 out of 165 stations reporting a significant correlation with it, though it also has a significant impact on annual and winter drought. The EAWR and MO indices' positive correlations were concentrated in winter by 67 and 50 stations, respectively, putting them second and third after the NCP index. Figure 9.12 represents the spatial distribution of all of these major associations. In most cases, the impact of the teleconnection patterns dominated in the southern Levant, especially in regions assciated with the PC-1 area, which encompassed, central and northern Palestine, north of Jordan, and south of Syria.

The effect of the NCP index on the SPI-12 (Figure 9.12a) is mainly concentrated in the southern areas of Palestine and Jordan, as well as in the west of Jordan (arid and semi-arid climate zones), with correlations ranging from 0.28 to 0.60. On the other hand, the influence of the ENSO index (Figure 9.12b) on the SPI-12 is localized in the southern areas from the Palestinian coast to the northwest of the West Bank, with correlations ranging from -0.29 to -0.39.

Index	WEMO		EAWR		NAO		EA		MO		NCP		ENSO	
	+	-	+	-	+	-	+	-	+	-	+	-	+	-
SPI-12	0	1	2	0	1	0	7	0	4	0	30	2	1	26
SPI-3 Feb.	0	1	67	0	11	0	1	0	50	0	74	0	0	27
SPI-3 May	0	58	0	0	4	0	0	12	3	0	43	0	0	3
SPI-3 Nov.	0	38	8	0	0	6	1	0	2	0	0	0	0	93

Table 9.5. Number of stations that showed significant ($p<0.05$) correlations between their annual and seasonal SPI time series ant the teleconection indices.

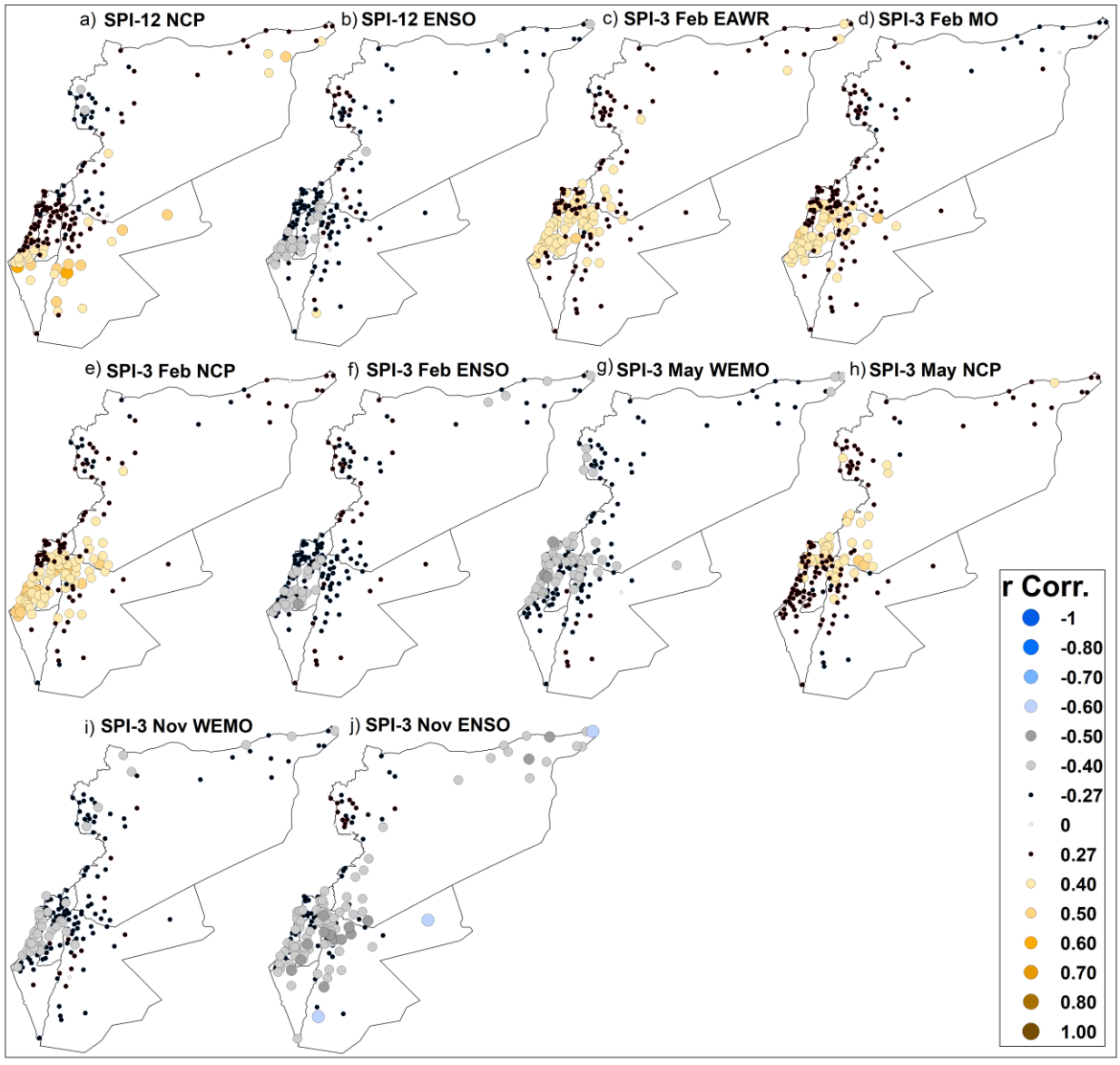

Figure 9.12. Spatial distribution of correlation coefficients between annual and seasonal SPI and some teleconnection indices, for the period 1970-2018. The limits of significant correlations are 27 and -27.

In winter (Figure 9.12c, d and e), the EAWR, MO, and NCP indices present higher frequency and magnitudes of significant correlations than other indices. Their significant effects on SPI-3 Feb occurred predominantly in south Levant, especially in central and northern Palestine, northern

Jordan, and southern Syria, with higher frequency and magnitude, up to 0.50 for the NCP index, up to 0.47 for the MO, and up to 0.42 for EAWR. As can be seen in Figure 9.11f, the ENSO index also exerts some influence on the winter drought in the southern stations of Palestinian coast and West Bank ($-0.49 < r < -0.28$).

During spring, the WEMO and NCP indices had a noticeable influence on SPI values (Figure 9.12 g and h) compared to other indices. The WEMO effect covered virtually all locations along the Palestinian coast, north of Palestine and Jordan, and many locations in Syrian coast with significant negative correlations between -0.28 and -0.41). Furthermore, the NCP index has exerted notably influence (correlation values from 0.28 to 0.49) on northern and northeastern parts of Palestine, north of Jordan, and southern Syria, including Damascus governorate.

The analysis clearly indicated the ENSO pattern is the main driver of the SPI autumn over the Levant (Figure 9.12j). Except for some stations in northern Palestine, Syrian coastal and western areas, all sites showed significant negative correlations with the ENSO index (with values from -0.37 to -0.56) during autumn. It had an influence on Jordan's and Palestine's southern regions as well (Figure 9.12j). Also, the WEMO index reported some effect (correlations values ranging from -0.27 to -0.39) in Palestinian coastal stations, the West Bank, and some northern Syrian locations (Figure 9.12i). Finally, as shown in Figures 6.23, 6.24, and 6.25, the findings were very similar to those obtained from observing the impact of large-scale circulation patterns on the Levant seasonal rainfall.

9.2.6 Covariability analysis

9.2.6.1 Covariability between SST and seasonal drought

By analyzing the covariance matrices of the two fields, the SVD was used to investigate the link between the SST and seasonal drought (SPI-3 Feb, SPI-3 May, and SPI-3 Nov) in the Levant region. The findings are represented by homogeneous and heterogeneous correlation maps (Wallace et al., 1992). Table 9.6 shows the statistics for the first three leading SVD modes, which includes the temporal correlation between pairs of expansion coefficients, strength of the coupling (STR), and percentage of squared covariance (SCF). Table 9.7 also shows how each mode explains the variance for the individual fields (SST, seasonal SPI values). The correlations between the left SST expansion coefficients of the selected SVD modes and the seven teleconnection indices chosen for this study are shown in Table 9.8. Only the coupling coefficients associated with the first three modes were evaluated in all SVD analyses because they accounted for 80% or more of the SCF. The SCF for the third mode drops below 7% in all cases, as shown in Table 9.6, indicating that the amount of information accounted for the third mode in relation to the two fields is not very relevant. Furthermore, there were fewer than seven stations that showed significant correlations with the third mode. Then, only the results corresponding to the first and second modes were discussed because of the reasons stated above. Figures 9.13, 9.14 and 9.15 show the homogeneous and heterogeneous maps along with the expansion coefficient time series for the selected coupled modes for winter, spring and autumn, respectively.

Season	Variable	STR			SST-seasonal drought SCF (%)			Total sig. stations (Heterogeneous)
		Mode1	Mode2	Mode3	Mode1	Mode2	Mode3	Modes (1,2,3)
Winter	**SPI-3 Feb**	0.44	0.52	0.61	58	14	7	(90,23,3)
Spring	**SPI-3 May**	0.40	0.36	0.54	45	22	6	(28,24,7)
Autumn	**SPI-3 Nov**	0.47	0.54	0.59	66	11	6	(106,7,23)

Table 9.6. Summary of the strength of the coupling (STR) and the square covariance fraction (SCF) corresponding to the selected modes obtained from the SVD of SST and seasonal drought for the period 1987-2017.

Season	Variable	SST variance (%)			Seasonal drought variance (%)		
		Mode1	Mode2	Mode3	Mode1	Mode2	Mode3
Winter	**SPI-3 Feb**	18	11	12	45	13	4
Spring	**SPI-3 May**	19	11	8	27	27	5
Autumn	**SPI-3 Nov**	17	13	7	49	5	8

Table 9.7. Explained variance by each coupled mode for the individual fields (SST and seasonal drought).

Season	Variable		WEMO	EA/WR	NAO	EA	MO	NCP	ENSO
Winter	**SPI-3 Feb**	**M1**	-0.28	0.10	**-0.46**	**-0.30**	-0.09	0.04	0.06
		M2	-0.02	**0.33**	**0.66**	0.04	**0.49**	**0.45**	-0.26
		M3	0.18	-0.12	0.10	-0.21	0.08	-0.05	-0.20
Spring	**SPI-3 May**	**M1**	0.07	-0.01	**-0.48**	0.04	-0.04	-0.26	-0.19
		M2	-0.21	0.13	**-0.43**	-0.07	0.01	0.01	-0.06
		M3	-0.09	0.07	0.40	-0.23	-0.11	0.31	0.08
Autumn	**SPI-3 Nov**	**M1**	0.12	0.15	**0.40**	0.07	0.10	0.11	**-0.40**
		M2	0.12	-0.07	0.16	0.05	-0.12	-0.19	0.04
		M3	**-0.34**	0.05	**-0.29**	0.21	-0.15	0.01	-0.01

Table 9.8. Correlations between the left expansion coefficients of the selected SST modes, obtained from the SVD of SST and seasonal drought, and the teleconnection indices.

9.2.6.1.1 Winter SST-SPI covariability

The first and second SVD modes account for 58% and 14% of the squared covariance between the SST and SPI-3 Feb, respectively (Table 9.6). For the first and second modes, the temporal correlation between pairs of expansion coefficients (STR) is 0.44 and 0.52, respectively, and both are significant at the 95% confidence level (Table 9.6, Figure 9.13c). Furthermore, the first pattern accounts for 18% of total SST variance and 45% of total Levant drought variance, while the second mode accounts for 11% and 13%, respectively (Table 9.7). The homogeneus map (Figure 9.13a, Mode 1) shows the Atlantic SST with two centers of action with positive correlations (up to 0.85) in the northernmost latitudes and in the tropical region, and two centers of action with negative correlations (up to -0.70) in the north-central Atlantic and the central Mediterranean Sea. This mode associates with a tripolar pattern of sea surface temperature (SST) anomalies that show one sign in the western midlatitudinal North Atlantic and the opposite in the subpolar and tropical North Atlantic. According to the correlation coefficients calculated between this SST first mode and the teleconnection indices (Table 9.8), only the NAO and EA indices presented significant negative correlations of -0.46 and -0.30, respectively.

The heterogeneous map (Figure 9.13b, Mode 1) revealed that this mode is strongly linked to winter drought in most Levant locations, with magnitudes of significant correlations around 0.30-0.49 in

northern Palestine, Jordan, and the majority of Syrian stations. It also has an impact on drought in a few isolated locations in eastern and southern Jordan. This means that during winter, when the northern and southern parts of the North Atlantic Ocean are unusually cold, the Levant experiences more drought.

For the second SVD coupled mode, the homogeneous SST map (Figure 9.13a, Mode 2) showed significant positive correlations (up to 0.70) to the northern and eastern of Europe (e.g., North Sea and Bay of Biscay) and for the central and southern Mediterranean Sea. This mode showed significant positive correlations (between 0.30-0.49) with winter SPI variability in the southern portions of the Palestinean coast. Furthermore, some stations in eastern Syria had a negative correlation with this mode. The EA/WR, NAO, and MO indices presented significant positive correlations with the left SST expansion coefficients in the range (0.33-0.49), wherase the correlations was highr with the NAO index by 0.66 (Table 9.8).

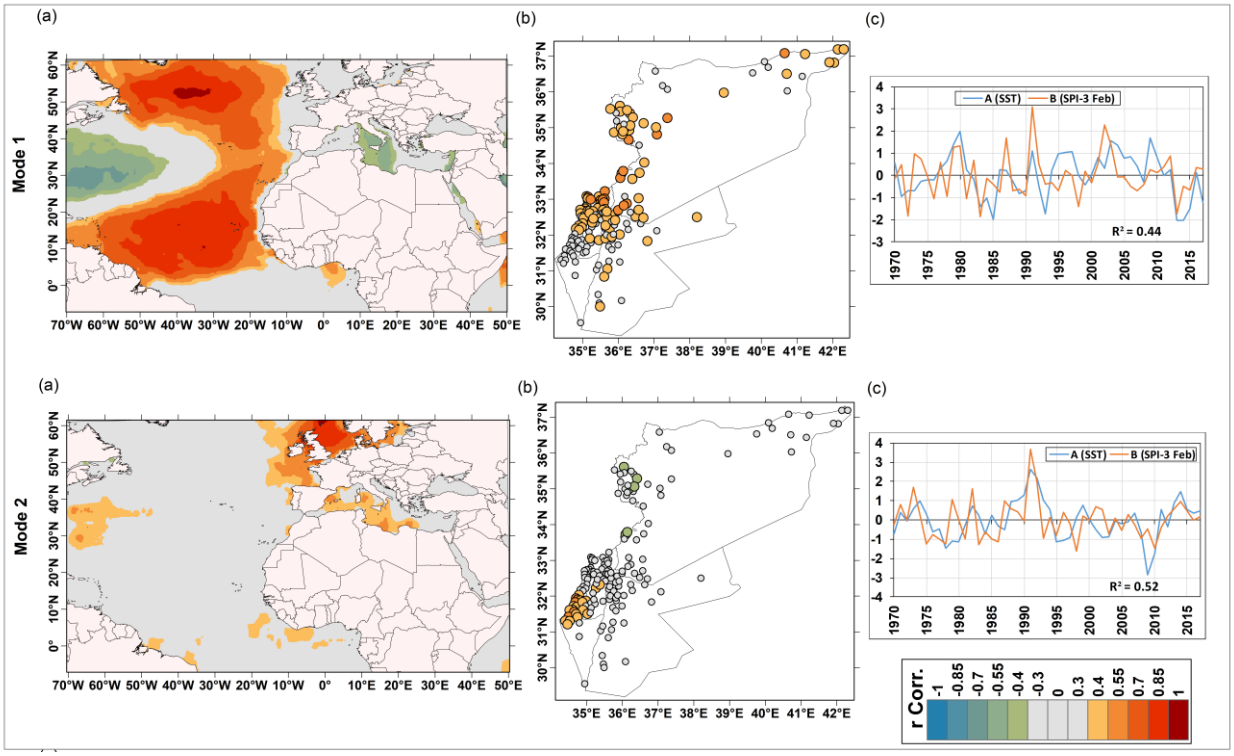

Figure 9.13. (a) Homogeneous maps, (b) heterogeneous maps, and (c) left (SST) and right (SPI-3 Feb) normalized expansion coefficient time series for the Mode 1 (upper panel) and Mode 2 (bottom panel). Colored areas and circles in homogeneous and heterogeneous maps represent regions and stations with significant correlations at 0.05 significance level (corresponding to correlation values higher than +0.30 and lower than -0.30).

9.2.6.1.2 Spring SST-SPI covariability

Figure 9.14 depicts the spatial patterns of the two variability modes of SST obtained by the SVD in spring (Figure 9.14, panel a), as well as the map of heterogeneous correlations for spring SPI values (Figures 9.14, panel b) and the temporal variability of each mode, as represented by the respective coefficients of expansion (Figure 9.14, panel c). With coupling strengths of 0.40 and

0.36, the first two coupled modes explain 45% and 22% of the fractional variance for the covarience matrix SST–SPI-3 May) (Table 9.6). Furthermore, the first mode alone accounts for 19% of total SST variability and 27% of total spring drought variability (Table 9.7). The second mode accounts for 11% of total SST variance and 27% of SPI values in spring (Table 9.7).

The first and second modes' homogeneous maps (Figure 9.14a, Mode 1 and 2) show a horseshoe shape with significant positive correlation in the Atlantic Ocean and significant negative correlation in the central Atlantic Ocean and western Mediterranean Sea. The heterogeneous map connected to the first mode, as shown in Figure 9.14b (Mode 1), showed significant negative correlations with 25 stations with values ranging from -0.30 to -0.46, mostly located in the south of the Levant, northern Palestine, and western Jordan. The heterogeneous map for the second mode, on the other hand, revealed significant positive correlations (values between 0.30 - 0.46) with 28 stations primarily in the northern Levant, west, and south of Syria. This pattern is responsible for an increase in drought events in the south of Levant and a decrease in drought "wetter conditions" in the north of Levant when it is abnormally warm. The correlations with teleconnection indices were only significant for the NAO index by -0.48 and -0.43 for both modes, with the same strength for the correlations between the left SST expansion coefficients and SPI spring values.

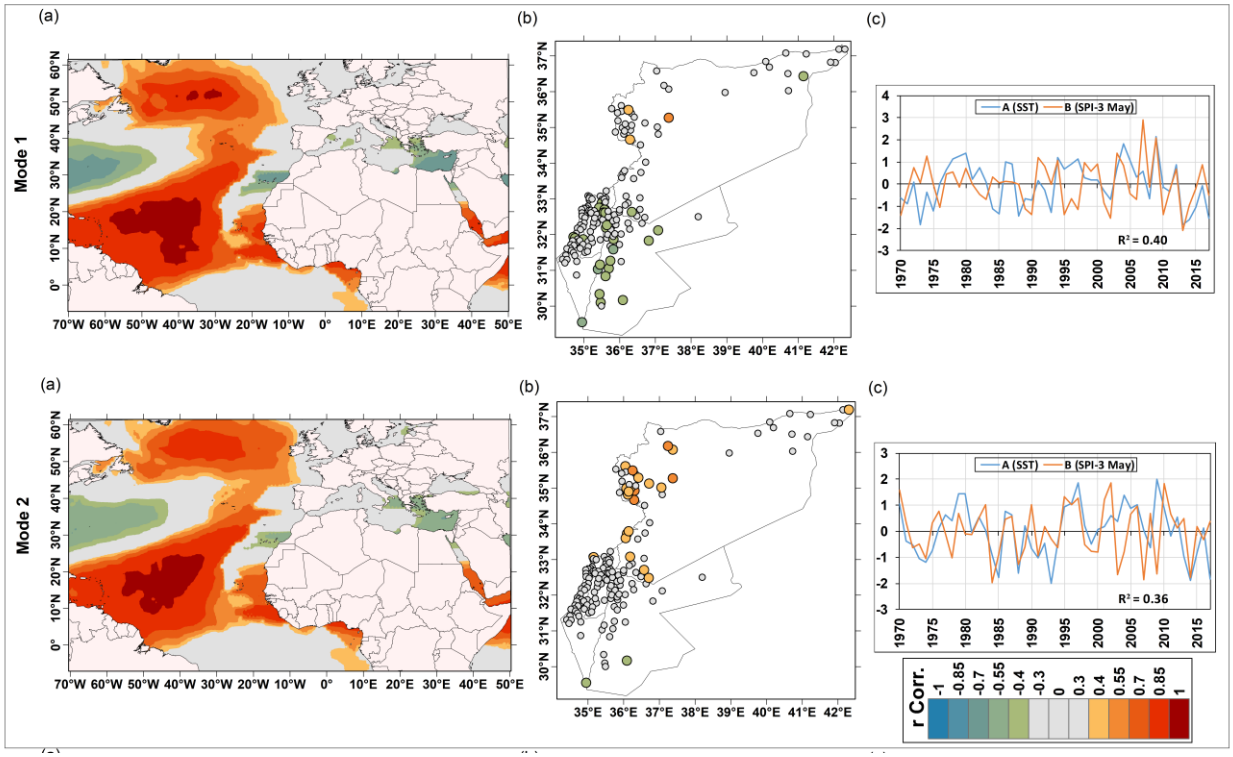

Figure 9.14. As Figure 9.13 but for drough in spring.

9.2.6.1.3 Autumn SST-SPI covariability

With a coupling strength of 0.47, the first coupled pattern is responsible for 66% of the SCF. Furthermore, the variance explained by the first mode in each field accounted for 17% of the total SST variance and 49% of the autumn drought variance (Table 9.7). In the north and tropical Atlantic Ocean, the homogeneous map (Figure 9.15a, Mode 1) shows a significant negative correlation (up to 0.70). With 106 stations covering all regions except Syria's coastal and northeastern areas, the heterogeneous map (Figure 9.15a, Mode 1) revealed significant positive correlations (between 0.30-0.51). The Levant has wetter conditions in autumn, when the SST in the northern and tropical Atlantic Ocean is remarkably cold, according to the homogeneous and heterogeneous maps. The correlations between the SST expansion coefficient time series and the NAO and ENSO indices were 0.40 and -0.40, respectively (Table 9.8).

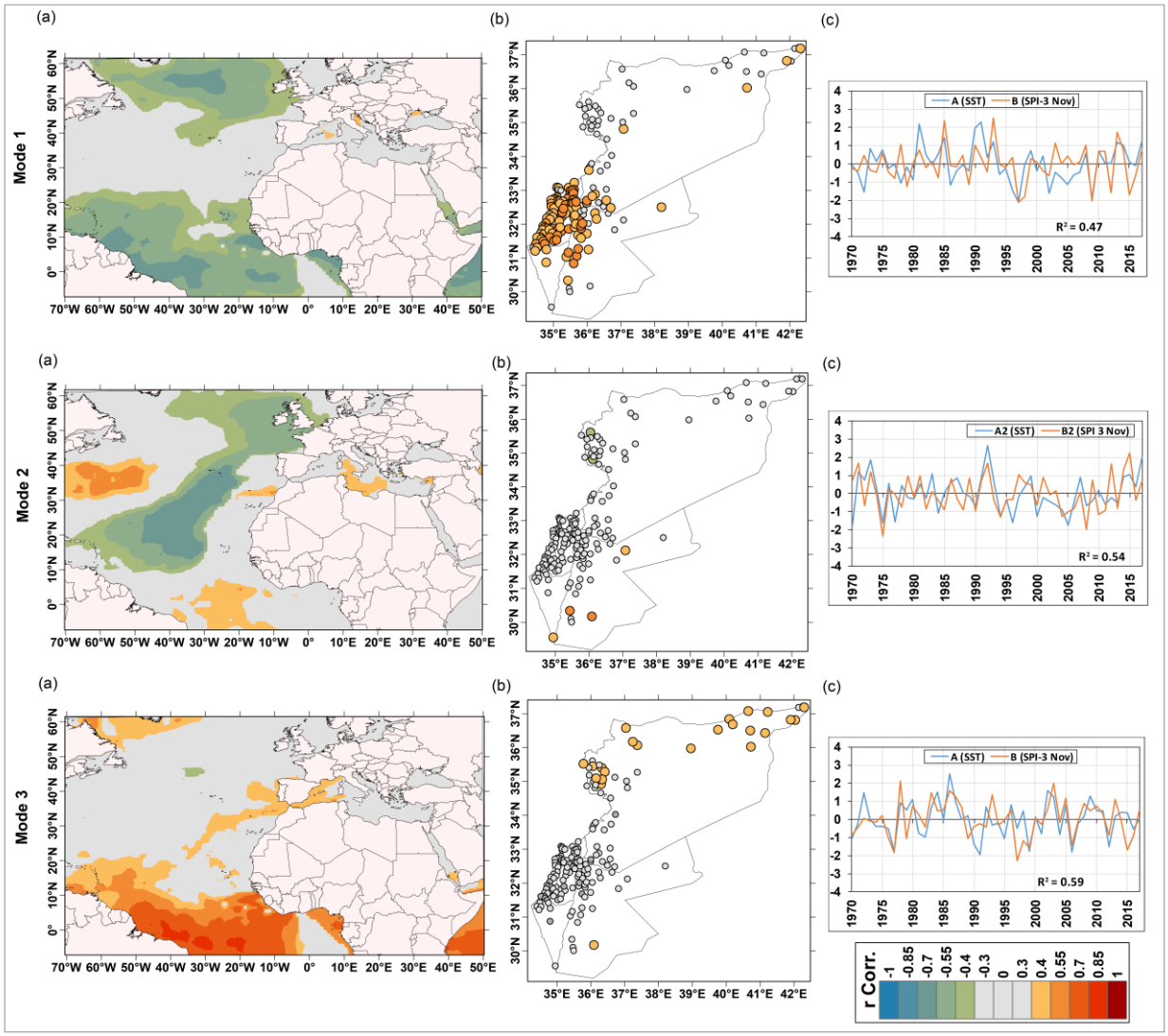

Figure 9.15. As Figure 9.13 but for drough in autumn.

The third coupled mode between the SST and the autumn drought (Figure 9.15, Mode 3) explains 6% of the SCF. The STR is 0.59, which is statistically significant at the 95% confidence level. For the third mode, the variance explained for each field was 13% of the total SST variance and 8% of the total SPI-3 Nov variance (Table 9.7). This pattern did not present a discernible relationship with the teleconnection indices (Table 9.8). Its SST homogeneous map revealed a strong correlation in the southern North Atlantic Ocean and the western Mediterranean Sea (Figure 9.15a, Mode 3). The heterogeneous map showed a significant positive correlation (between 0.30-0.54) with Syrian stations in the coastal and western areas, as shown in Figure 9.15b, Mode 3. This means that if the southern region of the North Atlantic Ocean is warmer than usual, the aforementioned Syrian regions will experience more humid conditions.

9.2.6.2 Covariability between SLP and seasonal drought

In this section, drought in the Levant and SLP relationships are investigated using SVD analysis. For the first three modes of the SVD analysis, Table 9.9 shows the percentage of the SCF and the temporal correlation between the pairs of expansion coefficients to give us an idea of the coupling strength. Table 9.10 also shows the variance explained by each mode for individual fields (SLP and seasonal drought). Table 9.11 shows the relationships between the teleconnection indices and the left (SLP) expansion coefficients of the selected SVD modes.

Season	Variable	STR			SLP-seasonal drought SCF (%)			Total sig. stations (Heterogeneous)
		Mode1	Mode2	Mode3	Mode1	Mode2	Mode3	Modes (1,2,3)
Winter	**SPI-3 Feb**	0.46	0.43	0.56	53	20	7	(74,26,5)
Spring	**SPI-3 May**	0.58	0.58	0.64	69	13	4	+(110,0,26) -(0,32,0)
Autumn	**SPI-3 Nov**	0.62	0.67	0.69	74	7	4	+(141,11,2) -(0,19,6)

Table 9.9. Summary of the strength of the coupling (STR) and the square covariance fraction (SCF) corresponding to the selected modes obtained from the SVD of SLP and seasonal drought for the period 1987-2017.

Season	Variable	SLP variance (%)			Seasonal drought variance (%)		
		Mode1	Mode2	Mode3	Mode1	Mode2	Mode3
Winter	**SPI-3 Feb**	16	14	12	39	19	5
Spring	**SPI-3 May**	19	8	5	39	17	8
Autumn	**SPI-3 Nov**	13	7	7	53	8	4

Table 9.10. Explained variance by each coupled mode for the individual fields (SLP and seasonal drought).

Season	Variable		WEMO	EA/WR	NAO	EA	MO	NCP	ENSO
Winter	**SPI-3 Feb**	**M1**	0.16	**-0.60**	**-0.52**	-0.15	**-0.37**	**-0.54**	**0.45**
		M2	-0.11	0.21	**0.74**	0.04	**0.44**	**0.51**	0.24
		M3	0.17	0.25	-0.14	0.57	-0.16	-0.10	-0.70
Spring	**SPI-3 May**	**M1**	**-0.36**	0.12	**0.57**	-0.02	0.51	**0.54**	-0.20
		M2	0.14	0.17	**0.54**	**0.30**	**0.53**	0.10	-0.16
		M3	-0.17	0.01	-0.13	-0.24	-0.08	0.06	0.28
Autumn	**SPI-3 Nov**	**M1**	**-0.29**	**0.36**	**0.38**	0.03	0.13	**0.31**	**-0.72**
		M2	0.02	0.08	**0.38**	0	-0.06	0.06	**-0.40**
		M3	-0.17	-0.01	0.65	-0.11	0.43	0.50	0.31

Table 9.11. Correlations between the left expansion coefficients of the selected SLP modes, obtained from the SVD of SLP and seasonal drought, and the teleconnection indices.

9.2.6.2.1 Winter SLP-SPI covariability

The first coupled mode in winter (Figure 9.16, left panels) explains 53% of the square covariance, and the strength of the coupling is 0.46, significant at the 95% confidence level (Table 9.9, Figure 9.16c). The first mode also explains 16% of the total SLP variance and 39% of the winter drought variance (Table 9.10). The homogeneous map (Figure 9.16a) shows a center of significant positive correlation ($r > 0.70$) extended over the north of Asia and Atlantic Ocean, which is responsible for increase drought in winter in south Levant, central Palestine, north Palestine and Jordan (Figure 9.16b). The homogeneous map also shows significant negative correlations ($-0.54 < r < -0.31$) over the equatorial Atlantic Ocean, south of Europe, Mediterranean Sea, Africa, western Indian Ocean. The SLP over these regions positively correlated with drought in in south Levant.

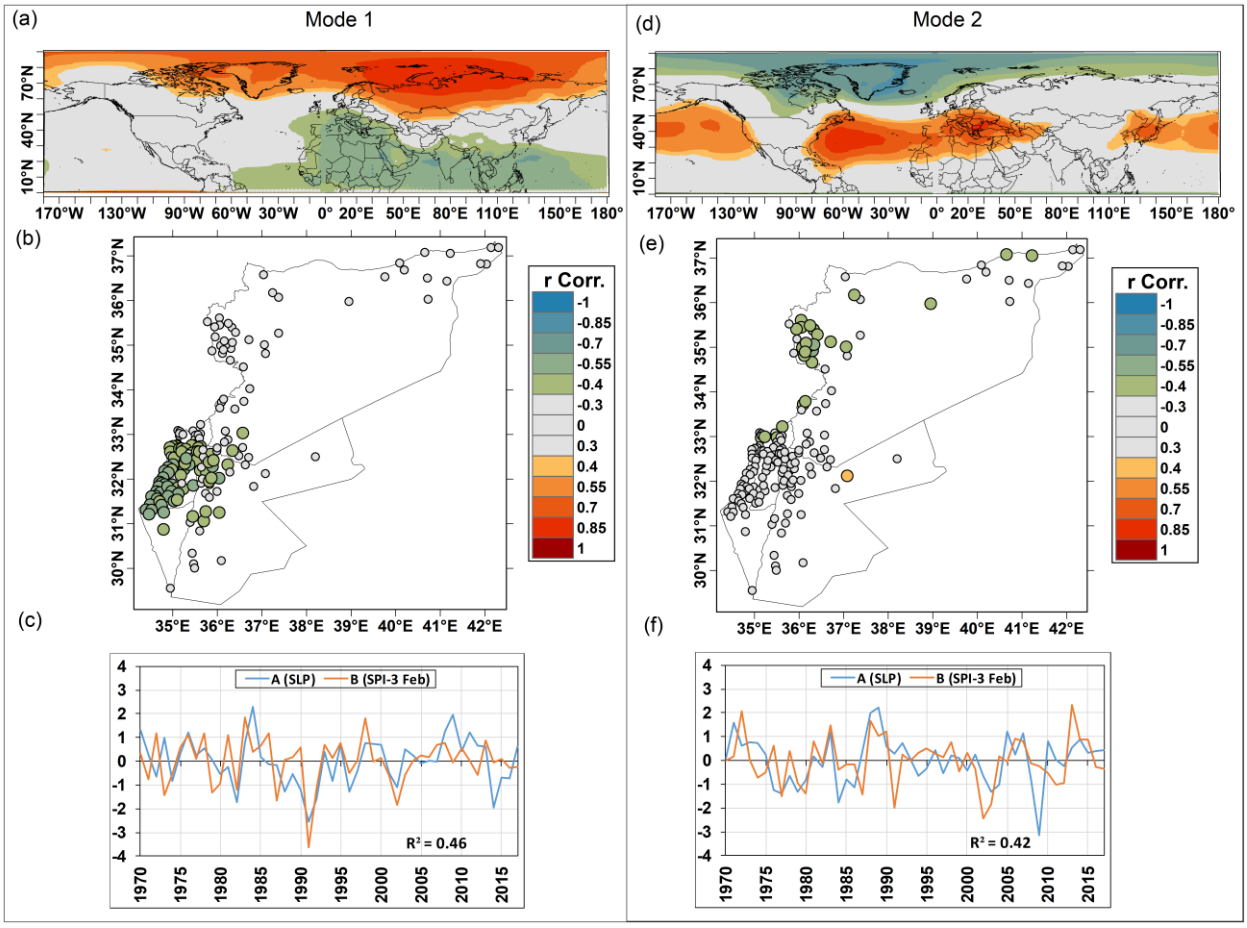

Figure 9.16. (a and d) Homogeneous map, (b and e) heterogeneous map, and (c and f) left (SLP) and right (SPI winter) normalized expansion coefficient time series for the Mode 1 and Mode 2. Colored areas and circles in homogeneous and heterogeneous maps represent regions and stations with significant correlations at 0.05 significance level (corresponding to values higher than +0.30 and lower than -0.30).

The second mode (Figure 9.16, right panel) explains 20% of the square covariance with a strength of the coupling of 0.46, significant at the 95% confidence level (Table 9.9, Figure 9.16f). Furthermore, the second mode accounts for 14% of total SLP variation and 19% of winter drought variability (Table 9.10). The homogeneous map (Figure 9.16d) shows a strong significant positive

correlation (up to 0.85) over the Atlantic Ocean's central region, which stretches all the way to the Mediterranean Sea and the over the higher and mid latitudes of the Pacific Ocean. It also shows negative correlations over Greenland, which extend into high latitudes for the entire globe. The teleconnection indices, NAO, MO, NCP, and ENSO significantly correlate with the left (SLP) expansion coefficients time series by -0.52, -0.37, -0.54, and 0.45, respectively (Table 9.11). As can be seen in the heterogeneous map (Figure 9.16e), the drought variability in the most north Palestine and Syrian coastal areas is negatively correlated with the SLP over the Atlantic Ocean's central region and positively with the SLP over the Greenland and high latitudes.

9.2.6.2.2 Spring SLP-SPI covariability

Figure 9.17 presents the results of the homogeneous correlation maps (Figures 9.17a and d) for the first two SLP modes obtained by the SVD in spring, together with the heterogeneous correlation maps for SPI-3 May (Figures 9.17b and e), and the temporal variability of each mode, represented by their respective expansion coefficient time series (Figures 9.17c and f).

The first mode explains 69% of the squared covariance, and the strength of the coupling reached 0.58 (Table 9.9, Figure 9.17c). Furthermore, the first SVD mode explains 19% and 39% of the total variance for the SLP and spring SPI fields, respectively (Table 9.10). The homogeneous map (Figure 9.17a) exhibits a pattern of positive correlations (r> 0.70) over Europe and western Mediterranean that extends through the Atlantic until North America with lower values (up to 0.55). The NCP, WEMO, and NAO indices significantly correlate with this left expansion coefficient time series by 0.54, -0.36, and 0.57, respectively (Table 9.11). The heterogeneous map couples this mode with drought variability in the southern Levant countries with high correlations (between 0.55-0.72) in the Palestine coast and northern locations (Figure 9.17b). This pattern is responsible for a generalized increase in SPI-3 May values (wetter conditions), mostly in south of Levant.

The second coupled mode (Figure 9.17, right panel) explains 13% of the SCF and presents a strength of the coupling of 0.58 (Table 9.9, Figure 9.17f). It explains 8% and 17% of the total variance of the SLP and spring drought, respectively (Table 9.10). From the homogeneous pattern (Figure 9.17d), the higher positive values of correlation (> 0.70) are located over west of Europe, extending through the central Atlantic Ocean to the eastern coasts of North America (Figure 9.17d), and it also has strong negative correlations over Greenland, which extend into high latitudes for the entire globe. This pattern presents significant correlations with the NAO, EA, and MO indices. The correlation between the time series of this SLP expansion coefficients and these teleconnection indices are between 0.30 and 0.54, significant at the 95% confidence level (Table 9.11). The heterogeneous correlation map (Figure 9.17e) shows significant negative correlations at the 95% confidence level over the Syrian coastal, western, and eastern areas. This implies that when the SLP over the west Europe and central North Atlantic Ocean has positive anomalies and the SLP over the Greenland and high latitudes has negative anomalies, the SPI decreases (more drought), and vice versa.

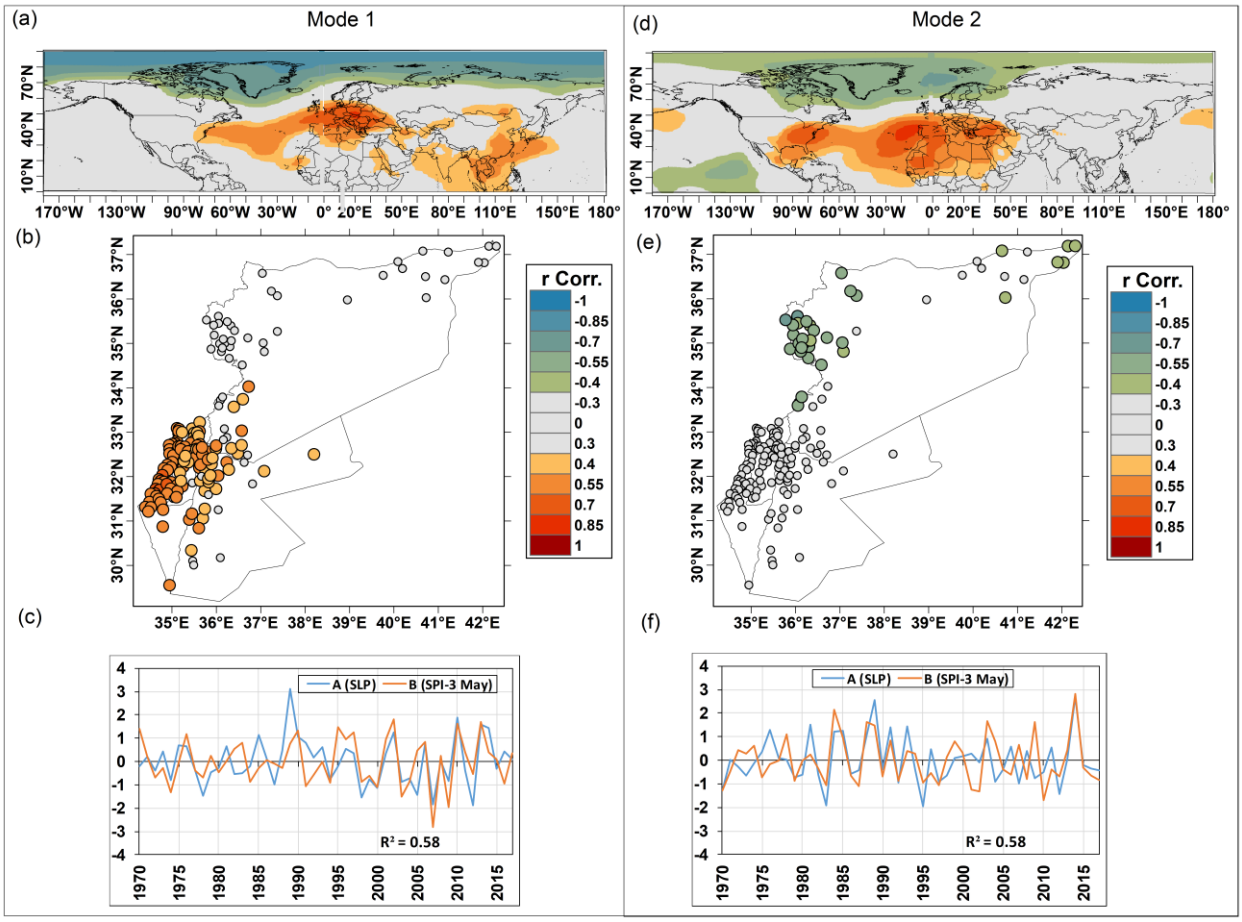

Figure 9.17. As Figure 9.16 but for spring**.**

9.2.6.2.3 Autumn SLP-SPI covariability

During autumn, the first coupled mode explains 74% of square covariance, with a couple of strength between the SLP and SPI-3 Nov of 0.62, which provides the highest square covariance among all the seasons (Table 9.9, Figure 9.18c). The first mode explains 53% of the total variance of the autumn drought and 13% of the SLP variance (Table 9.10). Its homogeneous SLP spatial pattern (Figure 9.18a) shows a structure associated with ENSO index, with two action centers varying in opposite phase located over the western and eastern parts of the tropical Pacific Ocean. The correlation between the SLP expansion coefficient time series associated with this first mode and the ENSO index is -0.72 (Table 9.11), being significant at the 95% confidence level. When the western Pacific SLP has positive anomalies and the eastern Pacific SLP has negative anomalies, the SPI rises (more humid conditions), and when the western Pacific SLP has negative anomalies and the eastern SLP has positive anomalies, the SPI falls (more drought). Additionallay, positive correlations were found in the southern part of the North Atlantic Ocean, South Africa and Asia, with high value in the north of Indian Ocean ($r > 0.85$) (Figure 9.18a). As shown in Figure 9.18b, all locations "except Syrian coastal area" showed positive and significant correlation with the SLP in these regions.

The second mode (Figure 9.18, left panel) explains 7% of the square covariance, and the strength of the coupling is 0.67, which is significant at the 95% confidence level (Table 9.9, Figure 9.18f). It also explains 7% of the total SLP variance and 8% of the autunm drought variance (Table 9.10). The homogeneous map (Figure 9.18b) shows a center of significant positive correlation (up to 0.75) over the North Asia and Siberia, which is associated with increasing drought in autumn in Syrian coast locations and a decrease in some southern locations from Jordan and Palestine when high SLP anomalies are presented over Asia.

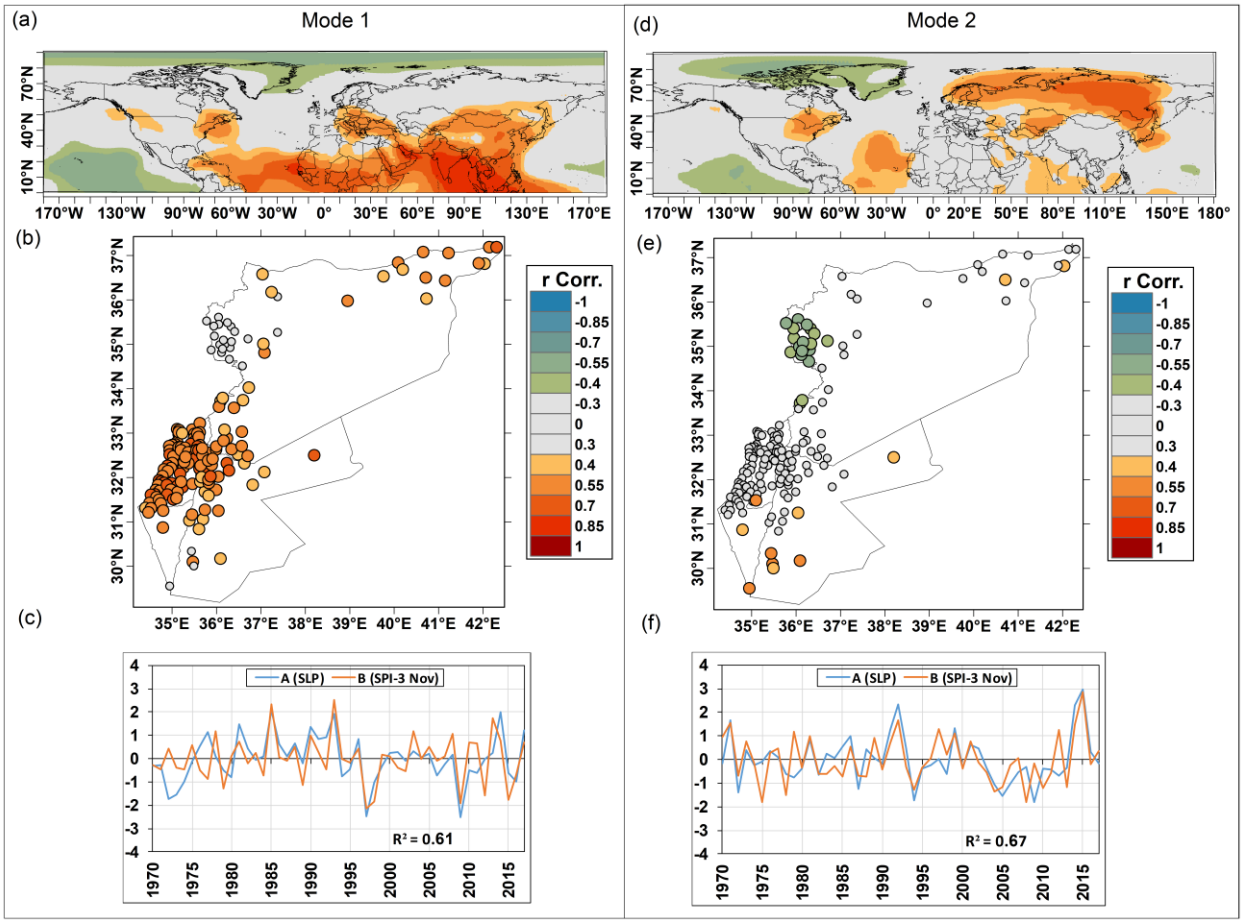

Figure 9.18. As Figure 9.16 but for autumn.

9.3 Conclusions and discusion

Using observational rainfall data from 165 meteorological stations, the standardized precipitation index (SPI) was computed at several timescales to assess the spatial and temporal variability of drought in the Levant from 1970 to 2018. The following conclusions may be drawn:

1. The temporal variation of the mean SPI over the Levant reveals that only the year 2008 had an extreme drought event for SPI-3 spring and SPI-6 spring/summer. In 1992, extremely wet conditions were observed for SPI-3 winter and SPI-6 autumn/winter. The wettest events were observed at many SPI timescales in 1991/1992, 1971, and 1988. Moderate and above drought events, on the other hand, were mostly observed at several

SPI timescales in 1998/1999, 2010, 2013/2014, and 2008. (e.g., 44% of the stations showed extreme drought events in 1999 for the SPI-12 months timescale). Furthermore, the Levant region experienced drought episodes in 1999-2001, 2006-2011, and 2014-2018, all of which were more severe at long-term drought scales.

Several studies have identified 1991/1992 as the wettest year on record for many Levantine countries, and 1998/1999, 2008, and 2010 as the worst drought years on record (Turco et. al., 2017; Inbar and Bruins, 2004; Haensel and Zurba, 2015; Kafle and Bruins, 2009; Salim and Wildi, 2005; Abu Hajar et al., 2019; Mustafa and Rahman, 2018; Yenigun and Ibrahim, 2019). Drought in Jordan, Syria, and Israel were also documented during the periods 1999-2001 and 2006-2011 (Mathbout et al., 2018; Kelley et al., 2015; Gleick, 2014; Mohammed et al., 2020; Al-Qinna et al., 2011; Inbar and Bruins, 2004). According to some of these studies, one of the causes of the civil war in Syria was the drought that struck the country between 2007 and 2011. Drought in central, southwest of Asia, and Middle East was studied by Barlow et al. (2002) and (2016), who identified severe droughts in 1998-2001 and 2007/2008, which they attributed to a cold phase ENSO (La Nina) event and unusually warm ocean waters in the western Pacific. Abbas and Kousar (2021) also found the strong ENSO in 1998/1999 contributed rise to a 5-year drought from 1998 to 2002 in the regions of South Asia. Significant negative correlations between the ENSO index and the SPI-12, -3 Feb, and -3 Nov were also detected in this study.

2. Drought characteristics have increased significantly in all regions and for all SPI timescales from 1995 to 2018, compared to the period 1970-1994. In general, the regions had higher values of drought parameters at long-term drought scales than at short- and mid-term drought scales, with the southern and eastern regions of the Levant showing this result more clearly. Identical spatial patterns for all SPI timescales were found between the TDS TDD, and DF maps.
3. According to the PCA analysis, the study area can be divided into three homogeneous PC regions for SPI-3, -6, and -12 months timescales, that explain 70.7%, 66.6% and 68.3% of the total variance, respectively, and four regions for SPI-24 months timescale that explain 72.3% of the total variance.
4. The least vulnerable regions to DF, TDD, and TDS are the central and northern locations of Palestine, northern Jordan, and southern Syria, associated with the PC-1 region at SPI-3 and -6 months timescale, and the central and northern locations of Palestine and northern Jordan (PC-1 region at SPI-12 and -24 timescales). The Syrian coastal and western locations, associated with the PC-2 region at SPI-3 and -6 months, on the other hand, had the highest values for all drought characteristics. At larger timescales, the eastern and southern locations of the Levant, associated with the PC-3 region for SPI-12 and with PC-3 and PC-4 regions for the SPI-24, generally showed the highest values of the DF, TDD, and TDS than other regions.
5. The study confirmed the trend toward drier conditions, especially after the mid-1990s. Drought has become more frequent and extended, within the region. Significant (at 0.05 level) decrasing trends were detected for the SPI-3 spring and SPI-6 spring/summer, with a significant change point detected in 1997. For SPI-3 spring, SPI-6 spring/summer, SPI-

12, and SPI-24, a strong increasing drought pattern from 1990 to 2018 was observed. Spatially, the widespread significant decreasing trends (> 27% of the total stations) were observed for SPI-3 May, SPI-3 spring/summer, and SPI-12 months timescales, and they mainly affected the central and northern locations in Palestine, northern Jordan, and east of Syria, while other regions showed few significant trends. As was documented in Chapter 6, Section 6.4.1, the significant decreasing trends for SPI-3 spring are accompanied by a significant temporal and spatial decline in spring precipitation for most Levant regions (see also the study of Ziv et al. (2014) for Israel). Moreover, dominant increasing trends were detected in the number of stations affected by different drought categories and at various SPI timescales.

6. Despite having the lowest DF, TDD, and TDS values, the PC-1 regions showed heavy significant increasing trends for the DF at SPI-3 and -12 months timescales. Furthermore, the MDS's significant decreasing trends were concentrated over the PC-1 and PC-3 regions. On the other hand, while the PC-2 (Syrian coast) had the highest DF, TDD, and TDS values, the DF and MDS showed mixed trends with no significance. In comparison to other regions with mixed trends, this indicates that significant changes will occur in central and northern Palestine, as well as eastern Syria.

These results are consistent with other studies conducted in the Levant sub-regions and the areas around them. Trends towards drier conditions in large parts of the Mediterranean region have been also observed in Palestine, Jordan, Syria, Israel, and Lebanon (Mahfouz et al., 2015; Aladaileh et al., 2019; Hameed et al., 2018; Haensel and Zurba 2015; Turco et al., 2017; Mathbout et al., 2018). Several studies have found that global trends in drought characteristics are on the rise (Dai et. al., 2004; Sheffield et al., 2012). According to Cook et al. (2016), the drought that hit the Levant region from 1998 to 2012 was the driest on the records in the past nine centuries. Mustafa and Rahman (2018) showed a significant increase in magnitude of drought with the rate 0.02 unit/year for the period 1980-2017 in Jordan. Haensel and Zurba (2015), based on grided data for the period 1950-2010, showed that dry anomalies for the first ten years of the 21st century were more abundant than wet anomalies in Palestine. Moreover, Mahfouz et al. (2016) studied the temporal variability of the SPI in Lebanon using gridded rainfall dataset for the period 1951–2000, and the results demonstraed extremely dry conditions in the year 1999 and 2014, and a decreasing trend of SPI-12 months timescale, for all selected regions, was detected. Mathbout et al., (2018) analysed the drought in Syria using data from 20 stations in 1961-2012, and their analysis suggests that Syria had a severe drought in the 1990s, which had been never observed before in the country. Furthermore, the 2007–2010 drought was the driest period in the instrumental record, happening just before the onset of the recent conflict in Syria.

Hameed et al. (2018) studied drought characteristics over Iraq in 1948-2009 and the results revealed a significant drought exacerbation over Iraq during the sub-period of 1998–2009. Two significant drought periods, 1998–1999 and 2007–2008, have been identified when severe to extreme droughts covered about 87% and 82% of Iraq, respectively. Mohammed et al., (2020) examinid the variability of drought in Syria at SPI-12 scale using data from 36 stations for the period 1990-2010, and the results indicated drought was more intensified in the early 1999–2001 and 2007–2010. The results also demonstrated a statistically significant decline in SPI-12 values

over Syria. Turco et al., (2017) studied the recent drought changes in Israel as a case study of the Eastern Mediterranean using grided data for the period 1980-2014, and they found significant decreasing trends for SPI-3 spring by -0.3 unit/decade and a decreasing trend for SP1-12 by -0.20 unit/decade. The results also showed that drought conditions in Israel have increased since 1980, regardless of the drought index considered.

According to Kafle and Bruins (2009), Israel's climate became more arid in most regions between 1970 and 2002. They discovered a significant warming trend, as well as a decrease in annual average precipitation and the annual aridity index. Shohami et. al. (2011) suggested that the EM region is experiencing a climate change manifested by an increased warming and drying. Changes of atmospheric conditions during winter and the transitional seasons such as increase in the SLP over the entire Mediterranean Basin, increased anticyclonic circulation, a weakening of the Eurasian thermal high, and a rising 500-hPa geopotential height, support drier conditions resulting from reduction in cyclogenesis and specific humidity over the EM. Shohami et al. (2011) also showed a summer–autumn SST increase in the Mediterranean, which points to a reduction in the Mediterranean Sea's cooling effect eastward, as well as an extension of the summer season into autumn.

7. Drought is primarily controlled by the NCP, WEMO, and ENSO indices in the winter, spring, and autumn, respectively. The NCP and WEMO had the greatest impact in the southern Levant, particularly on the PC-1 area, which included central and northern Palestine, north Jordan, and south Syria. The ENSO effect, on the other hand, covered the entire region in the autumn, with the exception of the Syrian coast. In addition, other indices also exhibited notable effects on the drought variability in the Levant regions but with less frequency and magnitude, such as MO and EA/WR on the SPI-winter, NCP on the SPI-spring, and WEMO on SPI-autumn.

There are no previous studies directly documenting the relationship between large-scale patterns and drought in the Levant at regional or local scales, making comparisons difficult. It is also worth noting that these teleconnection indices influenced rainfall variations in the Levant in a similar way. In Chapter 8, section 8.3, the physical mechanisms by which these indices influenced seasonal precipitation in the Levant, and thus the drought, were discussed. During positive NCP and EA/WR phases, the drought will decrease due to the cold air advection from the north towards the southern part of Europe and the eastern Mediterranean region, with increased moisture transport from the Black Sea. The ENSO influences the Middle East precipitation variability through an equatorward shift of the subtropical jet, if the jet stream shifts equatorward (El Niño) or poleward (La Niña) by a few degrees, significant changes in precipitation amounts can occur. During El Niño events, the polar jet streams moved further south causing increased storms and thus decreased drought.

8. From the SST/SLP-drought covariability analysis, a percent between 50-60% of the total seasonal drought variance can be explained by the first and second SST and SLP covariability modes. Additionally, the first coupled SLP-seasonal drought showed higher values of the SCF and STR compared to the first SST-drought for spring and autumn. It also explains higher drought variance in the Levant than the SST. On the other hand, the

first coupled SST-drought showed higher values of the SCF and STR for winter compared to the SLP-drought, and it explains higher SPI variance in winter than the SLP.

In most cases, the covariability analysis revealed the first SST/SLP-seasonal drought mode was significantly related to the southern Levant, while the second SST/SLP-seasonal drought mode was significantly related to the drought variability in the Syrian coast and northern areas. Similar results were obtained for the first and second SST/SLP-seasonal rainfall covariability modes in the Levant.

9. The first SST-winter drought coupled mode reflects the SST tripolar Atlantic pattern, which resembles the NAO signature. This SST pattern marks by a same sign in the north and south of the North Atlantic Ocean and a different one in the central Atlantic and the Mediterranean Sea. Furthermore, the drought in all regions, except for the southern location of the Palestinian coast were significantly connected with this pattern. For the second coupled mode, when the SST in the North and Baltic Seas, west of Europe, and southern parts of the Mediterranean Sea are abnormally warm, wetter conditions will occur in the southern location of the Palestinian coast. The second mode showed significant positive correlations with the NCP, EA/WR, and MO indices.
10. The first SLP-winter drought coupled mode indicates when the SLP over Europe, entire North Africa, North Indian Ocean and west Pacific Ocean is higher than normal, the drought in southern Levant decreases. For this mode, drought in the south of Levant was mainly correlated with the NCP index, where increase NCP “positive phase” leads to increase SPI values and increase rainfall. On the contrary, if the SLP over the northern latitudes increases, the drought will increase. The second SLP-winter drought coupled mode is only relevant in the western Syrian regions and some locations in most northern Palestine, where increasing SLP over the central Atlantic, Europe, Levant, Middle East, and North west and east of the Pacific Ocean is associated with increased drought in the Levant, while increasing SLP in northern latitudes is associated with decreased drought. Furthermore, the second mode resembles the NAO influence, where the positive phase of the NAO leads to decrease SPI values through a decrease in rainfall for the western Syrian regions and some locations in most northern Palestine.
11. Similar to the SLP-spring rainfall analysis, the first SLP-spring drought coupled mode indicates when the SLP over central Atlantic, central Europe, the North and Caspian Seas, central Mediterranean Sea, Africa's northern coast, and southeastern coastal of Asia is higher than normal, the drought in south of Levant decreases. The second SLP-spring drought coupled mode is only relevant in the Syrian coastal and eastern regions, where increasing SLP over the central Atlantic, Europe, the Mediterranean Sea, North Africa, and the Middle East is associated with increased drought, while increasing SLP in northern latitudes is associated with decreased drought. For the first mode, SPI values in the south Levant were positively correlated with the NCP index, but negatively correlated with the WEMO index. Furthermore, the second mode resembles the NAO index effect on the Syrian coastal and eastern regions.
12. Similar SST-autumn (drought and rainfall) coupled patterns were detected for the first mode. These patterns are characterized by increasing (decreasing) rainfall (drought) in all

Levant regions, except for the Syrian coast, when the SST in the north and subtropical Atlantic Ocean is abnormally cold. As mentioned in Chapter 8 (section 8.3), this pattern is associated with the ENSO index. For the second mode, very few information can be extracted from the coupled pattern, with very few stations significantly correlated with the SST pattern, and there is not any large-scale atmospheric circulations indices correlated with the left (SST) expansion coefficients. The third SST-drought mode exhibited same sign between the SST in (the west Mediterranean and subtropical Atlantic) and SPI in the north western and eastern locations from Syria. The left SST expansion coefficients showed significant negative correlation with the WEMO index.

13. The first and second covariability modes for SLP-autumn drought and SLP-autumn rainfall were also similar. The first SLP-autumn drought coupled mode revealed increasing SPI values in all Levant locations, except the Syrian coast, when the SLP increases over the tropical/subtropical Atlantic Ocean, extending through Africa, Indian Ocean, and western Pacific, Middle East and East Asia. The SLP pattern also indicated increased SPI values when the SLP over the east of the Pacific Ocean is abnormally low. The left (SLP) expansion coefficients exhibited a strong negative correlation of -0.72 with ENSO index, compared to other indices. Note that the SPI structure linked to the SLP patterns in the heterogeneous correlation map exactly coincide with the autumn SPI connected to the ENSO (Figure 9.12j). The second mode, which was related to the rainfall and drought in Syrian coast, showed when the SLP over the northeastern Asia, the Scandinavian Peninsula, and eastern coast of America is higher than normal the rainfall in the Syrian coast will decrease and the drought will increase.

CHAPTER 10
CONCLUSIONS

The main conclusions of this thesis are summarized, including data quality control, temperature and rainfall variability, extreme temperature and rainfall indices, drought characteristics, and the effects of large-scale circulation patterns on temperature and precipitation in the Levant region.

In this work, two climate variables have been used, the temperature (Tmax, Tmin, and DTR) and the precipitation. It was based on a large set of climate data that covers the entire Levant region (Palestine, Israel, Jordan, Lebanon, and Syria). All data were subjected to rigorous, station-by-station quality control. The final stations list consisted of data from 61 stations for temperature covering the period 1987-2018 and 165 stations for precipitation covering the period 1970-2018. The objective of this thesis is to investigate climate variability in the Levant. For this end, the spatio-temporal variability of temperature, precipitation, extreme temperature and precipitation indices, drought occurrence and its characteristics, and their relationships with the large-scale patterns in the Atlantic and Mediterranean Sea, as well as the influence of SST and SLP indicators, have been all analyzed.

- ***The results have demonstrated that the Levant region is experiencing high warming trends at various time scales (annual, seasonal, and monthly). The trends differ relatively in magnitudes from one country to another, from one region to another, and for maximum and minimum temperatures. The spatial distribution of the seasonal temperatures (both for Tmax and Tmin) was homogeneous across the study area. Decreasing trends were not detected at any time scale. For all time scales, more than 97% of the stations exhibited increasing trends, in both Tmax and Tmin, with the highest frequency of significant trends***

(> 74% of the stations) observed at the annual scale and for spring, February, March, and August. Specifically, the main results are:

- The annual, spring, summer, January, February, March, June, July, and August-Tmax and -Tmin means increased significantly over the Levant in 2001-2018 compared to 1987-2000. The most significant increases were observed for spring and March. Moreover, the annual and seasonal-Tmax and -Tmin means for the 10-years non-overlapping periods, 1987-1996, 1997-2006, and 2007-2018 gradually increased, with the last decade, 2007-2018, being significantly the hottest decade.
- Significant warming trends affected both Tmax and Tmin across the Levant in 1987-2018, but Tmax increased at a faster rate than Tmin in winter, summer, and spring. The Levant-Tmin, on the other hand, has warmed faster than Tmax in the autumn, May, and July.
- Over the study area, spring-Tmax and -Tmin, winter-Tmax, and autumn-Tmin all showed very strong and significant seasonal warming trends. On a monthly basis, March and February had the highest warming trends for both Tmax and Tmin.
- For the entire Levant, the DTR for the cold months (December-April) increased, while it decreased for the warm months (May-November). Significant DTR decreasing trends were detected for August and September. Furthermore, the highest DTR increasing trend was in March, although it was non-significant.
- For annual, spring, summer, and autumn, the southern Levant Tmax increased significantly at a higher rate than the northern Levant. Only in winter, the Tmax of northern Levant rose at a higher rate than southern Levant. On the contrary, the Tmin of the northern Levant rose at a higher rate than the south Levant at annual, winter, and autumn scales.
- For all countries, the highest significant warming trends were found in spring (for both Tmax and Tmin). Jordan had the highest significant increasing Tmax trends for annual, winter, spring, and summer, while Syria had the highest trend for autumn-Tmax. Furthermore, Syria-Tmin had the highest warming trend at annual, winter, and autumn, while Palestine and Jordan had the highest trends in spring-Tmin and summer-Tmin.
- In the summer months, Jordan-Tmax and -Tmin showed the highest (significant) increases. It also showed the highest increasing trends in September and October.
- The widespread significant warming trends (> 80% of the stations) were mainly observed in March, February, and August, both in Tmax and Tmin. Spatially, most stations from Jordan, northern and central areas of Palestine showed very high warming trends at annual scale, and for winter, spring, summer, and autumn for Tmax, with the highest value for spring. These regions also showed very high warming trends for the summer-Tmin and winter-DTR.

- ***Regards precipitation, at various time scales, the Levant presented a trend toward lower rainfall amounts and drier conditions, particularly in the spring and March. Except for Jordan in February, no significant increasing trends in precipitation were detected for the Levant as a whole and for its sub-regions at any time scale. The study area showed more***

spatial variability for seasonal rainfall than for seasonal temperatures, and it can be divided into three homogeneous regions: the central and north of Palestine and Jordan (PC-1), the coastal and western Syria (PC-2), and the eastern Syria and Jordan, and southern Palestine and Jordan (PC-3). Some relevant results are:

- For the periods 1993-1999, 2003-2008, and 2012-2018, the rainfall showed a decreasing trend, while in 2000-2003 and 2008-2012, it showed an increasing trend. Moreover, during the period under investigation, 1970-2018, the spring variability gradually decreased.
- Significant mean differences were noted only in spring rainfall for the Levant and Palestine in 2000-2018 compared to 1970-2018. Furthermore, the Levant as a whole, Palestine, and Jordan recorded significant decreases in their spring mean values for the period 1991-2018 compared to 1970-1990.
- Significant change points were observed in spring around 1992 for the Levant, Palestine, and Jordan, and around 1997 for Syria. The significant change points were also found in March for the Levant (in 2013), Palestine (in 2015), and Jordan (in 1999).
- A total of 91 out of 167 stations showed significant decreasing trends in spring, with the highest rates for Syria's easternmost locations, coastal stations, and northern Palestine. Only nine stations showed a significant downward trend in the autumn, with high rates in Palestine's central areas. Only the eastern parts of Syria experienced significant decreases in winter, while the rest of the regions experienced increases, but not significant, with the Syrian coastal region experiencing the highest rate.
- At monthly timescale, March had the highest frequency of significant downward trends. The highest trend values were detected for most stations in the West Bank, east to Haifa district, and Syria's most eastern stations. In April, significant decreasing trends were spatially concentrated in most eastern and coastal locations of Syria. On the other hand, a significant upward trend was observed in January and February for Jordan.

- ***For the study of extreme events, a total of 34 extreme rainfall and temperature indices developed by ETCCDI and ET-SCI (some of them modified to fit the study area) were analyzed for Palestine and Israel (southern Levant). Warmer and drier conditions are also on the rise. Extremes related to minimum night-time temperature indices denoted more intense trends at annual and seasonal scales than those related to maximum day-time temperature indices. The study area had longer periods of extreme dry spells (CDD) and shorter periods of extreme wet spells (CWD) in the winter, spring, and combined winter-spring seasons. Spring rainfall extreme indices showed negative trends for most of the indices, significantly for R1mm, R20mm, CWD, RX1day, RX3day, RX5day, and SDII indices.*** The main conclusion for the extreme events analysis are:
  - The southern Levant witnessed significant increasing trends in seven extreme temperature indices (TNx, TX90p, TN90p, SU25, SU30, TR20 and TR25) at annual scale, whereas it showed significant decreasing trends in the CSDI and TN10p indices.

- At annual scale, significant warming trends (> 82% of the stations) were intensively detected in SU25, TR20 TX90p, and TN90p indices. For the TNx, SU30, TR25, and WSDI indices, between 29%-46% of the stations exhibited significant increasing trends.
- At seasonal scale, significant decreasing trends were only found for TX10p-autumn, TN10p-spring, and TN10p-autumn. The most significant increasing trends were detected for summer-TXn, -TNn, and -TNx, for more than 90% of total stations. For TN90p-spring and TN90p-summer, 61% and 85% of the locations showed significant increasing trends, respectively.
- The annual averages for frequency-based precipitation extreme indices exhibited decreasing trends, significant for the R1mm and CDD indices, covering the northern, northeastern, and West Bank stations, for the R1mm index, and some southern coastal locations for the CDD index. Conversely, the percent and intensity based-extreme indices showed increasing trends, significant for the R99Ptot index.
- The significantly decreasing trend in the CDD index did not lead to an increase in the CWD index, which may points at a change in the temporal organization of the dry and wet days.
- Spring and autumn are the seasons that contribute the most to annual declines in the PRCPTOT, R1mm, R10mm, R20mm, and CDD indices, while winter is the season that contributes the most in the RX1day, RX3day, RX5day, and SDII indices.
- At seasonal scale, only the winter-R1mm index showed a declining trend. The increasing trend of the PRCPTOT index, together with the decreasing trend of the R1mm index, led to an increase of the simple daily intensity index (SDII), which is significant for the northwestern sites. In addition, the northern locations have experienced intensively rising trends in the RX1day index.
- The rising trends in RX1day and the SDII indices in the northern regions may indicate an increase in precipitation intensity and the possibility of flooding in these areas, particularly, for localities with an annual precipitation maximum of more than 1000 mm.
- For spring, extreme indices showed negative trends for most of the indices, significant for R1mm, R20mm, CWD, RX1day, RX3day, RX5day, and SDII mainly in stations covering central and northern locations. With the exception of the CDD index, there was a very consistent pattern of declining trends across the study area, with more than 75% of stations showing declining trends in all indices. During the autumn, significant decreases in RX1day, RX3day, and SDII were observed primarily in the central regions.

- ***Drought analysis shows that it has become more frequent and widespread in the region, particularly since the mid-1990s. In comparison to 1970-1994, drought features have increased significantly in all regions and for all SPI time scales in 1995-2018. According to the PCA, the study area can be divided into three homogeneous regions based on the SPI-3, -6, and -12 months, and into four regions based on the SPI-24 months time scale. The first PC represents the central and northern locations from Palestine, northern locations from Jordan, and south of Syria at SPI-3 and -6 months timescales. The second PC represents***

Syria's western and coastal regions. The third PC is associated with the Levant's eastern and southern locations. Little difference was detected for the SPI-12 and -24 months, when the second PC extended to cover many locations in north of Palestine at SPI-12 and -24. Furthermore, the third PC is restricted to Syria's eastern regions, whereas the southern Palestine and all stations in Jordan, with the exception of the northern stations, conformed to the fourth PC for the SPI-24 months. The main findings are summarized as follows:

- The wettest events were observed at many SPI time scales in 1991/1992, 1971, and 1988. Drought events of moderate and above, on the other hand, were mostly observed at several SPI timescales in 1998/1999, 2010, 2013/2014, and 2008. The Levant region experienced drought episodes in 1999-2001, 2006-2011, and 2014-2018, all of which were more severe on long-term hydrological drought.
- Significant decreasing trends were detected across the Levant for the SPI-3 spring and SPI-6 spring/summer, with a significant change point detected in 1997. For SPI-3 spring, SPI-6 spring/summer, SPI-12, and SPI-24, a strong downward trend from 1990 to 2018 was observed over the Levant. The widespread significant decreasing trends mainly affected the central and northern locations in Palestine, northern Jordan, and eastern Syria. The significant decreasing trends in SPI-3 spring are accompanied by a significant temporal and spatial decline in spring precipitation for most Levant regions.
- In general, the locations had higher values of drought characteristics on long-term hydrological drought than on short- and mid-term meteorological drought scales, with the southern and eastern regions of the Levant showing this result more clearly. The regions with lowest DF, TDD, and TDS values were in the central and northern locations of Palestine, northern Jordan, and southern Syria (PC-1 region for SPI-3 and -6 months), and for the central and northern locations of Palestine and north of Jordan (PC-1 region at SPI-12 and -24 months). The Syrian coastal and western locations (PC-2 region at SPI-3 and -6 months), on the other hand, had the highest values of all drought parameters.
- Despite having the lowest DF, TDD, and TDS values, the central and northern locations from Palestine, northern locations of Jordan, and southern and eastern Syria showed high significant increasing trends for the DF at SPI-3 and -12 months' time scales. Furthermore, they also showed MDS's significant decreasing trends.

- ***Regarding the influence of large-scale ocean-atmospheric circulation patterns on seasonal temperatures, precipitation and drought, the results show that, along with the complex topography of the Levant, many physical processes that are linked to large-scale ocean-atmospheric circulation interactions dominate the Levant temperatures and precipitation variability. The results strongly support the NCP, NAO, WEMO, and ENSO indices as potential predictors due to their high ability in explaining the temperatures and rainfall variability in different seasons. Additionally, the MO and EA/WR indices also present significant relationships with winter rainfall. The correlation of the NAO, NCP, MO, and EA/WR indices is always negative on temperatures and positive on rainfall, except for the NAO, which has an inverse effect on rainfall. On the other hand, the effect of the ENSO***

and WEMO indices is positive on temperatures and negative on the rainfall. In most cases, similar mechanisms and spatial patterns were detected between the SLP/SST-rainfall and SLP/SST-drought. The main findings are summarized as follows:

- The NCP index is the major influential atmospheric circulation index for the seasonal temperatures and rainfall over the Levant region
- The effect of the ENSO index was mainly restricted for the summer temperature and for autumn precipitation.
- The WEMO index notably exerted influence in spring, both for temperature and precipitation.
- Based on the SVD analysis, the SST (of the North Atlantic Ocean and Mediterranean Sea) and the SLP (North Hemisphere) explain temperature variability better than precipitation one, which could be due to the higher spatial and temporal variability of precipitation, mainly in transition months, compared to the more homogeneous temperature behaviour.
- The SST and winter temperatures/rainfall coupled modes reflect the SST tripolar Atlantic Ocean pattern, which is related with the NAO. During the NAO positive phase, the SST in the subpolar and tropical Atlantic will be colder than normal due to lose energy to the atmosphere by stronger westerly and northeast trade winds. Atlantic SST in the middle latitudes will be higher than normal due to lower wind speeds and a lower turbulent heat flux out of the ocean, resulting in a drop in winter Levant temperatures and rainfall (increase drought), and vice versa.
- The Mediterranean SST had little impact on seasonal rainfall. It is possible that the relationship between Mediterranean SST and seasonal precipitation in the Levant is not causal, or that distinct atmospheric processes influence both fields. On the other hand, the SST of the Eastern Mediterranean and Black Sea is strongly and positively related to all seasonal temperatures. If the westerlies are weak (negative NAO), another large-scale processes related to NCP and EA/WR indices may take over, bringing a local northeasterly cold wind regime over the Caspian and Black Seas. Northeasterly winds dominate over the Caspian and Black Seas during the positive phases of the NCP and EA/WR indices, bringing cold air to the region and causing a decrease in SST, which leads to lower seasonal Levant temperatures. Similarly, during the negative phases, the winds blow primarily from the southwest, bringing warm air from these regions and, as a result, increasing SST, which leads to higher seasonal temperatures.
- The SST and spring temperatures/rainfall coupled modes reflect the SSTs horseshoe Atlantic Ocean pattern, which not resembles the NAO signature, except for the second coupled mode of the SST-rainfall related to the Syrian coast. The Atlantic SSTs horseshoe shape showed a negative association with the temperature and rainfall, while the SST in the Mediterranean Sea, Black, North, and Red seas had positive correlations with the temperature and rainfall. This could indicate that regional atmospheric-ocean interactions (like Mediterranean SLP, and the NCP index) have a stronger influence in spring and autumn than the NAO index, as a natural result of the NAO's weaker influence in the transitional seasons.

- A similar SST structure was found for the SST-summer temperatures and the first SST-autumn rainfall coupled modes, distinguishable by the positive association between the SST in the north and tropical/subtropical Atlantic Ocean and summer temperatures, and a negative association between the SST in these regions and autumn rainfall. This SST variability mode is associated with the ENSO's positive and negative effects on summer temperatures and autumn rainfall, respectively. The ENSO-related Atlantic warmings occur as a result of reductions in the surface NE trade wind speeds, which in turn reduce latent and sensible heat losses (increasing SST) over the Tropical Atlantic, leading to increase summer temperatures in the Levant.
- With the exception of the summer, the SLP-seasonal temperatures coupled modes generally showed a negative correlation between the SLP over the North Africa, Mediterranean, Europe (except most north part), and central Atlantic (Azores) and seasonal temperatures, whereas positive correlations were found between the SLP in the north latitudes and seasonal temperatures. These coupled patterns reflect the signatures of the NAO, NCP, MO, WEMO, and EAWR indices. For the SLP-summer temperatures, increasing SLP in tropical/subtropical Pacific Ocean, associated with the ENSO signal, is associated with increased temperatures.

Future work

In this thesis all efforts have been aimed at offering an analysis of the spatio-temporal variability of the climate in the Levant region, trying to analyze the causal mechanisms responsible for it. Then, the results obtained are the starting point for the consideration of potential predictors for seasonal temperature, rainfall or extreme events such as drought occurrence. In this framework several key points could be improved in the future focused on the study of the climate predictability in this region. For this end, a better understanding the role of the large-scale circulation patterns in the seasonal temperature and precipitation is crucial. One way could be to complete the potential predictor fields, adding more teleconnection indices and expanding the spatial cover of the SST. Once a more complete set of possible predictors has been identified, their predictive ability should be analyzed. Different techniques could be used for the development of statistical models of seasonal climate prediction, such as the application of the SVD between the predictor fields and the temperature and precipitation of Levant at different seasonal lags, or the application of statistical linear regression models, among others.

Additionally, the region under study also could be expanded trough obtaining daily temperature and precipitation time series for Jordan and Syria, in order to analyze changes in extreme climate events in these regions, where this topic has never been explored before. Other important issue in this respect is related with the use of different drought indices for the analysis of this phenomenon in the region. For example, the use of the Standardized Precipitation Evapotranspiration Index (SPEI), which account for both rainfall and

potential evapotranspiration, could be used to better understand the impact of temperature on water demand and moisture variability under climate change conditions.

CAPÍTULO 10
CONCLUSIONES

Las principales conclusiones de esta Tesis, que incluyen el control de calidad de los datos, el estudio de la variabilidad de la temperatura y las precipitaciones y de los índices de temperatura y precipitaciones extremas, así como las características de la sequía y la influencia de los patrones de circulación a gran escala sobre la temperatura y la precipitación en la región de Levante, son resumidas en este capítulo.

En este trabajo se han utilizado dos variables climáticas, la temperatura (Tmax, Tmin y DTR) y la precipitación. El estudio se ha basado en un gran conjunto de datos climáticos que cubren toda la región del Levante (Palestina, Israel, Jordania, Líbano y Siria). Los datos de cada localidad se sometieron a un riguroso control de calidad. El conjunto final de datos analizados consistió en datos procedentes de 61 estaciones para la temperatura, que cubren el período 1987-2018, y 165 estaciones para la precipitación, que cubren el período 1970-2018.
El objetivo de esta Tesis es investigar la variabilidad climática en el Levante. Para ello, se ha estudiado la variabilidad espacio-temporal de la temperatura, la precipitación, los índices de temperatura y precipitación extrema, la ocurrencia de sequías y sus características, y sus relaciones con los principales patrones de teleconexión en el Atlántico y Mediterráneo, así como los principales modos de variabilidad acoplados entre la SST y SLP y las variables analizadas.

- ***Los resultados han demostrado que la región de Levante está experimentando altas tendencias de calentamiento en varias escalas de tiempo (anual, estacional y mensual). Las tendencias difieren relativamente en magnitud de un país a otro, de una región a otra y entre las temperaturas máximas y mínimas. La distribución espacial de las temperaturas estacionales (tanto para Tmax como para Tmin) fue homogénea en toda el área de estudio. No se detectaron tendencias decrecientes en ninguna escala de tiempo. Para todas las escalas de tiempo, más del 97% de las estaciones exhibieron tendencias crecientes, tanto en***

la Tmax como en la Tmin, con la mayor frecuencia de tendencias significativas (> 74% de las estaciones) observadas a escala anual y para la primavera, febrero, marzo, y agosto. En concreto, los principales resultados son:

- Las medias anuales, de primavera, verano y de los meses de enero, febrero, marzo, junio, julio y agosto, tanto para la Tmax como para la Tmin, aumentaron significativamente en el Levante en 2001-2018 en comparación con 1987-2000. Los incrementos más significativos se observaron en primavera y en el mes de marzo. Además, las medias anuales y estacionales de la Tmax y la Tmin para los períodos de 10 años no superpuestos, 1987-1996, 1997-2006 y 2007-2018 aumentaron gradualmente, siendo la última década, 2007-2018, significativamente la más cálida.
- Las tendencias de calentamiento significativas afectaron tanto a la Tmax como a la Tmin en todo el Levante en el periodo 1987-2018, pero la Tmax aumentó a un ritmo más rápido que la Tmin en invierno, verano y primavera. La Tmin, por otro lado, incrementó más que la Tmax en otoño, mayo y julio.
- En el área de estudio, las series de primavera de Tmax y Tmin, la de invierno de Tmax y las de otoño de Tmin mostraron tendencias de calentamiento estacional muy fuertes y significativas. Mensualmente, marzo y febrero tuvieron las tendencias de calentamiento más altas tanto para la Tmax como para la Tmin.
- Para todo el Levante, el DTR para los meses fríos (diciembre-abril) aumentó, mientras que disminuyó para los meses cálidos (mayo-noviembre). Se detectaron tendencias significativas a la baja de DTR para agosto y septiembre. Además, la mayor tendencia al alza de DTR se registró en marzo, aunque no fue significativa.
- Para la primavera, el verano y el otoño, la Tmax del Levante meridional aumentó significativamente a un ritmo mayor que la del Levante septentrional. Solo en invierno, la Tmax del norte del Levante aumentó a un ritmo mayor que la del sur. Por el contrario, la Tmin del norte de Levante aumentó a un ritmo mayor que el sur a escala anual, y para invierno y otoño.
- Para todos los países analizados, las tendencias crecientes significativas más altas se encontraron en primavera (tanto para la Tmax como para la Tmin). Para Jordania se encontraron las tendencias de aumento significativo de la Tmax más altas para la serie anual, de invierno, primavera y verano, mientras que para Siria la tendencia más alta de Tmax fue en otoño. Para la Tmin, Siria tuvo la mayor tasa de calentamiento anual, y en invierno y otoño, mientras que Palestina y Jordania mostraron las mayores tendencias en primavera y verano.
- Las tendencias generalizadas de calentamiento significativo (> 80% de las estaciones) se observaron principalmente en marzo, febrero y agosto, tanto en la Tmax como en la Tmin. Espacialmente, la mayoría de las estaciones de Jordania y las áreas norte y central de Palestina muestran tendencias de calentamiento muy altas para la Tmax anual, de invierno, primavera, verano y otoño, con el valor más alto para la primavera.

Estas regiones también muestran tendencias de calentamiento muy altas para la Tmin de verano y el DTR de invierno.

- ***Respecto a la precipitación, a diversas escalas de tiempo, el Levante presentó una tendencia hacia menores cantidades de lluvia y condiciones más secas, particularmente en la primavera y marzo. A excepción de Jordania en febrero, no se detectaron tendencias crecientes significativas en las precipitaciones para el Levante en su conjunto ni para sus subregiones en ninguna escala de tiempo. El área de estudio mostró más variabilidad espacial para las precipitaciones estacionales que para las temperaturas estacionales, pudiéndose establecer tres regiones homogéneas: el centro y norte de Palestina y Jordania (PC-1), la costa y el oeste de Siria (PC-2), y el este de Siria y Jordania y sur de Palestina y Jordania (PC-3).*** Algunos resultados relevantes son:
  - Para los períodos 1993-1999, 2003-2008 y 2012-2018, la precipitación mostró una tendencia decreciente, mientras que en 2000-2003 y 2008-2012 mostró una tendencia creciente. Además, durante el período investigado, 1970-2018, la variabilidad de la precipitación de primavera disminuyó gradualmente.
  - Se observaron diferencias medias significativas solo en las precipitaciones de primavera para la región en conjunto del Levante y para Palestina en el periodo 2000-2018 en comparación con el periodo 1970-2018. Además, el Levante en su conjunto, Palestina y Jordania registraron disminuciones significativas en sus valores medios de la precipitación de primavera para el período 1991-2018 en comparación con 1970-1990.
  - Se observaron puntos de cambio significativos en la precipitación de primavera alrededor de 1992 para el Levante en su conjunto, Palestina y Jordania, y alrededor de 1997 para Siria. Los puntos de cambio significativos también se encontraron en marzo para el Levante (en 2013), Palestina (en 2015) y Jordania (en 1999).
  - Un total de 91 de las 167 estaciones mostraron tendencias decrecientes significativas en la primavera, con las tasas más altas para las ubicaciones más orientales de Siria, las estaciones costeras y el norte de Palestina. Solo nueve estaciones mostraron una tendencia descendente significativa en el otoño, con tasas altas en las áreas centrales de Palestina. Solo las partes orientales de Siria experimentaron disminuciones significativas en invierno, mientras que el resto de las regiones experimentaron aumentos, aunque no significativos.
  - A escala de tiempo mensual, marzo tuvo la mayor frecuencia de tendencias significativas decrecientes. Los valores de tendencia más altos se detectaron para la mayoría de las estaciones en Cisjordania, al este del distrito de Haifa y las estaciones más al este de Siria. En abril, las tendencias decrecientes significativas se concentraron espacialmente en la mayoría de las ubicaciones costeras y orientales de Siria. Por otro lado, se observó una tendencia ascendente significativa en enero y febrero para Jordania.

- ***Para el estudio de eventos extremos, se analizaron un total de 34 índices de temperatura y precipitación extrema desarrollados por el ETCCDI y ET-SCI (algunos de los cuales fueron modificados para ajustarse al área de estudio) para Palestina e Israel (sur del Levante). Las condiciones más cálidas y secas también están aumentando. Los extremos relacionados con los índices de temperatura mínima nocturna denotaron tendencias más intensas en escalas anuales y estacionales que las relacionadas con los índices de temperatura máxima diurna. El área de estudio tuvo períodos más largos de períodos secos extremos (CDD) y períodos más cortos de períodos húmedos extremos (CWD) en invierno, primavera y en las temporadas combinadas de invierno-primavera. La mayoría de los índices extremos de lluvia de primavera mostraron tendencias negativas, significativas para los índices R1mm, R20mm, CWD, RX1day, RX3day, RX5day y SDII.*** Las principales conclusiones para el análisis de índices de extremos son:
  - El sur del Levante mostró tendencias crecientes significativas en siete índices de temperaturas extremas (TNx, TX90p, TN90p, SU25, SU30, TR20 y TR25) a escala anual, mientras que mostró tendencias decrecientes significativas en los índices CSDI y TN10p.
  - A escala anual, se detectaron tendencias de calentamiento significativas (> 82% de las estaciones) en los índices SU25, TR20 TX90p y TN90p. Para los índices TNx, SU30, TR25 y WSDI, entre el 29% y el 46% de las estaciones exhibieron tendencias crecientes significativas.
  - A escala estacional, solo se detectaron tendencias decrecientes significativas para los índice TX10p y TN10p de otoño y de primavera. Las tendencias crecientes más significativas se detectaron para los índices TXn, TNn y TNx de verano, para más del 90% del total de estaciones. Para TN90p de primavera y de verano, el 61% y 85%, respectivamente, mostró tendencias crecientes significativas.
  - Los valores anuales para los índices extremos de precipitación basados en la frecuencia exhibieron tendencias decrecientes, significativas para los índices R1mm y CDD, en localidades del norte, noreste y Cisjordania, para el índice R1mm, y algunas localizaciones costeras del sur para el índice CDD. Por el contrario, los índices de extremos basados en el porcentaje y la intensidad mostraron tendencias crecientes, significativas para el índice R99Ptot.
  - La tendencia significativamente decreciente en el índice CDD no condujo a un aumento en el índice CWD, lo que sugiere que las lluvias tienden a ocurrir en días más aislados.
  - La primavera y el otoño son las estaciones que más contribuyen a los descensos anuales en los índices PRCPTOT, R1mm, R10mm, R20mm y CDD, mientras que el invierno es la temporada que más contribuye en los índices RX1day, RX3day, RX5day y SDII.
  - A escala estacional, solo el índice R1mm de invierno mostró una tendencia a la baja. La tendencia creciente del índice PRCPTOT, junto con la tendencia decreciente del índice R1mm, llevó a un aumento del índice de intensidad diaria simple (SDII), que es

significativo para localidades del noroeste. Además, las ubicaciones del norte han experimentado tendencias ascendentes intensas en el índice RX1day.

- Las tendencias ascendentes tanto en los índices RX1day como SDII en las localidades del norte pueden indicar un aumento en la intensidad de las precipitaciones y la posibilidad de inundaciones en estas áreas, particularmente, para localidades con un máximo anual de precipitación de más de 1000 mm.
- Para la primavera, los índices extremos mostraron tendencias negativas para la mayoría de los índices, significativas para R1mm, R20mm, CWD, RX1day, RX3day, RX5day y SDII. Estos índices mostraron tendencias decrecientes significativas en las estaciones del centro y norte. Con la excepción del índice CDD, hubo un patrón muy consistente de tendencias decrecientes en el área de estudio, con más del 75% de las estaciones mostrando tendencias decrecientes en todos los índices. Durante el otoño, se observaron disminuciones significativas en RX1day, RX3day y SDII principalmente en las localidades centrales.

- ***El análisis de la sequía muestra que esta se ha vuelto más frecuente y generalizada en la región, particularmente desde mediados de la década de 1990. En comparación con 1970-1994, las características de la sequía han aumentado significativamente en todas las regiones y para todas las escalas de tiempo analizadas del SPI en el periodo 1995-2018. Según el PCA, el área de estudio se puede dividir en tres regiones homogéneas para el SPI en escalas de 3, 6 y 12 meses, y en cuatro regiones para el SPI a 24 meses. La primera PC representa las ubicaciones del centro y norte de Palestina, las ubicaciones del norte de Jordania y el sur de Siria en escalas de tiempo de 3 y 6 meses. La segunda PC representa las regiones costeras y occidentales de Siria. La tercera PC está asociado con las ubicaciones este y sur de Levante. Se detectó poca diferencia en las escalas de tiempo SPI-12 y -24, donde la segunda PC se extiende para cubrir muchas ubicaciones en el norte de Palestina. Además, la tercera PC está restringida a las regiones del este de Siria, mientras que el sur de Palestina y todas las estaciones en Jordania, con la excepción de las estaciones del norte, se asocian a la cuarta PC para el SPI-24 meses.*** Los principales hallazgos se resumen a continuación:
    - Los eventos más húmedos se observaron en diversas escalas de tiempo del SPI en los años 1991/1992, 1971 y 1988. Los eventos de sequía moderados y fuertes, por otro lado, se observaron principalmente en varias escalas de tiempo del SPI en 1998/1999, 2010, 2013/2014 y 2008. La región de Levante experimentó episodios de sequía en 1999-2001, 2006-2011 y 2014-2018, los cuales fueron más graves al poder catalogarse como sequía hidrológica a largo plazo.
    - Se detectaron tendencias decrecientes significativas en todo el Levante para el SPI-3 de primavera y SPI-6 de primavera/verano, con un punto de cambio significativo detectado en 1997. Para el SPI-3 de primavera, SPI-6 primavera/verano, SPI-12 y SPI-24, se observó una fuerte tendencia decreciente de 1990 a 2018 en el Levante. Las tendencias descendentes significativas generalizadas se observaron para las escalas de

tiempo SPI-3 de mayo, SPI-3 primavera /verano y SPI-12, y afectaron principalmente al centro y norte de Palestina, norte de Jordania y el este de Siria. Las tendencias decrecientes significativas en el SPI-3 de primavera están acompañadas por una disminución temporal y espacial significativa en la precipitación de primavera para la mayoría de las regiones del Levante.

- En general, las diversas áreas presentaron características más marcadas en la sequía hidrológica a largo plazo que en las escalas de sequía meteorológica a corto y medio plazo, siendo las regiones sur y este del Levante las que muestran este resultado con mayor claridad. Las regiones con valores más bajos de DF, TDD y TDS, en distintas escalas de tiempo, se encontraron en el centro y norte de Palestina, norte de Jordania y sur de Siria (región PC-1 para el SPI-3 y -6 meses), y para las ubicaciones del centro y norte de Palestina (región PC-1 para el SPI-12 y -24 meses). Las localidades costeras y occidentales de Siria (región PC-2 para el SPI-3 y -6 meses), por otro lado, presentaron los valores más altos de estos parámetros de sequía.
- A pesar de tener los valores más bajos de DF, TDD y TDS, las localidades del centro y norte de Palestina, las del norte de Jordania y el sur y este de Siria mostraron tendencias crecientes significativas para la DF en las escalas de tiempo del SPI-3 y -12 meses. Además, también mostraron tendencias decrecientes significativas de MDS. La costa siria tuvo los valores más altos de DF, TDD y TDS.

- ***En cuanto a la influencia de los patrones de circulación océano-atmosférica a gran escala en las temperaturas estacionales, las precipitaciones y la sequía, los resultados muestran que, junto con la compleja topografía del Levante, muchos procesos físicos que están vinculados a las interacciones de la circulación océano-atmosférica a gran escala podrían influir en la variabilidad de las temperaturas y las precipitaciones del Levante. Los resultados presentan firmemente a los índices de teleconexión NCP, NAO, WEMO y ENSO como potenciales predictores debido a su alta capacidad para explicar las temperaturas y la variabilidad de las precipitaciones en las diferentes estaciones. Además, los índices MO y EA/WR también presentan relaciones significativas con las lluvias invernales. La correlación de los índices NAO, NCP, MO y EA/WR es siempre negativa con las temperaturas y positiva con las precipitaciones, a excepción del NAO, que tiene un efecto inverso sobre las precipitaciones. Por otro lado, la correlación de los índices ENSO y WEMO es positiva con las temperaturas y negativa con las precipitaciones. En la mayoría de los casos, se detectaron relaciones y patrones acoplados de estructura espacial similares entre la SLP/SST y la precipitación, y entre la SLP/SST y la sequía.*** Los principales hallazgos se resumen a continuación:
    - El índice NCP es el índice de circulación atmosférica más influyente para las temperaturas estacionales y las precipitaciones en la región de Levante.
    - El efecto del índice ENSO se restringió principalmente a la temperatura de verano y a las precipitaciones de otoño.

- El índice WEMO parece ejercer una influencia notable durante la primavera, tanto en la temperatura como en las precipitaciones.
- Los resultados del SVD muestran que la SST (del Atlántico Norte y Mar Mediterráneo) y la SLP (del Hemisferio Norte) explican mejor la variabilidad de la temperatura que la de la precipitación, lo que podría deberse a la mayor variabilidad espacial y temporal de la precipitación, principalmente en los meses de transición, en comparación con el comportamiento más homogéneo de la temperatura.
- Los modos de variabilidad acoplados de la SST y la temperatura/precipitación, en invierno, reflejan el patrón tripolar de la SST del Océano Atlántico, que está relacionado con la NAO. Durante la fase positiva de NAO, la SST en el Atlántico subpolar y tropical tiende a ser más fría de lo normal debido a la pérdida de energía a la atmósfera debido a los vientos alisios del oeste y noreste más fuertes. La SST de Atlántico en las latitudes medias es más alta de lo normal debido a las velocidades del viento más bajas y a la reducción de los flujos de calor hacia la atmósfera, lo que resulta en una disminución en las temperaturas y precipitaciones de invierno en el Levante (y por tanto un aumento de la sequía), y viceversa.
- La SST del Mediterráneo presenta un impacto limitado en precipitación estacional. Es posible que la relación entre la SST mediterránea y la precipitación estacional en el Levante no sea causal, o que distintos procesos atmosféricos influyan en ambos campos. Por otro lado, la SST del Mediterráneo oriental y el Mar Negro están relacionadas fuerte y positivamente con todas las temperaturas estacionales. Note que, si los vientos del oeste son débiles (NAO negativo), otros procesos a gran escala relacionados con los índices NCP y EA/WR pueden tomar importancia, estableciendo un régimen local de vientos fríos del noreste sobre los Mares Caspio y Negro. Los vientos del noreste dominan estos mares durante las fases positivas de los índices NCP y EA/WR, estableciendo aire frío sobre la región y provocando una disminución de la SST, lo que conduce a temperaturas estacionales más bajas en el Levante. De manera opuesta, durante las fases negativas, los vientos soplan principalmente del suroeste, transportando aire cálido de estas regiones y, como resultado, aumentando la SST, lo que conduce a temperaturas estacionales más altas en el Levante.
- Los modos acoplados de la SST y la temperatura/precipitación, en primavera, reflejan el patrón en herradura de la SST del Atlántico Norte, que no muestra correlación con la NAO, excepto para el segundo modo acoplado de la SST y la precipitación relacionado con las localidades situadas en la costa de Siria. La forma de herradura de la SST del Atlántico muestra una correlación negativa con las temperaturas y las precipitaciones, mientras que la SST en los mares Mediterráneo, Negro, Norte y Rojo presenta correlaciones positivas con la temperatura y las precipitaciones. Esto podría indicar que otras interacciones atmosféricas-oceánicas regionales (como la SLP del Mediterráneo y el índice NCP) podrían tener una influencia más fuerte en primavera y

otoño que el índice NAO, como resultado natural de la influencia más débil de la NAO en las estaciones de transición.

- Se encontró una estructura similar de la SST para los primeros modos acoplados de la SST y la temperatura de verano, y de la SST y la precipitación de otoño. Esta estructura se distingue por la asociación positiva entre la SST en el norte y en el Océano Atlántico tropical/subtropical y las temperaturas de verano, y una correlación negativa entre la SST de estas regiones y las lluvias otoñales. Además, este modo de variabilidad de la SST está asociado con los efectos positivos y negativos del ENSO sobre las temperaturas de verano y las precipitaciones de otoño, respectivamente. El calentamiento de la SST del Atlántico, relacionado con el ENSO, ocurre como resultado de la reducción en la velocidad de los vientos alisios, que a su vez reducen las pérdidas de calor latente y sensible (aumentando la SST) sobre el Atlántico tropical, lo que lleva a un aumento de las temperaturas del Levante en verano.
- Excepto en verano, los modos de variabilidad acoplados entre la SLP y las temperaturas estacionales, mostraron en general una correlación negativa entre las SLP en el norte de África, el Mediterráneo, Europa (excepto la mayor parte del norte) y el Atlántico central (Azores), y las temperaturas estacionales, mientras que se encontraron correlaciones positivas entre la SLP en las latitudes más al norte y las temperaturas estacionales. Estos patrones acoplados reflejan, en parte, la influencia de los índices NAO, NCP, MO, WEMO y EA/WR. Para el acoplamiento de la SLP con la temperatura de verano, anomalías positivas de la SLP en la región tropical/subtropical del Océano Pacífico, asociadas con el ENSO, están relacionadas con un aumento de las temperaturas en el Levante.

Trabajo futuro

A lo largo de esta Tesis todos los esfuerzos se han dirigido a ofrecer un análisis de la variabilidad espacio-temporal del clima en la región del Levante, tratando de analizar los mecanismos causales responsables de la misma. Por tanto, los resultados obtenidos en este trabajo establecen un punto de partida para la consideración de potenciales predictores de la temperatura y precipitación estacionales, y de los eventos extremos como la ocurrencia de sequías. En este marco, varios puntos clave podrían mejorarse en el futuro centrados en el estudio de la predictibilidad climática en esta región. Para ello, resulta fundamental mejorar la comprensión del papel de los patrones de circulación a gran escala en la temperatura y las precipitaciones estacionales. Una forma podría ser completando los posibles campos predictores, por ejemplo, agregando más índices de teleconexión al estudio y expandiendo la cobertura espacial de la SST, limitada aquí al Atlántico Norte. Una vez que identificado un conjunto más completo de potenciales predictores, la capacidad predictiva de los mismos debería ser analizada. Para ello se podrían utilizar diferentes técnicas, con la finalidad de poder desarrollar modelos estadísticos de predicción climática estacional, como la aplicación de la SVD entre los campos predictores y la temperatura y precipitación del Levante

a diferentes retrasos estacionales, o la aplicación de modelos estadísticos de regresión lineal, entre otros.

Además, la región de estudio también podría ser ampliada a través de la obtención de series temporales de temperatura y precipitación diarias para Jordania y Siria, con el fin de analizar los cambios en los eventos climáticos extremos en estas regiones, donde esta temática no se ha sido explorado aún. Otro aspecto importante al respecto está relacionado con el uso de diferentes índices de sequía para el análisis de este fenómeno extremo en la región. Por ejemplo, el uso del Índice Estandarizado de Precipitación y Evapotranspiración (SPEI), que tiene en cuenta tanto la precipitación como la evapotranspiración potencial, podría utilizarse para comprender mejor el impacto de la temperatura en la demanda de agua y la variabilidad de la humedad en el Levante bajo condiciones de cambio climático.

APPENDIX A
TABLES

Table 1. The final list of the meteorological stations used in this study (monthly maximum and minimum temperatures).

Station	Name	Country	Long.	Latit.	Elev.	period	Missing (%)
1	Amman Airport	Jordan	31.98	35.98	767	1987-2017	0.0
2	Aqaba Airport	Jordan	29.55	35.01	53	1987-2017	0.0
3	Ghor Safi	Jordan	31.03	35.46	-350	1987-2017	0.3
4	H-4 Irwaished	Jordan	32.5	38.2	686	1987-2017	0.0
5	H-5 Safawi	Jordan	32.2	37.13	668	1987-2017	0.8
6	Irbid	Jordan	32.54	35.85	618	1987-2017	1.4
7	Maan	Jordan	30.16	35.78	1069	1987-2017	0.6
8	Mafraq	Jordan	32.36	36.25	686	1987-2017	0.6
9	Queen Alia Airport	Jordan	31.71	35.96	721	1987-2017	0.0
10	Guriat	Saudi arb.	31.4	37.26	509	1987-2017	0.0
11	Turaif	Saudi arb.	31.68	38.66	813	1987-2017	0.0
12	Iskenderun	Turkey	36.58	36.16	3	1987-2017	0.0
13	Gaziantep	Turkey	37.08	37.36	701	1987-2017	0.0
14	Elat	Israel	29.5526	34.9542	12	1987-2017	0.0
15	Yotvata	Israel	29.8851	35.0771	70	1987-2017	1.4
16	Sede Boqer	Israel	30.8704	34.7951	475	1987-2017	0.0
17	Sedom Man	Israel	31.0306	35.3919	-388	1987-2017	0.0
18	Arad Man	Israel	31.2552	35.2128	605	1987-2017	0.0
19	Beer Sheva Man	Israel	31.2515	34.7995	279	1987-2017	0.0
20	Besor Farm Man	Israel	31.2716	34.3894	110	1987-2017	0.3
21	Lahav Man	Israel	31.3812	34.8729	460	1987-2017	0.0
22	Lod Airport	Israel	31.995	34.897	40	1987-2017	0.3
23	Gat Man	Israel	31.6303	34.7913	140	1987-2017	0.1
24	Negba	Israel	31.6596	34.6796	90	1987-2017	0.0
25	Beit Jimal Man	Israel	31.7248	34.9762	355	1987-2017	4.2
26	Jerusalem Centre	Israel	31.7806	35.2217	810	1987-2017	0.0
27	Bet Dagan Man	Israel	32.0073	34.8138	31	1987-2017	0.0
28	Yavne'el Man	Israel	32.6978	35.5101	0	1987-2017	0.0
29	Hakfar Hayarok	Israel	30	34.83	432	1987-2017	0.3
30	Massada Man	Israel	32.6833	35.6008	-200	1987-2017	4.4
31	Avne Etan Man	Israel	32.8174	35.7622	375	1987-2017	0.6
32	Kefar Blum Man	Israel	33.1728	35.612	75	1987-2017	0.0
33	Ayyelet Hashahar	Israel	33.0219	35.5742	175	1987-2017	0.7

34	Zefat Har Kenaan	Israel	32.98	35.507	936	1987-2017	0.0
35	Harashim	Israel	32.956	35.3288	825	1987-2017	0.1
36	Elon Man	Israel	33.0653	35.2173	300	1987-2017	0.0
37	En Hahoresh Man	Israel	32.3877	34.9376	15	1987-2017	1.9
38	Galed (Even Yizhaq)	Israel	32.558	35.0742	185	1987-2017	0.0
39	Akko	Israel	32.9318	35.102	8	1987-2017	0.0
40	Leshem	Israel	32.8	35.24	345	1987-2017	0.3
41	Hebron	Palestine	31.5	35.1	1005	1987-2017	0.0
42	Dama0080	Syria	33.42	36.52	620	1987-2017	0.0
43	Hamaairport0558	Syria	35.12	36.71	305	1987-2017	0.0
44	Hmam0454	Syria	35.41	35.94	48	1987-2017	0.3
45	Kami0001	Syria	37.06	41.23	449	1987-2017	1.9
46	Lata0440	Syria	35.52	35.78	7	1987-2017	0.0
47	Safi0066	Syria	34.81	36.12	370	1987-2017	0.6
48	Alep0007	Syria	36.18	37.24	385	1987-2015	0.6
49	Deir0045	Syria	35.34	40.14	215	1987-2015	2.2
50	Hamaagric	Syria	35.11	36.75	316	1987-2015	0.6
51	Homs0055	Syria	34.73	36.73	483	1987-2015	0.6
52	Swed0067	Syria	32.71	36.57	1015	1987-2015	1.1
53	Tart0050	Syria	34.87	35.88	5	1987-2015	0.0
54	Palm0061	Syria	34.56	38.28	400	1987-2015	1.9
55	Maze0079	Syria	33.48	36.22	730	1987-2015	0.8
56	Qunitera	Syria	33.12	35.82	941	1987-2015	0.4
57	Kfardan	Lebanon	34.01	36.05	1049	1994-2017	1.1
58	Beyrouth	Lebanon	33.81	35.48	29	1994-2017	0.0
59	Tripoli	Lebanon	34.45	35.8	5	1994-2017	3.9
60	Houche-Oumara	Lebanon	33.81	35.85	920	1994-2017	5.3

Table 2. The final list of the meteorological stations used in this study (monthly precipitation).

Station	**Name**	**Country**	**Long.**	**Latit.**	**Elev.**	Period	**Missing (%)**
1	Kefar Rosh Haniqra	Israel	35.11	33.09	50	1970-2018	0
2	Bet Haemeq	Israel	35.15	32.97	50	1970-2018	0.03
3	Kefar Hamakkabbi	Israel	35.11	32.79	25	1970-2018	0
4	Yagur	Israel	35.08	32.74	25	1970-2018	0
5	Bet Oren	Israel	35.01	32.73	370	1970-2018	0
6	Atlit Salt	Israel	34.94	32.71	5	1970-2018	0.02
7	Ramat Hashofet	Israel	35.10	32.61	250	1970-2018	0
8	Nahsholim Plantations	Israel	34.95	32.61	15	1970-2018	0.05
9	Regavim	Israel	35.03	32.52	105	1970-2018	0
10	Binyamina Agr. Coun.	Israel	34.95	32.52	25	1970-2018	0
11	Barqay	Israel	35.03	32.47	65	1970-2018	0.01
12	Yad Hanna	Israel	35.01	32.33	55	1970-2018	0
13	Bene Deror	Israel	34.90	32.26	30	1970-2018	0
14	Eyal	Israel	34.98	32.21	75	1970-2018	0
15	Kefar Shemaryahu	Israel	34.82	32.18	30	1970-2018	0.01
16	Adanim	Israel	34.90	32.14	25	1970-2018	0
17	Miqwe Yisrael	Israel	34.78	32.03	20	1970-2018	0
18	Palmahim	Israel	34.71	31.93	20	1970-2018	0.02
19	Yavne	Israel	34.75	31.90	20	1970-2018	0.02
20	Kefar Bilu	Israel	34.82	31.88	65	1970-2018	0

21	Bet Hilqiyya	Israel	34.81	31.79	70	1970-2018	0.03
22	Nir Gallim	Israel	34.68	31.83	20	1970-2018	0.01
23	Nizzanim Kibbuz	Israel	34.64	31.72	30	1970-2018	0
24	En Zurim	Israel	34.72	31.70	55	1970-2018	0.01
25	Talme Yafe	Israel	34.61	31.62	75	1970-2018	0
26	Ziqim	Israel	34.52	31.61	30	1970-2018	0
27	Beror Hayil	Israel	34.65	31.56	75	1970-2018	0.01
28	Be'eri	Israel	34.49	31.42	90	1970-2018	0
29	Niroz	Israel	34.40	31.31	110	1970-2018	0
30	Yir'on	Israel	35.46	33.08	685	1970-2018	0
31	Mazzuva	Israel	35.16	33.06	110	1970-2018	0
32	Kabri	Israel	35.15	33.02	100	1970-2018	0.03
33	Yehi'am	Israel	35.23	33.00	380	1970-2018	0
34	Zefat Har Kenaan	Israel	35.51	32.98	936	1970-2018	0
35	Huqoq	Israel	35.50	32.88	5	1970-2018	0
36	Kefar Hittim	Israel	35.50	32.80	40	1970-2018	0
37	Sede Ilan	Israel	35.43	32.75	195	1970-2018	0
38	Kefar Yehoshua	Israel	35.15	32.68	60	1970-2018	0
39	Ramat Dawid	Israel	35.20	32.68	80	1970-2018	0
40	Mizra Plantation	Israel	35.29	32.67	100	1970-2018	0.01
41	Hayogev	Israel	35.20	32.61	100	1970-2018	0.06
42	Moledet	Israel	35.44	32.59	65	1970-2018	0
43	Kefar Yehezqel	Israel	35.36	32.57	10	1970-2018	0.01
44	Sheluhot	Israel	35.48	32.47	-110	1970-2018	0
45	Sha'alvim	Israel	34.98	31.87	180	1970-2018	0
46	Hulda	Israel	34.88	31.83	125	1970-2018	0
47	Qiryat Anavim	Israel	35.12	31.81	660	1970-2018	0.01
48	Jerusalem St Anne	Israel	35.24	31.78	740	1970-2018	0
49	Beit Jimal?Man	Israel	34.98	31.72	355	1970-2018	0
50	Rosh Zurim	Israel	35.13	31.67	955	1970-2018	0
51	Bet Guvrin	Israel	34.89	31.61	270	1970-2018	0
52	Ruhama	Israel	34.71	31.50	170	1970-2018	0
53	Shoval	Israel	34.75	31.41	225	1970-2018	0
54	Urim	Israel	34.52	31.30	100	1970-2018	0.01
55	Be'er Sheva	Israel	34.80	31.25	279	1970-2018	0
56	Gevulot	Israel	34.47	31.21	135	1970-2018	0.06
57	Sede Boqer Man	Israel	34.80	30.87	475	1970-2018	0
58	Hagosherim	Israel	35.63	33.22	110	1970-2018	0.01
59	Gadot	Israel	35.62	33.02	120	1970-2018	0.02
60	Mahanayim	Israel	35.57	32.99	270	1970-2018	0
61	Almagor	Israel	35.60	32.91	-10	1970-2018	0.01
62	Haon	Israel	35.62	32.73	-200	1970-2018	0
63	Deganya Bet	Israel	35.58	32.70	-195	1970-2018	0
64	Gesher	Israel	35.55	32.62	-200	1970-2018	0
65	Tirat Zevi	Israel	35.53	32.42	-220	1970-2018	0
66	Sedom?Man	Israel	35.39	31.03	-388	1970-2018	0.03

67	Nablus	Israel	35.26	32.23	550	1970-2018	0
68	Tubas	Israel	35.37	32.32	175	1970-2018	0.05
69	Salfit	Israel	35.18	32.08	570	1970-2018	0.02
70	Dura	Israel	35.03	31.51	850	1970-2018	0.03
71	Hebron	Israel	35.10	31.53	1005	1970-2018	0.01
72	Meithelon	Israel	35.27	32.35	380	1970-2018	0.01
73	Rammallah	Israel	35.20	31.90	856	1970-2018	0.01
74	Jenin	Israel	35.30	32.46	178	1970-2018	0.02
75	Jericho	Israel	35.46	31.86	-260	1970-2018	0.02
76	Elqana Pe'erim	Israel	35.04	32.11	275	1970-2018	0
77	Ma'on	Israel	35.16	31.42	780	1970-2018	0
78	Elat	Israel	34.95	29.55	11	1970-2018	0
79	Irbed	Jordan	35.85	32.56	754	1970-2018	0
80	Errabah	Jordan	35.45	31.16	963	1970-2018	0
81	Safawi	Jordan	37.08	32.12	711	1970-2018	0
82	Maan	Jordan	35.47	30.10	1112	1970-2018	0
83	Aljafer	Jordan	36.09	30.17	849	1970-2018	0
84	Irwished	Jordan	38.20	32.50	688	1970-2018	0
85	Quen Alia	Jordan	35.99	31.72	716	1970-2018	0
86	Mafraq Air Port	Jordan	36.24	32.32	676	1970-2018	0
87	Deir Alla	Jordan	35.62	32.19	-220	1970-2018	0
88	Burma	Jordan	35.78	32.22	607	1970-2018	0
89	Ma'in	Jordan	35.74	31.68	840	1970-2018	0
90	Mazar	Jordan	35.70	31.06	1242	1970-2018	0
91	Petra	Jordan	35.44	30.34	900	1970-2018	0
92	Ruseifa	Jordan	36.04	32.02	641	1970-2018	0
93	Turra	Jordan	35.99	32.63	463	1970-2018	0
94	Baqura Met.Station	Jordan	35.60	32.61	-227	1970-2018	0.01
95	South Shuna	Jordan	35.64	31.91	637	1970-2018	0
96	Deir Abi Said	Jordan	35.68	32.50	339	1970-2018	0.01
97	Sihan	Jordan	35.76	32.14	900	1970-2018	0
98	Jarash	Jordan	35.89	32.28	636	1970-2018	0
99	Kufranja Dam	Jordan	35.64	32.27	630	1970-2018	0
100	Ira	Jordan	35.67	32.01	700	1970-2018	0
101	Na'ur	Jordan	35.83	31.87	520	1970-2018	0
102	Tafile	Jordan	35.61	30.84	1300	1970-2018	0
103	Um Qeis	Jordan	35.68	32.65	347	1970-2018	0
104	Wadi Es-Sir	Jordan	35.82	31.95	1211	1970-2018	0
105	Jubeiha	Jordan	35.87	32.02	1012	1970-2018	0
106	Um El-Quttein	Jordan	36.63	32.32	896	1970-2018	0
107	Ras En-Naqb	Jordan	35.49	30.00	1539	1970-2018	0
108	Qatraneh	Jordan	36.05	31.25	779	1970-2018	0
109	Azraq	Jordan	36.82	31.83	521	1970-2018	0
110	Muleih	Jordan	35.82	31.59	684	1970-2018	0
111	Ras Muneif Evap.	Jordan	35.81	32.38	1154	1970-2018	0
112	En Nueiyime	Jordan	35.91	32.42	748	1970-2018	0

113	Wadi Dhuleli	Jordan	36.28	32.15	514	1970-2018	0
114	Rabba	Jordan	35.74	31.27	954	1970-2018	0
115	Ras Al3en	Syria	40.09	36.84	400	1970-2018	0.03
116	Busra Al Sham	Syria	36.49	32.52	800	1970-2018	0.02
117	Banias	Syria	35.95	35.18	20	1970-2018	0.06
118	Al Hiffa	Syria	36.05	35.61	335	1970-2018	0.03
119	Al Shadadah	Syria	40.73	36.03	280	1970-2018	0
120	Ezra3	Syria	36.24	32.88	570	1970-2018	0.02
121	Al Zabadani	Syria	36.09	33.72	145	1970-2018	0.05
122	Al Sanamin	Syria	36.18	33.08	640	1970-2018	0.02
123	Al 3areda	Syria	36.29	34.66	280	1970-2018	0
124	Al Qahtania	Syria	38.95	35.98	262	1970-2018	0
125	Al Manajer	Syria	40.19	36.69	345	1970-2018	0.02
126	Al Ya3robia	Syria	42.04	36.81	400	1970-2018	0.02
127	Al Karem	Syria	36.33	35.40	174	1970-2018	0.07
128	Tal Shehab	Syria	36.00	32.69	300	1970-2018	0.03
129	Al Soura Al Soghra	Syria	36.57	33.03	740	1970-2018	0.03
130	Salkhad	Syria	36.70	32.48	320	1970-2018	0
131	Shekh Meskin	Syria	36.16	32.83	528	1970-2018	0
132	Quirdaha	Syria	36.05	35.45	300	1970-2018	0
133	Al Basil Airpo	Syria	35.94	35.41	48	1970-2018	0
134	Azaz	Syria	37.04	36.58	555	1970-2018	0
135	Al Safera	Syria	37.38	36.07	335	1970-2018	0.05
136	Allepo	Syria	37.24	36.18	385	1970-2018	0
137	Tel Tammer	Syria	41.91	36.83	410	1970-2018	0.02
138	Derbasia	Syria	40.65	37.08	500	1970-2018	0.02
139	Mabroka	Syria	39.76	36.53	400	1970-2018	0.01
140	Tartus	Syria	35.88	34.87	5	1970-2018	0
141	Lattakia	Syria	35.78	35.52	7	1970-2018	0
142	Malkieh	Syria	42.14	37.19	500	1970-2018	0
143	Qamishli	Syria	41.23	37.06	449	1970-2018	0
144	Hasaka	Syria	40.71	36.50	307	1970-2018	0
145	Zuhireieh	Syria	42.31	37.19	350	1970-2018	0.04
146	Saeta	Syria	36.12	34.81	370	1970-2018	0
147	Shatha	Syria	36.25	35.49	250	1970-2018	0
148	Qusir	Syria	36.58	34.51	600	1970-2018	0.03
149	Makhram Foqani	Syria	37.08	34.81	600	1970-2018	0.01
150	Msefreh	Syria	36.34	32.64	685	1970-2018	0.03
151	Hama Airpo	Syria	36.71	35.12	305	1970-2018	0
152	En Halaquim	Syria	36.31	34.92	600	1970-2018	0
153	Alsalamieh	Syria	37.06	35.01	448	1970-2018	0
154	Maysalon	Syria	36.06	33.59	156	1970-2018	0
155	Sarghaya	Syria	36.14	33.79	409	1970-2018	0
156	Nabak	Syria	36.73	34.03	329	1970-2018	0
157	Al Swaida	Syria	36.57	32.71	15	1970-2018	0
158	Wadi Al3ouun	Syria	36.19	35.00	300	1970-2018	0.04

159	Al Se3en	Syria	37.38	35.27	440	1970-2018	0.05
160	Hamere	Syria	36.41	35.29	600	1970-2018	0.01
161	Mesiaf	Syria	36.34	35.06	530	1970-2018	0
162	Qatefeh	Syria	36.60	33.74	930	1970-2018	0.03
163	Duma	Syria	36.39	33.57	660	1970-2018	0.05
164	Shekh Bader	Syria	36.07	34.99	600	1970-2018	0.04
165	Qadamos	Syria	36.16	35.09	915	1970-2018	0.04
166	Drekish	Syria	36.14	34.90	500	1970-2018	0.01
167	Alhol	Syria	41.15	36.43	450	1970-2018	0

Table 3. The final list of the meteorological stations used in this study (daily maximum and minimum temperatures).

Station	Name	Elevation (m)	Longitude (ºE)	Latitude (ºN)	Period	Missing (%)
1	Elat	12	29.5526º	34.9542º	1987-2016	0
2	Yotvata	70	29.8851º	35.0771º	1987-2016	1.3
3	Sede Boqer	475	30.8704º	34.7951º	1987-2016	0
4	Sedom Man	-388	31.0306º	35.3919º	1987-2016	0
5	Arad Man	605	31.2552º	35.2128º	1987-2016	0
6	Beer Sheva Man	279	31.2515º	34.7995º	1987-2016	0
7	Besor Farm Man	110	31.2716º	34.3894º	1987-2016	0.3
8	Lahav Man	460	31.3812º	34.8729º	1987-2016	0
9	Lod Airport	40	31.9950º	34.8970º	1987-2016	0.3
10	Gat Man	140	31.6303º	34.7913º	1987-2016	0.1
11	Negba	90	31.6596º	34.6796º	1987-2016	0
12	Beit Jimal Man	355	31.7248º	34.9762º	1987-2016	4.1
13	Jerusalem Centre	810	31.7806º	35.2217º	1987-2016	0
14	Bet Dagan Man	31	32.0073º	34.8138º	1987-2016	0
15	Yavne'el Man	0	32.6978º	35.5101º	1987-2016	0
16	Hakfar Hayarok	432	30	34.83	1987-2016	0.3
17	Massada Man	-200	32.6833º	35.6008º	1987-2016	4.1
18	Avne Etan Man	375	32.8174º	35.7622º	1987-2016	0.5
19	Kefar Blum Man	75	33.1728º	35.6120º	1987-2016	0
20	Ayyelet Hashahar	175	33.0219º	35.5742º	1987-2016	0
21	Zefat Har Kenaan	936	32.9800º	35.5070º	1987-2016	0.7
22	Harashim	825	32.9560º	35.3288º	1987-2016	0.1
23	Elon Man	300	33.0653º	35.2173º	1987-2016	0
24	En Hahoresh Man	15	32.3877º	34.9376º	1987-2016	2
25	Galed (Even Yizhaq)	185	32.5580º	35.0742º	1987-2016	0
26	Akko	8	32.9318º	35.1020º	1987-2016	0
27	Hazeva Man	-135	30.7787º	35.2389º	1988-2016	0.8
28	Ariel	590	32.1063º	35.1774º	1990-2016	0.5

Table 4. The final list of the meteorological stations used in this study (daily precipitation).

Station	Name	Elevation (m)	Latitude (ºN)	Longitude (ºE)	Period	Missing (%)
1	Kefar Rosh Haniqra	50	35.1149	33.0861	1970-2018	0.23
2	Regba	20	35.0980	32.9755	1970-2018	0.33
3	Kefar Hamakkabbi	25	35.1134	32.7915	1970-2018	0.01
4	Haifa Port	5	34.9979	32.8223	1970-2018	0
5	Nir Ezyon	210	34.989	32.6990	1970-2018	0
6	Ramat Hashofet	250	35.0969	32.6121	1970-2018	0.09
7	Ma'yan Zevi Fields	10	34.9360	32.5756	1970-2018	0
8	Regavim	105	35.0336	32.5228	1970-2018	0.01
9	Binyamina Agr.	25	34.9469	32.5195	1970-2018	0
10	Yad Hanna	55	35.0072	32.3255	1970-2018	0.01
11	Bene Deror	30	34.9009	32.2629	1970-2018	0
12	Eyal	75	34.9797	32.2123	1970-2018	0.02
13	Kefar Shemaryahu	30	34.8185	32.1801	1970-2018	0
14	Adanim	25	34.9025	32.1430	1970-2018	0.02
15	Nahshonim	100	34.9510	32.0602	1970-2018	0.06
16	Miqwe Yisrael	20	34.7846	32.0318	1970-2018	0
17	Palmahim	20	34.7053	31.9340	1970-2018	0.37
18	Kefar Bilu	65	34.8223	31.8758	1970-2018	0.07
19	Nir Gallim	20	34.6831	31.8265	1970-2018	0.30
20	Kefar Menahem	115	34.8346	31.7333	1970-2018	0.02
21	Nizzanim Kibbuz	30	34.6352	31.7193	1970-2018	0
22	Negba	85	34.6841	31.6616	1970-2018	0
23	Talme Yafe	75	34.6148	31.6171	1970-2018	0.07
24	Ziqim	30	34.5243	31.6077	1970-2018	0.02
25	Nir Am	120	34.5791	31.5213	1970-2018	0
26	Nahal Oz	80	34.4947	31.4726	1970-2018	0
27	Magen	135	34.4253	31.301	1970-2018	0
28	Yir'on	685	35.4553	33.0778	1970-2018	0
29	Elon	320	35.2210	33.0630	1970-2018	0
30	Zefat Har Kenaan	936	35.5070	32.9800	1970-2018	0
31	Parod	450	35.4330	32.9322	1970-2018	0.02
32	Sede Ilan	195	35.4259	32.7525	1970-2018	0.21
33	Hazore'im	-65	35.5038	32.7433	1970-2018	0.06
34	Gazit	125	35.4472	32.6362	1970-2018	0
35	Kefar Yehoshua	60	35.1515	32.6810	1970-2018	0.02
36	Ginnegar	100	35.2563	32.6624	1970-2018	0.12
37	Giv'at Oz	105	35.1986	32.5559	1970-2018	0
38	Kefar Yehezqel	10	35.3617	32.5650	1970-2018	0.37
39	Hamadya	-165	35.5208	32.5199	1970-2018	0.01
40	Sha'alvim	180	34.9830	31.8698	1970-2018	0
41	Hulda	125	34.8838	31.8315	1970-2018	0.01
42	Qiryat Anavim	660	35.1199	31.8098	1970-2018	0
43	Jerusalem St Anne	740	35.2360	31.7808	1970-2018	0
44	Beit Jimal Man	355	34.9762	31.7248	1970-2018	0
45	Rosh Zurim	955	35.1264	31.6680	1970-2018	0.12
46	Bet Guvrin	270	34.8934	31.6139	1970-2018	0
47	Ruhama	170	34.7063	31.4974	1970-2018	0.05
48	Shoval	225	34.7460	31.4138	1970-2018	0
49	Eshel Hanasi	190	34.6986	31.3243	1970-2018	0.32
50	Urim	100	34.5245	31.3049	1970-2018	0.01

51	Omer	330	34.8490	31.2725	1970-2018	0.13
52	Gevulot	135	34.4676	31.2105	1970-2018	0.39
53	Revivim	280	34.7231	31.0448	1970-2018	0
54	Sede Boqer	475	34.7950	30.8702	1970-2018	0
55	Kefar Blum	75	35.6133	33.1716	1970-2018	0
56	Gadot	120	35.6208	33.0165	1970-2018	0.42
57	Almagor	-10	35.6006	32.9122	1970-2018	0.21
58	Haon	-200	35.6248	32.7275	1970-2018	0.01
59	Gesher	-200	35.5534	32.6192	1970-2018	0
60	Tirat Zevi	-220	35.5258	32.4222	1970-2018	0.03
61	Sedom Man	-388	35.3919	31.0306	1970-2018	0
62	Elat	11	34.9542	29.5526	1970-2018	0
63	Salfit	570	35.1805	32.0847	1970-2018	0.19
64	Nabils	550	35.2608	32.2250	1970-2018	0
65	Elqana	275	35.0381	32.1121	1982-2018	0.02
66	Karmel	740	35.1841	31.4294	1982-2018	0.14

Table 5. List of the stations where change points in daily rainfall was detected.

Station	Name	Latitude (ºN)	Longitude (ºE)	Change points
1	Regba	35.098	32.9755	6/2/2013
2	Kefar Hamakkabbi	35.1134	32.7915	22/10/2000
3	Nir Ezyon	34.989	32.699	1/2/2013
4	Ramat Hashofet	35.0969	32.6121	31/1/2013
5	Palmahim	34.7053	31.934	18/10/1989
6	Kefar Menahem	34.8346	31.7333	22/2/2016
7	Parod	35.4330	32.9322	17/3/1991
8	Hazore'im	35.5038	32.7433	12/2/2005
9	Kefar Yehezqel	35.3617	32.565	5/3/1976 , 25/12/1999
10	Hamadya	35.5208	32.5199	1/2/2013
11	Jerusalem St Anne	35.236	31.7808	25/1/1982
12	Shoval	34.746	31.4138	4/12/1994
13	Urim	34.5245	31.3049	14/12/2013
14	Revivim	34.7231	31.0448	11/2/1974
15	Gesher	35.5534	32.6192	10/12/1974

Table 6. List of the stations where change points in daily temperatures was detected.

Station	NAME	Tmax	Tmin
1	Elat		19971026
2	Yotvata		19931009/19880715
3	Sede Boqer		
4	Sedom Man		19911204/19930507
5	Arad Man		19901014/19910515 19930412/20080304
6	Beer Sheva Man	20091213/20110129	19971008
7	Besor Farm Man		20091206
8	Lahav Man		
9	Lod Airport	19910516/19920523	19890216/19900825 19931010
10	Gat Man		20091005
11	Negba		
12	Beit Jimal Man		20080304
13	Jerusalem Centre		

14	Bet Dagan Man		19931010/20080228
15	Yavne'el Man		19980409
16	Hakfar Hayarok		20090515/20120404
17	Massada Man		
18	Avne Etan Man		19931009/19941104
19	Kefar Blum Man		
20	Ayyelet Hashahar		
21	Zefat Har Kenaan		
22	Harashim		20080221
23	Elon Man		
24	En Hahoresh Man	19901014/19910515 19930412/20031107	
25	Galed (Even Yizhaq)	19910516/20030706 20041116/20080304 20110130/20120331	
26	Akko		19981000/19991200 20030300/20061100
27	Hazeva Man		19900828/19901031 19910516/19930514
28	Ariel	19980408/20091214	
Total		23 (82%)	12 (43%)

Table 7. Significant change points detected in the annual, seasonal, and monthly Tmax. Tmin, and DTR averages time series in 1987-2017.

Level	Tmax	Tmin	DTR
Annual	1997	2007	-
Winter	2002	1998	-
Spring	2002	2007	-
Summer	1997	2004	-
Autumn		2006	-
February	2008	2005	-
March	1999	2005	-
May	-	2012	-
June	1995	1997	-
July	2014	1997	-
August	2005	2005	2005
September	-	2005	2005

Table 8. The trends for the annual, seasonal, and monthly averages of Tmax, Tmin, and DTR for the Levant sub-regions during (1987-2017). (***) if trend at $\alpha = 0.001$ level of significance. (**) if trend at $\alpha = 0.01$ level of significance. (*) if trend at $\alpha = 0.05$ level of significance. (+) if trend at $\alpha = 0.1$ level of significance.

Month	Palestine (Tmax/Tmin/DTR)	Jordan (Tmax/Tmin/DTR)	Lebanon (Tmax/Tmin/DTR)	Syria (Tmax/Tmin/DTR)
Ann.	(0.32**/0.29***/-0.09)	(0.39***/0.28**/0.07)	(0.37+/0.34+/-0.03)	(0.34*/0.32**/-0.09)
Win.	(0.43+/0.32*/0.15)	(0.53*/0.20/0.34*)	(0.35/0.21/0.12)	(0.51*/0.35+/0.22)
Spr.	(0.53*/0.48**/-0.028)	(0.59**/0.47**/0.18)	(0.49*/0.48*/0.10)	(0.50*/0.47*/-0.14)
Sum.	(0.33*/0.33**/-0.19**)	(0.45*/0.38**/-0.08)	(0.25/0.08/0.02)	(0.40*/0.23+/-0.17*)
Aut.	(0.31+/0.41**/-0.19*)	(0.32+/0.42**/-0.11)	(0.33/0.49*/-0.17)	(0.38/0.58**/-0.24)
Jan.	(0.49/0.37/0.02)	(0.56/0.19/0.46*)	(0.23/-0.04/-0.05)	(0.54+/0.25/0.02)
Feb.	(0.85*/0.64*/0.29)	(0.98**/0.56*/0.50*)	(0.74/0.46/0.22)	(0.71*/0.75*/0.21)
Mar.	(1.1*/0.72*/0.34)	(1*/0.70*/0.38*)	(1.1+/0.81+/0.24)	(0.78+/0.71*/0.03)

Apr.	(0.50/0.45*/-0.06)	(0.63*/0.38/0.20)	(1.1*/0.61+/0.63+)	(0.63+/0.45+/0.01)
May	(0.18/0.47**/-0.22*)	(0.18/0.29/-0.04)	(0.04/0.25/-0.32)	(0.11/0.45*/-0.21)
June	(0.45*/0.22/-0.16)	(0.48*/0.40**/-0.12)	(0.22/-0.061/0)	(0.32+/0.26/-0.23+)
July	(0.44*/0.48**/-0.19)	(0.52*/0.57**/0.01)	(0.44/0.0/0.13)	(0.40+/0.29/-0.087)
Aug.	(0.47***/0.49**/-0.022)	(0.62**/0.59**/-0.01)	(0.38/0.45/-0.07)	(0.54***/0.51**/-0.29*)
Sept.	(0.33/0.45**/-0.14+)	(0.37+/0.48**/-0.20)	(0.49*/0.54*/-0.19)	(0.35*/0.55*/-0.34*)
Oct.	(0.16/0.34/-0.11)	(0.23/0.38/-0.08)	(0.63+/0.52/0.07)	(0.08/0.47+/-0.18)
Nov.	(0.36/0.39/-0.12)	(0.31/0.29/-0.03)	(0.01/0.48/-0.32)	(0.63/0.44/0)
Dec.	(0.47/0.40/0.072)	(0.42 /0.38/0.28)	(0.046 /-0.15/0.05)	(0.64+/0.22/0.37)

Table 9. Number of stations with positive or negative trends at annual, seasonal and monthly scales. Note: In bracket, the number of stations with significant positive or negative trends at the 95% confidence level.

Level	**Tmax**		**Tmin**		**Range**	
	+	-	+	-	+	-
Annual	59(50)	1(0)	57(50)	3(0)	36(13)	24(5)
Winter	58(38)	2(0)	55(21)	5(0)	46(22)	14(1)
Spring	59(44)	1(1)	58(47)	2(0)	37(11)	23(7)
Summer	59(44)	1(1)	59(40)	1(0)	20(7)	40(10)
Autumn	53(22)	7(1)	58(37)	2(1)	20(5)	40(18)
January	55(15)	5(0)	54(3)	6(0)	46(23)	14(0)
February	60(49)	0(0)	59(49)	1(0)	46(17)	14(2)
March	60(50)	0(0)	60(50)	0(0)	49(20)	11(0)
April	59(23)	1(0)	56(24)	4(1)	35(4)	25(7)
May	48(7)	12(0)	57(33)	3(0)	16(2)	54(0)
June	57(27)	3(0)	58(32)	2(0)	13(4)	49(11)
July	60(37)	0(0)	58(43)	2(0)	29(7)	31(9)
August	59(47)	1(1)	59(52)	1(1)	20(4)	40(13)
September	57(23)	3(0)	58(46)	2(0)	14(6)	46(20)
October	50(3)	10(0)	55(12)	5(0)	25(3)	35(10)
November	53(5)	7(0)	54(10)	6(0)	25(5)	35(3)
December	58(12)	2(0)	44(8)	16(0)	49(10)	11(0)

Table 10. Some fundamental statistics for the annual and seasonal (Tmax and Tmin) trends.

		Annual	**Winter**	**Spring**	**Summer**	**Autumn**
Tmax	Minimum	0.01	-0.29	-0.41	-0.38	-0.42
	Maximum	0.48	0.65	0.74	0.58	0.55
	1st Quartile	0.25	0.35	0.41	0.29	0.17
	Median	0.30	0.43	0.51	0.34	0.27
	3rd Quartile	0.35	0.51	0.59	0.40	0.41
	Mean	0.30	0.41	0.48	0.33	0.27
	Variance	0.00	0.00	0.00	0.00	0.00
	Standard deviation	0.09	0.15	0.19	0.15	0.19
Tmin	Minimum	-0.23	-0.05	-0.23	-0.36	-0.29
	Maximum	0.45	0.63	0.66	0.56	0.94
	1st Quartile	0.21	0.17	0.36	0.22	0.28
	Median	0.29	0.28	0.43	0.28	0.37
	3rd Quartile	0.33	0.35	0.49	0.36	0.48
	Mean	0.27	0.26	0.40	0.28	0.38
	Variance	0.00	0.00	0.00	0.00	0.00
	Standard deviation	0.12	0.15	0.15	0.13	0.22

Table 11. The whole cross correlation matrix between the annual and seasonal temperature and rainfall.

		Annual rainfall	Winter rainfall	Spring rainfall	Autumn rainfall
Annual	Tmax	**-0.465**	-0.329	-0.294	-0.261
	Tmin	-0.207	-0.124	-0.173	-0.116
	DTR	**-0.813**	**-0.633**	**-0.403**	**-0.454**
	Tmean	-0.348	-0.236	-0.240	-0.195
Winter	Rainfall	**0.890**	1	0.14	0
	Tmax	**-0.510**	**-0.526**	-0.022	-0.152
	Tmin	0.005	-0.031	0.049	0.059
	DTR	**-0.475**	**-0.463**	-0.057	-0.184
	Tmean	-0.347	**-0.378**	0.012	-0.072
Spring	Rainfall	**0.43**	0.14	1	0
	Tmax	**-0.363**	-0.259	**-0.460**	0.019
	Tmin	-0.248	-0.213	-0.258	0.033
	DTR	-0.133	-0.067	-0.211	-0.008
	Tmean	**-0.388**	-0.297	**-0.459**	0.032
Autumn	Rainfall	0.39	0	0	1
	Tmax	-0.151	0.052	-0.225	**-0.361**
	Tmin	-0.080	0.036	-0.174	-0.164
	DTR	-0.058	0.013	-0.046	-0.158
	Tmean	-0.157	0.060	-0.269	**-0.356**

Table 12. The cross-correlation matrix between the extreme rainfall indices and geographical features in the Levant for the period 1987-2018.

Index	1	2	3	4	5	6	7	8	9	10	11	12	13	14	15	16	17	18
prcptot	1	-0.72	0.86	0.89	0.99	0.99	0.83	0.99	0.71	0.97	0.69	0.92	0.93	0.95	0.89	0.49	0.66	0.43
Cdd	-0.72	1	-0.77	-0.82	-0.73	-0.66	-0.42	-0.68	-0.57	-0.66	-0.60	-0.52	-0.53	-0.56	-0.41	-0.67	-0.80	-0.17
Cwd	0.86	-0.77	1	0.98	0.90	0.79	0.46	0.80	0.58	0.77	0.64	0.68	0.71	0.74	0.62	0.64	0.88	0.23
r1mm	0.89	-0.82	0.98	1	0.93	0.83	0.52	0.84	0.59	0.81	0.65	0.71	0.74	0.76	0.65	0.67	0.89	0.29
r10mm	0.99	-0.73	0.90	0.93	1	0.97	0.75	0.96	0.67	0.94	0.68	0.88	0.90	0.92	0.85	0.53	0.72	0.38
r20mm	0.99	-0.66	0.79	0.83	0.97	1	0.87	0.98	0.70	0.97	0.67	0.93	0.94	0.96	0.91	0.43	0.56	0.48
r50mm	0.83	-0.42	0.46	0.52	0.75	0.87	1	0.89	0.71	0.89	0.58	0.91	0.90	0.90	0.90	0.14	0.21	0.50
r95	0.99	-0.68	0.80	0.84	0.96	0.98	0.89	1	0.76	0.99	0.71	0.96	0.96	0.97	0.91	0.42	0.57	0.46
r95ptot	0.71	-0.57	0.58	0.59	0.67	0.70	0.71	0.76	1.00	0.76	0.71	0.78	0.76	0.76	0.68	0.30	0.45	0.34
r99	0.97	-0.66	0.77	0.81	0.94	0.97	0.89	0.99	0.76	1.00	0.76	0.96	0.95	0.96	0.91	0.38	0.55	0.44
r99ptot	0.69	-0.60	0.64	0.65	0.68	0.67	0.58	0.71	0.71	0.76	1.00	0.68	0.64	0.66	0.56	0.44	0.57	0.25
rx1day	0.92	-0.52	0.68	0.71	0.88	0.93	0.91	0.96	0.78	0.96	0.68	1.00	0.99	0.99	0.98	0.21	0.40	0.46
rx3day	0.93	-0.53	0.71	0.74	0.90	0.94	0.90	0.96	0.76	0.95	0.64	0.99	1.00	1.00	0.98	0.24	0.42	0.45
rx5day	0.95	-0.56	0.74	0.76	0.92	0.96	0.90	0.97	0.76	0.96	0.66	0.99	1.00	1.00	0.97	0.27	0.45	0.45
Cdii	0.89	-0.41	0.62	0.65	0.85	0.91	0.90	0.91	0.68	0.91	0.56	0.98	0.98	0.97	1.00	0.14	0.31	0.45
X	0.49	-0.67	0.64	0.67	0.53	0.43	0.14	0.42	0.30	0.38	0.44	0.21	0.24	0.27	0.14	1.00	0.83	-0.01
Y	0.66	-0.80	0.88	0.89	0.72	0.56	0.21	0.57	0.45	0.55	0.57	0.40	0.42	0.45	0.31	0.83	1.00	0.01
Elv.	0.43	-0.17	0.23	0.29	0.38	0.48	0.50	0.46	0.34	0.44	0.25	0.46	0.45	0.45	0.45	-0.01	0.01	1.00

APPENDIX B
FIGURES

Figure 1. Spatial distribution of Pearson correlation coefficients between the EA/WR index and the extreme temperature indices at annual scale.

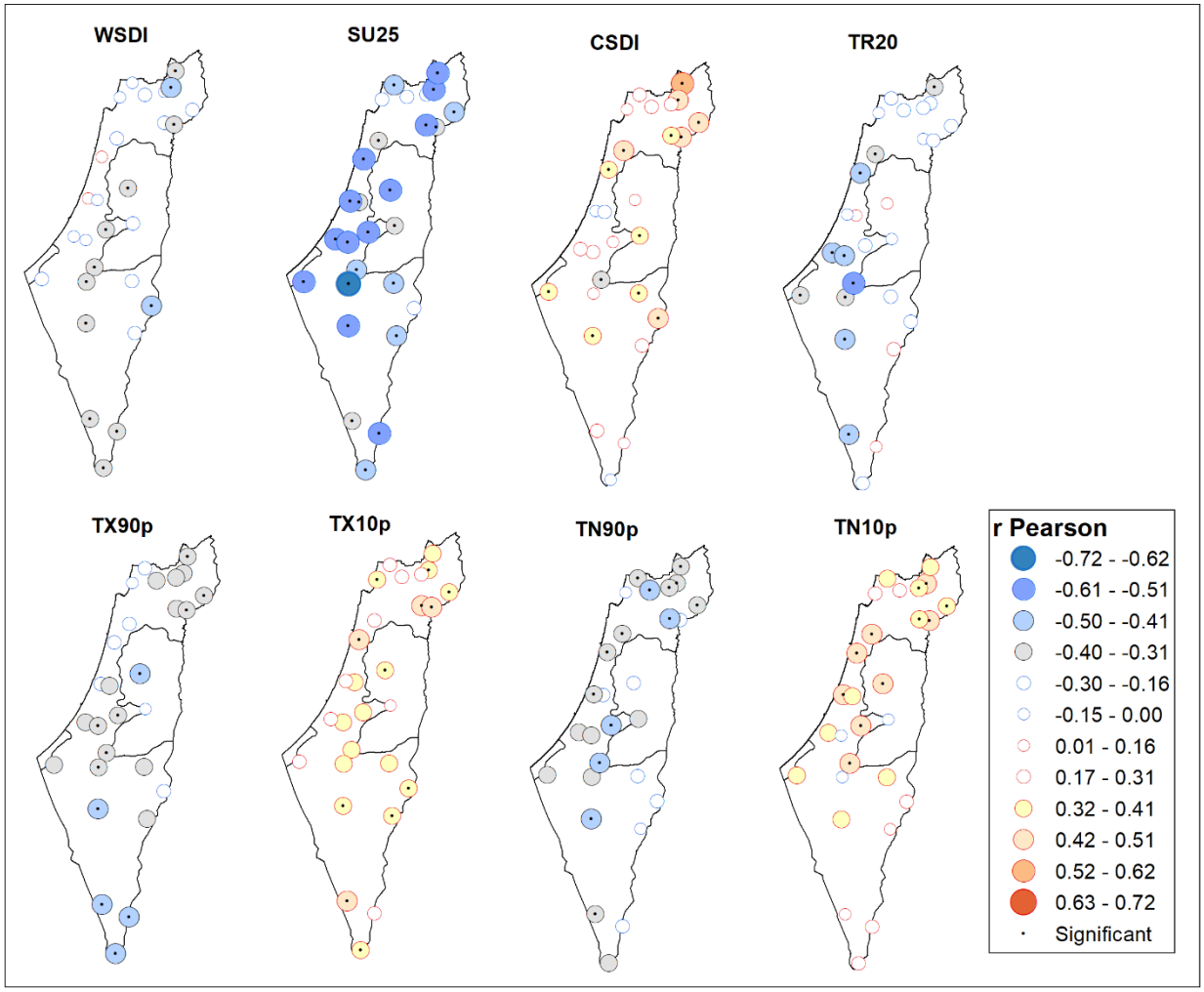

Figure 2. Spatial distribution of Pearson correlation coefficients between the NAO index and the TX90p and TN90p indices at annual scale.

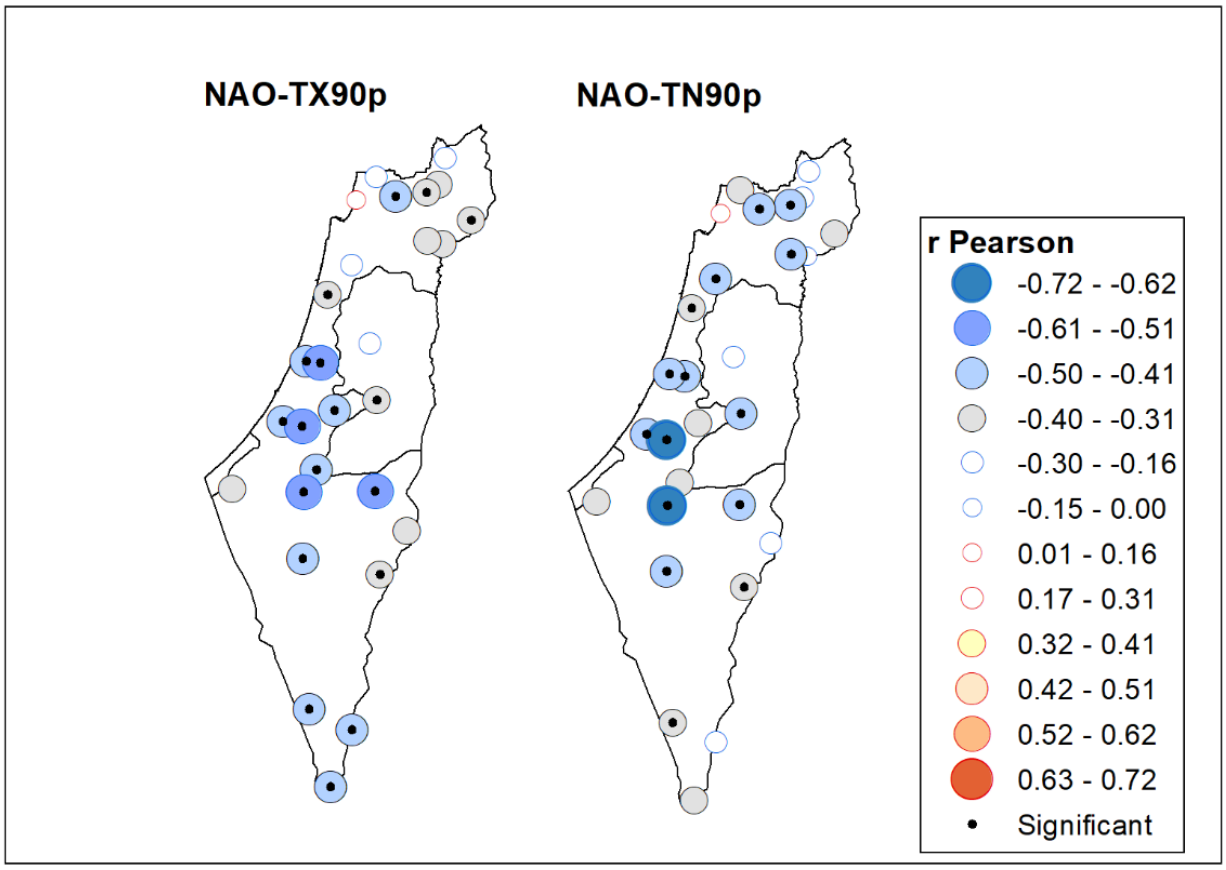

Figure 3. Spatial distribution of Pearson correlation coefficients between the EA/WR index and the extreme temperature indices at seasonal scale.

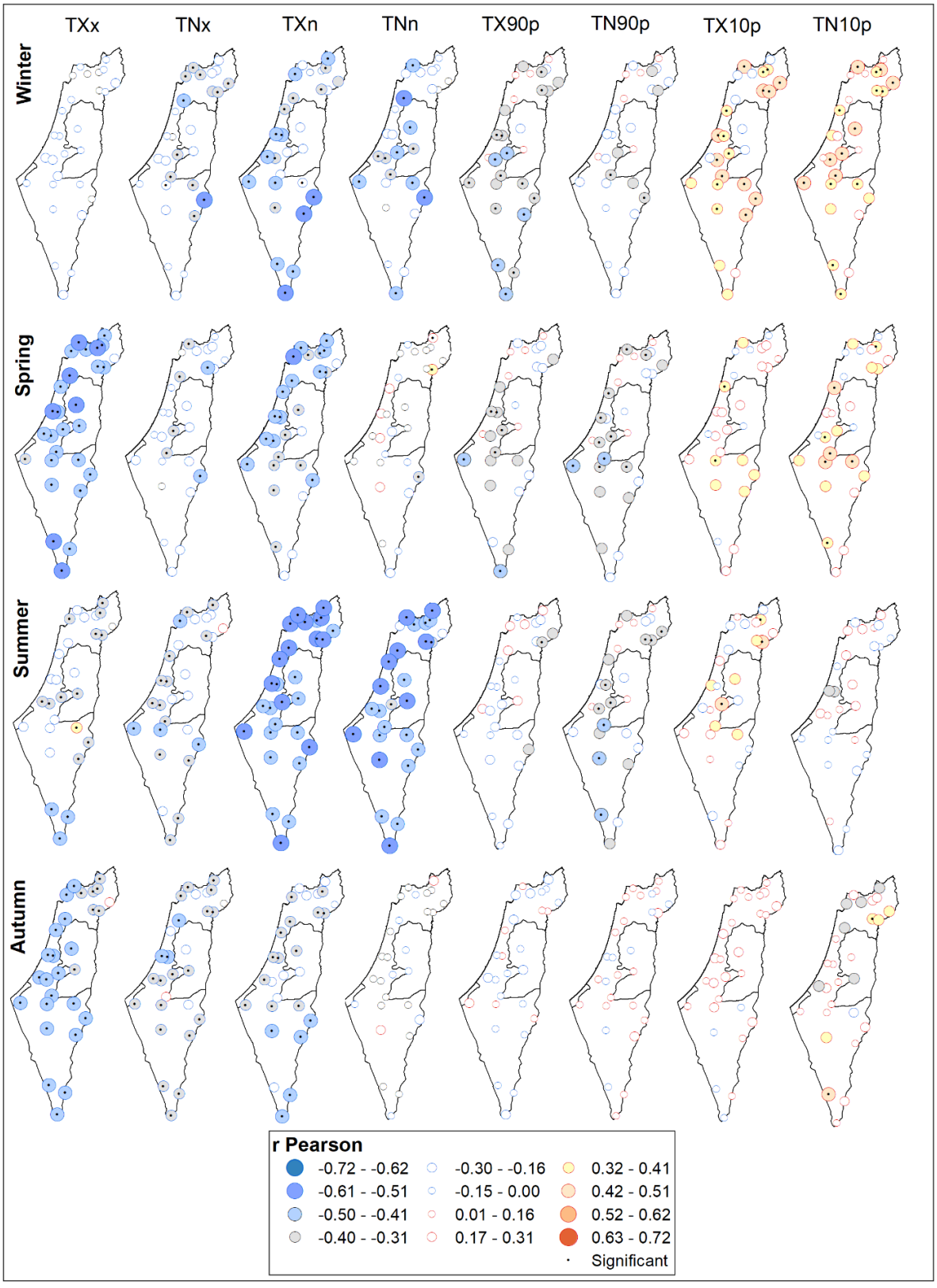

Figure 4. Spatial distribution of Pearson correlation coefficients between A) the NAO and SU25/30 in winter, and B) the ENSO and TX10p and TN10p in spring and summer.

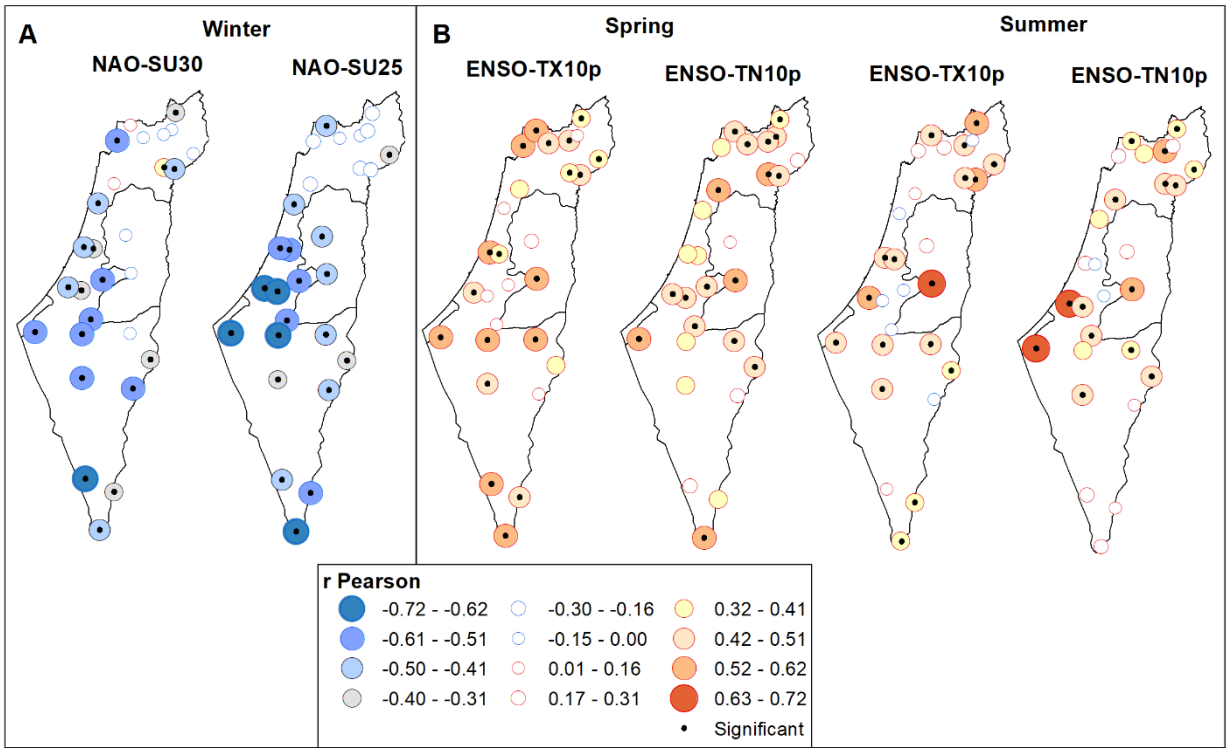

APPENDIX C
TESTS

1. Lowess smooth algorithm

Cleveland (1979) proposed the algorithm LOWESS, locally weighted scatter plot smoothing, as an outlier resistant method based on local polynomial fits. The basic idea is to start with a local polynomial (a k-NN type fitting) least squares fit and then to use robust methods to obtain the final fit. Specifically, one can first fit a polynomial regression in a neighborhood of x, that is, find $\beta \in R^{p+1}$ which minimize

$$n^{-1} \sum_{i=1}^{n} W_{ki}(x) \left(y_i - \sum_{j=0}^{p} B_i X^i\right) \quad \text{C1}$$

Where $W_{ki}(x)$ denote k-NN weights. Compute the residuals $\varepsilon_i\hat{}$ and the scale parameter and the scale parameter $\sigma\hat{}$ = median(ε_i). Define robustness weights $\delta_i = K(\varepsilon_i/6\hat{}\sigma)$, where $K(u) = (15/16)(1-u)^2$, if $|u| \leq 1$ and $K(u) = 0$, if otherwise. Then, fit a polynomial regression as in (C1) but with weights ($\delta_i W_{ki}\ (x)$). Cleveland suggests that $p = 1$ provides good balance between computational ease and the need for flexibility to reproduce patterns in the data. The smoothing parameter can be determined by cross-validation.

2. Precipitation concentration index

The Precipitation Concentration Index (PCI) proposed by Oliver (1980) and further developed by De Luis et al. (1997) was used for the calculation of the annual PCI as indicated in equation (C3),

$$PCI = \frac{\sum_{i=1}^{12} P^2}{(\sum_{i=1}^{12} P)^2} * 100 \quad \text{C3}$$

where P represents the monthly precipitation in month i that is calculated for each studied station and for each year throughout the observation period. For the study area, the previous equation was modified as indicated in equation 2 to be suitable for Climate of Levant which generally has recording rainfall data of nine months from September to May,

$$PCI = \frac{\sum_{i=1}^{9} P^2}{(\sum_{i=1}^{9} P)^2} * 75 \quad \text{C4}$$

According to Oliver (1980) and Zamani et al. (2018), PCI values below 10 denote a uniform monthly rainfall distribution throughout the year (low precipitation concentration); values ranging

from 11 to 15 indicate a moderate concentration of precipitation; values between 16 and 20 represent an irregular distribution; and values above 20 represent a strong irregularity (high precipitation concentration) in precipitation distribution. On theoretical bases, the lowest PCI value is 8.3, indicating the perfect uniformity in precipitation distribution (i.e., the same amount of rainfall occurs in each month. A PCI value of 16.7 indicates the total annual or seasonal rainfall is concentrated in ½ of the period and a PCI value of 25 means the total rainfall occurs in 1/3 of the period (i,e., total annual and seasonal rainfall occurred in 4 months and 1 month, respectively).

REFERENCES

Abbas, S., Kousar, S. (2021). Spatial analysis of drought severity and magnitude using the standardized precipitation index and streamflow drought index over the Upper Indus Basin, Pakistan. *Environ Dev Sustain*.

Abeysingha, N.S., M. Singh, V.K. Sehgal, M. Khanna, H. Pathak (2016). Analysis of trends in streamflow and its linkages with rainfall and anthropogenic factors in Gomti River basin of North India. *Theor. Appl. Climatol*., 123 (2016), pp. 785-799.

Abu Hajar, H.A., Murad, Y.Z., Shatanawi, K.M. (2019). Drought assessment and monitoring in Jordan using the standardized precipitation index. *Arab J. Geosci.* 12, 417.

Abualnaja, Y., Papadopoulos, V.P., Josey, S.A., Hoteit, I., Kontoyiannis, H. and Raitsos, D.E. (2015). Impacts of climate modes on air–sea heat exchange in the Red Sea, *Journal of Climate*, 28, 2665–2681.

Adarsh, S. and Janga Reddy, M. (2015). Trend analysis of rainfall in four meteorological subdivisions of southern India using nonparametric methods and discrete wavelet transforms, *Int. J. Climatol.*, 35: 1107-1124.

Adrian E. Gill. (1982). Atmosphere-Ocean Dynamics, Academic Press. ISBN 0-12-283520-4.

Agnew, C.T., A. (1999). Chappel. Drought in the Sahel. Geojournal, 48 (4), pp. 299-311.

Aguilar E, Auer I, Brunet M, Peterson TC, Wieringa J. (2003). Guidelines on Climate Metadata and Homogenization, *World Meteorological Organization*, WMO–TD No. 1186, WCDMP No. 53, Switzerland, Geneva.

Ahmad, I., Mahmood, I., Malik, I.R., Arshad, I.A., ul Haq, E. and Iqbal, Z. (2013). Probability analysis of monthly rainfall on seasonal monsoon in Pakistan. *Int. J. Climatol*., 34: 827-834.

Aieb, Amir, Khodir Madani, Marco Scarpa, Brunella Bonaccorso, Khalef Lefsih (2019). A new approach for processing climate missing databases applied to daily rainfall data in Soummam watershed, Algeria, *Heliyon*, V.5, Issue 2.

Al Qatarneh, G.N., Al Smadi, B., Al-Zboon, K. (2018). Impact of climate change on water resources in Jordan: a case study of Azraq basin, *Appl. Water Sci.*, 8, 50.

Aladaileh H, Al Qinna M, Karoly B, Al-Karablieh E, Rakonczai J. (2019). An investigation into the spatial and temporal variability of the meteorological drought in Jordan. *Climate* 7:82.

Alexander L, Zhang X, Peterson T, Caesar J, Gleason B, Klein Tank A, Haylock M, Collins D, Trewin B, Rahimzadeh F. (2006). Global observed changes in daily climate extremes of temperature and precipitation, *J. Geophys*. Res., Atmos. 111: D05109.

Alexander, L. and Herold, N. (2015). ClimPACTv2 Indices and Software. A Document Prepared on Behalf of the Commission for Climatology (CCl) Expert Team on Sector-Specific Climate Indices (ET-SCI). Sydney.

Alexandersson H. (1986). A homogeneity test applied to precipitation data, *International Journal of Climatology,* 6: 661–675.

Almazroui M, Islam MN, Dambul R, Jones PD. (2014). Trends of temperature extremes in Saudi Arabia, *International Journal of Climatology,* 34: 808–826.

Almazroui, M, Hasanean, HM. (2020). Saudi Arabia's summer surface air temperature and its association with circulation patterns, *International Journal of Climatology*, 1– 17.

Almazroui, M. (2019). Assessment of meteorological droughts over Saudi Arabia using surface rainfall observations during the period 1978–2017. *Arab J Geosci* 12, 694.

Almazroui, M., Nazrul Islam, M. Rahman, M. A. (2012). Recent climate change in the Arabian Peninsula: annual rainfall and temperature analysis of Saudi Arabia for 1978–2009, Int. J. Climatol., 32: 953-966.

Alpert P, Neeman BU, Shay-El Y. (1990). Climatological analysis of Mediterranean cyclones using ECMWF data. Tellus 42A: 65–77.

Alpert P, Reisin T. (1986). An early winter polar air mass penetration to the Eastern Mediterranean. Mon. Weather. Rev. 114:1411–1418.

Alpert, P., Abramsky, R., Neeman, B. U., (1990). The prevailing summer synoptic system in Israel. Subtropical high not Persian trough. Israel J. Earth Sci., 39, 93-102.

Alpert, P., Ben-Gai, T., Baharad, A., Benjamini, Y., Yekutieli, D., Colacino, M., Diodato, L., Ramis, C., Homar, V., Romero, R. and Michaelides, S. (2002). The paradoxical increase of Mediterranean extreme daily rainfall in spite of decrease in total values, *Geophysical Research Letters*, 29(11). 31–31.

Alpert, P., I. Osetinsky, B. Ziv, and H. Shafir (2004). Semi-objective classification for daily synoptic systems: Application to the eastern Mediterranean climate change, *International Journal of Climatology*, 24, 1001–1011.

Al-Qinna MI, Hammouri NA, Obeidat MM, Ahmad FY. (2011). Drought analysis in Jordan under current and future climates, *Climatic Change,* 106: 421–440.

Al-Salihi AM, Al-Lami AM, Altimimi YK. (2014). Spatiotemporal analysis of annual and seasonal rainfall trends for Iraq, *Al-Mustansiriyah J. Sci.*, 25(1):153–168.

AlSarmi S, Washington R. (2011). Recent observed climate change over the Arabian Peninsula, *Journal of Geophysical Research*, 116: D11109.

AlSarmi SH, Washington R. (2014). Changes in climate extremes in the Arabian Peninsula: analysis of daily data, *International Journal of Climatology*, 34: 1329–1345.

Ana Cristina M. Costa and Amílcar Soares. (2006). Identification of inhomogeneities in precipitation time series using SUR models and the Ellipse test. 7th International Symposium on Spatial Accuracy Assessment in Natural Resources and Environmental Sciences. Edited by M. Caetano and M. Painho.

Angstroem, A. (1935). Teleconnections of climate changes in present time, *Geogr. Ann.*, 17, 242-32258.

Arab Forum for Environment and Development (AFED) (2009). in Tolbaand, M.K. and Saab, N.W. (Eds), *Arab Environment: Climate Change*, Arab Forum for Environment and Development, Lebanon.

Araghi, A., Mousavi-Baygi, M., Adamowski, J. and Martinez, C. (2017). Association between three prominent climatic teleconnections and precipitation in Iran using wavelet coherence, *Int. J. Climatol.*, 37: 2809-2830.

Armon, M., E. Dente, J. A. Smith, Y. Enzel, and E. Morin (2018). Synoptic-Scale Control over Modern Rainfall and Flood Patterns in the Levant Drylands with Implications for Past Climates, *J. Hydrometeor.*, 19, 1077–1096.

Asakereh, H. (2020). Decadal variation in precipitation regime in northwest of Iran, *Theor. Appl. Climatol.*, 139, 461–471.

Asakereh, H., Khosravi, Y., Doostkamian, M. (2020). Assessment of Spatial Distribution and Temporal Trends of Temperature in Iran, *Asia-Pacific J. Atmos. Sci.*, 56, 549–561.

Asfaw, Amogne, Belay Simane, Ali Hassen, Amare Bantider (2018). Variability and time series trend analysis of rainfall and temperature in northcentral Ethiopia: A case study in Woleka sub-basin. Weather and Climate Extremes. V. 19, Pages 29-41.

Ashbel D. (1938). Great floods in Sinai Peninsula, Palestine, Syria and the Syrian Desert, and the influence of the Red Sea on their formation, *Quarterly Journal of the Royal Meteorological Society*, 64: 635–639.

Assaf, Chem, Adam Abramson, Nir Becher (2014). A tale of two rivers: pathways for improving water management in the Jordan and colorado river basin, Journal of Arid Environment 112:1-15.

Athar H. (2014). Trends in observed extreme climate indices in Saudi Arabia during 1979–2008. *International Journal of Climatology*, 34: 1561–1574.

Attada, R, Dasari, HP, Chowdary, JS, Yadav, RK, Knio, O, Hoteit, I. (2019). Surface air temperature variability over the Arabian Peninsula and its links to circulation patterns. *Int. J. Climatol.*, 39: 445– 464.

Ballesteros, E. (2006). Mediterranean coralligenous assemblages: a synthesis of the present knowledge, *Oceanogr. Mar. Biol. Annu. Rev*. 44:123−195.

Baltacı H, Akkoyunlu BO, Tayanç M. (2018). Relationships between teleconnection patterns and Turkish climatic extremes. *Theoretical and Applied Climatology,* 134: 1365-1386.

Baly, Denis. College, Kenyon, Ohio, Gambier (1984). The geography of Palestine and the Levant in relation to its history. *Cambridge University Press*. pp 1-24.

Barlow, M., Cullen, H., & Lyon, B. (2002). Drought in central and southwest Asia: La Niña, the warm pool, and Indian Ocean precipitation. *Journal of Climate*, 15, 697–700.

Barlow, M., Zaitchik, B., Paz, S., Black, E., Evans, J., & Hoell, A. (2016). A review of drought in the Middle East and Southwest Asia. *Journal of Climate*, 29, 8547–8574.

Barnston, A.G.; Livezey, R.E. (1987). Classification, seasonality and persistence of low frequency atmospheric circulation patterns. *Mon. Weather Rev.,* 115, 1083–1126.

Barrera-Escoda, A., Gonçalves, M., Guerreiro, D. (2014). Projections of temperature and precipitation extremes in the North Western Mediterranean Basin by dynamical downscaling of climate scenarios at high resolution (1971–2050). *Climatic Change*, 122, 567–582.

Bartzokas A, Metaxas DA. (1993). Covariability and climatic changes of the lower-troposphere temperatures over the northern hemisphere. Nuovo Cimento. 16C:359–373.

Bastos, A., Janssens, I. A., Gouveia, C. M., Trigo, R. M., Ciais, P., Chevallier, F., Peñuelas, J., Rödenbeck, C., Piao, S., Friedlingstein, P., and Running, S. W. (2016). European land CO2 sink influenced by NAO and East-Atlantic Pattern coupling. *Nat. Commun*., 7, 10315.

Ben-Gai T, Bitan A, Manes A, Alpert P, Kushnir Y. (2001). Temperature and surface pressure anomalies in Israel and the North Atlantic Oscillation. *Theoretical and Applied Climatology,* 69: 171–177.

Ben-Gai T, Bitan A, Manes A, Alpert P, Rubin S. (1998). Spatial and temporal changes in annual rainfall frequency distribution patterns in Israel. *Theor. Appl. Climatol.,* 61:177–190.

Ben-Gai T, Bitan A, Manes A, Alpert P. (1994). Long-term changes in annual rainfall patterns in southern Israel. *Theor. Appl. Climatol.,* 49:59–67.

Beranová, R., Kyselý, J. (2016). Links between circulation indices and precipitation in the Mediterranean in an ensemble of regional climate models. *Theor Appl Climatol*, 123, 693–701.

Bickici Arikan, B., Kahya, E. (2019). Homogeneity revisited: analysis of updated precipitation series in Turkey. *Theor Appl Climatol,* 135, 211–220.

Bilal, DA, Al-Jumaily KJ, Habbib EA. (2013). Air temperature trends in Baghdad, Iraq for the period 1941–2000. *Int. J. Sci. Res. Publ.,* 3(9).

Bisai, D., Chatterjee, S., Khan, A., and Barman, N. K. (2014). Application of sequential Mann-Kendall test for detection of approximate significant change point in surface air temperature for Kolkata weather observatory, West Bengal, *India International Journal of Current Research*, 6, 5319–5324.

Bitan A, Saaroni H. (1992). The horizontal vertical extension of the Persian Gulf trough. *Int. J. Climatol*. 12:733–747.

Black E. (2009). The impact of climate change on daily precipitation statistics in Jordan and Israel. *Atmospheric Science Letters,* 10: 192–200.

Black, E. (2011). The influence of the North Atlantic Oscillation and European circulation regimes on the daily to interannual variability of winter precipitation in Israel, *Int. J. Climatol.* 32, 1654–1664.

Bortz, J. (1993). Statistik fuÈr Sozialwissenschaftler. Berlin: Springer, 753 pp.

Braganza K, Karoly DJ, Arblaster JM. (2004). Diurnal temperature range as an index of global climate change during the twentieth century. *Geophys. Res. Lett.,* 31: 13, L13217.

Bretherton, C. S., C. Smith, and J. M. Wallace. (1992). An intercomparison of methods for finding coupled patterns on climate data. *J. Climate*, 5, 541–560.

Brito, S.S.B., Cunha, A.P.M.A., Cunningham, C.C., Alvalá, R.C., Marengo, J.A. and Carvalho, M.A. (2018). Frequency, duration and severity of drought in the Semiarid Northeast Brazil region. *Int. J. Climatol*, 38: 517-529.

Brunet, M., SaladiÉ, O., Jones, P., SigrÓ, J., Aguilar, E., Moberg, A., Lister, D., Walther, A., Lopez, D. and Almarza, C. (2006). The development of a new dataset of Spanish Daily Adjusted Temperature Series (SDATS) (1850–(2003). *Int. J. Climatol.*, 26: 1777-1802.

Brunetti M, Buffoni L, Maugeri M, Nanni T. (2000). Precipitation intensity trends in northern Italy. *Int. J. Climatol.,* 20(9):1017–1031.

Brunetti M, Buffoni L, Maugeri M, Nanni T. (2000). Trends in minimum and maximum daily temperatures in Italy from 1865 to 1996. *Theor. Appl. Climatol.,* 66: 49–60.

Brunetti M, Kutiel, H. (2011). The relevance of the North-Sea Caspian Pattern (NCP) in explaining temperature variability in Europe and the Mediterranean. *Natural Hazards and Earth System ehSciences,* 11: 2881–2888.

Brunetti M, Maugeri M, Monti F, Nanni T. (2006). Temperature and precipitation variability in Italy in the last two centuries from homogenised instrumental time series. *Int. J. Climatol.,* 26:345–381.

Brunetti M, Maugeri M, Nanni T. (2002). Atmospheric circulation and precipitation in Italy for the last 50 years. *International Journal of Climatology,* 22: 1455–1471.

Buishand TA. (1982). Some methods for testing the homogeneity of rainfall records. *Journal of Hydrology,* 58: 11–27.

Byun HR, Wilhite DA. (1999). Objective quantification of drought severity and duration. Journal of Climate 12, 2747-2756.

Cafiero, Carlo (2009). Study on Supply and Demand Prospects for the Major Syrian Agricultural Products. *Min-istry of Agriculture and Agrarian Reform* (NAPC). 8-9.

Cai, W. (2014). Increasing frequency of extreme El Niño events due to greenhouse warming, *Nat. Clim. Change*, 5(2). 1–6.

Caloiero T, Veltri S, Caloiero P, Frustaci F. (2018). Drought analysis in Europe and in the mediterranean basin using the standardized precipitation index. *Water* 10:1043.

Casanueva A, Rodríguez-Puebla C, Frías MD, González-Reviriego N. (2014). Variability of extreme precipitation over Europe and its relationships with teleconnection patterns. *Hydrol. Earth Syst. Sci.*, 18:709–725.

Cayan, D. R. (1992). Latent and sensible heat flux anomalies over the Northern Oceans: Driving the sea surface temperature. *J. Phys. Oceanogr*. 22, 859–881.

Chang, P., S.E. Zebiak. (2015). Tropical Meteorology & Climate, El niño and the southern oscillation. Encyclopedia of Atmospheric Sciences, (Second Edition).

Chen, S., Wu, R. (2020). Interdecadal changes in the relationship between interannual variations of spring North Atlantic SST and Eurasian surface air temperature. *J. Clim*. 30, 3771–3787.

Cherenkova, E.A., Semenov, V.A. (2017). A link between winter precipitation in Europe and the Arctic Sea ice, sea surface temperature, and atmospheric circulation. Russ. Meteorol. Hydrol. 42, 238–247.

chmidli J, Frei C. (2005). Trends of heavy precipitation and wet and dry spells in Switzerland during the 20th century. *International Journal of Climatology,* 25: 753–771.

Chow V.T., Maidment D.R. and L.W. Mays (1988). Applied Hydrology, Mc Graw. Hill Book Company, ISBN 0-07-010810-2.

Christensen, J.H., Hewitson, B., Busuioc, A. (2007). Regional climate projections. In: S. Solomon. Climate change, the physical science basis. Contribution of Working Group I to the Fourth Assessment Report of the Intergovernmental Panel on Climate Change. *Cambridge: Cambridge University Press*.

Ciarlo`, J. M., & Aquilina, N. J. (2015). An analysis of teleconnections in the Mediterranean region using RegCM4. *International Journal of Climatology*, 36(2), 797–808.

Cleveland WS. (1979). Robust locally weighted regression and smoothing scatterplots. *Journal of the American Statistical Association,* 74: 829–836.

Cleveland WS. (1981). LOWESS: A program for smoothing scatterplots by robust locally weighted regression. *The American Statistician,* 35: 54.

Conrad V, Pollak C. (1950). Methods in Climatology. 2nd ed. *Harvard University Press*. Cambridge, MA, 459 pp.

Conte M, Giuffrida A, Tedesco S. (1989). The Mediterranean Oscillation, impact on precipitation and hydrology in Italy. Proceedings of Conference on Climate, Water. *Publications of the Academy of Finland*, Helsinki, p. 121–137.

Cook BI, Anchukaitis KJ, Touchan R, Meko DM, Cook ER. (2016). Spatiotemporal drought variability in the Mediterranean over the last 900 years. *J. Geophys. Res. Atmos.* p 121:2060–2074.

Correia, F.N., Santos, M.A. and Rodrigues, R.R. (1991). Reliability in Regional Drought Studies. In: Ganoulis, J. (Ed.) *Water Resources Engineering Risk Assessment*. NATO ASI Series, Vol. 29, pp. 43–62.

Costa AC, Soares A. (2009). Homogenization of climate data: review and new perspectives using geostatistics. *Math. Geosci.,* 41:291–305.

Costa, A.C. and Soares, A. (2009). Trends in extreme precipitation indices derived from a daily rainfall database for the South of Portugal. *Int. J. Climatol.*, 29: 1956-1975.

Criado-Aldeanueva F, Soto-Navarro FJ. (2013). The Mediterranean Oscillation Teleconnection Index: Station-Based versus Principal Component Paradigms. *Advances in Meteorology*, ID738501.

Criado-Aldeanueva F, Soto-Navarro J. (2020). Climatic Indices over the Mediterranean Sea: A Review. *Applied Sciences*. 0(17):5790.

Criado-Aldeanueva, F., Soto-Navarro, F. J., García-Lafuente, J. (2014). Large-Scale Atmospheric Forcing Influencing the Long-Term Variability of Mediterranean Heat and Freshwater Budgets: Climatic Indices. *Journal of Hydrometeorology*, 15(2), 650–663.

Croitoru, Adina-Eliza, Brîndușa-Cristina Chiotoroiu, Veneta Ivanova Todorova, Vasile Torică (2013). Changes in precipitation extremes on the Black Sea Western Coast, *Global and Planetary Change*, Volume 102, Pages 10-19.

Cruz RV, Harasawa H, Lal M, Wu S. (2007). Asia. In: Parry ML, CanzianiOF, Palutikof JP, van der Linden PJ, Hanson CE (eds) Climatechange 2007: impacts, adaptation and vulnerability. Contributionof Working Group II to the Fourth Assessment Report of theIntergovernmental Panel on Climate Change. CambridgeUniversity Press, *Cambridge*, p 420,

Cullen HM, Kaplan A, Arkin PA, Demenocal PB. (2002). Impact of the North Atlantic Oscillation on Middle Eastern climate and stream flow. *Clim Chang*, 55:315–338.

Cullen, H.M., Kaplan, A., Arkin, P.A. (2002). Impact of the North Atlantic Oscillation on Middle Eastern Climate and Streamflow. Climatic Change. 55, 315–338.

Czaja, A., and C. Frankignoul (2002). Observed impact of Atlantic SST anomalies on the North Atlantic Oscillation. *J. Clim.*, 15, 606–623.

D.A. Wilhite, M.H. Glantz.(1985). Understanding the drought phenomenon: the role of definitions. Wood (Eds.), Planning for Drought, *Vest view Press*, Boulder, CO, pp. 11-27.

Da Costa, E., A. Colin de Verdiere, (2002). The 7.7-year North Atlantic Oscillation. *Quart. J. Roy. Meteor. Soc.*, 128, 797–818.

Dabanli İ, Mishra AK, Şen Z. (2017). Long-term spatio-temporal drought variability in Turkey. *J Hydrol* 552:779–792.

Dai A, Trenberth KE, Qian T. (2004). A global dataset of Palmer Drought Severity Index for 1870–2002: relationship with soil moisture and effects of surface warming. *J. Hydrometeorol.* 5(6): 1117–1130.

Dai A. (2011). Drought under global warming: a review. *Wiley Interdiscip. Rev. Clim. Chang.*, 2:45–65.

Deser, clara, Michael A. Alexander, Shang-Ping Xie, Adam S. Phillips (2010). Sea Surface Temperature Variability: Patterns and Mechanisms. *Annual Review of Marine Science*, 2:1, 115-143.

De Lima, M. I. P., S. C. P. Carvalho, J. L. M. P. de Lima. (2010). Investigating annual and monthly trends in precipitation structure: an overview across Portugal, Nat. Hazards Earth Syst. Sci. 10, 2429–2440.

De Lima, M., Espı ´rito Santo, F., Ramos, A., & De Lima, J. (2013). Recent changes in daily precipitation and surface air temperature extremes in mainland portugal, in the period 1941–2007. *Atmospheric Research*, 27, 195–209.

De Luis, M., González-Hidalgo, J.C., Raventós, J., Sánchez, J.R. and Cortina, J. (1997). Distribución espacial de la concentración y agresividad de la lluvia en el territorio de la comunidad valenciana. *Cuaternario Y Geomorfologia*, 11, 33–44.

De Pauw, Wu. (2010). Climate change, drought and potential for water harvesting in Palestine. WFP-ICARDA2010.

del Rı´o, S., R. Fraile, L. Herrero, and A. Penas. (2007). Analysis of recent trends in mean maximum and minimum temperatures in a region of the NW of Spain (Castilla y Leon). *Theor. Appl. Climatol.*, 90, 1–12.

del Río S, Cano-Ortiz A, Herrero L, Penas A. (2012). Recent trends in mean maximum and minimum air temperatures over Spain (1961–2006). *Theor. Appl. Climatol.*, 109:605–626.

Deng, Y., Jiang, W., He, B., Chen, Z., & Jia, K. (2018). Change in intensity and frequency of extreme precipitation and its possible teleconnection with large-scale climate index over the China from 1960 to 2015. *Journal of Geophysical Research: Atmospheres*, 123, 2068– 2081.

Deser C, Alexander MA, Xie S-P, Phillips AS. (2010). Sea surface temperature variability: patterns and mechanisms. *Annu. Rev. Mar. Sci*., 2: 115–143.

Deshpande NR, Nandargi SS, Dhar ON. (2011). Some characteristic features of hourly rainfall over the Upper Krishna basin in Maharashtra. *Indian Journal of Power and River Valley Development*, 53: 47– 53.

Dhorde, Amit G., Mohammad Zarenistanak (2013). Three-way approach to test data homogeneity: An analysis of temperature and precipitation series over southwestern Islamic Republic of Iran. *J. Ind. Geophys*. Union. Vol.17, No.3, pp. 233-242.

Diao, Y., S. Xie, D. Luo (2015). Asymmetry of winter European surface air temperature extremes and the North Atlantic Oscillation. *J. Climate*, 28, 517–530.

Dickson, R.R., Osborn, T.J., Hurrell, J.W., Meincke, J., Blindheim, J., Adlandsvik, B., Vinje, T.,Alexseev, G., and Maslowski, W. (2000). The Arctic Ocean response to the North Atlantic Oscillation. *J. Climate*, 13, 2671–2696.

Dikbas F, Firat M, Koc A, Güngör M. 2010. Homogeneity test for Turkish temperature series. Balwois 2010. 25–29 May.

Diodato N. (2007). Climatic fluctuations in Southern Italy since 17th century: reconstruction with precipitation records at Benevento. Climatic Change 80: 411–431.

Domonkos P. (2013). Measuring performances of homogenization methods. *Q. J. Hung. Meteorol. Serv.*, 117(1):91–112.

Domroes, M. and El-Tantawi, A. (2005). Recent temporal and spatial temperature changes in Egypt, Int. J. Climatol., 25: 51-63.

Donat MG, Peterson TC, Brunet M, King AD, Almazroui M, Kolli RK, Boucherf D, Al-Mulla AY, Nour AY, Aly AA, Nada TAA, Semawi MM, Al Dashti HA, Salhab TG, El Fadli KI, Muftah MK, Dah Eida S, Badi W, Driouech F, El Rhaz K, Abubaker MJY, Ghulam AS, Erayah AS, Mansour MB, Alabdouli WO, Al Dhanhani JS, Al Shekaili MN. (2014). Changes in extreme temperature and precipitation in the Arab region: long-term trends and variability related to ENSO and NAO. *International Journal of Climatology*, 34: 581–592.

Donat, M.G., L.V. Alexander, N. Herold, A.J. Dittus. (2016). Temperature and precipitation extremes in century-long gridded observations, reanalyses, and atmospheric model simulations. J. *Geophys. Res. Atmos*., 121, pp. 11174-11189.

Dos Santos, C.A.C., Neale, C.M.U., Rao, T.V.R. and da Silva, B.B. (2011). Trends in indices for extremes in daily temperature and precipitation over Utah, USA. *Int. J. Climatol.*, 31: 1813-1822.

Douguedroit, A. (1998). Que peut-on dire d'une oscillation Mediterraneenne? Climate and Environmental Change, Proceedings of the Meeting of the Commission on Climatology of the IGU Evora, Portugal, 135-136.

Droogers, P. W. W. Immerzeel. W. Terink. J. Hoogeveen. M. F. P. Bierkens. L. P. H. van Beek and B. Debele. (2012). *Hydrol. Earth Syst. Sci.*, 16, 1–14, Water resources trends in Middle East and North Africa towards 2050.

Dünkeloh, A. and Jacobeit, J. (2003). Circulation dynamics of Mediterranean precipitation variability 1948–98. *International Journal of Climatology*, 23(15): 1843–1866.

Easterling DR, Evans JL, Ya Groisman P, Karl TR, Kunkel KE, Ambenje P. (2000). Observed variability and trends in extreme climate events: a brief review. *Bull. Am. Meteorol. Soc.,* 81(3):417–425.

Efthymiadis, D., Goodess, C.M. and Jones, P.D. (2011). Trends in Mediterranean gridded temperature extremes and large-scale circulation influences. *Natural Hazards and Earth System Sciences,* 11, 2199–2214.

Ehsan, M.A., Nicolì, D., Kucharski, F. (2020). Atlantic Ocean influence on Middle East summer surface air temperature. npj *Clim. Atmos. Sci.* 3, 5.

Eischeid J, Baker CB, Karl T, Diaz HF. (1995). The quality control of long-term climatological data using objective data analysis. *J. Appl. Meteorol.,* 34(12):2787–2795.

El Kenawy A, López-Moreno JI, Stepanek P, Vicente-Serrano SM. (2013). An assessment of the role of homogenization protocol in the performance of daily temperature series and trends: application to northeastern Spain. *International Journal of Climatology,* 33: 87–108.

El Kenawy, A.M., McCabe, M.F., Vicente-Serrano, S.M., Robaa, S.M. and Lopez-Moreno, J.I. (2016). Recent changes in continentality and aridity conditions over the Middle East and North Africa region, and their association with circulation patterns. *Climate Research,* 69, 25– 43.

El Kenawy, Ahmed, M. Vicente-Serrano. (2009). Temperature trends in Libya over the second half of the 20th century, *Theoretical and Applied Climatology*.

El-Fandy MG. (1948). The effect of Sudan monsoon low on the development of thundery conditions in Egypt, Palestine and Syria. *Quarterly Journal of the Royal Meteorological Society*, 74: 31–38.

Enfield, D. B., E. T. Alfaro (1999). The dependence of Caribbean rainfall on the interaction of the tropical Atlantic and Pacific Oceans. *J. Climate,* 12, 2093–2103.

Enfield, D. B., Mayer, D. A. (1997). Tropical Atlantic sea surface temperature variability and its relation to El Niño-Southern Oscillation. *J. Geophys. Res*. 102, 929–945.

Enzel, Yehouda, Rivka Amit, Uri Dayan, Onn Crouvi, Ron Kahana, Baruch Ziv, David Sharon (2008). The climatic and physiographic controls of the eastern Mediterranean over the late Pleistocene climates in the southern Levant and its neighboring deserts, *Global and Planetary Change*, Volume 60, Issues 3–4, Pages 165-192, ISSN 0921-8181.

Erian, W.; Abbashar, A.; Abo-Swaireh, L. (2011). Drought Vulnerability in the Arab Region - Case Study Drought in Syria; Ten Years of Scarce Water (2000 – 2010). *ACSAD*, Damascus, 15-18.

Erlat E, Türkeş M. (2013). Observed changes and trends in numbers of summer and tropical days, and the 2010 hot summer in Turkey. *International Journal of Climatology,* 33: 1898–1908.

Eshel G, Farrell BF. (2000). Mechanisms of eastern Mediterranean rainfall variability. J. Atmos. Sci. 57:3219–3232.

Esterling DR, Evans LG, Groisman PY, Karl TR, Kunkel KE, Ambenje P. (2000). Observed variability and trends in extreme climate events: A brief review. *Bulletin of the American Meteorological Society,* 3: 417–425.

Evans JP. (2009). 21st century climate change in the Middle East. *Clim. Chang.,* 92:417–432.

Everitt, B.S., T. Hothorn (2011). An Introduction to Applied Multivariate Analysis with R. *Springer*, New York.

Fallah-Ghalhari, G., Shakeri, F. & Dadashi-Roudbari, A. (2019). Impacts of climate changes on the maximum and minimum temperature in Iran. *Theor. Appl. Climatol.,* 138, 1539–1562.

Farzana, F., Sinha, N.C., Rahman, M.M. (2019). Comparison of missing value estimation techniques in rainfall data of Bangladesh. *Theor. Appl. Climatol*. 136, 1115–1131.

Fathian, F., Ghadami, M., Haghighi, P. (2020). Assessment of changes in climate extremes of temperature and precipitation over Iran. *Theor. Appl. Climatol.,* 141, 1119–1133.

Fauchereau, N. S.Trzaska, M. Rouault, and Y. Richard (2003). Rainfall variability and changes in Southern Africa during the 20th century in the global warming context. *Natural Hazards*, 29, 139-154.

Feng R, Yu R, Zheng H, Gan M. (2018). Spatial and temporal variations in extreme temperature in Central Asia. *International Journal of Climatology*, 38 (Suppl.1): e388-e400.

Finkelstein, Israel and Dafna Langgut. (2014). Dry Climate in the Middle Bronze I and Its Impact on Settlement Patterns in the Levant and Beyond: New Pollen Evidence. *Journal of Near Eastern Studies*, Vol. 73, No. 2, pp. 219-234.

Fiorillo F, Guadagno FM. (2010). Karst spring discharges analysis in relation to drought periods, using the SPI. *Water Resour*. Manage. 24: 1867–1884.

Firat, Mahmut. Fatih Dikbas, A. Cem Koc¸ Mahmud Gungor. (2010). Missing data analysis and homogeneity test for Turkish precipitation series, Vol. 35, Part 6, pp. 707–720. © *Indian Academy of Sciences*.

Fogt, R. L., Bromwich, D. H., and Hines, K. M. (2011). Understanding the SAM influence on the South Pacific ENSO teleconnection, *Clim. Dynam*., 36, 1555–1576.

Folland CK, Miller C, Bader D, Crowe M, Jones P, Plumner N, Richman M, Parker DE, Rogers J, Scholefield P. (1999). Temperature Indices for Climate Extremes. Climatic Change, Workshop on Indices and indicators for Climate Extremes, *Asheville*, NC, USA, 3-6 June 1997, Breakout Group C. 42, 31–43.

Fonseca D, Carvalho MJ, Marta-Almeida M, Melo-Gonçalves P, Rocha A. (2016). Recent trends of extreme temperature indices for the Iberian Peninsula. *Physics and Chemistry of the Earth*, 94: 66–76.

Ford, T. and Labosier, C.F. (2014). Spatial patterns of drought persistence in the Southeastern United States. Int. J. Climatol., 34: 2229-2240.

Fortin, G. and Hétu, B. (2014). Estimating winter trends in climatic variables in the Chic-Chocs Mountains, Canada (1970–2009). *Int. J. Climatol.*, 34: 3078-3088.

Founda D, Papadopoulos KH, Petrakis M, Giannakopoulus C, Good P. (2004). Analysis of mean, maximum, and minimum temperature in Athens from 1897 to 2001 with emphasis on the last decade: trends, warm events, and cold events. *Global Planet Change,* 44: 27–38.

Fränti, Pasi, and Sami Sieranoja (2018). K-Means Properties on Six Clustering Benchmark Datasets. *Applied Intelligence,* 48: 4743–59.

Freiwan, M. and Kadioğlu, M. (2008). Climate variability in Jordan. *Int. J. Climatol.*, 28: 69-89.

Freiwan, M. and Kadioglu, M. (2008). Spatial and temporal analysis of climatological data in Jordan. *Int. J. Climatol.*, 28: 521-535.

Frumkin, A., & Stein, M. (2004). The Sahara-East Mediterranean dust and climate connection revealed by strontium and uranium isotopes in a Jerusalem speleothem. *Earth and Planetary Science Letters*, 217(3–4). 451–464.

Fujibe F. (2009). Detection of Urban Warming in Recent Temperature Trends in Japan. *International Journal of Climatology,* 29: 1811–1822.

Gado TA, El-Hagrsy RM, Rashwan IMH. (2019). Spatial and temporal rainfall changes in Egypt. *Environ Sci. Pollut Res.,* 26(27):28228–28242.

Gámiz-Fortis, S.R., Esteban-Parra, M.J., Pozo-Vázquez, D. and Castro-Díez, Y. (2011). Variability of the monthly European temperature and its association with the Atlantic sea-surface temperature from interannual to multidecadal scales. *International Journal of Climatology*, 31, 2115–2140.

Garnaut R. (2008). The Garnaut climate change review. *Cambridge University Press*, Melbourne, Victoria, Australia.

Gastineau, G., and C. Frankignoul (2015). Influence of the North Atlantic SST variability on the atmospheric circulation during the twentieth century. *J. Clim*., 28, 1396–1416.

Geerts, B. Empirical estimation of the monthly-mean daily temperature range. *Theor. Appl. Climatol*. 74, 145–165 (2003).

Gerstengarbe, F. W. Werner P. C. (1999). Estimation of the beginning and end of recurrent events within a climate regime, *Clim. Res*., 11, 97–107.

Ghanem, A. A. (2011). Climatology of the areal precipitation in Amman/Jordan. *Int. J. Climatol.*, 31: 1328-1333.

Ghasemi AR, Khalili D. (2008). The association between regional and global atmospheric patterns and winter precipitation in Iran. *Atmospheric Research,* 88: 116–133.

Ghasemi AR, Khalili D. (2008). The effect of the North Sea-Caspian pattern (NCP) on winter temperatures in Iran. *Theoretical and Applied Climatology,* 92: 59–74.

Ghasemi, A. R. (2015). Changes and trends in maximum, minimum and mean temperature series in Iran. Atmos, Sci. Lett., 16: 366-372.

Giannakopoulos C, Le Sager P, Bindi M, Moriondo M, Kostopoulou E, Goodess CM. (2009). Climatic changes and associated impacts in the Mediterranean resulting from a 2 °C global warming. *Glob. Planet Chang,* 68(3): 209–224

Giorgi, F. (2006). Climate change Hot-Spots. *Geophys. Res*. Lett., 33, L08707.

Gleick PH. (2014). Water, drought, climate change, and conflict in Syria. Weather, Climate, and Society 6:331–340.

Glickman T.S. (2000). Glossary of Meteorology. 2nd Edition, American Meteorological Society, Boston, 855 pp.

Gocic M, Trajkovic S. (2014). Spatio-temporal patterns of precipitation in Serbia. *Theor. Appl. Climatol.,* 117:419–431.

Göktürk, O.M., Bozkurt, D., Şen, Ö.L. and Karaca, M. (2008), Quality control and homogeneity of Turkish precipitation data. *Hydrol. Process*., 22: 3210-3218.

Goldreich Y, Moses H, Rosenfeld D. (2004). Radar analysis of cloud systems and their rainfall yield in Israel. *Israel Journal of Earth Sciences,* 53: 63–76.

Goldreich Y. (2003). The Climate of Israel. Observation, Research and Applications. *Kluer Academic/Plenum Publishers*: New York.

Golian, S., Mazdiyasni, O. AghaKouchak, (2015). A. Trends in meteorological and agricultural droughts in Iran. *Theor. Appl. Climatol.* 119, 679–688.

Gonzalez-Hidalgo, J. C., Peña-Angulo, D. (2016). Recent trend in temperature evolution in Spanish mainland (1951–2010): from warming to hiatus, Int. J. Climatol., 36: 2405-2416.

González-Rouco J F, Jiménez J L, Quesada V, Valero F. (2001). Quality control and homogeneity of precipitation data in the southwest of Europe; *J. Climate*, 14(5) 964–978.

Goodess CM, Jones PD. (2002). Links between circulation and changes in the characteristics of Iberian rainfall. *Int. J. Climatol.,* 22:1593–1615.

Greatbatch, R. (2000). The North Atlantic Oscillation. Stochastic Environmental Research and Risk Assessment 14, 213–242.

Groisman, P.Ya. R.W. Knight, T.R. Karl,D.R. Easterling, B.Sun, and J.M. Lawrimore (2004). Contemporary Changes Of The Hydrological Cycle Over The Contiguous United States: Trends Derived From In-Situ Observations. *J. Hydrometeorol*., 5, 64-85.

Groisman,P.Y.,Knight,R.W.,Easterling,D.R.,Karl,T.R.,Hegerl,G.C., and Razuvaev, V. N. (2005). Trends in intense precipitation in the climate record. *J. Clim*., 18(9). 1326–1350.

Gu, Chaojun, Xingmin Mu, Peng Gao, Guangju Zhao, Wenyi Sun & Pengfei Li (2017). Effects of climate change and human activities on runoff and sediment inputs of the largest freshwater lake in China, Poyang Lake, *Hydrological Sciences Journal*, 62:14, 2313-2330.

Gumus, V. and Algin, H.M. (2017). Meteorological and hydrological drought analysis of the Seyhan-Ceyhan River Basin, Turkey. *Meteorological Applications*, 24, 62–73.

Guttman NB. (1999). Accepting the standardized precipitation index: a calculation algorithm. *J. Am. Water Resour*. Assoc. 35(2): 311–322.

H.K. Kafle, H.J. Bruins. (2009). Climatic trends in Israel 1970–2002: warmer and increasing aridity inland. *Clim. Chang*. 96, pp. 63-77.

Hadi, S. J., Tombul, M. (2018). Long-term spatiotemporal trend analysis of precipitation and temperature over Turkey, Met. Apps.

Haensel S, Zurba K. (2015). Precipitation characteristics and trends in the Palestinian territories during the period 1951–2010. FOG-FREIBERG Online Geosci. 39:103–130.

Hamed, K.H., 2009. Enhancing the effectiveness of prewhitening in trend analysis of hydrologic data. *Journal of Hydrology*, 368, 143–155.

Hameed M, Ahmadalipour A, Moradkhani H. (2018). Apprehensive drought characteristics over Iraq: results of a multidecadal spatiotemporal assessment. *Geosciences* 8:58.

Hammad AA, Salameh AM. (2018). Temperature analysis as an indicator of climate change in the Central Palestinian Mountains. *Theoretical and Applied Climatology*.

Han, Z., F. Luo, and J. Wan (2016). The observational influence of the North Atlantic SST tripole on the early spring atmospheric circulation. *Geophys. Res. Lett.,* 43, 2998–3003.

Hansen, J., Ruedy, R., Sato, M., Imhoff, M., Lawrence, W., Easterling, D. R., Peterson, T. C., and Karl, T. R. (2001). A closer look at United States and global surface temperature change, *J. Geophys*. Res., 106, 23947–23963.

Hartigan J, Wong M. (1979). A K-means clustering algorithm. *Applied Statistics,* 28: 100–108.

Hasanean HM. (2001). Fluctuations of surface air temperature in the Eastern Mediterranean, *Theor. Appl. Climatol.,* 68:75–87.

Hasanean HM. (2004). Winter surface temperature in Egypt in relation to the associated atmospheric circulation. *Int. J. Climatol.,* 24:985–999.

Hasanean, H.M. and Abdel Basset, H. (2006). Variability of summer temperature over Egypt. *International Journal of Climatology*, 26, 1619–1634.

Hasanean, H.M. and Almazroui, M. (2016). Teleconnections of the tropical sea surface temperatures to the surface air temperature over Saudi Arabia in summer season. *International Journal of Climatology,* 37, 1040–1049.

Hatzaki M, Flocas HA, Asimakopoulos DN, Maheras P. (2007). The eastern Mediterranean teleconnection pattern: identification and definition. *International Journal of Climatology,* 27(6): 727 – 737.

Hatzaki M, Flocas HA, Oikonomou C, Giannakopoulos C. (2010). Future changes in the relationship of precipitation intensity in Eastern Mediterranean with large scale circulation. *Adv. Geosci., 23:31–36.*

Hawkins D. (1980). Identification of Outliers. Chapman and Hall, Kluwer Academic Publishers, Boston/Dordrecht/London.

Haylock, M., and N. Nicholls (2000). Trends in extreme rainfall indices for an updated high quality data set for Australia, 1910-1998. *Int. J. Climatol.*, 20, 1533-1541.

Herceg Bulic, I., Brankovi C., and Kucharski, F. (2011). Winter ENSO teleconnections in a warmer climate, *Clim. Dynam.*, 38, 1593–1613, 2011.

Hertig, E., Seubert, S., Paxina, A., Vogt, G., Paeth, H., & Jacobeit, J. (2013). Changes of total versus extreme precipitation and dry periods until the end of the twenty-first century: Statistical assessments for the Mediterranean area. *Theoretical and Applied Climatology*, 111, 1–20.

Hirsch RM, Slack JR, Smith RA. (1982). Techniques of trend analysis for monthly water quality data. *Water Resour. Res.* 18: 107–121.

Hirsch, R.M., Helsel, D.R., Cohn, T.A. and Gilroy, E.J. (1992). Statistical Analysis of Hydrologic Data. Handbook of Hydrology. New York, NY: McGraw-Hill.

HMSO 1962. Weather in the Mediterranean I: General Meteorology. 2nd edn. Her Majesty's Stationery Office: London, 362.

Hochman, A., Mercogliano, P., Alpert, P., Saaroni, H. and Bucchignani, E. (2018). High-resolution projection of climate change and extremity over Israel using COSMO-CLM. *International Journal of Climatology*, 38(14). 5095–5106.

Houghton JT, Ding Y, Griggs DJ, Noguer M, van der Linden PJ, Dai X, Maskell K, Johnson CA (eds). (2001). Climate Change: The Scientific Basis. *Cambridge University Press*: Cambridge, UK.

Huang, Y.F., Puah, Y.J., Chua, K.C. and Lee, T.S. (2015). Analysis of monthly and seasonal rainfall trends using the Holt's test. *Int. J. Climatol*., 35: 1500-1509.

Hunt, G. (2007), "Climatic outliers". International Journal of Climatololy, 27, 139-156.

Hurrell, J. W. (1995). Decadal trends in the North Atlantic Oscillation: Regional temperatures and precipitation. *Science*, 269(5224). 676-679.

Hurrell, J. W., Kushnir, Y., Ottersen, G., and Visbeck, M. (2003). An Overview of the North Atlantic Oscillation, in The North Atlantic Oscillation: Climatic Significance and Environmental Impact, edited by: Hurrell, J. W., Kushnir, Y., Ottersen, G., and Visbeck, M., American Geophysical Union, Washington, D.C., *Geophysical Monograph Series*, Vol. 134, American Geophysical Union, 1–35.

Hurrell, J.W & Kushnir, Yochanan & Ottersen, Geir & Visbeck, Martin. (2003). The North Atlantic Oscillation. 10.1029/134GM01.

Hurrell, J.W. (2000). The North Atlantic Oscillation: Climatic Significance and Environmental Effect. *American Geophysical Union*: Washington, DC, USA, EOS 84, No. 8.

Huschke, Ralph E. (Ed.). (1959). Glossary of Meteorology, *Am. Meteorol. Soc.*, Boston, Mass.

Inbar, M. and Bruins, H.J. (2004). Environmental impact of multi-annual drought in the Jordan Kinneret watershed, Israel. *Land Degrad. Dev*., 15: 243-256.

IPCC (2007b). Climate change: the physical science basis. In: Solomon S, Qin D, Manning M, Chen Z, Marquis M, Averyt KB, Tignor M, Miller HL (eds) Contribution of Working Group I to the Fourth Assessment Report of the Intergovernmental Panel on Climate Change. Cambridge University Press, Cambridge, UK, p 996.

IPCC (2013). Summary for policymakers. In: Climate change 2013: The physical science basis (Contribution of Working Group I to the fifth assessment report of the Intergovernmental Panel on Climate Change). Cambridge University Press, Cambridge.

IPCC. (2007). Fourth Assessment report: Working group II report Impacts, Adaptation and Vulnerability.

Iqbal, M.J., Hameed, S. Khan, F. (2013). Influence of Azores High pressure on Middle Eastern rainfall. Theor. Appl. Climatol. 111, 211–221.

Islam MN, Almazroui M., Dambul R, Jones PD, Alamoudi AO. (2015). Long-term changes in seasonal temperature extremes over Saudi Arabia during 1981–2010. *International Journal of Climatology* 35: 1579–1592.

Itzhak-Ben-Shalom H, Samuels R, Potchter O, Alpert P. (2016). Recent Trends and Future Predictions until 2060 of Urban Warming in Four Israeli Cities Employing the RegCMClimate Model. *American Journal of Climate Change* 05: 464–484.

Jain, Anil K. (2010). Data Clustering: 50 Years Beyond K-Means, *Pattern Recognition Letters* 31 (8): 651–66.

Jain, S., & Kumar, V. (2012). Trend analysis of rainfall and temperature data for India. *Current Science*, 102(1), 37-49.

Jasim, A.I., Awchi, T.A. (2020). Regional meteorological drought assessment in Iraq. *Arab J. Geosci.* 13, 284 (2020).

Jason, P., Smith, R.B., and Oglesby, R. J. (2004).Middle East Climate Simulation andDominant Precipitation Processes. *International Journal of Climatology*. 24, 1671–1694.

Jenkins, K., Warren, R. (2015). Quantifying the impact of climate change on drought regimes using the Standardised Precipitation Index. *Theor. Appl. Climatol*. 120, 41–54.

Jerez, S. and Trigo, R. M. (2013). Time-scale and extent at which largescale circulation modes determine the wind and solar potential in the Iberian Peninsula. *Environ. Res. Lett.*, 8, 044035.

Jiang FQ, Hu RJ, Wang SP, Zhang YW, Tong L. (2012). Trends of precipitation extremes during 1960–2008 in Xinjiang, the Northwest China. *Theor. Appl. Climatol.* 111: 133–148.

Jing, Y., Li, Y., and Xu, Y. (2020). Assessment of responses of North Atlantic winter sea surface temperature to the North Atlantic Oscillation on an interannual scale in 13 CMIP5 models, *Ocean Sci.*, 16, 1509–1527.

Jinming, F., Yonghe, L. & Zhongwei, Y. (2015). Analysis of surface air temperature warming rate of China in the last 50 years (1962–2011) using k-means clustering. *Theor. Appl. Climatol.* 120, 785–796.

Jordan's Third National Communication on Climate Change (2014). Submitted to The United Nations Framework Convention on Climate Change (UNFCCC).

Kadioğlu, M. (1997). Trends in surface air temperature data over Turkey. *Int. J. Climatol.*, 17: 511-520.

Kafle, H. and Bruins, H. (2009). Climatic trends in Israel 1970–2002: warmer and increasing aridity inland. *Climatic Change* 96(1-2): 63-77.

Kalnay E, Kanamitsu M, Kistler R, Collins W, Deaven D, Gandin L, Woollen J. (1996). The NCEP/NCAR 40-year reanalysis project. *Bull. Am. Meteorol. Soc*. 77(3): 437–471.

Kamal Ahmed, Shamsuddin Shahid, Tarmizi Ismail, Nadeem Nawaz and Xiao-Jun Wang (2018). Absolute homogeneity assessment of precipitation time series in an arid region of Pakistan, *Atmósfera*, 31(3). 301-316.

Kang HF, Yusof F. (2012) Homogenity test on daily rainfall series in Peninsular Malasiya. *Int J Contemp Math Sci* 7(1):9–22.

Karabulut M. (2015). Drought analysis in Antakya-Kahramanmaras Graben, Turkey. *J. Arid Land* 7: 741–754.

Karl TR, Trenberth KE (2003). Modern global climate change. *Science* 302:1719–1723.

Katiraie-Boroujerdy, P., Ashouri, H., Hsu, K. (2017). Trends of precipitation extreme indices over a subtropical semi-arid area using PERSIANN-CDR. *Theor. Appl. Climatol.* 130, 249–260.

Katsnelson, J. (1964). The variability of annual precipitation in Palestine. *Arch. Met. Geoph.* Biokl. B. 13, 163–172.

Kazmin, A. S., & Zatsepin, A. G. (2007). Long-term variability of surface temperature in the Black Sea, and its connection with the large-scale atmospheric forcing. Journal of Marine Systems, 68(1-2), 293–301.

Katz, R.W. and Brown, B.G. (1992). Extreme events in a changing climate: variability is more important than averages. *Climatic Change*, 21, 289–302.

Kelley CP, Mohtadi S, Cane MA, Seager R, Kushnir Y. (2015). Climate change in the Fertile Crescent and implications of the recent Syrian drought. *Proc Natl Acad Sci* 112:3241–3246.

Kelley, C., Ting, MF. Seager, R., and Kushnir, Y.: (2012). Mediterranean precipitation climatology, seasonal cycle, and trend as simulated by CMIP5, *Geophys. Res. Lett.*, 39, L21703.

Kendall MG, Stuart A. (1977). The advanced theory of statistic. Charles Griffin and Company: London, *High Wycombe*. 400-401.

Kendall, M.G. (1955). Rank Correlation Methods. London: *Charles Griffin*.

Keyantash, J. A., Dracup, J. A. (2004). An aggregate drought index: Assessing drought severity based on fluctuations in the hydrologic cycle and surface water storage. *Water Resources Research*, 40, 1–14.

Kim KJ, Ahn H. (2008). A recommender system using GA K-means clustering in an online shopping market. *Expert Syst. Appl*. 34:1200–1209.

Kim, C.J., Park, M.J. and Lee, J.H. (2014). Analysis of climate change impacts on the spatial and frequency patterns of drought using a potential drought hazard mapping approach. *Int. J. Climatol*. 34: 61-80.

Klein Tank A, Können G. (2003). Trends in indices of daily temperature and precipitation extremes in Europe, 1946–99. *J. Clim.* 16: 3665–3680.

Klein Tank AMG, Zwiers FW, Zhang X. (2009). Guidelines on analysis of extremes in a changing climate in support of informed decisions for adaptation. *Climate data and monitoring WCDMP*-No. 72, WMO-TD No. 1500, 56 pp.

Klein Tank, A.M.G., Können, G.P., (2003). Trends in indices of daily temperature and precipitation extremes in Europe, 1946–99. *J. Climate* 16, 3665–3680.

Klok EJ, Klein Tank AMG. (2009). Updated and extended European dataset of daily climate observations. *International Journal of Climatolology* 29: 1182–1191.

Kostopoulu E, Jones PD (2005). Assessment of climate extremes in the Eastern Mediterranean. *Clim. Res.* 89: 69–85.

Kousari MR, Ekhtesasi MR, Tazeh M, Naeini MAS, Zarch MAA. (2011). An investigation of the Iranian climatic changes by considering the precipitation, temperature, and relative humidity parameters. *Theor Appl Climatol* 103(3–4):321–335.

Krichak S.O., Breitgand JS, Gualdi S, Feldstein SB. (2013). Teleconnection-extreme precipitation relationships over the Mediterranean region. *Theor. Appl. Climatol.*

Krichak SO, Alpert P. (2005). Decadal trends in the east Atlantic–west Russia pattern and Mediterranean precipitation. *International Journal of Climatology* 25: 183–192.

Krichak SO, Kishcha P, Alpert P. (2002). Decadal trends of main Eurasian oscillations and the Mediterranean precipitation. *Theor. Appl. Climatol*. 72: 209–220.

Krichak, S., Tsidulko, M., Alpert, P. (2000). Monthly Synoptic Patterns Associated with Wet/Dry Conditions in the Eastern Mediterranean. Theor. Appl. Climatol. 65, 215–229.

Kumar, K.N., Molini, A., Ouarda, T.B.M.J. (2017). North Atlantic controls on wintertime warm extremes and aridification trends in the Middle East. *Sci. Rep.* 7, 12301.

Kundzewicz, Z. W. (2005). Summer floods in Central Europe— Climate change track? *Nat. Hazards*, 36(1–2). 165–189.

Kunkel KE, Andsager K, Easterling DR. (1999). Long-term trends in extreme precipitation events over the conterminous United States and Canada. *J. Clim.* 12: 2515–2527.

Kutiel H, Benaroch Y. (2002). North Sea – Caspian Pattern (*NCP*) – an upper level atmospheric teleconnection affecting the Eastern Mediterranean: Identification and definition. *Theoretical and Applied Climatology* 71: 17–28.

Kutiel H, Maheras P, Turkis M, Paz S. (2002). North Sea - Caspian Pattern (*NCP*) - an upper level atmospheric teleconnection affecting the eastern Mediterranean - implications on the regional climate. *Theoretical and Applied Climatology* 72: 173–192.

Kutiel H, Paz S. (1998). Sea level pressure departures in the Mediterranean and their relationship with monthly rainfall conditions in Israel. *Theoretical and Applied Climatology* 60: 93–109.

Kutiel H, Türkes M. (2005). New evidence for the role of the North Sea—Caspian Pattern on the temperature and precipitation regimes in continental Central Turkey. *Geografiska Annaler Series* a-Physical Geography 87A(4): 501–513.

Lawson, M.P., Balling, R.C., Jr., Peters, A.J. and Rundquist, D.C. (1981), Spatial analysis of secular temperature fluctuations. *J. Climatol.,* 1: 325-332.

Lelieveld, J., Hadjinicolaou, P., Kostopoulou, E., Chenoweth, J., El Maayar, M., Giannakopoulos, C., Hannides, C., Lange, M. A., Tanarhte, M., Tyrlis, E., & Xoplaki, E. (2012). Climate change and impacts in the Eastern Mediterranean and the Middle East. *Climatic change*, 114(3-4). 667–687.

Lelieveld, J., P. Hadjinicolaou. E. Kostopoulou. C. Giannakopoulos. A. Pozzer. M. Tanarhte. E. Tyrlis. (2013). Model projected heat extremes and air pollution in the eastern Mediterranean and Middle East in the twenty-first century. *Reg. Environ. Change.*

Li Z. (2015). Spatial and Temporal Variation of Climate Extremes in Southwestern China. In: Study on Climate Change in Southwestern China. Springer Theses (Recognizing Outstanding Ph.D. Research). *Springer*, Berlin, Heidelberg.

Lim, Y.-K. (2014). The East Atlantic/West Russia (EA/WR) teleconnection in the North Atlantic: climate impact and relation to Rossby wave propagation. *Climate Dynamics*, 44(11-12), 3211–3222.

Lionello P (ed). (2012). The Climate of the Mediterranean Region,From the past to the Future. *Elsevier: Amsterdam*, 502 pp. ISBN:9780124160422.

Lionello, Planton S., P., Artale, V., Aznar, R., Carrillo, A., Colin, J., Congedi, L.,. Dubois, C., Elizalde, A., Gualdi, S., Hertig, E., Jacobeit, J., Jordà, G., Li, L., Mariotti, A., Piani, C., Ruti, P., Sanchez-Gomez, E., Sannino, G., Sevault, F., Somot, S., Tsimplis, M. (2012). The Climate of the Mediterranean Region in Future Climate. Amsterdam: *Elsevier* (NETHERLANDS), Projections 449-502.

Liu G., Tan Y., Yu L., Liu J., Gao J. (2013). Application Research of Modified K-Means Clustering Algorithm. In: Qi E., Shen J., Dou R. (eds) The 19th International Conference on Industrial Engineering and Engineering Management. *Springer*, Berlin, Heidelberg.

Longobardi A, Villani P. (2010). Trend analysis of annual and seasonal rainfall time series in the Mediterranean area. *Int. J. Climatol.* 30:1538–1546.

López-Moreno, J. I., and S. M. Vicente-Serrano (2008). Positive and negative phases of the wintertime North Atlantic Oscillation and drought occurrence over Europe: A multitemporal-scale Approach, *Journal of Climate*, 21(6). 1220-1243.

Lu J, Vecchi GA, Reichler T (2007). Expansion of the Hadley cell under global warming. *Geophys. Res Lett*. 34:L06805.

Luterbacher J, Liniger MA, Menzel A, Estrella N, Della-Marta PM, Pfister C, Rutishauser T, Xoplaki E (2007). Exceptional European warmth of autumn 2006 and winter 2007: historical context, the underlying dynamics, and its phenological impacts. *Geophys. Res. Lett*. L12704.

Lv, M.-q., Chen, J.-L., Mirza, Z.A., Chen, C.-D., Wen, Z.-F., Jiang, Y., Ma, M.-h. and Wu, S.-J. (2016). Spatial distribution and temporal variation of reference evapotranspiration in the Three Gorges Reservoir area during 1960–2013. *Int. J. Climatol.*, 36: 4497-4511.

M. Brunetti, M. Maugeri, and T. Nanni. (2002). Atmospheric circulation and precipitation in Italy for the last 50 years. *International Journal of Climatology*, vol. 22, no. 12, pp. 1455–1471.

M. Charrad, N. Ghazzali, V. Boiteau, A. Niknafs (2014). NbClust: An R package for determining the relevant number of clusters in a data set. *J. Stat. Softw*. 61, 1–36.

M. Tanarhte, P. Hadjinicolaou, J. Lelieveld. (2012). Intercomparison of temperature and precipitation data sets based on observations in the Mediterranean and the Middle East. *J. Geophys. Res. Atmos.*, 117, Article D12102.

Mac Queen, J., (1967). Some methods for classification and anal-ysis of multivariate observations (pp. 281–297). In: Le Cam, L.M., Neyman, J. (Eds.). Proc. 5th Berkley Symp. On Mathematical Statistics and Probability, vol. I. *Universityof California Press*. xvii pp. 666.

Machiwal, D., Dayal, D. and Kumar, S. (2017). Long-term rainfall trends and change points in hot and cold arid regions of India. *Hydrological Sciences Journal*, 62(7). 1050–1066.

Maheras, P., & Kutiel, H. (1999). Spatial and temporal variations in the temperature regime in the Mediterranean and their relationship with circulation during the last century. *International Journal of Climatology*, 19(7), 745–764.

Mahfouz P, Mitri G, Jazi M, Karam F. (2016). Investigating the temporal variability of the standardized precipitation index in Lebanon. *Climate* 4:27.

Maldonado J. (2011). Climate Change in Israel.. USDA Foreing Agricultural Service, Global Agricultural Information Network, GAIN Report Number: IS1109, Regional Agricultural Attaché, U.S. Embassy, Cairo.

Malekian A, Kazemzadeh M. (2016). Spatio-temporal analysis of regional trends and shift changes of autocorrelated temperature series in Urmia lake basin. *Water Resour. Manag.* 30(2):785–803.

Manfred A. Lange (2019). Impacts of Climate Change on the Eastern Mediterranean and the Middle East and North Africa Region and the Water–Energy Nexus. *Energy, Environment and Water Research Center*, The Cyprus Institute; P.O. Box 27456, CY1645 Nicosia, Cyprus.

Mann, H.B. (1945) Non-parametric tests against trend. *Econometrica*, 13, 245–259.

Marco Turco, Noam Levin, Naama Tessler, Hadas Saaroni (2017). Recent changes and relations among drought, vegetation and wildfires in the Eastern Mediterranean: The case of Israel, *Global and Planetary Change*, V. 151, P. 28-35, ISSN 0921-8181.

Mariotti A, Dell'Aquila A. (2012). Decadal climate variability in the Mediterranean region: roles of large-scale forcing's and regional processes. *Clim. Dyn.* 38: 1129–1145.

Mariotti, A., N. Zeng, and K. M. Lau (2002). Euro-Mediterranean rainfall and ENSO a seasonally varying relationship, *Geophys. Res. Lett*., 29(12).

Marshall, J., Johnson, H. Goodman, J. A. (2001). Study of the interaction of the North Atlantic Oscillation with oOcean circulation. *J. Climate*, 14, 1399–1421.

Mart, Yossi, William B.F. Ryan, Oxana V. Lunina, (2005). Review of the tectonics of the Levant Rift system: the structural significance of oblique continental breakup, *Tectonophysics*, Volume 395, Issues 3–4, PP209-232, ISSN 0040-1951.

Martín, M.L., Valero, F., Morata, A., Luna, M.Y., Pascual, A. and Santos-Muñoz, D. (2011). Springtime coupled modes of regional wind in the Iberian Peninsula and large-scale variability patterns. *Int. J. Climatol.*, 31: 880-895.

Martin-Vide, J. and Lopez-Bustins, J.-A. (2006). The Western Mediterranean Oscillation and rainfall in the Iberian Peninsula. *Int. J. Climatol.*, 26: 1455-1475.

Marullo, S., Artale, V. Santoleri, R. (2011). The SST Multidecadal Variability in the Atlantic-Mediterranean Region and Its Relation to AMO. *J. Climate* 24, 4385–4401.

Masih, I., Maskey, S., Mussa, F.E.F. and Trambauer, P. (2014). A review of droughts on the African continent: a geospatial and long-term perspective. *Hydrology and Earth System Sciences*, 18(9), 3635–3649.

Mathbout S, Lopez-Bustins JA, Martin-Vide J, Bech J, Rodrigo FS. (2018). Spatial and temporal analysis of drought variability at several time scales in Syria during 1961–2012. *Atmos. Res.* 200:153–168.

Matulla, C., Scheifinger, Helfried., Menzel, Annette., Koch, Elisabeth (2004). Exploring two methods for statistical downscaling of Central European phenological time series. International journal of biometeorology. 48. 56-64. 10.1007/s00484-003-0186-y.

McCabe, G.J. and D.M. Wolock, (2014). Variability Common to Global Sea Surface Temperatures and Runoff in the Conterminous United States. *J. Hydrometeor*., 15, 714–725.

McKee, T.B.; Doesken, N.J.; Kleist, J. (1993). The Relationship of Drought Frequency and Duration to Time Scales. In Proceedings of the Eighth Conference on Applied Climatology, Anaheim, CA, USA, 17–22; pp. 179–184.

Meddi, M., Toumi, S., Assani, A. A., Eslamian, S., (2014). Regionalization of Rainfall Erosivity in Northern Algeria, *Int. J. Hydrology Science and Technology*, Vol. 4, No. 2, 155-175.

Micu D.M., Dumitrescu A., Cheval S., Birsan MV. (2015). Observed Variability and Trends from Instrumental Records. In: Climate of the Romanian Carpathians. Springer Atmospheric Sciences. *Springer*, Cham.

Mills, G.F. (1995). Principal Component Analysis of precipitation and rainfall regionalization in Spain. *Theor Appl Climatol* 50, 169–183.

Ministry of Water and Irrigation (MWI) (2009). Water for life: Jordan's water strategy 2008–2022. Ministry of Water and Irrigation, Amman, Jordan.

Ministry of Water and Irrigation (MWI) and German Technical Cooperation (GTZ) (2005). National Water Master Plan, Amman, Jordan.

Mishra AK, Singh VP, Desai VR. (2009). Drought characterization: a probabilistic approach. Stoch. Environ. *Res. Risk Assess*. 23: 41.

Moberg A, Jones PD, Lister D, Walther A, Brunet M, Jacobeit J, Alexander LV, Della-Marta PM, Luterbacher J, Yiou P, Chen D,. Klein Tank AMG, Saladiée O, Sigró J, Aguilar E, Alexandersson H, Almarza C, Auer I, Barriendos M, Begert M, Bergström H, Böhm R, Butler CJ, Caesar J, Drebs A, Founda D, Gerstengarbe F-W, Micela G, Maugeri M, Österle H, Pandzic K, Petrakis M, Srnec L, Tolasz R, Tuomenvirta H, Werner PC, Linderholm H, Philipp A, Wanner H, Xoplaki E (2006). Indices for daily temperature and precipitation extremes in Europe analyzed for the period 1901–2000. *J. Geophys. Res.* 111:D22106.

Modarres R, Sarhadi A (2009). Rainfall trends analysis of Iran in the last half of the twentieth century. *J. Geophys. Res.* 114:D03101.

Modarres, R. and Sarhadi, A. (2011). Statistically-based regionalization of rainfall climates of Iran. *Global and Planetary Change*, 75, 67–75.

Mohammad Reza Najafia and Saber Moazamib. (2016). Trends in total precipitation and magnitude–frequency of extreme precipitation in Iran, 1969–2009. INTERNATIONAL JOURNAL OF CLIMATOLOGY *Int. J. Climatol.* 36: 1863–1872.

Mohammadrezaei, M., Soltani, S. & Modarres, R. (2020). Evaluating the effect of ocean-atmospheric indices on drought in Iran. *Theor. Appl. Climatol*. 140, 219–230.

Mohammed Matouq, Tayel El-Hasan, Hussam Al-Bilbisi, Monther Abdelhadi, Muna Hindiyeh, Saeid Eslamian & Salman Duheisat (2013). The climate change implication on Jordan: A case study using GIS and Artificial Neural Networks for weather forecasting, *Journal of Taibah University for Science,* 7:2, 44-55.

Mohammed, S., Alsafadi, K., Al-Awadhi, T. (2020). Space and time variability of meteorological drought in Syria. *Acta Geophys*. 68, 1877–1898.

Mooley, D.A., Parthasarathy, B. (1984). Fluctuations in All-India summer monsoon rainfall during 1871–1978. *Climatic Change* 6, 287–301.

Moore, G. W. K. and Renfrew, I. A. (2012). Cold European winters: interplay between the NAO and the East Atlantic mode. *Atmos. Sci. Lett.*, 13, 1–8.

Müller, W. A. and Roeckner, E. (2008). ENSO teleconnections in projections of future climate in ECHAM5/MPI-OM, *Clim. Dynam.*, 31, 533–549.

Mulugeta, S.; Fedler, C.; Ayana, M. (2019). Analysis of Long-Term Trends of Annual and Seasonal Rainfall in the Awash River Basin, Ethiopia. Water, 11, 1498.

Muslih, K.D., Błażejczyk, K. (2017). The inter-annual variations and the long-term trends of monthly air temperatures in Iraq over the period 1941–2013. Theor Appl Climatol 130, 583–596.

Mustafa A, Rahman G. (2018). Assessing the spatio-temporal variability of meteorological drought in Jordan. *Earth Syst. Environ* 2:247–264.

Nair, A., Mohanty, U.C. & Acharya, N. (2013). Monthly prediction of rainfall over India and its homogeneous zones during monsoon season: a supervised principal component regression approach on general circulation model products. *Theor Appl Climatol* 111, 327–339.

Najafi MR, Moazami S (2017). Trends in total precipitation and magnitude–frequency of extreme precipitation in Iran, 1969–2009. Int J Climatol 36(4):1863–1872.

Najafi MR, Moradkhani H. (2014). A hierarchical Bayesian approach for the analysis of climate change impact on runoff extremes. *Hydrol. Process*. 28(26): 6292–6308.

Nalbantis I. (2008). Evaluation of a hydrological drought index. Eur. *Water* 23: 67–77.

Nastos PT, Zerefos CS. (2007). On extreme daily precipitation totals at Athens, Greece. *Advances in Geosciences* 10: 59–66.

Nastos, P. T., Philandras, C. M., Founda, D., & Zerefos, C. S. (2011). Air temperature trends related to changes in atmospheric circulation in the wider area of Greece. *International Journal of Remote Sensing*, 32(3), 737–750.

Nazemosadat MJ, Samani N, Barry DA, Molaii Niko M. (2006). ENSO forcing on climate change in Iran: precipitation analyses. *Iranian Journal of Science & Technology*, Transaction B, Engineering 30(B4): 47–61.

Neelin JD, Münnich M, Su H, Meyerson JE, Holloway CE (2006). Tropical drying trends in global warming models and observations. *Proc. Natl. Acad. Sci.* 103:6110–6115.

New M, Hewitson B, Stephenson DB, Tsiga A, Kruger A, Manhique A, Gomez B, Coelho CA, Masisi DN, Kululanga E. (2006). Evidence of trends in daily climate extremes over southern and west Africa. *J. Geophys. Res. Atmos*. 111: 1–11.

New, M., M. Hulme, and P. D. Jones (2000), Representing twentieth century space-time climate variability. Part 2: development of 1901–96 monthly grids of terrestrial surface climate, *J. Clim.*, 13, 2217– 2238.

Newman, M., and P. D. Sardeshmukh (1995). A caveat concerning singular value decomposition. *J. Climate*, 8, 352–360.

Nicholls, N., (2015). Tropical Meteorology & Climate, El niño and the southern oscillation. *Encyclopedia of Atmospheric Sciences* (Second Edition).

Niedzielski, Tomasz. (2014). El Niño/Southern Oscillation and Selected Environmental Consequences. In Advances in Geophysics.

North, G. R. T. L. Bell, R. F. Cahalan, and F. J. Moeng (1982). Sampling errors in the estimation of Empirical Orthogonal Functions, *monthly weather review*, 110(7), 699-706.

Oguz, T. (2005). Black Sea ecosystem response to climatic variations. *Oceanography* 18 (2), 122–133.

Oikonomou, C., Flocas, H., Hatzaki, M., Nisantzi, A., & Asimakopoulos, D. (2010). Relationship of extreme dry spells in em with large-scale circulation. *Theoretical and Applied Climatology*, 100, 137–151.

Olbers, Dirk & Willebrand, Jürgen & Eden, Carsten (2012). Ocean Dynamics. 10.1007/978-3-642-23450-7.

Oliver, J.E. (1980) Monthly precipitation distribution: a comparative index. Professional Geographer, 32, 300–309.

Onoz, B. and Bayazit, M. (2003). The power of statistical tests for trend detection. *Turkish Journal of Engineering and Environmental Sciences*, 27(2003). 247–251.

Önöz, B. and Bayazit, M. (2012), Block bootstrap for Mann–Kendall trend test of serially dependent data. *Hydrol. Process*., 26: 3552-3560.

Osborn, T. J., M. Hulme, P. D. Jones, and T. A. Basnett (2000). Observed trends in the daily intensity of United Kingdom precipitation. *Int. J. Climatol.*, 20, 347-364.

Osborne JW, Overbay A. (2004). The power of outliers (and why researchers should always check for them). *Practical Assessment, Research & Evaluation* 9: 1–8.

Osofsky, Hari M. (2014). transition to a clean energy future: the role of climate change litigation in shaping our regulatory path, forthcoming, *cambridge university press*.

Ouachani, R., Z. Bargaoui, and T. B. M. J. Ouarda (2011). Power of teleconnection patterns on precipitation and streamflow variability of upper Medjerda Basin, *Int. J. Climatol*., 33, 58–76.

Ouarda TBMJ, Charron C, Kumar KN, Marpu PR, Ghedira H, Molini A, Khayal I. (2014). Evolution of the rainfall regime in the United Arab Emirates. *J. Hydrol*. 514: 258–270.

Özgür, E., Koçak, K. (2019). Climatology of snowfall/total precipitation days over Turkey. *Theor Appl Climatol* 137, 2487–2495.

Pal I, Al-Tabbaa A. (2011). Assessing seasonal precipitation trends in India using parametric and non-parametric statistical techniques. *Theor Appl Climatol* 103:1–11.

Palmer WC. (1965). Meteorological drought. *Research Paper* No. 45, p 58, U.S. Dep. Commer. Weather Bur. Washington, DC. Research.

Palutikof JP, Conte M, Casimiro Mendes J, Goodess CM, Esprito Santo F. (1996). Climate and Climatic Change. In: Brandt CJ, Thornes JB (eds.) Mediterranean desertification and land use. Wiley, New York, pp 43–86.

Palutikof, J. P.. (2003). Analysis of Mediterranean climate data: measured and modelled in Mediterranean Climate: Variability and Trends. *Springer,* Berlin, Germany.

Papadimas, C. D. & Bartzokas, Aristides & Lolis, Christos & Hatzianastassiou, N. (2012v). Sea-level pressure–air temperature teleconnections during northern hemisphere winter. Theoretical and Applied Climatology. 108. 173-189. 10.1007/s00704-011-0523-8.

Parker DE. (2004). Large-scale warming is not urban. *Nature* 432: 290–291.

Parmesan C, Root TL, Willig MR. (2000). Impacts of extreme weather and climate on terrestrial biota. *Bulletin of the American Meteorological Society* 81: 443–450.

Parmesan, C.: (2006). Ecological and evolutionary responses to recent climate change. *Annu. Rev. Ecol. Evol. Syst*. 37, 637–669.

Partal T, Kucuk M. (2006). Long-term trend analysis using discrete wavelength components of annual precipitations measurements in Marmara region (Turkey). *Phys. Chem. Earth.* 31:1189–1200.

Patakamuri, Sandeep Kumar. O'Brien, Nicole. (2020). Modified Versions of Mann Kendall and Spearman's Rho Trend Tests. R package version 1.5.0.

Peterson T C, Vose R, Schmoyer R and Razuvaëv V. (1998). Global Historical Climatology Network (GHCN) quality control of monthly temperature data; *Int. J. Climatol.*18(11) 1169–1179.

Peterson TC, Folland C, Gruza G, Hogg W, Mokssit A, Plummer N. (2001). Report of the activities of the Working Group on Climate Change Detection and Related Rapporteurs 1998-2001. ICPO Publication Series 48, Southampton, *UK. International CLIVAR Project Office* 144 pp.

Peterson, T.C., Zhang, X.B., India, M.B., Aguirre, J.L.V. (2008). Changes in North American extremes derived from daily weather data. *Journal of Geophysical Research*.

Pettitt AN. (1979). A non-parametric approach to the change-point detection. *Applied Statistics* 28: 126–135.

Philandras CM, Nastos PT, Kapsomenakis J, Douvis KC, Tselioudis G, Zerefos CS. (2011). Long term precipitation trends and variability within the Mediterranean region. *Nat. Hazards Earth Syst. Sci*. 11:3235–3250.

Pingale, S.M., D. Khare, M.K. Jat, J. Adamowski. (2016). Trend analysis of climatic variables in an arid and semi-arid region of the Ajmer District, Rajasthan, India J. Water Land Dev., 28, pp. 3-18.

Pinto, J. G. and Raible, C. C. (2012). Past and recent changes in the north Atlantic oscillation. *WIRFs Clim. Change*, 22, 4014.

Popov, T., Gnjato, S., Trbic, G. and Ivaniševic, M. (2018). Recent trends in extreme temperature indices in Bosnia and Herzegovina Carpathian Journal of Earth and Environmental Sciences, 13, 211–224.

Posio J, Leiviskä K, Ruuska J, Ruha P. (2008). Outlier Detection for 2D Temperature Data. Proceedings of the 17th World Congress, *The International Federation of Automatic Control Seoul*, Korea.

Preisendorfer, R. W. (1988). Principal Component Analyses in Meteorology and Oceanography. *Elsevier*.

Presti, Lo. R., Barca, E. & Passarella, G. A (2010). Methodology for treating missing data applied to daily rainfall data in the Candelaro River Basin (Italy). Environ Monit Assess 160, 1 (2010).

Prezerakos NG. (1984). Does the extension of the Azores anticyclone towards the Balkans really exists. Arch. Meteor. Geophys. Bioclimatol Ser. A 33:217–227.

Price, C., Stone, L., Rajagopalan, B., Alpert, P. (1998). A possible link between El Niño and precipitation in Israel. *Geophys. Res. Lett*., 25, 3963±3966.

Proedrou M, Theoharatos G, Cartalis C. (1997). Variations and trends in annual and seasonal air temperature in Greece determined from ground and satellite measurements. *Theor Appl Climatol* 57:65–78.

prohaska j. (1976). A technique for analyzing the linear relationships between two meteorological fields. *Mon. Wea. Rev.* 104: 1345-1353.

Quadrelli R, Wallace JM. (2004). Varied expressions of the hemispheric circulation observed in association with contrasting Polarities of prescribed patterns of variability. *Journal of Climate* 21: 4245–4253.

R. Batehup, S. McGregor, and A. J. E. Gallant. (2015). The influence of non-stationary teleconnections on palaeoclimate reconstructions of ENSO variance using a pseudoproxy framework. *Clim. Past*, 11, 1733–1749, 2015.

R. H. Heiblum, I. Koren, and O. Altaratz (2011). Analyzing coastal precipitation using TRMM observations, *Atmos. Chem. Phys*., 11, 13201–13217.

R.H. McCuen. (1998). Hydrologic Analysis and Design. Prentice-Hall, Englewood Cliffs, NJ.

Radinović, D., Ćurić, M. (2009). Deficit and surplus of precipitation as a continuous function of time. *Theoretical and Applied Climatology* 98, 197–200.

Rahimi M, Hejabi S. (2018). Spatial and temporal analysis of trends in extreme temperature indices in Iran over the period 1960–2014. *International Journal of Climatology* 38: 272–282.

Rahimzadeh, F., Asgari, A. and Fattahi, E. (2009). Variability of extreme temperature and precipitation in Iran during recent decades. *Int. J. Climatol.*, 29: 329-343.

Raja, N.B., Aydin, O., Türkoğlu, N. (2017). Space-time kriging of precipitation variability in Turkey for the period 1976–2010. *Theor Appl Climatol* 129, 293–304 (2017).

Rajagopalan, B., E. Cook, U. Lall, and B. K. Ray (2000). Spatiotemporal variability of ENSO and SST teleconnections to summer drought over the United States during the twentieth century. *J. Climate*, 13, 4244–4255.

Ramadan, H.H., Ramamurthy, A.S. & Beighley, R.E. Inter-annual temperature and precipitation variations over the Litani Basin in response to atmospheric circulation patterns. *Theor. Appl. Climatol*. 108, 563–577 (2012).

Rayner, N. A., Parker, D. E., Horton, E. B., Folland, C. K., Alexander, L. V., Rowell, D. P., Kent, E. C., and Kaplan, A. (2003). Global analyses of sea surface temperature, sea ice, and night marine air temperature since the late nineteenth century, *J. Geophys. Res.*, 108, 4407.

Razavi T, Switzman H, Arain A, Coulibaly P. (2016). Regional climate change trends and uncertainty analysis using extreme indices: A case study of Hamilton, Canada. *Climate Risk Management* 13: 43–63.

Raziei T, Bordi I, Pereira L (2008). A precipitation-based regionalization for Western Iran and regional drought variability. *Hydrol. Earth Syst. Sci.* 12:1309–1321.

Raziei, T., Daryabari, J., Bordi, I. (2014). Spatial patterns and temporal trends of precipitation in Iran. *Theor Appl Climatol* 115, 531–540.

Redolat, D., Monjo, R., Lopez-Bustins, J.A. (2019). Upper-Level Mediterranean Oscillation index and seasonal variability of rainfall and temperature. *Theor. Appl. Climatol.*, 135, 1059–1077.

Rehman, S. (2010), "Temperature and rainfall variation over Dhahran, Saudi Arabia, 1970–2006". International Journal of Climatololy, 30: 445-449.

Repapis CC, Philandras CM, Kalabokas PD, Zanis P, Zerefos CS. (2007). Is the last years abrupt warming in the National Observatory of Athens records a climate change manifestation? *Glob NEST* J 9:107–116.

Repapis, C. C,, Philandras, C. M. (1988). A note on the air temperature trends of the last 100 years as evidenced in the Eastern Mediterranean time series. *Theor. Appl. Climatol*., 39, 93-97.

Revadekar J V and Preethi B (2010). Statistical analysis of the relationship between summer monsoon precipitation extremes and food grain yield over India; *Int. J. Climatol.*

Rixen, M., J. Beckers, S. Levitus, J. Antonov, T. Boyer, C. Maillard, M. Fichaut, E. Balopoulos, S. Iona, H. Dooley, M. Garcia, B. Manca, A. Giorgetti, G. Manzella, N. Mikhailov, N. Pinardi, M. Zavatarelli. (2005). The Western Mediterranean Deep Water: a proxy for climate change. *Geophys. Res. Lett.*, 32 (12), p. L12608.

Robaa ESM, Al-Barazanji Z. (2015). Mann-Kendall trend analysis of surface air temperatures and rainfall in Iraq. IDOJARAS 119(4):493–514.

Robaa SM, and AL-Barazanji ZJJ. (2013). Trends of Annual Mean Surface Air Temperature over Iraq, 11(12);138–145.

Rodriguez-Puebla C, Encinas AH, Nieto S, Garmendia J. (1998). Spatial and temporal patterns of annual precipitation variability over the Iberian Peninsula. *Int. J. Climatol.*18: 299–316.

Rosenzweig C, Iglesias A, Yang XB, Epstein PR, Chivian E. (2001). Climate change and extreme weather events: implications for food production, plant diseases, and pests. *Glo. Chang Hum. Health.* 2:90–104.

Rummel, Bernard (2014). Probability Plotting: A Tool for Analyzing Task Completion Times. *Journal of usability studies (JUS).* Vol. 9, Issue 4, August 2014 pp. 152-172.

Saaroni H, Ziv B, Edelson J, Alpert P. (2003). Long term variations in summer temperature over the eastern Mediterranean. *Geophys. Res. Lett.* 30:1946–1949.

Saaroni, H., Halfon, N., Ziv, B., Alpert, P. and Kutiel, H. (2010). Links between the rainfall regime in Israel and location and intensity of Cyprus lows. *Int. J. Climatol.*, 30: 1014-1025.

Saaroni, H., Ziv, B., Lempert, J., Gazit, Y. and Morin, E. (2015). Prolonged dry spells in the Levant region: climatologic-synoptic analysis. *Int. J. Climatol*, 35: 2223-2236.

Sabziparvar, A.A., Mirmasoudi, S.H., Tabari, H., Nazemosadat, M.J. and Maryanaji, Z. (2011). ENSO teleconnection impacts on reference evapotranspiration variability in some warm climates of Iran. *Int. J. Climatol.*, 31: 1710-1723.

Sagarika, S., Kalra, A. and Ahmad, S. (2016). Pacific Ocean SST and Z500 climate variability and western U.S. seasonal streamflow. *Int. J. Climatol.*, 36: 1515-1533.

Sahai, A., Pattanaik, D., Satyan, V. (2003). Teleconnections in recent time and prediction of Indian summer monsoon rainfall. *Meteorol. Atmos. Phys*. 84, 217–227.

Sahour, H., Vazifedan, M. & Alshehri, F. (2020). Aridity trends in the Middle East and adjacent areas. *Theor. Appl. Climatol*.

Sahsamanoglou HS, Makrogiannis TJ. (1992). Temperature trends over the Mediterranean region 1950–1988. *Theor Appl Climatol* 45:183–192.

Salameh, A. M. Ala, Yolanda Castro-Díez, Maria-Jesus Esteban-Parra, S. R. Gámiz-Fortis. (2018). Spatio-temporal analysis of maximum and minimum temperatures over Levant region (1987-2017). Conference: EL CLIMA: AIRE, AGUA, TIERRA Y FUEGO, *Asociación Española de Climatología; Agencia Estatal de MeteorologíaAt: University of Murcia*.

Salameh, Ala, AM. Gámiz Fortis SR, Castro-Díez Y, Abu Hammad A, EstebanParra MJ. (2019). Spatio-temporal analysis for extreme temperature indices over the Levant region. *Int. J .Climatol*.;1–27.

Salameh, Ala, Fallah, R. (2018). Changes in Air Temperature and Precipitation over the Syrian Coastal Region. *Cuadernos Geográficos* 57(3), 140-151.

Salas, J.D. (1993). In: Maidment, D.R. (Ed.) Analysis and Modeling of Hydrologic Time Series. Handbook of Hydrology. *New York*, NY: McGraw-Hill.

Salehi, S, Dehghani, M, Mortazavi, SM, Singh, VP. (2020). Trend analysis and change point detection of seasonal and annual precipitation in Iran. *Int. J. Climatol.;* 40: 308– 323.

Salehnia, N., Salehnia, N., Ansari, H. (2019). Climate data clustering effects on arid and semi-arid rainfed wheat yield: a comparison of artificial intelligence and K-means approaches. *Int. J. Biometeorol.* 63, 861–872.

Salim, N., and Wildi, W. (2005). Impact of global climate change on water resources in the Israeli, Jordanian and Palestinian region, *Terre et Environnement* 50, 125–140.

Salinger MJ, Griffiths GM. (2001). Trends in New Zealand daily temperature and rainfall extremes. *International Journal of Climatology,* 21: 1437–1452.

Salman, S.A., Shahid, S., Ismail, T. (2018). Unidirectional trends in daily rainfall extremes of Iraq. *Theor. Appl. Climatol.* 134, 1165–1177.

Santos M, Fragoso M, Santos JA. (2017). Regionalization and susceptibility assessment to daily precipitation extremes in mainland Portugal. *Appl. Geogr.* 86:128–138.

Sarricolea, P., Meseguer-Ruiz, Ó., Serrano-Notivoli, R., Soto, M.V., & Martin-Vide, J., (2019). Trends of daily precipitation concentration in Central-Southern Chile. Atmospheric Research (215), 85-98.

Scorzini AR, Di Bacco M, Leopardi M. (2018). Recent trends in daily temperature extremes over the central Adriatic region of Italy in a Mediterranean climatic context. *International Journal of Climatology* 38(S1): e741–e757.

Seager R, Liu H, Henderson N, Simpson I, Kelley C, Shaw T. (2014). Causes of increasing aridification of the mediterranean region in response to rising greenhouse gases. *J Clim* 27:4655–4676.

Semawi M. 2012. Climate change predictions and projections and extreme events indices in the Arab Region. Regional Workshop on Climate Change 13-16 March 2012 Casablanca, Morocco. Jordan Meteorological Department JMD.

Sen PK. (1968). Estimates of the Regression Coefficient Based on Kendall's Tau. *Journal of the American Statistical Association,* 63: 1379–1389.

Serhat, Sensoy, Necla Türkoğlu, Alper Akçakaya, Mithat Ekici, Mesut Demircan, Yusuf Ulupinar, Hakkı Atay, Arzu Tüvan, Hatice Demirbaş (2013). Trends In Turkey Climate Indices. *6th Atmospheric Science Symposium* - ATMOS 2013 3 - 5 Haziran 2013, İstanbul.

Serra C, Burgue~no A, Lana X. (2001). Analysis of maximum and minimum daily temperatures recorded at Fabra observatory (Barcelona, NE Spain) in the period 1917–1998. *Int. J. Climatol.* 21: 617–636.

Shadeed, S. 2013. Spatio-temporal Drought Analysis in Arid and Semiarid Regions: A Case Study from Palestine. *Arabian Journal for Science & Engineering* 38: p. 2303-2313.

Shafran-Nathan R, Svoray T, Perevolotsky A. (2012). The resilience of annual vgetation primary production subjected to different climate change scenarios. *Clim. Chang*.

Shahabfar A, Eitzinger J. (2013). Spatio-temporal analysis of droughts in semi-arid regions by using meteorological drought indices. *Atmosphere* 4: 94–112.

Shaman, J., and E. Tzipperman (2011). An Atmospheric teleconnection linking ENSO and Southwestern European precipitation, *J. Clim*., 24, 124–139.

Shamsniya A, Pirmoradian N and Amiri N. (2008) Drought modeling in Fars Province using time series analysis; *Geogr. Plan.* 28 165–189.

Sharon, D. and Kutiel, H. (1986), The distribution of rainfall intensity in Israel, its regional and seasonal variations and its climatological evaluation. *J. Climatol*., 6: 277-291.

Sheffield J, Wood EF, Roderick ML. (2012). Little change in global drought over the past 60 years. *Nature* 491(7424): 435–438.

Shifa, M.; Lopez-Bustins, J.A.; Martin-Vide, J.; Becha, J.;Rodrigo, F. (2018). Spatial and temporal analysis of drought variability at several time scales in Syria during 1961–2012. *Atmospheric Research*, 153-168.

Shlomi Y, Ginat H (2009). Rainfall in the Arava 1950-2008, Preliminary report. Scientific report submitted to the water and the Arava drainage authorities, *Dead Sea and Arava Science Center*, 23 p. (in Hebrew).

Shohami, D., , U. Dayan, , and E. Morin, (2011) Warming and drying of the eastern Mediterranean: Additional evidence from trend analysis. *J. Geophys. Res*., 116, D22101.

Shukla, J., (1998). Predictability in the midst of chaos: a scientific basis for climate forecasting Science, 282, pp. 728-731.

Sibson R. (1981). A brief description of natural neighbour interpolation, in Interpreting Multivariate Data. In Barnett V. (Ed.). Interpreting Multivariate Data, *John Wiley & Sons*, New York, 21–36 pp.

Sillmann J, Roeckner E. (2008). Indices of extreme events in projections of anthropogenic climate change. *Clim. Chang.* 86:83–104.

Simolo, C., Brunetti, M., Maugeri, M. and Nanni, T. (2010), Improving estimation of missing values in daily precipitation series by a probability density function-preserving approach. *Int. J. Climatol.*, 30: 1564-1576.

Simone, Stefan (2011). Adapting to climate change in the water sector in the Mediterranean: situation and pros-pects. Plan Bleu, *UN Environment*.

Singh, V. P. (1994). Elementary Hydrology. Prentice Hall of India, New Delhi.

Sirdas S, Sen Z. (2003). Spatio-temporal drought analysis in the Trakya region, Turkey. *Hydrol. Sci. J.* 48: 809–820.

Skaf, M. Mathbout, S. (2010). Drought changes over last five decades in Syria. Options Méditerranéennes, A no. 95, Economics of drought and drought preparedness in a climate change context.

Skliris, N. (2011). Decadal scale variability of sea surface temperature in the Mediterranean Sea in relation to atmospheric variability. *Ocean Dynam*. 62, 13–30.

Skliris, N. S. Sofianos, A. Gkanasos, P. Axaopoulos, A. Mantziafou, V. Vervatis. (2011). Long-term sea surface temperature variability in the Aegean Sea, Adv. Oceanogr. Limnol., 2 (2), pp. 125-139.

Smiatek, G., , Kunstmann H. , and Heckl A. (2011). High-resolution climate change simulations for the Jordan River area. *J. Geophys. Res*., 116, D16111.

Sneyers, R. (1990). Technical note no. 143 on the statistical analysis of series of observations, *World Meteorological Organization*, Geneva.

Snyder, R.L., R. Moratiel , Zhenwei Song, A. Swelam, I. Jomaa, T. Shapland (2011). evapotranspiration response to climate change. *Acta. Horticulturae.* 922(922):91-98.

Soltani M, Laux P, Kunstmann H, Stan K, Sohrabi MM, Molanejad M, Zawar-Reza P. (2015). Assessment of climate variations in temperature and precipitation extreme events over Iran. *Theor Appl Climatol* 126(3-4):1–21.

Some'e, B. Shifteh, Azadeh Ezani, Hossein Tabari, (2012). Spatiotemporal trends and change point of precipitation in Iran, Atmospheric Research, 113,1-12.

Soukup, Tyrel & Oubeidillah, Abdoul & Tootle, Glenn & Piechota, Thomas & Wulff, Shaun. (2009). Long lead-time streamflow forecasting of the North Platte River incorporating oceanic–atmospheric climate variability. *Journal of Hydrology*. 368. 131-142. 10.1016/j.jhydrol.2008.11.047.

Sousa, P. M., Trigo, R. M., Aizpurua, P., Nieto, R., Gimeno, L., and Garcia-Herrera, R.: Trends and extremes of drought indices throughout the 20th century in the Mediterranean, Nat. Hazards Earth Syst. Sci., 11, 33–51.

Sowers J, Vengosh A, Weinthal E. (2011). Climate change, water resources, and the politics of adaptation in the Middle East and North Africa. *Climatic Change* 104: 599–627.

Spinoni J, Vogt JV, Naumann G, Barbosa P, Dosio A. (2018). Will drought events become more frequent and severe in Europe? *Int J Climatol* 38:1718–1736.

Spinoni, J., Naumann, G., Carrao, H., Barbosa, P. and Vogt, J. (2014). World drought frequency, duration, and severity for 1951–2010. *Int. J. Climatol.*, 34: 2792-2804.

Stedinger JR, Vogel RM, Foufoula-Georgiou E. (1993). Frequency analysis of extreme events. In: Maidment DR (ed) Handbook of hydrology. McGraw-Hill, New York, pp 1810–1823.

Štěpánek P, Zahradníček P, Farda A. (2013). Experiences with data quality control and homogenization of daily records of various meteorological elements in the Czech Republic in the period 1961–2010. *IDŐJÁRÁS Quarterly Journal of the Hungarian Meteorological Service* 117: 123–141.

Stephanie, Hänsel, Deusdedit M. Medeiros, Jörg Matschullat, Reinaldo A. Petta and Isamara de Mendonça Silva. (2016). Assessing Homogeneity and Climate Variability of Temperature and Precipitation Series in the Capitals of North-Eastern Brazil, *Atmospheric science*.

Stott, P. A., D. A. Stone, and M. R. Allen (2004). Human contribution to the European heatwave of (2003). *Nature*, 432, 610–614.

Sugimoto S, Hanawa K. (2010). The wintertime wind stress curl field in the North Atlantic and its relation to atmospheric teleconnection patterns. *J. Atmos. Sci.* 67: 1687-1694.

Suhaila J, Deni SM, Jemain AA. (2008). Detecting inhomogeneity of rainfall series in Peninsular Malaysia. *Asia Pac. J. Atmos. Sci.* 44(4):369–380.

Suhaila, J., Yusop, Z. (2018). Trend analysis and change point detection of annual and seasonal temperature series in Peninsular Malaysia. *Meteorol. Atmo.s Phys.* 130, 565–581.

Sutarya D, Mahendra A. (2014). Outlier Filtering for Hydrogen Temperature and Flow Rate Time series data in Sintering Process. *Proceeding Conference on Applied Electromagnetic Technology (AEMT)*. Lombok, 11-15 April. 86 p.

Sutton, R. T. Dong, B. (2012). Atlantic Ocean influence on a shift in European climate in the 1990s. *Nat. Geosci.* 5, 788–792.

Sutton, R. T. Hodson, D. L. R. (2005). Atlantic ocean forcing of North American and European summer climate. *Science* 309, 115–118.

Svoboda M, Lecomte D, Hayes M, Heim R, Gleason K, Angel J, Rippey B, Tinker R, Palecki M, Stooksbury D, Miskus D, Stephens S. (2002). The drought monitor. Bull. *Am. Meteorol. Soc*. 83: 1181–1190.

T.B. McKee, N.J. Doesken, J. Kleist (1993). The Relationship of Drought Frequency and Duration to Time Scales, Paper Presented at 8th Conference on Applied Climatology, American Meteorological Society, Anaheim, CA.

T.B. McKee, N.J. Doesken, J. Kleist (1995). Drought Monitoring with Multiple Time Scales, Paper Presented at 9th Conference on Applied Climatology, American Meteorological Society, Dallas, Texas.

Tabari H, Marofi S, Aeini A, Talaee PH, Mohammadi K. (2011). Trend analysis of reference evapotranspiration in the western half of Iran. *Agric. For. Meteorol.* 151:128–136.

Tabari, H. and M. B. Aghajanloo (2013). Temporal pattern of aridity index in Iran with considering precipitation and evapotranspiration trends, *International Journal of Climatology*, vol. 33, no. 2, pp. 396–409.

Tabios, G.Q. III, J.D. Salas. (1985). A comparative analysis of techniques for spatial interpolation of precipitation Water Resources Bulletin, 21, pp. 365-380.

Tan, Chunping, Yang, Jianping, Man Li. (2015). Temporal-Spatial Variation of Drought Indicated by SPI and SPEI in Ningxia Hui Autonomous Region, *China. Atmosphere*. 6, 1399-1421.

Tan, L., Li, C., Xia, J., Cao, J. (2019). Application of self-organizing feature map neural network based on K-means clustering in network intrusion detection. *Comput. Mater. Continua* 61(1). 275–288.

Tan, M.L., Chua, V.P., Li, C. (2019.) Spatiotemporal analysis of hydro-meteorological drought in the Johor River Basin, Malaysia. *Theor Appl Climatol* 135, 825–837.

Tan, M.L.; Samat, N.; Chan, N.W.; Lee, A.J.; Li, C. (2019). Analysis of Precipitation and Temperature Extremes over the Muda River Basin, Malaysia. *Water*, 11, 283.

Tanarhte M, Hadjinicolaou P, Lelieveld J. (2015). Heat wave characteristics in the eastern Mediterranean and Middle East using extreme value theory. *Climate Research* 63: 99-113.

Tangborn, Wendell (2003). Winter Warming Indicated by Recent Temperature and Precipitation Anomalies, *Polar Geography*, 27:4, 320-338.

Tao, H., Fraedrich, K., Menz, C. (2014). Trends in extreme temperature indices in the Poyang Lake Basin, China. *Stoch. Environ. Res. Risk Assess.* 28, 1543–1553.

Tebaldi C, Hayhoe K, Arblaster J, Meehl G. (2006). Going to the extremes: an intercomparison of model-simulated historical and future changes in extreme events. *Clim. Chang.* 79:185–211.

Terink W, Immerzeel WW, Droogers P. (2013). Climate change projections of precipitation and reference evapotranspiration for the Middle East and Northern Africa until 2050. *International Journal of Climatology* 33: 3055–3072.

Thompson D, Wallace J. (1998). The Arctic oscillation signature in the wintertime geopotential height and temperature fields. *Geophys. Res. Lett*., 25:1297–1300.

Thompson, D. W. J. and Wallace, J. M. (2000). Annular Modes in the Extratropical Circulation. Part I. Month-to-Month Variability, *J. Climate*, 13, 1000–1016.

Tian, L, Quiring, SM. (2019). Spatial and temporal patterns of drought in Oklahoma (1901–2014). *Int. J. Climatol*; 39: 3365– 3378.

Tian, L., Yuan, S. and Quiring, S.M. (2018). Evaluation of six indices for monitoring agricultural drought in the south-central United States. *Agricultural and Forest Meteorology*, 249, 107–119.

Tonbol, K. M., El-Geziry, et al. (2018). Evaluation of changes and trends in air temperature within the Southern Levantine basin, Weather, 73: 60-66.

Toreti A, Desiato F (2008). Temperature trend over Italy from 1961 to 2004. *Theor Appl Climatol* 91:51–58.

Tornros, Tobias (2013). On the relationship between the Mediterranean Oscillation and winter precipitation in the Southern Levant. *Atmospheric science letters Atmos. Sci. Let*. 14: 287–293.

Toros H. (2012). Spatio-temporal variation of daily extreme temperatures over Turkey. *International Journal of Climatology* 32: 1047–1055.

Trenberth KE (2011). Changes in precipitation with climate change. *Clim. Res.* 47:123–138.

Trenberth KE, Jones PD, Ambenje P, Bojariu R, Easterling D, Klein Tank A, Parker D, Rahimzadeh F, Renwick JA, Rusticucci M, Soden B, Zhai P (2007). Observations: surface and atmospheric climate change. In: Solomon S, Qin D, Manning M, Chen Z, Marquis M, Averyt KB, Tignor M, Miller HL (eds) Climate change 2007: the physical science basis. Contribution of working group I to the fourth assessment report of the intergovernmental panel on climate change. Cambridge University Press, Cambridge, United Kingdom and New York, NY, USA.

Trenberth, K.E., and T. J. Hoar, (1997). El niño and climate chamge, Geophys. *Res. Lett*., 24, 3057-3060.

Trewin, B. (2010). Exposure, instrumentation, and observing practice effects on land temperature measurements, WIREs, *Clim. Change*, 490–506.

Trewin, B. (2013). A daily homogenized temperature data set for Australia. *International Journal of Climatology*, 33, 1510–1529.

Trigo RM, Osborn TJ, Corte-Real J. (2002). The North Atlantic oscillation influence on Europe: climate impacts and associated physical mechanisms. *Climate Research* 20: 9–17.

Turco M, von Hardenberg J, AghaKouchak A, Llasat MC, Provenzale A, Trigo RM. (2017). On the key role of droughts in the dynamics of summer fires in Mediterranean Europe. *Sci. Rep.* 7:81.

Türkes M, Erlat E. (2009). Winter mean temperature variability in Turkey associated with the North Atlantic Oscillation. *Meteorology and Atmospheric Physics* 105(3): 211–225.

Türkeş M, Utku M, Demir I. (2002). Re-evaluation of trends and changes in mean, maximum and minimum temperatures of Turkey for the period 1920–1999. *Int. J. Climatol.* 22: 947–977.

Türkeş, M. and Tatlı, H. (2009). Use of the standardized precipitation index (SPI) and a modified SPI for shaping the drought probabilities over Turkey. *Int. J. Climatol.* 29: 2270-2282.

Tutsak, Ersin. Sözer, Adil. Özsoy, Emin. Gündüz, Murat (2015). Connections between climate indices and Caspian Sea surface temperature. *J. Sci. Tech.*, Vol: 5, No: 1,29-36.

Ulbrich U, Christoph M. (1999). A shift of the NAO and increasing storm track activity over Europe due to anthropogenic greenhouse gas forcing. *Climate Dynamics* 15: 551–559.

Ulbrich U., P. Lionello, P. Malanotte-Rizzoli, R. Boscolo, (2006). The Mediterranean climate change under global warming. Mediterranean Climate Variability, Elsevier, Amsterdam, pp. 398-415.

Unal, Y.S., Deniz, A., Toros, H. and Incecik, S. (2012). Temporal and spatial patterns of precipitation variability for annual, wet, and dry seasons in Turkey. *Int. J. Climatol.*, 32: 392-405.

Unkaševic M, Tošić I (2013). Trends in temperature indices over Serbia: relationships to large-scale circulation patterns. *Int. J. Climato.l* 33:3152–3161.

Unkašević M, Tošić I. (2001). Trends in temperature indices over Serbia: relationships to large-scale circulation patterns. *International Journal of Climatology* 33: 3152–3161.

Uvo, C.B., C.A. Repelli, S.E. Zebiak, Y. Kushnir. (1998). The relationships between tropical pacific and atlantic SST and northeast brazil monthly precipitation. *J. Clim.*, 11 (4). pp. 551-562.

Van Loon, H., and J. C. Rogers. (1978). The seesaw in winter temperatures between Greenland and Northern Europe. Part I: General Description, *Monthly Weather Review*, 106(3). 296310.

Van Rooy, MP. (1965) A Rainfall anomaly index (RAI) independent of time and space. Notos 14:43–48.

Van Zeist, W. Bottema, S. (1991). Late Quaternary vegetation of the Near East. Wiesbaden: Dr. Ludwig Reichert Verlag.

Venegas, S. A., l. a. mysak, and d. n. straub. (1995). Atmosphere–Ocean Coupled Variability in the South Atlantic. *Journal of climate*, v.10.

Venema, V., Mestre, O., Aguilar, E., Auer, I., Ja, G., Domonkos, P., Vertacnik, G., Szentimrey, T., Štěpánek, P., Zahradnicek, P., Viarre, J., Müller-Westermeier, G., Lakatos, M., Cn, W., Menne, M., Lindau, R., Rasol, D., Rustemeier, E., Kolokythas, K., Marinova, T., Andresen, L., Acquaotta, F., Fratianni, S., Cheval, S., Klancar, M., Brunetti, M., Gruber, C., Prohom Duran, M., Likso, T., Esteban, P. and Brandsma, T. (2012). Benchmarking homogenization algorithms for monthly data. *Climate of the Past*, 8, 89–115.

Ventura F, Rossi P, Ardizzoni E. (2002). Temperature and precipitation trends in Bologna (Italy) from 1952 to 1999. *Atmos. Res.* 61: 203–214.

Vicente-Serrano SM, Beguería S, López-Moreno JI. (2010). A multi scalar drought index sensitive to global warming: the standardized precipitation evapotranspiration index. *J. Clim*. 23: 1696–1718.

Vieux, B.E. (2001). Distributed Hydrologic Modeling using GIS, Water Science and Technology Library. *Kluwer Academic Publishers*.

Villafuerte, M.Q., II, Matsumoto, J. and Kubota, H. (2015). Changes in extreme rainfall in the Philippines (1911–2010) linked to global mean temperature and ENSO . *Int. J. Climatol*., 35: 2033-2044.

Vincent LA, Peterson TC, Barros VR, Marino MB, Rusticucci M, Carrasco G, Ramirez E, Alves LM, Ambrizzi T, Berlato MA, Grimm AM, Marengo JA, Molion L, Moncunill DF, Rebello E, Anunciação YMT, Quintana J, Santos JL, Baez J, Coronel G, Garcia J, Trebejo I, Bidegain M, Haylock MR, Karoly D. (2005). Observed trends in indices of daily temperature extremes in South America 1960–2000. *Journal of Climate* 18: 5011–5023.

Viola F, Liuzzo L, Noto LV, Lo Conti F, La Loggia G (2013). Spatial distribution of temperature trends in Sicily. *Int. J. Climatol.*

Visbeck M.H., Hurrell J.W., Polvani L., Cullen H.M. (2001). The North Atlantic Oscillation: past, present, and future. *Proc. Natl. Acad. Sci*., U.S.A., 98, 23, 12876-12877.

Visbeck M, Chassignet EP, Curry RG, Delworth TL, Dickson RR, Krahmann K. 2003. The ocean's response to North Atlantic Oscillation variability. See Hurrell et al. 2003, pp. 113–46

Vogt JV, Barbosa P, Hofer B, Magni D, De Jager A, Singleton A, Horion S, Sepulcre G, Micale F, Sokolova E, Calcagni L, Marioni M, Antofie TE. (2011). Developing a European Drought Observatory for Monitoring, Assessing and Forecasting Droughts across the European Continent. In AGU Fall Meeting Abstracts 1, NH24A-07.

Von Neumann J. (1941). Distribution of the ratio of the mean square successive difference to the variance. *Annals of Mathematical Statistics* 13: 367–395.

Von Storch H. (1995). Misuses of statistical analysis in climate research, in Analysis of Climate Variability: Applications of Statistical Techniques, edited by H. von Storch, and A. Navarra, *Springer*, New York, pp. 11–26.

Von Storch, H. and F. W. Zwiers (1999). Statistical Analysis in Climate Research. *Cambridge University Press*, 494.

Von Storch, H., and A. Navarra, Eds., (1995). Analyses of Climate Variability—Applications of Statistical Techinques. *Springer*, 334 pp.

Von Storch, Hans (2008). In: Assessment of Climate Change for the Baltic Sea Basin. Regional Climate Studies. *Springer*, Berlin, Heidelberg.

Vörösmarty CJ, Green P, Salisbury J, Lammers, RB. (2000). Global water resources: vulnerability from climate change and population growth. *Science* 289: 284–288. *science*. 289.5477.284.

Wagesho, Negash, N.K. Goel & M.K. Jain (2013). Temporal and spatial variability of annual and seasonal rainfall over Ethiopia, *Hydrological Sciences Journal*, 58:2, 354-373.

Walker GT, Bliss EW. (1932). World weather V. *Mem. Roy. Meteor. Soc.* 4:53-84.

Walker GT. (1924). Correlations in seasonal variations of weather IX. Mem Ind Meteor Dept. 24:275-332.

Wallace, J. M., C. Smith, and S. Bretherton (1992). Singular value decomposition of winter time sea surface temperature and 500-mb heights anomalies. *J. Climate*,5, 561–576.

Wallace, J-M., C. Smith, Q. Jiang (1990). Spatial patterns of atmosphere ocean interactions in the northern winter. *J. Climate*, 3, 990–998.

Wallace, John M.; Gutzler, David S. (1981). Teleconnections in the Geopotential Height Field during the Northern Hemisphere Winter. *Monthly Weather Review*. 109 (4): 784.

Walther, GR., Post, E., Convey, P. (2002). Ecological responses to recent climate change. Nature 416, 389–395 (2002).

Wang GX, Bai W, Li Y, Hu HC (2011). Climate changes and its impact on tundra ecosystem in Qinghai-Tibet Plateau, China. *Clim. Chang.* 106:463–482.

Wang XL, Chen H, Wu Y, Feng Y, Pu Q. (2010). New techniques for the detection and adjustment of shifts in daily precipitation data series. *J. Appl. Meteorol. Climatol*. 49: 2416–2436.

Wang XL, Feng Y. (2013). RHtests_dlyPrcp User Manual. Climate Research Division, Atmospheric Science and Technology Directorate, Science and Technology Branch, *Environment Canada*, Toronto, Ontario, Canada, Retrieved February 25, 2014.

Wang, Hui & Ting, M. (2000). Covariabilities of Winter U.S. Precipitation and Pacific Sea Surface Temperatures. *Journal of Climate*. 13. 3711-3719.

Wang, Q-x., Fan, X-h., Qin, Z-d., Wang, M.-b. (2012). Change trends of temperature and precipitation in the Loess Plateau Region of China, 1961–2010. *Global and Planetary Change* 138–147.

Wang, S., Jiang, F. and Ding, Y. (2015). Spatial coherence of variations in seasonal extreme precipitation events over Northwest Arid Region, China. *Int. J. Climatol.*, 35: 4642-4654.

Wang, X. L. (2008). Accounting for autocorrelation in detecting mean shifts in climate data series using.

Wang, X. L., Q. H. Wen, and Y. H. Wu. (2007). Penalized maximal t test for detecting undocumented mean.

Wang, X.L. and Swail, V.R. (2001). Changes of extreme wave heights in Northern Hemisphere oceans and related atmospheric circulation regimes. *Journal of Climate*, 14, 2204–2220.

Wang, X.L., Feng, Y. (2010). RHtestsV3 User Manual. Published online at http://cccma. seos.uvic.ca/ETCCDMI/software.shtml (January 2010 (updated in June 2010).

Wanner, Heinz. Brönnimann, S., Casty, Carlo, Gyalistras, Dimitrios, Luterbacher, Jürg, Schmutz, Christoph, Stephenson, David, Xoplaki, Elena. (2001). North Atlantic Oscillation – Concepts And Studies. *Surveys in Geophysics*. 22. 321-381.

Westra S, Alexander LV, Zwiers FW. (2013). Global increasing trends in annual maximum daily precipitation. *J. Clim*. 26(11): 3904–3918.

Wijngaard JB, Klein Tank AMG, Können GP. (2003). Homogeneity of 20th century European daily temperature and precipitation series. *International Journal of Climatology* 23: 679–692.

Wilhite D, Buchannan-Smith M (2005). Drought as hazard: understanding the natural and social context. *Technology and Management Issues*, Taylor & Francis, London, p 399.

Wilhite DA. (2000). Drought as a natural hazard: concepts and definitions. In Drought: A Global Assessment, *Routledge*: New York, NY.

Wilks DS. (1995). Statistical Methods in the Atmospheric Sciences: An Introduction. *Academic Press:* San Diego.

WMO. (2012). Standardized Precipitation Index User Guide (M. Svoboda, M. Hayes and D. Wood). WMO-No.1090 , Geneva.

Woldeamlak, B., D. Conway. (2007). A note on the temporal and spatial variability of rainfall in the drought-prone Amhara region of Ethiopia. Int. J. Climatol., 27, pp. 1467-1477, 10.1002/joc.1481.

World Bank (2007). Making the most of scarcity. Accountability for better water management results in the Middle East and North Africa MENA Development Report.

World Bank (2013). Jordan Overview. Online document.

World Meteorological Organization - WMO (2013). The Global Climate 2001–2010. WMO – No 1119, Geneva, Switzerland.

World Meteorological Organization - WMO (2019). WMO Statement on the State of the Global Climate in 2019– No 1248, Geneva, Switzerland.

World Meteorological Organization -WMO (1966). Climatic Change, WMO Technical Note No. 79, WMO No. 195-TP-100, World Meteorological Organization, Geneva.

World Metrology Organization (WMO) (2012). Standardized Precipitation Index User Guide WMO-No. 1090 7 ISBN 978-92-63-11091-6.

Wu, C. and Huang, G. (2016). Projection of climate extremes in the Zhujiang River basin using a regional climate model. *Int. J. Climatol.*, 36: 1184-1196.

Wu, H.; Hayes, M.J. (2005). Wilhite, D.A.; Svoboda, M.D. The effect of the length of record on the standardized precipitation index calculation. *Int. J. Climatol*. 25, 505–520.

Xiong, Z.Y., Chen, R.T., Zhang, Y.F.: (2011). An effective method for initialization of clustering centers in K-means clustering. *Comput. Appl. Res*.

Xoplaki E, González-Rouco JF, Luterbacher J, Wanner H. (2004). Wet season Mediterranean precipitation variability: influence of large-scale dynamics and trends. Clim. Dyn. 23:63–78.

Xoplaki E, González-Rouco JF, Luterbacher J. (2003). Mediterranean summer air temperature variability and its connection to the large-scale atmospheric circulation and SSTs. *Climate Dynamics* 20: 723–739.

Xoplaki E. (2002). Climate variability over the Mediterranean. Ph.D., Thesis University of Bern 512 Switzerland.

Xu, Z. X., K. Takeuchi, and H. Ishidaira (2003). Monotonic trend and step changes in Japanese precipitation, *Journal of Hydrology*, vol. 279, no. 1–4, pp. 144–150.

Y. Avni, N. Porat, J. Plakht, G. Avni. (2006). Geomorphic changes leading to natural desertification versus anthropogenic land conservation in an arid environment, the Negev Highlands, *Israel Geomorphology*, 82 (3), pp. 177-200.

Yenigun, K, Ibrahim, WA. (2019). Investigation of drought in the northern Iraq region. *Meteorol. Appl*. 2019; 26: 490– 499.

Yilmaz, Abdullah Gokhan (2015). The effects of climate change on historical and future extreme rainfall in Antalya, Turkey, *Hydrological Sciences Journal*, 60:12, 2148-2162.

Yizhak Y, Hadas S, Pinhas A. (2009). Trends in Daily Rainfall Intensity Over Israel 1950/1-(2003)/4. *The Open Atmospheric Science Journal* 3: 196–203.

Yosef, Y., Aguilar E, Alpert P. (2019) Changes in extreme temperature and precipitation indices. Using an innovative daily homogenized database in Israel. *Int J Climatol*; 1–24.

Yosef, Y., Saaroni, H. and Alpert, P. (2009). Trends in daily rainfall intensity over Israel 1950/1-(2003)/4. *Open Atmospheric Science Journal*, 3, 196–203.

yosi tsvieli and abraham zangvil (2005). Synoptic climatological analysis of 'wet' and 'dry' red seatroughs over Israel. *International journal of climatology*. 25: 1997–2015.

Yozgatligil, C., Aslan, S., Iyigun, C. (2013). Comparison of missing value imputation methods in time series: the case of Turkish meteorological data. Theor Appl Climatol 112, 143–167.

Yue S, Pilon P, Cavadias G. (2002). Power of the Mann-Kendall andSpearman's Rho tests for detecting monotonic trends in hydrologicseries. *Journal of Hydrology* 259(1–4): 254– 271.

Zakhem BA, Kattaa B. (2016). Investigation of hydrological drought using cumulative standardized precipitation index (SPI 30) in the eastern Mediterranean region (Damascus, Syria). *J. Earth Syst. Sci*. 125(5):969–984.

Zamani, R., Mirabbasi, R., Nazeri, M., Meshram, S.G. and Ahmadi, F. (2018) Spatio-temporal analysis of daily, seasonal and annual precipitation concentration in Jharkhand state, India. Stochastic Environmental Research and Risk Assessment, 32(4), 1085–1097.

Zanchettin D, Franks S, Traverso P, Tomasino M. (2008). On ENSO impacts on European wintertime rainfalls and their modulation by the NAO and the Pacific multi-decadal variability described through the PDO index. *International Journal of Climatology* 28(8): 995–1006.

Zangvil A, Karas S, Sasson A. (2003). Connection between Eastern Mediterranean seasonal mean 500 hPa height and sea-level pressure patterns and the spatial rainfall distribution over Israel. Int. J. Climatol. 23:1567–1576.

Zeinali B and Safarian Zengir V. (2017) Drought monitoring in Urmia Lake Basin using fuzzy index; *J. Environ. Risks* 6(12) 37–62 (in Persian).

Zeng, W., Jiang Y., Huo Z., Hu K. (2020). Clustering Analysis of Extreme Temperature Based on K-means Algorithm. In: Sun X., Wang J., Bertino E. (eds) Artificial Intelligence and Security. ICAIS 2020. Lecture Notes in Computer Science, vol 12240. *Springer*, Cham.

Zhang X B, Feng Y, (2004). R ClimDex (1.0). User Manual. Climate research branch environment Canada Downs view, Ontario Canada.

Zhang X, Aguilar E, Sensoy S, Melkonyan H, Tagiyeva U, Ahmed N, Kutaladze N, Rahimzadeh F, Taghipour A, Hantosh TH, Albert P, Semawi M, Ali MK, Al-Shabibi MHS, Al-Oulan Z, Zatari T, Khelet IAD, Hamoud S, Sagir R, Demircan M, Eken M, Adiguzel M, Alexander L, Peterson TC, Wallis T. (2005). Trends in Middle East climate extreme indices from 1950 to (2003). *Journal of Geophysical Research-Atmospheres* 110.

Zhang X, Yang F. (2004). RClimDex (1.0) User Manual. Climate Research Branch Environment, Canada Downsview, Ontario.

Zhang, B., Muradov, K. & Dada, A. (2020). Principal component analysis-assisted selection of optimal denoising method for oil well transient data. *J. Petrol. Explor. Prod. Technol*.

Zhang, Q., Xu, C.-Y., Becker, S., Zhang, Z.X., Chen, Y.D. and Coulibaly, M. (2009), Trends and abrupt changes of precipitation maxima in the Pearl River basin, *China. Atmosph. Sci. Lett*., 10: 132-144.

Zhang, Q., Zhang, J., Guo, E. (2015). The impacts of long-term and year-to-year temperature change on corn yield in China. *Theor. Appl. Climatol.* 119, 77–82.

Zhang, X, Alexander L, Hegerl GC, Jones P, Tank AK, Peterson TC, Trewin B, Zwiers FW. (2011). Indices for monitoring changes in extremes based on daily temperature and precipitation data. *Climatic Change* 2: 851–870.

Zhang, X, Vincent LA, Hogg WD, Niitsoo A. (2000). Temperature and precipitation trends in Canada during the 20th century. *Atmosphere-Ocean* 38: 395–429.

Zhang, X. (2005). Trends in Middle East climate extreme indices from 1950 to 2003, J. Geophys. Res., 110, D22104.

Zhang, X., Vincent, L.A., Hogg, W.D. and Niitsoo, A. (2000). Temperature and precipitation trends in Canada during the 20th century. *Atmosphere-Ocean*, 38, 395–429.

Zheng, F., J. Li, R. T. Clark, and H. C. Nnamchi (2013). Simulation and projection of the Southern Hemisphere annular mode in CMIP5 models, *J. Clim.*, 26(24). 9860–9879.

Zhou, Y. Wu, Z. (2016). Possible impacts of mega-El Niño/Southern Oscillation and Atlantic Multidecadal Oscillation on Eurasian heatwave frequency variability. *Q. J. R. Meteorol. Soc.* 142, 1647–1661.

Ziv B, Dayan U, Kushnir Y, Roth C, Enzel Y. (2006). Regional and global atmospheric patterns governing rainfall in the southern Levant. *International Journal of Climatology* 26: 55–73.

Ziv B, Dayan U, Sharon D. (2005). A mid-winter, tropical extreme flood-producing storm in southern Israel: Synoptic scale analysis. *Meteorology and Atmospheric Physics* 88: 53–63.

Ziv B, Saaroni H, Baharad A, Yekutieli D, Alpert P. (2005). Indications for aggravation in summer heat conditions over the Mediterranean Basin. *Geophysical Research Letters* 32: L12706.

Ziv, B., Saaroni, H., Pargament, R. (2014). Trends in rainfall regime over Israel, 1975–2010, and their relationship to large-scale variability. *Reg. Environ Change* 14, 1751–1764.

Zohary, M. (1982). Vegetation of Israel and adjacent areas. *Wiesbaden*: Dr. Ludwig Reichert Verlag.

Zubiate, L., McDermott, F., Sweeney, C., and O'Malley, M. (2017). Spatial variability in winter NAO-wind speed relationships in western Europe linked to concomitant states of the East Atlantic and Scandinavian patterns. *Q. J. Roy. Meteorol. Soc.,* 143, 552–562.